The Use of Seismic Wave Velocities in the Measurement of Stiffness of a Residual Soil

Cristiana Maria da Fonseca Ferreira

Supervised by
Antonio Viana da Fonseca [FEUP]
Co-supervised by
David Nash [UoB] and Paul Greening [UCL]

A dissertation submitted to the Faculty of Engineering of the University of Porto
in accordance with the requirements of the degree of Doctor in Civil Engineering
Dissertação apresentada à Faculdade de Engenharia da Universidade do Porto
para a obtenção do Grau de Doutor em Engenharia Civil

DEC
Porto, 2008

To grandma Emilia

I am among those who think that science has great beauty.
A scientist in his laboratory is not only a technician:
he is also a child placed before natural phenomena which impress him like a fairy tale.

[Marie Curie]

Abstract

Measurement of seismic wave velocities is a practical, non-destructive, frequently non-invasive, cost-effective means of determining small-strain stiffness of soils. Given the particulate nature of soils, wave-based techniques present unique advantages to study geomaterials without affecting fabric or structural equilibrium and inherent mechanical properties.

In the laboratory, the most widely-used of the methods of determining V_S makes use of piezoelectric transducers. Bender elements, as well as other piezoceramic transducers, have opened a new window in laboratory testing, by enabling to perform standard mechanical, static or cyclic, tests simultaneously with seismic wave dynamic tests. These transducers enable transmitting and receiving shear and/or compression waves and can be installed virtually in any conventional soil testing device, most commonly in the oedometer or the triaxial chamber, but also in more complex systems such as calibration chambers, centrifuges, resonant columns and even cubical true triaxial apparatuses.

Seismic wave velocities in soils are influenced by a number of factors, such as the stress state, void ratio, structure, inherent anisotropy, among others, and it is important to be able to isolate each of these factors. The ability to measure wave velocities in different propagation and polarization directions in a general fully-controlled three-dimensional stress state is made possible in true triaxial apparatuses, where the influence of each of the different factors has been effectively investigated.

The main objective of this research work is the use and application of seismic wave velocities, in the field and mainly in the laboratory, for the measurement of reference soil parameters, such as the stiffness moduli, and indirectly for the definition of other relevant state parameters and dynamic and static properties. The applications of bender element results in geotechnical engineering and design are demonstrated, using natural intact and remoulded residual soil from Porto granite. Important issues such as the identification of destructuration and assessment of sampling quality; comparison of dynamically- and statically-determined stiffnesses; assessment of anisotropy; process monitoring: consolidation, saturation; evaluation of porosity, among others, are analysed in detail.

Resumo

A medição das velocidades das ondas sísmicas é um meio prático, não destrutivo, frequentemente não invasivo e económico, de determinação da rigidez dos solos a muito pequenas deformações. Dada a natureza particulada dos solos, as técnicas baseadas em ondas apresentam vantagens únicas no estudo dos materiais geotécnicos, sem que a fábrica ou o equilíbrio estrutural do solo e as suas propriedades mecânicas inerentes sejam afectadas.

No laboratório, o método mais correntemente usado para determinação das V_S recorre a transdutores piezoeléctricos. Os *bender elements*, assim como outros transdutores piezocerâmicos, vieram abrir novos horizontes às práticas laboratoriais, por facultarem a realização de ensaios mecânicos correntes, estáticos ou cíclicos, em simultâneo com os ensaios dinâmicos de ondas sísmicas. Estes transdutores permitem a transmissão e recepção das ondas de corte e/ou de compressão e podem ser instalados em praticamente todos os equipamentos de ensaios de solos convencionais, mais frequentemente em edómetros e em câmaras triaxiais, mas também em sistemas mais complexos, como em câmaras de calibração, centrifugadoras, colunas ressonantes e inclusivamente em sistemas triaxiais cúbicos verdadeiros.

As velocidades das ondas sísmicas em solos são influenciadas por um grande número de factores, nomeadamente o estado de tensão, índice de vazios, estrutura, anisotropia inerente, entre outros, sendo fundamental conseguir isolar o efeito de cada um destes factores. A capacidade de medição de ondas sísmicas em direcções de propagação e polarização diferentes, em quaisquer condições controladas de tensões tridimensionais genéricas, tornou-se possível com recurso a sistemas de ensaio triaxiais verdadeiros, onde a influência de cada um dos diferentes factores pode efectivamente ser investigada.

O principal objectivo deste trabalho de investigação é a utilização e aplicação das velocidades das ondas sísmicas, no campo e sobretudo no laboratório, para a medição de parâmetros de referência dos solos, nomeadamente os módulos de rigidez, e para a definição indirecta de outros parâmetros relevantes de estado do solo e propriedades estáticas e dinâmicas. As aplicações dos resultados de ensaios de *bender elements* na engenharia e no projecto geotécnicos são demonstradas, utilizando-se para tal amostras naturais intactas e remoldadas de solo residual do granito do Porto. A identificação da desestruturação e a avaliação da qualidade de amostragem, a comparação entre rigidezes determinadas dinâmica e estaticamente, a monitorização de processos, como os de consolidação e saturação, a avaliação da porosidade, são alguns dos importantes aspectos em análise detalhada.

Résumé

La mesure de la vitesse des ondes séismique en laboratoire est une méthode pratique, non destructive, fréquemment non invasive et économique pour la détermination de la rigidité des sols soumis à très petites déformations. Comme les sols sont constitués par particules, les techniques concernant les ondes présentent des avantages uniques pour l'étude des matériaux géotechniques vu que la fabrique ou l'équilibre structurel du sol bien que ses propriétés mécaniques ne sont pas affectées.

Dans le laboratoire, la méthode plus généralement utilisé pour la détermination de la vitesse des ondes S emploie des transducteurs piézoélectriques. Les *bender elements* et d'autres transducteurs piezocéramiques ont apportés des nouveaux horizons pour les pratiques de laboratoire car la réalisation des essais mécaniques courants, statiques et cycliques, peuvent être faits au même temps que les essais dynamiques des ondes séismiques. Ces transducteurs permettent la transmission et la réception des ondes de cisaillement et/ou de compression et ils peuvent êtres installés dans presque tous les équipements classiques d'essais de sols. Les plus utilisés sont les oedomètres et les chambres triaxiaux mais ils sont installés aussi dans des systèmes plus complexes comme les chambres de calibration, les centrifugeuses, les colonnes résonnantes et même dans les vrais systèmes triaxiaux cubiques.

La vitesse des ondes séismiques en sols est influencée par un grand nombre de facteurs notamment l'état de contrainte, l'indice des vides, la structure, l'anisotropie inhérente, etc. … donc, il est très important de séparer l'influence de chaque facteur. La capacité de mesure des ondes séismiques en directions de propagation et polarisation différentes, dans quelques conditions contrôlées de contraintes tridimensionnelles génériques, a été possible grâce à l'utilisation de systèmes de vrais essais triaxiaux, où l'influence de chaque facteur peut être effectivement investigué.

Le principal objectif de ce travail d'investigation est l'utilisation et l'application de la vitesse des ondes séismiques, in situ et surtout en laboratoire, pour la mesure des paramètres de référence en sols, notamment les modules de rigidité, et pour la définition indirect d'autres paramètres remarquables de l'état du sol et de ses propriétés statiques et dynamiques. Les applications des résultats d'essais de *bender elements* au génie civil et dans le projet géotechnique sont démontrées, en utilisant des échantillons naturels intacts et remoulés de sol résiduel du granite du Porto. Quelques aspects très importants analysés en détaille sont l'identification de la déstructuration et l'évaluation de la qualité d'échantillonnage, la comparaison entre les rigidités déterminées de façon dynamique et statique, la surveillance de processus comme la consolidation et la saturation et l'évaluation de la porosité.

Acknowledgements

This research work would not have been possible without the financial support of FCT (Portuguese Foundation for Science and Technology) in the form of the PhD grant SFRH/BD/11363/2002 and the grant from the research project POCI/55589/2006.

I would like to acknowledge the many people who, in so many ways, helped me to get to this point. I feel blessed for having so many people to thank for:

First to all, to Professor Antonio Viana da Fonseca, who exceeded being supervisor of this work and never seemed to stop believing in my capabilities, who always demonstrated the utmost confidence in my work, proving it so many times by delegating important tasks, from the organization of conferences and events, to the participation in workshops and meetings around the world - from Sao Paulo, to Perth, to Sydney, to Lyon, to London, to Osaka, to Rome, and soon to Atlanta - to discuss our research and promote our University and our country.

To Professor David Nash, who co-supervised this work and always made time for my enquiries about research and just about everything else; who first triggered my curiosity for geotechnical research and especially for seismic waves. Thank you for your friendship, hospitality, care and generosity at all times.

To Professor Paul Greening, also co-supervisor of this research, for suggesting challenges and making me feel like I could achieve whatever I aimed at; for your friendship and hospitality.

To Professor Martin Fahey, for being such a wonderful adviser, teacher, friend and positive person; and to his wife, Annie, for your generosity and hospitality, for making me feel at home on the other side of the world.

To all the staff of the Geotechnical Group of the Civil Engineering Department of FEUP, especially to Professor Matos Fernandes, for the support and friendship.

To Professor Jaime Santos, from IST, for the dedicated collaboration in research, for guidance and informal supervision.

To Professor Mostafa Ismail, from UWA, with whom I learnt a whole new and inventive approach to laboratory problems and who originally conceived the true triaxial apparatus applied in this research.

To Professor Martin Lings, from UoB, who kindly answered all my questions and provided so many important advice and suggestions.

To Professors Antonio Gomes Correia, Carlos Santamarina, David Muir Wood, Diego Lo Presti, Fernando Schnaid, Fumio Tatsuoka, Giovanni Cascante, Paul Mayne, Sebastiano Foti, Serge Leroueil, which whom I had the privilege of discussing my research interests.

And to Marcos Arroyo, Susie Gourvenec, Joao Rio, Tarek Sadek, Jiraroth Sukolrat [May] and Erdin Ibraim, for their friendship and companionship abroad.

Ao Senhor Armando Pinto, sempre surpreendente pela capacidade de resolução de problemas, experiência e sabedoria, acompanhados de generosidade e total disponibilidade;

A toda a equipa do LabGEO da FEUP: à Cláudia, pela amizade sincera, pela disponibilidade e pela competência profissional; à Sofia, pela ternura, curiosidade e pela ajuda generosa e preciosa na realização dos ensaios, sobretudo os triaxiais cúbicos; ao Carlos, pelo companheirismo, pela ajuda e pela disponibilidade; e ao Luís Miguel, pela ajuda prestada na fase inicial destes trabalhos.

A todos os meus amigos, amigas e colegas, que por serem tantos nem sempre são mencionados, mas sobretudo: Patrícia e Rui, Alexandra, Carla, Mafalda, Elisabete, Sara, Javier, Isabel, Fernando, Topa, Rodrigo, Raquel, André, …

Aos meus amigos e colegas do CSCP, em particular ao Pe. Amorim, pelo incentivo, pela amizade e por sentirem a minha falta.

E ainda:
A toda a minha família, sobretudo ao Nelo, à Gina e Jorge e ao Pedro; aos meus Padrinhos; à Laide e Nelo, à Diana e à Catarina; ao Carlos e Mónica e ao Gonçalo; à D. Rita e Sr. Joaquim; a todos muito obrigada pela compreensão, pelo incentivo e pela amizade sincera;

À Susana e Simon e ao Daniel, pela disponibilidade, hospitalidade e amizade sincera;

À Luísa e ao Paulo, pela cumplicidade e amizade, e ao Carlos Alexandre, por trazer a luz no seu sorriso e me inundar de felicidade;

À minha avó, a quem dedico este trabalho e de quem acredito ter herdado os genes da inteligência, da generosidade e da simpatia;

Aos meus pais, por me oferecerem tudo, todos os dias;

E ao Paulo, por sermos um só e assim me tornar uma pessoa melhor a cada dia.

A todos, a minha profunda gratidão.
Thank you all.

Table of Contents

1. Introduction 1

1.1. Background on the use of seismic wave velocities 1

1.2. Objectives 4

1.3. Thesis layout 5

2. Overview of Stiffness Measurements Using Static and Dynamic Methods 9

2.1. Introduction 9

2.2. Stiffness measurements in situ 13

2.2.1. Geophysical methods 13

2.2.1.1. Surface Reflection Method 14

2.2.1.2. Surface refraction method 14

2.2.1.3. Surface wave methods 15

2.2.1.4. Cross-hole method 16

2.2.1.5. Down-hole method 17

2.2.1.6. Seismic cone penetrometer testing (SCPT) 17

2.2.2. Other field methods 18

2.3. Stiffness measurements in the laboratory 19

2.3.1. Resonant-column testing 20

2.3.2. Piezoelectric transducers 20

2.3.3. Triaxial apparatuses 21

2.3.4. Calibration chambers 21

2.3.5. True triaxial apparatuses 23

3. Laboratory Prototypes and Equipment 27

3.1. Introduction 27

3.2. Piezoelectric transducers 28

3.2.1. Piezoelectricity 28

3.2.2. Types of transducers in use 28

3.2.3. Shear-plates 29

3.2.4. Compression transducers 30

3.2.5. Bender elements 31

3.2.6. Bender/extender elements 32

3.2.6.1. Manufacturing bender or bender/extender elements 34

3.2.7. Associated electronics equipment 35

3.2.8. Specific seismic wave measurement software 37

3.2.9. Performance and calibration checks 39

3.3. Standard triaxial testing apparatuses with bender elements and local strain instrumentation 42

3.3.1. ISMES-Enel.Hydro triaxial cell [TX70] 42

3.3.2. FEUP standard triaxial cell [TX100] 44

3.3.2.1. Equipment modifications 44

3.3.2.2. BE checks and installation 45

3.3.3. Bishop-Wesley stress-path cell [SP100] 46

3.4. Modified resonant-column [RC] 48

3.4.1. Equipment details 48

3.4.2. Installation of the BE 50

3.5. True triaxial apparatuses 51

3.5.1. FEUP true triaxial chamber [TT] 51

3.5.1.1. Installation and equipment details 51

3.5.1.2. GDS controllers 53

3.5.1.3. Volume change measurement 55

3.5.1.4. Displacement transducers 55

3.5.1.5. Control and data acquisition software 57
3.5.1.6. Data acquisition application and user interface details 58
3.5.1.7. Seismic wave measurements 61
3.5.2. UoB cubical cell [CC] 65
3.5.2.1. Installation and equipment details 65
3.5.2.2. Control and data acquisition 66
3.5.2.3. Displacement transducers [LVDT] 68
3.5.2.4. LVDT Calibration 70
3.5.2.5. Seismic wave measurements 78
3.6. Conclusions 83

4. Interpretation and Analysis of Bender Element Results 85

4.1. Introduction 85
4.2. BE-related phenomena 86
4.2.1. BE installation 87
4.2.2. Cross-talk 88
4.2.3. Environment noise 90
4.2.4. Near-field effects 90
4.2.5. Boundary conditions and sample geometry effects 94
4.2.6. Models for the BE test system 96
4.3. Monitoring the behaviour of BE 99
4.3.1. "Self-monitoring" bender elements 100
4.3.2. Accelerometer measurements 101
4.3.3. Laser-beam measurements 102
4.3.4. BE in direct contact 103
4.4. Interpretation techniques 104
4.4.1. Introduction 104
4.4.2. Effective travel length 105
4.4.3. Input signal configuration 107

4.4.3.1. Square signals 108
4.4.3.2. Sinusoidal signals 109
4.4.3.3. Random noise 110
4.4.4. Travel time determination 110
4.4.4.1. First direct arrival of the output wave 110
4.4.4.2. Time interval between characteristic points of the input and output waves 112
4.4.4.3. Second arrival of the output wave 113
4.4.4.4. Cross-correlation of input and output signals 115
4.4.4.5. Discrete method: □-point identification 116
4.4.4.6. Continuous method: sweep input signal 118
4.4.4.7. Discussion of current methods 121
4.5. Proposed BE interpretation framework 123
4.5.1. Description and methodology 123
4.5.2. Methodology 124
4.5.3. Application examples of the TD-FD framework 127
4.5.3.1. Experimental setup 127
4.5.3.2. Test results on residual soil from Porto granite 128
4.5.3.3. Test results on Toyoura sand 136
4.5.3.4. Comparison of the results of the two soils 139
4.6. Summary and conclusions 141

5. Characterization of the Residual Soil from Porto Granite..... 143

5.1. Residual soils 143
5.1.1. Introduction to the origin and formation of residual soils 143
5.1.2. Classification of residual soils 145
5.1.3. Residual soils from Porto granite 147
5.1.3.1. Typical profiles 147
5.1.3.2. Mineralogy 149
5.1.3.3. Geotechnical parameters 151

5.2. ES1: CICCOPN experimental site 153
5.2.1. Description 153
5.2.2. Geotechnical characterization 154
5.3. ES2: CEFEUP experimental site 160
5.3.1. Description 160
5.3.2. Geological setting and characterization 162
5.3.3. Geophysical characterization 167
5.3.4. Geomechanical characterization 171
5.3.4.1. Derived profile and results from in situ mechanical tests 171
5.3.4.2. Classification based on mechanical indices from in situ test results 175
5.3.4.3. General physical properties 180
5.3.4.4. Strength correlations 182
5.4. Summary and conclusions 185

6. Sampling and Laboratory Testing Programme 187

6.1. Introduction 187
6.2. Sampling programme 188
6.2.1. Introduction to sampling methods 188
6.2.2. Block sampling 189
6.2.3. Tube sampling 192
6.2.3.1. Overview 192
6.2.3.2. GMPV sampler 194
6.2.3.3. ST85 sampler 194
6.2.3.4. NT81 sampler 195
6.2.3.5. Mazier sampler 197
6.2.3.6. Osterberg sampler 198
6.2.3.7. Shelby sampler 199
6.2.4. Other sampling methods 200
6.3. Sample preparation 200

6.3.1. Natural samples 200
6.3.1.1. Standard triaxial and stress-path natural samples 201
6.3.1.2. Resonant-column natural samples 203
6.3.1.3. True triaxial natural samples 204
6.3.1.4. Cubical cell natural samples 206
6.3.2. Reconstituted specimens 210
6.3.2.1. Standard triaxial specimens 210
6.3.2.2. True triaxial specimens 211
6.4. Laboratory testing programme 213
6.4.1. Setup and testing procedures 213
6.4.2. ES1 testing programme 214
6.4.3. ES2 testing programme 216
6.5. Summary and conclusions 217

7. Laboratory Test Results 219

7.1. Introduction 219
7.1.1. Theoretical background on stiffness at very small strains 220
7.2. Very small strains 223
7.2.1. Introduction 223
7.2.2. Resonant-column and BE tests 223
7.2.2.1. BE interpretation process 225
7.2.2.2. RC measurements and calculations 231
7.2.2.3. Comparison of BE and RC results 232
7.2.2.4. The influence of the shear strain even at very small strains 236
7.2.3. Triaxial tests on reconstituted specimens of residual soil 243
7.2.3.1. Definition of references indices from reconstituted specimens 244
7.2.3.2. Definition of the void ratio function in isotropic conditions 245
7.2.3.3. Definition of the stress indices from reconstituted specimens 249
7.2.4. Triaxial tests on undisturbed samples of residual soil 251

7.2.4.1. Test results from ES1 251
7.2.4.2. Test results from ES2 257
7.2.4.3. Isotropic test on an undisturbed sample from ES2 260
7.2.4.4. Comparison between ES1 and ES2 undisturbed samples 263
7.2.5. True triaxial tests 265
7.2.5.1. Seismic wave measurements in the TT 265
7.2.5.2. TT tests on reconstituted residual soil specimens 272
7.2.5.3. TT tests on natural block samples of residual soil 283
7.2.6. Cubical cell true triaxial tests 292
7.2.6.1. Introduction 292
7.2.6.2. Seismic wave measurements 293
7.2.6.3. CC test results on natural undisturbed samples 293
7.2.6.4. Comparison of results for the three CC undisturbed samples 301
7.3. Small to large strains 303
7.3.1. Introduction 303
7.3.2. Resonant-column tests 303
7.3.3. Triaxial tests 307
7.3.3.1. Internal versus external strain measurements 307
7.3.3.2. Stress-strain response of undisturbed samples from ES1 308
7.3.3.3. Stiffness-strain response of undisturbed samples from ES1 310
7.3.3.4. Stress-strain response of undisturbed samples from ES2 314
7.3.4. True triaxial tests 317
7.3.4.1. Stress-strain-stiffness response of reconstituted samples 318
7.3.4.2. Stress-strain-stiffness response of undisturbed samples 330
7.3.4.3. Comparison between undisturbed and reconstituted samples 340
7.3.5. Cubical cell tests 343
7.4. Summary and conclusions 348

8. Discussion 351

8.1. Introduction 351

8.2. Developments in bender testing 352

8.2.1. BE testing methods and interpretation techniques 352

8.2.2. Comparison of RC and BE measurements 353

8.3. Comparison of stiffness measurements in the laboratory 356

8.3.1. Resonant-column and standard triaxial results 356

8.3.2. Standard triaxial and true triaxial results 358

8.3.3. True triaxial and cubical cell results 361

8.4. Assessment of sampling quality 363

8.4.1. Introduction 363

8.4.2. Fabric inspection 365

8.4.3. Measurement of initial mean effective stress 366

8.4.4. Measurement of strains during reconsolidation 367

8.4.5. Comparison between laboratory and in situ measurements of seismic wave velocities or maximum shear modulus 368

8.5. Other applications of seismic wave measurements 375

8.5.1. Assessment of structure 375

8.5.2. Assessment of anisotropy 379

8.5.3. Evaluation of porosity 382

8.6. Other correlations between laboratory and in situ tests 385

8.7. Key findings 389

9. Conclusions 391

9.1. Key findings revisited 391

9.2. Further work and limitations 393

List of Figures

Figure 1.1 -Most common field and laboratory methods for determining shear modulus (after Schneider et al., 1999) 2

Figure 2.1 - Non-linear characteristic stiffness-strain behaviour of soil (after Atkinson and Sallfors, 1991 and Mair, 1993) 12

Figure 2.2 - Field arrangements used in surface reflection testing: a) normal moveout; b) common offset; c) common depth point (Stokoe and Santamarina, 2000) 14

Figure 2.3 - Field arrangement in surface refraction testing (after Stokoe and Santamarina, 2000) 15

Figure 2.4 - Field arrangement used in SASW testing with common-receivers midpoint geometry (after Stokoe and Santamarina, 2000) 15

Figure 2.5 - SWM method: multistation acquisition scheme (Lopes et al., 2004) 16

Figure 2.6 - Field arrangements used to perform intrusive seismic tests: a) CH; b) DH; c) SCPT; d) suspension logging (after Stokoe and Santamarina, 2000) 18

Figure 2.7 - Schematic diagram of embedded geophones and electronics used in seismic measurements in a calibration chamber (Brignoli et al., 1997) 22

Figure 2.8 - Calibration chamber at the University of Western Australia (drawings after Ismail et al., 2004) 22

Figure 2.9 - Arrangement of platens in Cambridge true triaxial apparatus (Muir Wood, 1981). ... 24

Figure 2.10 - Flexible boundary true triaxial apparatus: a) isometric view of the frame; b) sections through face plate, cell and pressure bag (Sadek, 2006) 24

Figure 3.1 - Shear-plate schematic: a) connections, polarization and deformation (after Brignoli et al., 1996; b) design of a miniature SP (Ismail and Rammah, 2005); c) SP from UWA: the miniature transducer on the right is just 15 mm in diameter. 30

Figure 3.2 - Compression transducer: a) schematic of connections, polarization and deformation; b) movement under sinusoidal excitation 31

Figure 3.3 - Bender element: a) movement diagrams; b) Dyvik and Madshus (1985) model 32

Figure 3.4 - Typical BE wiring details and operation: a) transmitter; b) receiver (after Lings and Greening, 2001) 32

Figure 3.5 Typical EE wiring details and operation: a) transmitter; b) receiver (after Lings and Greening, 2001) 33

Figure 3.6 - BE and B/EE from UoB: a) standard size B/EE before coating; b) mould for epoxy coating; c) final single BE pair; d) miniature pair of B/EE during assembly 35

Figure 3.7 - BE or B/EE from UWA: a) mould for one transducer; b) wired pair of B/EE; c) potting the epoxy resin in the capsule probe; d) final T-shaped B/EE 35

Figure 3.8 - Screenshots of the programs used for seismic data acquisition in the time domain: a) WaveStar; b) OpenChoice Tektronix; c) PicoScope 38

Figure 3.9 - Data acquisition results using ABETS: a) setup; b) screenshot of the acquisition worksheet; c) program output 39

Figure 3.10 - Photographs of the ISMES triaxial system at LabGEO 42

Figure 3.11 - CT and BE in the ISMES-Enel.Hydro triaxial cell 43

Figure 3.12 - Schematic of seismic wave testing in the ISMES apparatus (after Brignoli et al., 1996) 43

Figure 3.13 - New and modified platens of the FEUP triaxial cell: a) top; b) bottom; c) pedestal 45

Figure 3.14 - Polarity check for the BE in FEUP triaxial cell (from Ferreira, 2003) 45

Figure 3.15 - BE and B/EE mounting scheme in FEUP triaxial platens 46

Figure 3.16 - BE electronics equipment in use for the FEUP triaxial cell (Ferreira, 2003) 46

Figure 3.17 - Stress-path triaxial system at LabGEO: a) overview; b) B/EE and porous stone details; c) lateral miniature BE and outlet holes for the cables 47

Figure 3.18 - Photographs of the complete stress-path system: a) stress-path control and acquisition; b) seismic wave measurement setup 48

Figure 3.19 - Resonant column device with bender elements: a) original porous stone; b), c) installation of B/EE; d) modified platens; e) overview of the testing apparatus 51

Figure 3.20 - FEUP true triaxial apparatus: a) overview; b) nomenclature for the platens 52

Figure 3.21 - Schematic of the FEUP true triaxial apparatus: schematic diagram and details of the location of the BE 53

Figure 3.22 - Diagram of a GDS standard pressure controller (GDS Instruments, 2001) 54

Figure 3.23 - Volume change measurements in the TT apparatus, using burettes 55

Figure 3.24 - Potentiometers for platen displacement measurement: a) diagram; b) PT1 during calibration; c) PT1 in use at the apparatus. 56

Figure 3.25 - Stability test on the displacement transducers at fixed positions 57

Figure 3.26 - Menu tabs of the LabView application: configuration of communications 59

Figure 3.27 - Menu tabs of the LabView application: a) order sequence input; b) data acquisition setup and plots of pressure and volume 60

Figure 3.28 - Menu tabs of the LabView application: real-time monitoring of pressures, volumes and displacements 61

Figure 3.29 - Arrangement of the B/EE in the apparatus: a) 3D view and notation for each transducer; b) direct [□] and inclined [□] wave measurements 62

Figure 3.30 - Seismic wave calibration of the TT filled with water: a) view of the test; b) example of results: TD signals for P-waves using B/EE HV from X1 to X2 64

Figure 3.31 - CC chamber: schematic diagram (after Sadek, 2006) and photograph of the frame . 66

Figure 3.32 - General layout of the instrumentation components of the CC testing system (adapted from Dihoru et al., 2005 and Sadek, 2006) 67

Figure 3.33 - Pressure panel: photographs and detailed diagram (adapted from Sadek, 2006) 67

Figure 3.34 - LVDTs: a) clear identification; b) modular unit and voltage limiter; c) inside the voltage limiter and connector boxes 68

Figure 3.35 - LVDTs: a) paper model; b) location of LVDTs in platens X2, Y2 and Z2; c) "unfolded" cube with the layout of all platens; d) colour code and numbering in each platen 69

Figure 3.36 - Fixing the LVDT magnets on the cushions 70

Figure 3.37 - LVDT calibrator in use 71

Figure 3.38 - LVDTs on X and Y platens: a) evidence of the misalignment of the rods due to gravity and the application of different tips for the LVDTs; b) platens positioned according to their arrangement in the frame 72

Figure 3.39 - LVDT calibration of the Z platens: a) Z1 (bottom platen); b) Z2 (top platen) 72

Figure 3.40 - Evolution of LVDT1 measurements with time, at a fixed position 74

Figure 3.41 - LVDT1 logging for 18h at a fixed position and zoomed view of 1st hour readings ... 75

Figure 3.42 - X1 platen LVDTs and temperature logged overnight: results of 3-hour readings 76

Figure 3.43 - Room temperature variation: air conditioning effect (ON versus OFF) 77

Figure 3.44 - Overcoming LVDT limitations: a) specific LabView calibration routine; b) installation of a rudimental yet efficient shade for the apparatus (aluminium foil sheet) 78

Figure 3.45 - 90 ° rotation of the apparatus: a) schematic diagram; b) photographs of the process 80

Figure 3.46 - Stages of the 90 ° rotation process: from vertical to horizontal positions 80

Figure 3.47 - Front view of the cell in the vertical and horizontal positions: a) schematic; b) photograph of the apparatus in the horizontal (90 ° rotated) position 81

Figure 3.48 - B/EE arrangement in the cubical cell: a) initial tests (direct measurements only); b) final tests (direct and inclined measurements) 82

Figure 3.49 - Installation of B/EE in the cubical cell 83

Figure 4.1 - BE measurements in different testing setups: a) no evidence of cross-talk; b) clear presence of cross-talk in the output signals 89

Figure 4.2 - Typical BE traces: a) experimental tests (Ferreira, 2003); b) numerical simulations for an unbounded specimen (Rio, 2006) 91

Figure 4.3 - Signal type and near-field effect in the time domain (Arroyo et al., 2003) 93

Figure 4.4 - Time history of received pulse signals for model A (100x50 mm) and model B (100x75 mm): a) non-absorbing models A and B, and absorbing model B; b) non-absorbing and absorbing model A and reflected signal (Rio, 2006) 96

Figure 4.5 - Dynamic systems for modelling BE testing: a) with internal subsystems (Blewett et al. (2000); b) without and with internal subsystems (Arroyo et al., 2006)..... 98

Figure 4.6 - Sequence of frequency response functions in a BE installation (Lee and Santamarina, 2005)..... 99

Figure 4.7 - Self-monitoring BE: schematic of strain-gauged BE and respective frequency response and phase (Greening and Nash, 2004) 100

Figure 4.8 - Monitoring BE behaviour with an accelerometer (Brocanelli and Rinaldi, 1998): a) dynamic model of the pedestal and transmitting element; b) frequency response to the BE sinusoidal signal excitation 101

Figure 4.9 - Monitoring the BE behaviour using a laser velocimeter: a) general setup; b) measurements with the BE embedded in a specimen (Rio, 2006) 102

Figure 4.10 - Schematic of monitoring BE in direct contact 103

Figure 4.11 - Definition of travel distance: a) direct arrival for a triaxial cylindrical specimen; b) direct and inclined waves for a true triaxial specimen [FEUP-TT]..... 107

Figure 4.12 - Definition of travel length for reflected wave arrival: example from the multiple reflections methods (after Lee and Santamarina, 2005) 107

Figure 4.13 - Example of time domain interpretation methods: first direct arrival 111

Figure 4.14 - Evidence of second shear wave arrival 114

Figure 4.15 - Cross-correlation results (Mohsin and Airey, 2003): a) input, output and cross-correlation signals; b) Gmax predicted from different peaks in the cross-correlation during isotropic compression 116

Figure 4.16 - Discrete □-points method: a) manual sweeping of input frequency; b) XY plots showing Lissajous figures in the oscilloscope; c) determination of travel time 118

Figure 4.17 - FD results for the residual soil (p' = 100 kPa): a) input and output signals in timescale; b) coherence; c) wrapped and d) unwrapped phase angle against frequency; e) summary of results..... 119

Figure 4.18 - Evidence of superimposed results using the □-points and sweep methods for different stress conditions (isotropic 50 kPa and 200 kPa) on Toyoura sand..... 122

Figure 4.19 - Example of TD results: use of various S-wave wave signals at different frequencies, complemented by P-wave measurements..... 125

Figure 4.20 - Data acquisition spreadsheet: ABETS 126

Figure 4.21 - Post-processing and analysis spreadsheet: abets-PLUS 126

Figure 4.22 - Variation of shear wave velocity with isotropic consolidation stress on Porto residual soil (test R2-isoCF1, w = 30%) 128

Figure 4.23 - TD results for input sine waves for the residual soil (p' = 100 kPa): a) at resonant frequency of 6.07 kHz; b) 2, 4, 6.07, 8, 12, 20 kHz and P-waves for 25 kHz input 129

Figure 4.24 - TD results for input sine waves for the residual soil (p' = 800 kPa): a) at resonant frequency of 18.1 kHz; b) 4, 6, 8, 10, 12, 18.1, 20 kHz and P-waves for 25 kHz input 130

Figure 4.25 - FD results for the residual soil (p' = 800 kPa): a) input and output signals in timescale; b) coherence; c) wrapped and d) unwrapped phase angle against frequency; e) summary of results 133

Figure 4.26 - FD analysis results for the residual soil (p' = 100 kPa): a) coherence for the initial window (100 Hz-20 kHz); b) travel time spectra 134

Figure 4.27 - FD analysis results for the residual soil (p' = 800 kPa): a) coherence for the initial window (100 Hz-20 kHz); b) travel time spectra 135

Figure 4.28 - Variation of shear wave velocity with isotropic consolidation stress on Toyoura sand 136

Figure 4.29 - TD results for input sine waves of 2, 4, 6 kHz on Toyoura sand: a) at 100 kPa; b) at 400 kPa. [Note: S-wave outputs in reversed polarity] 137

Figure 4.30 - FD results for Toyoura sand (p' = 100 kPa): a) coherence; b) unwrapped phase angle against frequency; Toyoura sand (p' = 400 kPa): c) coherence; d) unwrapped phase angle against frequency; e) summary of results 138

Figure 4.31 - FD analysis results for Toyoura sand (p' = 100 kPa): a) coherence; b) travel time spectra 139

Figure 5.1 - Schematic diagram of a typical residual soil profile (after Little, 1969) 145

Figure 5.2 - Excavation works around Porto, on residual soils 148

Figure 5.3 - Microscope photographs of the clay fraction of a residual soil from Porto (Begonha, 1989) 149

Figure 5.4 - Microstructure characterisation by degree of decomposition (Viana da Fonseca, 2003, after Collins, 1985) 150

Figure 5.5 - Location of ES1 at CICCOPN in the geological chart of Portugal, Sheet 9-C (adapted from Vieira de Sousa, 2002, after Costa and Teixeira, 1957) 154

Figure 5.6 - ES1: a) location of the in situ tests (Vieira de Sousa, 2002); b) schematic profile (Ferreira, 2003) 155

Figure 5.7 - ES1: a) overview; b) layout of the boreholes 155

Figure 5.8 - Grain-size distribution curve of ES1 soil specimens, framed with the typical grain-size fuse for Porto residual soil 156

Figure 5.9 - In situ testing at ES1: a) plate load tests (Vieira de Sousa, 2002); b) cross-hole and down-hole tests (Ferreira, 2003) 157

Figure 5.10 - ES1 in situ test results: VS [CH], N60 [SPT], qc [CPT], qd [DPL], Epm and pl* [PMT] (Viana da Fonseca et al., 2003) 157

Figure 5.11 - Relative positioning of the plate load tests and schematic of the stress bulbs in serviceability conditions and classical failure wedges (Vieira de Sousa, 2002) 159

Figure 5.12 - Pressure-settlement curve of the PLT: a) direct; and, b) normalized representation (adapted from Viana da Fonseca et al., 2003) 159

Figure 5.13 - Simplified geological maps of the Porto area and of the CEFEUP experimental site (Viana da Fonseca et al., 2006, adapted from Pereira, 1992) 161

Figure 5.14 - General layout of the ES2 experimental site 162

Figure 5.15 - Textural aspect of the formation of silimanite from biotite (Viana da Fonseca et al., 2006) 163

Figure 5.16 - a) Granular hypautomorphic texture in the granite; b) K feldspar with poekilitic inclusions (Viana da Fonseca et al., 2006) 164

Figure 5.17 - Grain size analysis 165

Figure 5.18 - Electronic microscope photographs of two samples of CEFEUP soil: a) and b) block sample B4; c) and d) disturbed tube sample S1 166

Figure 5.19 - Refraction testing at ES2 and resulting S-wave travel time plots 167

Figure 5.20 - Refraction tomography P-wave model (Carvalho et al., 2004) 168

Figure 5.21 - Refraction tomography SH velocity model overlaid by geophysical results (Carvalho et al., 2004) and geological model used for seismic reflection interpretation (Almeida et al., 2004) 169

Figure 5.22 - Electric resistivity image (Carvalho et al., 2004) 169

Figure 5.23 - Processed radargram with interpreted events overlaying the resistivity and CH model and N-SPT values in boreholes S3 and S1 (Carvalho et al., 2004) 169

Figure 5.24 - Integration of the interpreted partial models: a) interval velocity model; b) stacked seismic reflection section (Viana da Fonseca et al., 2006) 170

Figure 5.25 - Geotechnical profile and photos of the samples obtained in boreholes (S3 - Figure 5.14) 172

Figure 5.26 - In-situ tests profile: a) CPTU: qc, fs; b) PMT: pf, pLM, EM; c) DMT: Ed, Kd, Id173

Figure 5.27 - Shear modulus and Poisson's ratio from CH sections and DH in borehole S3 174

Figure 5.28 - Soil behaviour classification chart (after Robertson, 1990) 175

Figure 5.29 - Soil behaviour classification chart (after Eslami & Fellenius, 1997) 176

Figure 5.30 - Soil behaviour classification profiles (Costa, 2005), based on the proposals of Robertson (1990) and Eslami & Fellenius (1997) 176

Figure 5.31 - Profile identification from distinct tests based classifications 177

Figure 5.32 - Relationship between Go and qc for residual soils (after Schnaid et al., 2004) 178

Figure 5.33 - Correlation between G0 and N60 for residual soils (after Schnaid et al., 2004) 180

Figure 5.34 - Grain size distribution curves from ES2, compared with Porto silty sand 181

Figure 5.35 - Soil index properties in depth from a number of samples 181

Figure 5.36 - Relation between qc values, in situ at rest effective stress, σ'v0, and the angle of shearing resistance, □' (adapted from Robertson and Campanella, 1983) 182

Figure 5.37 - Ranges of qc/N versus D50 on Brazilian residual soils, compared with the experimental site results (based on Danziger et al., 1998) 183

Figure 6.1 - Stages in tube sampling and soil specimen preparation for laboratory testing (after Hight, 2000) 189

Figure 6.2 - Illustrative diagrams of the block sampling stages (after JGS, 1995) and photographs of the work at experimental site ES1 (after Ferreira, 2003) 190

Figure 6.3 - Photographs of the block sampling work at experimental site ES2 at different depths: a) B1 and B2 at 1.65 m; b) B3 and B4 at 2.75 m; c) B5 and B6 at 4.25 m .. 191

Figure 6.4 - ES1 at CICCOPN: a) view of the experimental site during sampling; b) layout of the boreholes 193

Figure 6.5 - GMPV thick-walled sampler: a) photographs of the sampling process; b) schematic diagram 194

Figure 6.6 - Soil sampling with the ST85 sampler 195

Figure 6.7 - NT 81 sampler: a) schematic diagram; b) photographs of the steel liner and of the sampler during sampling stage in ES1 at CICCOPN 196

Figure 6.8 - Photographs of tube sampling works in ES2 at CEFEUP using NT 81 sampler: sampling, immediate extraction of the liner and cling film wrapping 196

Figure 6.9 - Schematic details and principle of operation of the Mazier sampler (GCO, 1987); photographs of the sampling process with this sampler in ES1 197

Figure 6.10 - Osterberg composite hydraulic fixed piston sampler (Osterberg, 1973, in Clayton et al, 1995). 198

Figure 6.11 - Shelby thin-walled open-drive sampler: a) schematic; b) photographs of the sampler and the insulating lids 199

Figure 6.12 - CEFEUP site: continuous borehole sampling 200

Figure 6.13 - Preparation of undisturbed tube samples: a) cutting the PVC liner into eight parts using a rotary disc; b) removing the liner by vertically sliding each part 202

Figure 6.14 - Example of a coarse-grained natural sample, evidencing problematic preparation . 202

Figure 6.15 - Trimming cylindrical 70 and 100 mm diameter samples for standard triaxial testing from block samples B3 and B5. 203

Figure 6.16 - Preparation of a resonant-column test: a) saturation of the porous stones; b) preparation of the filter paper disc with the slots for the column blades; c) installation 204

Figure 6.17 - Sequence of preparation of a block sample [B2] in the true triaxial apparatus 205
Figure 6.18 - Preparation of an undisturbed sample (B6-RS2) for the cubical cell..... 207
Figure 6.19 - Preparation of the cubical cell membrane for tests with BE 208
Figure 6.20 - Installation of an undisturbed natural sample in the cubical cell 209
Figure 6.21 - Stages of preparation of remoulded specimens: a) spooning a weighed amount of soil corresponding to one layer; b) light static compaction by layers; c) detail of the layer marks in the piston; d) remoulded specimen in the mould; e) ready for installation in the triaxial cell 210
Figure 6.22 - Preparation of a wet reconstituted sample in the true triaxial apparatus 212
Figure 6.23 - Preparation of a dry reconstituted sample in the true triaxial apparatus 212

Figure 7.1 - Differences between reference void-ratio functions against void ratio 222
Figure 7.2 - RC+BE sample S1.2.4: TD results at 50 kPa..... 226
Figure 7.3 - RC+BE sample S1.2.4: FD results at 50 kPa, ABETS automatic results 227
Figure 7.4 - RC+BE sample S1.2.4: FD results at 50 kPa, input and output in a timescale 228
Figure 7.5 - RC+BE sample S1.2.4: FD results at 50 kPa, complete frequency range 229
Figure 7.6 - RC+BE sample S1.2.4: FD results at 50 kPa, travel time spectra..... 229
Figure 7.7 - RC+BE sample S1.2.4: FD results at 50 kPa, travel time spectra for R2¿0.98 230
Figure 7.8 - RC+BE sample S1.2.4: evolution of G0 with mean effective stress 233
Figure 7.9 - Variation of G0 with p' for all samples, from BE measurements in TD and FD 234
Figure 7.10 - Variation of G0 with p' for all samples, from RC and BE measurements..... 234
Figure 7.11 - G0 values derived from the RC versus from the two BE methods 235
Figure 7.12 - RC+BE sample S1.2.4: evolution of the G0 ratios with RC shear strain..... 237
Figure 7.13 - Comparison between RC-CT (hollow symbols) and RC-RN (solid symbols) (after Santos et al., 2007) 238
Figure 7.14 - RC+BE sample B5-1-RC: evolution of G0 with mean effective stress 239
Figure 7.15 - RC+BE sample B5-1-RC: evolution of the G0 ratios with RC shear strain 239
Figure 7.16 - Variation of the G0 ratios with RC shear strain for all RC+BE tested samples 241
Figure 7.17 - Schematic of the stress path for the definition of the void ratio function 244
Figure 7.18 - Isotropic test on sample R2-isoCF1: a) start and b) end of the test 245
Figure 7.19 - R2-isoCF1 test results: shear moduli obtained by BE-TD and BE-FD against a) mean effective stress; b) void ratio..... 246
Figure 7.20 - R2-isoCF1 test results: shear moduli from BE-TD and BE-FD against mean effective stress and normalised to different void ratio functions..... 247
Figure 7.21 - Shear moduli from BE-FD and BE-TD against void ratio, with trends taken at the same isotropic stresses..... 248

Figure 7.22 - Comparison between absolute and normalised G0 to the defined void ratio function against isotropic stress 249

Figure 7.23 - Comparison between R2-isoCF1 (from ES2) and B2.0.70 (from ES1) of the normalised G0 against p' 250

Figure 7.24 - Generic stress-path of undisturbed samples in standard triaxial tests 252

Figure 7.25 - Examples of the application of the π-points method in test S1.2.1: a) load stage 5 (σ'v = 46.5 kPa, σ'h = 22.5 kPa) ; b) load stage 22 (σ'v = 119.2 kPa, σ'h = 22.5 kPa) 254

Figure 7.26 - Examples of the FD (using π-points method) and TD results for three different undisturbed samples from ES1: S1.2.1, S3.2.2 and S6.2.2 (all from a depth of 2 m) .. 255

Figure 7.27 - ES1 undisturbed samples results, normalised G0 against: a) mean effective stress, b) vertical and horizontal stresses 256

Figure 7.28 - ES2 undisturbed samples results, normalised G0 against: a) mean effective stress, b) vertical and horizontal stresses 259

Figure 7.29 - B5-isoSP: schematic of the isotropic stress-path 260

Figure 7.30 - B5-isoSP: isotropic consolidation test on an undisturbed sample, normalised G0 against mean effective stress (or isotropic stress) 261

Figure 7.31 - B5-isoSP: FD travel time spectra at different stages (#11 and #14) for the same isotropic stress of 400 kPa 262

Figure 7.32 - ES1 and ES2 undisturbed samples: normalised G0 against mean effective stress ... 263

Figure 7.33 - Schematics of a B/EE pair in one of the true triaxial platen 266

Figure 7.34 - Direct and inclined seismic wave measurements using BE transmitters in platens: a) X1; b) Y1; c) Z1 266

Figure 7.35 - Time domain results for sample R4D-TT, on X1ch1 direction, at stage #02 [σ'x=6 kPa, σ'y=7 kPa and σ'z=25 kPa] 270

Figure 7.36 - Frequency domain for sample R4D-TT, on X1ch1 direction, at stage #02 [σ'x=6 kPa, σ'y=7 kPa and σ'z=25 kPa]: a) coherence; b) travel time spectra for R2¿0.98 . 271

Figure 7.37 - Example of a datasheet for TT travel time records (in μs) 272

Figure 7.38 - R2W-TT: Schematic of the stress stages 274

Figure 7.39 - R2W-TT: G0 results for direct and inclined measurements from: a) TD; b) FD 274

Figure 7.40 - R2W-TT: global normalised G0 results from TD and FD measurements 275

Figure 7.41 - R8D-TT: Schematic of the stress stages 276

Figure 7.42 - R8D-TT: G0 results from direct FD measurements 277

Figure 7.43 - R8D-TT: G0 against void ratio, from direct FD measurements 277

Figure 7.44 - R8D-TT: G0 results from direct FD measurements 278

Figure 7.45 - R8D-TT: G0* results in relation to the wave polarisation direction in normally consolidated conditions, from direct FD measurements 279

Figure 7.46 - R4D-TT: Schematic of the stress stages 280

Figure 7.47 - R4D-TT: normalised G0* against: a) stress corresponding to the wave propagation direction, b) mean effective stress 282

Figure 7.48 - Block sample B3: impossibility of trimming a true triaxial specimen due to a large discontinuity across the sample 283

Figure 7.49 - B2-TT: schematic of the isotropic stress-path 284

Figure 7.50 - B2-TT: G0 results against isotropic stresses 285

Figure 7.51 - B5-TT: stress-path followed, partially with zero horizontal deformation 286

Figure 7.52 - B5-TT: normalised G0* against: a) corresponding stresses, b) stresses in the wave propagation and polarisation directions, c) mean effective stress 287

Figure 7.53 - B5-TT: normalised G0* against: a) stresses in the wave propagation and polarisation directions and b) mean effective stress 289

Figure 7.54 - B4-TT: preparation of the sample for testing 291

Figure 7.55 - B4-TT: BE measurement the Xhh direction at stage #4 (σ'x= σ'h=30 kPa; σ'z=65 kPa) for an input frequency of 4 kHz 291

Figure 7.56 - B6-RS1: schematic of the stress-path 294

Figure 7.57 - B6-RS1: normalised G0 against: a) corresponding stresses, b) stresses in the wave propagation and polarisation directions, c) mean effective stress 295

Figure 7.58 - B6-RS2: schematic of the stress-path 296

Figure 7.59 - B6-RS2: normalised G0 against: a) corresponding stresses, b) stresses in the wave propagation and polarisation directions, c) mean effective stress 297

Figure 7.60 - B4-RS3: photographs of the trimming process and the evidence of a central discontinuity in the specimen (a hand-drawn sketch indicates the position pf this discontinuity in relation to the platens of the cubical cell) 299

Figure 7.61 - B4-RS1: schematic of the stress-path 299

Figure 7.62 - B4-RS3: normalised G0 against: a) corresponding stresses, b) mean effective stress, c) stresses in the wave propagation and polarisation directions 300

Figure 7.63 - Normalised G0 against corresponding stresses for the 3 CC samples 302

Figure 7.64 - Resonant-column test results on ES2 samples: stiffness versus shear strain, for different confining stresses 303

Figure 7.65 - Resonant-column test results on ES2 samples: normalized stiffness and damping ratio versus shear strain, for different confining stresses 304

Figure 7.66 - Resonant column results: normalized stiffness and damping ratio versus normalised shear strain 305

Figure 7.67 - RC+BE samples: reference shear strain, as a function of mean effective stress 306

Figure 7.68 - ES2 test S2-3-TX: example of internal and external strain measurements, a) full test data; b) measurements below 100 kPa and 0.7% 308

Figure 7.69 - ES1 undisturbed samples: summary of stress-paths 308

Figure 7.70 - ES1 undisturbed samples: summary of the stress-strain curves, a) deviatoric stress against internal axial strain; b) normalised deviatoric stress against internal axial strain 309

Figure 7.71 - ES1 undisturbed samples: volumetric against internal axial strains 310

Figure 7.72 - ES1 undisturbed samples: summary of the stiffness-strain curves, including the estimate of E0 from BE measurements 311

Figure 7.73 - ES1 undisturbed samples: Young's modulus degradation curves plotted as Es/Es0 versus (q/qmax) 313

Figure 7.74 - ES1 undisturbed samples: normalised Young's modulus versus normalised strain .. 314

Figure 7.75 - ES2 undisturbed samples: summary of the stress-paths 315

Figure 7.76 - ES2 undisturbed samples: summary of the stress-strain curves, a) deviatoric stress and b) normalised deviatoric stress, against internal axial strain 316

Figure 7.77 - ES2 undisturbed samples: Young's modulus degradation curves plotted as Es/Es0 versus (q/qmax) 317

Figure 7.78 - R2W-TT: stress-strain curves: a) complete data and consolidation curves per stress direction; b) 3D plot of axial strains 319

Figure 7.79 - R2W-TT: stiffness moduli against mean effective stress during isotropic consolidation: a) secant Young's modulus, Es; b) zoom on secant Young's modulus to observe variations at high stresses; c) maximum shear modulus, G0BE. 320

Figure 7.80 - R2W-TT: Young's moduli against axial strain: a) Es from X, Y and Z axial strain measurements; b) E0 from BE measurements 322

Figure 7.81 - R8D-TT stress-strain results: a) conventional plot; b) 3D view of axial strains 323

Figure 7.82 - R8D-TT: stiffness moduli against mean effective stress during isotropic consolidation: a) secant Young's modulus, Es; b) zoom on secant Young's modulus to observe variations at high stresses; c) maximum shear modulus, G0BE. 325

Figure 7.83 - R8D-TT: Young's moduli against axial strain: a) Es0; b) E0 from BE and Es0 326

Figure 7.84 - R4D-TT: stress-strain results (test under K0 conditions, so strains are only visible in the Z direction) 327

Figure 7.85 - R4D-TT: secant Young's moduli against a) stresses; b) axial strains 328

Figure 7.86 - Secant Young's moduli against strain for the 3 reconstituted samples 329

Figure 7.87 - Compressibility curves for reconstituted samples in true triaxial conditions 329

Figure 7.88 - B2-TT: stress-strain curves: a) conventional plot; b) 3D view of axial strains 331

Figure 7.89 - B2-TT: secant Young's moduli against a) isotropic stress; b) axial strains 332

Figure 7.90 - B2-TT: anisotropy ratios for the two X and Y horizontal directions in relation to the Z vertical direction 333

Figure 7.91 - B5-TT: stress-strain curves: a) complete results; b) strains in the X and Y directions; c) strains in the Z direction 334

Figure 7.92 - B5-TT: distortional stress and volumetric strain against distortional strain 335

Figure 7.93 - B5-TT: secant Young's moduli against mean effective stress 336

Figure 7.94 - B4-TT: stress-strain curves, a) complete set of data; b) zoom-in for horizontal stresses; c) vertical stress 337

Figure 7.95 - B4-TT: distortional stress and volumetric strain against distortional strain 338

Figure 7.96 - B4-TT: secant Young's moduli against a) mean effective stress; b) axial strains ... 339

Figure 7.97 - Compressibility curves of the undisturbed and reconstituted samples 340

Figure 7.98 - Secant Young's moduli obtained from isotropic consolidation: comparison between undisturbed B2 and reconstituted R2W samples 341

Figure 7.99 - Secant Young's moduli from anisotropic K0 consolidation, comparison between undisturbed B5 and reconstituted R4D samples: a) X and Y horizontal direction; b) Z vertical direction 342

Figure 7.100 - B6-RS1: stress-strain curves 343

Figure 7.101 - B6-RS1: secant Young's moduli against axial strains 344

Figure 7.102 - B6-RS2: stress-strain curves 344

Figure 7.103 - B6-RS2: secant Young's moduli against axial strains 345

Figure 7.104 - B4-RS3: stress-strain curves 345

Figure 7.105 - B4-RS3: secant Young's moduli against axial strains 346

Figure 7.106 - Distortional stress and volumetric strain against distortional strain for all tested CC specimens 346

Figure 7.107 - B6-RS2: end of the test 347

Figure 8.1 - Variation of the ratios of G0 measured by BE methods with those determined by RC methods: a) FD; b) TD 354

Figure 8.2 - Maximum shear moduli measured by RC-CT, RC-RN, BE-TD and BE-FD as a function of the shear strain of measurement 355

Figure 8.3 - Normalised G0 of three specimens from block B5, tested in the resonant-column and the standard triaxial apparatuses 357

Figure 8.4 - Comparison between reconstituted samples in isotropic conditions in the standard triaxial and the true triaxial: a) G0 against stress; b) G0* against stress 359

Figure 8.5 - Comparison of G0* against stress between undisturbed samples in different stress conditions in the standard triaxial and the true triaxial 360

Figure 8.6 - Comparison of G0* in X and Y directions against stresses, from undisturbed samples in different stress conditions in the true triaxial and the cubical cell apparatuses 361

Figure 8.7 - Comparison of G0* in the Z direction against stresses, from undisturbed samples in different stress conditions in the true triaxial and the cubical cell apparatuses 362

Figure 8.8 - Definition of the geometric parameters of a tube sampler 364

Figure 8.9 - Fabric inspection: a) disturbance on a laminated clay sample with sand and silt layers spaced every 10 mm (Morecombe Bay), Rowe (1972); b) clearly disturbed residual soil sample collected from CEFEUP experimental site (ES2) 365

Figure 8.10 - Stress-path during tube sampling and specimen preparation of centreline element of low OCR clay (Ladd and Lambe, 1963, Baligh et al., 1987, in Ladd and DeGroot, 2003) 366

Figure 8.11 - Measurement of G0 from shear wave velocities in: a) laboratory tests; b) in situ tests (Atkinson, 2000) 369

Figure 8.12 - Normalized shear wave velocities for ES1 specimens 370

Figure 8.13 - Normalized shear wave velocities for ES2 specimens 371

Figure 8.14 - Normalized shear wave velocities for all tested specimens 372

Figure 8.15 - Proposed classification of sampling quality based on the comparison of normalised shear wave velocities in the field and in the laboratory 373

Figure 8.16 - Shear wave velocities for ES2 block samples tested in true triaxial conditions 375

Figure 8.17 - Structural framework for a natural clay (Nash et al., 2006) 377

Figure 8.18 - Assessment of structure, from the normalised G0 as a function of the effective stresses for undisturbed and reconstituted specimens 378

Figure 8.19 - Comparison of estimated and measured porosity 385

List of Tables

Table 2.1 - General applicability of selected non-invasive geophysical methods to typical site assessments and monitoring objectives (Stokoe and Santamarina, 2000, after NRC, 2000) 13

Table 3.1 - Bender element testing: associated electronics equipment used 36

Table 4.1 - Estimated signal loss at each interface and in each material (Pennington, 1999) 97

Table 4.2 - Input wave shape suggested by different authors 108

Table 4.3 - Time interval between characteristic points of the input and output signals 113

Table 4.4 - Time interval between characteristic points of the first and second arrival of the shear wave in the output signal 114

Table 5.1 - Typical values of uniaxial compression strength for different weathering classes (Viana da Fonseca, 2003) 151

Table 5.2 - Common natural physical parameters (Viana da Fonseca, 2003) 151

Table 5.3 - Typical values of permeability by classes of weathering of Porto granite (Viana da Fonseca and Coutinho, 2008) 152

Table 5.4 - Geotechnical characterisation results (after Vieira de Sousa, 2002) 154

Table 5.5 - Secant, Es, and unload-reload, Eur, Young's moduli (MPa) from PLT tests at different stress levels (Viana da Fonseca et al., 2003) 160

Table 5.6 - The mineralogical semi-quantitative results obtained by DRX (Viana da Fonseca et al., 2006) 165

Table 5.7 -Estimated values of qc/NSPT for different residual soils 184

Table 5.8 - Strength parameters from in situ and laboratory tests 185

Table 6.1 - Tube sampler used in each borehole 193

Table 6.2 - List of the main laboratory tests on ES1 natural samples 215

Table 6.3 - List of the main laboratory tests on ES1 reconstituted specimens 215
Table 6.4 - List of the main laboratory tests on CEFEUP natural samples 216
Table 6.5 - List of the main laboratory tests on CEFEUP reconstituted specimens 217

Table 7.1 - Reference void ratio functions (from Ferreira, 2003) 222
Table 7.2 - Testing conditions and physical characteristics of ES1 specimens in the RC..... 224
Table 7.3 - Testing conditions and physical characteristics of ES2 specimens in the RC..... 224
Table 7.4 - Test results on RC+BE sample S1.2.4: BE and RC small strain parameters 232
Table 7.5 - Test results on RC+BE sample S1.2.4: ratios of G0 obtained by the 3 methods..... 237
Table 7.6 - Maximum amplitudes of oscillation for two different BE, in air and embedded in a sample for pulse and sweep signal excitation (adapted from Rio, 2006)..... 242
Table 7.7 - Reconstituted specimens used for definition of reference indices 243
Table 7.8 - Linear regressions 247
Table 7.9 - Values of the references stress dependency indices determined from tests on reconstituted specimens..... 251
Table 7.10 - Physical properties and testing conditions of undisturbed ES1 specimens 252
Table 7.11 - Physical properties and testing conditions of undisturbed ES2 specimens 258
Table 7.12 - B5-isoSP: correlation parameters for the different stress-dependency approaches.... 260
Table 7.13 - Combination of possible seismic wave measurements in the TT apparatus 265
Table 7.14 - Equations for the determination of the travel lengths of the 14 different wave measurements in the true triaxial apparatus 267
Table 7.15 - Results of the calibration test with the chamber filled with water 268
Table 7.16 - Summary of physical properties of the reconstituted specimens tested in the TT ... 273
Table 7.17 - R2W-TT: regression parameters per wave direction, from TD and FD 275
Table 7.18 - R8D-TT: correlation parameters for each wave direction..... 279
Table 7.19 - R4D-TT: correlation parameters for three stress-dependency approaches..... 281
Table 7.20 - Physical properties of the natural block samples tested in the TT..... 284
Table 7.21 - B5-TT: regression parameters for the stress-dependency approaches..... 288
Table 7.22 - Summary of physical properties of the undisturbed specimens tested in the CC 293
Table 7.23 - B6-RS1: correlation parameters for two stress-dependency approaches..... 294
Table 7.24 - B6-RS2: correlation parameters for the three stress-dependency approaches 298
Table 7.25 - B4-RS3: correlation parameters for the three stress-dependency approaches 301
Table 7.26 - RC+BE samples: summary of stiffness degradation results..... 306

Table 8.1 - Criteria for the assessment of sampling quality from volumetric strains (from Lunne et al., 1997) 367

Table 8.2 - Example of the application of the method of Lunne et al. (1997) for assessing sample quality, from the initial and reconsolidation void ratios from ES1 samples ... 368

Table 8.3 - Differences between VS* measured in situ and in the laboratory 372

Table 8.4 - Proposed classification of sampling quality and sample condition based on the comparison of normalised shear wave velocities in the field and in the laboratory 373

Table 8.5 - Parameters of the shear stiffness dependency with stress (σ'v.σ'h) 378

Table 8.6 - Anisotropy ratios for reconstituted specimens 381

Table 8.7 - Anisotropy ratios for undisturbed specimens 382

Table 8.8 - Stiffness (Young's) moduli E deduced in triaxial tests on undisturbed samples 387

Table 8.9 - Ratios between Young's moduli from in situ tests 388

Table 8.10 - Average ratios between Young's modulus and in situ tests 388

Table 8.11 - Ratios between Young's moduli determined in triaxial tests and in situ CH tests... 388

1.

Introduction

1.1. Background on the use of seismic wave velocities

In the past couple of decades, it has been recognized that the so-called 'elastic' stress-strain response of practically all soils and soft rocks is in fact highly non-linear. This has led to the development of methods of foundation analysis and settlement/deformation prediction that take this into account, such that stiffness non-linearity is now routinely incorporated into many standard computer codes. These achievements have been paralleled by developments in both in situ and laboratory testing methods that allow the details of the stress-strain response to be examined, even at strains as low as 10^{-6}.

Measurement of seismic wave velocities is a practical, non-destructive, frequently non-invasive, cost-effective means of determining small-strain stiffness of soils. Given the particulate nature of soils, wave techniques present unique advantages to study geomaterials without affecting fabric or structural equilibrium and inherent mechanical properties (Fam and Santamarina, 1995). New demands in civil engineering require advanced characterization techniques to assess in-situ conditions

and to monitor processes. Challenges include aging infrastructure, construction in critical/sensitive zones, restrictions created by the urban environment, trenchless construction, installation of new infrastructures, environmental demands and protection. Near-surface geophysical methods can play a critical role in satisfying these needs (Stokoe and Santamarina, 2000).

The use of geophysical in situ tests to compliment conventional drilling, sampling, and laboratory testing has become an expedient and cost-effective way to determine strength and stiffness parameters over an entire site. Although correlations can be used to estimate the in-situ shear modulus of the soil (e.g. Mayne and Rix, 1993), a direct measurement of the soil property is desirable. Field measurements of shear wave velocity include crosshole tests (CHT), downhole tests (DHT), suspension logging, seismic reflection, seismic refraction, and spectral analysis of surface waves (SASW). A representation of these test procedures is shown in Figure 1.1.

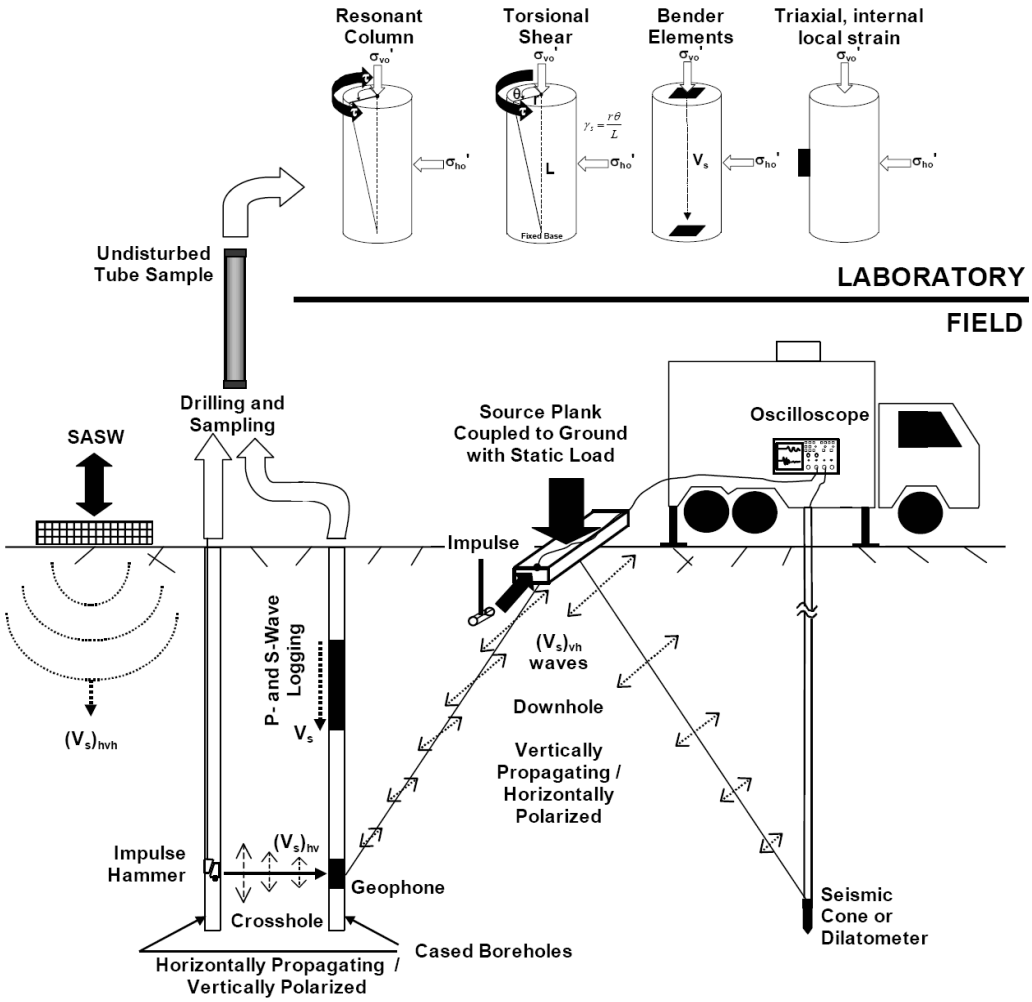


Figure 1.1 -Most common field and laboratory methods for determining shear modulus (after Schneider et al., 1999)

Most wave-based geophysical methods are used to measure propagation velocities. Attenuation-based measurements are infrequently used because of difficulties in analyzing these measurements as noted earlier in the discussion on material damping. Yet, attenuation-based measurements have the potential to be very valuable, especially in combination with wave velocity measurements.

Field testing methods can be classified as active or passive. Active-type methods are generally employed, whereby a wave is radiated into the medium from a source that is energized as part of the test. Passive-type methods are used less frequently. However, a passive system can be selected when the background noise can be used as the excitation or illumination source. Field testing methods can also be classified as non-intrusive if all instrumentation is mounted on the surface, or intrusive when boreholes or penetrometers are used. The most common stress-wave based methods in field use today are reviewed in the following chapter.

One of the advantages of these seismic wave-based tests is that the same tests that are performed in the field can be performed in the laboratory as well. Both intact and reconstituted specimens are used in the laboratory, with the choice often controlled by the ability to obtain high-quality samples. Laboratory tests provide the opportunity to conduct parametric studies which can greatly enhance the analysis of field data (Stokoe and Santamarina, 2000).

In the laboratory, the most widely-used of the methods of determining V_S makes use of piezoelectric transducers, such as bender elements (BE), shear plates and also bender-extender elements. Bender elements, as well as other piezoceramic transducers, have opened a new window in laboratory testing, by enabling to perform standard mechanical, static or cyclic, tests simultaneously with seismic wave dynamic tests. These transducers enable transmitting and receiving shear and/or compression waves and can be installed virtually in any conventional soil testing device, most commonly in the oedometer or the triaxial chamber, but also in more complex systems such as calibration chambers, centrifuges, resonant columns and even cubical true triaxial apparatuses.

Seismic wave velocities in soils are influenced by a number of factors, such as the stress state, void ratio, structure, inherent anisotropy, among others, and it is important to be able to isolate each of these factors. The ability to measure wave velocities in different propagation and polarization directions in a general fully-

controlled three-dimensional stress state is made possible in true triaxial apparatuses, where the influence of each of the different factors can be investigated.

1.2. Objectives

The main objective of this research work is the use and application of seismic wave velocities, measured in the field and in the laboratory, for the measurement of reference soil parameters, mainly the stiffness moduli, and its contribution to the definition of other relevant soil characteristics, namely dynamic and static properties, soil state and conditions. It is commonly recognized that important factors such as the stress state, void ratio, structure, inherent anisotropy, among others, influence the seismic wave velocity response in soils. The ability to measure wave velocities in different propagation and polarization directions in a general fully-controlled three-dimensional stress state is made possible in true triaxial apparatuses, where the influence of each of the different factors can be investigated and established.

Although both in situ and laboratory testing methods are used and thoroughly applied, the focus of the research work is the use of piezoelectric transducers for seismic wave measurement, installed in a multitude of apparatuses for laboratory soil characterization. Some novelty adaptations in the testing devices, as well as new designs for testing prototypes have been conceived, to overcome some limitations of more conventional devices, providing the necessary tools for the purposes of the research programme.

The University of Porto has dedicated many years of research to the geomechanical characterization of the residual soil from Porto granite. The complexity of its behaviour has led to its recognition as an unusual geomaterial, thus requiring specific and more detailed investigation. As a sequence to previous works, this study also aims at providing further insight to the behaviour of this natural and regionally dominant material.

1.3. Thesis layout

The work presented in this thesis has been divided in nine chapters. Following this chapter, Chapter 2 presents a general overview of the static and dynamic methods currently used for stiffness measurements, both in situ and in the laboratory. Emphasis is given to the use of the wave-based measurements, from which the elastic stiffness moduli are derived.

Chapter 3 describes the many apparatuses employed during the course of this research. The common denominator of virtually all tests is the use of seismic waves, transmitted and received by piezoelectric transducers, as a means to measure stiffness moduli. The characteristics and particularities of the piezoelectric transducers systematically present in the experimental programme are introduced, as well as the associated electronics equipment required for testing. Different types of these transducers have been installed in various testing apparatus for complementary and comparative purposes, namely in standard triaxial, stress-path cells, resonant-column and also in true triaxial cubical apparatuses. For the installation of the piezoelectric transducers, it was often necessary to conceive and implement some adaptations in the testing devices, as well as to devise and develop new designs for testing prototypes, which could overcome some limitations of more conventional devices. Given the novelty of some modifications and the new designs of other testing equipments, its characteristics, functioning, calibration and testing procedures are presented in some detail.

Chapter 4 focuses on the issues involved in the interpretation of bender element results. Bender-element related phenomena are discussed, namely the conditions of installation of the transducers, interferences such as cross-talk and noise, dispersion due to near-field effects and to wave reflections at the boundaries. Important technical requirements are suggested as means to minimize errors. Methods for monitoring the bender element behaviour are presented and commented, which have been providing evidence of a more complex 3D response of the transducers to the induced excitations. The most common methods for the interpretation of BE tests are introduced and debated. A practical framework for BE testing, based on the comparison of different interpretation techniques is proposed, in order to obtain the most reliable value for the travel time. This new procedure consists on the application of a methodical, systematic, and objective approach for the interpretation of the results, in the time and frequency domains. The use of an automated tool enables unbiased information to be obtained regarding variations in the results to assist in the decision of the travel time.

Chapter 5 deals with the general characterization of the residual soils and focuses in the two experimental sites on residual soil from Porto granite used for the research. A residual soil is a soil-like material derived from the in-situ weathering and decomposition of rock which has not been transported from its original location. The peculiarities of these naturally bonded soils are examined. The characteristics of residual soils can be quite distinctively different from those of transported soils and the specific features of residual soils do not adequately fit in the conventional soil classification methods. The identification and characterisation of residual soils demands for other criteria apart from those conventionally integrated in classical Soil Mechanics classifications. Comparisons are established between the characterization results of the two experimental sites of this research and previous works on residual soils from Porto.

Chapter 6 introduces the sampling programme, from the sampling methods used for the collection of undisturbed soil samples, to the sample preparation techniques prior to testing. The experimental objectives and testing programmes for the soil samples retrieved from the two experimental sites are detailed. Due to the specificity of the laboratory tests carried out, namely the cubical cell and true triaxial tests, the procedures for sample preparation of cylindrical and cubical specimens are described, for both natural and remoulded conditions.

Chapter 7 presents the main results obtained from the testing programme. Given the influence of the strain level in the stiffness response of the soil, the presentation of results is divided in stiffness measurements at very small strains and at small to large strains.

Chapter 8 discusses and analyses the obtained results, comparing and combining test methods both in situ and in the laboratory. The information provided by the seismic wave measurements serves multiple applications, namely the assessment of sampling quality, assessment of structure and anisotropy, evaluation of porosity, among others. A new classification of sampling quality is proposed for these materials, based on the comparison between in situ and laboratory shear wave velocities. The comparison between biaxial standard triaxial and true triaxial conditions is established in terms of the stiffness response in the three orthogonal directions at very small strains and at small and large strains. By combining data from different tests and using appropriate normalised parameters, the effects of stress state, void ratio, structure, inherent anisotropy, among others, are effectively isolated, providing interesting insight in the behaviour of this natural soil.

Chapter 9 summarizes the conclusions gathered throughout the research work and discussed in the previous chapters. The limitations and obstacles encountered in this research are also revealed, which suggest room for further improvements and developments.

2.

Overview of Stiffness Measurements Using Static and Dynamic Methods

2.1. Introduction

In this chapter, an overview of the most common in situ and laboratory methods for the measurement of stiffness at different strain levels will be presented, with emphasis to wave-based techniques.

First, it is important to distinct different stiffness parameters, depending on the stress and strain relationships. In terms of elasticity theory, the general three-dimensional form of Hooke's law of elasticity relates strains and stresses through a compliance matrix $[C]$ comprising 36 coefficients C_{ij} in the form:

$$\begin{bmatrix} \varepsilon_{xx} \\ \varepsilon_{yy} \\ \varepsilon_{zz} \\ \gamma_{yz} \\ \gamma_{zx} \\ \gamma_{xy} \end{bmatrix} = \begin{bmatrix} C_{11} & C_{12} & C_{13} & C_{14} & C_{15} & C_{16} \\ C_{21} & C_{22} & C_{23} & C_{24} & C_{25} & C_{26} \\ C_{31} & C_{32} & C_{33} & C_{34} & C_{35} & C_{36} \\ C_{41} & C_{42} & C_{43} & C_{44} & C_{45} & C_{46} \\ C_{51} & C_{52} & C_{53} & C_{54} & C_{55} & C_{56} \\ C_{61} & C_{62} & C_{63} & C_{64} & C_{65} & C_{66} \end{bmatrix} \begin{bmatrix} \sigma_{xx} \\ \sigma_{yy} \\ \sigma_{zz} \\ \tau_{yz} \\ \tau_{zx} \\ \tau_{xy} \end{bmatrix} \qquad [2.1]$$

Anisotropy describes the directional dependency of elasticity. Love (1927) concluded that the compliance matrices for anisotropic elastic materials must be symmetrical. Hence the number of independent coefficients reduces from 36 to 21 since $C_{ij} = C_{ji}$. Moreover, most natural materials show some form of symmetrical behaviour, thus the number of coefficients can be reduced even more. Crampin (1981) presented the six most common anisotropic symmetry systems, including: isotropic (2 independent elastic constants); cubic (3 independent elastic constants); hexagonal (5 independent elastic constants); trigonal (6 independent elastic constants); tetragonal (6 or 7 independent elastic constants); orthorhombic (9 independent elastic constants) and monoclinic (13 independent elastic constants).

In geotechnical engineering, it is common to consider soil properties in terms of vertical and horizontal directions. When the soil properties in any horizontal direction are considered identical, the soil is transversely isotropic, or cross-anisotropic, thus referring to a hexagonal anisotropy state (e.g. Crampin, 1981; Graham and Houlsby, 1983; Sadek, 2006). The soil element can then be fully described by means of five independent elastic constants. The relationship between strain and effective stress increments for a cross-anisotropic material can be expressed in the form:

$$\begin{bmatrix} \Delta\varepsilon_{xx} \\ \Delta\varepsilon_{yy} \\ \Delta\varepsilon_{zz} \\ \Delta\gamma_{yz} \\ \Delta\gamma_{zx} \\ \Delta\gamma_{xy} \end{bmatrix} = \begin{bmatrix} \frac{1}{E'_h} & -\frac{\nu'_{hh}}{E'_h} & -\frac{\nu'_{vh}}{E'_v} & . & . & . \\ -\frac{\nu'_{hh}}{E'_h} & \frac{1}{E'_h} & -\frac{\nu'_{vh}}{E'_v} & . & . & . \\ -\frac{\nu'_{hv}}{E'_h} & -\frac{\nu'_{hv}}{E'_h} & \frac{1}{E'_v} & . & . & . \\ . & . & . & \frac{1}{G'_{hv}} & . & . \\ . & . & . & . & \frac{1}{G'_{hv}} & . \\ . & . & . & . & . & \frac{1}{G'_{hh}} \end{bmatrix} \begin{bmatrix} \Delta\sigma'_{xx} \\ \Delta\sigma'_{yy} \\ \Delta\sigma'_{zz} \\ \Delta\tau_{yz} \\ \Delta\tau_{zx} \\ \Delta\tau_{xy} \end{bmatrix} \qquad [2.2]$$

where E'_v = Young's modulus in the vertical direction;
E'_h = Young's modulus in the horizontal direction
ν'_{vh} = Poisson's ratio for horizontal strain due to vertical strain
ν'_{hv} = Poisson's ratio for vertical strain due to horizontal strain
ν'_{hh} = Poisson's ratio for horizontal strain due to horizontal strain at right angle
G'_{hv} = Shear modulus in the vertical plane
G'_{hh} = Shear modulus in the horizontal plane

These seven parameters, defined in this matrix, correspond to only five independent elastic constants, since:

$$G'_{hh} = \frac{E'_h}{2(1+\nu'_{hh})} \qquad [2.3]$$

and

$$\frac{\nu'_{hv}}{E'_h} = \frac{\nu'_{vh}}{E'_v} \qquad [2.4]$$

Other formulations of these equations have been presented, especially to provide more conventional expressions from which these parameters can be derived, namely by Graham and Houlsby (1983), Muir Wood (1990), Lings et al. (2000), Lings (2001).

In the past couple of decades, it has been recognized that the so-called 'elastic' stress-strain response of practically all soils and soft rocks is in fact highly non-linear. This has led to the development of methods of foundation analysis and settlement/deformation prediction that take this into account, such that stiffness non-linearity is now routinely incorporated into many standard computer codes. These achievements have been paralleled by developments in both in situ and laboratory testing methods that allow the details of the stress-strain response to be examined, even at strains as low as 10^{-6}.

Figure 2.1 illustrates a typical stiffness-strain curve for soil and includes typical ranges of strain for laboratory testing and for structures. At small strains the stiffness is relatively large; at strains close to failure the stiffness is small: this is soil being non-linear (Atkinson, 2000). The ranges of strain for the different testing techniques in the figure are similar to those given by Atkinson and Sallfors (1991), while the typical strain ranges for structures are those given by Mair (1993). A typical

characteristic strain in the ground is 0.1%; this represents a movement of 10 mm across a gauge length of 10 m (Atkinson, 2000).

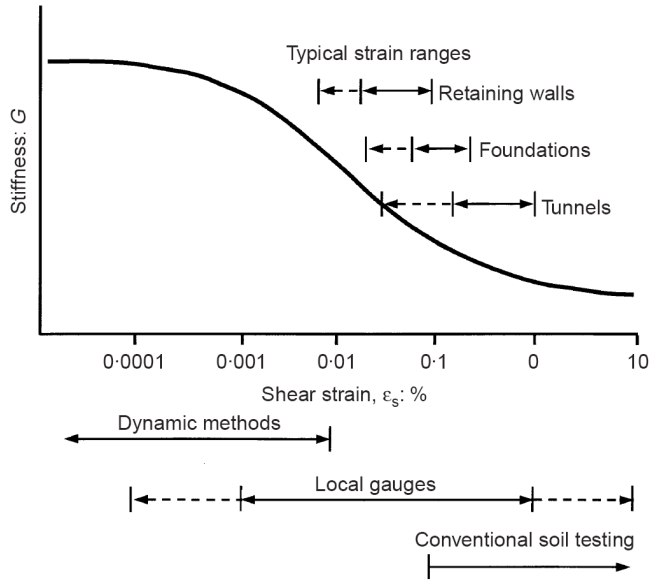


Figure 2.1 - Non-linear characteristic stiffness-strain behaviour of soil (after Atkinson and Sallfors, 1991 and Mair, 1993)

Measurement of seismic wave velocities is a practical, non-destructive, frequently non-invasive, cost-effective means of determining small-strain stiffness of soils. Given the particulate nature of soils, wave techniques present unique advantages to study geomaterials without affecting fabric or structural equilibrium and inherent mechanical properties (Fam and Santamarina, 1995). New demands in civil engineering require advanced characterization techniques to assess in-situ conditions and to monitor processes. Challenges include aging infrastructure, construction in critical/sensitive zones, restrictions created by the urban environment, trenchless construction, installation of new infrastructures, environmental demands and protection. Near-surface geophysical methods can play a critical role in satisfying these needs (Stokoe and Santamarina, 2000).

In what follows, the most significant and common methods for stiffness measurement in situ and in the laboratory will be briefly introduced. The information in the following sections was compiled from reference works in the literature, namely from Lo Presti (1995), Stokoe and Santamarina (2000), Lo Presti et al. (2001), Santamarina et al. (2001), Muir Wood (2004), among others.

2.2. Stiffness measurements in situ

2.2.1. Geophysical methods

As pointed out by Stokoe and Santamarina (2000), most wave-based geophysical methods are used to measure propagation velocities. Field testing methods can be classified as active or passive. Active-type methods are generally employed, whereby a wave is radiated into the medium from a source that is energized as part of the test. Passive-type methods are used less frequently. However, a passive system can be selected when the background noise can be used as the excitation or illumination source. Field testing methods can also be classified as non-intrusive if all instrumentation is mounted on the surface or intrusive when boreholes or penetrometers are used. The most common stress-wave based methods in field use today are briefly reviewed below. Their applicability to typical site characterisation objectives is summarised in Table 2.1

Table 2.1 - General applicability of selected non-invasive geophysical methods to typical site assessments and monitoring objectives (Stokoe and Santamarina, 2000, after NRC, 2000)

Example Objectives	Seismic Refraction	Seismic Reflection	Ground-Penetrating Radar	Electrical Resistivity	Electromagnetics	Induced Polarization	Microgravity	Airborne Sensing	Magnetics
Geologic mapping	❶	❶	❶	❶	❶	②	②	②	②
Hydrogeology characteristics	❶	②	❶	❶	❶	③	②	③	na
Water table depth	❶	②	②	❶	❶	③	na	②	na
Top of bedrock	❶	❶	③	❶	❶	③	②	③	na
Cavity detection	②	②	❶	❶	❶	③	❶	③	③
Disposal trench mapping	③	②	❶	❶	❶	na	②	②	②
Nature of trench fill	③	na	❶	❶	❶	?	❶	na	❶
Inorganic contaminant plume	na	na	❶	❶	❶	❶	na	②	na
Organic contaminant plume	na	na	②	?	?	?	na	②	na
Disposal container (metal drum)	na	na	❶	②	❶	③	③	na	❶
Underground storage tanks	③	③	❶	②	❶	③	②	na	❶
UXO detection	na	na	❶	❶	❶	na	na	③	❶

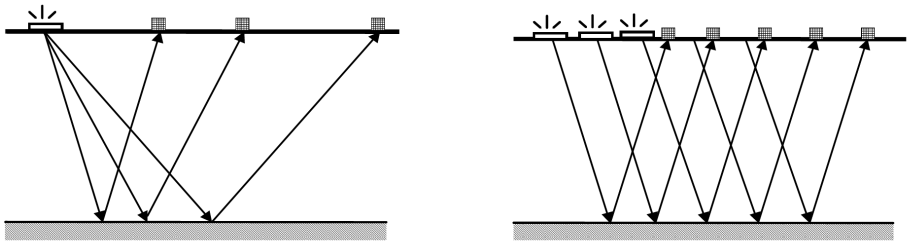
KEY: ❶ = primary applicability; ② = secondary supporting applicability; ③ = limited applicability; na = no general applicability or not widely used; and ? = area of active research and rapidly evolving technology or questionable application.

(Note: UXO stands for unexploded ordinance)

Non-intrusive methods eliminate the time and cost of drilling are eliminated, avoid the potential environmental consequences of drilling and permit effectively covering large areas. Obviously, the optimum approach is the combination of different testing methods so that the strengths and weaknesses of each method are counter-balanced.

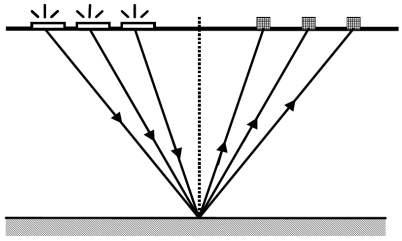
2.2.1.1. Surface reflection method

One of the oldest and most common seismic methods is the surface reflection method. This method appears in various geophysics textbooks (e.g., Dobrin and Savit, 1988; and Burger, 1992). The main principle of the seismic reflection method is illustrated in Figure 2.2. Both the active source and receivers are placed on the ground surface. Typically, compression wave measurements are performed using either mechanical sources that are vertically oriented or explosive sources. Waves reflected from interfaces at depth are monitored with vertically-sensitive geophones.



a. Normal moveout (NMO)

b. Common offset



c. Common depth point (CDP)

Figure 2.2 - Field arrangements used in surface reflection testing: a) normal moveout; b) common offset; c) common depth point (Stokoe and Santamarina, 2000)

2.2.1.2. Surface refraction method

The surface refraction method is an established geophysical method for non-intrusively identifying soil stiffnesses and layer interfaces at depth. The method is based on the ability to detect the arrival of wave energy that is critically refracted from a higher velocity layer which underlies a lower velocity sediment. Seismic signals are generated with an active source, and wave arrivals are detected on the surface with an array of receivers as shown in Figure 2.3. Similarly to the surface

reflection method, compression wave measurements are typically performed using vertical mechanical sources or explosives. The arrivals of refracted waves on the ground surface are monitored with vertically-sensitive geophones. Seismic refraction testing is appropriate to detect boundaries and dipping layers at shallow depths.

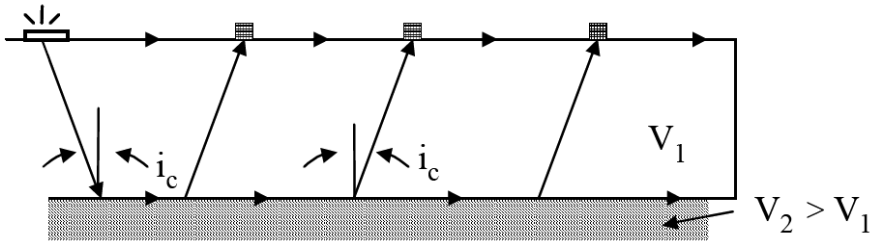


Figure 2.3 - Field arrangement in surface refraction testing (after Stokoe and Santamarina, 2000)

2.2.1.3. Surface wave methods

The use of surface waves in geotechnical engineering applications was introduced with the SASW (spectral analysis of surface waves) method (Nazarian and Stokoe, 1984). Surface wave testing can involve Rayleigh and Love waves, and testing has been conducted on land and offshore (Stokoe et al., 1994b; Stoll et al., 1994; Tokimatsu, 1995; and Luke and Stokoe, 1998). The SASW test method involves actively exciting Rayleigh wave energy at one point and measuring the resulting vertical surface motions at various distances (receiver points) away from the source. A typical field testing arrangement is shown in Figure 2.4 for one set of source-receiver spacings. Measurements are performed at multiple source-receiver spacings along a linear array placed on the ground surface.

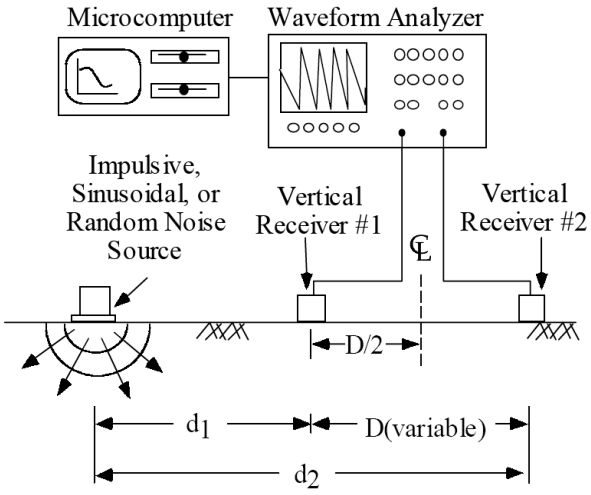


Figure 2.4 - Field arrangement used in SASW testing with common-receivers midpoint geometry (after Stokoe and Santamarina, 2000)

The basis of the SASW method is the dispersive characteristics of Rayleigh waves when propagating in a (horizontally) layered system. The phase velocity V_R depends primarily on the material properties, namely shear wave velocity, mass density, and Poisson's ratio or compression wave velocity, over a depth of approximately one wavelength. As a result of the varying shear stiffnesses of the layers, waves with different wavelengths travel at different phase velocities. A surface wave dispersion curve is the variation of V_R with λ or f. The dispersion curve is interpreted to determine the shear wave velocity profile with depth. The simplest interpretation is based on the fact that longer wavelengths sample deeper portions of the near surface. Formal mathematical inversion has already being implemented in practice (Nazarian, et al. 1994; Joh, 1996; Gangi, et al., 1998; Rix, et al., 2000).

Recently, an acquisition scheme with multiple receivers, usually 24 or more, has been introduced which has a faster field procedure and more accurate results due to the higher spectral integrity of the acquired data (Gabriels et al., 1987; Park et al., 1999; Foti, 2000; Strobbia, 2003; Lopes et al., 2004). This is usually known as the Surface Wave Method (SWM), which is schematically illustrated in Figure 2.5.

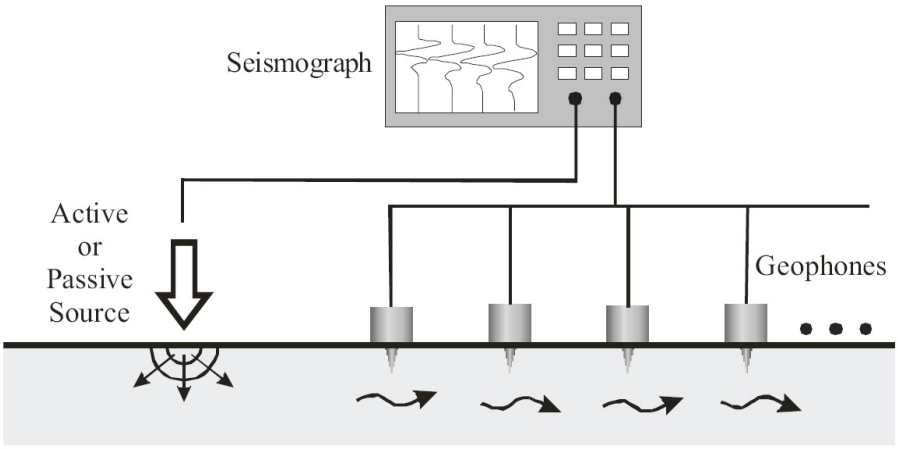


Figure 2.5 - SWM method: multistation acquisition scheme (Lopes et al., 2004)

2.2.1.4. Cross-hole method

Shear and compression wave velocities can be determined from the measurement of the travel time between a source and one or more receivers. The cross-hole (CH) method is a time-of-travel measurement where the source and receivers are placed at the same depth in adjacent boreholes, as illustrated in Figure 2.6a. This measurement then involves generating and monitoring horizontally propagating shear

waves with vertical particle motion; hence SV waves. Shear wave velocities are determined by dividing the borehole spacings at the testing depth by the respective travel times. The test is repeated at multiple depths to compile a complete profile of shear and compression wave velocities versus depth. This method is one of the most commonly used in geophysical site characterisation.

The CH method is capable of overcoming some of the resolution issues associated with surface geophysics, since the location of the boreholes can be selected according to the most relevant areas. A string of receivers (geophones or hydrophones) is lowered in one of the boreholes. The source is fired and the arrival times at all receivers are recorded. The next step is to change the location of the source and to acquire new arrival times. When multiple-source to multiple-receiver data are obtained, a tomographic inversion can be implemented, similar to applications in the medical field. There are several advantages associated with cross-hole testing: the source and receivers are placed closed to the material/target to be evaluated, thus enhancing resolution; measurements can be gathered along multiple inclined ray paths which can be processed together to render a tomographic image of the cross section (Menke, 1989; Santamarina and Fratta, 1998); different wave directions (P, S_{HH}, S_{HV} and S_{VH}) can be generated and measured.

2.2.1.5. Down-hole method

The down-hole (DH) method is similar to the cross-hole, but in this case the excitation is applied at the surface and hence only one borehole is necessary, as shown in Figure 2.6b. Travel distances are typically based on assuming straight ray paths between the source and receivers, although the analysis may sometimes account for refracted travel paths. The main disadvantage of this method is that wave energy has to travel increasingly larger distances as the depth of testing increases.

2.2.1.6. Seismic cone penetrometer testing (SCPT)

The cone penetration test (CPT) is a well established tool for characterizing soil properties by measuring tip and side resistances on a probe pushed into the soil (Lunne et al., 1997). The SCPT test is a modification of the CPT which allows measurement of shear wave velocities in a DH testing arrangement (Campanella et al., 1986). Seismic energy is generated at the surface near the insertion point of the cone. Usually, a horizontal impact on an embedded anvil is used to generate the

horizontally polarised waves. Travel times of the shear wave energy, either direct or interval, are measured at one or more locations above the cone tip as shown in Figure 2.6c. After testing at one depth, the cone is penetrated further into the soil, and the test is repeated. One of the important benefits of this method is that the seismic data can be combined with the cone resistance values to build a clearer picture of soil type, strength, stiffness, and layering. As concluded by Stokoe and Santamarina (2000), this is an excellent example of using multiple techniques to investigate sites.

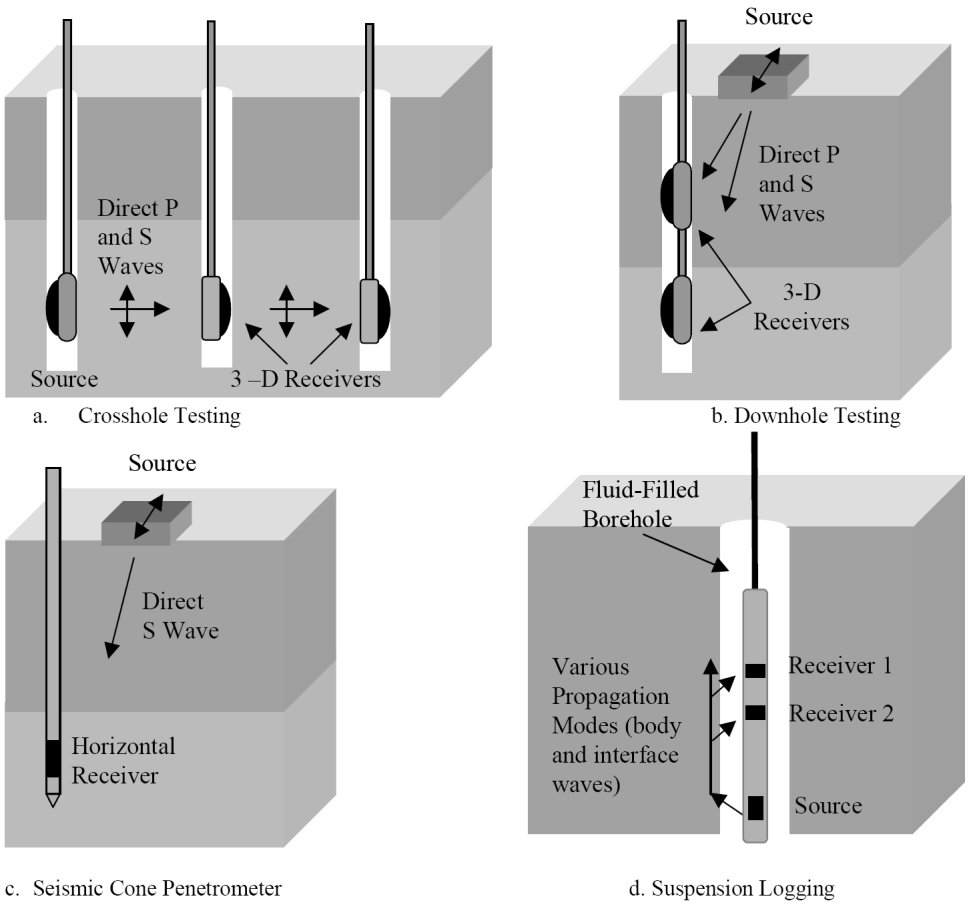


Figure 2.6 - Field arrangements used to perform intrusive seismic tests: a) CH; b) DH; c) SCPT; d) suspension logging (after Stokoe and Santamarina, 2000)

2.2.2. Other field methods

There are also a number of field testing methods that provide measurements of the stiffness of the soil. According to Schnaid et al. (2004), these field techniques can be broadly divided into: i) non-destructive or semi-destructive tests that are carried out

with minimal overall disturbance of soil structure and little modification of the initial mean effective stress during the installation process; and ii) invasive, destructive tests were inherent disturbance is imparted by the penetration or installation of the probe into the ground. Examples of non-destructive methods comprise the self-boring pressuremeter (SBPT) and plate loading tests (PLT), where a set of tools is generally suitable for rigorous interpretation of test data under a number of simplified assumptions. On the other hand, examples of invasive-destructive techniques include cone (CP) and Menard's pressuremeters (PMT) and the Marchetti's flat plate dilatometer (DMT). The self boring pressuremeter (SBPT) is the most sophisticated, useful and informative technique, as it is capable of in situ determination of a number of fundamental parameters, namely the in situ at rest state and the stiffness modulus (Wroth, 1982; Campanella, 1994; Robertson et al., 1994; Fahey, 1998, 2001; Gomes Correia et al. 2004; Fahey et al. 2003, 2007).

Given the focus of this research work on the application of seismic-wave based techniques for stiffness measurement, the description of these field methods is considered beyond its scope.

2.3. Stiffness measurements in the laboratory

Several reviews on the laboratory apparatuses and testing techniques available for the assessment of soil stiffness have been presented over the years, namely Woods (1978, 1991), Tatsuoka (1988), Saada (1988), Arthur (1988), Jamiolkowski et al. (1991), Ladd (1991), Tatsuoka and Shibuya (1992), Lo Presti (1995), among others.

Measurements of stiffness in the laboratory are usually grouped, according to the type of tests from which it is inferred, in dynamic and static tests. According to Dobry and Vucetic (1987) and Tatsuoka and Shibuya (1992), the term 'dynamic tests' indicates tests involving fast (monotonic or cyclic) loading conditions (Lo Presti, 1995). These are generally divided into: seismic tests (using piezoelectric transducers) and resonant-column tests. One of the advantages of seismic wave-based tests is that the same test in the field can be also performed in the laboratory. On the other hand, static monotonic loading tests include: standard triaxial tests, torsional shear tests, and true triaxial tests, whereby the three principal stresses can be independently controlled.

2.3.1. Resonant-column testing

The resonant-column (RC) test is a classical dynamic laboratory test (ASTM D4015, 2000), in which the vibration frequency can be varied, in order to induce resonance of the system. Its main advantage lies on the reliability of the derived parameters, which are based on one-dimensional wave propagation theory. This test enables to determine the shear stiffness and damping of a soil specimen for a wide range of strains, usually from 10^{-6} to 10^{-2}.

The first application of this technique, according to Woods (1978) is attributed to Ishimoto and Iida (1937). The testing configurations involve either fixed-free (Hall and Richart, 1963) or free-free boundary conditions (Drnevich et al., 1978), where the fixed-free torsional resonant column is the most widely used method in testing soils.

This testing method was applied in this research and further details regarding its functioning and the determination of the stiffness parameters are presented in Chapters 3 and 7.

2.3.2. Piezoelectric transducers

Bender elements, as well as other piezoceramic transducers, have opened a new window in laboratory testing, by enabling to perform standard mechanical, static or cyclic, tests simultaneously with seismic wave dynamic tests.

In the laboratory, the most widely-used of the methods of determining V_S makes use of piezoelectric transducers, such as bender elements (BE), shear plates and also bender-extender elements. These transducers enable transmitting and receiving shear and/or compression waves and can be installed virtually in any conventional soil testing device, most commonly in the oedometer or the triaxial chamber, but also in more complex systems such as calibration chambers, centrifuges, resonant columns and even cubical true triaxial apparatuses.

These transducers are the basis of the experimental work carried out in this research. For this reason, their operation, installation, interpretation and other issues involving BE testing are the main subject of Chapter 4.

2.3.3. Triaxial apparatuses

In this category are included the standard triaxial, torsional shear and hollow cylinder apparatuses. The development in laboratory techniques and equipments and the diffusion of automation in control and data acquisition has increased the capability of performing reliable laboratory tests under a generalised state of stress. The standard triaxial (TX) is still the most popular testing system both in research and in industry (Lo Presti, 1995).

The possibility of measuring small strains in the TX, thus enabling to determine small strain stiffness parameters during static monotonic loading tests, was made possible by means of the installation of local axial and radial strain transducers (Ampadu, S.F.; Tatsuoka, F., 1993; Cuccovillo and Coop, 1997). These measurements eliminate many errors inherent to externally measured axial strains, namely the compliance of the system, including seating and bedding errors.

In this research, standard triaxial and stress-path apparatuses will be used and their descriptions will be provided in the following chapter.

2.3.4. Calibration chambers

Calibration chambers are generally used to load carefully constructed samples of soil with known boundary conditions. Models or prototype systems are then inserted into the soil to evaluate their performance in a known geotechnical environment. Evaluation of the performance of in situ devices is a typical use of these chambers. Well known results include the Gibbs and Holtz (1957) standard penetration test (SPT) relationships, the Schmertmann (1976) cone penetration test (CPT) relationships and numerous studies conducted by the NGI, and ENEL and ISMES in Italy (e.g., Baldi et al., 1981). An example of these chambers is illustrated in Figure 2.7. Ismail et al. (2004) also devised a calibration chamber for investigating artificially cemented sands, shown in Figure 2.8.

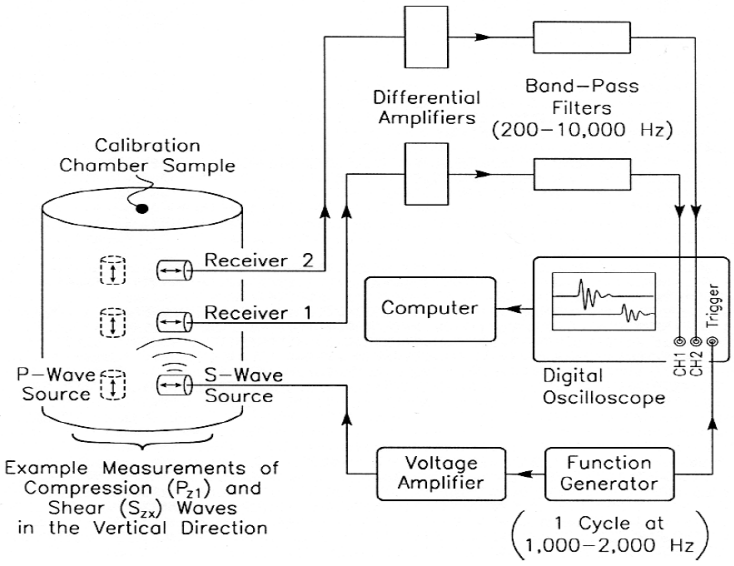


Figure 2.7 - Schematic diagram of embedded geophones and electronics used in seismic measurements in a calibration chamber (Brignoli et al., 1997)

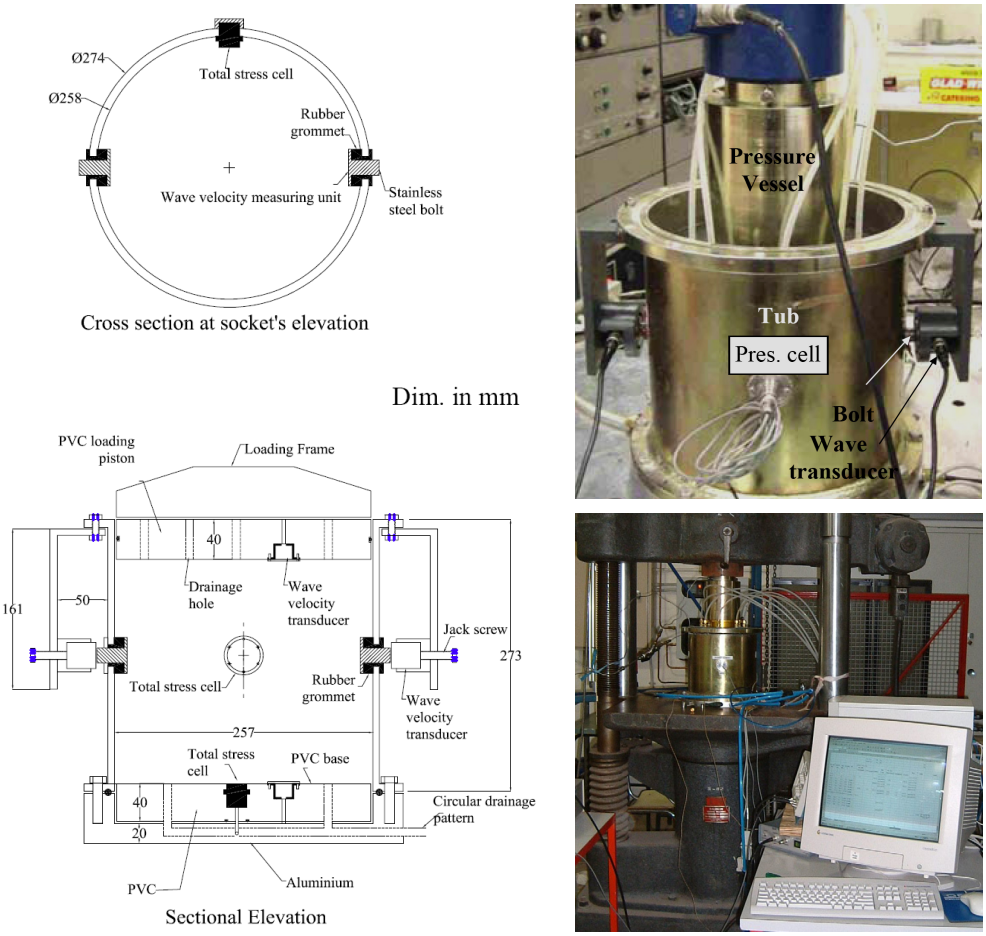


Figure 2.8 - Calibration chamber at the University of Western Australia (drawings after Ismail et al., 2004)

2.3.5. True triaxial apparatuses

True triaxial apparatus provide the capability of applying three independent principal stresses or strains to cubical specimens of soil and thus provide one more degree of freedom that the conventional triaxial apparatus. Several models of true triaxial apparatuses have appeared over the years, all of which fall with three main categories: a) strain-controlled rigid boundaries; b) stress-controlled flexible boundaries; c) mixed boundary apparatuses.

Ideally, laboratory experiments would be performed on single elements of soil in order that predictions may be made of the behaviour of the soil in any prototype situation. While a complete programme of exploration of stress or strain space towards constructing a complete numerical model for the response of the soil to all possible stress or strain paths is unfeasible, it is possible to restrict exploration to areas of stress or strain space which are known to be of interest in particular prototype situations (Muir Wood, 1981). This approach requires, however, the identification of the relevant stress paths to be used when testing soil samples.

Certain situations are, however, statically or kinematically determinate so that relevant stress or strain path can be readily defined. Installation and loading of piles form on situation for which predictions of response are needed. In the absence of accurate soil models for use as input to competent finite element programs, some success has been obtained in drawing an analogy between the processes of driving a cylindrical pile into the ground and of rapidly expanding (or creating) a long cylindrical cavity in the soil (for example, Randolph et al., 1979). The path applied in the rapid expansion of a cylindrical cavity is strain-controlled, which can be applied in an appropriate testing apparatus to produce a corresponding stress path.

One of the oldest designs of a true triaxial apparatus was devised by Hambly (1969). This advanced type of true triaxial apparatus was described by Muir Wood (1974) in which a cuboidal sample of soil is contained with six linked rigid platens, as schematically illustrated in Figure 2.9. A soil element is constrained between six identical rigid platens, each of which is mechanically linked to two other platens.

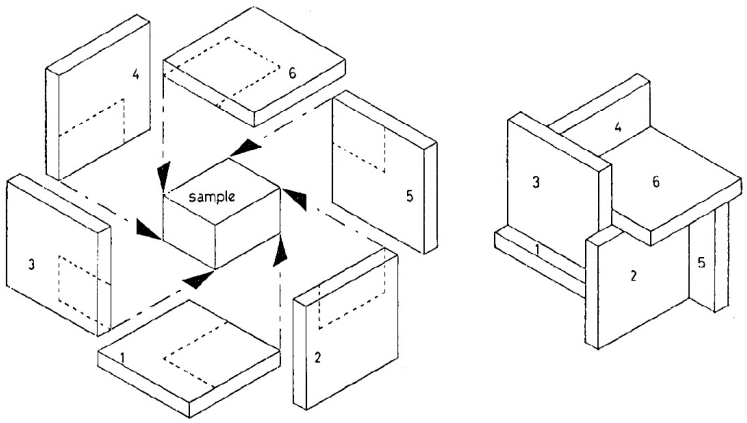


Figure 2.9 - Arrangement of platens in Cambridge true triaxial apparatus (Muir Wood, 1981).

Based on this design, a rigid boundary true triaxial apparatus was constructed and used by Pearce (1970) to study the behaviour of soft clay. Muir Wood (1974) improved the performance of the existing device and adopted it to investigate the mechanical response of kaolin clay under a wide range of true triaxial states of stress and strain. Afterwards, various true triaxial apparatus with rigid boundaries were built and used at different laboratories around the world, namely Wood (1974), Lanier and Zitouni (1988), Airey and Wood (1988), Matsuoka et al. (2002), Ibsen and Praastrup (2002), Sadek (2006). Probably the most recent type of rigid boundary true triaxial (TT) apparatus is that described by Ismail et al. (2005), identical to the one used in the present research work, presented in detail in the following chapter.

Flexible boundary true triaxial apparatus, also called cubical cell (CC) apparatus, contain an arrangement of six pressurised bags which surround the sample within a loading frame (see Figure 1.5).

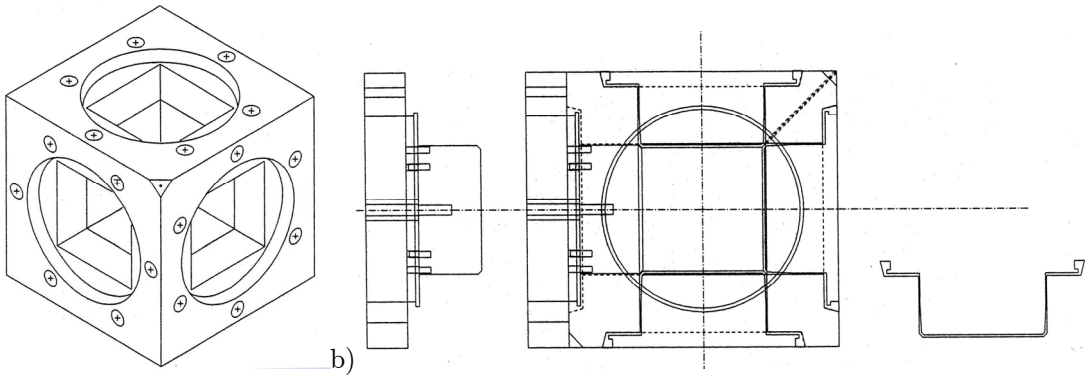


Figure 2.10 - Flexible boundary true triaxial apparatus: a) isometric view of the frame; b) sections through face plate, cell and pressure bag (Sadek, 2006)

The original cubical cell device was described by Ko and Scott (1967). They emphasised that such testing equipment is capable of measuring the true

deformational behaviour of soils. There have been a number of variants of the basic design since that time, as reported by Arthur and Menzies (1972), Alawaji et al. (1990), Reddy et al. (1992), Dewoolkar et al. (1997), Callisto and Calabresi (1998), Callisto and Rampello (2002), and Penumadu and Prashant (2005).

Details regarding the operation and testing procedures of a flexible boundary cubical cell apparatus, similar to that of Dewoolkar et al. (1997) and Sadek (2006) are given in Chapter 3.

Finally, it is worth introducing the mixed-boundary true triaxial apparatuses. The most widely used design originated from Lade and Duncan (1973) in which different principal stresses can be applied to a cubical specimen using a specially designed horizontal loading system. Reported works on mixed-boundary true triaxial tests include Michelis (1988), Silvestri et al. (1988), Lewin and Allman (1993), Hayano et al. (1999), Macari and Hoyos Jr (2001), Wang and Lade (2001), AnhDan and Koseki (2003) and Shapiro and Yamamuro (2003). These systems consist of a combination of rigid and flexible boundaries, thus lack the essential symmetry of the rigid boundary or flexible boundary apparatuses previously described. According to Sadek (2006), these conditions usually limit the regions of principal stress space that can be explored. Moreover, it is likely that preferential directions of failure are developed.

The use of either six flexible boundaries or six rigid boundaries appears to be a more suitable approach for examine soil behaviour in three-dimensional stress conditions, as suggested by Airey and Wood (1988).

In this research, a number of laboratory testing apparatuses were used, all of which incorporated bender element transducers to provide seismic wave measurements. These testing conditions enabled to simultaneously combine the benefits of very small strain stiffness measurements, by means of BE, with the small to large strain stiffness measurements of each apparatus.

3.

Laboratory Prototypes and Equipment

3.1. Introduction

Given the experimental focus of this work, many different devices and testing equipments were applied. The common denominator of virtually all tests is the use of seismic waves, transmitted and received by piezoelectric transducers, as a means to measure stiffness moduli. These transducers have been installed in different testing apparatus for complementary and comparative purposes, namely in standard triaxial, stress-path, resonant-column and also in true triaxial cubical apparatuses. For the installation of the piezoelectric transducers, it was often necessary to conceive and implement some adaptations in the testing devices, as well as to devise and develop new designs for testing prototypes, which could overcome some limitations of more conventional devices. Given the novelty of some modifications and the new designs of other testing equipments, it is worth detailing its characteristics, functioning and testing procedures.

Firstly though, it is relevant to present the particularities of the piezoelectric transducers systematically used in this experimental programme.

3.2. Piezoelectric transducers

3.2.1. Piezoelectricity

Pierre and Jacques Curie were the first to publish in 1880 the experimental demonstration of the connection between macroscopic piezoelectric phenomena and crystallographic structure, by measuring surface surcharges on especially prepared crystals when subjected to mechanical stress. This property, known as piezoelectricity, refers to the ability of converting electrical into mechanical energy, or vice-versa, and can be found in nature in some particular crystals, such tourmaline, quartz, or topaz, among others. Piezoelectricity can also be artificially obtained by polarization of certain ceramics such as lead zirconate titanate (PZT), barium titanate, and lead titanate (Piezo Systems Inc., 1994). The deformation of the polarized piezoceramic element essentially depends on its shape, composition, polarization direction and on the applied electrical field. Hence, different transducers can be manufactured to generate compression-extension or shear movements. Furthermore, since the piezoelectric effect is reversible, the transducers can operate as actuators, sensors, or as both (Brignoli et al., 1996).

3.2.2. Types of transducers in use

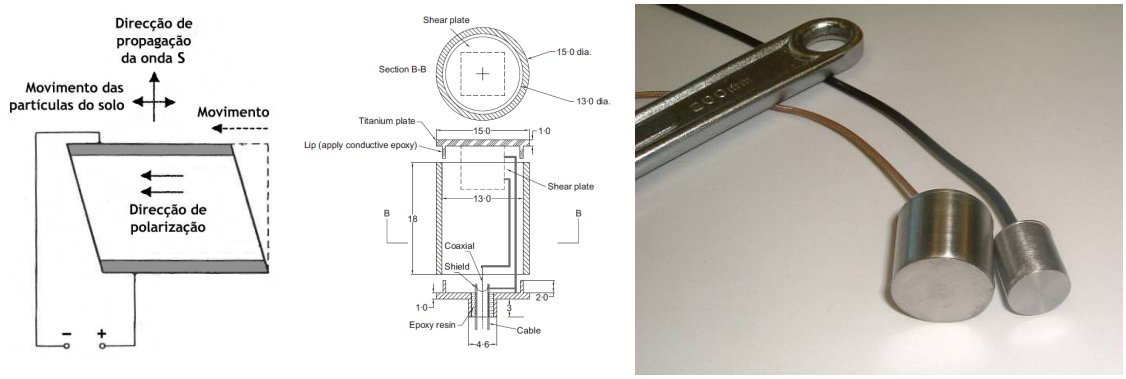
Shear-plates and bender elements are examples of piezoelectric transducers, which can transmit and receive S-waves; similarly, extender elements and compression transducers can transmit and receive P-waves. Focusing on shear-wave transducers, shear-plates were reportedly the first to be employed in soil specimens (Lawrence, 1963, 1965; Brignoli et al., 1996). Shear-plates, despite being more robust and easier to use in stiff or coarse undisturbed materials because for their non-invasive nature, require much higher driving voltages, have larger dimensions and lower efficiency for the typically low confining stresses of soils, resulting on a large mismatch between the characteristic impedances of the transducer and the soil specimen (Shirley, 1978; Shirley and Hampton, 1978). Given the limitations of the shear-plates, these authors have proposed a different type of transducer, the bender element, where most of the disadvantages of the shear-plate were overcome. Later, Dyvik and Madshus (1985) introduced a more detailed bender element design model, which formed the basis of much of the subsequent development and which is still followed at present. Lings and Greening (2001) described a new construction technique, in which a single transducer is modified, by a few simple changes to the wiring, to become a bender-extender element, capable of transmitting and receiving both types of body waves, S- and P-waves, through the soil, with evident practical benefits. On the other hand, Ismail

and Rammah (2005) have proposed a smaller and more efficient shear-plate as an attractive alternative, namely for very demanding testing conditions, such as harsh environments or particularly high stresses.

All these piezoelectric transducers can be installed in a wide variety of soil testing devices, from conventional to non-conventional, from static to dynamic equipments. The triaxial cell is probably the most common apparatus where these transducers are used, but its use in other devices have also been reported, namely in the oedometer (Fam and Santamarina, 1995; Zeng and Grolewski, 2005) and direct shear apparatus (Dyvik and Olsen, 1989), the centrifuge (Ismail and Hourani, 2003), in the hollow cylinder apparatus (Di Benedetto et al., 1999; Geoffroy et al., 2003) and in true triaxial and cubical cell apparatuses (Ismail et al., 2005; Sadek, 2006). Its installation in the platens of a resonant-column testing apparatus has also been reported (Souto et al., 1994; Fam et al., 2002; Ferreira et al., 2007) and this is particularly interesting as a means to assess the potentialities of the BE technique, and to compare and calibrate its measurements.

3.2.3. Shear-plates

A shear-plate [SP] consists of a single piezoceramic element, generally prismatic, where the electrode surfaces, applied to two faces parallel to the polarization direction, are series-connected. As illustrated in Figure 3.1, the deformation induced by the electrical signal is distortional, thus producing shear waves (Brignoli et al., 1996). Shear-plates were the first piezoelectric transducers used for soil testing by Lawrence (1963, 1965), though scarcely applied mainly due to the large difference in characteristic impedances of these transducers and most soils, which limited its efficiency in shear wave measurements especially at low confining stresses. To overcome these limitations, bender elements were later developed, as detailed below, and became far more popular in soil testing. Nevertheless, for undisturbed stiff soils and coarse-grained soils, shear plates are better suited than bender elements since SP do not penetrate into the soil, as concluded by Brignoli et al. (1996). Recently, Ismail and Rammah (2005) presented a smaller and more efficient shear-plate, designed for very demanding testing conditions, such as harsh environments or particularly high stresses, where other transducers, namely bender elements, are likely to be less appropriate. Illustrations of this new SP are also presented in Figure 3.1.



a) b) c)

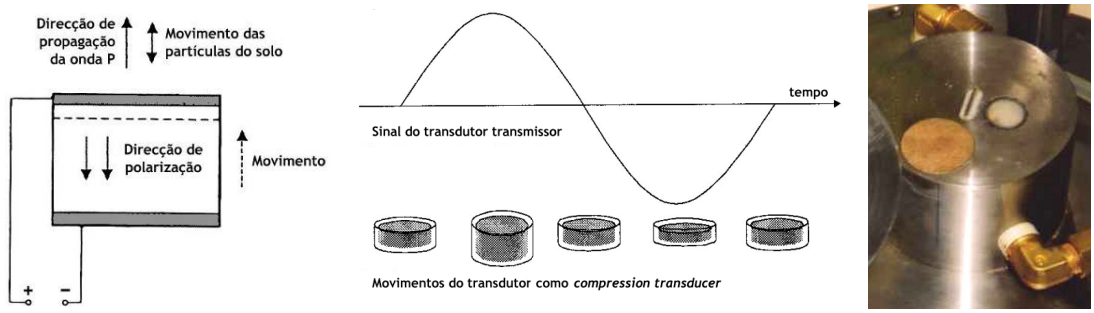
Figure 3.1 - Shear-plate schematic: a) connections, polarization and deformation (after Brignoli et al., 1996; b) design of a miniature SP (Ismail and Rammah, 2005); c) SP from UWA: the miniature transducer on the right is just 15 mm in diameter.

Shear-plates transducers, such as the miniature SP from UWA, were employed in the preliminary tests of the UWA-FEUP true triaxial apparatus, following the proposal of Ismail et al. (2005). In this application, the shear-plate transducer was used externally to the sample, with the advantage of requiring a single pair of transducers for the measurement of shear waves in the three propagation directions, by placing the transducers in the different pairs of platens (X, Y and Z). The ability to rotate the transducers in place, to polarise the movement of soil particles in any polarisation direction is another interesting feature of this setup.

3.2.4. Compression transducers

A compression transducer, similarly to a shear-plate, consists of a single piezoceramic element, though its polarization is in the thickness direction. The electrodes are located in the external surfaces and series-connected. In this configuration, the application of an electrical excitation results in compression-extension movements of the transducer, thus enabling the propagation of P-waves.

It is generally a small cylindrical transducer of about 2 mm thickness and 8 mm diameter. Figure 3.2 presents a schematic of its connections, polarization, and deformation (adapted from Brignoli et al., 1996) and a diagram of its movement induced by a sinusoidal pulse excitation.



a) b) c)

Figure 3.2 - Compression transducer: a) schematic of connections, polarization and deformation; b) movement under sinusoidal excitation

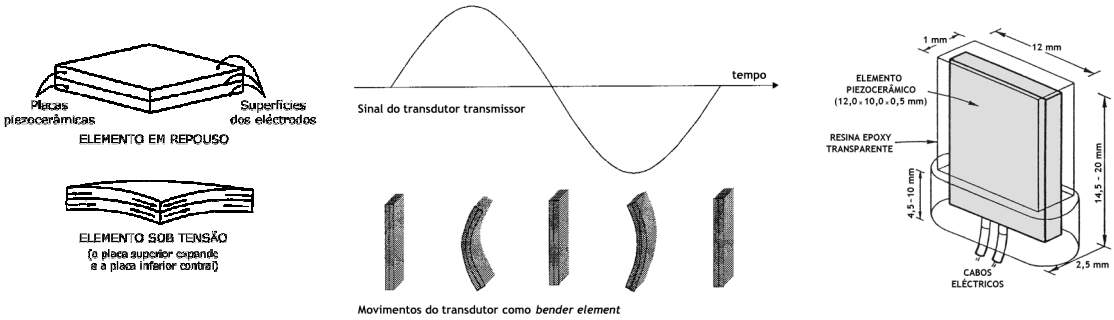
This type of transducer was only used in the ISMES-Enel.Hydro triaxial apparatus and provided in general very clear and sharp signals. The use of this or other P-wave transducers is strongly advocated as complement to S-wave measurements, since the interpretation of the signals is facilitated.

3.2.5. Bender elements

A bender element [BE] is a double piezoceramic transducer composed of two thin piezoceramic plates, rigidly bonded to a central metallic sheet and to electrodes on its outer surfaces. The metallic sheet acts as reinforcement, since the piezoceramic plates are extremely fragile. This assembly is protected with a rigid epoxy resin coating, in order to electrically isolate and prevent direct contact with the soil and, more importantly, with water. The electrical connection to the plates is made in relation to the polarization directions of the two plates, in order to ensure proper flexural movement: plates polarized in opposite directions are series-connected, while plates polarized in the same direction are parallel-connected. The performance of the transducers is also related to its capability of transmitting or sensing shear waves: a series connection is preferable for the receiver element, as a higher output is obtained for the same movement, twice the energy of a parallel connection; conversely, a parallel connection is more suitable for the transmitter element, since the distortional movement of the transducer is greater for a given input, hence achieving double the efficiency of series-connected BE if used as transmitters (Dyvik and Madshus, 1985; Brignoli et al., 1996).

The model presented by Dyvik e Madshus (1985), in Figure 3.3, is still the basis of current design, though variations have been made, namely to its size and to arrangements (usually T-shaped) of pairs of transducers in a single probe. These variations are consequences of the need to adjust to new testing challenges: in order

to observe vertical and horizontal homogeneity in triaxial specimens, and thus assess anisotropy, the standard-sized BE is not appropriate, as it is too large in relation to the travel distance and too heavy to be sustained by the sample (and the membrane). The combination of two BE placed orthogonally in a single probe has also resulted from the interest in measuring vertically- and horizontally-polarized waves. And so, the miniature and/or T-shaped BE have been developed and manufactured with great success, especially when horizontally mounted in a triaxial specimen (Pennington et al., 1997, 2001).



a) b) c)

Figure 3.3 - Bender element: a) movement diagrams; b) Dyvik and Madshus (1985) model

3.2.6. Bender/extender elements

Bender/extender elements [B/EE] were "accidentally" discovered when the typical BE connection scheme was incorrectly performed (Fuertes, 1999). Lings and Greening (2001) detail its manufacture. The most interesting feature of this transducer is its reversibility of functions: a parallel-connected bender-extender element works as an S-wave transmitter [BT] and a P-wave receiver [ER]; on the other hand, a series-connected B/EE is both a P-wave transmitter [ET] and an S-wave receiver [BR]. Figure 3.4 and Figure 3.5 detail its configuration and wiring for S- and P-wave measurement, respectively.

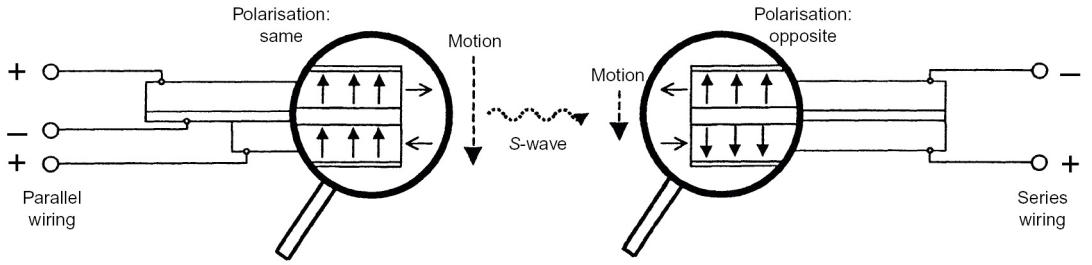


Figure 3.4 - Typical BE wiring details and operation: a) transmitter; b) receiver (after Lings and Greening, 2001)

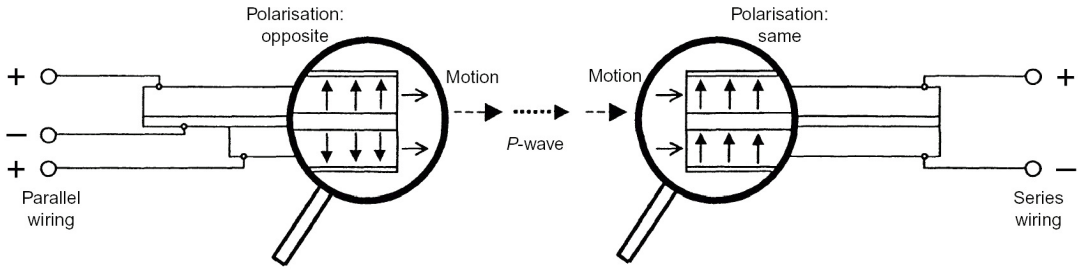


Figure 3.5 Typical EE wiring details and operation: a) transmitter; b) receiver (after Lings and Greening, 2001)

These bender (and bender/extender, to a smaller scale) elements have become the most common laboratory shear wave transducer worldwide, mainly due its simplicity and ease of application, offering a convenient and increasingly popular method of small-strain stiffness measurement. References to its use in soil characterization are increasingly recurrent in the literature, reporting test results in many different apparatuses, namely in the:

- oedometer (Thomann and Hryciw, 1990; Fam and Santamarina, 1995; Zeng and Ni, 1998; Grolewski and Zeng, 2001);
- direct shear apparatus (Dyvik and Olsen, 1989);
- triaxial cell: top and bottom platens (Brignoli et al., 1996; Viggiani and Atkinson, 1995; Ferreira, 2003);
- triaxial cell: horizontally mounted (Pennington et al., 1997, 2001; Lo Presti et al., 1999; Kuwano et al., 2000; Fioravante and Capoferri, 2001; Clayton et al., 2004);
- cyclic triaxial apparatus (Huang et al., 2005)
- resonant-column testing apparatus (Souto et al., 1994; Fam et al., 2002; Ferreira et al., 2007; Camacho-Tauta et al., 2008);
- centrifuge (Gohal and Finn, 1991; Ismail and Hourani, 2003);
- hollow cylinder apparatus (Di Benedetto et al., 1999; Geoffroy et al., 2003);
- true triaxial and cubical cell apparatuses (Ismail et al., 2005; Sadek, 2006);
- other testing prototypes: tomography scale models (Lee et al., 2005); calibration chamber (Ismail et al., 2004).

The applications of bender element results are numerous, as will be detailed in the following chapters and include:

- definition of the elastic stiffness parameters (Atkinson, 2000; Lings, 2001);
- comparison of dynamically- and statically-determined stiffness moduli (Pennington, 1999; Viana da Fonseca et al., 2003);
- assessment of sampling quality (Ferreira, 2003; Landon et al., 2007; Sukolrat, 2007);

- identification of destructuration (Nash et al., 2006; Sukolrat, 2007);
- assessment of anisotropy (Pennington et al., 1997; Pennington, 1999; Fioravante, 2000; Kuwano et al., 2000; Ng et al., 2004)
- process monitoring: consolidation, curing, cementation (Ismail et al., 2004);
- evaluation of porosity (Arroyo et al., 2006);
- identification and control of suction (Silva et al., 2002);
- assessment of liquefaction potential (Andrus and Stokoe, 1998; Yang, 2002).

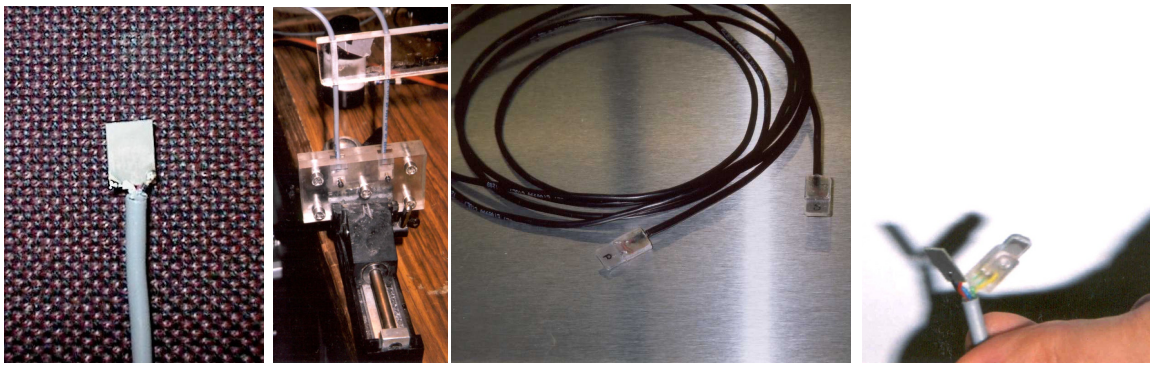
3.2.6.1. Manufacturing bender or bender/extender elements

In this research programme, various pairs of BE and B/EE have been used, though its production and assembly was carried out elsewhere. From co-operation projects with other universities and institutions, different transducers have been obtained and employed, namely:

- single BE and B/EE, and one miniature T-shaped pair of BE from the University of Bristol [UoB];
- T-shaped pairs of B/EE and a small pair of SP from the University of Western Australia [UWA];
- BE and CP installed in a triaxial cell, from ISMES-Enel.Hydro.

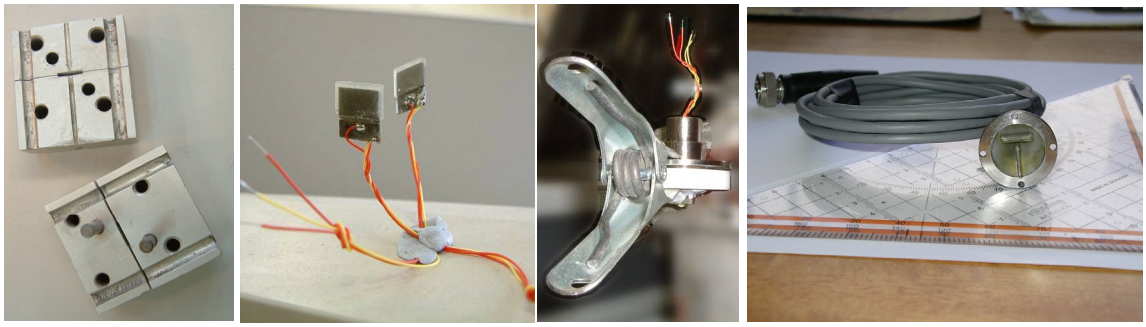
It does not seem appropriate to detail herein the process of preparation of the piezoceramic material and manufacture of the transducers. However, since those procedures were closely observed, parts of the manufacturing process are presented below, for illustrative purposes. Important aspects regarding insulation, grounding and wiring have been carefully observed, towards producing transducers with high standards of quality and reliability.

In Figure 3.6, some photographs are provided of standard and miniature transducers, during their production at the University of Bristol. Similarly, the manufacturing process of BE or B/EE at the University of Western Australia is reported in Figure 3.7. A specifically designed mould is used to coat the piezoceramic plates with epoxy resin (Figure 3.6c and Figure 3.7a). This produces a thin, even and uniform protective surface for the transducer, providing adequate insulation and robustness. For T-shaped probes, each pair of coated BE or B/EE is placed inside a brass or stainless steel capsule (or casing) and a second epoxy filling and respective mould are necessary to fix the two transducers orthogonally in place.



a) b) c) d)

Figure 3.6 - BE and B/EE from UoB: a) standard size B/EE before coating; b) mould for epoxy coating; c) final single BE pair; d) miniature pair of B/EE during assembly



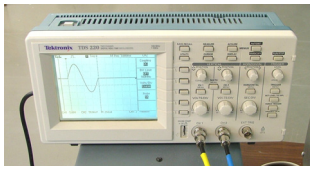
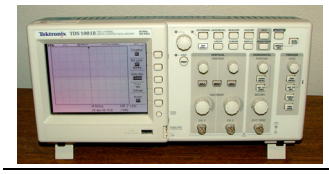
a) b) c)

Figure 3.7 - BE or B/EE from UWA: a) mould for one transducer; b) wired pair of B/EE; c) potting the epoxy resin in the capsule probe; d) final T-shaped B/EE

3.2.7. Associated electronics equipment

For the measurement of seismic waves, having piezoelectric transducers is not enough. An external signal source is necessary, as well as an acquisition device for viewing and recording the wave results. Amplification is often fundamental in order to appropriately visualise and interpret the signals. Hence, a set of electronics equipment is usually required and the most frequently used in this experimental programme are listed and detailed in Table 3.1. During the course of this research, given the number of different testing apparatuses with piezoelectric transducers running tests nearly simultaneously, this set of electronics equipment was installed in a trolley, thus facilitating commutation between them.

Table 3.1 - Bender element testing: associated electronics equipment used

	a programmable **function generator** (TTi) capable of generating an electrical signal with various user-defined configurations (sinusoidal, square, ramp, arbitrary, in continuous or triggered mode); these configurations can be stored as functions for easy access and fast switching;
	a 2-channel **amplifier** (specifically developed by ISMES-Enel.Hydro manufacturers) of both the input and the output signals, which amplifies the input signal by 10x and the output by 10x (1000%);
	two 6-channel **multiplexers** [MUX] and output **amplifiers**, designed and manufactured at COFS-UWA, for managing and manual switching between different channels in the same test: one MUX is for transmitters, the other MUX is for receivers, with amplification of the output signal by 2x; it works with 2 channels connected in the same 6-pins plug, and enables any combination of transmitter and receiver channels, particularly suited for inclined measurements.
 	dual-channel **oscilloscopes** (Tektronix TDS210, TDS220 and TDS1001B) for visualizing and directly identifying the travel time and acquiring the signals; its RS-232 or USB [*] serial port connections with a PC enable data transfer using specific software program and storage in different formats for post-processing and interpretation. [*: *TDS1001B only*]
	a low-cost **oscilloscope** and FFT-based **spectrum analyser** (PicoScope ADC-216): dual-channel; 16-bit resolution, though 333kS/s sampling rate, which is just about enough for the current range of frequencies (for stiffer materials, higher sampling rates may be required, so the use of other models, such as the ADC-212 is recommended); this FFT-based spectrum analyser digitises the signal using an analog-to-digital converter and the stored values are then processed using the Fast Fourier Transform (FFT) algorithm.

The signals from the oscilloscopes can be directly transferred and stored in a personal or laptop computer, connected using series and/or parallel ports.

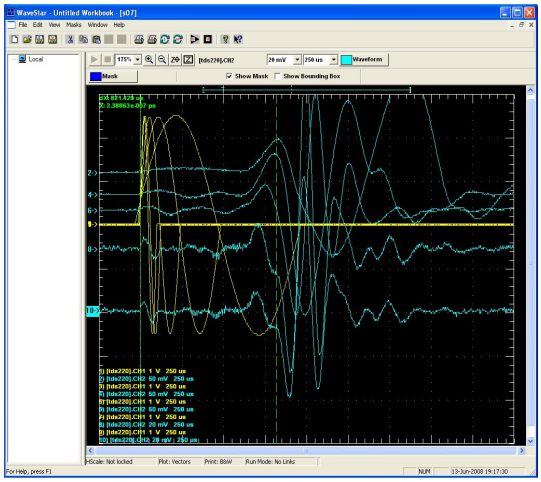
3.2.8. Specific seismic wave measurement software

The use of all these different equipment connected to different computers requires specific software for dealing with data acquisition and storage. While some of that equipment already provided suitable operating software, other new pieces of software were still necessary and had to be developed, to better suit the experimental objectives. As will be described in the following chapter, seismic wave measurements can be made in the time and in the frequency domain. For the use of techniques in both domains, it is important to have a flexible and robust system, with adequate software.

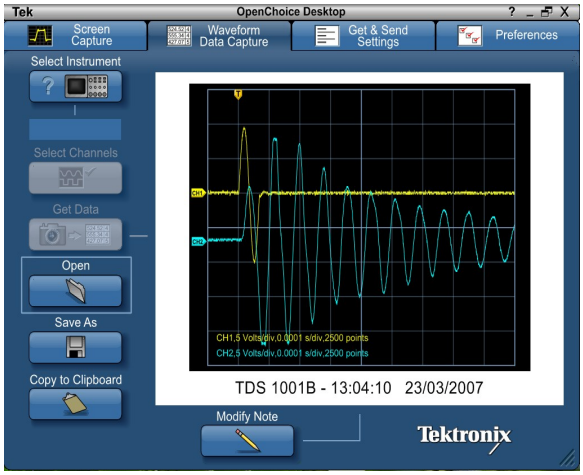
For seismic wave measurements, both Tektronix and PicoTech oscilloscopes are provided with data acquisition programs, WaveStar (and OpenChoice Tektronix, for TDS1001B) and PicoScope respectively, both of which were used for registering the wave traces in the time domain. The analyses in time domain are varied, as will be discussed in the following chapter, but the measurements are identical, that is, time-based readings of the transmitted and received signals. Screenshots of the different programs in use are presented in Figure 3.8.

Given the difficulties in automating time domain measurements, as reported by other researchers (Arroyo et al., 2003) with limited success, this option was not considered useful or reliable. Hence, time-domain readings were manually and individually analysed, based on the best-practice interpretation principles, to be discussed in the following chapter. In sum, an educated eye and experienced judgement are essential requirements towards a reliable interpretation of BE results in the time-domain.

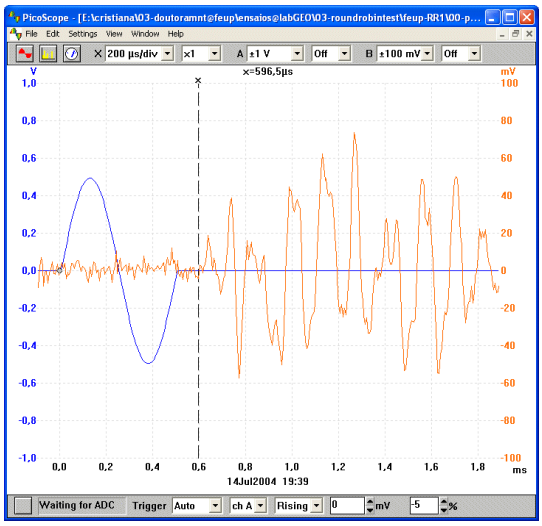
On the other hand, frequency-domain methods can be automated and, despite requiring some degree of user intervention, provide a broader view on the response of the system to the imposed excitation, as will be debated in Chapter 4. After a number of preliminary tests and experiments, the solution for wave measurement and acquisition in FD was inspired by the original work of Greening et al. (2003) and Greening and Nash (2004). An algorithm, based on Fast Fourier Transforms (FFT), has been created and embedded onto a Microsoft Excel spreadsheet ABETS: Automatic Bender Element Testing System. This user-friendly program, which enables measurements and analyses in the time and the frequency domain, has been applied and further developed, as will be detailed in depth in Chapter 4.



a)



b)



c)

Figure 3.8 - Screenshots of the programs used for seismic data acquisition in the time domain: a) WaveStar; b) OpenChoice Tektronix; c) PicoScope

A screenshot of this program and views of the data acquisition results are provided in Figure 3.9. The FD analyses are performed automatically for a predefined set of parameters, from which estimates of travel time, velocity and modulus are immediately computed. Although further data processing is required to derive the final values, this process enables to establish comparisons with time domain results, providing more information than other existing techniques, namely on the response of the system for a broadband range of input frequencies.

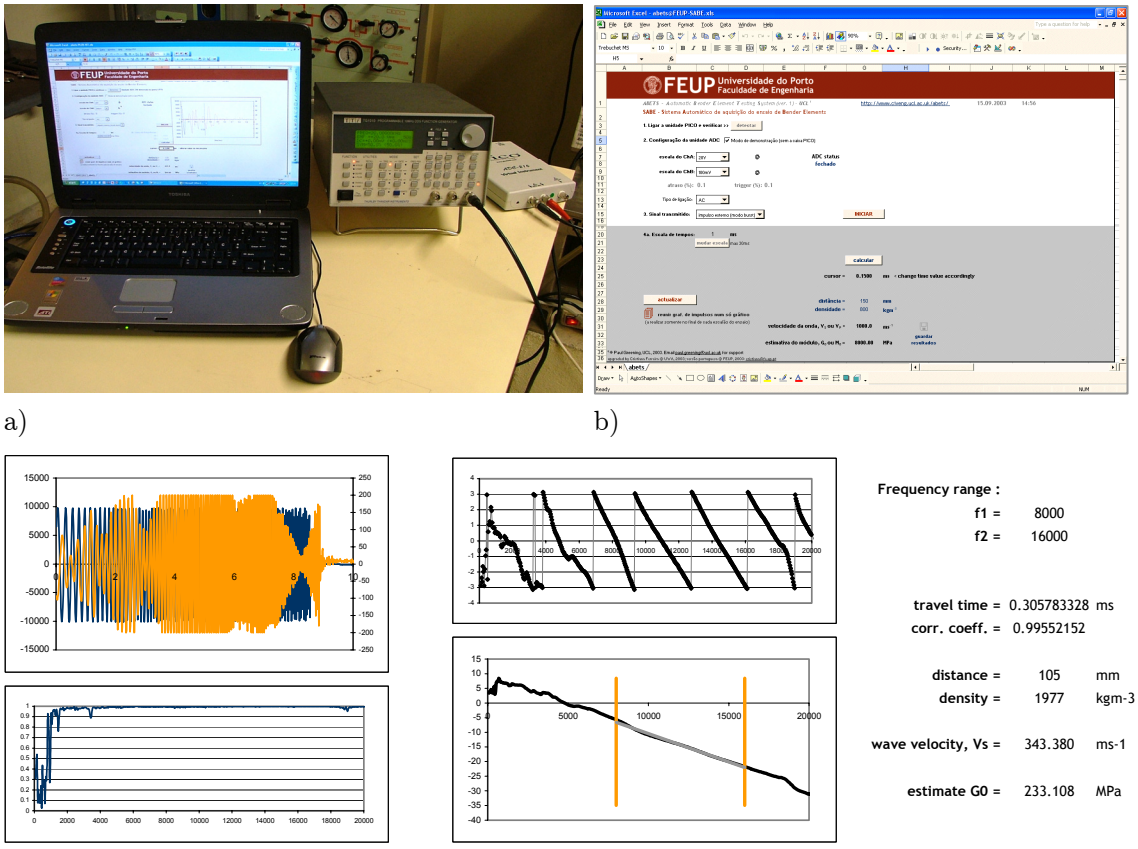


Figure 3.9 - Data acquisition results using ABETS: a) setup; b) screenshot of the acquisition worksheet; c) program output

3.2.9. Performance and calibration checks

Prior to soil testing with these transducers, it is important to carry out a few tests on its functioning and on the system's calibration and polarity. The first test consists on checking that each transducer, directly connected to the function generator, "sings" when an audible input signal is generated, usually for continuous sinusoidal signals within the 1-15 kHz frequency range. Despite being more or less efficient in transforming such input signal into movement, that is, whether it is to be used as transmitter or as receiver, each transducer should respond clearly to the excitation signal, in an audible manner. If so, then the transducer is operational and can be used as intended, as a transmitter or a receiver.

The second test is more informative and the setup consists of manually holding both transducers in direct contact. The results derived from this exercise are extremely relevant, providing information on three different aspects:

- the minimum time delay or calibration time;

- the polarity of the input-to-output signals; and,
- the optimal performance in relation to function.

The minimum time delay between transmitter and receiver BE can be observed when both transducers are placed in direct contact. An input signal is fed to the transmitter and the output signal of the receiver is observed in the oscilloscope. In theory, the time delay should be null, since the tips of the transducers are in contact, that is, at null travel distance. Despite the direct contact of the transducers, the obtained signals are a reflection of the whole BE testing setup, which is in fact a system composed not only by the transducers but also by the electronic devices and cables. All these elements introduce some delay, even if minimal. Hence, from the instant the signal is generated to the instant it is picked up by the receiver, even when in direct contact with the transmitter, a time lag may be expected. This interval should be quantified and, if relevant, defined as the system's calibration time. In the present work, the following was considered:

- for the case of the extender elements, the time lag is less than 3 μs, which corresponds to a maximum error of about 2% in V_P; this error was computed considering the minimum travel time (or maximum velocity) for a 200 mm high saturated specimen, in which the P-wave velocity is about 1500 m/s, close to the velocity of sound in water;
- for the case of bender elements, the time lag varies from 4 to 16 μs, thus resulting in a maximum error in V_S of about 2%, and consequently of 4% in Gmax; this value was estimated considering the in-situ velocities of these residual soils around 200 m/s.

Given the relatively larger errors associated with the interpretation methods and the measurement of the testing parameters (such as the travel distance and density), this time delay is considered negligible in this work, and no correction was introduced to account for this effect.

Another important conclusion can be drawn from this check, which refers to the polarity of the input-to-output signals. When the transmitter and the receiver BE are in direct contact, the wave traces should be very similar in the oscilloscope, but the polarity may be positive or negative (inverted signal). By rotating one of the transducers by 180 degrees, the polarity should reverse and the positions corresponding to positive polarity can be simply marked on one side of each transducer for identification. This characteristic of reversible polarity is exclusive to shear-wave transducers, hence only applicable to bender elements and shear-plates.

The transducers must be installed taking the polarity into account, defining the direction of the first true arrival of the wave: upwards for positive polarity and downwards for inverse polarity. From practical experience, the polarity check should be done at a frequency below resonance, especially if using continuous waves. This information is essential to the correct interpretation of the signals in the time domain. In fact, when propagating a shear wave through a soil specimen, the wave is inevitably altered by a number of factors, such as reflections, distortions and noise, as will be discussed in Chapter 4. Hence, when the wave is picked up by the receiver transducer, its shape is not identical to the input electrical signal, insomuch that its polarity may be nearly inverted, confusing the interpretation. Running this polarity check and bearing this information in mind avoids mistakes, reduces the uncertainty, and clarifies the interpretation.

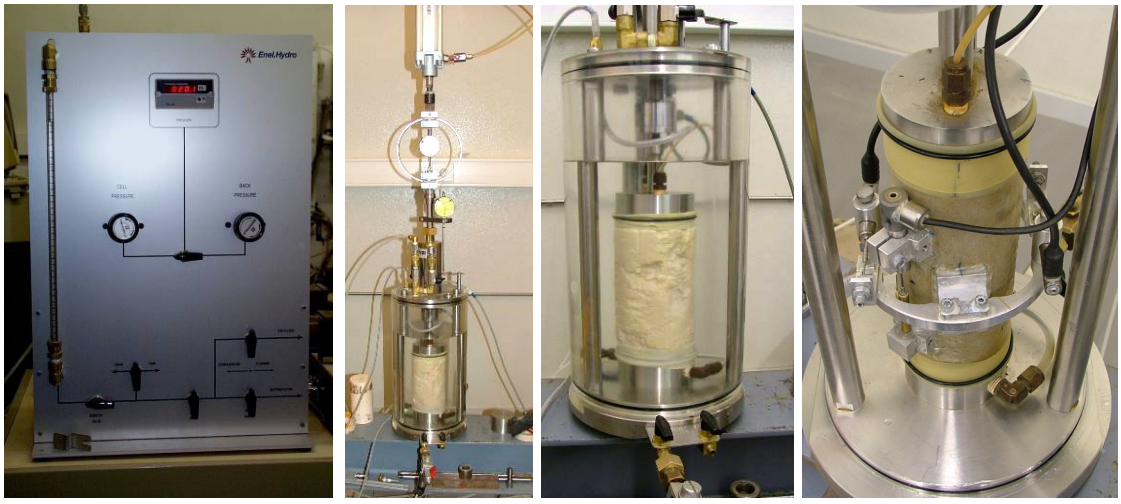
This check also enables to confirm the efficiency of the transducer as transmitter. As mentioned above, the type of polarization and the electrical connection of each transducer influence its performance in relation to the respective function as transmitter or receiver. The magnitude of the response of a parallel-connected BE to an input signal should be greater (theoretically double) than that of a series-connected BE, which would operate more effectively as a receiver.

3.3. Standard triaxial testing apparatuses with bender elements and local strain instrumentation

3.3.1. ISMES-Enel.Hydro triaxial cell [TX70]

The first triaxial cell at the Geotechnical Laboratory of FEUP [LabGEO] equipped with piezoelectric transducers was manufactured and supplied by ISMES-Enel.Hydro. This apparatus enables triaxial testing of cylindrical specimens of 70 mm in diameter and 140 mm in height, and measurement of seismic P- and S-waves by means of compression transducers and bender elements, respectively.

Contrary to most triaxial chambers, in this apparatus the confining pressure is directly applied by means of compressed air, exerting the pressure defined in the panel, on an air-water interface located above the specimen, inside the chamber. The original pressure control panel for both confining and back pressures, presented in Figure 3.10a, is particularly straightforward and easy to use. A burette enables visual measurement of the volume change in saturated specimens. However, in order to facilitate data acquisition and monitoring, including external and internal strains, and axial load measurements, most tests were carried out using other stress control panels, also available at the laboratory, more suitable for the purposes of this research. In Figure 3.10b, different test setups are illustrated with internal load and local strain measurements.

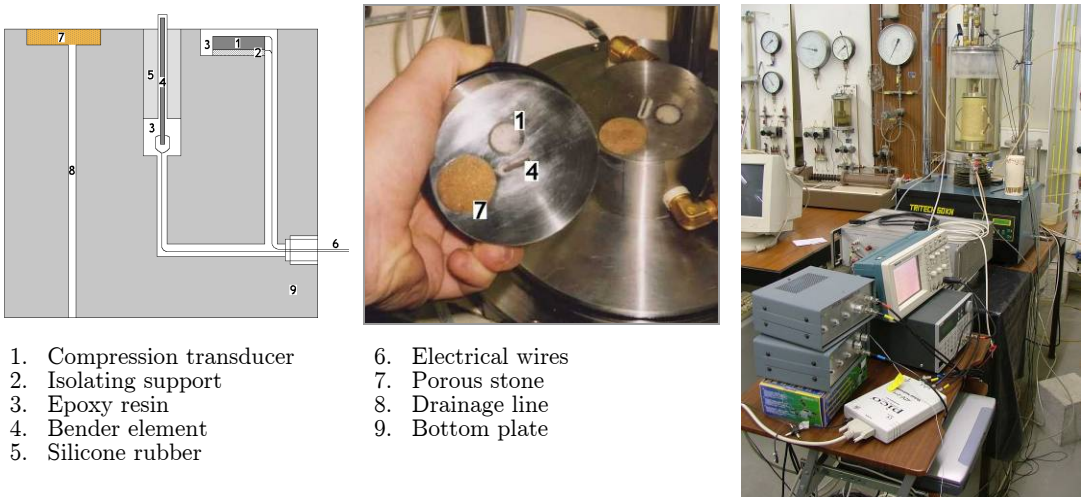


a) b)

Figure 3.10 - Photographs of the ISMES triaxial system at LabGEO

For seismic wave measurement, piezoelectric transducers have been installed in the top and bottom platens, with the transmitters located at the bottom, hence wave

propagation is upwards. A central pair of bender elements enables shear wave measurement, while another pair of compression transducers measures P-waves, as detailed in Figure 3.11. The schematic of seismic wave measurement in this apparatus is presented in Figure 3.12.



1. Compression transducer
2. Isolating support
3. Epoxy resin
4. Bender element
5. Silicone rubber
6. Electrical wires
7. Porous stone
8. Drainage line
9. Bottom plate

Figure 3.11 - CT and BE in the ISMES-Enel.Hydro triaxial cell

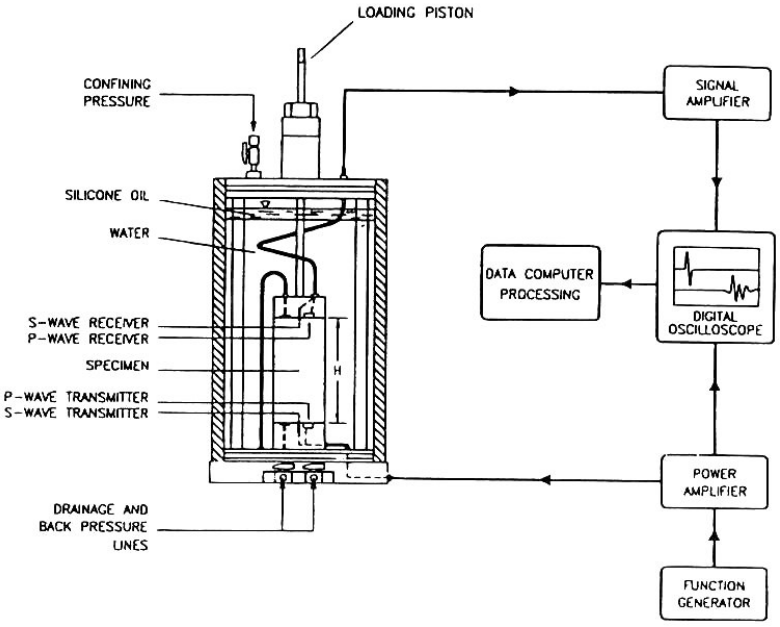


Figure 3.12 - Schematic of seismic wave testing in the ISMES apparatus (after Brignoli et al., 1996)

Being a fully calibrated testing system, this apparatus has also served for the calibration of the other modified triaxial cells, where the piezoelectric transducers were locally implemented. The calibration consisted of the comparison of test results

on identical reconstituted soil specimens, under the same stress conditions in both apparatuses, as reported in Ferreira (2003).

3.3.2. FEUP standard triaxial cell [TX100]

A conventional triaxial cell was selected for the installation of piezoelectric transducers for seismic wave measurement. Specimen size is 100 mm diameter and 200 mm height. Some alterations were required in order to accommodate the transducers, as briefly described below and further detailed in Ferreira (2003). For seismic wave measurements, one pair of BE and another of B/EE, both from the University of Bristol, were installed.

3.3.2.1. Equipment modifications

The alterations in the triaxial chamber for the installation of the BE consisted on the design of new top and bottom platens with slots for the transducers, on the opening of slots in the porous stones and in the base pedestal. Other modifications include the paths of the electrical cables and the plugs for insulation and sealing, all of which were also specifically designed, to minimize the interference with the existing setup and accessories. It is important to ensure that the introduced changes are compatible with the use of other instrumentation, namely for local strain measurement during testing. Some of the modifications required for the various components of this apparatus are summarized in what follows.

The top platen has a central concavity to fit the dome tip of the load piston, thus ensuring a perfectly vertical load, with no restrictions on rotation of the top cap. For this reason, the transducers had to be located slightly off-centred to enable the passage of the cables without interfering with the loading area. These constraints led to an increase in the thickness of the platen, which resulted on the decision of manufacturing a new platen using acrylic, instead of stainless steel or even duralumin, to minimize the effect of its weight especially over soft samples. Adequate drainage was incorporated and appropriate cable insulation was provided by specifically designed screws and o-rings (Figure 3.13a). The position of the transducers in the top platen was mirrored in a new bottom platen, and similar modifications were made regarding insulation and drainage. Slots in both porous stones were machined for passing the transducers (Figure 3.13b).

The base pedestal was modified to provide outlet of the cables from the top and bottom transducers, which also required proper insulation and sealing, using specific

plugs (Figure 3.13c). An additional pedestal disc was also required to facilitate the passage of cables, which could otherwise get trapped especially during setup and installation at the load frame.



a) b) c)

Figure 3.13 - New and modified platens of the FEUP triaxial cell: a) top; b) bottom; c) pedestal

3.3.2.2. BE checks and installation

Prior to the installation of the transducers in the platens, the performance and calibration checks were carried out, in order to verify their functioning and especially to decide on the most suitable configuration. When there are no restrictions to the configuration, it is natural to select a positive polarity and install the transducers accordingly. In Figure 3.14 are presented the wave traces from a polarity check of the transducers in direct contact, where the polarity reversibility is clear, resulting from the rotation by 180 degrees of one transducer in relation to the other.

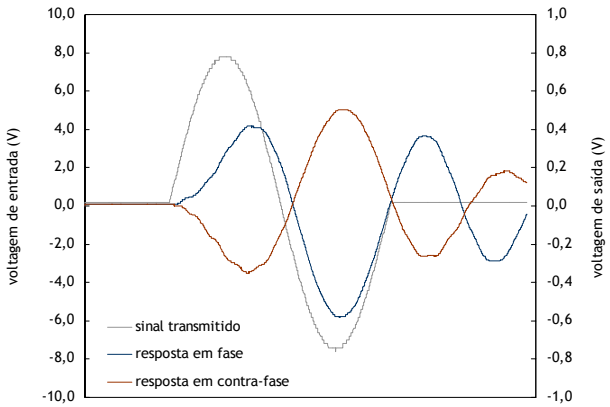


Figure 3.14 - Polarity check for the BE in FEUP triaxial cell (from Ferreira, 2003)

Each transducer was mounted so that its full length is divided in thirds between the platen, the porous stone and the protrusion to the soil specimen, of less than 4 mm. The slots in the platens and porous stones were made slightly larger than the BE

dimensions to avoid constraining the transducers, and all gaps were filled with silicone sealant, to avoid the penetration of any soil particles.

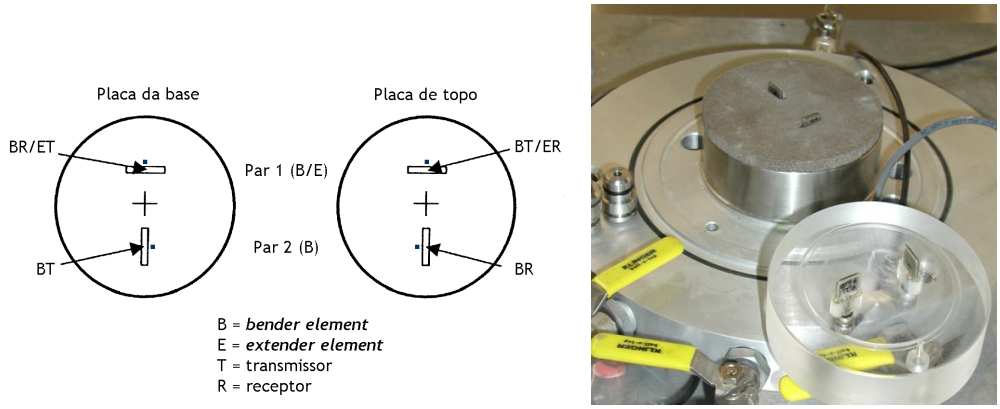


Figure 3.15 - BE and B/EE mounting scheme in FEUP triaxial platens

The setup of seismic wave measurement in this apparatus is identical to the ISMES triaxial cell, detailed in Figure 3.12. A photograph of the equipments used during testing is provided in Figure 3.16.

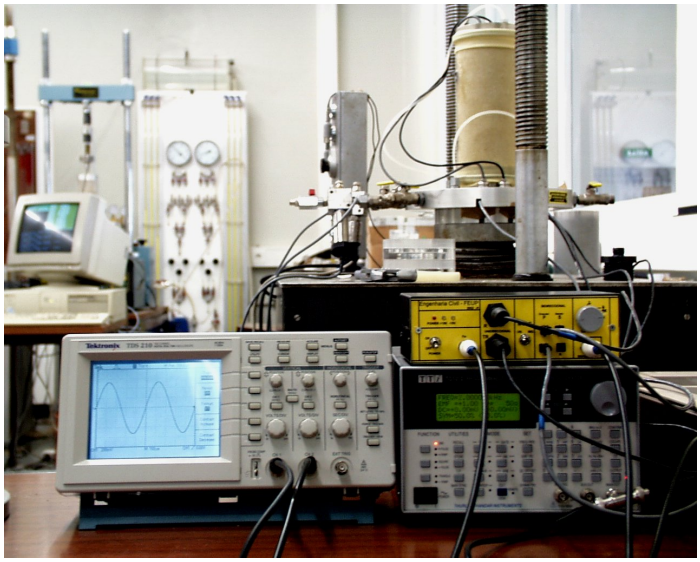


Figure 3.16 - BE electronics equipment in use for the FEUP triaxial cell (Ferreira, 2003)

3.3.3. Bishop-Wesley stress-path cell [SP100]

One of the Bishop-Wesley stress-path cells available at the Geotechnical Laboratory of FEUP enables testing 70 mm and 100 mm diameter specimens. For the purpose of BE testing, new 100 mm platens were designed to accommodate the transducers. Despite the differences in the design of this stress-path chamber in relation to a

standard triaxial, the procedure for modification of the cell and installation of the transducers was similar to that previously detailed. Some of the differences include the nature and shape of the transducers, the type of porous stone, and the location of the outlet holes for the cables.

The transducers used for this apparatus are bender-extender elements from UWA, consisting of T-shaped pairs encased in stainless steel casings. This casing is particularly useful for an easy removal of the B/EE, for example in case of damage or for running standard tests - without seismic wave measurements -, in which case the slot can be sealed with a dummy piece (Figure 3.17b).

The use of thin sintered stainless steel porous stone plates is more adequate in this apparatus, due to limitations of height inside the chamber. Top and bottom platens were redesigned to accommodate the 2 mm porous stones, with the top platen being made in acrylic to reduce the weight over the sample, similarly to the FEUP triaxial cell. Taking advantage of the configuration of the base of the chamber, the outlet holes for the cables were drilled through its side, thus facilitating the installation of the specimen and the setup of the chamber without entangling the cables (Figure 3.17c). Additional outlet holes for horizontally-mounted miniature BE from UoB were also included.

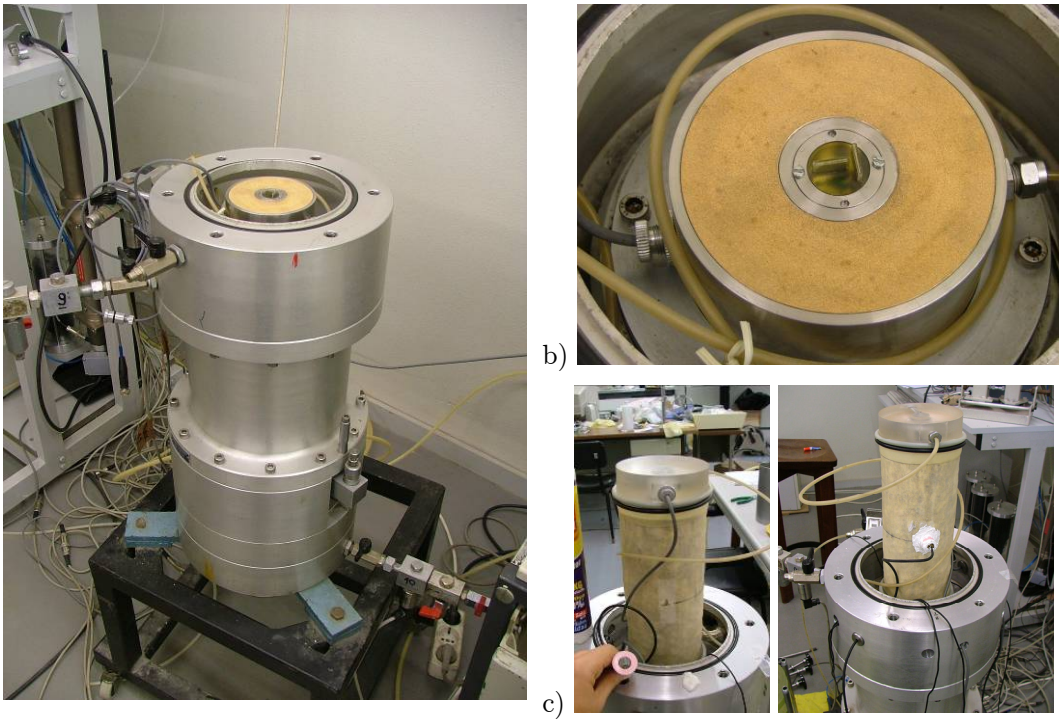


Figure 3.17 - Stress-path triaxial system at LabGEO: a) overview; b) B/EE and porous stone details; c) lateral miniature BE and outlet holes for the cables

As before, an identical seismic wave measurement setup has been adopted, as illustrated in Figure 3.18b. The control of the stress-path apparatus has been automated using the TRIAX software, running in a BBC basic for Windows, developed in the University of Bristol (Nash, 2002; Sukolrat, 2007), from the original DOS version by Toll (1993).



a) b)

Figure 3.18 - Photographs of the complete stress-path system: a) stress-path control and acquisition; b) seismic wave measurement setup

3.4. Modified resonant-column [RC]

3.4.1. Equipment details

The resonant-column apparatus used for this work is a Hardin-type oscillator, manufactured by Seiken (Japan), and it is installed at the Geotechnical Laboratory of IST, in Lisbon. Details regarding the design, functioning and operation of this resonant-column system, prior to the installation of bender/extender elements, can be found in Santos (1999).

In conventional resonant-column testing, a cylindrical specimen is subjected to torsional vibration in the form of continuous sine excitation. The frequency of the sine signal is gradually changed until resonance is reached. Under the resonant condition, it is possible to obtain the shear modulus G, using the following equation (Santos, 1999; Santos et al., 2007; Camacho-Tauta, 2007).

$$G \cdot I_p \frac{2\pi \cdot f_T}{\sqrt{\frac{G}{\rho}}} + t \cdot g \cdot \left(\frac{2\pi \cdot f_T \cdot L}{\sqrt{\frac{G}{\rho}}} \right) \cdot \left(K - J_A \cdot (2\pi \cdot f_T)^2 \right) = 0 \qquad [3.1]$$

where

I_P polar moment of inertia of the cylindrical specimen

f_T system resonance frequency for torsional motion

ρ soil mass density

L specimen length

K active end torsional apparatus spring constant

J_A rotational inertia of the active end platen system

In terms of the RC test procedure, the resonance frequency of the system is experimentally obtained at each test stage. For the present research, the laboratory procedure was performed without any kind of automatic closed-loop control, thus resulting in a relatively time-consuming process. This, however, could be improved with the use of a automated system. Within the scope of another research project (Santos et al., 2007; Camacho-Tauta, 2007, 2009), various options were analysed:

- application of few cycles at a fixed frequency with the measurement of the phase lag between the input and output signals; the system modifies the frequency by a defined increment and then the process is repeated until the signals are in phase
- application of a sine sweep (signal in which the frequency is linearly increased with time, within a preset range of frequencies and interval); the amplitude of the response varies with frequency; the frequency to which the transfer function reaches a peak is the resonant frequency (f_T) of the system
- use of random noise instead of sine sweep; the energy is distributed by all frequencies and it is possible to measure very low strains (Cascante and Santamarina, 1997); the frequency content from f_1 to f_2 may be adjusted after a preliminary broadband test in order to obtain better results.

The latter option was subsequently implemented in an automatic system to solve this problem, providing more solutions to resonant-column testing (Santos et al., 2007).

For the definition of the resonance frequency of the system, a few cycles of a continuous sinusoidal wave at an initial frequency are applied. The computer software, acquiring data from the electronic equipments of the RC, provides measurements of the phase lag between the input and output signals. The input frequency is then manually adjusted until the signals are in phase, whilst keeping the shear strain, measured by the output amplitude, as low as possible. The values of resonance frequency, current, output amplitude and displacement of the sample are recorded, for the final computation of the RC results. An algorithm, previously developed by Santos (1999), was directly used to process the data, after verification of the calibration parameters. This program automatically provides the shear strain, shear modulus, damping ratio and void ratio for each test stage.

3.4.2. Installation of the BE

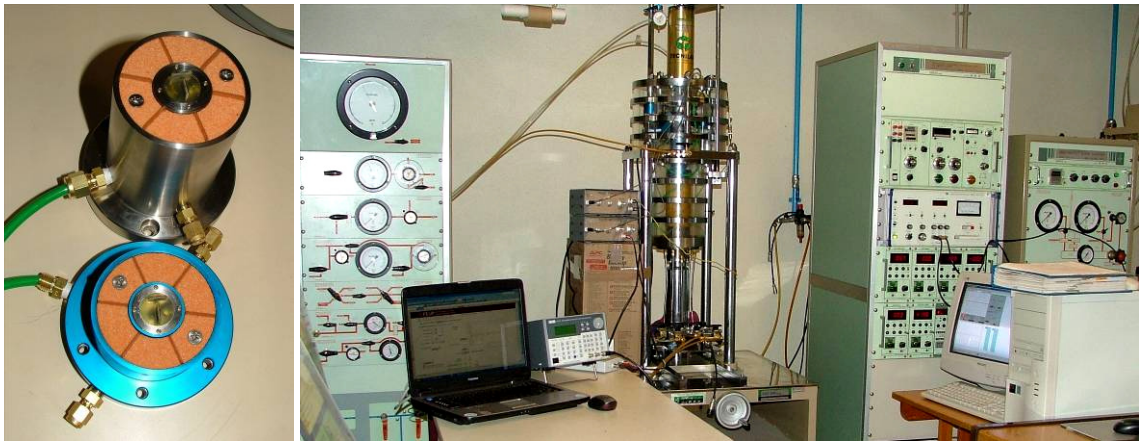
Similarly to the previously described triaxial apparatuses, modifications in the platens were required for the installation of the BE. These were designed in co-operation with IST and new platens were ordered and made by the manufacturer, to ensure optimal adaptability and quality. The bender elements used were also a T-shaped pair of B/EE encased in a stainless steel casing, manufactured at UWA (Figure 3.19).

During installation of the B/EE, special attention was given to ensure that the cables would not interfere with the movement of the free active-end. Nevertheless, this modification in the setup introduced slight variations in the mass and inertia of the top cap, which are likely to affect the calibration parameters of the apparatus and consequently the computed results. As detailed by Camacho-Tauta et al. (2008), the apparatus was re-calibrated using the method proposed by Tatsuoka and Silver (1980) to determine the new parameters of the apparatus equipped with BE.

In this setup, it is possible to make practically simultaneous measurements of RC and BE, using two (or more) interpretation methodologies for the BE technique, at any stage of testing. Hence, this setup enables determining which BE method most closely matches the shear wave velocity measured by the RC, taking into account the respective strain level. Figure 3.19 shows photographs of the apparatus, with focus to the modified platens equipped with the T-shaped pair of B/EE.



a) b) c)



d) e)

Figure 3.19 - Resonant column device with bender elements: a) original porous stone; b), c) installation of B/EE; d) modified platens; e) overview of the testing apparatus

The usual set of electronic equipments for BE measurements has been used: programmable function generator; UWA input and output multiplexers; an oscilloscope and/or a PICOScope, both connected to a PC, acquiring using ABETS.

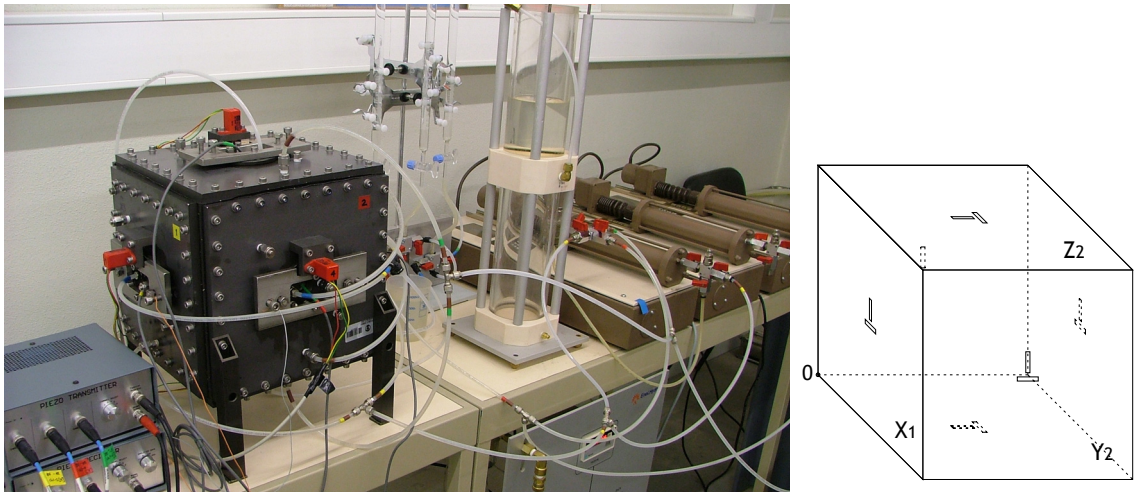
3.5. True triaxial apparatuses

3.5.1. FEUP true triaxial chamber [TT]

3.5.1.1. Installation and equipment details

A new true triaxial testing apparatus has been developed, in a collaborative project between FEUP and the University of Western Australia. Its original design is thoroughly described in Ismail et al. (2005). This apparatus is made of anodized aluminium and consists of six pairs of square platens mounted in a cubical frame of 250 mm internal side length. Uniform strains are applied in the three orthogonal directions by means of rigid platens. A thick rubber diaphragm, between each piston

and an outer plate, is pressurized using a water pressure controller. Hence, for the application of independent stresses in the three directions (X, Y and Z), three GDS pressure and volume controllers were used, which distribute the pressure to each pair of platens of the same direction, as illustrated in Figure 3.20a. As a convention, the two horizontal directions were taken as X and Y, while the vertical direction was taken as Z (Figure 3.20b). For the nomenclature of the platens, a virtual origin of the platens was considered at the furthest lower left corner, as indicated in the figure (point 0), defining the intersection of the first platens of each direction, that is, X1, Y1 and Z1.



a) b)

Figure 3.20 - FEUP true triaxial apparatus: a) overview; b) nomenclature for the platens

Each platen is attached to a guide in contact with the outer plate, which limits the movement of each piston inside the chamber to 10 mm. Hence, for an initial sample length of 250 mm, the maximum linear strain in any direction is 8% (considering the movement of both faces). Given the simplicity of this design, there is a limitation in this apparatus regarding the corners. In fact, there is no control of the stresses exerted on the corners; however, considering the large size of the specimen, this effect is considered to be negligible. For the measurement of displacements, a potentiometer-type displacement transducer is fixed to the outer wall of each platen, directly measuring the relative displacements of the guide (and consequently of the inner platen) and a fixed point outside the chamber (Figure 3.20 and Figure 3.21). The arrangement of the different elements of the platen, including the guide, is such that there is no possibility of tilt of the guide. Drainage is achieved by an 8-mm diameter hole fitted with a porous stone in each of the platens, and volume change is measured in three independent burettes.

The most innovative aspect of this equipment, in relation to previous designs of rigid-boundary true triaxial apparatuses, is the capability of measuring seismic wave velocities in all directions. For this purpose, a cylindrical hole has been drilled at the centre of each wall (across each platen, guide and outer plate) for the installation of the piezoceramic transducers (Figure 3.21).

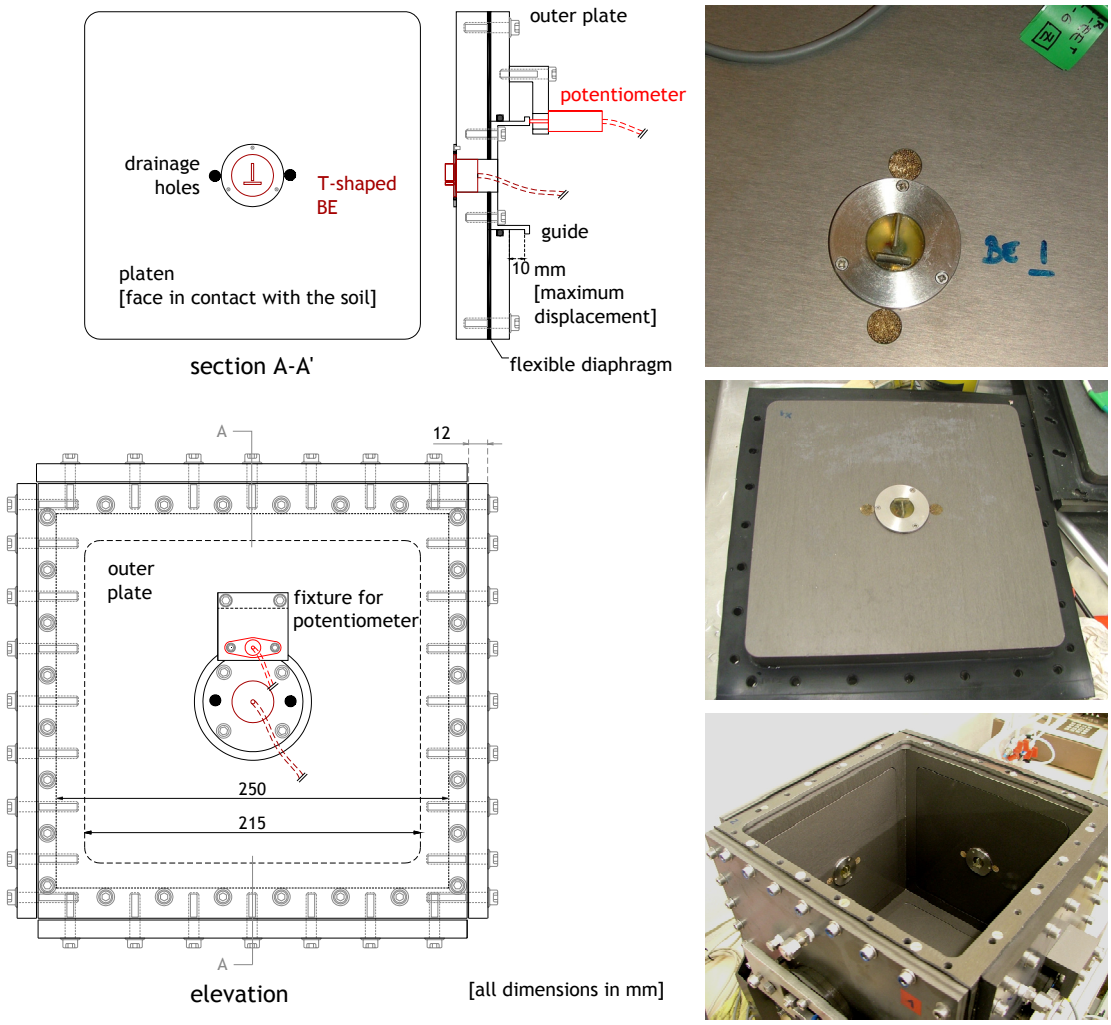


Figure 3.21 - Schematic of the FEUP true triaxial apparatus: schematic diagram and details of the location of the BE

3.5.1.2. GDS controllers

The GDS hydraulic controllers [STDDPC model] are pressure or volume controlled, using deaerated water (or oil) as pressurizing fluid. Each comprises a stepper motor acting on a piston, which moves and directly applies pressure to the water, as illustrated in Figure 3.22. The control is made in closed loop circuit and enables variations as low as 1 mm^3 per motor step, while operating up to 1 MPa and/or 200

cm^3. In stand alone mode, the instrument can work as a constant pressure source, a volume change gauge, a flow pump and/or a digital pipette. It can also be programmed through its own keypad to ramp or cycle pressure and volume change linearly with time. In computer control mode, the instrument fully enables computer-automated test control and data logging via the RS-232 computer interface (GDS Instruments, 2001). In order to use more than one controller, a multiplexer is provided to connect up to four controllers to a PC via the serial port.

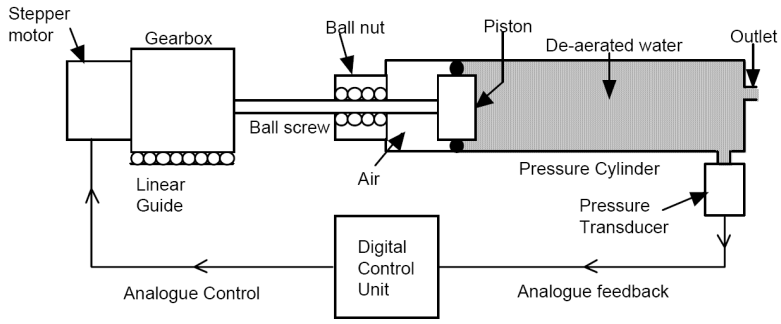


Figure 3.22 - Diagram of a GDS standard pressure controller (GDS Instruments, 2001)

Given the quality and reliability of these instruments, the calibrations were minimal and limited to control checks and to the validation of the measured quantities by direct comparison with pressure transducers and volume change measurements.

As mentioned above, each of these controllers stores up to 200 cm^3 of deaerated water. This volume is clearly insufficient to fill the two platens in each direction with water during the setup and installation of a new test and occasionally during the course of a test. Ideally, greater capacity controllers should be used (for instance, the 1000 cm^3 GDS controllers), but another solution was devised to successfully overcome this limitation during setup. A pressure tank, left open at atmospheric pressure, was installed in between the controllers and the apparatus. Its volume of several litres enables filling all platens at a rapid flow (Figure 3.20a; Figure 3.23). A block of valves and connectors separates each pair of platens per axis (and per GDS), providing further control over the filling process.
Despite being generally used as a pressure-controlled apparatus, it is important to minimize the amount of air trapped in the space between the platens and the flexible membrane. For that purpose, at the start of each test (except for undisturbed samples), each platen is fixed at the maximum deformation position (protruding inwards) and filled with water, while air is released by the bleeding valve, until the water starts to flow through this valve. Then, the platen is manually pulled to the minimum deformation position (inline with the face of the inner cube), forcing the air

out to the atmosphere at the pressure tank and also at the bleeding valve. This procedure is performed twice to ensure maximum air removal, in all six platens.

3.5.1.3. Volume change measurement

The movement of the platens is monitored by the potentiometers and is also related with the volume change in the controllers (initial differences are expected due to the air possibly entrapped between the platen and the membrane). The actual volumetric change of the soil specimen inside the apparatus is also related with the movement of the platens, but can be more accurately determined for saturated samples by measuring the volume of water in and out of the specimen in each direction. For that purpose, an assembly of three 100 ml burettes has been added to the apparatus and connected to each pair of platens in the same direction. In each platen, two small holes adjacent to the BE, are equipped with porous stones: one of these is used for percolating pore water and measure volume changes using the burettes; the other is currently not in use, though a pore pressure sensor can be fitted to provide accurate and continuous measurements. This system enables not only variations in pore water to be observed, but also to flood the soil at a very low water pressure, corresponding to the maximum height at the top of the burettes, with benefits in terms of the integrity of the soil structure. The burettes, valves and connections are shown below in Figure 3.23.

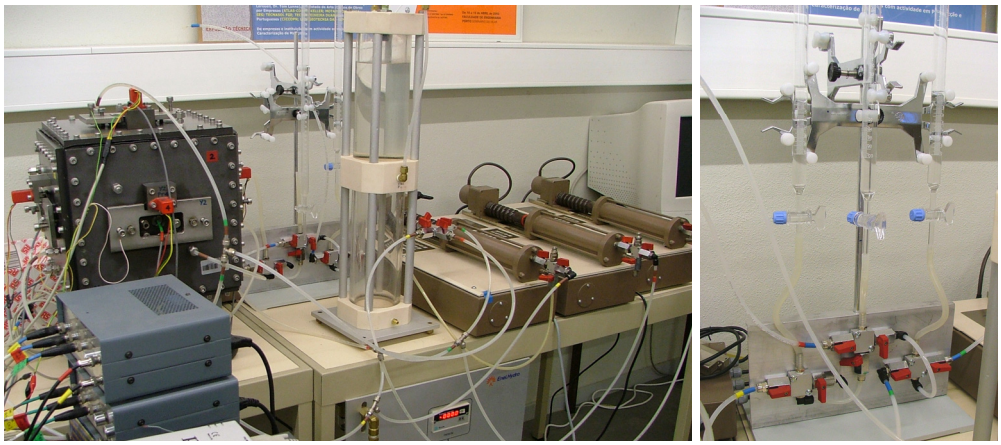


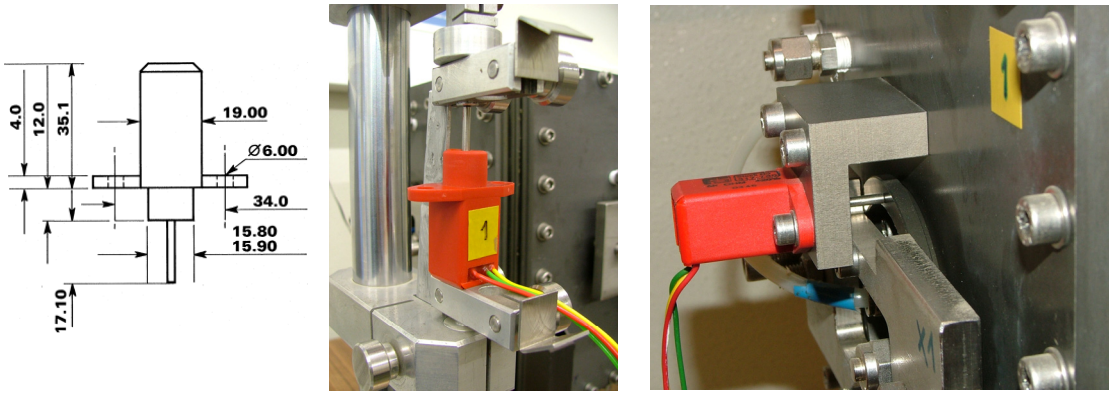
Figure 3.23 - Volume change measurements in the TT apparatus, using burettes

3.5.1.4. Displacement transducers

For the measurement of displacements, potentiometer-type transducers [PT] were used, manufactured by RS [ref. 317-780] (Figure 3.24a). The effective travel of the PT is 10 mm ± 0.5 mm and its mechanical travel is 12.5 mm, which fits the

maximum movement of the platens, mentioned above, of 10 mm. These low-cost transducers are small and perfectly suited for external measurements in each of the faces of the apparatus. For data acquisition, the potentiometers are connected to a NI SCB-98 terminal board, which is in turn connected to a NI PCI-6221 data acquisition card, installed in the computer. The potentiometers are connected to the terminal board as differential input channels. The air temperature sensor available at the board is switched on, to enable temperature monitoring. For the calibration of these transducers, shown in Figure 3.24b, a micrometer calibrator was employed and the linearity parameters were directly computed.

Each PT is positioned in place using a specific accessory fixture and its inner rod is in direct contact with the guide of the platen, as illustrated in Figure 3.24c.



a) b) c)

Figure 3.24 - Potentiometers for platen displacement measurement: a) diagram; b) PT1 during calibration; c) PT1 in use at the apparatus.

Since there is one potentiometer in each platen, the numbering of the PT logically followed that of the platens: PT1 in X1, PT2 in X2, PT3 in Y1..., and PT6 in Z2.

The stability of these transducers was analysed in detail in different situations, to assess the resolution of the measurements. One of those experiments consisted of placing all six potentiometers in the respective platen at a fixed position and recording the measurements over an extended period of time. The graph presented in Figure 3.25 corresponds to partial readings of that experiment, taken at the first period of 200 minutes, where the fluctuation of the values measured by the measurements is lower than 0.008 mm, thus can be considered acceptable for monitoring small strain deformations.

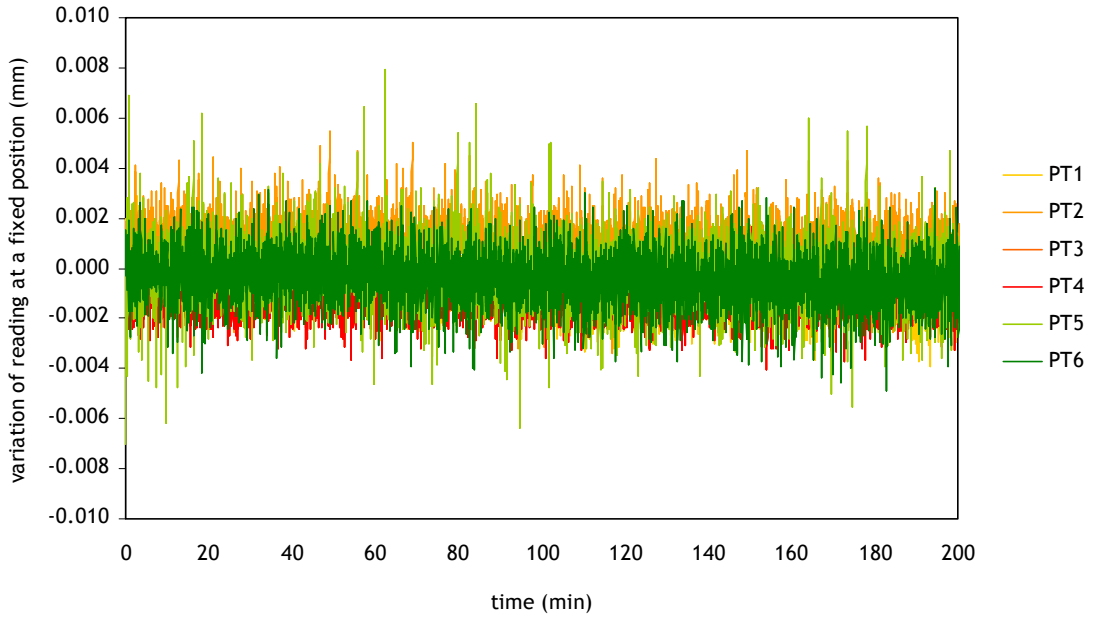


Figure 3.25 - Stability test on the displacement transducers at fixed positions

3.5.1.5. Control and data acquisition software

Taking into account the variety and complexity of the equipments involved in each test and the volume of data to acquire, appropriate software for control, monitoring, and acquisition of the pressure controllers and the displacement transducers was required. In the absence of suitable commercial programs, a new software tool was conceived and implemented as a control and data acquisition system.

For continuous data logging and acquisition of stresses and volumetric changes in the controllers and displacements in the potentiometers, LabVIEW™-based software was developed for this apparatus, while fully controlling the application of stresses, under any stress-path. LabVIEW (abbreviation for Laboratory Virtual Instrumentation Engineering Workbench) is a platform and visual programming language from National Instruments. Its graphical language is simple, intuitive, and well-suited for data acquisition, instrument control, and industrial automation. The selection of this programming language also reflects the intention of producing an open-source tool, allowing for future changes and adjustments; the flexibility and easy-to-use interface of this application facilitate these objectives.

For an adequate operation, the pressure controllers should not only apply the predefined pressures independently to the respective platens, but also follow a three-dimensional stress-path, in a synchronous manner. These hydraulic actuators have

internal pressure and volume control, thus the program needs to establish the communication with each actuator, in order to send the desired orders (target pressures and path) and acquire the real-time response for monitoring, data acquisition and file storage.

On the other hand, for the controlled deformation tests, it is further required that the system responds interactively, by combining the response of the displacement transducers with the volume adjustment of the controllers and the measurement of the corresponding pressures induced by the soil in each fixed direction. In this case, the directions of null deformation (generally, both horizontal) and of imposed loading (usually the vertical direction) need to be predefined. Using this program routine, the null deformation condition is kept by adjusting the volume of water inside the controllers in those directions, thus necessarily altering the pressures, which are in fact induced by the soil. Since there are two displacement measurements per axis, the deformation control considers the averaged value of those readings. The relation between vertical imposed pressure and the measured horizontal pressures enables to establish a correspondence with the at rest stress state.

3.5.1.6. Data acquisition application and user interface details

In order to comply with the requirements of this system, the developed application was divided into four parts, separated by menu tabs. The first menu tab is the starting point, where the configurations of the system, the communication with the controllers and the correspondence between the actuators and the platens of the cube are established (Figure 3.26). For the definition of new control orders, the user should be acquainted with this type of systems, having the option of controlling pressures and volumes (via the GDS controllers), or deformations (from measurements of the potentiometers). The orders introduced in the application are defined for each actuator, as shown in Figure 3.27a, and three main types of control are available: linear variation, hold present value, or hold other user-defined value. The no-control option is also provided, enabling measurement of pressure changes without volumetric change.

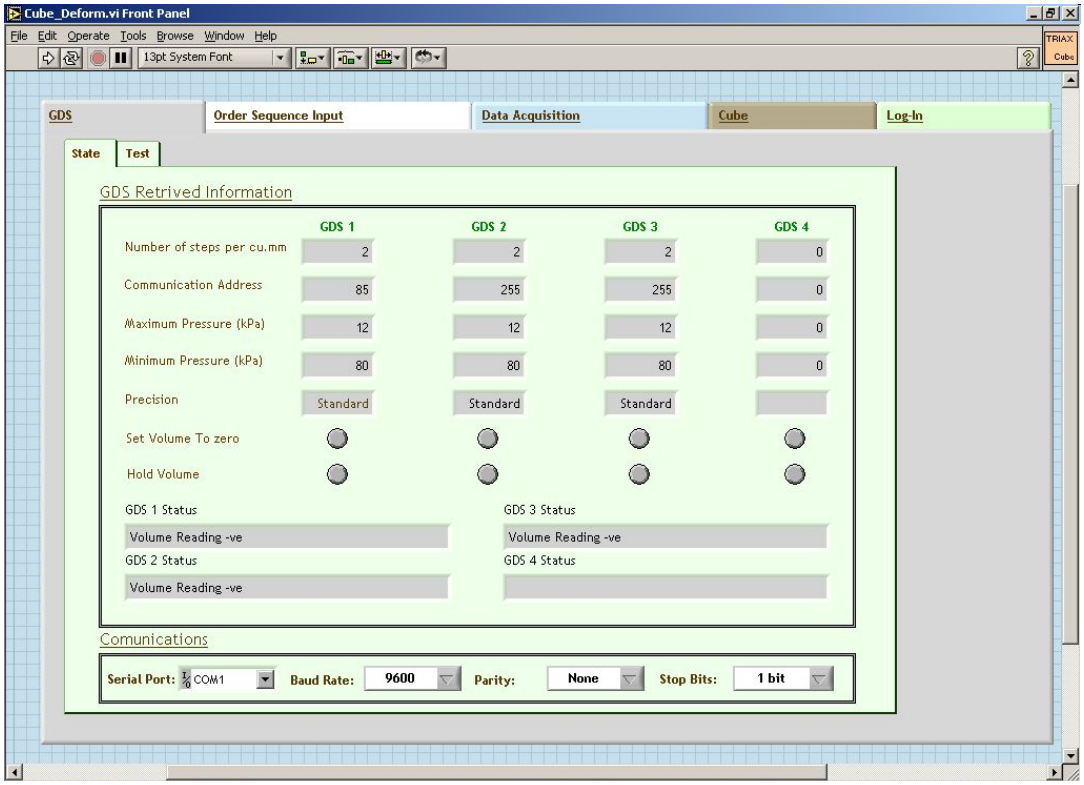
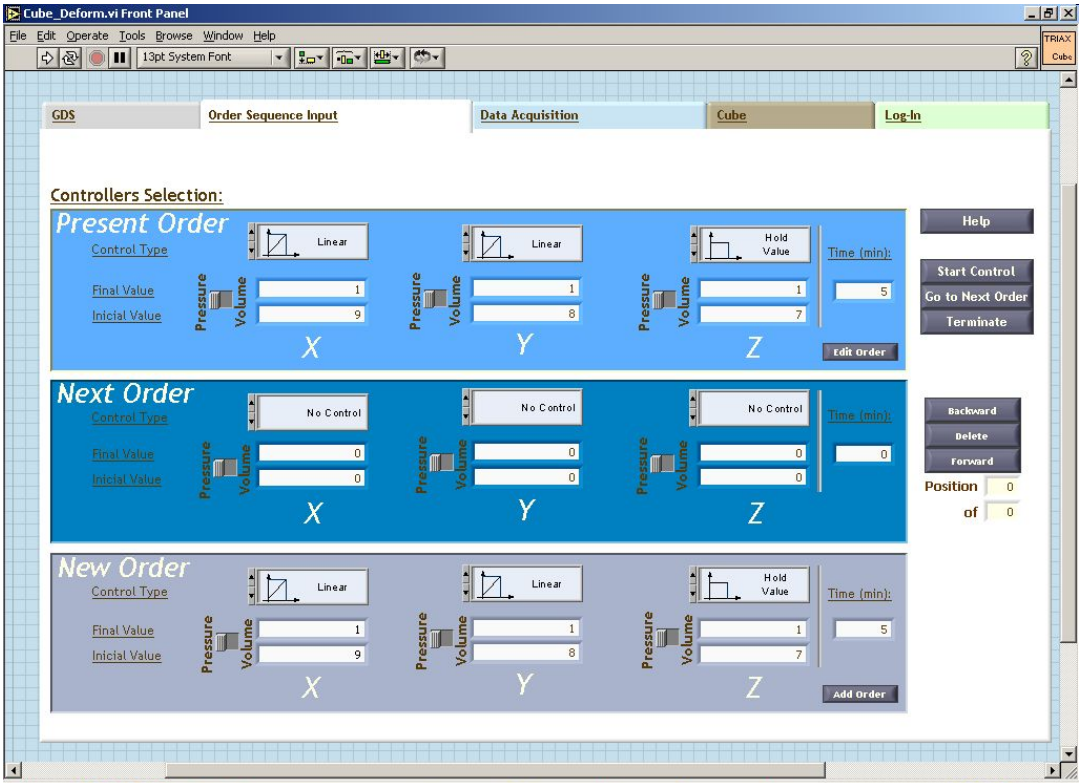


Figure 3.26 - Menu tabs of the LabView application: configuration of communications

In terms of data acquisition, the values of pressure and volume of the GDS controllers are continuously recorded, as well as the displacements of the faces of the "cube". Data storage to a predefined location is set by the user at a defined rate, generally 30, 60, or 120 s (2 s minimum), as presented in Figure 3.27b. In order to facilitate visualizing the evolution of the test, the various acquired parameters are presented in different charts, in separate screens (or menu tabs). In one of the tabs, two charts are presented, for pressure and volume against time, respectively, for all the selected actuators (Figure 3.27b). On another tab (Figure 3.28), real-time displacement values per transducer and per axis are displayed, alongside with the values of pressure and volume in each direction, complete with the corresponding graphs. This software application was checked and tested in real operating conditions, prior to its use in valid soil tests.

a)



b)

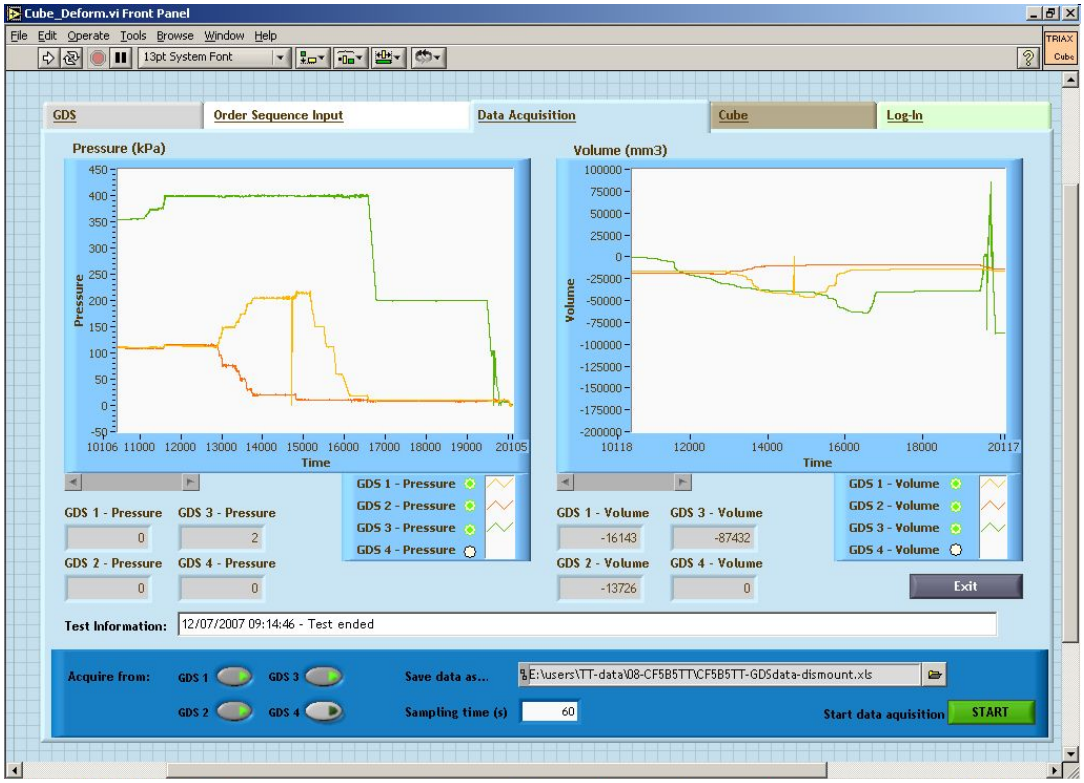


Figure 3.27 - Menu tabs of the LabView application: a) order sequence input; b) data acquisition setup and plots of pressure and volume



Figure 3.28 - Menu tabs of the LabView application: real-time monitoring of pressures, volumes and displacements

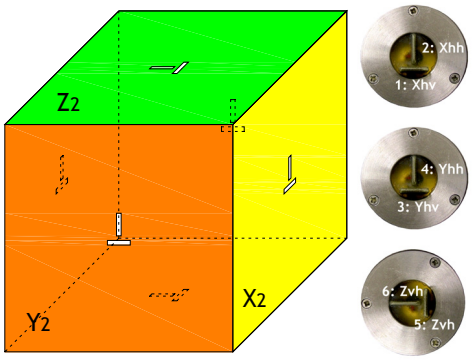
3.5.1.7. Seismic wave measurements

Ismail et al. (2005) employed shear-plates in this apparatus, where a single pair of transducers outside the chamber was moved to each pair of platens in turn, for the measurement of shear waves in all three directions. A titanium or stainless steel disc, fixed to the inside of each platen, but accessible from the outside through a threaded hole, served as coupling element. The calibration of the seismic wave measurements was made to take this element into account. The possibility of testing under harsh conditions, whether chemically-aggressive or at elevated pressures, without affecting the transducers and the ability to rotate the transducers to polarise the movement of soil particles in different orientations are other important advantages of this setup.

This solution was initially applied in the present research, successfully but unsatisfactorily. Despite being a cost-effective solution with interesting features, in practical terms and for the testing conditions of this research, on natural materials at relatively low pressures, it is very time-consuming and hence inconvenient. As detailed below, fourteen differently polarised and propagated shear wave velocities are to be measured and the use of a single pair to cover all these measurements is not feasible with the desired level of reliability. Issues such as coupling, perfect

positioning and alignment, grounding, among other, have to be considered, checked and, if necessary, resolved in each measurement, leading to unacceptable testing times (over 2 hours per loading stage), incompatible with the normal course of a test.

As an alternative, T-shaped pairs of B/EE fixed to the inside of each of the six platens have been used, which enable waves to be propagated in two orthogonal directions, with clear benefits in terms of operation. The possibility of installing bender elements in each of the platens of this apparatus enables not only measurement of orthogonal seismic waves in the horizontal [X and Y] and vertical [Z] directions, but also in diagonal (or inclined) directions. The arrangement of the bender elements inside the chamber has been selected in order to maximize the number of wave propagation and polarization directions, as illustrated in Figure 3.29a. Note that measurements in the YZ direction are not considered, since the alignment of the transducers does not permit these measurements to be made. This combination of direct and inclined measurements is redundant, but at the same time necessary: given the uncertainty and subjectivity of these measurements, the possibility of duplicating results is useful. However, for the present study, the measurement of shear (and compression) waves in all possible directions can rapidly become a cumbersome task: there are fourteen possible shear wave measurements, as shown in Figure 3.29b, which double if compressional waves are also to be separately recorded.



a)

output / input	ch1: X2hv	ch2: X2hh	ch3: Y2hv	ch4: Y2hh	ch5: Z2vh	ch6: Z2vh
ch1: X1hv	→		↗		↗	
ch2: X1hh		→		↗		↗
ch3: Y1hv	↗		→			
ch4: Y1hh		↗		→		
ch5: Z1vh	↗				→	
ch6: Z1vh		↗				→

b)

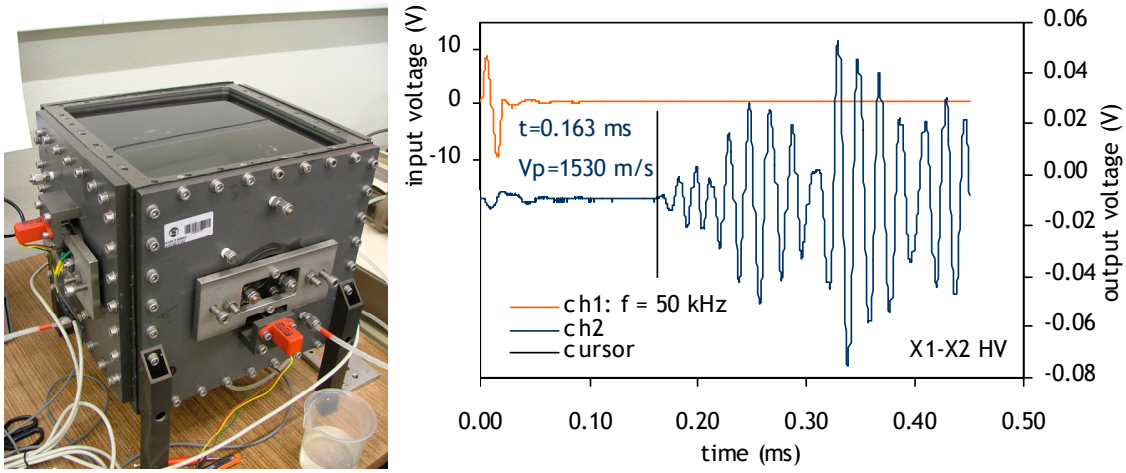
Figure 3.29 - Arrangement of the B/EE in the apparatus: a) 3D view and notation for each transducer; b) direct [→] and inclined [↗] wave measurements

Even more than in other apparatuses, in this case a solid, objective yet flexible method of obtaining and interpreting seismic wave measurements is paramount. For that reason, after a series of tests and experiments, the ABETS software was considered most adequate, for its unbiased approach to BE results. Although initially the use of both time and frequency domain techniques was unquestionable, it was

later decided to narrow acquisition to frequency domain data, for the following reasons: a) the comparison of both techniques provide consistent parallelism, similar to that observed in other tests, namely in axisymmetric triaxial conditions; b) despite having automated many steps in the data acquisition process, the proposed variety of wave directions analysed via both techniques required a time window incompatible with the desired course of a test; c) an automatic post-processing tool was developed, as will be detailed in the following chapter in section 4.5, which further reduces the variability of the FD results, by the consideration of different frequency moving-windows to compute travel time.

Nevertheless, occasional measurements in TD were made at particular points and specific conditions, whenever necessary. The setup consisted, as before, of the function generator, 6-channel transmitter and receiver multiplexers and a spectrum analyzer-oscilloscope (PicoScope) connected to a PC. Both multiplexers, designed at UWA, enable to manually switch channels, and any input-output channel combination is accepted, as required for inclined measurements.

Due to the nature and configuration of this apparatus, there was a suspicion that shear waves could travel directly through the platens, from which a high shear wave velocity would result. As a means of calibrating the seismic wave measuring system, the apparatus was filled with water and the propagation of P- and S-waves was tested, to assess grounding and shielding (Figure 3.30a). This calibration test revealed that, using appropriate grounding, shear wave propagation through the platens was negligible. On the other hand, it was possible to ascertain the performance of the B/EE for the measurement of P-waves, which were measured in direct and inclined directions. As the example in Figure 3.30b, the measured V_P values in all testing directions ranged from 1500 to 1550 m/s, typical of the velocity of sound in water.



a) b)

Figure 3.30 - Seismic wave calibration of the TT filled with water: a) view of the test; b) example of results: TD signals for P-waves using B/EE HV from X1 to X2

3.5.2. UoB cubical cell [CC]

3.5.2.1. Installation and equipment details

A flexible boundary true triaxial Cubical Cell apparatus [CC] has been used at the Geomechanics Laboratory of the University of Bristol. This stress-controlled CC enables exploring the stress-strain response of soils under any pre-determined monotonic and non-monotonic stress paths. It can be used for testing dry, partially saturated and fully saturated specimens, in drained or undrained conditions. The design of this apparatus was inspired by the one developed at the University of Colorado at Boulder (Dewoolkar et al., 1997). This apparatus and its application to the characterisation of the multiaxial behaviour of sand are detailed in Sadek (2006).

The apparatus consists of a stainless steel frame, which creates the inner chamber where the soil specimen is installed. In each face of the frame, a flexible rubber cushion is pressurized by air and used to transmit uniform controlled normal stresses to the surface of the sample. Six stainless steel external walls, fixed by six bolts each, ensure sealing of the pressurised cushion. Figure 3.31 shows a schematic view of the CC chamber including the frame, walls, rubber cushions and local instrumentation. Two diagonal cylindrical ports are machined through the frame providing the potential to connect the specimen to back pressure, drainage or vacuum lines. Two inlet connections are located on each external wall, one for the application of air pressure to the cushion, and consequently to the sample, and another for rapid pressure release, namely at the end of a test. For the installation of piezoelectric transducers, a threaded hole with a specially-designed insulating plug is used in the centre of the wall, enabling the B/EE cable to pass securely from the inner chamber to the outer side of the apparatus. Three linear variable differential transformers [LVDT], each consisting of an external stainless steel tube and an inner rod, are mounted on each face of the apparatus, in a total of eighteen LVDTs, for measuring local displacements. The LVDTs are arranged to form an equilateral triangle, centred with the centre of the wall. The external LVDT tube is fixed to the respective wall and covered with epoxy to prevent any leakage of pressurised air inside the cell, whereas the tip of the inner rod is kept permanently in contact with the rubber cushion by means of disc magnets.

The frame is fixed to a specially designed steel stand by six stainless steel bars, connected in six of the eight corners of the apparatus (the remaining two corners are unsupported due to the existence of the diagonal ports), as illustrated in Figure 3.31.

The installation of casters beneath the stand provides effortless mobility of the apparatus around the laboratory.

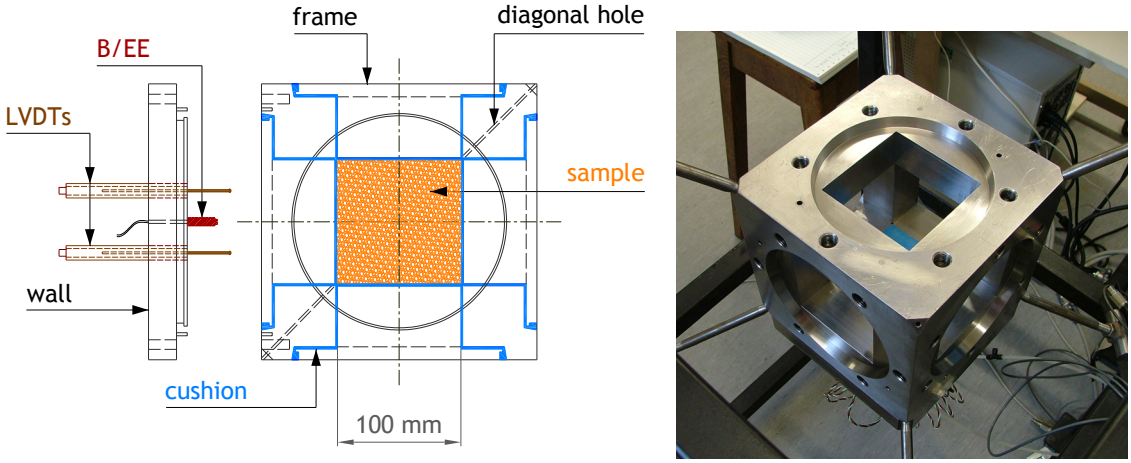


Figure 3.31 - CC chamber: schematic diagram (after Sadek, 2006) and photograph of the frame

3.5.2.2. Control and data acquisition

The operation of this true triaxial apparatus requires a complex system of sophisticated instrumentation, precise control, and adequate acquisition. A general layout of the system and instrumentation components is presented in Figure 3.32, as reported by Dihoru et al. (2005) and detailed by Sadek (2006). In this apparatus, the pressure fluid is air. Using specific software, the pressures applied to the platens are controlled by three pressure regulators [PR] and monitored by three pressure transducers [PT]. For strain monitoring, three linear variable differential transformers [LVDT] have been installed in each of the six faces of the cubical cell, in a total of eighteen transducers.

LabView™ software was used for control and data acquisition and a vast number of programmes were especially developed for this device by previous researchers (Dihoru et al., 2005; Sadek, 2006) to fulfil the testing requirements, namely for the different loading conditions and stress paths. The computer dedicated to this system has been equipped with in-board analogue input and output cards, both from National Instruments, Inc [NI]. Each of these cards is complemented with an external box, to which the wires from all instruments are connected. In order to automatically control the application of pressures, the NI PCI-6713 analogue output card has been installed, which sends the orders defined in the computer to the pressure regulators.

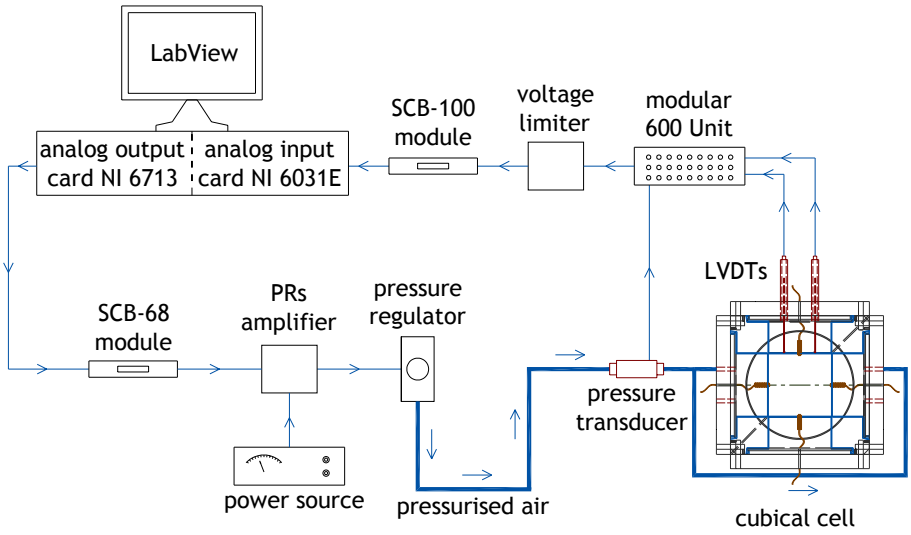


Figure 3.32 - General layout of the instrumentation components of the CC testing system (adapted from Dihoru et al., 2005 and Sadek, 2006)

The pressure values measured by the pressure transducers are fed back to the computer and the orders are reconfigured to reach the desired values. Being an air-pressured system, its application is nearly instantaneous; consequently, the program should be configured to produce a gradual and balanced pressure increase, instead of an abrupt pressure change.

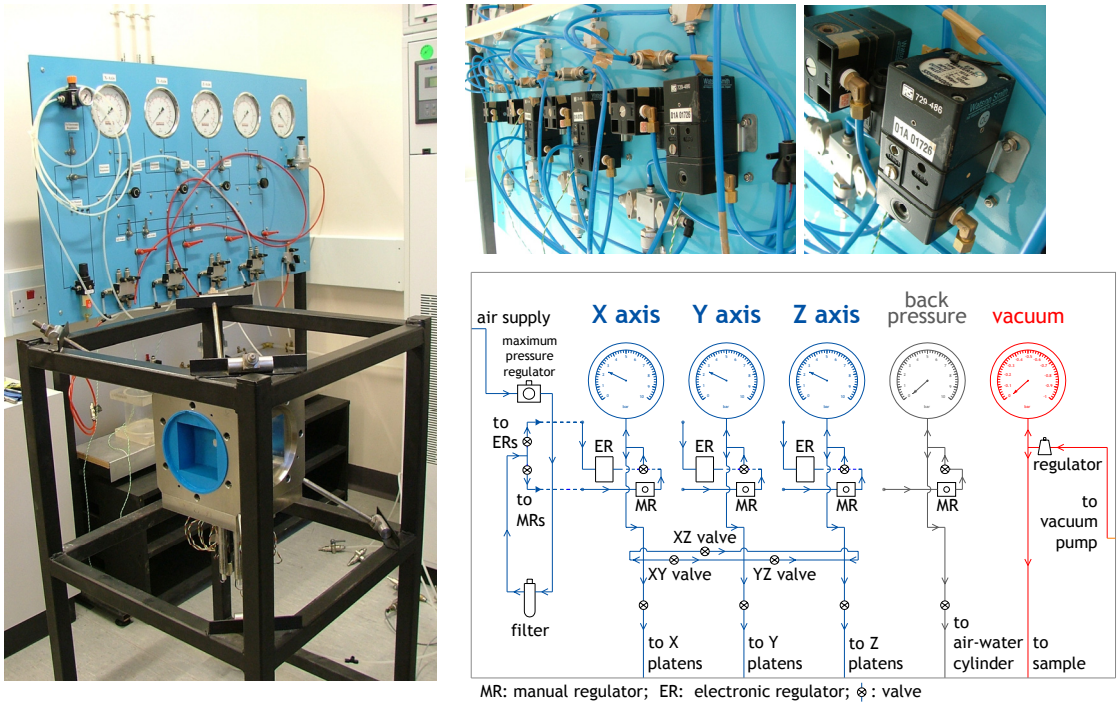
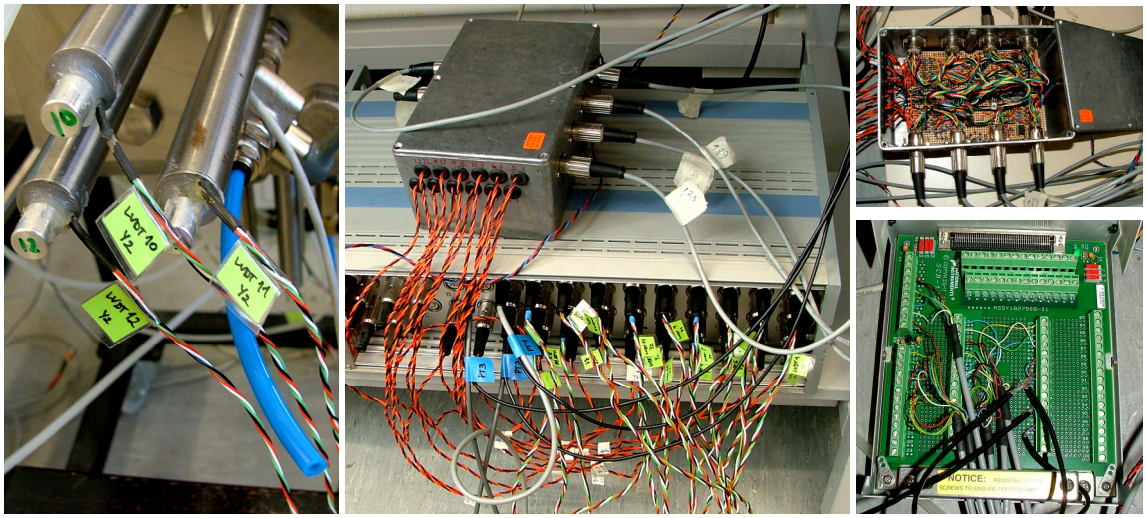


Figure 3.33 - Pressure panel: photographs and detailed diagram (adapted from Sadek, 2006)

For data acquisition, the NI PCI-6031E analogue input card was used, complemented by a SCB-100 connector block (or box). All eighteen LVDTs and the three PTs are connected in this box. In order to wire all the cables from the instruments correctly, it is necessary to know how the card recognizes each channel, as provided by its quick reference chart. After allocating each channel to each transducer, these must be correctly introduced in the software for correct channel configuration, using LabView's Measurement and Automation Explorer [MAX]. This is usually a one-time operation (for details, see Appendix A3).



a) b) c)

Figure 3.34 - LVDTs: a) clear identification; b) modular unit and voltage limiter; c) inside the voltage limiter and connector boxes

3.5.2.3. Displacement transducers [LVDT]

For the measurement of displacements, each platen is equipped with three Linear Variable Differential Transformers [LVDT], placed in a triangular arrangement, in a total of eighteen. The LVDT have been manufactured by MacroSensors (see appendix for details). The numbering of the LVDT is an important step in the planning of the tests, given the number of transducers in use, in order to have a clear and unambiguous perception of the movement of the specimen inside the cell. For example, corresponding transducers, that is, those face-to-face in the same alignment in opposite platens, should be promptly identified using a simple mnemonic. Bearing these considerations in mind, the numbering in the platens has been altered from the original configuration and made as logical and simple as possible. The logic underlying the new numbering configuration comprised:

1. sequential ordering by axes and by pairs of platens of the same axis: X1 X2 → Y1 Y2 → Z1 Z2;
2. sequential numbering of corresponding pairs of LVDTs by the addition of 3 (e.g. LVDT1 in platen X1 faces LVDT4 in platen X2; LVDT15 in platen Z1 faces LVDT18 in platen Z2);
3. considering the first LVDT in each platen as "single" or as "the tip of the triangle", that is, as the one not horizontally nor vertically aligned with any other; this should also be the transducer facing two screw holes of the platen.
4. numbering the LVDTs of the odd platens (X1, Y1, Z1) in the opposite clockwise direction of the even platens; this is necessary to make the LVDTs correspondence (between facing platens) work. Looking at the sample, the LVDTs on odd platens are numbered anti-clockwise; conversely, looking at the inside of the platens, these are numbered clockwise.

The following table and figures clarify this configuration. Using a paper model has proved particularly helpful in this as well as in other tasks.

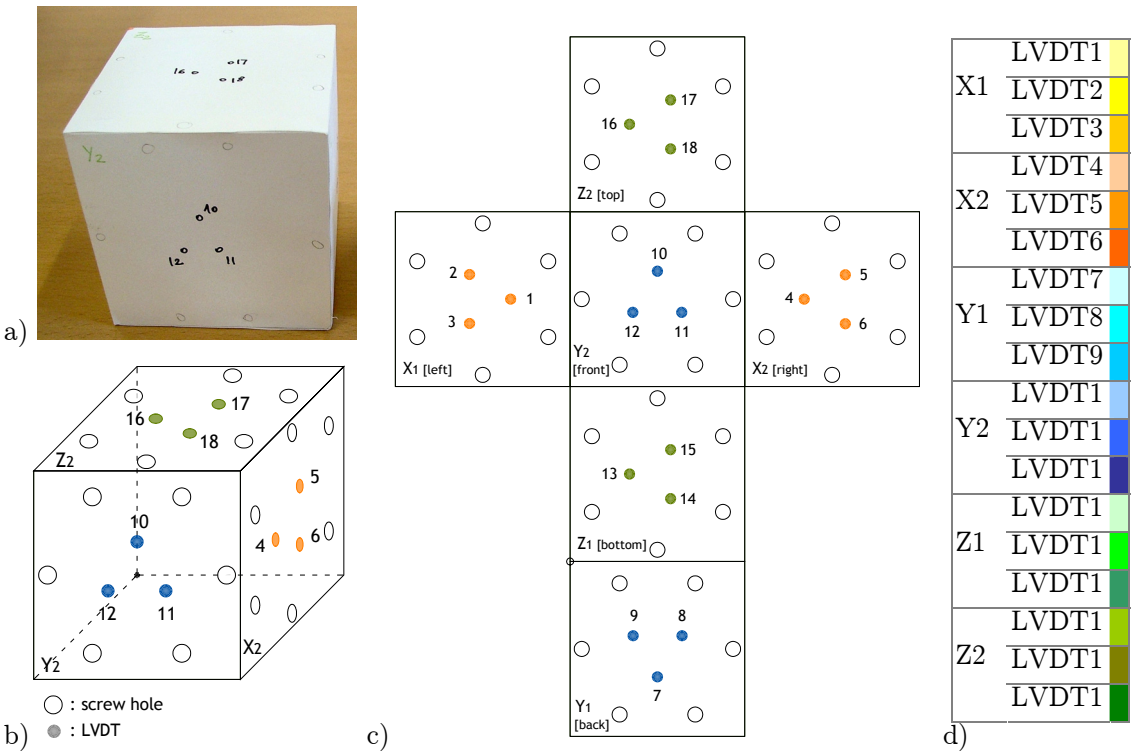


Figure 3.35 - LVDTs: a) paper model; b) location of LVDTs in platens X2, Y2 and Z2; c) "unfolded" cube with the layout of all platens; d) colour code and numbering in each platen

As illustrated earlier in Figure 3.34a, clear identification of the LVDTs is also fundamental not only to minimize errors during setup, but also for rapid assessment of internal movements and displacements during the tests.

Each LVDT is intended (and required) to be in permanent contact with the pressurizing cushion, in order to monitor the movements and displacements experienced during testing. Originally the LVDTs were provided with springs, but during the first experiments with the system, it was observed that its movement was not entirely steady and smooth, thus incompatible with the desired performance and reliability of strain measurements. For that reason, the springs were removed and in order to maintain contact with the cushion, magnets were used instead. Three miniature magnetic discs were required to ensure proper contact: while the first disc magnet has to be glued in the cushion, the others are bonded together by the magnetic force (Figure 3.36). The magnet to cushion bond is an important issue, because it is crucial that it is long-term stable and especially under testing pressures. Finding an adequate glue to bond the steel magnet to the rubber cushion can be somewhat challenging, due to the distinct characteristics of both materials. Several glues and bonding materials were experimented, but the only satisfactory bond was obtained for a silicone-based adhesive sealant (Loctite 595-Superflex), which was used to glue all the eighteen "first" magnets.

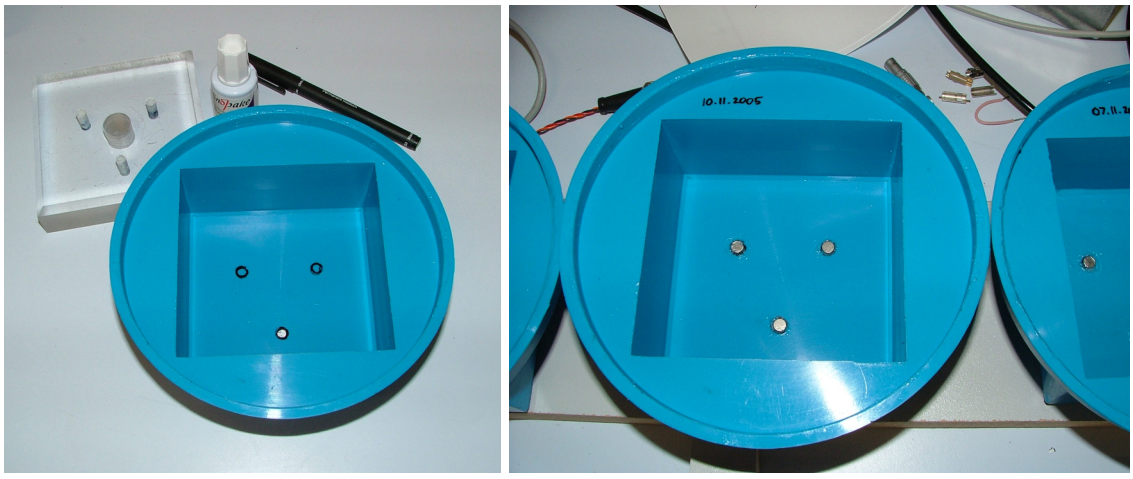


Figure 3.36 - Fixing the LVDT magnets on the cushions

3.5.2.4. LVDT Calibration

For the calibration of each LVDT, a micrometer was used, with a range of 25 mm and an accuracy of 1 μm. The calibrator consisted of the micrometer fixed to an aluminium arm, which was attached on the other end to a long threaded steel rod.

Making use of the screw holes in each platen, the calibrator was fastened in place and positioned exactly in line with the LVDT. The photo explains the setup.

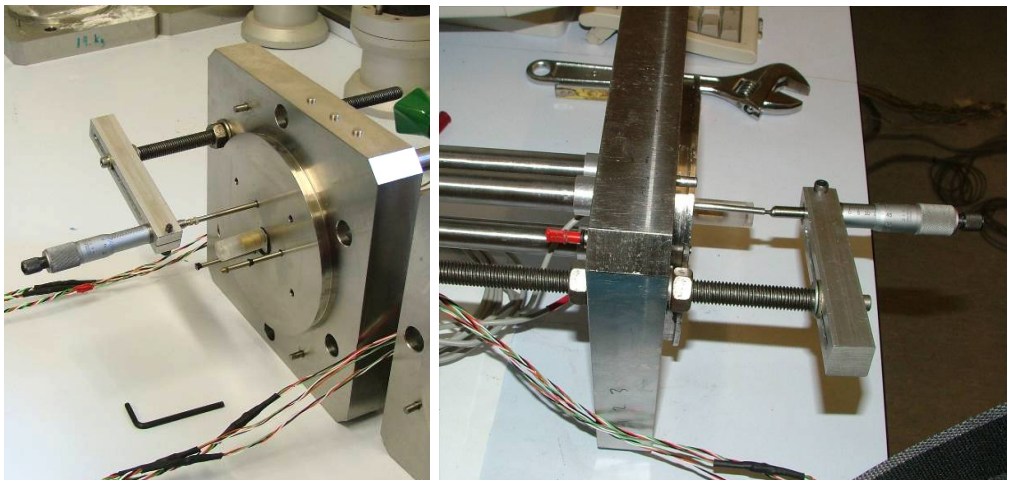
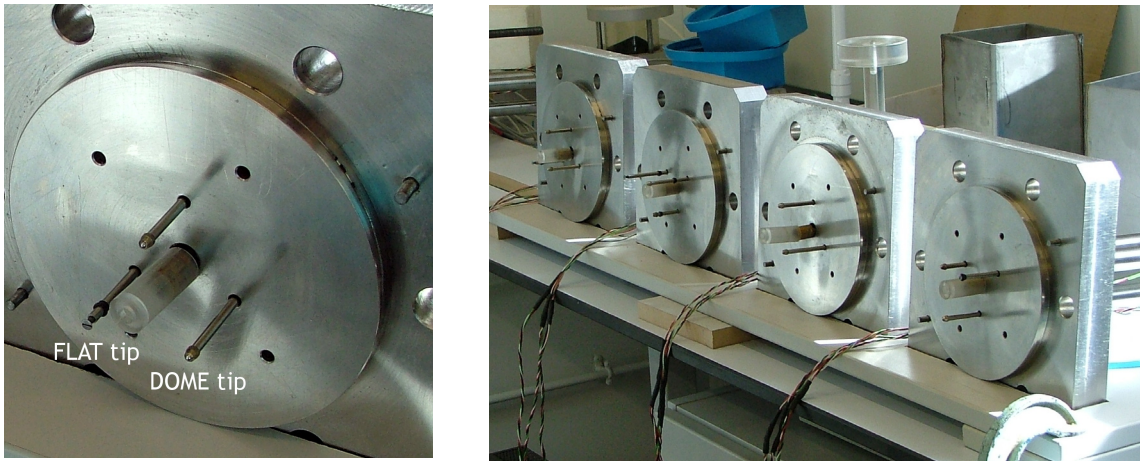


Figure 3.37 - LVDT calibrator in use

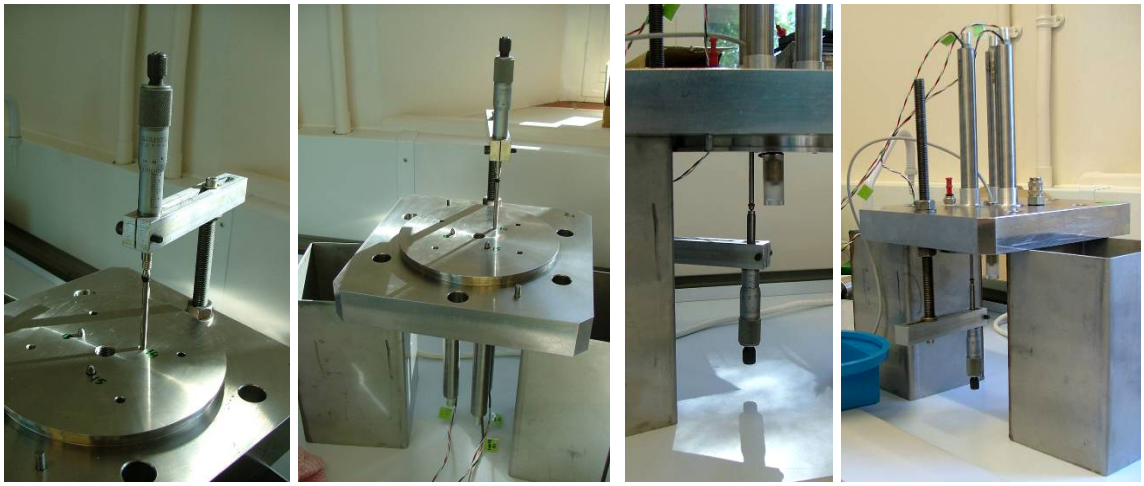
Previous tests showed different fluctuations in the displacement readings, somewhat linked to the respective directions of the platens, namely between the vertical and horizontal platens. Issues such as side friction inside the LVDT hole and misalignment of the rod due to gravity are likely to cause such differences and affect the readings, but these are particularly hard to quantify. In order to minimize the influence of these aspects, the calibration process was carried out taking into account the final positioning of the platen in the frame. For that, all X and Y axes platens were calibrated in the vertical position, with the LVDTs placed in the same arrangement as when in the apparatus frame. As shown in Figure 3.38, the LVDT tend to rest in the base of the hole due to gravity, causing a misalignment of the rod inside the hole thus inducing side friction.

Similarly, both Z platens were calibrated in the horizontal position, with the LVDTs moving vertically. The following photographs in Figure 3.39 show the calibration of each platen and demonstrate the setup.



a) b)

Figure 3.38 - LVDTs on X and Y platens: a) evidence of the misalignment of the rods due to gravity and the application of different tips for the LVDTs; b) platens positioned according to their arrangement in the frame



a) b)

Figure 3.39 - LVDT calibration of the Z platens: a) Z1 (bottom platen); b) Z2 (top platen)

The LVDTs operate within a range of approximately ±10 mm, with zero taken at the contact with the cushion, distancing 50 mm from the internal face of the platen. The calibration process consisted on reading and recording the voltage of the LVDT positioned at every millimetre from -10mm to +10 mm. Following the usual convention in Soil Mechanics, compression is considered positive displacement, i.e., the LVDT moving away from the platen, and inversely, extension corresponds to negative displacement, that is, towards the platen.

Originally, the LVDTs calibration had been carried out using LabView's MAX ("Measurement and Automation Explorer") which provides real-time voltage values of

the respective LVDT (unrecorded). These voltage measurements at every millimetre of the considered range of ±10 mm were plotted together and the best fit linear regression equation would provide the calibration factor and offset. Whilst following this procedure for re-calibrating all LVDTs, some fluctuation in voltage was often observed. This voltage fluctuation occurred during reading at a fixed position, but uneven intervals between consecutive positions were also observed. While this was at first considered acceptable due to the high correlation factors obtained, looking in greater depth to the results, it was decided to reduce this variability by replacing the tip of the LVDT.

The tip of the LVDT rod, depicted in Figure 3.38, was initially designed to be flat, consisting of a screw attached to the rod, in order to maximize the area in contact with the magnet, thus ensuring a good contact. However, it was observed that despite the rather flat surface of the tip, it would still retain some friction with the magnet. This has particularly evident during calibration, since the calibrator is operated in circular movements, accentuating the friction and the unevenness of the contact. This would possibly induce erroneous readings, especially for larger strains where the cushion surface is no longer perpendicular to the LVDT. As an alternative, a dome tip was used, providing a constant contact point despite the orientation of the magnets, that is, even for large strains. On the other hand, it required a stronger magnetic force, due to the limited contact area. Three magnets were sufficient to fix the LVDT to the cushion at all times, including in the most demanding conditions such as during setup and installation, and even for the inverted platen (Z1).

Nevertheless, some variability persisted especially with time. In fact, it was clear that the voltage measured in the LVDT at a given position at a certain instance in time was different from that at another time, a few minutes apart. The following example in Figure 3.40 evidences this observation. The readings were taken for only ten seconds each at different times, for LVDT1 at a fixed position, in contact to the calibrator. Despite not being plotted in a time base, as a time stamp was not initially considered in the readings, it is clear that there is some phenomena affecting and influencing the voltage response of LVDT1.

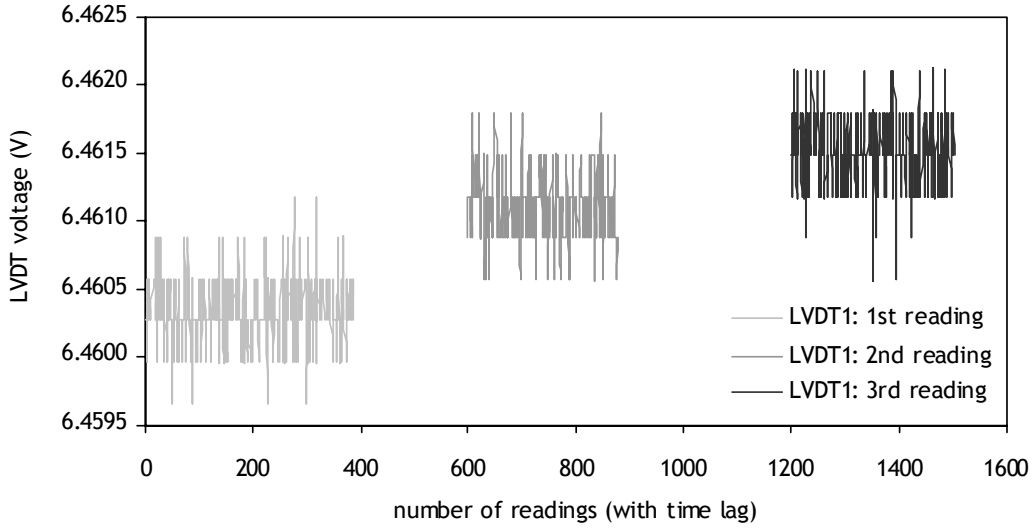


Figure 3.40 - Evolution of LVDT1 measurements with time, at a fixed position

Based on these observations, the same LVDT was logged for a few days at a fixed position. The results of such exercise are partially illustrated in Figure 3.41, for the first 18 h readings, taken at the maximum sampling rate - about 0.25 s -, reduced to every 2 seconds and filtered. The "10% filter" is a common feature of data scanners, by which 90% of the accumulated previous reading plus 10% of the current reading are calculated, for each reading point. This filter is effective in smoothing the data and eliminating much of the noise, whilst maintaining the overall variation. Observing the same results for the first hour interval, it is possible to identify a periodic variation in the response of the transducer. The maximum voltage oscillation in 1 hour is of about 1.7 mV, corresponding to a displacement of 0.003 mm, that is, about 3 x 10^{-5} strain for the 100 mm cubical specimens.

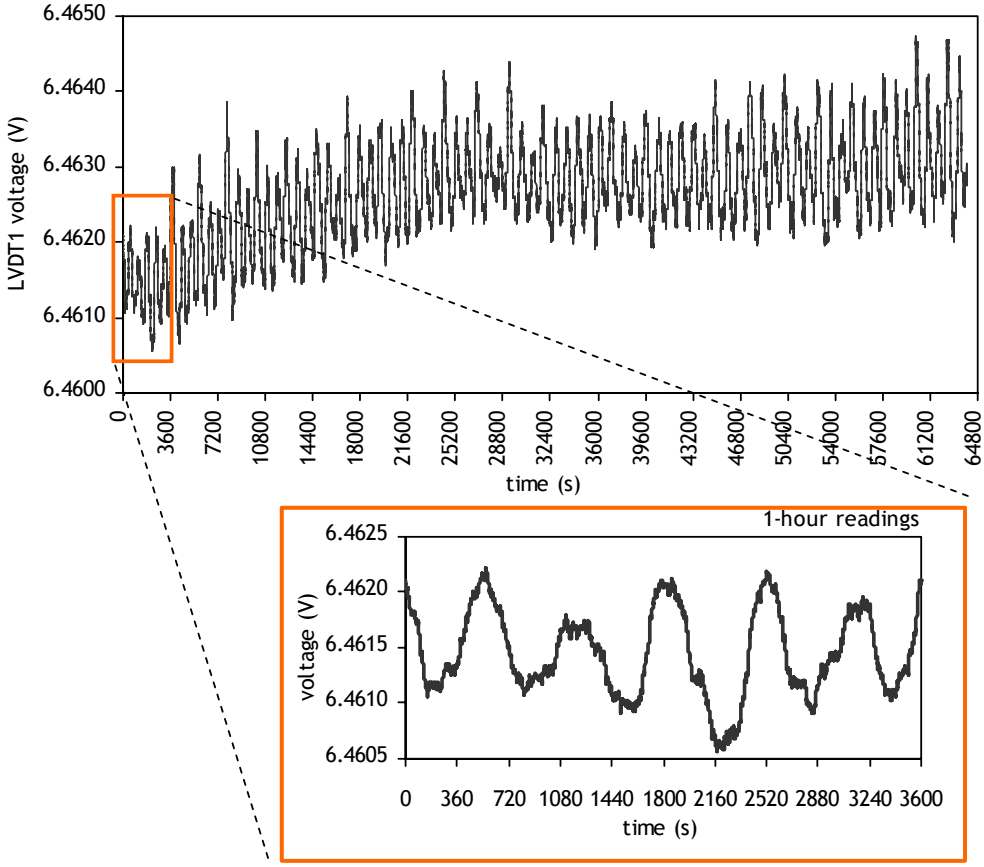


Figure 3.41 - LVDT1 logging for 18h at a fixed position and zoomed view of 1st hour readings

The first plausible explanation to such recurring variation would be the temperature, which at the time was being controlled by an air conditioning tower, located adjacent to the apparatus, set at 20 ° C.

Further experiments were carried out, including tests with other transducers as a means of verifying similarities in its behaviour. Simultaneous logging of room temperature was also initiated, using a temperature gauge available at the laboratory, attached to one of the sides of the frame, with data acquired through a DATASCAN to a PC running TRIAX. These first comparisons between LVDT readings and room temperature exhibited some interesting similarities, but it was necessary to investigate in which extent this applies, that is, to determine if the same behaviour occurs evenly in other transducers and for different temperature ranges. On another test, all the LVDTs in one platen were logged overnight, at fixed positions, as well as the room temperature. The results for 3 h readings are presented below, in Figure 3.42.

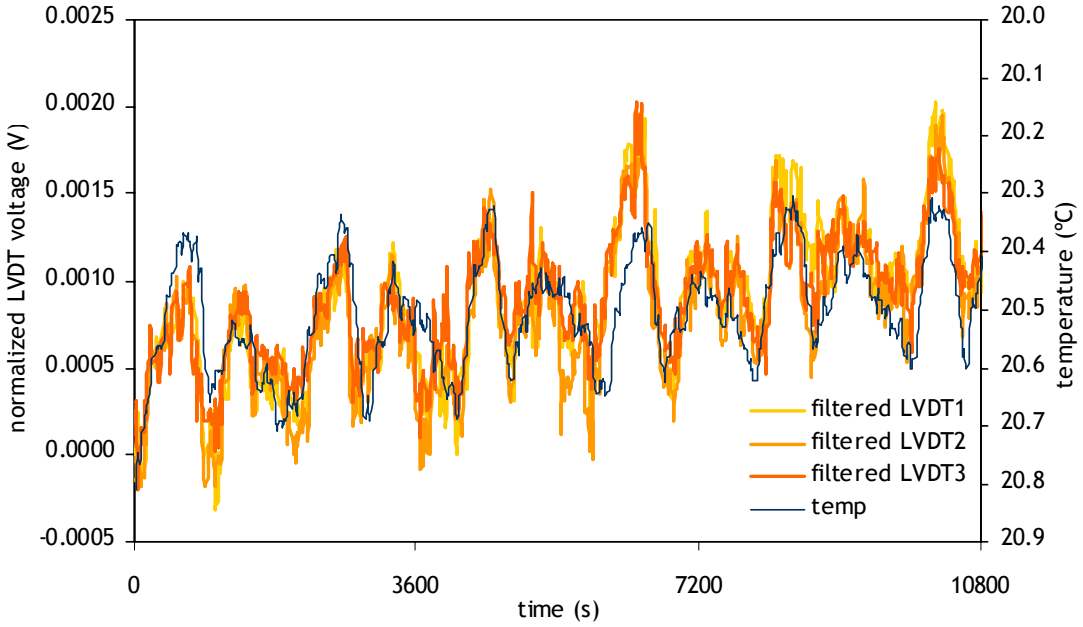


Figure 3.42 - X1 platen LVDTs and temperature logged overnight: results of 3-hour readings

The similarities in the behaviour of the three LVDTs were remarkable, with the temperature clearly dominating such response. It should be noted that the temperature axis is presented inverted in the graphs as this eases interpretation.

Supported by these findings, the number of LVDTs logged was widened and the same procedure was followed, with all LVDTs fixed at the zero position (or as close as possible to it). A logging period of approximately 66 hours was considered to account for the day effect, especially when the temperature rises due to direct sunlight in the laboratory. From this experiment, it became clear that, despite the use of air conditioning, the room temperature indeed increased significantly during that period and as a consequence, the voltage measured by the LVDTs would vary, roughly inversely proportional to temperature. This trend is not completely followed by some LVDTs. A possible explanation for this divergence may reside on the fact that those transducers were in shade at all times, while the others would be heated by the sunlight, whenever it entered the room. As a consequence of these observations, it was considered relevant to turn off the air conditioning, leaving the room to a more naturally controlled temperature. For the purposes of comparison, in the same period in different days, the temperature was recorded for nearly 20 hours and the results are provided in the next plot (Figure 3.43).

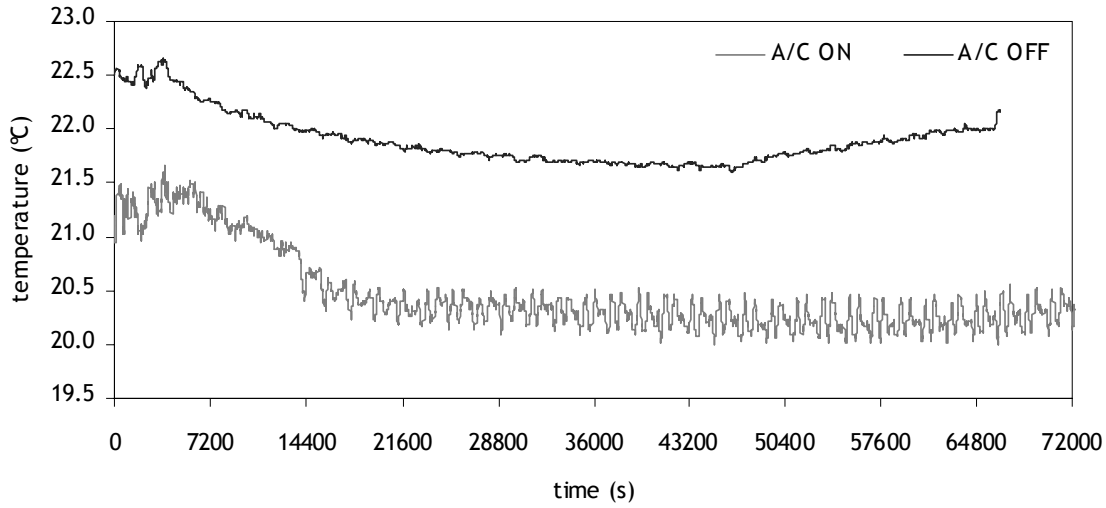


Figure 3.43 - Room temperature variation: air conditioning effect (ON versus OFF)

Whilst the temperature control would keep the room between 20.0 and 20.5 °C (except during the "sunny hours"), the natural room temperature was observed to be around 21.5 to 22 °C. It is remarkable though that despite the uncontrolled nature of the latter, it is much less variable than that induced by the air conditioning. For longer periods of time, the same variation was observed. Having concluded that the air conditioning is incompatible with this type of transducer, for the desired range of measurement, it was decided to leave it turned off during the testing period.

Many other experiments were carried out to further explain the behaviour of these transducers in fixed positions: the effects of temperature, sunlight versus shade, with the platens at the bench top versus fixed to the apparatus, calibration using a aluminium cube, among others. Previous work (Dihoru et al., 2005; Sadek, 2006) had already investigated the response of the LVDTs, having opted for neural network analyses as a means to predict errors in these measurements. In this case, a different path was followed, seeking to minimise or, if possible, neutralise the influence of the laboratory conditions in the response of the system. It has been concluded that, under a naturally-controlled room temperature, at about 21 °C, there is no need to account for the relation between LVDTs readings and temperature. The use of a calibration period of 10 s at each calibration position (every millimetre) has been considered satisfactory to obtain good reliable values and discard erroneous measurements. No significant differences have been observed in the selected range of measurement between extension-to-compression and compression-to-extension paths, evidencing linearity. As a precaution, the LVDTs have been calibrated in both directions, and the calibration factor was taken as the average of the two correlation

factors. A specific LabView routine has been prepared to automate this calibration process and record the results, as illustrated in Figure 3.44.

During the testing period, the air conditioning of the laboratory was turned off to avoid additional fluctuations in measurements. The effect of sunlight, acting only on some of the transducers, was found to be another source of variability. In the absence of a more sophisticated long-term solution, mainly due to time restrictions, a large aluminium foil sheet, fixed to the apparatus but easily removable, was used and found to be perfectly efficient, keeping the transducers in shade at all times.

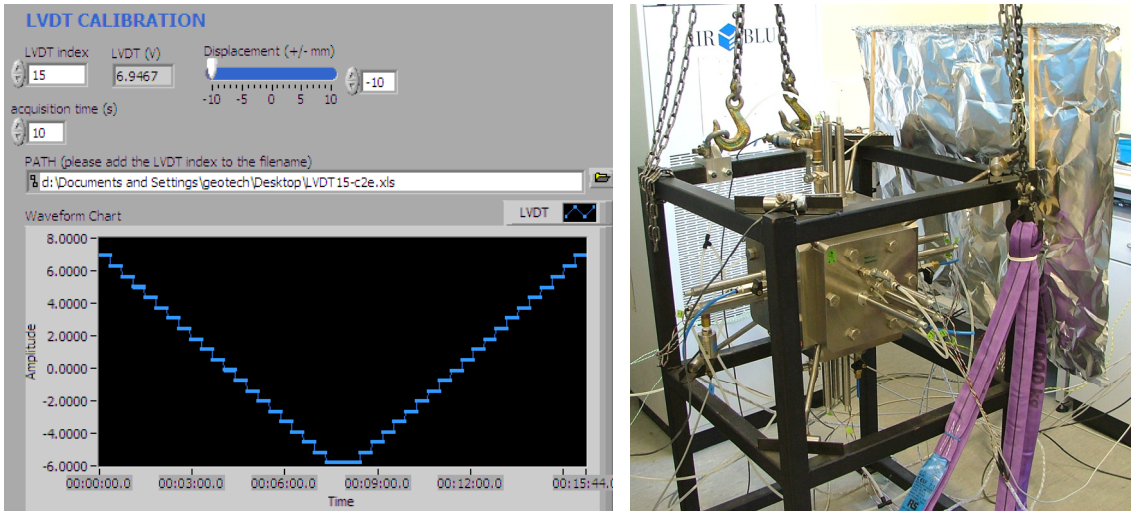


Figure 3.44 - Overcoming LVDT limitations: a) specific LabView calibration routine; b) installation of a rudimental yet efficient shade for the apparatus (aluminium foil sheet)

3.5.2.5. Seismic wave measurements

Sadek (2006) manufactured miniature T-shaped bender/extender elements for seismic P- and S- wave measurements for installation in this apparatus. In his work, it was originally planed to mount B/EE in each face of the cubical cell enabling the investigation of the orthorhombic anisotropy of pluviated sand specimens, where nine independent material constants are deduced. According to the author, it was not possible to install a transducer at the bottom face of the apparatus at the time, due the need to retain the pressurised cushion for supporting the sand. As a consequence, only four B/EE were used, mounted in the side faces (platens X and Y) of the CC, thus restricting the exploration of elastic anisotropy to an elastic cross-anisotropic model with five independent material constants.

In the context of the present work, the relevance of the use of this apparatus is fundamentally related with the possibility of measuring stiffness by seismic waves

propagated in all three orthogonal directions. Hence, these limitations had to be overcome in order to fully justify the use of this apparatus and thus accomplish the present research purposes.

3.5.2.6. 90° rotation of the apparatus

A possible solution to this issue consists of a 90° rotation of the apparatus on the X axis, moving Y1 and Y2 platens to a horizontal position (as bottom and top, respectively) and bringing Z1 and Z2 to a vertical position (as front and back, respectively), as sketched in Figure 3.47a. At such position, the installation of BE in the Z direction could be made according to the standard procedure, previously restricted to X and Y directions.

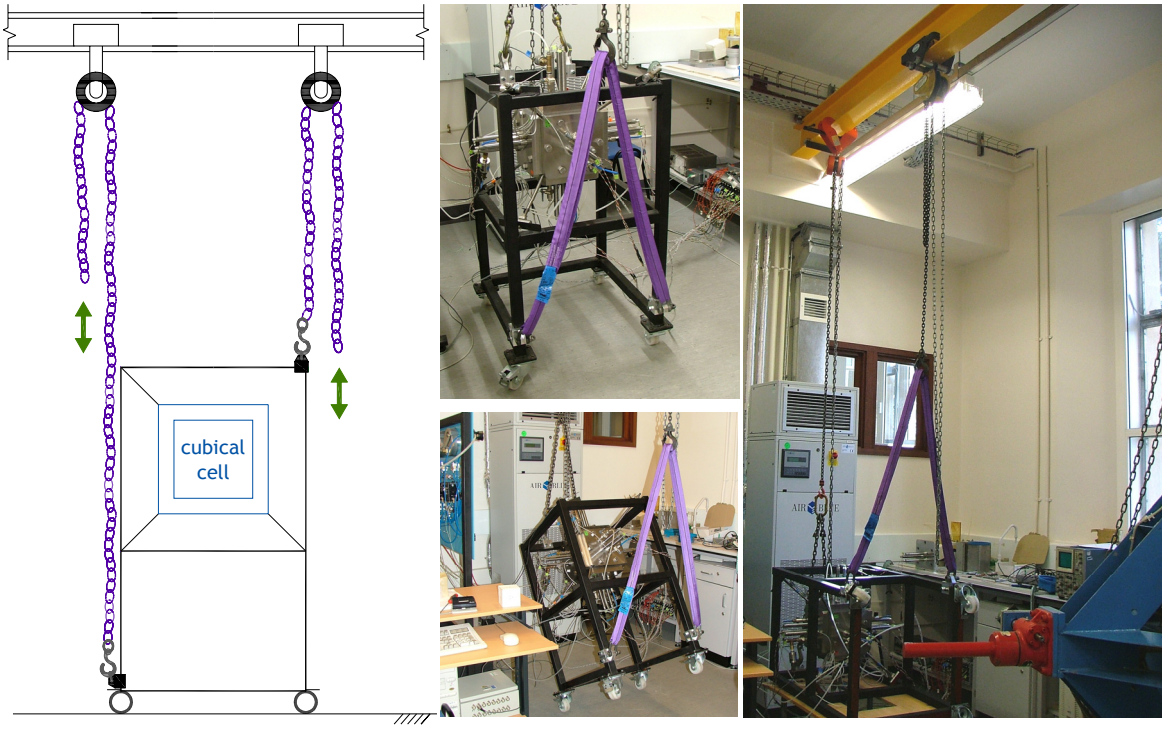
A study of the possibility of rotation of the cubical cell was carried out, considering several options for the rotation method, including changes in the current support frame to enable pivoting on a secondary stand; removal of the current support stand and design of a smaller, lighter support frame to be manually moveable, similar to the original prototype (Dewoolkar et al., 1997); replacement of the current support frame with a rotary rail with locked positions; or, the lifting and rotation of the whole apparatus, using chains and pulleys rolling in the laboratory rail beam in the ceiling.

Taking into account that the cubical cell itself is completely made of stainless steel, hence quite heavy, any new support stand would have to be stiff enough to handle such weight without inducing shear stresses and distortions in the cube. It should be noted that only six of the eight corners of the apparatus can be used for the support. Under these circumstances, a new support frame would hardly be possible to handle and rotate manually.

On the other hand, with the help of highly skilled technicians, lifting and rotating the apparatus using appropriate chains and pulleys appeared to be the most convenient, simple and straight-forward process. The full weight of the apparatus was estimated to be of about 250 kg, and the safety requirements for handling such weight were thoroughly considered in the selection of all devices.

Finally, the 90° rotation process was successfully implemented, requiring minimal effort. Figure 3.45 presents a schematic diagram of the setup along with photographs of the rotation process. This process can be systematised in six basic stages, according to the movement of the chains, as illustrated in Figure 3.46. At the 6th

stage, the apparatus is lowered to a table on casters for stability and safety. This low table has a central open slot to give room to the protruding LVDT rods.



a) b)

Figure 3.45 - 90 ° rotation of the apparatus: a) schematic diagram; b) photographs of the process

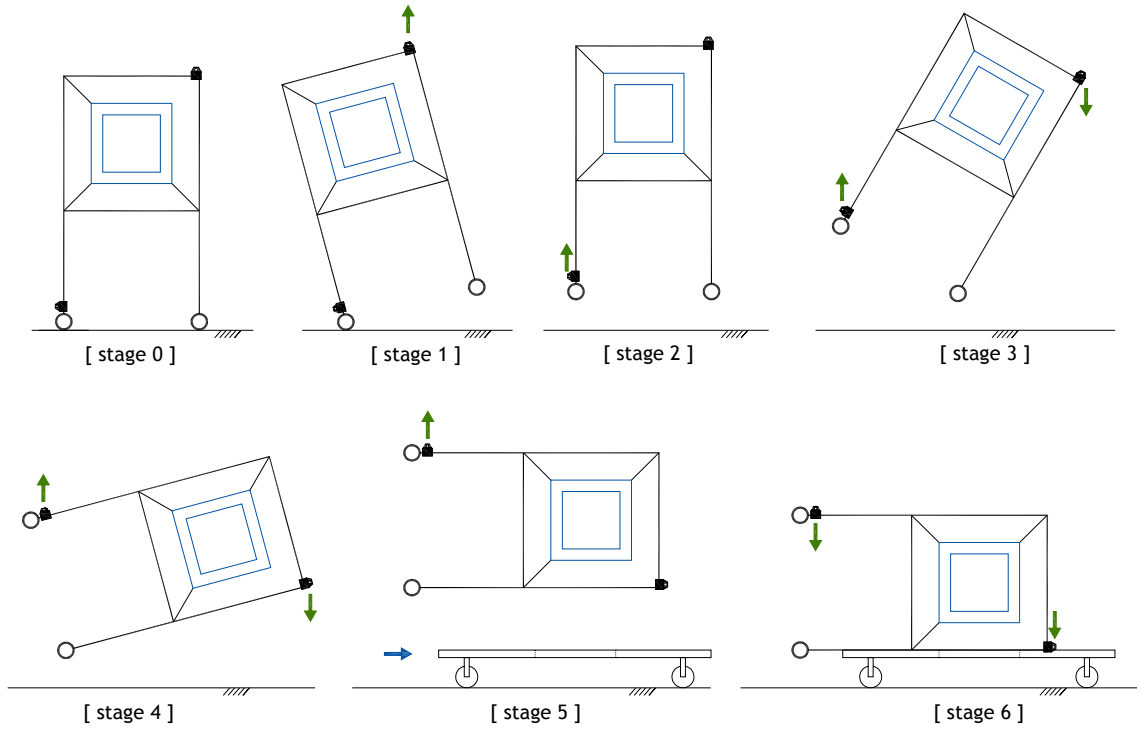
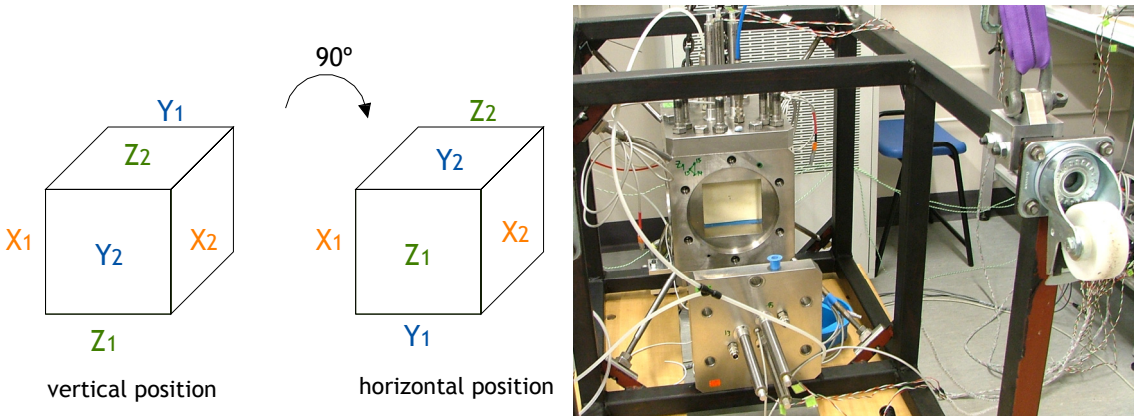


Figure 3.46 - Stages of the 90 ° rotation process: from vertical to horizontal positions

The vertical position is the original position of the apparatus, upright. The 90° clockwise [CW] rotation moves the apparatus to the horizontal position, as depicted in Figure 3.47. In fact, experience showed that this is the most suitable position for the installation of the specimen at the start of a test, since the soil specimen inside the cell undergoes a single counter clockwise [CCW] rotation, minimizing potential disturbances or other hazards during the process.



a) b)

Figure 3.47 - Front view of the cell in the vertical and horizontal positions: a) schematic; b) photograph of the apparatus in the horizontal (90° rotated) position

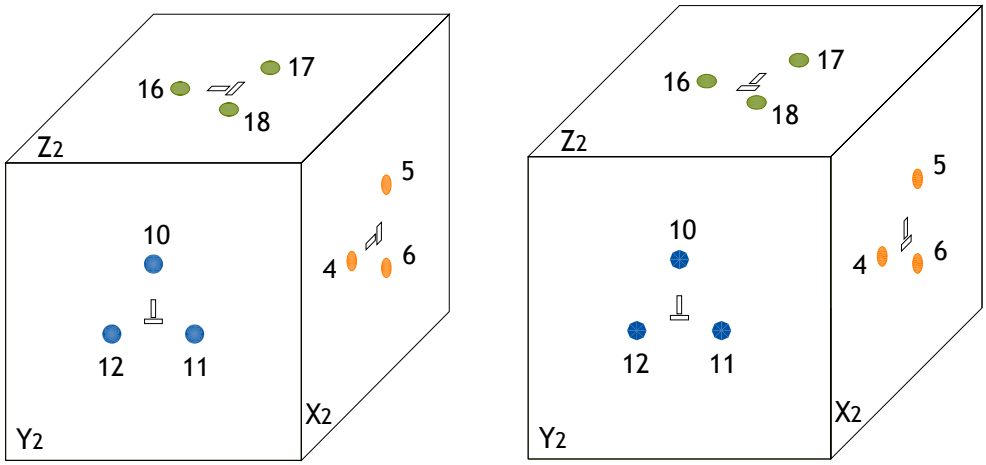
3.5.2.7. Selection of the BE positioning

Since the bender/extender elements are fixed for each test directly onto the specimen, the arrangement of the bender/extender elements may differ from test to test, according to specific test requirements. For the first tests in this apparatus, only direct wave measurements were made, resulting in a total of twelve measurements of P- and S-waves. As a simple mnemonic, the initial configuration of the B/EE followed the triangular shape of the LVDTs in each platen (Figure 3.48a).

Measuring inclined waves was not considered at start but occasional difficulties in measuring in certain directions led to the decision of complementing the results with such measurements. Evidently, the combination of direct and inclined measurements is redundant, but it may also prove quite useful at times.

The initial BE arrangement did not enable inclined measurements due to the misalignment of the transducers. For that, a new configuration has been devised to maximize the number of wave propagation and polarization directions. Similarly to the true triaxial apparatus at FEUP, there is one direction where the alignment of

the transducers does not permit these measurements to be made. In this case, inclined measurements are possible in all directions, except in the XZ direction (Figure 3.48b). Again, this combination of P- and S-wave directions amount to a total of forty-eight different measurements per load stage.



a) b)

Figure 3.48 - B/EE arrangement in the cubical cell: a) initial tests (direct measurements only); b) final tests (direct and inclined measurements)

3.5.2.8. B/EE installation

The installation of the miniature T-shaped B/EE is a delicate process, as it is crucial that all the elements are properly sealed and insulated, especially the cushion to transducer connection. A rubber grommet is placed around the transducer, providing a larger surface for gluing and fixing on both sides. Silicone sealant is applied between the grommet and the specimen membrane, while “CopyDex” adhesive solution is used at the back in the grommet-cushion connection, in order to guarantee an airtight pressure system. A curing time of at least one hour is required before mounting the platen on the apparatus. If the grommet-cushion seal is not broken in consecutive tests, this process is accelerated and the installation of the transducer is simplified. The B/EE cable is fed through a hole in the centre of the platen, which is tightened and sealed using a specially-designed threaded plug.

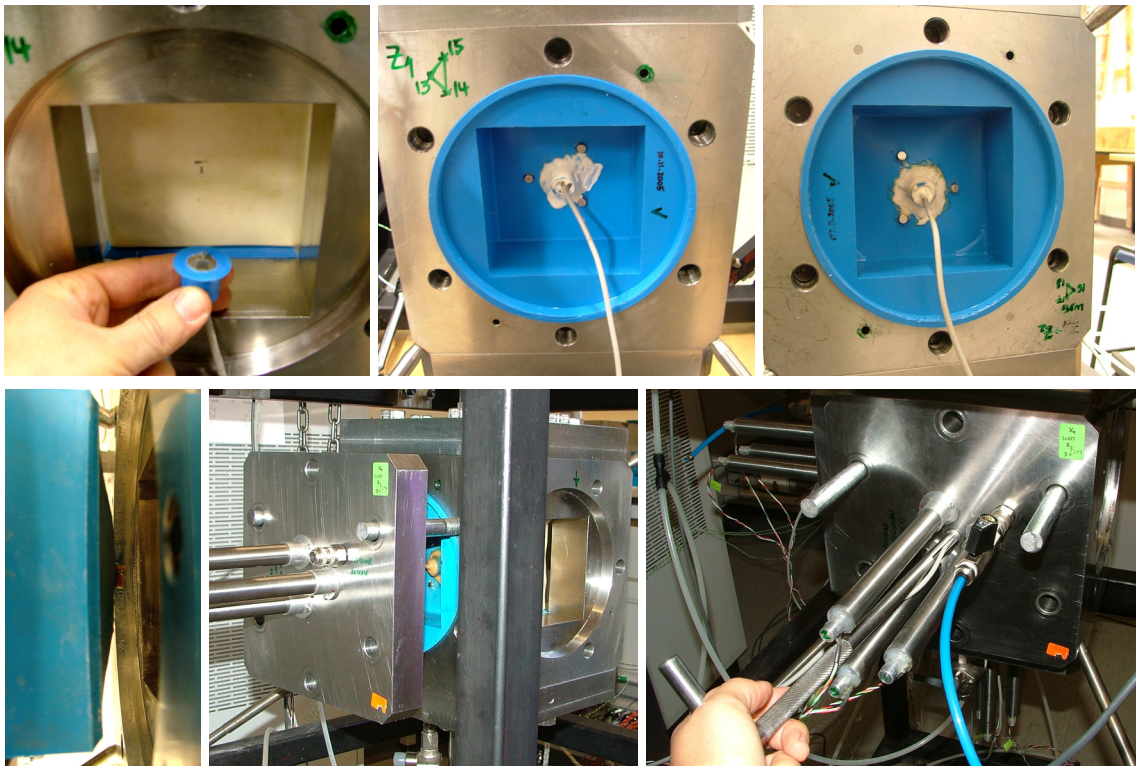


Figure 3.49 - Installation of B/EE in the cubical cell

The different level of detail in these descriptions derives from the fact that different levels of complexity are associated with the operation of each of these apparatuses. Clearly, true triaxial apparatuses pose additional challenges in relation to standard triaxial chambers, mainly due to the multiplication of the number of measurind devices, from pressure to displacement transducers, and also to the seismic wave measurements.

3.6. Conclusions

This chapter focused on the detailed description of the various laboratory testing apparatuses used in the research work. Almost all tests were carried out with simultaneous measurement of seismic wave velocities by means of piezoelectric transducers, which are also thoroughly presented in terms of characteristics, operation

The installation of these transducers in different testing apparatus is illustrated, since it is particularly useful for complementary and comparative purposes, namely in standard triaxial, stress-path, resonant-column and also in true triaxial cubical apparatuses. For the installation of the piezoelectric transducers, it was often necessary to conceive and implement some adaptations in the testing devices, as well

as to devise and develop new designs for testing prototypes. Given the novelty of some modifications and the new designs of other testing equipments, their characteristics, functioning and testing procedures were also addressed in this chapter.

4.

Interpretation and Analysis of Bender Element Results

4.1. Introduction

Bender elements, as well as other piezoceramic transducers, have opened a new window in laboratory testing, by enabling to perform standard mechanical, static or cyclic, tests simultaneously with seismic wave dynamic tests.

The attraction of the BE technique is its apparent simplicity: one of the transducers is excited at one end of a specimen using a single pulse excitation, and the time required for this to be registered by the receiving bender element at the other end of the specimen can be simply read off an oscilloscope, to obtain the travel time, and hence the shear wave velocity. The installation of these transducers is relatively straightforward and quick; the necessary electronics equipments (function generator, oscilloscope, spectrum analyser, PC data acquisition card) do require some investment, however it may rapidly pay off when these devices are shared among multiple users running different tests in the same laboratory. Therefore, piezoelectric transducers are an inexpensive and versatile solution for laboratory seismic wave

measurement. Furthermore, its capabilities in monitoring the evolution of stiffness with effective stresses, influenced by factors such as cementation, curing, load stabilisation, among others, by means of shear waves and also in observing other processes, namely saturation, using compression waves, are particularly appealing.

However, as the method was implemented and used by both research and commercial laboratories around the world, it gradually became apparent that there were various issued to be resolved to do with the hardware used, the conduct of the test, and the interpretation of the results. Finally, there has been much discussion on the details of the test procedure and the most appropriate method of interpreting the results to obtain the shear wave velocity. In the following sections, these issues will be analysed and discussed in detail.

In summary, the potential and benefit of bender element testing is clear; the interpretation of its results, unfortunately, is not so, as demonstrated by many authors (Viggiani and Atkinson, 1995; Brignoli et al., 1996; Jovicic et al., 1996; Arulnathan et al., 1998; Greening et al., 2003; Greening and Nash, 2004; Leong et al., 2005; Viana da Fonseca et al., 2009). In effect, despite the various advantages of the bender element technique, namely its simplicity and ease of use and application, there is not yet a standard procedure and interpretation framework, developed for this technique. The interpretation of the results remains subjective, requiring some degree of judgement.

A practical framework for bender element testing, based on the comparison of different interpretation techniques in order to obtain the most reliable value for the travel time, is required in order to have a methodical, systematic, and objective approach to the results. Before presenting the results of this research, it is worthwhile detailing the most common methods for the interpretation of bender element tests.

4.2. BE-related phenomena

Several authors have investigated the many aspects related with wave propagation using bender elements, namely the various phenomena that may occur during BE testing affecting its performance (Sanchez-Salinero et al., 1986; Mancuso and Vinale, 1988; Viggiani and Atkinson, 1995; Jovicic et al., 1996; Arulnathan et al., 1998; Pennington, 1999; Arroyo et al., 2002; Hardy et al., 2002; Rio et al., 2003; Jovicic, 2004; Lee and Santamarina, 2005, among others). The conditions of installation of the transducers, interferences such as cross-talk and noise, dispersion phenomena

namely near-field effects and wave reflections at the boundaries are some of the aspects under intense research over the years, which are addressed below.

4.2.1. BE installation

There are several difficulties associated with bender element installations, which result in a number of potential (inherent and induced) factors of error involved in BE testing. Some of these errors derive from the properties and quality of the transducers, the details of the insulation, electrical crosstalk due to electromagnetic coupling through the soil, mixed radiation of both P- and S-waves, near field effects, all leading towards uncertainty in the detection of first arrivals.

With regard to the BEs themselves, most issues have already been addressed in the previous chapter, namely the design details of the elements and its insulation and installation procedures. In practical terms, a number of technical requirements and boundary conditions should be accomplished, as recommended by Jovicic (2004) and Lee and Santamarina (2005). These requirements comprise:

- optimal wiring of the layers of the element (parallel or series) to obtain greater efficiency;
- adequate shielding of the piezoceramic layers and grounding of the transducer;
- properly connected and encased BEs;
- leak-free connections; and,
- noise free environment.

Since these transducers are rather fragile in comparison with the surrounding soil, it is important to occasionally assess its wear-and-tear degradation. The insulating epoxy coating and the cable shielding are particularly susceptible to this type of deterioration, leading towards short-circuiting. Santamarina and Fam (1997) presented examples of typical responses for a BE with deteriorated insulation in a saturated silty soil, evidencing early energy arrival often confused with near field effects. The authors provided solutions for minimising this problem by the use of more durable coating materials, and presented suggestions for mitigating its effects, if the short-circuit condition develops during testing.

Other issues also play a part, especially spatial and boundary conditions, such as:

- alignment of the BE;
- reflections of the wave on the edges and sides of the sample;

- near field effects (relative distance between transmitter and receiver);
- contact between the BE and the soil, which might induce poor coupling, especially at low confining pressures; and,
- overshooting at high frequencies, at which the bender element changes its mode shape, resulting in a more complex response.

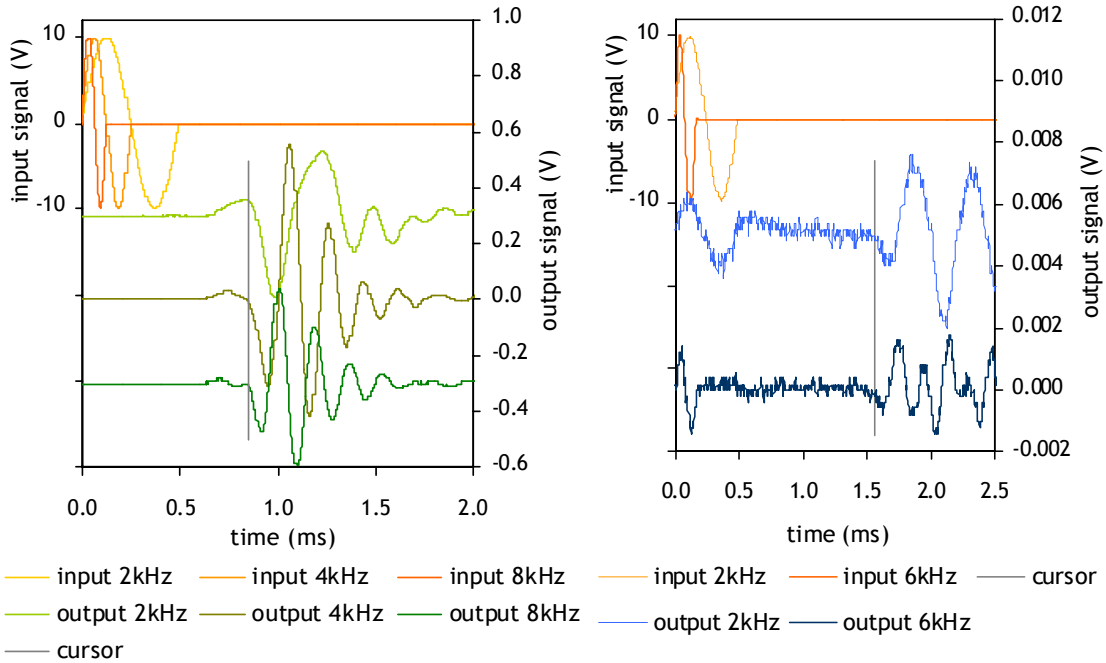
There has also been considerable discussion with regard to the choice of ancillary hardware - pulse and function generators, PC sound cards as generators, power and signal amplifiers, oscilloscopes, spectrum analysers, A-D converters, etc. The equipment used in this research, already introduced in Chapter 3, was found to be well suited for the frequency range of interest. Nevertheless, recent test results on stiffer materials, namely artificially cemented soil specimens, have posed new challenges to BE measurements, due to the requirement of much higher frequencies (above 50 kHz for shear waves), approaching the frequency range limitations of some of these equipments (Rios Silva et al., 2008). In the light of these data, it appears that the choice of electronics equipment should be made considering a wider spectrum of working frequencies in order to efficiently test materials with distinct stiffnesses.

4.2.2. Cross-talk

In bender element traces, when an early component quasi-simultaneous with the input signal appears in the output signal, it indicates the presence of cross-talk, usually associated with electromagnetic coupling between transmitter and receiver elements, as suggested by Santamarina (2001). This type of cross-talk is predominant in conductive soils, namely in saturated soils. One solution involves appropriately grounding the BE and the use of parallel to series BE combination (Lee and Santamarina, 2005). Brocanelli and Rinaldi (1998) coated the BE with conductive silver paint over the insulating epoxy resin and grounded it, thus avoiding transmission of the input signal and observing improvements in the received signal.

However, the leakage of the transmitted electric signal to the received BE can also result from other sources at different points of the circuit (Rio, 2006). The physical proximity of the plugs in the electronics equipments and the lack of grounding of the testing apparatus are some of the aspects that may contribute to the presence of cross-talk. Moreover, cross-talk has been observed with different magnitudes in different testing conditions, though the reasons for such differences are often unclear. In sum, though this effect should be minimised as much as possible, it may sometimes be nearly impossible to eliminate.

Figure 4.1 presents examples of BE measurements in two different setups in the laboratory, using different BE installed in different apparatuses. In Figure 4.1a, the output signal is perfectly flat up to the arrival of the shear wave, with no evidence of cross-talk. This is likely due to the high magnitude of the output signal, resulting on a high signal-to-noise ratio, favourable for its interpretation. In contrast, in Figure 4.1b, the presence of cross-talk is clearly visible and enhanced by the low voltage of the actual shear wave, corresponding to a very low signal-to-noise ratio. Despite the cross-talk in the second figure, the identification of first arrival in the time domain is not substantially affected, assuming that the user is aware of this phenomenon and is capable of distinguishing it from the actual wave. Additionally, it is necessary to use sufficiently high input frequencies to allow for the complete dissipation of the cross-talk effects before the arrival of the shear wave. Specifically, this means that the input frequency should be such that its signal finishes at least at half the travel time, i.e., at least two wavelengths should travel in the length of the specimen. In those conditions, it is relatively easy to visually disregard the cross-talk portion of the signal and focus on the far field where the true shear wave appears.



[note: the polarity of the output signals is inverted in relation to the input signals]

a) b)

Figure 4.1 - BE measurements in different testing setups: a) no evidence of cross-talk; b) clear presence of cross-talk in the output signals

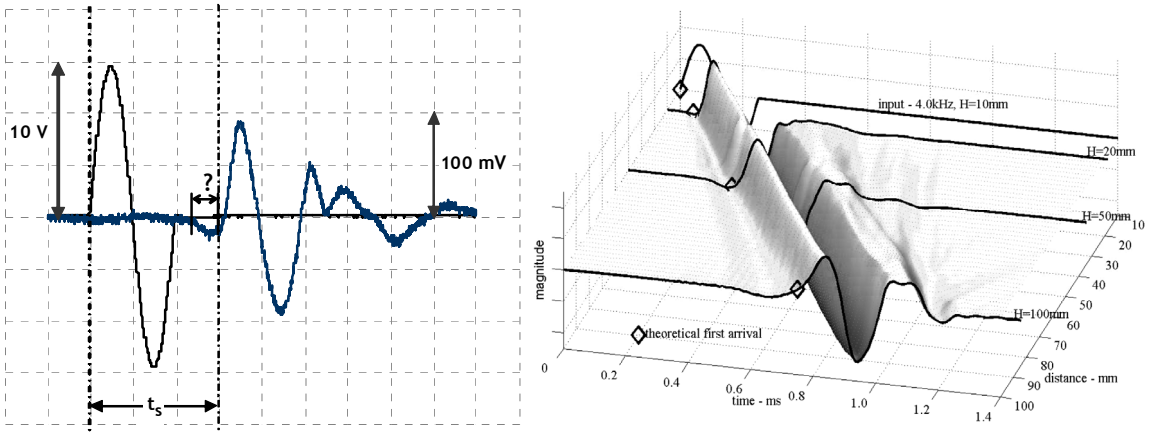
On the other hand, cross-talk is in fact a contamination of the output signal with the content of the input signal. Since cross-talk has frequently a magnitude comparable with that of the received signal, this may result in a considerable source of error, especially if the signals are to be analysed in the frequency domain (Rio, 2006). In this case, one possible solution may reside on the use of numerical tools to remove the initial portion of the signal, similar to the use of specific filtering, since the frequency and location of this error are known. Then, the equivalent filtered signals can be used for frequency domain analyses.

4.2.3. Environment noise

As mentioned above, one of the technical requirements for optimising BE measurements refers to a noise-free environment. In most laboratories, it is virtually impossible to completely remove environment noise, namely background noise from electromagnetic noise and mains supply. This noise affects mainly the output signal, and even though it is random in nature, a typical low frequency of 50 Hz is often visible in the oscilloscope. Noise at very high frequencies (above 100 kHz) is also often apparent in the output signal. If the quality of the signal is low, the level of noise becomes more visible and the use of double insulation of the equipment and apparatus should be experimented, in order to reduce its influence. In general, the use of stacking for averaging results (standard procedure in this research is 128 stacked signals in the oscilloscope) is sufficient to provide clear results. Post-processing analytical filters can also be used to clarify the signal numerically, though its routine use is not advocated here, since other relevant features of the signals may accidentally be eliminated in the filtering process.

4.2.4. Near-field effects

A BE test consists of the application of an input voltage of defined shape and frequency to the transmitter to generate a shear wave, the propagation of this wave through the soil specimen, and the sensing of the arrival of this wave by the receiver, resulting in an output signal. The output signal is heavily attenuated, more distorted and more complex than the input signal. While it is sometimes easy to determine the first arrival of the shear wave, it is often the cause of much uncertainty. This behaviour is illustrated in Figure 4.2, which presents typical BE traces from experimental tests and also from three-dimensional numerical simulations for an unbounded specimen (Rio, 2006), where any dispersion can only be caused by near-field effects.



a) b)

Figure 4.2 - Typical BE traces: a) experimental tests (Ferreira, 2003); b) numerical simulations for an unbounded specimen (Rio, 2006)

In both traces, an initial bump in the output signal is visible which, in the case of Figure 4.2a, corresponds to a margin of error of about 20%. In contrast, Arroyo (2001) presented an experimental database in which different estimates of travel time, which should be equal according to the assumptions of the model, differed by up to 50% of their average value, resulting in a 100% uncertainty in the shear stiffness modulus, G_{max}, determination.

Much of the uncertainty and subjectivity in bender element testing is commonly, yet often erroneously, attributed to near-field effects. The consideration of near-field effects in geotechnical testing practice was introduced by Sanchez-Salinero et al. (1986), whose work focused on the analysis of field cross-hole tests. The propagation of a single sinusoidal pulse in an infinite isotropic elastic medium is assumed, considering theoretical records from two receivers, placed at different distances, and analytical solutions for the three-dimensional wave propagation in such medium and conditions were defined. Their model is based on Stokes' fundamental solution, who in 1849, described the movements generated by a unit impulsive force isolated in an infinite elastic medium (Arroyo et al., 2003).

The solutions for the equations of motion of compression and shear waves, presented by Sanchez-Salinero et al. (1986) are composed of three terms. The wave components of a shear wave can be generally represented as:

$$\Gamma = \Gamma_1 + \Gamma_2 - \Gamma_3 \text{ or } = F_S + N_P - N_S \qquad [4.1]$$

where F_S is the far-field component of the shear wave, and N_P and N_S are the near field components travelling at the compression and the shear wave velocities, respectively. In simplified terms, two of the components of a shear wave propagate at the shear wave velocity V_S, while the other component propagates at the compression wave velocity V_P. The terminology "far-field" and "near-field" denote different attenuations with distance. The near-field components attenuate much faster than the far-field so, although their contribution is important very near to the source, it rapidly decreases with distance from the source. The detailed expressions of the far-field and the near-field are not presented here, since analytical studies of this phenomenon fall beyond the scope of this work and have already been thoroughly investigated and reported elsewhere (Aki and Richard, 2002; Arroyo et al., 2003; Rio, 2006).

Based on these findings, Sanchez-Salinero et al. (1986) provided limits to the relative distance between transmitter and receiver transducers, expressed by a minimum number of wavelengths. For shear waves, the ratio between distance d (or travel length, L) and wavelength N or R_d (Jovicic et al., 1996) representing the number of wavelengths between the two transducers, was suggested, with the following limit:

$$N = R_d = \frac{L}{\lambda} = \frac{L \cdot f}{V_s} \text{ with } N > 2 \qquad [4.2]$$

In BE tests, due to the specific dimensions of soil specimens, it is more common and convenient to select high input frequencies than to change of the distance between transmitter and receiver, as a means to minimise near-field effects and work in far-field conditions. Many researchers (Brignoli et al., 1996; Jovicic et al., 1996; Arulnathan et al., 1998) have applied these limits in their bender element tests, showing evidence of near-field effects in shear wave signals for small relative distances to the wave source, typically for N lower than 2. While Jovicic et al. (1996) used the input frequency (or apparent input frequency, as set-up in the function generator) to calculate N, Brignoli et al. (1996) considered more appropriate to measure the frequency of the received signal and used it to compute N.

Lee (2003) proposed an alternative solution for extracting shear wave velocity from measurements with pronounced near-field effects, by means of the "signal-matching" method. This technique consists of matching experimental waveforms with analytically computed waveforms and takes into consideration the shear wave velocity, the operating frequency and the installation. The mathematical formulation

and the recommended step-by-step procedure for signal matching are summarised in Lee and Santamarina (2005).

On the other hand, other researchers were less successful and reported difficulties in obtaining clear arrivals even when the minimum frequency rule was followed (Gajo et al., 1997; Pennington, 1999; Viana da Fonseca et al., 2008, among others). Arroyo et al. (2003) demonstrated that the abilities of the model proposed by Sanchez-Salinero et al. (1986) were rather limited in effectively reducing the uncertainty associated with BE testing. According to their analysis of near-field effects, if phase or group velocity is measured at more than about 1.6 normalised distances (or travel lengths) from the source, the possible excess induced by Stokes' near field over the shear velocity, V_S, will stay below 5%. The frequency adjustment to limit near-field influence to 5% has been translated into the following expression:

$$f_{\lim} = \frac{V_S}{\lambda} > \frac{V_S}{1.6 \cdot L} \qquad [4.3]$$

These authors suggested quantifying the near-field relative height, that is, the magnitude of the initial bump of the output signal, due to the near-field term, in comparison with its maximum peak. Using four different shapes of input signals under the same testing conditions, the authors studied the relative height of the near-field, depicted in Figure 4.3. They concluded that the limit proposed by Sanchez-Salinero et al. (1986), though indicative, is not valid for all kinds of input signal, corresponding roughly to a policy of ignoring bumps in the output signal lower than 10% of the maximum magnitude of the response to a single sine input.

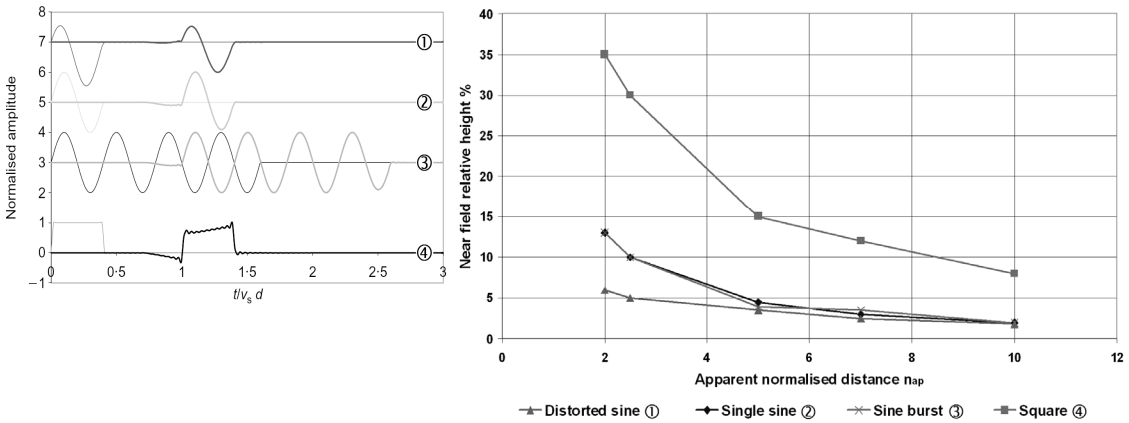


Figure 4.3 - Signal type and near-field effect in the time domain (Arroyo et al., 2003)

As pointed out by Arroyo et al. (2003), these results suggest that, although Stokes' isolated source model may be an adequate model for field pulse tests, it might not be

directly translated to laboratory practice. One obvious difference is that wave transmission seems more unbounded in the field than in the laboratory. More elaborate elastodynamic models are required to provide insight on these issues, since errors due to near-field effects are not sufficient to fully explain the scatter observed in laboratory BE measurements. For example, Rio (2006) has shown the importance of waveguide and sample geometry effects, mainly due to lateral boundary reflections, in bender element testing.

4.2.5. Boundary conditions and sample geometry effects

The general interpretative model of a bender element test, usually implicit, considers a shear bulk plane wave travelling between source and receiver. The plane wave geometry of transmission has also been questioned, as a follow-up to the discussion of near-field effects. Arroyo et al. (2003) tested a cylindrical clay sample, varying the height-to-width ratio, or slenderness, between 1.9 and 0.8, proving that near-field effects were unable to justify the observed measurement uncertainty. However, the results of Lee & Santamarina (2005) on short oedometer specimens of slenderness 0.33 pointed towards a very good match with the near-field model. These opposite findings directly suggest the existence of other limitations in the wave transmission model, namely those regarding boundary conditions and sample geometry.

It is commonly recognised that the propagation of waves in a confined medium, such as that of a laboratory soil specimen, is influenced by the reflection of wave components at its boundaries. As a result, the presence of reflected waves in bender element tests is likely to be dependent on the geometric properties of the soil specimen. The importance of sample size and geometry in BE testing has been suggested and discussed by a number of researchers (Blewett et al., 2000; Arroyo et al., 2002; Theron et al., 2003; Greening & Nash, 2004; Arroyo et al., 2006; Rio, 2006).

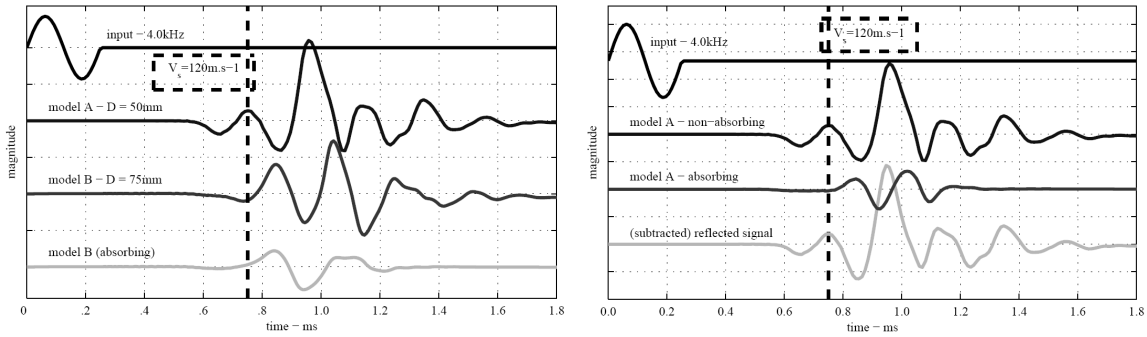
Sample geometry effects will depend on the type of test. Most BE tests are carried out in cylindrical soil specimens, generally in the triaxial and the oedometer, where BE are most commonly installed. Moreover, BE tests generally consist of the propagation of seismic waves along the axis of the specimen, that is, the cylinder. On the other hand, the slenderness has been found to have great importance in measurement uncertainty. Arroyo (2001) and Rio (2006) examined the problem of sample-size effects, namely those related with end reflections at the platens, and those due to reflections at the lateral boundaries. Some of the findings of their work are discussed here.

As Rio (2006) explains, wave reflection is a complex process, varying according to the nature of the boundaries, or interfaces, as well as the type of waves. In general, P- and S-waves can propagate in solid medium, whereas only P-waves can propagate in a fluid medium; no wave propagation is possible in vacuum. Hence, each combination of media results in a different solution for wave reflection. The relevant cases for BE testing on soil specimens involve a boundary with an interface between solid and either fluid or air media. In the most common apparatuses, such as triaxial cells and oedometers, the soil specimen is surrounded by water, or less frequently, by oil. Occasionally, BE tests are carried out directly on a bench, for which the consideration of an interface between solid and air is appropriate. These two cases can be translated into two opposite types of lateral boundary conditions: reflecting and absorbing boundaries.

Arroyo et al. (2006) described the analogy between these boundary conditions and laboratory setups very clearly. In most BE tests, the lateral boundaries are provided either by a metallic interface (oedometers) or by a membrane, separating the soils from a confining fluid (triaxial). In general, the higher the impedance of the confining media relative to that of the soil, the higher the proportion of energy reflected back into the sample. This means that oedometer tests with metallic boundaries will be very close to the perfectly reflecting case; the same will apply for dry soil and triaxial conditions. The case of saturated soil and triaxial conditions is less clear-cut, and probably intermediate between the perfectly absorbing and perfectly reflecting conditions.

Rio (2006) developed a sophisticated 3D numerical model of BE wave propagation, providing impressive and elucidative figures of the wave reflection phenomena. As an example, the simulation results for a standard triaxial specimen (model A of 100 x 50 mm, with a slenderness of 2) are compared with those of specimen model B of different geometry (100 x 75 mm), for the cases of reflecting (non-absorbing) and absorbing boundaries, represented below in Figure 4.4.

The influence of the reflected wave components in the received signals are clearly evident in the figures and appear to depend on the sample geometry and boundary conditions. For the absorbing model B (third output signal in Figure 4.4a), simulating a supposedly unbounded situation, the response is the least distorted, and first arrival occurs at the expected instant. Larger distortions appear in non-absorbing model A, representing the highest wave reflection situation, where an early first arrival appear with a substantial difference with the expected arrival.



a) b)

Figure 4.4 - Time history of received pulse signals for model A (100x50 mm) and model B (100x75 mm): a) non-absorbing models A and B, and absorbing model B; b) non-absorbing and absorbing model A and reflected signal (Rio, 2006)

The estimate of the reflected wave signal, shown in Figure 4.4b, results from the decomposition of the signals for non-absorbing and absorbing conditions in model A. The similarity with the non-absorbing signal is quite significant, which indicates that, for non-absorbing conditions, the signal is dominated by reflected wave components and direct wave propagation is hardly noticeable. These recent findings highlight the importance of wave reflection caused by sample geometry and boundary conditions, which are complex issues, especially for the interpretation of BE results in the time domain.

4.2.6. Models for the BE test system

The generic interpretative model of a bender element test, usually implicit, considers a shear bulk plane wave travelling between source and receiver. However, the transmission of shear waves from the source to the transmitter, through the soil specimen and into a receiver, eventually through instrumentation, involves attenuation or partial loss of the signal, which depends on the quality of these series of interfaces. Based on practical experience, Pennington (1999) compiled the factors influencing the transmission across the interfaces or connections and through materials between transmitter to receiver BE. The signal strength at each stage of the propagation was estimated, as directly reproduced in Table 4.1.

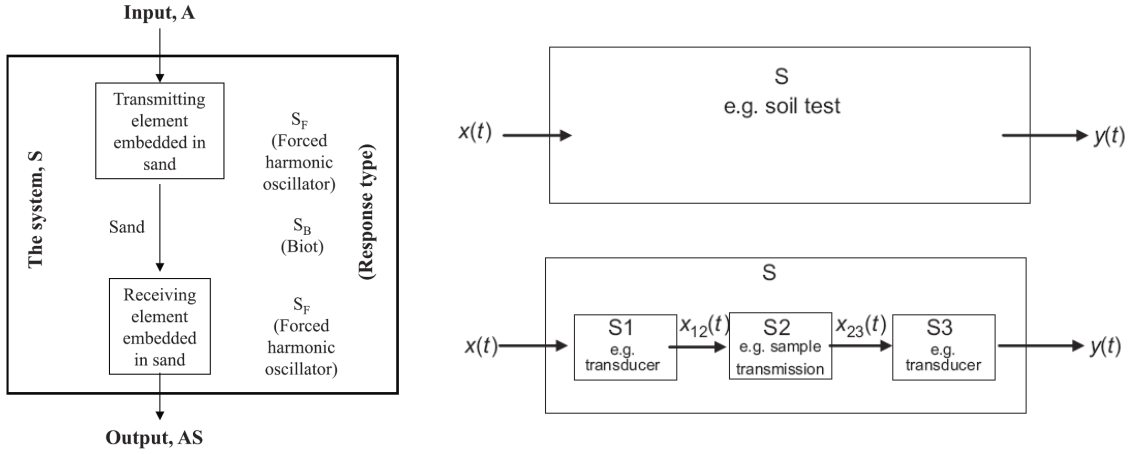
Table 4.1 - Estimated signal loss at each interface and in each material (Pennington, 1999)

Transmission interface / material	Factors influencing	Factors leading to improvement	Estimated loss in signal	Signal amplitude (V)
driver signal to piezoceramic	impedance of connections	quality of soldering of connectors to piezoceramic	<1%	≈20
piezoceramic	variations in purity of piezoceramic	manufacturing variations unavoidable	2 - 5%	19.8
piezoceramic to resin	quality of bond between ceramic and resin	fully de-grease and clean piezoceramic before potting	10 - 20%	19
resin	elastic modulus of resin, quality of casting process	use fresh resin, fully de-air before injection into mould, fully cure	10 - 20%	16
resin - soil	fit between transducer and soil, soil type and state	accuracy and control in the insertion of the BE, amount of consolidation following insertion	70 - 90%	12
soil	soil type and state	dry sands best, wet normally consolidated clays worst	30 - 70%	1.4
soil - resin	fit between transducer and soil, soil type and state	accuracy and control in the insertion of the BE, amount of consolidation following insertion	70 - 90%	0.5
resin	elastic modulus of resin, quality of casting process	use fresh resin, fully de-air before injection into mould, fully cure	10 - 20%	0.06
resin to piezoceramic	quality of bond between ceramic and resin	fully de-grease and clean piezoceramic before potting	10 - 20%	0.05
piezoceramic	variations in purity of piezoceramic	manufacturing variations unavoidable	2 - 5%	0.04
piezoceramic to received signal	impedance of connections	quality of soldering of connectors to piezoceramic	<1%	0.04

Unsurprisingly, the largest source of attenuation, suggested in the table, is at the interfaces between BE and soil, resulting on the received signal that is smaller by many orders of magnitude than the transmitted signal. Nevertheless, the variability proposed in the BE-soil interface points towards the importance of the coupling at this interface, for a good transmission and reception. Pennington (1999) also refers that quality of the coupling is directly related with quality of the fabrication of bender elements, since the more regular and parallel are the surfaces of the transducer, the better will it fit when inserted into the soil.

A mechanical analogy of the system BE-soil transmission has been suggested by Santamarina and Fam (1997) and detailed by Blewett et al. (2000), as represented in Figure 4.5. The input electrical signal drives the first BE which is embedded in the soil medium; this can be regarded as a damped, forced harmonic oscillator with response S_F. The waveform then propagates into and across the soil specimen, which is generally considered to respond to shear waves as described by Biot (1956a, 1956b), labelled S_B. The shear-wave energy finally drives the second BE as a

harmonic oscillator, again damped by the sand in which it is embedded. Blewett et al. (2000) considered the response of the two elements to be practically identical, hence incorporated it into a single S_F. Each of these responses corresponds to transfer function of the two interface materials. Given that the responses of the elements and medium compose the response of the larger system, S, once the subsystem responses, or transfer functions, S_F and S_B, are defined, the output for any arbitrary input waveform can be understood. However, as discussed by Arroyo and Greening (2002), the results obtained with this new model were not very satisfactory. For any symmetric experimental arrangement, where the source and receiver are identical, the transfer function of both sub-systems should cancel out. This is generally the case, especially for the mounting arrangements of BE in triaxial and oedometer cells.



a) b)

Figure 4.5 - Dynamic systems for modelling BE testing: a) with internal subsystems (Blewett et al. (2000); b) without and with internal subsystems (Arroyo et al., 2006)

Although dispersion manifests itself in the time domain it is best addressed in the frequency domain; "picking" of arrival times in traces needs to be guided by a proper dispersive model of any particular experiment.

The decomposition of the BE installation, including the electronics equipments, in a series of frequency response functions has been proposed by Lee and Santamarina (2005), as illustrated in Figure 4.6. This sequence of interfaces includes $H_{p\text{-}in}$, the input peripheral electronics such as power amplifiers and cables; $H_{BE\text{-}in}$, the bender element-soil response at the source; H_{soil}, the soil; $H_{BE\text{-}out}$, the bender element-soil response at the receiver; and $H_{p\text{-}out}$, the response of peripheral electronics at the output. Considering quasi-linear soil behaviour and adequate peripheral electronics, the measured global frequency response is strongly determined by the frequency response of the bender element-soil pair, i.e., $H_{BE\text{-}in}$ x $H_{BE\text{-}out}$, similar to what Arroyo et al. (2006) suggested.

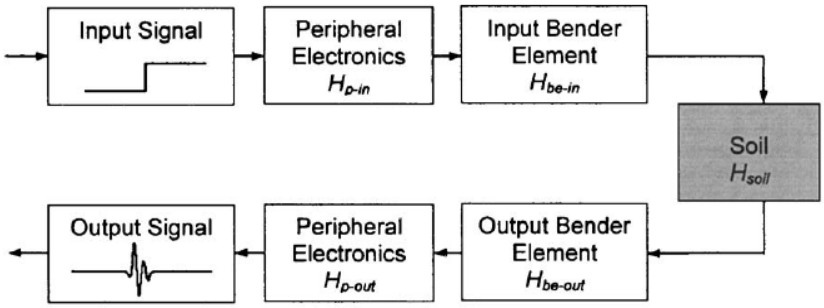


Figure 4.6 - Sequence of frequency response functions in a BE installation (Lee and Santamarina, 2005)

From these findings, it appears that transducer effects should be taken into account, in order to obtain the desired true H_{soil} in BE tests. As previously discussed for sample geometry effects, transducer effects also introduce changes in the wave traces, affecting its characteristic points, and thus a consistent and accurate identification of travel time may be compromised. Alternative interpretation techniques, namely in the frequency domain, have been explored to minimise the influence of transducer effects. However, such techniques must relate signals of the same nature or include the various frequency response functions already identified (examples provided in Brocanelli and Rinaldi, 1998; Blewett et al., 2000; Arroyo et al., 2003; Lee and Santamarina, 2005).

4.3. Monitoring the behaviour of BE

As mentioned earlier, peripheral effects, namely the frequency response of the transmitter and of the electronics, exist in bender element testing, which means that the excitation actually applied to the specimen is not necessarily exactly the same as the electrical input. The actual transfer function of the BE-specimen system is very difficult to measure, as it is strongly affected by coupling, that is, the arrangement of the soil particles around the transducer at the time of testing, as well as by the stiffness of the surrounding material and the level of confinement, among others. The degree of coupling is particularly variable and difficult to predict.

However, measurements of the behaviour of the BE have been done on occasion by a few researchers using diverse setups, including “self-monitoring” elements.

4.3.1. "Self-monitoring" bender elements

Schultheiss (1982) devised the "self-monitoring" bender element, by which the piezoelectric ceramic of the transmitting element is wired to two independent electric circuits. One is wired as a standard BE transmitter and the other returns the response of the transmitter to the input wave as an electric signal. Tests using these BEs provided evidence of the occurrence of overshooting at high frequencies, demonstrated by discontinuities in the signals. The frequencies at which overshooting starts to appear were found to be dependent of the relative impedances of the soil and the transducers, as well as the type of input signal (Jovicic et al., 1996). Pennington (1999) also used self-monitoring BEs as a means to assess the accuracy of travel time measurements, having observed a constant time delay of about 5 μs for a wide frequency range of 2 to 16 kHz.

This monitoring procedure, though quite ingenious, reproduced the input signal rather too faithfully, thus proved incapable of translating its true behaviour (Greening and Nash, 2004). Such a result can be explained by an electric leakage, where the exciting electric signal directly reaches the wiring circuit, responsible for monitoring the response (Rio, 2006).

Alternatively, Greening and Nash (2004) used another type of "self-monitoring" BE and analysed the frequency response of an instrumented bender element. A strain-gauge, mounted directly onto the bimorph prior to encapsulation in epoxy, provides a sensitive feedback of the bending of the element, thus measures the actual movement of the BE (Figure 4.7). Preliminary tests with these elements provided useful indications regarding the resonant frequency of the testing BE. However, a significant phase shift between transmitter and receiver BEs was also revealed, which was attributed to differences in the mounting arrangement of the transducers.

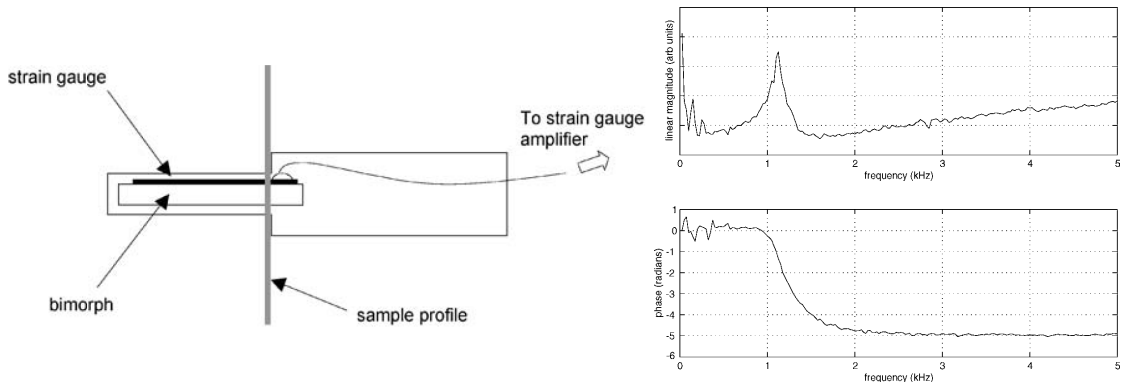
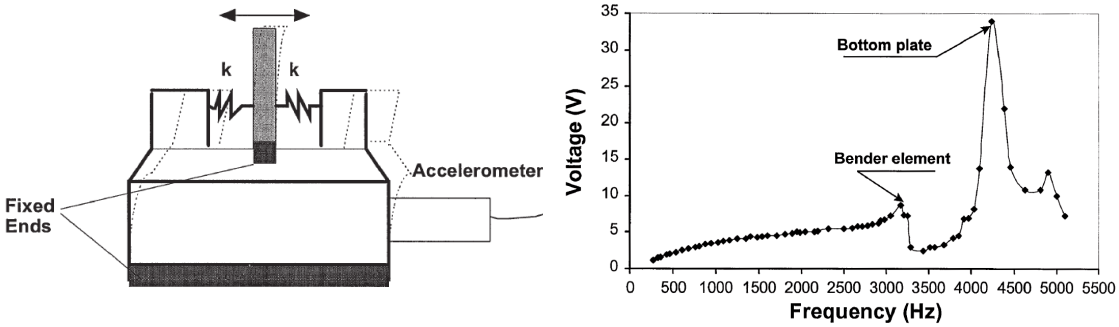


Figure 4.7 - Self-monitoring BE: schematic of strain-gauged BE and respective frequency response and phase (Greening and Nash, 2004)

A disadvantage of this method is the complex and delicate manufacturing process, in order to successfully affix the gauge to the piezoelectric ceramic. A perfect coupling between the BE and the strain-gauge is difficult to achieve, and the actual transfer function between the two elements cannot be accurately assessed. Moreover, given the size and geometry of the BE, the presence of the strain-gauge may introduce relevant changes in the response of the transducer.

4.3.2. Accelerometer measurements

Brocanelli and Rinaldi (1998) used an accelerometer, fixed to the bottom plate where the transmitting bender element is installed, to measure its response (Figure 4.8a). The vibration response of this system to an external excitation and to a BE sinusoidal signal are recorded by the accelerometer. The comparison of the frequency content of the responses to both excitations enabled to distinguish and derive the dynamic properties of the bottom plate and the transmitter element, namely its resonant frequencies, presented in Figure 4.8b.



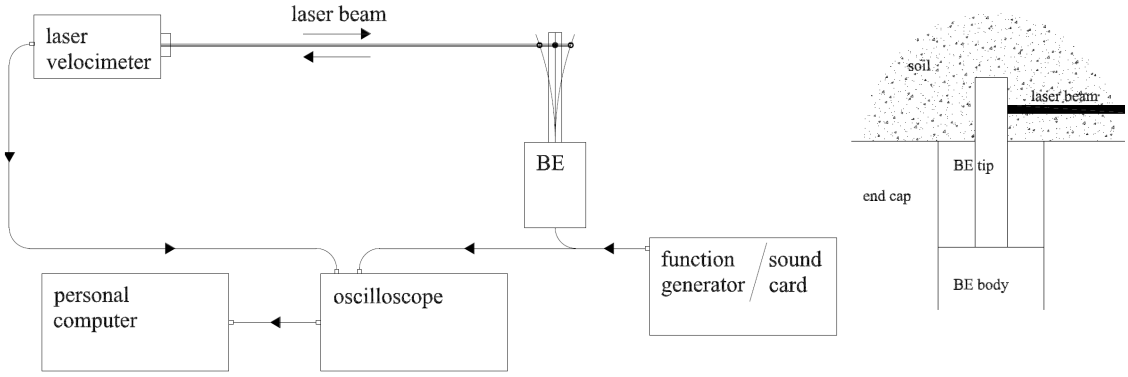
a) b)

Figure 4.8 - Monitoring BE behaviour with an accelerometer (Brocanelli and Rinaldi, 1998): a) dynamic model of the pedestal and transmitting element; b) frequency response to the BE sinusoidal signal excitation

Rio (2006) argued that, since the accelerometer is connected to the plate rather than to the BE, the results are dominated by the behaviour of the plate and are thus less reliable in terms of the actual BE response. However, a more detailed and accurate determination of the effective frequency response of the BE can be obtained by the use of different BE excitation signals with several measurements of the vibration response of the system, with an accelerometer at various points in the bottom platen, namely very close to the transducer.

4.3.3. Laser-beam measurements

The movement of the BEs can also be determined using a laser velocimeter, pointing towards a fixed target in the surface of the transducer. The non-contact nature of this type of monitoring is its main advantage, since the laser measurements are taken without any interference in the behaviour of the BE. The setup for this test is very simple, as depicted in Figure 4.9: the laser beam is aimed at the monitoring target, where it is reflected and returns to its source. This path needs to be unobstructed; hence, this setup is only achievable in air, where the BE acts as a free cantilever.



a) b)

Figure 4.9 - Monitoring the BE behaviour using a laser velocimeter: a) general setup; b) measurements with the BE embedded in a specimen (Rio, 2006)

These measurements of the BE in air can be used to study the actual properties of the bender element. However, in order to better understand BE tests, it is most relevant to know how the bender element interacts with the medium where it is embedded, as in normal BE testing conditions. It is virtually impossible to use the laser velocimeter for monitoring the behaviour of a bender element embedded in a soil sample. Rio (2006) conceived an alternative measurement of the movement of the BE, when embedded in an artificial polyurethane sample, which behaviour resembles that of a soft clay. The compromise consisted in opening a small slot in the side of the sample, thus enabling the laser beam to reach, unobstructed, its target at the BE surface.

From his results, Rio (2006) concluded that BE behave as mechanical frequency filters, since there is a maximum frequency after which its response is no longer relevant, which is applicable both in air or when embedded in a sample. This maximum frequency, which should be taken in account when testing, is a property of the transducers, but also depends of the medium. The overall mechanical response of the BE is proportional to the stiffness of the medium and to the degree of coupling with the medium. In terms of the response of the transducers to different excitation

signals, Rio (2006) observed significant discrepancies for pulse input signals as opposed to continuous input signals. When input pulse signals are used, a transient response is obtained, dominated by the natural frequency of the transducer rather than the frequency of the signal, and dispersive phenomena cannot be effectively controlled. In contrast, the use of harmonic continuous signals enables the establishment of a steady-state of vibration, and thus the selection of this type of signal is recommended.

4.3.4. BE in direct contact

Since bender elements work as transmitters and receivers, it is possible to use the receiver BE to monitor the movement of the transmitter BE, when in direct tip-to-tip contact, as suggested by Lee and Santamarina (2005) and Leong et al. (2005), among others. In the present research, this method was applied. Some assumptions are required for the application of this method, namely a perfect coupling between the BE tips. Moreover, the monitoring of the movement of the BE tip is not fully accurate, since the BE movement, as a cantilever beam, involves the whole transducer. In comparison with laser beam measurements, this method is less reliable, however it is simple and immediate, readily available and can easily be made in any BE test setup.

The response of the BE to the electrical excitation of the function generator was monitored using the receiver BE as the measuring tool. The setup consists in using exactly the same setup of electronics as in standard soil testing conditions, and placing the tips of the two BE (transmitter and receiver) in direct contact, as illustrated in Figure 4.10. The concept is similar to a polarity check setup, described in the previous chapter. In such conditions, the received signal will incorporate all the potential interferences from the transducers and electronics.

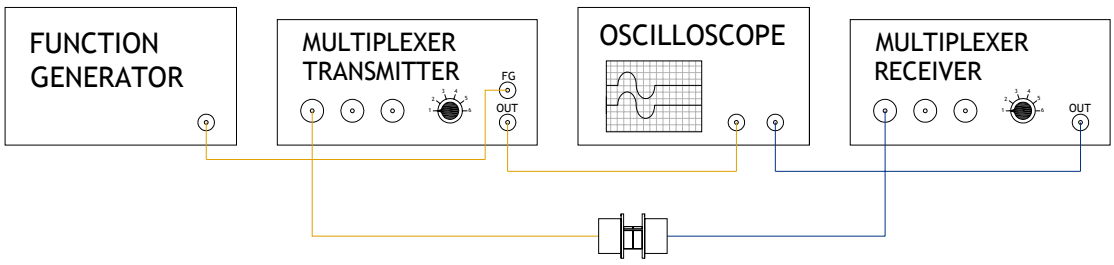


Figure 4.10 - Schematic of monitoring BE in direct contact

The direct comparison of transmitted and received signals is useful and enables to observe how the BE respond to the different input signals. Leong et al. (2005)

observed that the received signal has a different time history than that of the transmitted signal, with a different frequency and shape; particularly after the transmitted signal has ended. The received signal indicates some further movement from the transducers, as would be caused by inertia effects.

From comparisons of this method with laser beam measurements, Rio (2006) concluded that the use of BE to directly compare the transmitted and received signals in the time domain is not ideal. A frequency dependent phase delay is added at each mechanical interface of the bender element test system. In a normal bender element test, four such interfaces exist, and as a consequence any direct time comparison between the transmitted and received electric signals is inevitably affected. A signal comparison, done in relative terms by comparing different received signals in the frequency domain, is capable of overcoming the effect of the mentioned delays at each interface, and its use is therefore advisable.

It would be interesting to include figures with the results of the BE calibrations, in the time domaind and with FFTs for better understanding the frequency content of the signals

4.4. Interpretation techniques

4.4.1. Introduction

As already mentioned, the attraction of the BE technique is its apparent simplicity, both in respect to the test itself and to the interpretation of the results. Many authors have dealt with the difficulties of interpretation of results (Viggiani and Atkinson 1995; Brignoli et al. 1996; Jovicic et al. 1996; Arulnathan et al. 1998; Greening et al. 2003; Greening and Nash 2004; Leong et al. 2005). In essence, it is clear from all of these authors that the interpretation of the results remains subjective, requiring some degree of judgment, and no single ideal method of interpretation has been agreed upon.

For the derivation of the seismic velocities, two measurements are required: the travel length and the travel time. Although the second is by far the most complex parameter, as the output signals are always very different from the input signals, different proposals for the measurement of travel length have also been advised.

For interpretation of the received signals towards the determination of the travel time, diverse methodologies have been proposed over the years, ranging from the simplest method based on the immediate observation of the wave traces and measurement of the time interval between starting points, to more elaborate techniques, supported by signal processing and spectrum analyses tools. Alternative options for the selection of the input wave configuration have also been proposed, not only in terms of its shape, but also in its frequency, with obvious impact in terms of output clarity and ease of interpretation. The most common methodologies for interpreting BE results are generally grouped into time-domain and in the frequency-domain methods. A short description of the main principles and applications of each method is provided in the sections that follow.

4.4.2. Effective travel length

The length effectively travelled by the seismic waves is defined as the actual distance between the transmitter and receiver BE at the time of wave propagation. Since the wave velocity, and thus the corresponding modulus, is directly dependent of the travel length, its accurate determination is fundamental, especially given the relatively small dimensions of laboratory specimens.

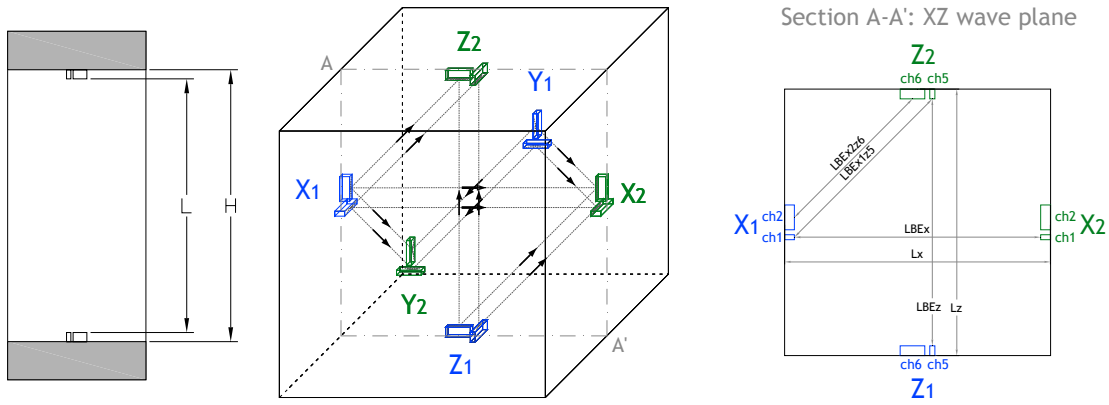
Some discrepancies appear in the literature with regard to the selection of the travel length. Fam and Santamarina (1995) computed velocities using the distance between mid-height of the free-ends of the BE, though no further justification was given. As cited by Sadek (2006), Porovic (1995) considered the distance between the centres of the transducers as the effective travel length, having concluded that such a travel length provided optimum agreement between the shear stiffness obtained from resonant-column tests and bender element measurements. Rio (2006) carried out a series of BE tests on artificial polyurethane samples, at several heights for a large range of geometries, having concluded from back-analyses of the results that the travel distance measured between transducers tip-to-tip appeared to be unsuitable. Instead, the results indicated that the travel distance should be measured between the centres of dynamic pressure exerted by the transducers on the surrounding soil, roughly at 60% of the embedded height. Further research on this matter appears to be urgent.

Nevertheless, the effective distance is most commonly taken as the bender elements tip-to-tip distance, which for the case of triaxial tests generally corresponds to the height of the soil specimen, H at the time of testing less the protrusion of each element, l_{BE}. The protrusion varies according to the transducer dimensions and its

setup in the apparatus, hence the travel length, L should be verified prior to each test (Figure 4.11a). As a confirmation of this assumption, Viggiani and Atkinson (1995) carried out tests on a set of reconstituted specimens of different heights under various stress conditions, to assess the relation between specimen height and travel time, observing an intercept corresponding to the protrusion of the BE. Obviously, this protrusion correction is only necessary for bender and extender elements, since shear-plates and compression transducers do not penetrate the specimen.

The tip-to-tip distance has been herein adopted, supported by the results of Dyvik and Madshus (1985), Viggiani and Atkinson (1995), Brignoli et al. (1996), Lee and Santamarina (2005), among others, which demonstrated that the shortest distance between transducers is most accurate. During the course of a test, the deformation experienced by the specimen has to be duly taken into account, and included in the computation of travel length.

In the present work, both direct (straight) and inclined (diagonal) wave measurements were performed and recorded. For the case of inclined measurements in triaxial or true triaxial tests, the selection of the effective tip-to-tip distance is less clear-cut. When the transducers are located in adjacent orthogonal directions, the shortest distance corresponds to the nearest corners at the tips of the transducers. However, since the wave is generated by the movement of the whole transducer, the consideration of a centre-to-centre tip distance appears to be more realistic. Sadek (2006) analysed the results of freshly pluviated Hostun sand samples and observed that the velocities of direct and inclined measurements in the horizontal plane of the specimen (assumed cross-anisotropic) would coincide if the tip-to-tip distance measured from the centreline of the elements were used. Therefore, the centre-to-centre tip distance was considered the effective travel length for inclined body wave measurements, as illustrated in Figure 4.11b. Given the arrangement and positioning of the transducers in the true triaxial chamber, most of the inclined wave distances are slightly different and need to be computed separately, as will be detailed later in Chapter 7 with the test results.



a) b)

Figure 4.11 - Definition of travel distance: a) direct arrival for a triaxial cylindrical specimen; b) direct and inclined waves for a true triaxial specimen [FEUP-TT]

When a second arrival of the wave, caused by reflection at the ends of the specimen, is visible, the travel time can be also measured by comparison of the first and the second arrival of the wave in the output signal using the second arrival method (Arulnathan et al., 1998) or the multiple reflections method (Lee and Santamarina, 2005) as will be described below. In this case, the travel length is different, as it refers to the distance between the first and second arrival (Figure 4.12), which corresponds exactly to twice the plate-to-plate distance, that is, twice the height of the specimen, which can be deduced from the following expression:

$$L_{reflect} = 2(L + 2l_{BE}) = 2H \qquad [4.4]$$

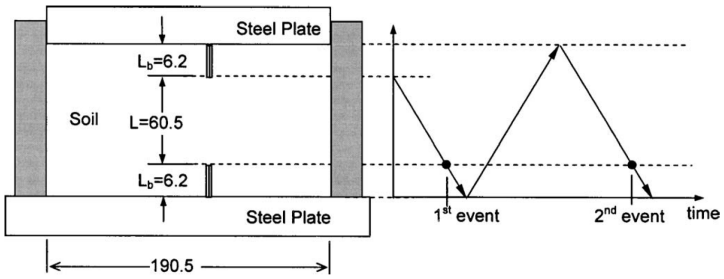


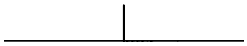
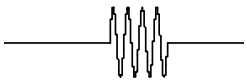
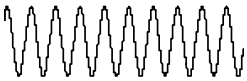
Figure 4.12 - Definition of travel length for reflected wave arrival: example from the multiple reflections methods (after Lee and Santamarina, 2005)

4.4.3. Input signal configuration

Many different configurations of the input signal have been used for BE testing. The configuration refers to the shape of the electric signal generated by the function generator or by another device, namely a computer sound card, which is sent directly

or via an amplifier, to the transmitter bender element. The most common input signal configurations reported in the literature are summarised in Table 4.2

Table 4.2 - Input wave shape suggested by different authors

Input wave shape		Reference
	Square or step signal	Dyvik and Madshus (1985); Fam and Santamarina (1995)
	Impulse signal	Lee and Santamarina (2005)
	Sine wave	Viggiani and Atkinson (1995); Brignoli et al. (1996)
	Sine pulse [90 ° phase shift]	Pennington et al. (2001)
	Distorted sine wave [typically 30 ° phase shift]	Jovicic et al. (1996)
	Forced oscillation [sine wave cycles at resonance frequency]	Jovicic et al. (1996)
	Continuous sine wave of constant frequency	Greening and Nash (2004)
	Sine sweep of frequencies [typically 100 Hz to 20 kHz]	Greening and Nash (2004); Ferreira et al. (2007)
random signal [or noise]	Stochastic random noise	Roesler (1979); Santos et al. (2007)

In what follows, each of the listed input wave configurations will be introduced and discussed in the context of BE testing and interpretation.

4.4.3.1. Square signals

Most early studies using BEs (Dyvik and Madshus, 1985; Bates, 1989) used a single square-wave pulse, as this signal has a very sharp, well-defined start. According to Bodare and Massarsch (1984), square signals resemble the impact loads used in the cross-hole test method, where the first direct arrival of the wave is used to estimate its travel time. However, while this instantaneous variation of voltage can be mathematically expressed and electrically reproduced by a digital function generator, mechanical devices and materials with finite mass and stiffness cannot respond in

such manner. Due to the presence of inertia forces, it is not possible to obtain instantaneous variations in motions, equivalent to infinite accelerations (Rio, 2006). Moreover, the initial sharp rise of the signal results in a very broad frequency content with no particular main frequency.

It is yet unclear how the transmitter BE actually responds to this excitation. As a result, the response signal provided by the receiver is more difficult to compare with the square input signal sent by the function generator. In the absence of self-monitoring BE, analyses in the frequency domain using these two signals (the electrical signal from the FG and the receiver BE signal) may be even more misleading, due to the uncertainty regarding the transfer function of the transmitting element. In view of these limitations, square signals were not used in this research.

4.4.3.2. Sinusoidal signals

Sinusoidal signals have become more popular, as these have been shown to give more reliable time measurements, primarily because they reduce the frequency components and thus minimize velocity dispersion (Blewett et al., 2000). Given the configuration of sinusoidal signals, its interpretation in time domain is straightforward and intuitive.

In this type of signals, several variations have been adopted, with different durations and shape. Pulse-type signals include the complete sine wave pulse, the positive sine pulse [90 ° phase shift], the distorted sine [typically 30 ° phase shift, proposed by Jovicic et al. (2006)] and the forced oscillation signal [sine wave cycles at resonance frequency]. Continuous signals have also been used, such as the continuous sine wave of constant frequency and the sine sweep of frequencies [typically 100 Hz to 20 kHz].

The pulse input signals are usually identified by its single input frequency, although in reality the frequency content of pulse signals is broad. Results from the BE monitoring process carried out in this research, as well as those reported by other authors, suggest that the actual frequency of the BE may differ from that sent to the transducer. In the absence of an accurate feedback measurement of the frequency of the transmitted signal, in this text, whenever the frequency of a sinusoidal input (pulse or continuous) wave is provided, it refers to the apparent input frequency, as selected in the function generator.

According to Arroyo et al. (2003), it is now apparent that the square-shaped input signal is the least favourable shape and the distorted sine wave, suggested by Jovicic et al. (1996) is the most favourable, as experimentally observed.

4.4.3.3. Random noise

Low strain measurements using random noise excitation or ambient vibration have been used by several researchers, mainly in resonant-column tests (Aggour et al., 1988, Amini et al., 1988, Cascante and Santamarina, 1997). Amini et al. (1988) proposed the use of random noise in a resonant column device as an alternative method to obtain the first mode of vibration. The transfer function between the input and output signals is used to identify the resonance frequency of the system. The procedure involves the adjustment of the input signal by modifying its frequency content according to a first identification of the maximum peak in the frequency response curve and the use of a number of tests to eliminate undesirable noise. Usually, a PC computer is used to control the system with the possibility to generate bandwidth random noise. Random noise imposes all frequencies simultaneously, spreading the energy in the selected frequency band and thus facilitating low strain measurements (Cascante and Santamarina, 1997).

Ambient vibration measurement can also be used, requiring modal identification techniques, since the input excitation is unknown. This type of input signal is simple and readily available, since excitation devices are not necessary; every harmonic component corresponding to a natural frequency of the system has an amplified response due to resonance; as a result, the obtained modal parameters, i.e., natural frequencies, mode shapes and damping ratio, provide information regarding the inherent dynamic properties of the soil specimen.

Although these techniques have been developed for resonant-column testing, this type of input signal can also be used in bender element testing, as reported by Santos et al. (2007).

4.4.4. Travel time determination

4.4.4.1. First direct arrival of the output wave

The direct measurement of the time interval between the input and output waves is the most immediate and intuitive interpretation technique, similar to the method

used in field geophysical testing (Abbiss, 1981; Dyvik and Madshus, 1985; Jamiolkowski et al., 1995; Jovicic et al., 1996; Pennington, 1999). This method of interpretation assumes plane wave-fronts and the absence of any reflected or refracted waves (Arulnathan et al., 1998). Figure 4.13 shows an example of a typical sine-wave input pulse (OABC) and the resulting output signal. The identification of the instant of first inflection of the output wave is simple but subjective: that is, different users may select different arrival points, as indicated by the multiple 'arrow' indicators in the upper signal in Figure 4.13.

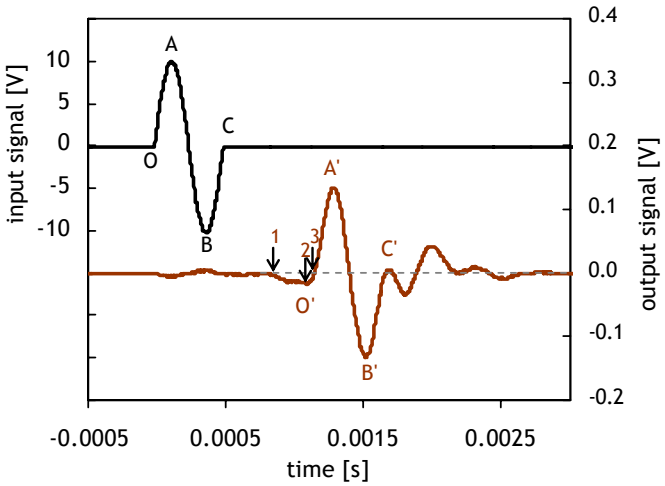


Figure 4.13 - Example of time domain interpretation methods: first direct arrival

In the context of this work, this method was applied systematically. The complete framework for interpretation of BE tests in this research is provided in the final sections of this chapter. Using the example in Figure 4.13, there is a range of possible locations for the shear wave first arrival, usually taken between arrows 1 and 3. As previously demonstrated, there are a number of phenomena involved in bender element testing, which influence and distort the BE response signal, complicating its interpretation. These effects or disturbances seem to be present in this example and therefore an appropriate and systematic approach must be used, in order to obtain comparable and reliable results. A practical, yet empirical set of guidelines has been defined for the interpretation and selection of the travel time by first arrival in the time domain.

The first step in the interpretation consists in visualizing the complete wave. The oscilloscope window should be adjusted to provide a clear view of the complete signal or, in case of a long wave, of its initial and most energised section. From the observation of this example, the response contains one strong sinusoidal wave followed by a couple of smaller sine cycles. The main cycle of the response appears to have a frequency close to that of the input signal and positive polarity (as expected

from the polarity check test). Arrow number 1 indicates the very first deflection of the shear wave; however it is downwards, contrary to the expected wave polarity. This usually results from dispersion, either by near-field effects or wave reflections at the boundary conditions, as already discussed. Hence, this point does not correspond to the first arrival of the shear wave. Arrow number 2 is located at the first trough of the wave, at the start of the main sinusoidal cycle. Arrow 3 indicated the point where the main cycle crosses zero, as depicted in the figure by the zero intercept dashed line. The first arrival of the shear wave is most likely located between arrows 2 and 3. In the absence of further information, the selection of first arrival would be, in the context of this research, taken at arrow 2, as the position of arrow 3 corresponds to a point where the main cycle has already started.

The usual procedure is however to use several input signals, at different frequencies, about four or five, to obtain additional information of the response. The set of response signals will obviously have diverse shapes, more or less cycles, and more or less amplitude. In the vast majority of cases, a common feature point is usually encountered, corresponding to the first trough in some signals and to more discrete points, such as a slight inflection, in other response signals. The underlying assumption, without which this interpretation would be unfeasible, is that the travel time is independent of the input frequency, at least within the selected range of frequencies (typically from 1 kHz to 10 kHz).

4.4.4.2. Time interval between characteristic points of the input and output waves

Characteristic points of the input and output waves, such as peaks, troughs and zero intercepts, are easy to identify, and the intervals between corresponding points (AA' and BB' in Figure 4.13) can be considered to represent the travel time of the shear wave, again under the assumption of plane wave propagation and absence of reflections or refractions (Viggiani and Atkinson 1995; Arulnathan et al. 1998). However, given the damping, attenuation, and different frequency content of the signals, successive intervals AA' and BB' are not identical, with later intervals tending to be greater than early ones, so the use of this method is not recommended. In the example traces of the figure, the following time intervals were measured:

Table 4.3 - Time interval between characteristic points of the input and output signals

Characteristic points		time interval
input	output	[in ms]
O	O'1	0.868
O	O'2	1.104
O	O'3	1.156
A	A'	1.180
B	B'	1.184
C	C'	1.200

Jovicic et al. (1996) proposed an alternative method, which also makes use of characteristic points of the input and output waves for the determination of travel time. The method consists in adjusting the frequency of the input wave as to give forced oscillation of the receiver at one of its natural frequencies, inducing resonance, in about five input sinusoidal cycles. The resonant frequency can be determined by manually sweeping the frequency of a continuous sinusoidal input signal (in the function generator), while observing the Lissajous response in an XY plot in the oscilloscope, until a straight line is obtained.

In that case, the arrival time is taken from one of the peaks or troughs of the input signal and the corresponding point in the output signal, usually the peak of highest magnitude. Again, this method was not applied in the context of the present research.

4.4.4.3. Second arrival of the output wave

Arulnathan et al. (1998) observed that the transmitted wave propagates along the specimen and is detected by the receiver transducer, but it is also reflected in the receiver platen and propagated in the opposite direction to the transmitter platen where it is reflected again, returning to the receiver a second time. Figure 4.14 illustrates a larger window of the same test result in Figure 4.13, where the second arrival of the wave is visible in the output signal.

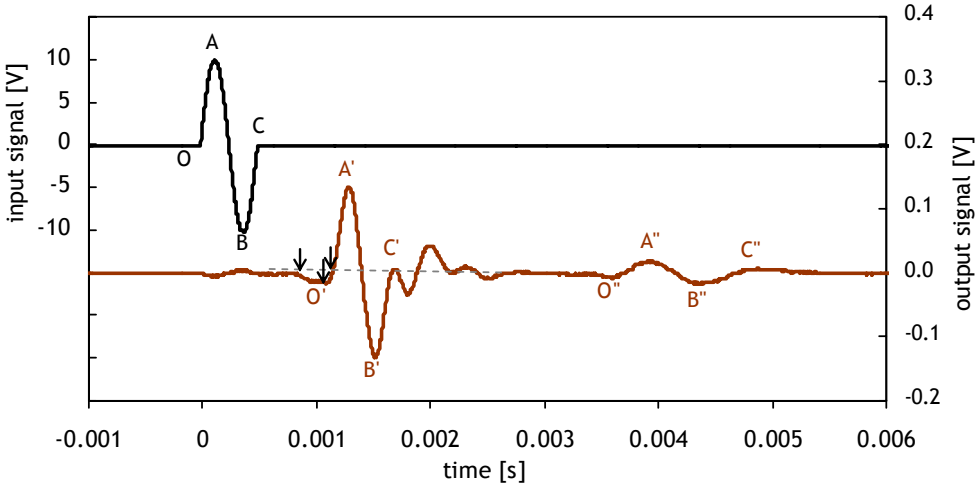


Figure 4.14 - Evidence of second shear wave arrival

The time between first and second arrival of the wave corresponds to twice the travel time. The second arrival of the wave obviously contains less energy than the first; hence it is often undetected in the signal, though further amplification of the output signal may be useful in this regard. Overall, the technique works only for certain combinations of travel distance, soil properties and boundary characteristics. For example, it is easier to observe second-wave arrivals in BE tests in the oedometer than in standard triaxial tests, due to the short travel length and to the nature of the top and bottom platens.

The direct comparison of time intervals between time intervals of characteristic points of the first and second arrival of the shear wave in the output signal is valid, since these are measurements of the same transducer. The results for this example are provided in the following table. The exact location of point C'' was hard to define, due to the low amplitude of the signal at that point, hence the time interval C'-C'' was not considered.

Table 4.4 - Time interval between characteristic points of the first and second arrival of the shear wave in the output signal

Characteristic points		time interval*	corresponding travel
input	output	[in ms]	time [in ms]
O'2	O''	2.510	1.207
A'	A''	2.644	1.271
B'	B''	2.812	1.352

[*] corresponds to less than the half the time interval, since the travel distance is exactly twice the height of the specimen (as schematically shown in Figure 4.12)

The corresponding travel times (for the standard travel length) obtained from this method and indicated in Table 4.4, are larger than those directly measured between characteristic points of the signals, in Table 4.3.

Lee and Santamarina (2005) also used a method based on second arrival of the output wave, which they called 'multiple reflections method'. They developed a systematic approach to interpreting the results based on the separation of the two events of wave arrival and on the selection of the peak of maximum cross-correlation between the two events as the travel time for twice the plate-to-plate distance. Since the two events are measured with the same transducer, the response cancels all the peripheral effects of the system, and hence this method is very robust. However, the same observation applies: second arrivals are often undetected.

In this research, due to the large travel distances and also on the low-reflective nature of the boundaries of the specimen, only in a few occasions was the second arrival visible in the output signal. As a result, this method was not applied in general. Whenever possible, the additional information provided by the second arrival of the shear wave was used to double-check the selection of the instant of first arrival.

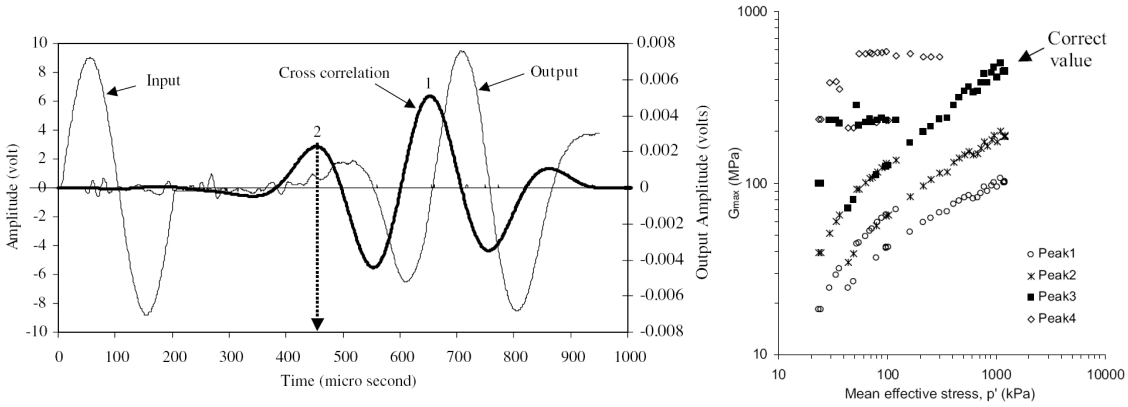
4.4.4.4. Cross-correlation of input and output signals

Based on the same assumptions as above, Viggiani and Atkinson (1995) suggested the use of the cross-correlation function, which is a measure of the degree of correlation of two signals. The cross-correlation of a single frequency pulse input wave with its response produces a peak at a time shift that is taken as the wave travel time between the two points (Mohsin and Airey 2003; Airey et al. 2003).

One of the main limitations of the use of cross-correlation is the fact that in most cases, the first peak of the output signal of a BE measurement does not correspond to the highest peak of the signal. This results on a maximum cross-correlation peak that is frequently inconsistent with the first arrival of the shear wave. The example of Figure 4.15 demonstrates an erroneous cross-correlation output, from Mohsin and Airey (2003). In this case, the maximum peak of cross-correlation does not correspond to the travel time, which is generally provided by the second highest peak. The authors do point out the major limitation of this technique is that it is difficult to determine which is the correct peak in the cross correlation signal. To select the correct peak, the authors suggested that a "visual check" should be performed at some stage of the test. Although it is unclear what this "visual check"

consists of, it is possibly referring to the identification of direct first arrival (described in section 4.4.4.1).

The data in Figure 4.15 show that the arrival times predicted by the different peaks in the cross correlation tend to vary proportionately during the test, resulting in nearly parallel curves. It should be noted, however, that the curve labelled as indicative of the correct value results at first from the selection of the second peak, and at higher stresses from the selection of the third peak. This demonstrates the instability of the method, thus questioning its validity for the correct interpretation of BE test results.



a) b)

Figure 4.15 - Cross-correlation results (Mohsin and Airey, 2003): a) input, output and cross-correlation signals; b) G_{max} predicted from different peaks in the cross-correlation during isotropic compression

Based on these uncertainties, it is not clear what, if any, is the advantage in using it for matching a single-pulse input signal and a more complex output signal, such as the example shown here. Moreover, such a technique is strictly applicable for signals of the same nature, requiring the frequencies of both waves to be of the same magnitude (Santamarina et al., 1997; Jovicic et al., 1996). For these reasons, this technique was not applied in this research.

4.4.4.5. Discrete method: π-point identification

The use of continuous sinusoidal input waves has been advocated by many researchers, mainly as a means to minimise distortion associated with different frequency components (Brocanelli and Rinaldi, 1998; Blewett et al., 1999, 2000; Greening et al., 2003). Naturally, it is not possible to read the wave travel time directly in the time domain (Kaarsberg, 1975; Sasche and Pao, 1978; Greening and Nash, 2004). The π-point identification method uses continuous harmonic waves as

input. In this method, the transmitted and received signals are observed directly on an oscilloscope, set to display a XY plot of channels A and B, which is time independent. The screen shows the Lissajous figures, as illustrated in Figure 4.16, which give an indication of the phase relationship between the channels: perfectly in-phase and out-of-phase correspond to positive and negative straight lines, respectively. Each of the frequencies producing a perfect phase shift between the signals is a π-point, or phase frequency, since the phase angle between the waves is a multiple of π (or - π). This technique is based on the wave propagation theory, in which velocity V is a function of the frequency f and the wavelength λ, or alternatively, of the travel length L and the corresponding phase angle $\Phi(f)$, as expressed by:

$$V = \lambda \cdot f = 2\pi \cdot f \frac{L}{\phi(f)} \qquad [4.5]$$

The plot of the phase frequencies against the respective phase angles produces an approximately linear relationship, the slope of which is proportional to the travel time. For practical reasons, it is more convenient to use the parameter N (the number of wavelengths) in the graph, as it takes multiple values of 0.5 for each phase angle multiple of π:

$$N = \frac{\phi(f)}{2\pi} \qquad [4.6]$$
$$\phi(f) = k\,\pi$$

from which

$$N = \frac{k}{2} \qquad [4.7]$$

Relating N with travel time results in:

$$t = \frac{L}{V} = \frac{N}{f} \qquad [4.8]$$

The slope of the plot in Figure 4.16c directly provides the travel time of the wave along the specimen. This approach is more objective, but it requires manual sweeping of the input frequency to allow the π-points to be determined.

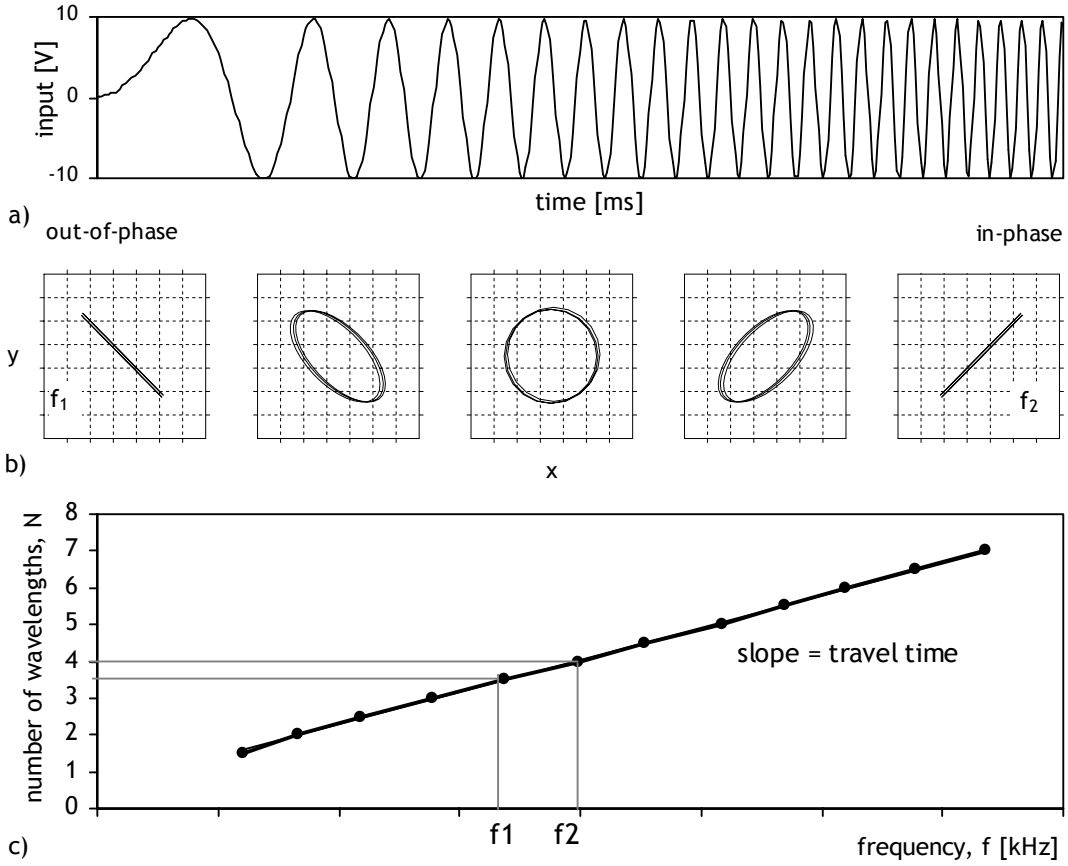


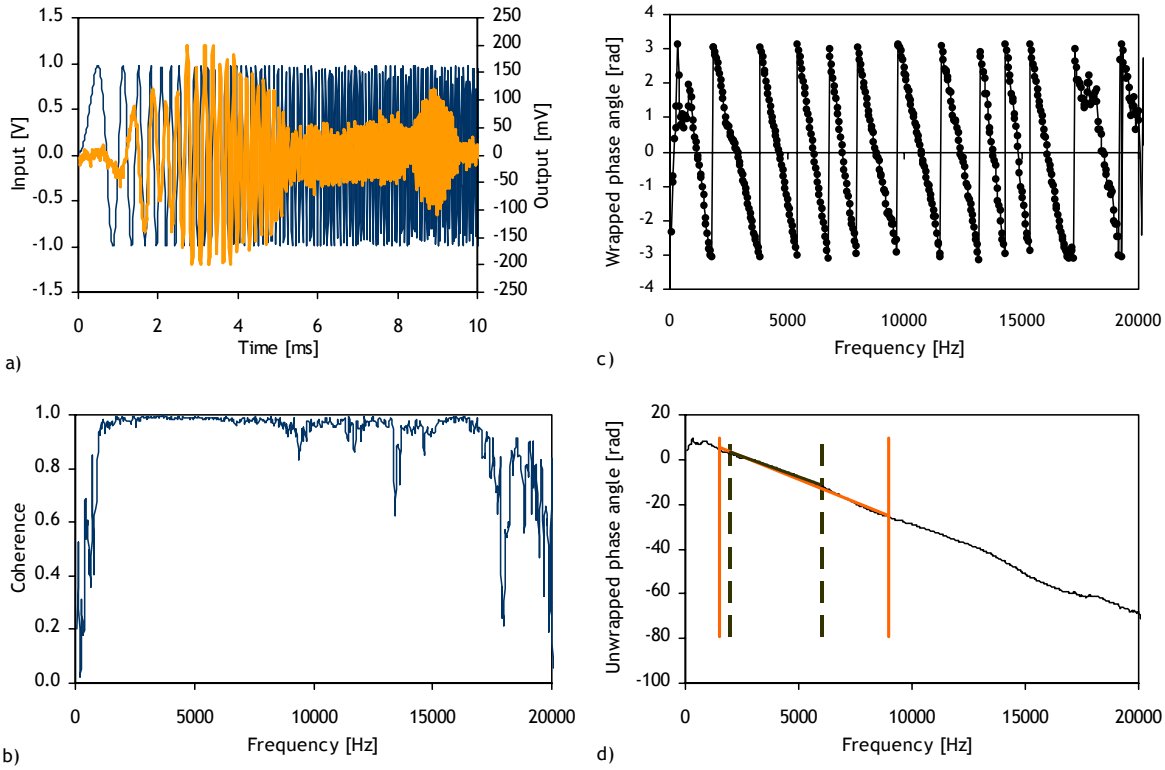
Figure 4.16 - Discrete π-points method: a) manual sweeping of input frequency; b) XY plots showing Lissajous figures in the oscilloscope; c) determination of travel time

This method has the disadvantage of being time-consuming, which becomes impractical especially when testing with multiple pairs of transducers, as in the true triaxial cell. An automated version of this method has been developed, as follows.

4.4.4.6. Continuous method: sweep input signal

The information provided by the discrete method could be established less onerously using an automated frequency sweep as input signal and a spectrum analyzer. Sweep signals, in the context of bender element testing, are non-harmonic sinusoidal continuous signals. The continuous sweep input method enables the acquisition of a continuous phase angle versus frequency relationship (Greening et al., 2003; Greening and Nash, 2004). These authors suggested a low-cost setup, consisting of a spectrum analyzer system loaded into a PC to control a high-speed dual-channel data acquisition unit.

For the purpose of illustrating the output of the program, an example for a test on a residual soil sample is reproduced in Figure 4.17.



	Frequency ranges	f1 [Hz]	f2 [Hz]	travel time [ms]	correlation coefficient	wave velocity, V_S [m/s]	modulus estimate, G_0 [MPa]
e)	———	1500	9000	0.6577	0. 9915	182.5	64.9
	- - -	2000	6000	0.5664	0. 9945	211.9	87.5

Figure 4.17 - FD results for the residual soil (p' = 100 kPa): a) input and output signals in timescale; b) coherence; c) wrapped and d) unwrapped phase angle against frequency; e) summary of results

A sweep sine signal, generally with a 100 Hz to 20 kHz bandwidth, is used as input and the output signal can be observed in the time domain, where it is not feasible to determine a direct arrival time (Figure 4.17a). The software processes this data (a few series of shots are used) and displays the coherence function and the relative wrapped and unwrapped phase angle, from which the travel time is derived.

This frequency bandwidth was considered suitable for testing these natural soils. Other input frequency ranges can be adopted to comply with the response of the system. From practical experience, a wider range of 100 Hz to 50 kHz has provided

clearer and more satisfactory results for tests on stiffer materials, namely compacted soil and soil-cement samples (Rios Silva et al., 2008).

The coherence between the two signals against input frequency, presented in Figure 4.17b, serves as an indication of how well correlated are the two signals. The coherence function indicates how much of the energy in the output signal is caused by the energy in the input signal (Hoffman et al., 2006). The extent of the relationship between the signals is expressed from 0 to 1, where unity represents maximum correlation, hence maximum coherence.

The relative phase angle against frequency can be provided "wrapped", that is, ranging from - π to π, or "unwrapped", starting at or near zero and continuously increasing, as shown in Figure 4.17c and d, respectively. The travel time is derived directly from the slope of the best-fit straight line to the plot of unwrapped phase angle against frequency, for a selected frequency range. A slightly non-linear relationship between the relative phase angle and the signal frequency is generally observed, showing that the 0 to 20 kHz range is too broad to provide reasonable results. However, it is still useful to start with this wide frequency range to provide an overview of the full coherence function as well as the complete relationship between unwrapped phase angle and frequency, which aids in making the decision on the most appropriate ranges to select for detailed analysis. Selection of a range showing high coherence is necessary to obtain low variation in the results, indicated by a high correlation coefficient of the best-fit line to the unwrapped phase angle versus frequency data. Finally, having decided on the most appropriate range, the travel time is determined directly from the slope of the best-fit line, and the shear wave velocity and shear modulus are automatically computed.

This continuous method is an interesting alternative, since it is automated and can be rapidly performed in conjunction with other methods. Since it requires the selection of a specific frequency range, undefined at the start and not automatically selected by the software, it is still a flexible and interactive system, where practical experience is combined effectively with the overall detailed information obtained in the process. The comparison of this and the π-point method, both in the frequency domain, is discussed in the following section.

It is also important to consider the differences between phase and group velocity (detailed in Greening and Nash, 2004; Rio, 2006).

4.4.4.7. Discussion of current methods

The exercise of applying all these diverse interpretation methods in a single BE test of a given soil specimen is both interesting and challenging, inevitably revealing significant variation in deduced travel times. Some techniques are not applicable in most cases, such as the second-arrival method or the multiple-reflections method, due to the rapid attenuation of the wave. Others are more or less elaborate representations of the same principle, as is the case of the π-point method and the continuous-sweep method (Greening and Nash, 2004; Ferreira, 2004).

In Table 4.3, considerable differences were obtained between time intervals of characteristic points of the input and the output. The maximum differences correspond to 28% of the maximum interval. On the other hand, in Table 4.4, the differences between time intervals of characteristic points of the same signal were less significant. The differences in the table amount to 11% of the maximum value. Apart from the obvious improvement in terms of the uncertainty in the determination of travel time, the use of comparisons between signal features of the same transducer, such as first and second arrivals, is more correct, as it is a "self-healing" measurement. Although not widely used in this research, the second-arrival or the multiple-reflections methods are recommended.

A comparison of the results of applying the π-point method and the continuous-sweep method is provided in Figure 4.18. This figure shows the unwrapped phase angle π plotted against frequency f, where π is related to the results from both methods, in tests at two different effective confining stresses of a Toyoura sand specimen (the confining stresses - 50 and 200 kPa - are indicated in the legend). The straight-line portion of these plots corresponds to the straight-line plot in Figure 4.16c, but with the latter plotted as N versus f rather than π versus f (where N and π are related by equation 4.5). These results were obtained in the context of an international benchmarking exercise (Ferreira and Viana da Fonseca, 2005; Yamashita et al., 2007). This example clearly demonstrates that the results of these methods superimpose, in terms of the overall slope of the curve. This good agreement between both methods serves as an important quality check to the transfer function algorithm of the continuous method, providing confidence in the automatic process. However, even in this type of plot, the sweep results provide more information, and, as will be demonstrated later, allow much more information to be extracted to clarify what part of the data should be used (Ferreira and Viana da Fonseca, 2005).

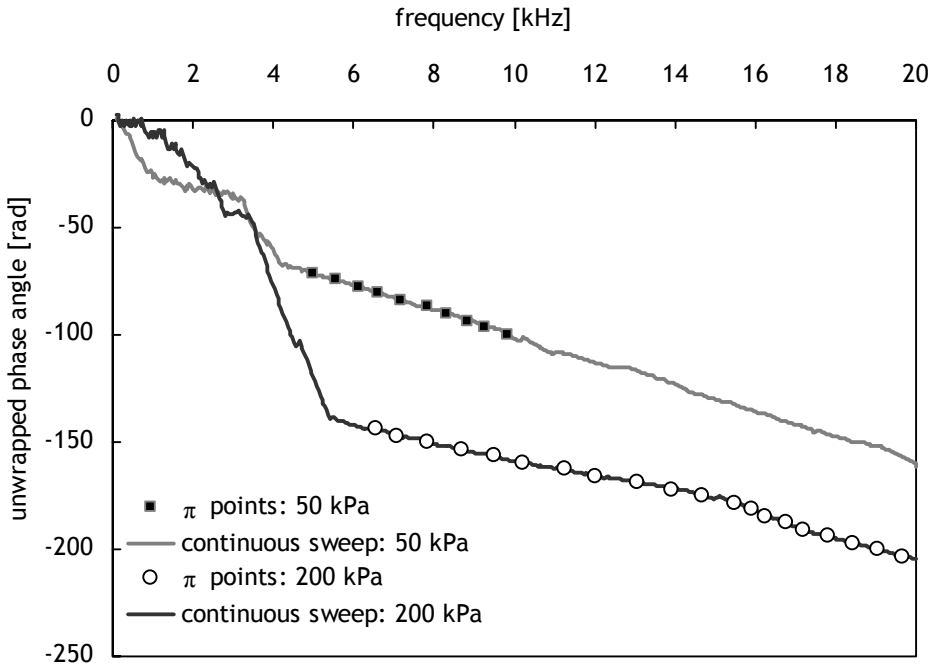


Figure 4.18 - Evidence of superimposed results using the π-points and sweep methods for different stress conditions (isotropic 50 kPa and 200 kPa) on Toyoura sand

All of the interpretation methods listed in the previous sections have been shown by their proponents to produce satisfactory results in the studies they have published. However, other researchers applying the same techniques to different test conditions or different materials have found less satisfactory performance, and moreover, the same method, applied by the same researcher in the same testing apparatus, may provide different levels of reliability in the interpretation, simply because the soil in study is different (Alvarado and Coop, 2009; Ferreira, 2004; Ferreira and Viana da Fonseca, 2005). The reasons for this are not yet fully understood. The lack of consistent results represents a clear obstacle to the standardization of this technique. Therefore, there is a need to improve, alter, or even ignore some methods, while pursuing new approaches.

In current (particularly commercial) practice, automation of procedures is currently almost as crucial as the interpretation method itself, and hence there is a demand for automated determination of the best estimates of travel time based on different interpretation techniques. This requirement is even more relevant for the case of large testing programs, where the time required for data processing is an important factor to be taken into account. For this reason, some researchers have attempted to develop programs to automatically identify first arrivals. For instance, Arroyo et al. (2003) suggested the use of automated picking of first arrivals by specifying that wave amplitudes below 10% of the maximum trace amplitude were to be ignored to

account for near-field effects, as previously commented. However, this procedure is not always applicable.

Others have been slightly more successful in achieving automation by automating frequency domain techniques (Greening et al., 2003; Ferreira and Viana da Fonseca, 2005; Viana da Fonseca et al., 2008). However, entirely automatic measurements have not yet been reported.

4.5. Proposed BE interpretation framework

4.5.1. Description and methodology

The framework for BE testing and interpretation proposed in this work does not rely solely on a single method of interpretation of the results, but rather involves the use of a combination of methods for an enhanced interpretation, thus leading to a higher reliability in the computed travel time. The final estimate of travel time still requires an educated judgment, but in the case of BE testing, information redundancy is actually necessary in order to make an informed decision.

The proposed framework for interpreting the BE tests assumes that the data are collected in such a way that they can be subsequently manipulated in both the time and frequency domains, as detailed below. The conduct and interpretation of the test is then carried out as follows:

- application of several input sine-wave signals at various frequencies, including at resonant frequency, using the first direct arrival method to determine travel time in the time domain (TD); hence, a unique value of travel time is assumed for all input frequencies;
- application of a continuous sine sweep input wave, using specific software to automatically acquire data and compute travel time in the frequency domain (FD);
- post-processing of the FD results, using the capabilities of the software, to derive the best estimate of travel time;
- comparison and combination of the results of both TD and FD method, for a final value of travel time.

In TD measurements, the resonant frequency of the system is, in general, taken to be the optimal input for a single-period sinusoid, since this enhances the response of the

BE (Lee and Santamarina, 2005). This frequency can be readily determined by manually sweeping the frequency of a continuous sine input signal while observing the Lissajous response in the oscilloscope in the XY plot, until a straight line is obtained (as for the π-points method). As the soil stiffness changes with the loading conditions, so does the resonant frequency of the system, and hence it needs to be determined at each stage of testing.

One of the complicating factors in determining the first shear wave arrival is the prior arrival of compression waves, due to near-field or wave reflections. Therefore, complementary information from P-wave measurements is also useful in distinguishing the arrival of the S-wave (Brignoli et al., 1996; Ferreira, 2003). In the course of this research, independent measurements of both waves were made.

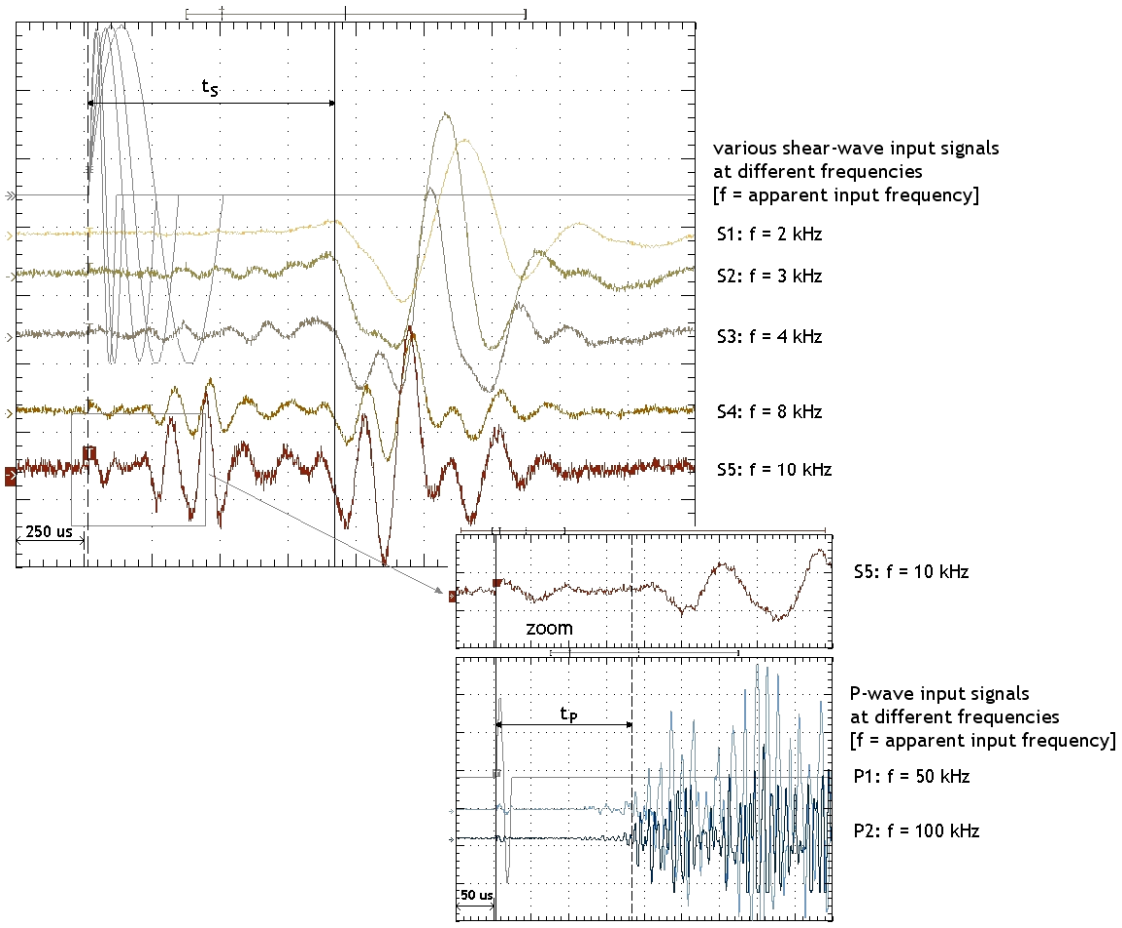
In FD methods, the application of cross-spectral analysis methods to the signals does not require a sine sweep, but this input signal is indeed favourable, because it is an unbiased selection, has a very broad frequency spectrum and so has the potential of providing a near-continuous response curve from a single signal, sufficient to cover virtually any soil stiffness (Rio, 2006). Frequently, this procedure is sufficient to guarantee good confidence in the estimated travel time, but this is not always the case. In fact, when the convergence of results is not immediately obtained, a more detailed analysis of the results is required. In practice, post-processing of the data is always recommended. Details are presented with the application examples below.

The suggestions included on a recent report of the Technical Committee TC29 of the International Society for Soil Mechanics and Geotechnical Engineering, ISSMGE (Jardine and Shibuya, 2005) converge with this procedure. In this document, it is strongly recommended to employ more than one technique with different input wave shapes and frequencies in BE testing.

4.5.2. Methodology

The proposed framework for BE interpretation combining time and frequency domain measurements is essentially divided into two stages: i) TD and FD data acquisition, at selected testing moments; ii) data interpretation and combined analysis for TD and FD results, which can be carried out immediately after data acquisition, or at a later, more convenient time. In either case, a preliminary estimate of travel time in the time domain should be determined, while in the frequency domain the estimated results are automatically provided.

For the time domain method of identification of first arrival, any of the oscilloscopes listed in the equipment can be used, as well as the ABETS software. In Figure 4.19, an example is provided, illustrating the number of different signals used for a single BE reading, as well as the additional information provided by P-wave measurements.



[note: the polarity of the output signals is inverted in relation to the input signals]
Figure 4.19 - Example of TD results: use of various S-wave wave signals at different frequencies, complemented by P-wave measurements

For frequency domain measurements, using the continuous method described above, a continuous sine-sweep input wave is preset at the function generator and the acquisition was carried out via the spectrum analyzer-oscilloscope using specific open-source software ABETS, short for Automated Bender Element Testing System. The software details, namely regarding the algorithm for data acquisition and processing, can be found in Greening et al. (2003). This program is user-friendly and runs in Microsoft Excel™. Some modifications have been introduced to the program, namely for post-processing and analysis, and a new version has been implemented, "abets-PLUS". Screenshots of this program, in its FEUP version, and of the post-processing and analysis spreadsheet are presented in Figure 4.20 and Figure 4.21, respectively.

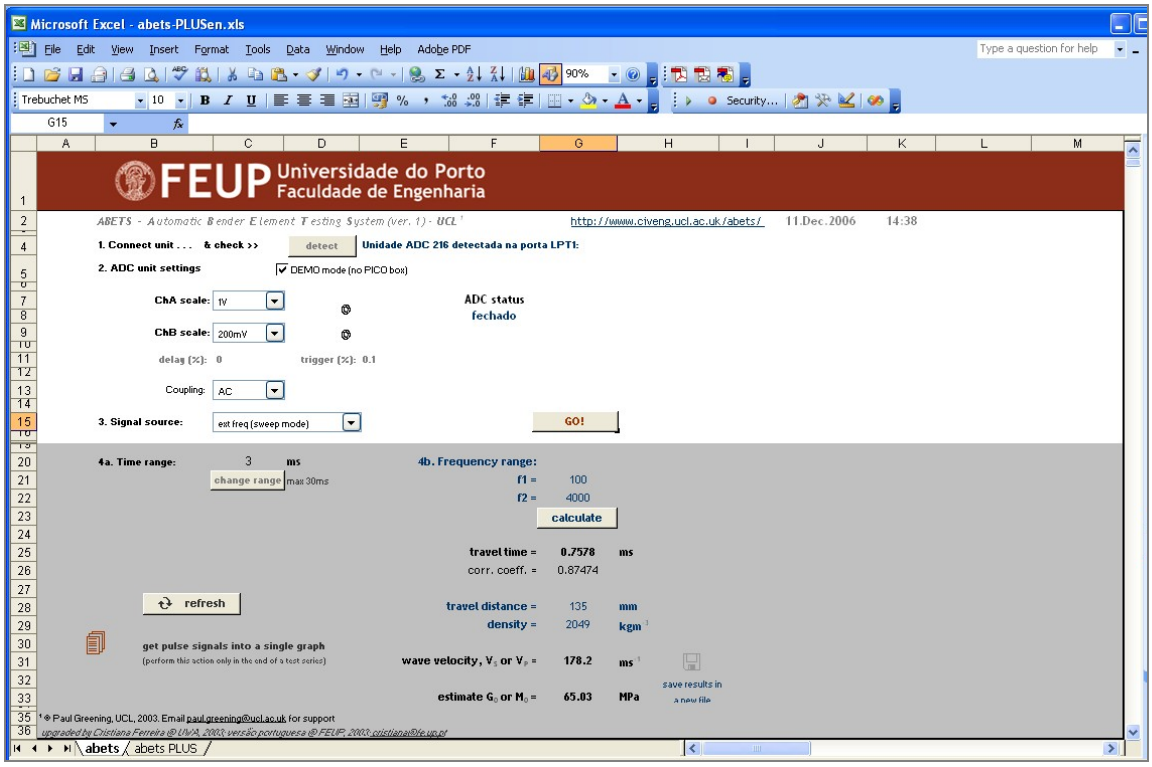


Figure 4.20 - Data acquisition spreadsheet: ABETS

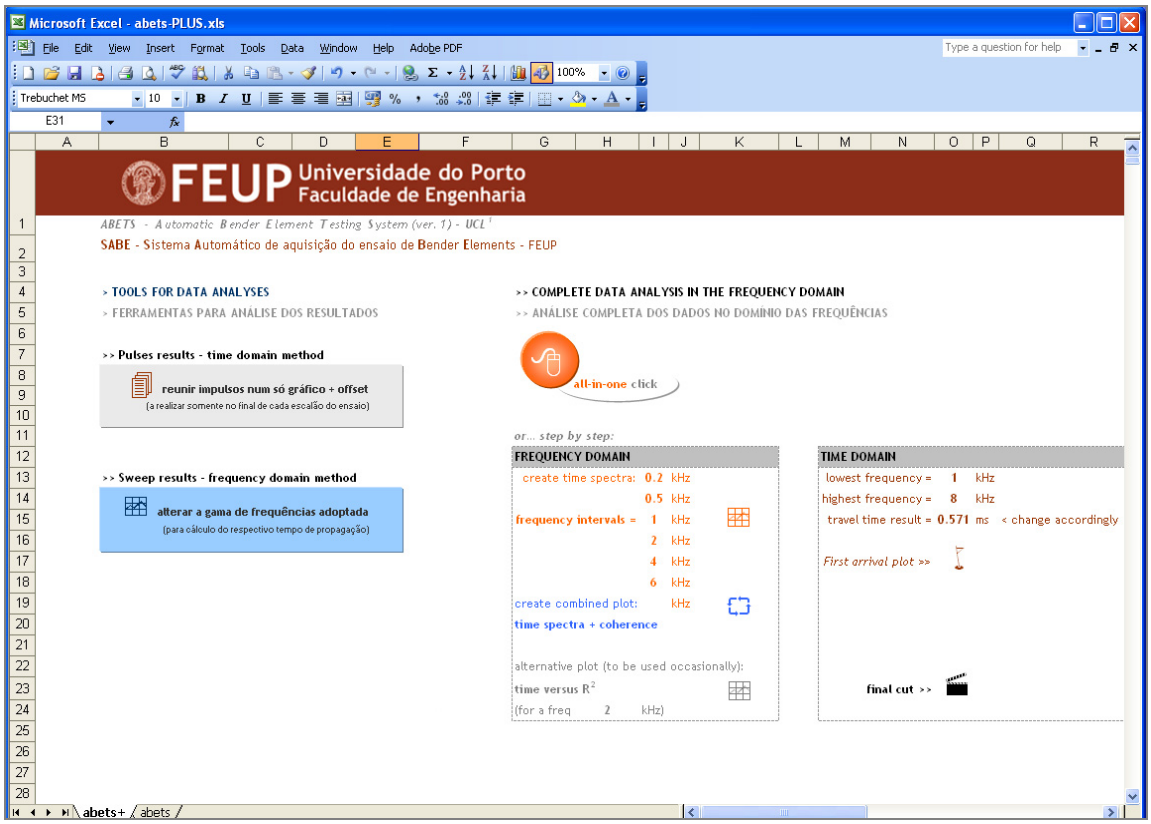


Figure 4.21 - Post-processing and analysis spreadsheet: abets-PLUS

The data acquisition results spreadsheet is detailed in the application examples (for example, **Error! Reference source not found.** and Figure 4.25). The acquisition is triggered by the user and, by means of the embedded frequency-domain analysis algorithm, the travel time, wave velocity and shear modulus are immediately computed by the software. These parameters can be recalculated for different frequency ranges. Best results have been obtained for a sweep sine input signal with a 0.1 - 20 kHz bandwidth (Greening & Nash, 2004). Narrower frequency ranges should be selected for computing travel time, mainly based on the results of the coherence function (further details on the application example).

4.5.3. Application examples of the TD-FD framework

4.5.3.1. Experimental setup

Specimens of natural residual soil from Porto granite (Viana da Fonseca, 2003; Viana da Fonseca et al., 2006) and reconstituted Toyoura sand were tested in a triaxial apparatus. The initial dimensions of the specimens were 140 mm height and 70 mm diameter (a height-to-diameter ratio, H/D, of 2.0). The bender elements are 10 mm wide, 1 mm thick, with a protrusion distance of 2 mm. These tests were carried out in the ISMES triaxial system, described in the previous chapter. The function generator (TTi TG1010), input-output amplifier (specifically designed by ISMES-Enel.Hydro), oscilloscope (Tektronix TDS 220) and/or spectrum analyzer-oscilloscope (PicoScope ADC-216), both connected to a PC for data acquisition, were used for BE testing. This system enables not only the travel time to be measured from the display of the oscilloscope, but also the signals to be transferred to a computer to further post-process the results using different approaches.

For the time-domain measurements, sine-wave input pulses were used at various preset frequencies (1, 2, 4, 6, 8, 10 kHz, provided the response obtained appeared relevant) and at one of the resonant frequencies of the sample-BE system. The output signals were captured in the oscilloscope, directly transferred to the PC and plotted together. For the frequency-domain measurements, a continuous sine-sweep input wave was applied and the acquisition was carried out via the spectrum analyzer-oscilloscope using ABETS. The acquisition is triggered by the user and, by means of the embedded frequency-domain analysis algorithm, the travel time, wave velocity and shear modulus are immediately computed by the software. These parameters can be recalculated for different frequency ranges. Narrower frequency ranges are then selected for computing travel time, mainly based on the results of the coherence function (further details provided below).

4.5.3.2. Test results on residual soil from Porto granite

Residual soil from Porto granite is a well-studied geomaterial (Viana da Fonseca 2003; Viana da Fonseca et al. 2006), as will be described in depth in the next chapter. For this case study example, an isotropic consolidation test was performed on a remoulded residual soil (RS) specimen with an initial water content of 30 %. The soil was spooned into the sample mould and set up on the triaxial base. The top cap is then attached in the usual way. At this water content, the BEs penetrated into the sample without any difficulty. The test comprised an initial pre-consolidation at 10 kPa, saturation by increments up to a backpressure of 300 kPa (corresponding to parameter B = 1.00 and V_P = 1545 m/s, measured by P-wave transducers), and drained isotropic consolidation at 50, 100, 200, 400, 600, 800, 1000 kPa. The variation of shear wave velocity with isotropic confinement for the two TD and FD methods is presented in Figure 4.22.

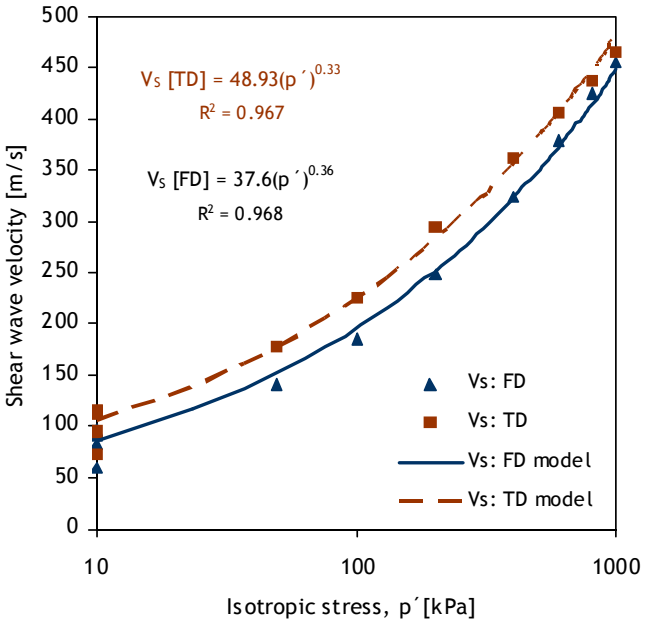


Figure 4.22 - Variation of shear wave velocity with isotropic consolidation stress on Porto residual soil (test R2-isoCF1, w = 30%)

The two methods produced similar results, but with the FD method giving consistently lower V_S values. The maximum observed difference is less than 20% in wave velocity, which is not negligible. Identical conclusions were reported by Greening and Nash (2004), and therefore this appears to be a systematic difference. The reasons for such systematic differences are not yet fully understood, though Arroyo et al. (2003) suggest that the TD methods are more likely than FD methods

to give overestimates of Vs due to interference from near-field effects. New insights regarding these differences were derived from the comparative tests on the resonant-column equipped with BE, as will be presented and discussed in Chapters 7 and 8.

For the purpose of comparison, results from two distinct stages of the isotropic consolidation test on sample R2-isoCF1 have been chosen (p' = 100 kPa and p' = 800 kPa). The input and output signals for these two test stages are shown in Figure 4.23 and Figure 4.24, respectively. It should be noted that the S-wave outputs are in reversed polarity in relation to the input signal.

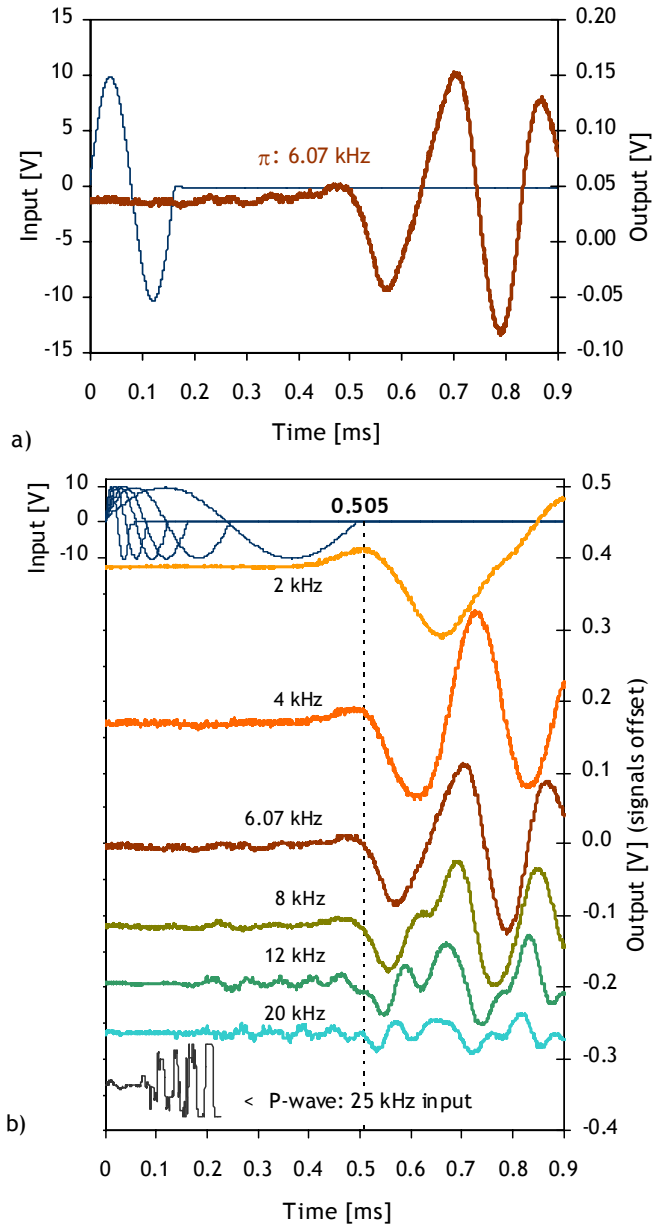


Figure 4.23 - TD results for input sine waves for the residual soil (p' = 100 kPa): a) at resonant frequency of 6.07 kHz; b) 2, 4, 6.07, 8, 12, 20 kHz and P-waves for 25 kHz input

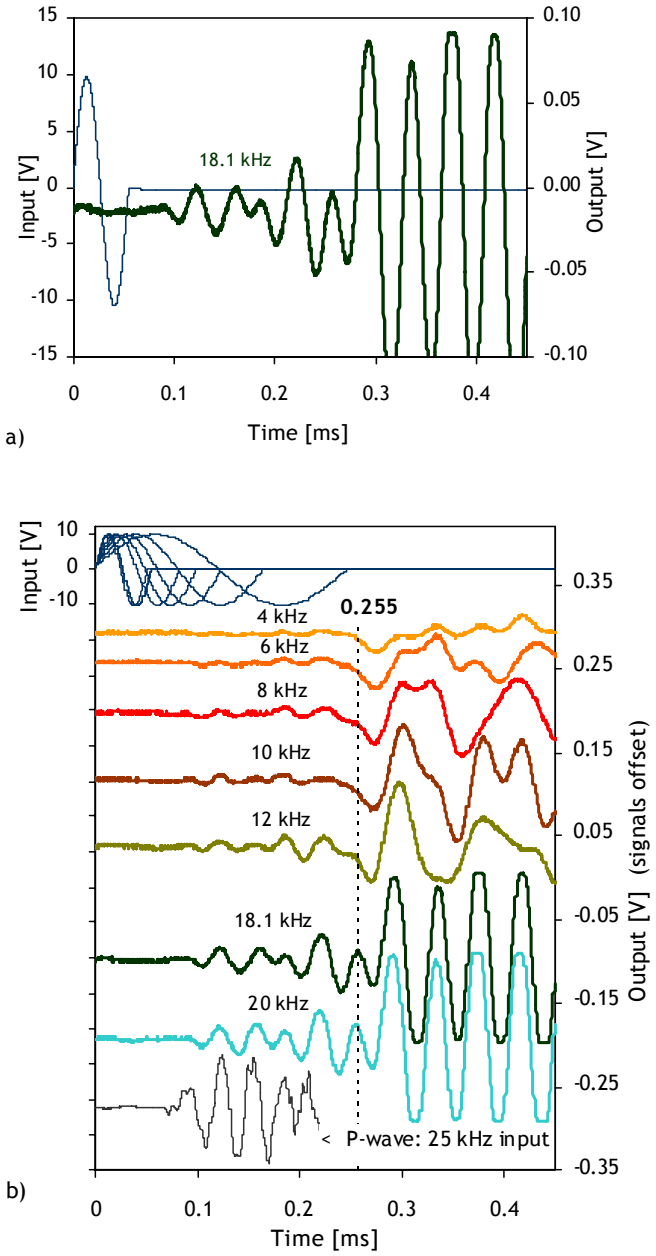


Figure 4.24 - TD results for input sine waves for the residual soil (p' = 800 kPa): a) at resonant frequency of 18.1 kHz; b) 4, 6, 8, 10, 12, 18.1, 20 kHz and P-waves for 25 kHz input

The ratio of sample length to wavelength, L/λ varies between 1 and 10 for frequencies between 1 and 20 kHz, for the first case, and between 1 and 5 for the second case. For the lower frequencies used here, the L/λ ratio is smaller than the minimum value of 1.6, required to avoid near-field effects, as proposed by Arroyo et al. (2006). Nevertheless, there is still considerable benefit to be derived within the presented framework in considering these lower frequencies, as the information

provided allows an appreciation of the complete response.

Figure 4.23a indicates that at p' = 100 kPa, the determination of the direct travel time is quite straightforward; however, Figure 4.24a indicates that at high stresses (p' = 800 kPa), interpretation is ambiguous. Each shows the response to a single sine input wave at resonant frequencies of 6.07 and 18.1 kHz, respectively. It should be noted that these resonant frequencies have been obtained for the full system under continuous signals, that is, at a steady state. However, as previously discussed, the actual frequencies of the pulses at the input and output ends of the specimen are not necessarily identical to those of the corresponding electrical pulses because of the inherent response characteristics of the transducers. In the example, for the results at higher confining stress, the signal can be visually divided into three parts and it is unclear which part corresponds to the arrival of the shear wave. Hence, interpretation of this result requires complementary analysis – for example, by comparing the response for other input frequencies. Thus, Figure 4.23b and Figure 4.24b show superimposed results from different frequencies for the p' = 100 kPa and p' = 800 kPa cases, respectively. In each case, while the resonant frequencies produced the maximum response signal of the system, lower frequencies assist favourably in the selection of the location of the shear wave arrival, which is refined with the sharper response of higher frequencies.

As previously mentioned, it is also helpful to have independent P-wave travel time information (from P-wave measurements carried out on the same specimen at the same time as the S-wave), to enable P-wave components of the BE signals to be more easily differentiated from S-wave components (Figure 4.23b and Figure 4.24b). The presence of P-waves in the shear wave signals is particularly noticeable at higher frequencies; for the present case, P-waves start to appear in the BE traces for frequencies above 12 kHz. The advantage of these independent P-wave measurements, by means of different transducers, is the possibility to confirm the compressional nature of the initial part of the shear wave signal. This is more evident in Figure 4.24b, where the shapes of the BE signals at 12, 18.1 and 20 kHz, prior to the true S-wave arrival, and of the P-wave signal are coincident.

The proposed approach is easy and quick to perform (not much more time required than for a single frequency). It is often possible to acquire more than one resonant frequency, which can be advantageous. For example, the results presented later in Figure 4.25 show that the response of the system is maximum at two main frequencies, which are likely to be related to resonant frequencies. As previously described, finding those frequencies is a relatively simple and rapid process and

applying them as additional input pulses for TD domain testing is favourable, since the amplitude of the resulting output signal will be at its highest.

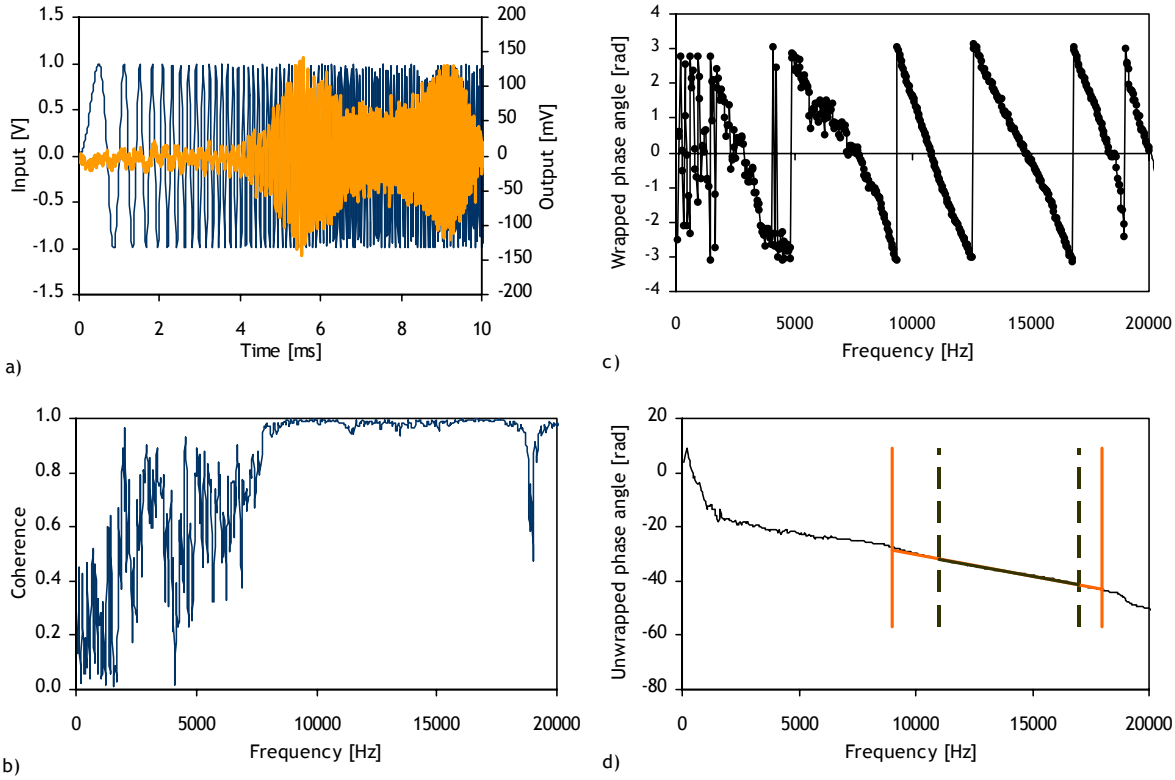
Finally, it is important to display all readings in the same graph, perhaps with a vertical offset to ease readability and interpretation, as illustrated in Figure 4.23 and Figure 4.24. As shown in this example, the measurement of shear waves at high confinement stresses and in saturated conditions is frequently more difficult, as the difference between the travel times of the two waves narrows, for several reasons:

- V_P remains nearly constant (around 1500 to 2000 m/s), while V_S increases significantly with increasing confining stress, such that the P-wave effects are still present when the first S-wave arrival occurs (in this case, the V_P/V_S ratio at 100 kPa is 7.45, while at 800 kPa it is 4.25);
- the amplitude of the P-wave response is much higher after saturation, and may even approach the amplitude of the S-wave response, making it difficult to separate them in the received signal;
- the input frequency for BEs is limited (preferably below 20 kHz), due to the characteristics of the transducers, filters and amplifiers and the resolution of the acquisition system, and hence it may not be possible to apply sufficiently-high input frequencies to cover a wider range for higher confining stresses.

The input and output signals for this sample from a sine-wave sweep measurement, plotted in the time domain, for the confining stress p' = 100 kPa were already presented in Figure 4.17.

The travel time is derived directly from the slope of best fit to the curve in Figure 4.17d, for a selected range of frequencies, by means of Equation 4.8. The coherence plot (Figure 4.17b) is used to aid in determining the optimum frequency range. In this case, the low coherence below 1 kHz and above 16 kHz indicated in Figure 4.17b suggests that noise dominates the signal outside these frequencies. Using a sweep frequency range wider than required (0 to 20 kHz in this case) is useful as an overview of the full coherence function, allowing the most appropriate to be chosen for the analysis. In this example, two frequency ranges have been selected corresponding to 1.5 to 9 kHz and 2 to 6 kHz, indicated in Figure 4.17d by the vertical solid and dashed lines, respectively. The deduced travel time, correlation coefficient, S-wave velocity and stiffness value for each range are shown in the inset table on Figure 4.17e. Despite the high correlation coefficients for both ranges, the

resulting travel times are considerably different. Similar conclusions apply to the second case (p' =800 kPa) in Figure 4.25.



e)

Frequency ranges	f1 [Hz]	f2 [Hz]	travel time [ms]	correlation coefficient	wave velocity, V_S [m/s]	modulus estimate, G_0 [MPa]
———	9000	18000	0.259	0.995	463.6	419.1
– – –	11000	17000	0.235	0.997	509.8	506.9

Figure 4.25 - FD results for the residual soil (p' = 800 kPa): a) input and output signals in timescale; b) coherence; c) wrapped and d) unwrapped phase angle against frequency; e) summary of results

Given the variability of the results, further analysis of the data should be performed to complete the process. A useful sensitivity analysis of frequency-domain measurements consists of selecting different frequency sampling ranges or windows to observe the changes in the travel time deduced with change in frequency. For this purpose, a simple Visual Basic program was implemented, to manipulate the sweep data using unbiased pre-established moving frequency windows (0.5, 1, 2, 4 and 6 kHz), to continuously calculate the best-fit line and corresponding travel times for each window location. The generated curves of time versus frequency for each window, which are termed arrival-time spectra, are presented in Figs 10 and 11, and

each curve contains a marker indicating the maximum correlation coefficient (maximum value of R2). The corresponding first arrival results from the TD analysis (the horizontal dashed line) are also included and the coherence plot is presented above the graph, for guidance. In general, the wider-frequency windows (2, 4 and 6 kHz) provide lower variability, as these tend to smooth and average the results, while the arrival-time spectra for narrower windows (0.5 and 1kHz) are highly variable and more sensitive to noise interferences in the signal.

Since these narrow-window spectra are similar to the original signal, they are almost representative of single-frequency travel times, which serve as a useful check on the validity of the other spectra. For example, for a central window frequency of 10 kHz, Figure 4.26b shows an almost identical travel time from all windows, including the narrowest one. From this process, the selection of the arrival time is based upon the position of the markers of maximum correlation, selected automatically in the software. As in Figure 4.26b and Figure 4.27b, knowledge of the TD arrival time helps in the final selection.

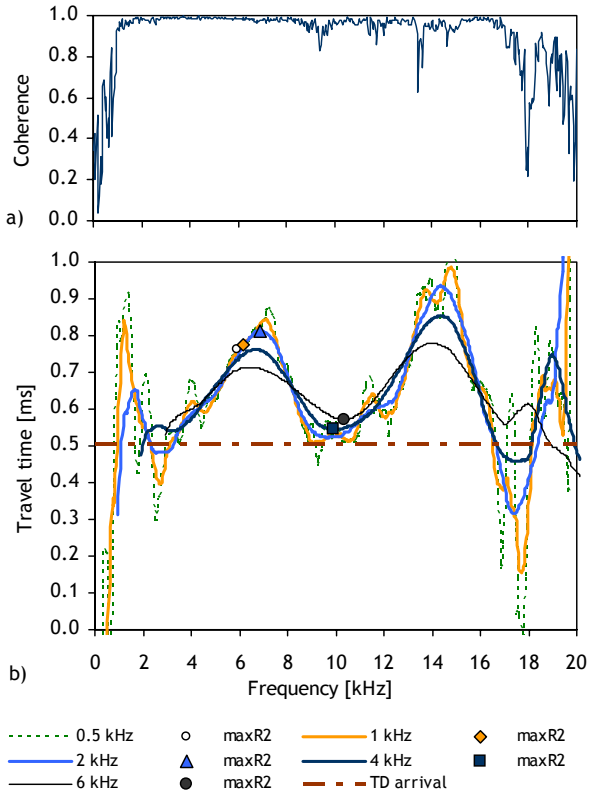


Figure 4.26 - FD analysis results for the residual soil (p' = 100 kPa): a) coherence for the initial window (100 Hz-20 kHz); b) travel time spectra

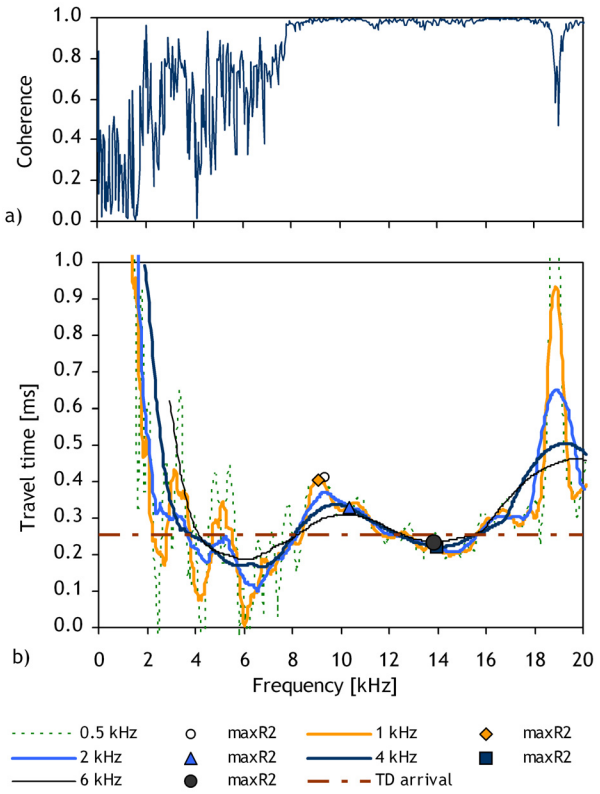


Figure 4.27 - FD analysis results for the residual soil (p' = 800 kPa): a) coherence for the initial window (100 Hz-20 kHz); b) travel time spectra

Figure 4.26b shows significant fluctuation in the arrival time between 1.5 and 9 kHz, corresponding to the high-coherence section in Figure 4.26a, and this fluctuation was not noticeable in the original data. In Figure 4.27b, the arrival-time spectra again show considerable variability, despite the high coherence values from 6 to 20 kHz indicated in Figure 4.27a.

Therefore, the initial concept of a selection based solely on coherence values close to unity is clearly not sufficient to guarantee an accurate determination of the travel time. Instead, the selection of the maximum correlation points of the arrival-time spectra, especially for higher ranges of frequency (4 or 6 kHz) appears to be more consistent. This procedure is also apparently able to overcome the limitations regarding the global transfer function of the BE system, which are likely to be partly responsible for the variability of the travel-time spectra.

As illustrated in this section, the technique of using travel-time spectra is useful and practical for selecting the most adequate travel time, besides enabling an overview of the variation of travel time. The combination of arrival-time spectra results and TD results gives confidence in the validity of the final travel time selected.

4.5.3.3. Test results on Toyoura sand

Similar analyses to those just described were also carried out for a series of BE measurements on a dry Toyoura sand specimen, also under isotropic consolidation conditions. The Toyoura sand is a well-known Japanese standard sand, with a D_{50} of 0.17 mm and a uniformity coefficient of 1.6.

The specimen was air pluviated, resulting in a void ratio of 0.69 (Ferreira and Viana da Fonseca 2005). Four isotropic stress stages (p' of 50, 100, 200 and 400 kPa) were applied. The shear-wave velocities obtained using the time-domain (TD, square symbols) and frequency-domain (FD, triangle symbols) approaches are plotted against the applied isotropic stress in Figure 4.28. The best-fit power function to the TD results is included as a solid line, and a similar line is included for the FD results, but in this case, only the two highest-stress results are used in the fit, since the lower-stress data do not seem to fit the same trend, as discussed below.

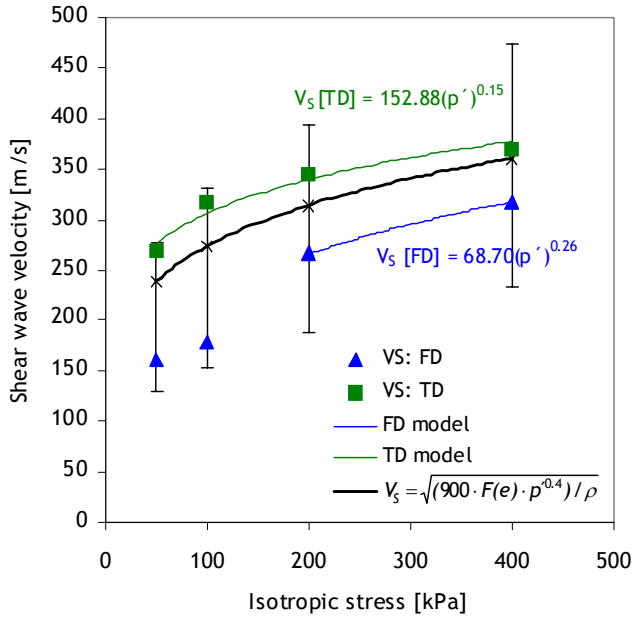


Figure 4.28 - Variation of shear wave velocity with isotropic consolidation stress on Toyoura sand

Figure 4.28 also shows a relationship obtained from resonant column tests by Iwasaki and Tatsuoka (1977), which is often taken to be a reference curve for this material. This relationship was found to give a good overall fit to the average of the results obtained from the recent round-robin set of tests conducted on this soil by a number of institutions around the world (Yamashita et al., 2007). Also included on this curve are error bars, which indicate the range of the results from this exercise. This indicates that the results from the tests described here are within the range of the

results from the other institutions, but with the TD results lying above the reference curve, and the FD results lying below it.

This plot indicates a significant difference between the results of the two approaches. The FD analysis gives lower values of V_S, corresponding to only 65% of V_S obtained from the TD approach at the lowest stress. There is a significant convergence at higher stresses, which is likely associated with a higher coupling between the soil and the BE, aided by the stiffening of the soil under the higher confining stress. The FD results also show two distinct trends, one for p' of 50 and 100 kPa, and another for p' of 200 and 400 kPa. The power function fitted to the upper two points gives an exponent of 0.26. To illustrate the application of the full framework in this case, two stages (at p' of 100 and 400 kPa) are presented in detail. The TD results for these stages are shown in Figure 4.29a and Figure 4.29b. Unfortunately, P-wave measurements were not made in this case, so independent P-wave arrival times cannot be shown.

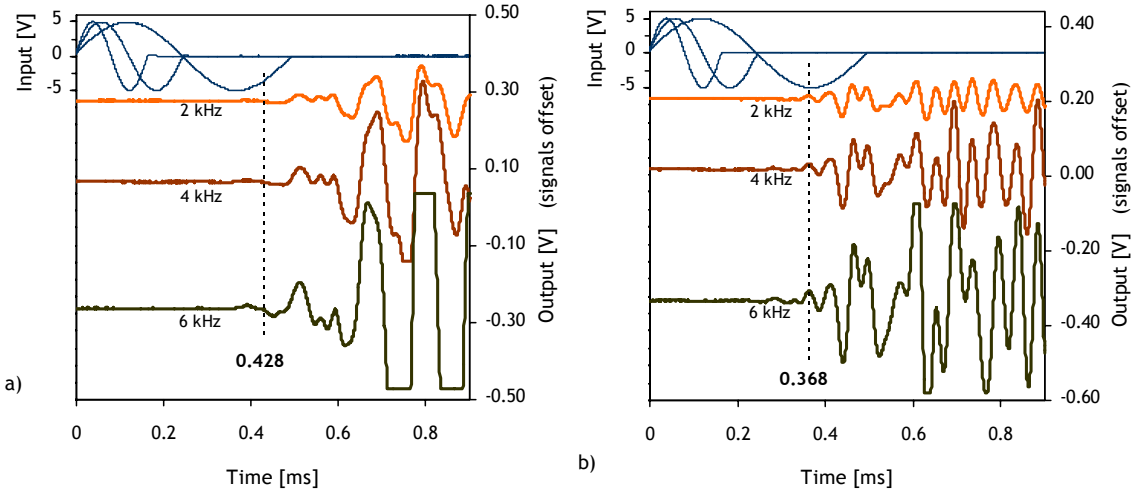
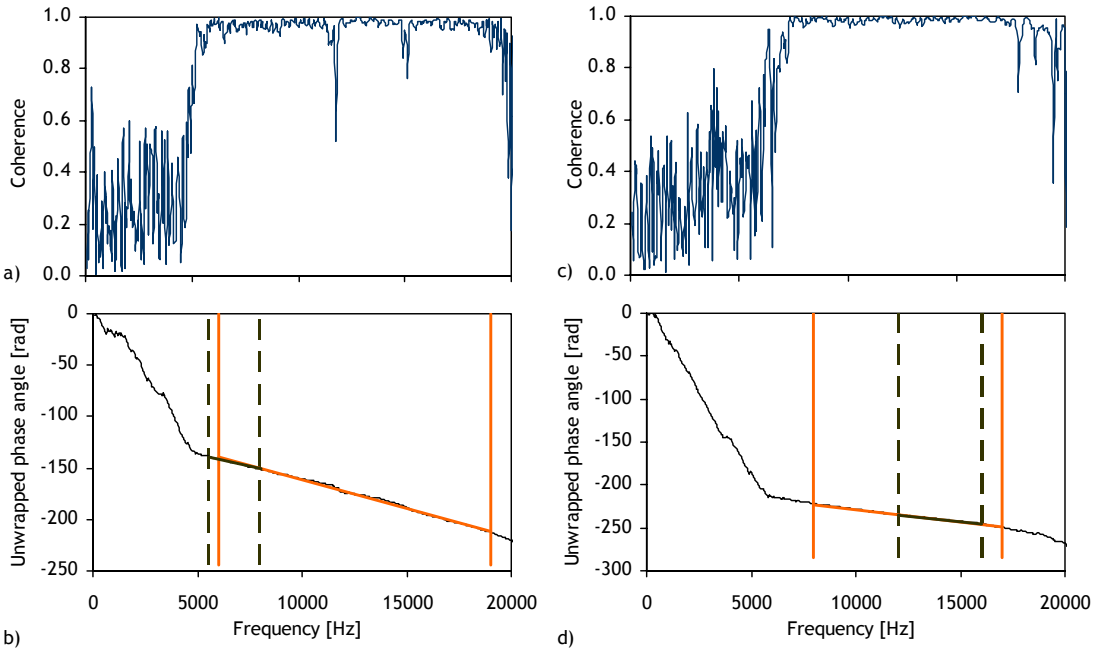


Figure 4.29 - TD results for input sine waves of 2, 4, 6 kHz on Toyoura sand: a) at 100 kPa; b) at 400 kPa. [Note: S-wave outputs in reversed polarity]

Frequency-domain plots for this test are presented in Figure 4.30, along with tabulated results for the p' = 100 kPa and p' = 400 kPa stages. The arrival-time spectra for both stages have been generated automatically, as shown in Figure 4.30and Figure 4.31. It is clearly more difficult to select a travel time for the 100-kPa stage than for the 400-kPa stage. For the former case, the best estimate from the arrival-time spectra approach is about 60% greater than that from the TD first-arrival approach.



e)

Test stages	Frequency ranges	f_1 [Hz]	f_2 [Hz]	Travel time [ms]	Correlation coefficient	Wave velocity, V_S [m/s]	Shear modulus, G_0 [MPa]
100 kPa	———	6000	19000	0.878	0.996	153.7	36.4
	– – –	5500	8000	0.788	0.998	171.3	45.2
400 kPa	———	8000	17000	0.464	0.997	291.1	130.4
	– – –	12000	16000	0.427	0.995	315.8	153.5

Figure 4.30 - FD results for Toyoura sand (p' = 100 kPa): a) coherence; b) unwrapped phase angle against frequency; Toyoura sand (p' = 400 kPa): c) coherence; d) unwrapped phase angle against frequency; e) summary of results

The fluctuations of travel time with frequency for the various frequency windows decrease substantially with stress increase, as do the differences in the travel time measured by the first-arrival method. This fact is likely to be associated with a higher coupling between the soil and the BE, aided by the densification and stiffening of the soil.

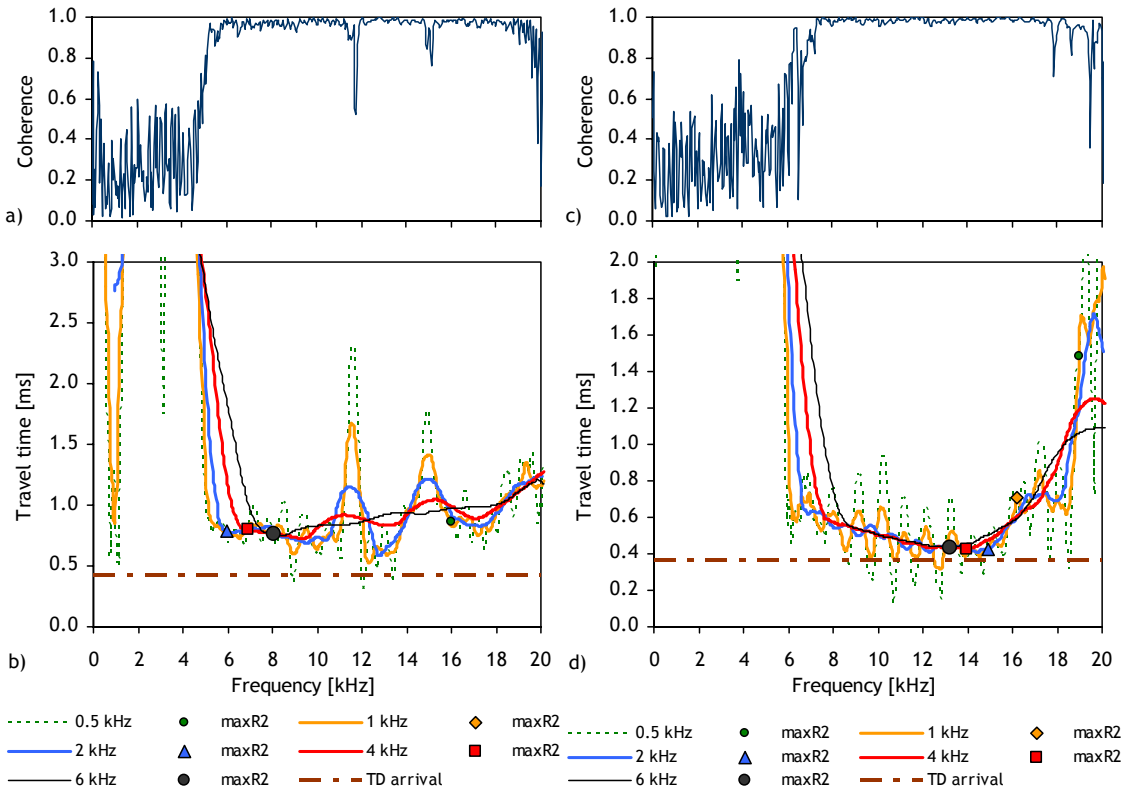


Figure 4.31 - FD analysis results for Toyoura sand (p' = 100 kPa): a) coherence; b) travel time spectra

4.5.3.4. Comparison of the results of the two soils

Bender element testing of these two natural soils, using the same testing apparatus and identical sample dimensions and procedures, has provided significantly different levels of reliability in the results obtained via TD and FD methods. Figure 4.22 and Figure 4.28 illustrate the variation of the shear-wave velocity with isotropic confining stress as provided by each of the methods, and clearly demonstrate greater variability and divergence in the results for the Toyoura sand compared to those from the residual soil. Additionally, the wave traces shown in Figure 4.23 and Figure 4.29a for the two soil specimens under the same confining stress are significantly different: the number of cycles in the output signals for the Toyoura sand specimen is much higher than for the residual soil, revealing longer reverberation time and hence lower damping.

An important factor that may be influencing the quality of the results for the Toyoura sand is that these tests were carried out in a dry condition. It has been pointed out by a number of authors (e.g. Lee and Santamarina, 2005; Arroyo et al. 2006) that side reflections of P-waves are less likely in a saturated triaxial sample

than in a dry one, because the impedance difference between the saturated soil and the cell water is much smaller than between the same dry soil and cell water.

However, these different saturation conditions cannot completely account for such differences in the results, which are believed to be also related to the nature and characteristics of each soil. The mean grain size D_{50} of these soils is similar, but one striking difference between these soils relates to their grain-size distributions: the Toyoura sand is a uniform sand (Cu = 1.6), while the residual soil is a (clayey) silty sand (Cu=90). Even though there are not enough data to establish any definite conclusion, it is plausible that a well-graded material would facilitate better wave propagation than a poorly-graded material, given the continuity provided by the packing of the grains in the well-graded material. Moreover, with a well-graded material, the coupling with the BE is aided by the arrangement of the finer particles around the transducers. The lower dependence of V_S on confining stress obtained with the residual soil specimen corroborates this hypothesis. Hence, it seems plausible that the quality of BE results, and hence the reliability in interpreting the results, depends to some extent on the degree of uniformity in the grain-size distribution.

Another important factor is that, with the much higher velocities in the Toyoura sand compared to the Porto residual soil, the L/λ ratios were consistently lower - in the range of 0.8 to 2.6 at p' = 200 kPa and 0.7 to 2.2 at p' = 400 kPa, for the frequency range of 2 to 6 kHz. These ratios are such that near-field effects are more likely to affect the output signals, being less than the value of 3.0 suggested by Arroyo et al. (2006) as the limit above which such effects should not be present. Ideally, this would be overcome using higher frequencies, but in this case, the response at higher frequencies was too weak to allow sensible analysis.

In the discussion of dispersion effects, this issue of frequency is extremely relevant. Santamarina et al. (2001) proposed a simplified relationship for soils in a saturated condition, in the light of Biot (1956) theory of propagation of seismic waves in fluid-saturated porous materials, and defined the frequency threshold for dispersion (the 'characteristic' frequency), directly related with porosity and hydraulic conductivity. As noted by Santamarina et al. (2001), as permeability decreases with increasing fines content (and increasing specific surface), the characteristic frequency increases and the Biot dispersion effects lose relevance. For the residual soil considered here, ($k \sim 10^{-6}$ m/s), the critical frequency is about 1 MHz, while for the Toyoura sand (if it were saturated), it is just of the order of 10 kHz. As a result, higher dispersion would be expected for the sand in a saturated condition than for the residual soil. On the

other hand, Yamashita et al. (2007) shows a comparison between BE results on dry and saturated Toyoura sand, clearly revealing greater scatter in dry conditions, which suggests that the problem is not related to (Biot-type) dispersion. Consequently, it appears that a dry clean sand, such as the Toyoura sand used here, poses a challenge for BE testing for standard testing frequencies, while the residual soil appears to be unaffected.

In a different study, Arroyo (2001) applied Krautkrämer and Krautkrämer's (1990) experience in ultrasonic testing of materials – natural materials, composed of grains – to derive the operating frequencies above which scattering-related attenuation starts to appear. The interpretation of wave absorption and scattering done by Krautkrämer and Krautkrämer (1990) was expressed by Arroyo (2001) as follows: "scattering of elastic waves, i.e. partial reflection and deviation of energy, is due to the granular nature of (any) material, and dependent on the relation between the wavelength of the impeding wave and the size of the obstacle (grain) or inhomogeneity. This introduces a frequency dependence on attenuation and imposes a practical higher limit to the movement frequency."

Using grain size and V_S values, Arroyo (2001) presented a graph in which the frequency limit is inversely proportional to the grain size, showing clearly that for a granular material, independently of its water content (or degree of saturation), the operating frequency range is relatively low, and hence frequencies above the order of 10 kHz would pose serious attenuation problems for sands.

Both studies corroborate the present results, and the greater complexity of interpreting BE results on the Toyoura sand specimen seems to be explained by the dispersion due to the use of inappropriately high frequencies, at which the response of the sand is strongly attenuated (Viana da Fonseca et al., 2009).

4.6. Summary and conclusions

In this chapter, the important issue of the interpretation of BE test results was analysed in detail. The phenomena related with this wave propagation conditions were discussed, which are influenced by a variety of factors, including installation details, cross-talk, environment noise, near-field effects, boundary conditions and sample geometry effects.

Different models have been proposed to represent the BE test system, which are also discussed.

In order to understand the behaviour of these transducers, the simplest process is to place the two transducers in direct contact. However, evidence suggest that this is an unreliable method and diverse solutions for monitoring the BE behaviour have been presented, namely self-monitoring BE, accelerometer and laser-beam measurements.

Numerous interpretation techniques have appeared over the years, most of which were introduced and discussed in this chapter. Finally, the interpretation method adopted in this research was described, which consists of a combination of time and frequency domain techniques, as a means to reduce the uncertainty and subjectivity often attributed to BE testing.

This work has shown that the results presented from the frequency-domain method vary significantly for slight changes in the frequency window used in the analysis. Therefore, the use of the automated tool developed in this research is recommended. This tool enables the variability, even at high coherence values, of the results from the sweep method to be dealt with and the travel time to be deduced from the highest correlation coefficient obtained from different moving windows. Finally, it provides unbiased information to assist the decision of the travel time, as has been demonstrated with the two case studies.

The exercise of comparing two different soils provided interesting results. The two soils used had different grain-size distributions, with one being tested completely saturated and the other in dry conditions. Both of these factors seem to have had an influence on the results. In particular, the occurrence of side reflections, which affect the quality of the received signals, is likely to be more pronounced in the dry sand than in the saturated Porto residual soil, which may explain the relatively greater difficulty in interpretation of the results from the Toyoura sand. The grain-size uniformity of the sand is also likely to attenuate at much lower frequencies than the residual soil, adding further complexity to BE testing results.

The most important conclusion from the work is that the combined use of time-domain and frequency-domain methods can aid effectively in the analysis and interpretation of BE tests in the laboratory.

5.

Characterization of the Residual Soil from Porto Granite

5.1. Residual soils

5.1.1. Introduction to the origin and formation of residual soils

In 1985, a review on the international practice of sampling and testing on residual soils concluded that there was no universally accepted definition of residual soils (Brand and Phillipson, 1985). A general definition of a residual soil was later suggested by Blight (1997): 'A residual soil is a soil-like material derived from the in-situ weathering and decomposition of rock which has not been transported from its original location'. The origin and peculiar features of these naturally structured soils requires a more specific approach to the understanding and characterisation of the behaviour beyond those traditionally considered for transported soils.

The formation of residual soils occurs by the in-situ weathering of the parent rock, by three major processes: physical, chemical and biological. In the weathering process,

the rock and its minerals are gradually broken, releasing internal energy and forming substances with a lower internal energy, hence more stable. Stress release by erosion, differential thermal strains or ice and salt crystallization are examples of physical processes, which degrade the rock, expose its surface to potential chemical attacks and increase its permeability (Blight, 1997). On the other hand, decomposition, leaching, dehydration and oxidation are some of the chemical processes, which tend to alter the rock minerals into clay minerals. Biological processes may include both physical and chemical actions, such as splitting by the intersection with roots or bacteriological oxidation.

Residual soils are often distinguished into the following two types (Viana da Fonseca, 1996):

- saprolites or young residual soils, which can be physically and mechanically considered a soil, while preserving a profile with the original structure and fabric of the parent rock. For example, a saprolite derived from a shale often retains the bedding and jointing patterns of the original rock (Blight, 1997);
- laterites or mature residual soils, in which the weathering processes caused by leaching and chemical processes create new inter-particle bonds, and where the structure and fabric of the original rock has completely disappeared.

Physical weathering is more predominant in dry and moderate climates, while chemical weathering processes are directly related with the humidity and temperature, thus more evident in sub-tropical and tropical zones. In moderate climates, such as in Portugal, the residual soils are almost exclusively saprolites, which are the main subject of this research.

The degree of weathering and extent to which the original structure of the rock mass is destroyed, generally varies with depth from the ground surface. This led to the definition of a typical residual soil profile consisting of three indistinctly divided zones (Vargas and Pichler, 1957; Ruxton and Berry, 1957; Little, 1969; Blight, 1997), depicted in Figure 5.1. The upper zone usually consists of highly weathered, eventually leached soil; the intermediate zone also consists of highly weathered material, though some features of the structure of the parent rock remain, including occasional intact blocks.

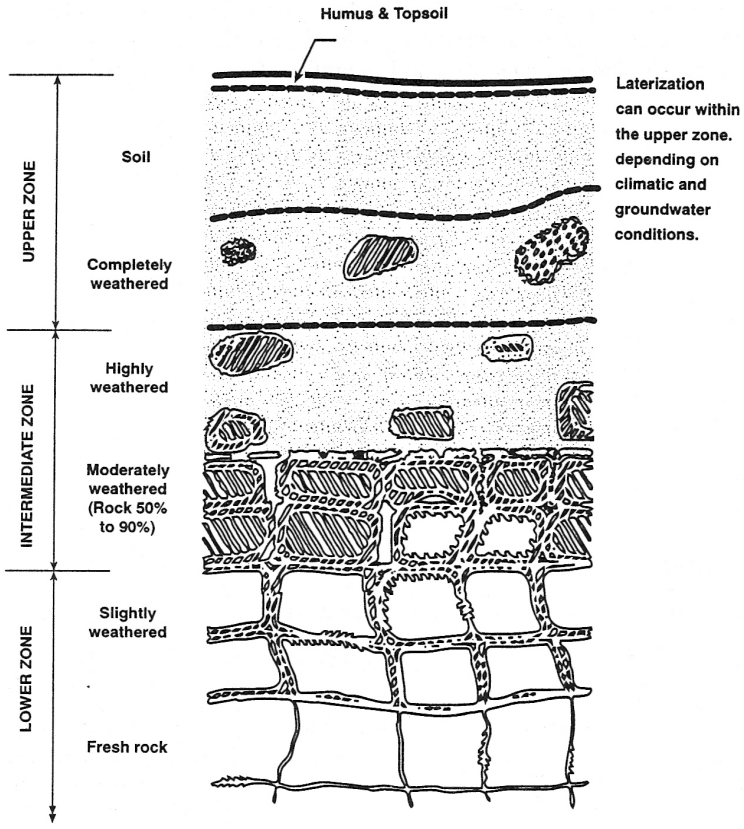


Figure 5.1 - Schematic diagram of a typical residual soil profile (after Little, 1969)

5.1.2. Classification of residual soils

The characteristics of residual soils can be quite distinctively different from those of transported soils. For example, the conventional concept of a soil grain or a particle size may be inaccurate or inapplicable to many residual soils. Particles of residual soil often consist of aggregates or crystals of weathered mineral matter, which break down and become progressively finer as the soil is subjected to mechanical actions. A coarse sand gravel in the field may deteriorate to a fine sandy silt during excavation, mixing and compaction (Blight, 1997). Also, the permeability of a residual soil is essentially governed by its micro- and macro-fabric and by jointing, and not directly related to its grain-size distribution, as usually considered for transported soils.

Several authors agree that there are specific features of residual soils that do not adequately fit in the conventional soil classification methods, namely the Unified Soil Classification system [USCS] (Cook and Newill, 1988; Viana da Fonseca, 1996; Wesley and Irfan, 1997). The identification and characterisation of residual soils demands for other criteria apart from those usually integrated in classical Soil Mechanics classifications. The identification as hard soils or weak rocks does not

include indicative signs for the expected mechanical behaviour. Due to their specific genesis, such soils present complex characteristics, due to their overall variability, heterogeneity and of the spatial arrangement and distribution of the particles and pore spaces. The parameters resulting from identification tests of this soil in remoulded conditions, such as Atterberg limits, relative density, grain size distribution or fines content, largely informative about the stiffness and strength of transported or sedimentary soils, do not reveal or classify the real geotechnical behaviour of these residual soils (Vaughan, 1988). In fact, the standard processes of remoulding and preparing the soil mass clearly affect its characterisation, especially for natural condition responses, due to the strong influence of its natural structure and fabric. As a result, the use of laboratory processes for characterisation of these materials is limited and may lead to erroneous classifications.

Viana da Fonseca (1996) summarised the current knowledge on residual soils, both in terms of its characterisation and its properties, in the following:

- heterogeneous masses, with highly variable weathering profile;
- wide grain-size distributions, ranging from silty sands to clayey sands to sandy silts, with variable fines content;
- presence of bonding bridges between particles, inherited from the parent rock, which rapidly degrade with stress relief, with exposure to chemical agents and even with water content variations;
- undefined and hard-to-predict at rest stress state, ranging from high values if considering the influence of the original rock, to low values, if an analogy with transported soils is assumed;
- limited knowledge regarding stiffness behaviour, where effects such as creep of the solid skeleton may be relevant;
- complex behaviour of the compacted material, not fully described by a single parameter;
- difficulty in obtaining undisturbed samples for high-quality laboratory characterisation;
- limited correlation between in situ results and strength and stiffness properties.

In these circumstances, it becomes apparent that an important research effort is still mandatory for understanding and anticipating the behaviour of these residual soils.

As suggested by several authors, residual soils fit the definition of "non-textbook materials" or, more appropriately, "unusual geomaterials", coined by Schnaid et al. (2004) to describe those soils that satisfy any one or more of the following criteria:

- classical constitutive models do not offer a close approximation of its true nature
- it is difficult to sample or to be reproduced in the laboratory (interpretation is therefore solely based on in situ test data)
- very little systematic experience has been gathered and reported
- values of parameters are outside the range that would be expected for more commonly encountered soils such as sand and clay
- the soil state is variable due to complex geological conditions

Among the unusual geomaterials, residual soils can be considered an example of bonded soils. Schnaid et al. (2004) highlighted the following general characteristics of the behaviour of these soils:

- Bonding and structure are important components of shear strength
- Cohesive-frictional nature (characterized by ϕ' and c')
- Anisotropy derived from relic structures of the parent rock
- Structure and fabric may be developed in situ by weathering process
- Very variable fabric and mineralogy
- Destructuration in shear
- Stress-history relatively unimportant

5.1.3. Residual soils from Porto granite

5.1.3.1. Typical profiles

In the North-Western region of Portugal, residual soils from granite are dominant (Viana da Fonseca, 1988, 1996; Begonha, 1989; Viana da Fonseca et al., 1994). Geologically, granite rocks prevail and, the typical Porto granite is a leucocratic alkaline rock, with two micas and medium-to-coarse grains (Costa and Teixeira, 1957). The chemical and mineralogical constitution of this rock varies naturally, generating a fairly heterogeneous mass. The main weathering factors acting on granite masses seem to be the degree of discontinuities - that is, number, spacing, orientation and continuity of joints - and the proximity of different tectonic events that determine the creation of weak zones where the water actions tends to increase by flow on discontinuities. Weathering factors and processes relevant to these

residual soils are the following: (i) localization; (ii) topography (particularly natural surface slopes); (iii) mass jointing and composition of the parent rock; (iv) climate, rainfall intensity, temperature gradients, humidity; (v) hydrology (water levels, seasonal gradients, percolation); (vi) vegetation (Viana da Fonseca, 2003). The typical weathering depths range from 0 to 20 m, though more commonly around 5 to 9 metres. The photographs in Figure 5.2 illustrate examples of residual soils from Porto granite, where some heterogeneity is evident.

Due to their specific genesis, these residual soils present complex characteristics, which are a consequence of the overall variability and heterogeneity of the rock, as well as of the spatial arrangement and distribution of the particles and pore spaces. The resulting residual soil is characterized by the presence of a bonded structure and fabric, which has significant influence on its engineering behaviour, particularly in its small-strain stiffness properties (Viana da Fonseca, 2003). It is usually classified as silty (SM) or well graded (SW) sand, or more rarely as clayey sand (SC), according to ASTM D 2487-85.



Figure 5.2 - Excavation works around Porto, on residual soils

Due to its specificity and to the need to characterize this geomaterial for design purposes, some researchers, mainly from the University of Porto, have reported studies on these residual soils, providing valuable contributions to its characterization (Silva Cardoso, 1986; Viana da Fonseca, 1988, 1996; Begonha, 1989; Viana da Fonseca et al., 1994; 2006; Cruz, 1995; Vieira de Sousa, 2002; Ferreira, 2003, among others). A synthesis on the specific approaches to the characterisation of residual soils was recently published (Viana da Fonseca and Coutinho, 2008).

5.1.3.2. Mineralogy

Viana da Fonseca (1996) studied in detail the evolution pattern of the mineralogical constituents of Porto granite, having concluded that:

- quartz is naturally very stable and its stability can even be increased by silica concentration;
- potassic feldspar (orthoclase) evolves to kaolinite and, to a lesser extent, to muscovite, which is directly related to small losses of K_2O;
- sodic feldspars (albite) - quite important in this alkaline type of granite - and calcareous feldspars (anortite) - present only in small quantities - are extensively transformed into kaolin and muscovite.

Microscope photographs of the clay fraction of typical residual soils from Porto are presented in Figure 5.3.

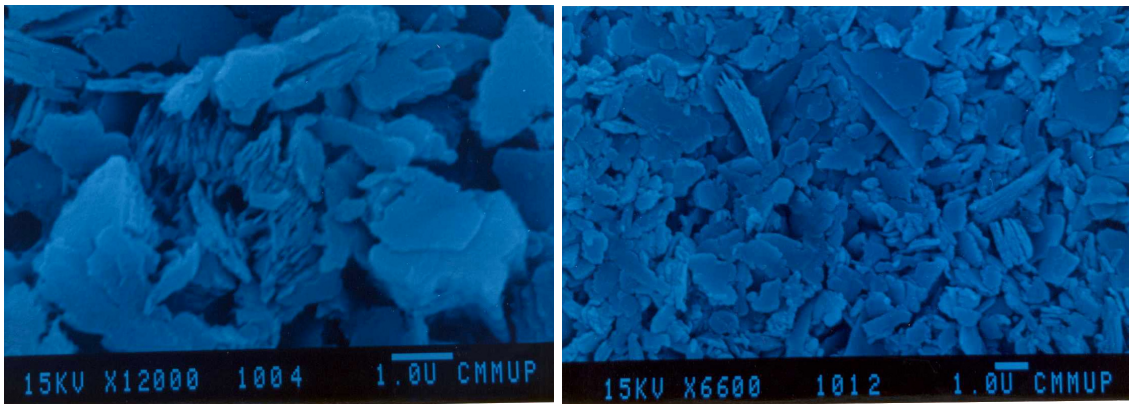


Figure 5.3 - Microscope photographs of the clay fraction of a residual soil from Porto (Begonha, 1989)

The relation of all these transient constituents to the stable amount of quartz is usually used as a classification weathering index, but other primary elements such as zircon, tourmaline, can also be used. Lumb (1962) defined the degree of decomposition for granitic rock as a function of the quartz and feldspar existing in both the parent rock and the residual soil:

$$X_d = (1 - W_f / W_{f0}) / (1 + W_f / W_q) \quad [5.1]$$

where W_q is the weight of quartz, "unaltered" by weathering, and W_f and W_{f0} are the weights of feldspar in the residual soil and in the parent rock, respectively.

The values obtained for X_d for residual soil from Porto granite ranged between 0.59 and 0.63, clearly reflecting a high degree of weathering. These X_d values correspond, in the Collins (1985) chart of microstructure characterisation, to a meta-stable zone, associated with a porous but cemented inter-particle matrix, as shown in Figure 5.4. This means that this saprolitic soil is composed of coarse quartz grains bonded by a porous clay matrix, resulting from the chemical alteration of the plagioclases. These feldspars lead to important lixiviation processes (Viana da Fonseca, 2003).

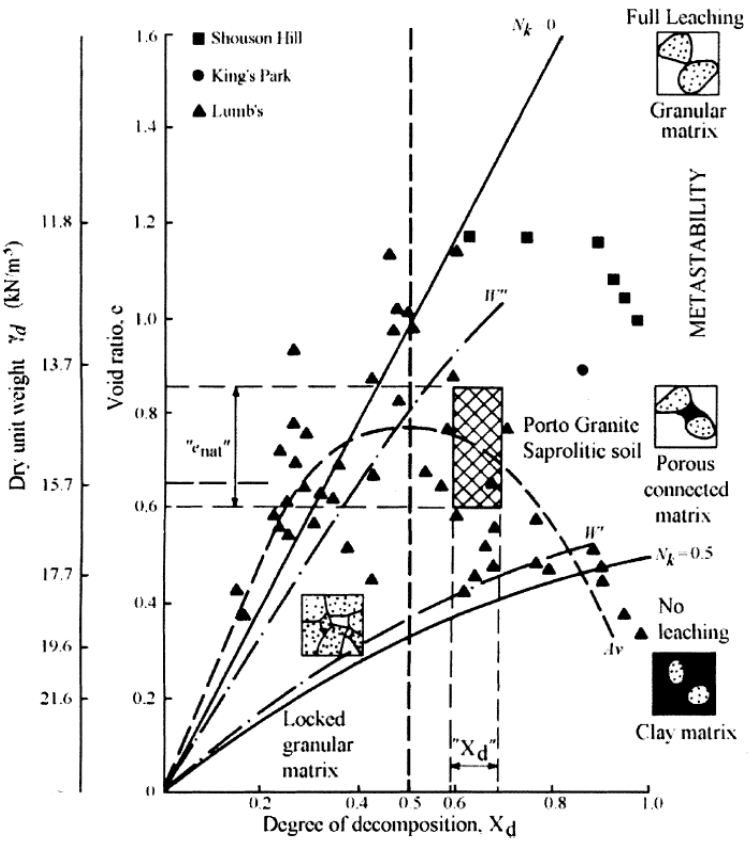


Figure 5.4 - Microstructure characterisation by degree of decomposition (Viana da Fonseca, 2003, after Collins, 1985)

5.1.3.3. Geotechnical parameters

Void ratio and dry density have already been mentioned as inadequate for predicting the mechanical response of residual soils. In these saprolitic soils, those physical parameters usually take the following values for dry apparent densities ($d = \gamma_d / \gamma_w$):

- Sound granites (W_1): 2.55 - 2.70
- Medium to compact weathered altered granites (W_2 - W_4): 2.30 - 2.60
- Saprolitic soils (decomposed granites, W_5): 1.45 - 1.77

The distinction between the intermediate weathering degrees is made by means of other specific indices, namely those of Rock Mechanics classifications for geotechnical design, such as RMR (Bieniawski, 1976) or Q (Barton et al., 1974). These different weathering degrees can be classified according to the uniaxial compressive strengths and characteristics of joints, defining each geomechanical unit (ranging from W_1 to W_5), as presented in Table 5.1.

Table 5.1 - Typical values of uniaxial compression strength for different weathering classes (Viana da Fonseca, 2003)

Weathering degree	W_2-W_3 W_3-W_2	W_3	W_3-W_4 W_4-W_3	W_4	W_4-W_5	W_5
σ_u (MPa)	≈ 10	≈ 35	≈ 20	≈ 15	≈ 10	0.03-0.14

A clear but smooth decrease is evident between the apparent densities of the sound rock and the weathered granites, with a steep density reduction at the highest weathering degree. Nevertheless, the macro-structure and fabric of the parent rock are in general preserved in the saprolitic soils.

Typical values of the most common physical parameters for saprolitic residual soils from Porto are presented in Table 5.2. The relatively low values of total unit weight, typically between 17 and 19 kN/m^3, are associated with a flocculated structure, with open continuous voids in a cemented, bonded structure (Viana da Fonseca, 2003).

Table 5.2 - Common natural physical parameters (Viana da Fonseca, 2003)

γ_s [kN/m^3]	w [%]	γ_d [kN/m^3]	S_r [%]	e	k [m/s]
25.7 - 26.5	15 - 25	15.0 - 18.5	80 - 100	0.40 - 0.70	10^{-6} - 10^{-5}

The influence of relict structures from the parent rock (fissures, discontinuities, etc.) has proved to be determinant in the water flow conditions of these granite weathering profiles (Costa Filho and Vargas Jr., 1985; Viana da Fonseca, 2003). Factors such as macro-pores and open channels in cemented and flocculated matrices also appear to be more relevant to permeability characteristics than microstructural arrangement of the soil. Deere & Patton (1971) suggested a classification of permeability in relation to the degree of weathering, where these saprolitic soils, or young residual soils, are considered medium to high permeability materials. Recent results from in situ permeability tests confirmed the range defined in Table 5.2, as shown in Table 5.3.

According to the degree of weathering of this residual soil, medium permeability is associated with the presence of sandy and silty grains aggregated in large pore sizes (flocculated matrices) while higher permeability in the more weathered rock masses is due to the highly fractured matrix. Variations of permeability with depth are small and mainly related to stable open microstructures and homogeneous dispersion of discontinuities. More kaolinite-rich matrices present permeability values that are lower than the indicated ranges by one order of magnitude.

Table 5.3 - Typical values of permeability by classes of weathering of Porto granite (Viana da Fonseca and Coutinho, 2008)

Class of rock weathering (W_i from ISRM, 1981)	**Permeability** [1] (m/s)	**Experimental results** [2]
Decomposed rock – soil with no relic structure (W_6)	Low	$\approx 10^{-7}$
Completely weathered rock - saprolitic soil (W_5)	Medium	10^{-6} -10^{-5} (3)
Highly weathered (W_4) and fractured (F_4-F_5) rock	High to medium	$10^{-5} - 10^{-4}$ (3)
Moderately weathered (W_3) and fractured (F_3-F_4) rock	Medium to high	$10^{-5} - 10^{-6}$
Slightly weathered rock (W_2)	Medium	$10^{-6} - 10^{-7}$

[1] Trends from Deere & Patton (1971), Dearman (1976), Costa Filho and Vargas Jr (1985)

[2] Experimental values obtained in head tests through sections in boreholes or pump tests, with surrounding piezometers

[3] More kaolinitic matrices present permeability values that are lower than the indicated ranges by one order of magnitude

Borehole permeability tests are considered the most appropriate method for characterizing these soils, since the micro- and macro-structural variability determine the in situ behaviour (Costa Filho and Vargas Jr., 1985; Viana da Fonseca, 2003). The presence of fissures and cracks are extremely important in the resulting overall high values of permeability. However, for saprolitic residual soils, the macro-structural features are less relevant, resulting in fairly uniform values of permeability with depth. In field measurements, the risk of reduction of the effective stresses due

to swelling should be taken into account, which might result in an overestimate of permeability. Laboratory evaluation of this parameter is difficult, due to scale effects and representativity issues and the use of high-quality undisturbed samples is imperative.

Two experimental sites were used for the purposes of this research, which are described in detail below. Extensive characterization data will be analysed and frequently compared with results from Viana da Fonseca (1996; 2003). Many of the results and discussions were already published in Viana da Fonseca et al. (2004, 2006) and more thoroughly analysed and compared with other residual soils in Viana da Fonseca and Coutinho (2008).

5.2. ES1: CICCOPN experimental site

5.2.1. Description

For the selection of an experimental site, it is fundamental to consider a location where the soil characteristics are expected to be approximately constant and homogeneous within the area of study. The first experimental site (ES1) is located in the region of Porto, in the grounds of the technical school CICCOPN (Figure 5.5). This location has been subject to prior geological and geotechnical surveys, from which a number of research works have been published (Cruz, 1995; Vieira de Sousa, 2002; Ferreira, 2003).

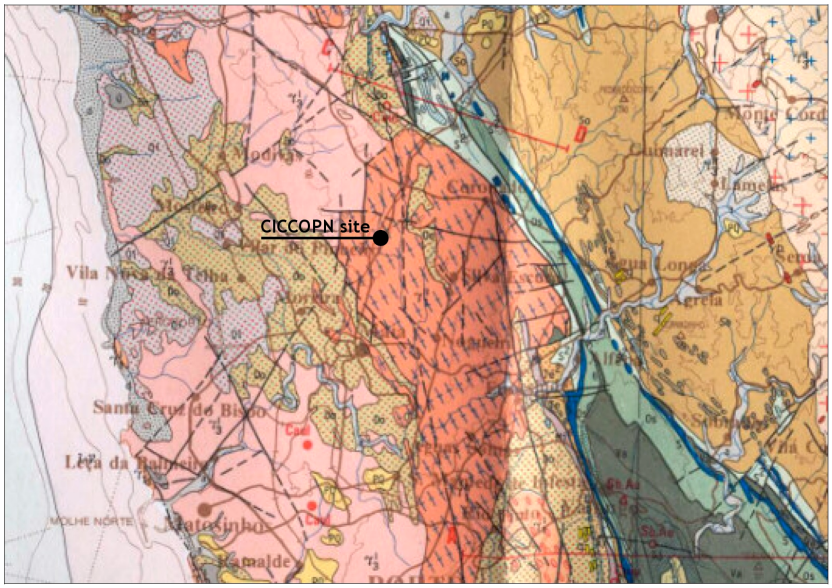


Figure 5.5 - Location of ES1 at CICCOPN in the geological chart of Portugal, Sheet 9-C (adapted from Vieira de Sousa, 2002, after Costa and Teixeira, 1957)

This site presents a typical saprolite residual soil, resulting from the weathering of granite, commonly known as Porto granite. This soil is essentially composed of alkaline granite, coarse to medium grains, two mica and albite as main feldspar. The natural variability of soil characteristics within the study area was considered to be acceptable for the purposes of this research.

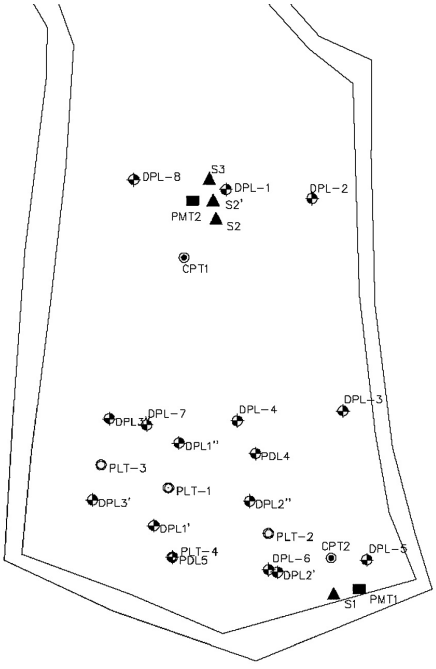
5.2.2. Geotechnical characterization

A wide range of in situ tests were carried out at this site, as depicted in Figure 5.6a, which included 3 SPT, 2 CPT, 7 PMT, 4 PLT, as well as 16 DPL and several high-quality tube samples of different diameters for laboratory testing (detailed in Vieira de Sousa, 2002). In Table 5.4 are summarised some of the results of the geotechnical characterisation of ES1 from previous surveys. The average resistance parameters obtained from compression triaxial tests (CID) on undisturbed block samples were of an effective cohesive intercept of 8 kPa and an effective friction angle of 38°. In view of these characterisation results and the relative homogeneity of the profile (Figure 5.6b), the site was considered suitable for further research analyses, namely for the assessment of the sampling quality produced by different samplers in this geomaterial.

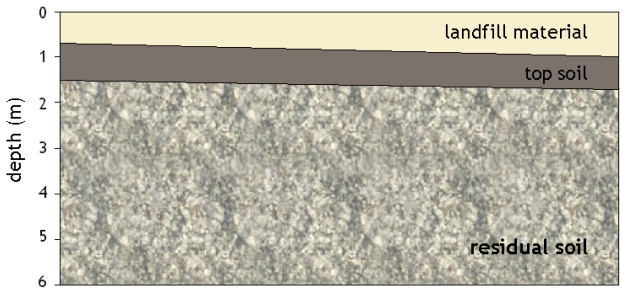
Table 5.4 - Geotechnical characterisation results (after Vieira de Sousa, 2002)

Depth	Soil type	N_{60}	q_c [*] (MPa)
1.5	top soil	---	---
3.0		7.5	3.5
4.5	residual soil	9.3	5.0
6.0		11.8	7.0

[*] average value every 0.5 m



a)



b)

Figure 5.6 - ES1: a) location of the in situ tests (Vieira de Sousa, 2002); b) schematic profile (Ferreira, 2003)

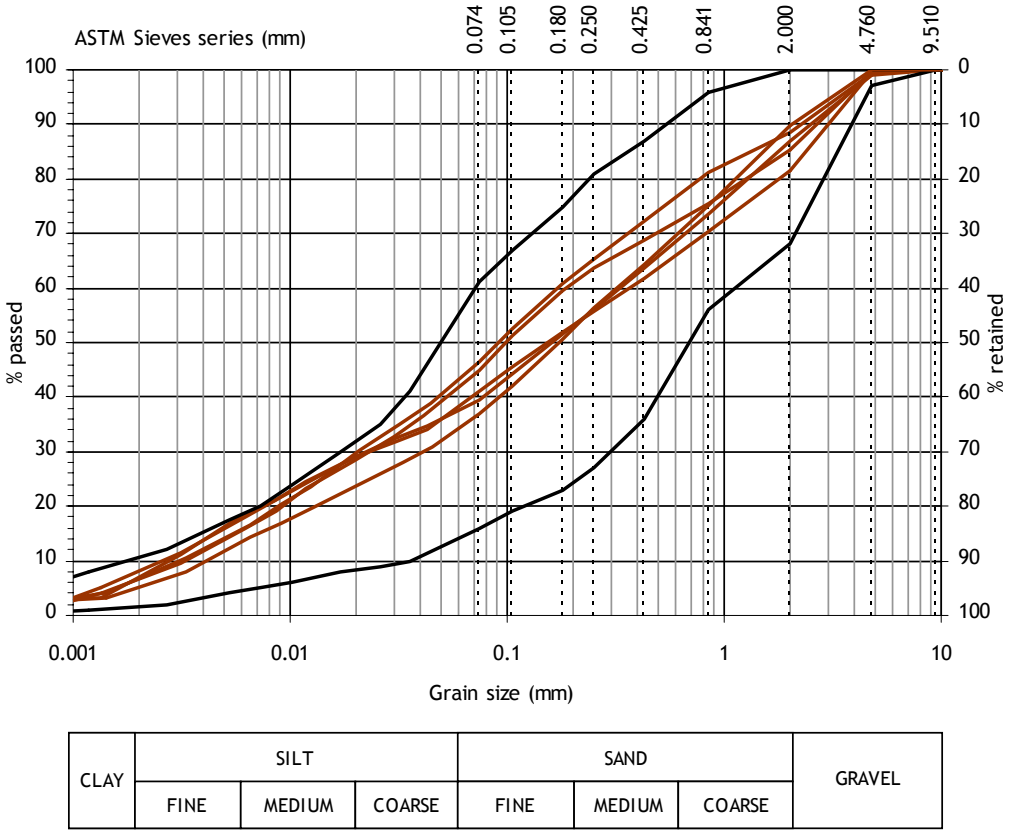
A large number of high-quality tube samples and undisturbed block samples were collected, which were subsequently tested in the laboratory, mainly in triaxial conditions. A photograph of this experimental site after the sampling survey is presented in Figure 5.7, as well as the schematic layout of the sampling boreholes. A triangular arrangement was adopted, with an even spacing of 4 m, to facilitate the execution of in situ cross-hole testing (Ferreira, 2003).



a) b)

Figure 5.7 - ES1: a) overview; b) layout of the boreholes

Several laboratory identification tests were performed on the collected material, namely water content, Atterberg limits, density, and grain-size distribution tests. The values for the liquid limit w_L ranged from 30% to 33% while the plasticity index I_P varied between 4% and 10%. The grain-size distribution curve of the tested soil specimens for the working depth of 2 m is presented in Figure 5.8, evidencing low variability. The figure also includes the envelopes of more than one hundred grain-size distribution curves obtained in previous works on residual soil from Porto granite, compiled by Viana da Fonseca (1996). The results of this experimental site fit well inside these envelopes curves, demonstrating the representativity of this soil as a typical residual soil from Porto granite.



[the lower and upper boundaries - in black - were defined, based on more than one hundred curves (from Viana da Fonseca, 1996)]

Figure 5.8 - Grain-size distribution curve of ES1 soil specimens, framed with the typical grain-size fuse for Porto residual soil

A more thorough geotechnical characterization results was carried out in this experimental site, as illustrated in Figure 5.9. Some field tests were developed on a restricted zone in order to compare the values for drained Young's modulus, E, derived from SPT, CPT, DPL, PMT and triaxial testing, and those considered as reference benchmarks: the dynamic values taken from CH techniques. The main results collected in this campaign can be resumed in the plots of these parameters with depth, as presented in Figure 5.10.

a)



b)



Figure 5.9 - In situ testing at ES1: a) plate load tests (Vieira de Sousa, 2002); b) cross-hole and down-hole tests (Ferreira, 2003)

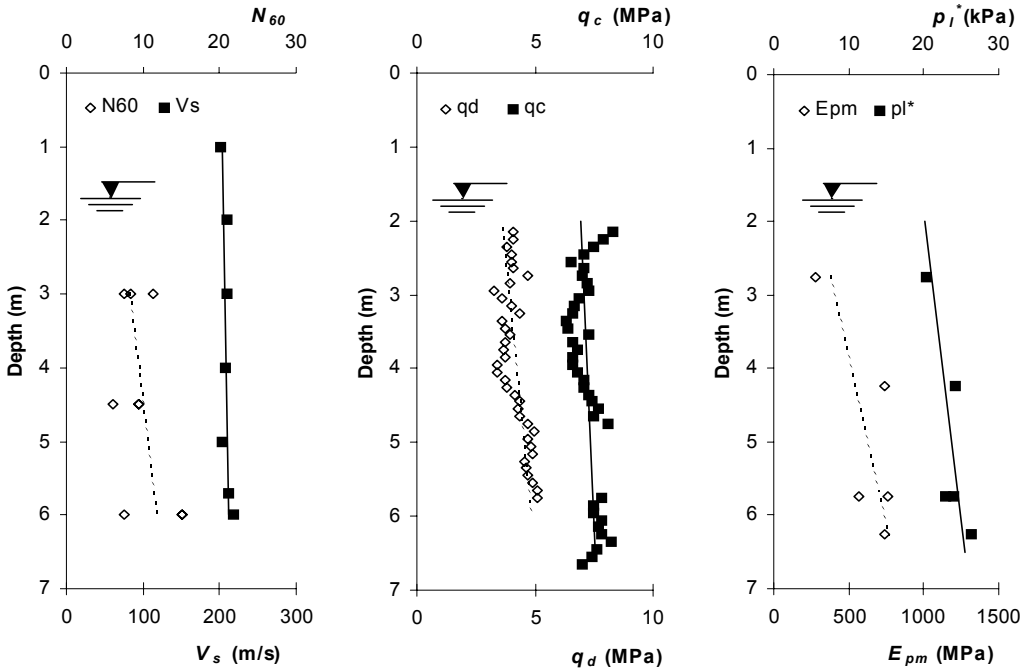


Figure 5.10 - ES1 in situ test results: V_S [CH], N_{60} [SPT], q_c [CPT], q_d [DPL], E_{pm} and p_l^* [PMT] (Viana da Fonseca et al., 2003)

From these results, the profile appears to be fairly homogeneous in depth, in terms of stiffness properties, although not equally revealed by the different parameters:

- values of shear wave velocities, determined by cross-hole (CH) are almost constant in depth, with a similar shape to the penetration point resistance of CPT and DPL;
- values of N_{SPT} increase slightly with depth, closer to PMT trends.

These differences are likely to be related with the distinct evidence of structure produced by the diverse testing methods. Seismic and CPT tests are more sensitive to the natural structure of soil, especially due to the reduced disturbance associated with these tests. On the other hand, in SPT or PMT, induce larger disturbances in the ground during testing, thus destroying the weak structure of the soil. This effect is clearly more pronounced at lower depths.

Samples collected at different depths demonstrated that some horizons have more pronounced kaolinised matrices than others; a clear presence of this dispersion was identified: while the soil matrix at 2 to 3 m of depth is fine, there is a coarser weathered granite in between 3.5 to 5 m of depth, changing to a relevant kaolinised zone between 5 to 6.5 m from the surface. Fines percentages are relevant in the samples taken from 2 to 2.5 m and 5.5 to 6.0 m deep (around 40%), while the samples in the intermediate horizon (≈ 4m) are coarser, with 25% of fines. There is a change in weathering degrees, as demonstrated by these signs. However, all the horizons are classified as W_5 weathering; hence, the overall pattern is comparable (Viana da Fonseca et al., 2003).

The possibility of carrying out more than one loading test has the advantage of an integrated analysis of the different responses, as means of studying the importance of the relation between stiffness and depth of influence. Some plate loading tests were performed at a previously excavated soil platform to ensure contact with the residual soil (at a depth of around 1.5 - 2 m). Different sizes plates of 45, 60 and 90 cm in diameter (Figure 5.11) were loaded with the purpose of evaluating the influence of stiffness variation in depth and controlling with it a reliable deduction of the Young's modulus.

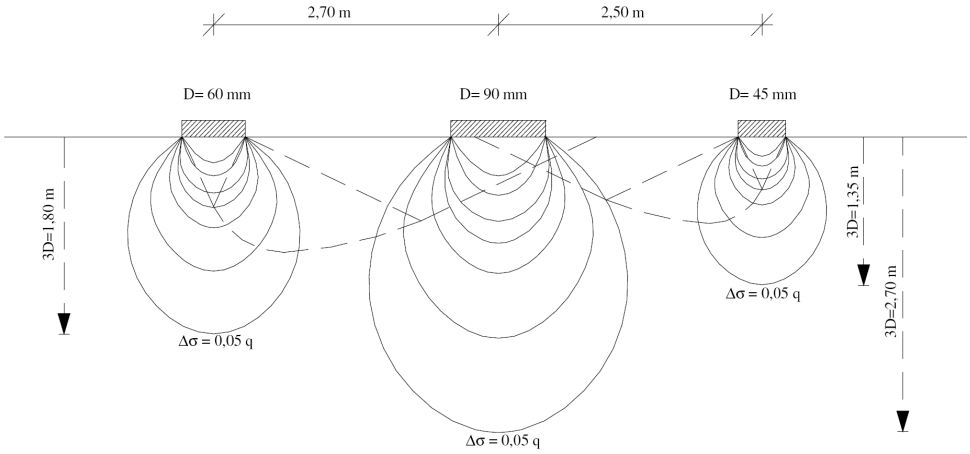


Figure 5.11 - Relative positioning of the plate load tests and schematic of the stress bulbs in serviceability conditions and classical failure wedges (Vieira de Sousa, 2002)

The resulting curves are plotted together, in Figure 5.12a. The same tests results are presented in a normalized scale, i.e., the ratio of the current pressure over the ultimate load (as defined by the set of results) against the relative settlement (towards the plate diameter) in Figure 5.12b.

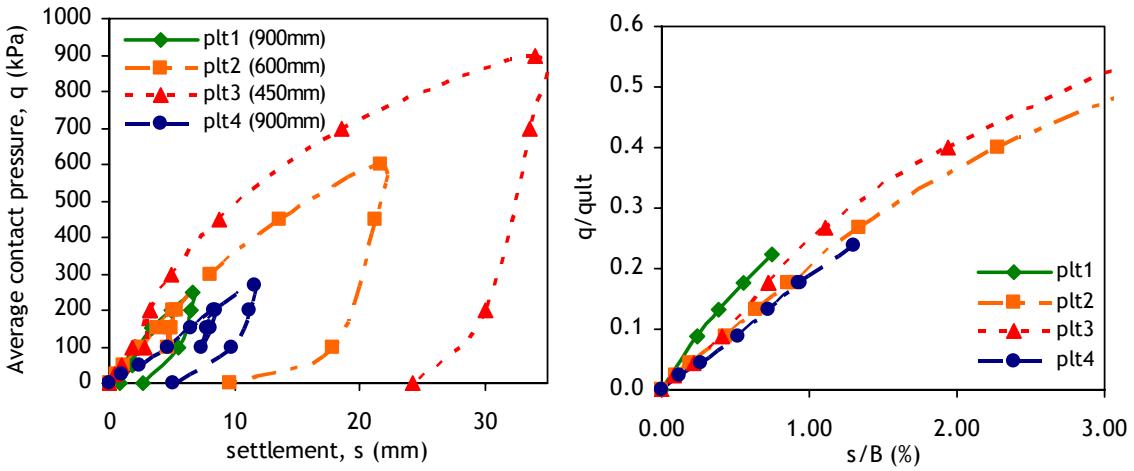


Figure 5.12 - Pressure-settlement curve of the PLT: a) direct; and, b) normalized representation (adapted from Viana da Fonseca et al., 2003)

The Young's moduli of the soil at different load stages obtained by back-analysis of the plate loading test (using formulations from the theory of elasticity) are summarised in Table 5.5.

Table 5.5 - Secant, E_s, and unload-reload, E_{ur}, Young's moduli (MPa) from PLT tests at different stress levels (Viana da Fonseca et al., 2003)

Criteria Plate (D)	s/B=0.1%	s/B=1%*	F_s=10	F_s=5	Unload-reload
900mm	---	23.24	29.36	24.46	106.93
600mm	19.81	14.73	15.94	17.00	73.66
450mm	20.06	20.07	22.59	25.07	69.06
900mm	15.64	15.57	14.94	15.22	100.44

* nearly corresponding to the allowable pressure for serviceability limit state design

These calculations assume a linear elastic layer with constant modulus underlain by a rigid base at a depth that will not interfere with the induced strains. The pressure surface was assumed rigid. It should be noted that the second value shown in the table corresponds approximately to the allowable pressure, according to the criterion of Decourt (1989) for residual soils. There is a reasonable constancy in E values, which is typical in these soils where loading develops a punching deformation. A relation between the unload-reload and the secant moduli (E_{ur}/E_s) for low strain levels (those expressed in the table corresponding to s/B=0.1% or $F_s=q/q_{ult}$=10) range between 3 and 6, with a medium value of around 5, giving a clear sign of the inelastic behaviour of the soil at the early stages of the plate loading.

In the context of this research, the results from this experimental site will be applied mainly for the assessment of the quality of sampling of the different samplers used, which will be described in the following chapter. The comparison of cross-hole and down-hole test results with laboratory bender element tests will serve as basis for the assessment of sampling quality. The results from the in situ tests presented above will also be used for the comparison of stiffnesses between different methods.

5.3. ES2: CEFEUP experimental site

5.3.1. Description

The second experimental site (ES2) considered in this work is located, within the campus of FEUP, illustrated in Figure 5.13 and Figure 5.14. This site, also referred to as CEFEUP, was initially defined for an international pile prediction event, within the scope of ISC'2 (International Conference on Site Characterisation) held in Porto in 2004 (Viana da Fonseca et al., 2004). Essentially, the site is geologically formed by an upper layer of heterogeneous saprolite residual soil from granite of variable thickness, overlaying a weathered granite, in contact with high-grade metamorphic rocks (gneisses and migmatites). The thickness of these residual saprolitic horizons

may vary between few meters to more than 20 metres with common values of 5 to 9 m. Although they often present strong heterogeneity, it is frequently observed an average gradual change of characteristics with depth, especially regarding their mechanical properties. Nevertheless, an accurate mapping of the spatial variability of the mechanical properties, necessary for geotechnical design, is often very challenging (Viana da Fonseca et al., 2006).

The extensive in situ investigation and characterization of this experimental site comprised the application of several geotechnical and geophysical surface and borehole techniques, namely SPT, CPT, DMT, surface and borehole seismic, electrical resistivity and GPR (Viana da Fonseca et al., 2004). A large number of samples, including high-quality undisturbed tube and block samples, provided material for a thorough laboratory characterization, which included identification analyses, direct shear, oedometer, triaxial, stress-path triaxial, resonant-column, and true triaxial tests, many of which with simultaneous BE measurements. The compiled data offered a valuable and unique opportunity to compare different methodologies and assess their relative advantages and limitations (Viana da Fonseca et al., 2006; Viana da Fonseca and Coutinho, 2008).

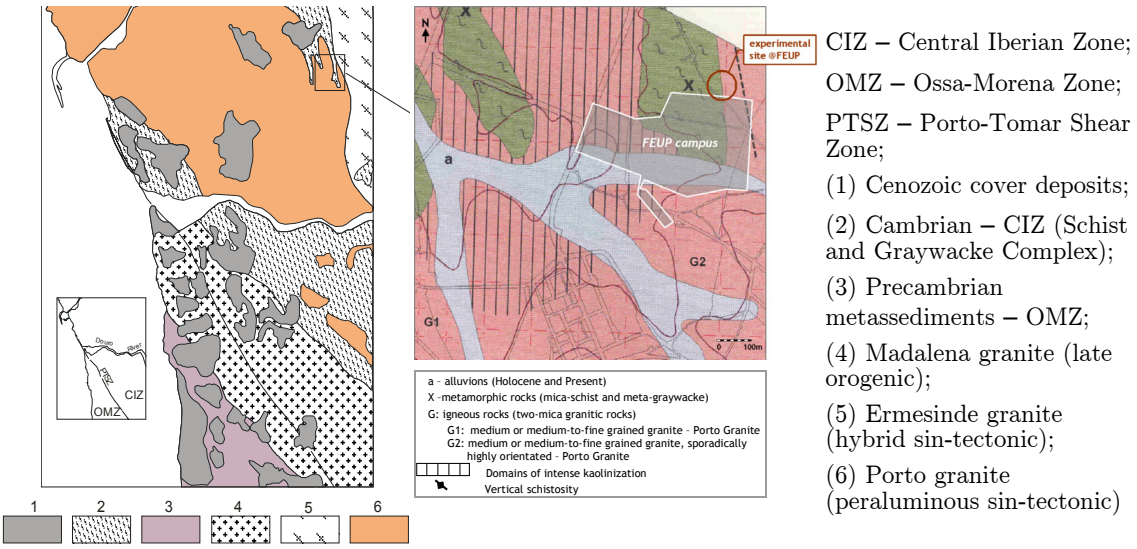


Figure 5.13 - Simplified geological maps of the Porto area and of the CEFEUP experimental site (Viana da Fonseca et al., 2006, adapted from Pereira, 1992)

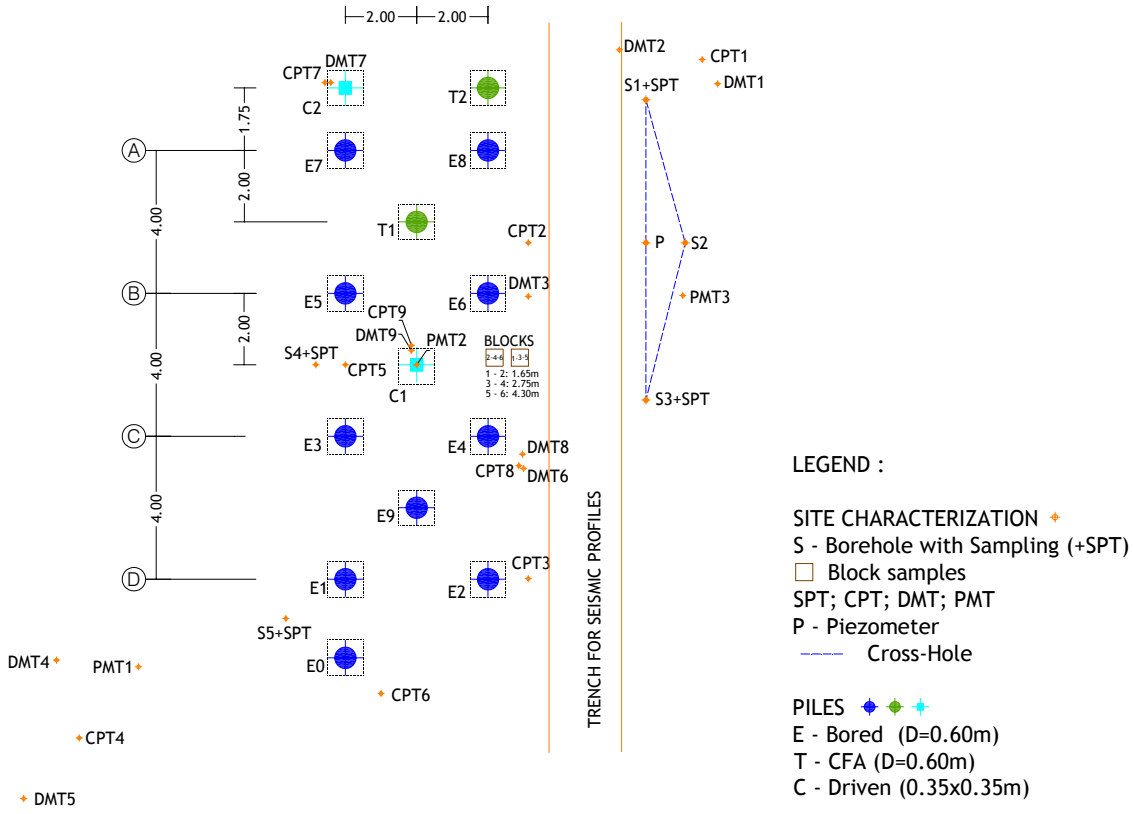


Figure 5.14 - General layout of the ES2 experimental site

5.3.2. Geological setting and characterization

An accurate and detailed geological study was carried out by INETI (Instituto Nacional de Engenharia, Tecnologia e Inovação, Porto) in order to understand the regional and local geology of this experimental site. The conclusions of such study are summarily reproduced below and further details can be found in appendix A5 (extracted from Viana da Fonseca et al., 2006). The simplified geological maps, depicted in Figure 5.13, evidence the geological and geotechnical complexity of this experimental site.

In this Porto area, fresh outcrops of basement rocks are rare. In fact, the site is geologically formed by a thin upper layer of soil of varying thickness, overlaying more or less weathered granite (saprolite) contacting an older gneissic migmatite with dominant sub-vertical foliation. This sub-vertical structural anisotropy can be considered a determining factor to understand the geophysical response of the related residual soils resulting from the weathering process. The geological materials identified by the drill-hole cores are very heterogeneous: biotitic gneisses, migmatitic

gneisses, gneisses cut by granite veins and a weathered two-mica peraluminous granite (Viana da Fonseca et al., 2006). This rock shows a typical gneissic foliation with quartz-feldspatic layers alternating with mica-rich layers. The occurrence of thin veins of granite materials cutting that gneissic structure is interpreted as a sign of the partial melting of the gneiss (Figure 5.15).

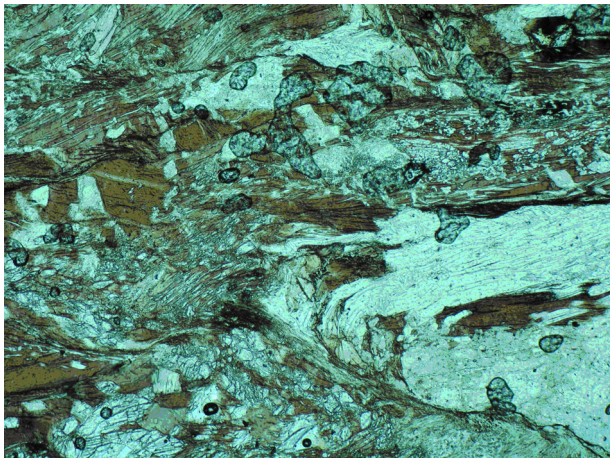
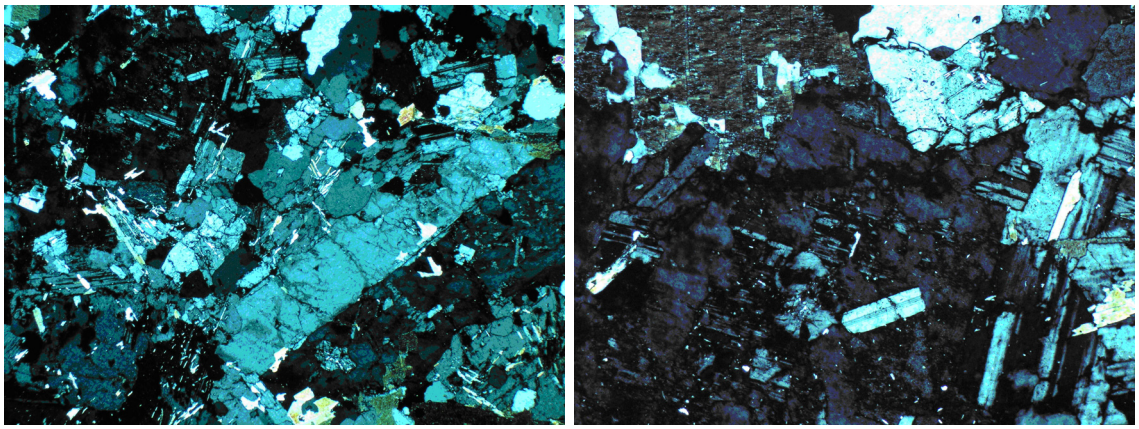


Figure 5.15 - Textural aspect of the formation of silimanite from biotite (Viana da Fonseca et al., 2006)

The essential minerals present include quartz, oligoclase, biotite; siliminanite formed from biotite and muscovite; muscovite in phenoblasts; K-feldspar formed from Al minerals. The rock is classified as gneiss, in the silimanite + K feldspar zone, in which the process of partial melt is apparent: formation of perthitic K feldspar from the consumption of silimanite and muscovite.

The two-mica granite is a leucocratic medium grain size with sparse megacristals. Despite its sintectonic genesis and installation, the rock is isotropic without any foliation. Under the microscope the rock exhibits a granular hypautomorphic texture with the biotite cristals slightly oriented (Figure 5.16a). Some post-magmatic reactions can be seen: a richer primary plagioclase is transformed in lamelar muscovite; in extreme cases, the same plagioclase suffers albitization forming perthitic K feldspar. When the K feldspar has poekilitic inclusions of albite remains, then it is anorthose (sodic microcline) that evolves to form microcline-perthite (Figure 5.16b). Essential minerals are anedric quartz; microcline and anorthose; two plagioclase types: primary oligoclase and neoformed albite; muscovite and rarely biotite, sometimes clorithized. Other minerals are also present, namely zircon; apatite; Fe, Ti oxides and titanite.



a) b)

Figure 5.16 - a) Granular hypautomorphic texture in the granite; b) K feldspar with poekilitic inclusions (Viana da Fonseca et al., 2006)

In order to compare the slightly weathered granite (FE2), collected far from the experimental site, with the weathered granite (FE1), obtained at the experimental site from drill-hole cores, chemical analysis of major and minor elements were made. In addition, the crust genesis of these granites is also suggested by the profile of incompatible elements. The strong crustal contribution in the genesis and evolution of the granitic magma can be highlighted by the fact that the amount of incompatible elements LIL is higher than the amount of incompatible elements HFS, when compared with a primitive material of chondritic composition.

An intense planar anisotropy (gneissic foliation) can be observed in local drill-hole gneissic cores having an orientation in accordance with the known NW - SE strike and 60° eastwards dipping of the regional variscan structure. The 1:50000 Porto geological map (Teixeira, 1955) shows a clear contact line between the gneissic metassediment and the granitic mass. In this complex structural and metamorphic zone it is admitted that the type of regional transition between the two bodies is not a single discontinuity surface but rather a gradual one, consisting in an eastward "probabilistic" decreasing of feldspar bands maintaining the local trend of geological planar anisotropy. Nevertheless, locally, there are zones of sudden lithologic changes. The differences in the weathering processes of granites and gneisses are the main factor for the irregular weathering profile of these rock formations, leading to a quite irregular spatial distribution. As previously mentioned, the thickness of these residual granitic soils (saprolitic formations) varies generally from a few meters to, sometimes, more than 20 m with more common values of 5 to 9 m. Some samples were taken from the borehole cores to study the weathered materials, in particular the changes in grain size and mineralogy with depth.

In terms of the weathered granite mineralogy, kaolinite is the dominant mineral and mica is, as usual, the second mineral. Some samples from borehole S3 are an exception, where quartz takes the place of mica as second mineral. Accessory minerals, such as K feldspar, Na feldspar and hematite, are the remaining minerals. Grain size analyses were carried out using a laser beam particle size analyser (Coulter LS130) and by wet sieving. The results are presented in Table 5.6 and graphically summarized in Figure 5.17.

Table 5.6 - The mineralogical semi-quantitative results obtained by DRX (Viana da Fonseca et al., 2006)

	Depth (m)	<2 um	2-63 um	>63 um
Borehole 1	0.10-1.70	8.24	41.59	50.17
	1.80-2.75	5.03	29.11	65.86
	3.00-3.65	5.79	30.10	64.11
	4.50-7.15	4.55	29.91	65.54
	7.50-9.65	4.56	29.00	66.44
	9.75-12.65	4.07	30.23	65.70
	12.80-12.95	3.17	26.35	70.48
	13.50-13.65	3.34	20.52	76.14
	13.75-16.65	2.37	23.83	73.80
	16.75-19.60	3.02	24.25	72.73
Borehole 3	0.3-2.2	7.39	38.33	54.28
	2.45-3.7	3.52	19.64	76.84
	5.5-5.95	2.64	14.76	82.60
	6.2-7.9	2.47	13.85	83.68
	8.15-10.95	1.92	13.08	85.00
	11.2-12.7	2.08	13.39	84.53
	12.95-16.7	1.40	10.50	88.10
	16.95-21.1	0.50	4.61	94.89

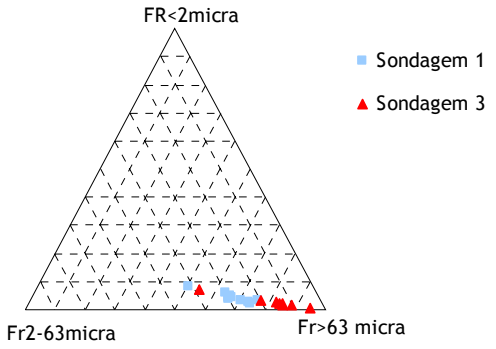
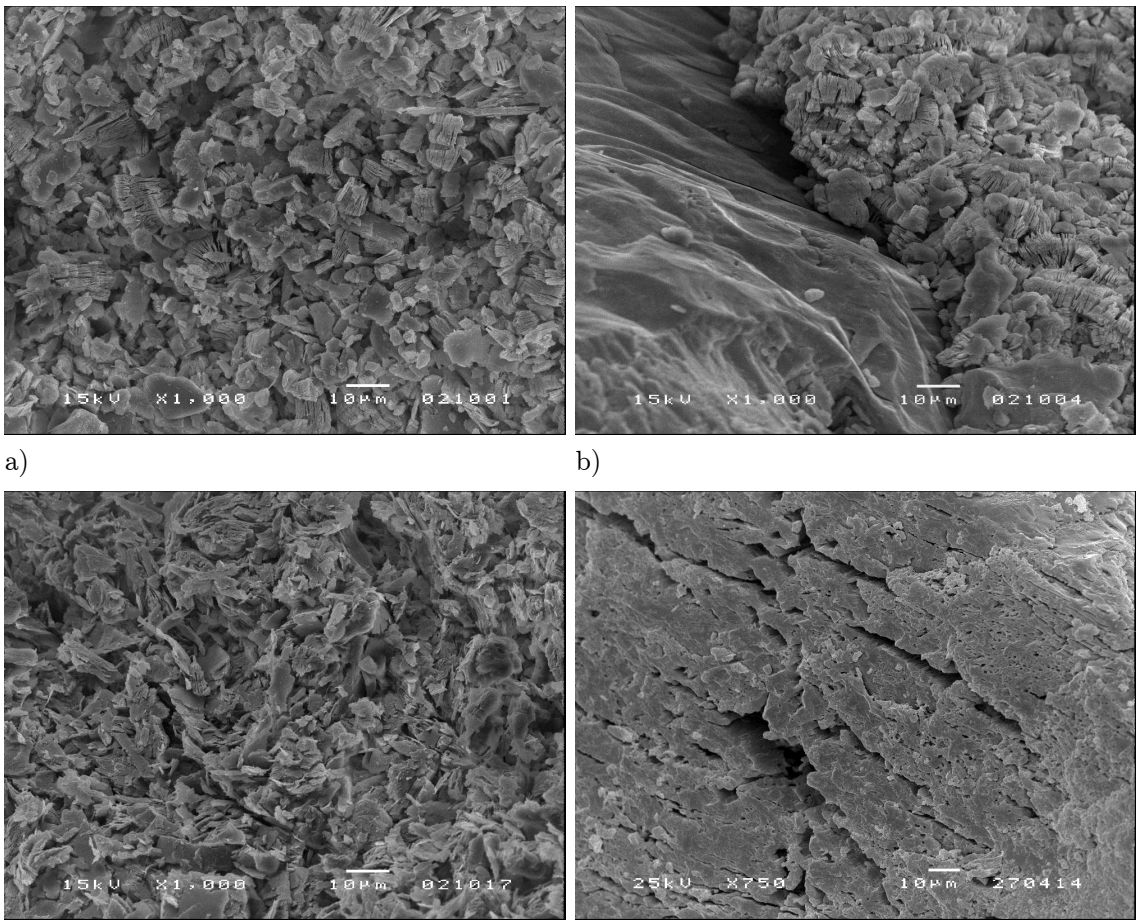


Figure 5.17 - Grain size analysis

The results of the grain size analyses show that both the clay and the silt particles decrease with increasing depth whereas the sand particle size increases with depth. These facts are more relevant in the samples of borehole S3. In terms of the clay fraction mineralogy, kaolinite is the main mineral. However, a slight decrease in its quantity is observed with increasing depth. This fact is in agreement with rock weathering. The high quantity of quartz in borehole S3, when compared with borehole S1, suggests different weathering degrees. The chloritization of micas is more important in the rock sample from borehole S3. It is worth mentioning the probable existence of a percolation level at 12.7 m in borehole S3 and at 12.9 m in borehole S1 suggested by the increasing content of kaolinite at these depths.

More recently, a second set of specimens was prepared for obtaining more electronic microscope photographs of this residual soil, in particular to observe the differences, if any, between block and tube samples. A few of those photographs are included in Figure 5.18. Figure 5.18a and b refer to block B4. In Figure 5.18a, a concentration of clay minerals is visible, containing ilite and kaolinite (kaolinite resembles harmonicas, whereas ilite looks like sheets of paper). Figure 5.18b corresponds to a contact between a feldspar grain and the clay matrix due to weathering. This block sample, contains, as would be expected in this type of soil, kaolinite as the dominant clay mineral. Figure 5.18c refers to the clay fraction of a sample from borehole S1 at 6 m, where in this case, there is a predominance of ilite over kaolinite. It should be noted that this is an unusual situation. Figure 5.18d is also from borehole S1, but at 11.8 m, and the photograph clearly shows the internal degradation of a feldspar grain, evidencing that the effects of weathering directly affect the soil minerals.



a) b)

c) d)

Figure 5.18 - Electronic microscope photographs of two samples of CEFEUP soil: a) and b) block sample B4; c) and d) disturbed tube sample S1

5.3.3. Geophysical characterization

An extensive site characterization campaign has been held, including a large variety of geophysical borehole and surface methods, namely P and S-wave seismic conventional and tomographic refraction (RT), high resolution shallow reflection, cross-hole (CH), down-hole (DH), electrical resistivity imaging (RC) and ground probing radar (GPR). Direct and derived results from the applied methods and techniques were compared between them, as well as with some of the available geological and geotechnical information (Carvalho et al., 2004; Almeida et al., 2004).

The generic layout map of the site in Figure 5.14 shows the location of the seismic, electrical and GPR, around a 50 m long trench, adjacent to three boreholes, S1, S2 and S3, in which undisturbed soil samples were collected, prior to geophysical data acquisition. The CH survey took place between boreholes S1-S2, S2-S3 and S1-S3. In borehole S3, a DH survey was conducted.

Seismic refraction data acquisition was performed along a 44.5 m long traverse, having 1.5 m spacing between geophones and nine shot points. The generic refracted S-wave and P-wave travel time patterns are illustrated in Figure 5.19, indicating an average gradual increase of velocity with depth.

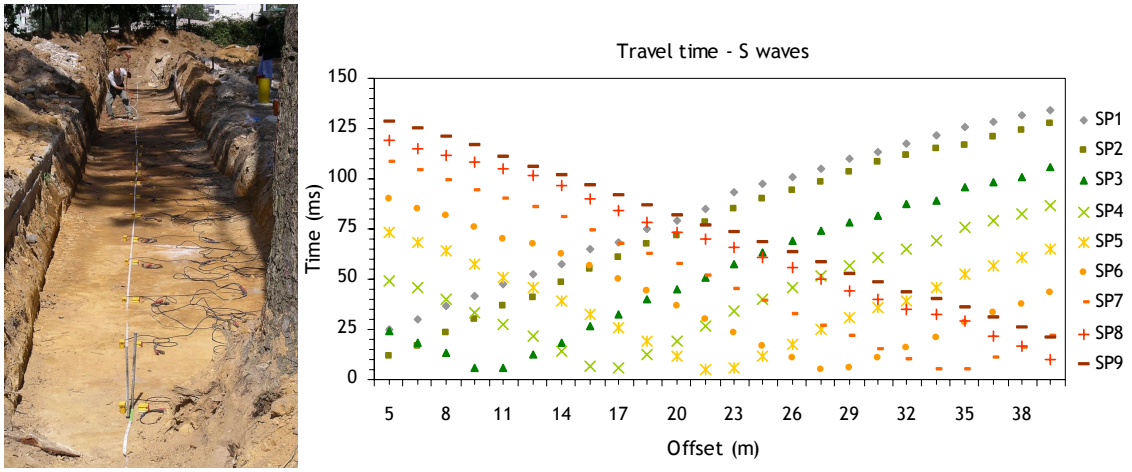


Figure 5.19 - Refraction testing at ES2 and resulting S-wave travel time plots

The conventional delayed time interpretation was done with software SIPT2 provided by Rimrock Geophysics® and the tomographic inversion was performed with the software SeisOpt22D provided by Optim software®. The corresponding S-wave velocity (V_S) values are consistent for both models and with those obtained from CH and RT. The P-wave velocity section resulting from tomographic inversion is

presented in Figure 5.20 and Figure 5.21 shows the V_S section resulting from tomographic inversion, overlaid by the obtained Time Delay method three layers model (dotted lines).

The overall pattern of velocity variability matches the one obtained with electric resistivity imaging: two traverses using the pole-pole method were developed parallel to the seismic refraction traverse and one of the resulting sections from the inversion interpretation method is shown in Figure 5.22.

In both seismic and electrical interpretations, a sub-vertical "contact" appears on the right side of the section separating zones of overall different seismic velocities and apparent resistances. The lower value zone, on the right side, corresponds to a higher seismic velocity zone signed by RC sections and clearly confirmed in RT S-wave section.

The high resistivity anomaly above water level (referred above) is interpreted as being related to a lesser kaolin band dipping 60° eastwards. The high RT V_S zone (also referred above) is well correlated with that high resistivity anomaly. The lower V_S zone in the middle of the profile is interpreted as a clayey band due to the fact that V_P do not change significantly along the horizontal direction therefore, within this lower V_S zones, Poisson's ratio will increase to a clayey domain.

The RC method shows two interfaces (dotted lines in Figure 5.21 and Figure 5.23) where velocity changes: the lower one is interpreted as being related to seasonal water level and the upper one is very consistent namely with the tomographic and reflection velocity fields (Figure 5.20 and Figure 5.22) as well as with GPR results (Figure 5.23 and Figure 5.24). In the processed radargram (Figure 5.23) a reflector with very good agreement with the RC model first interface is visible; the N_{SPT} values increase between 3m and 4m deep which supports the existence of a transition zone. There are some visible diffractions, and a possible less weathered zone between 0m and 5m along the transect line and from the surface to 3.5m depth.

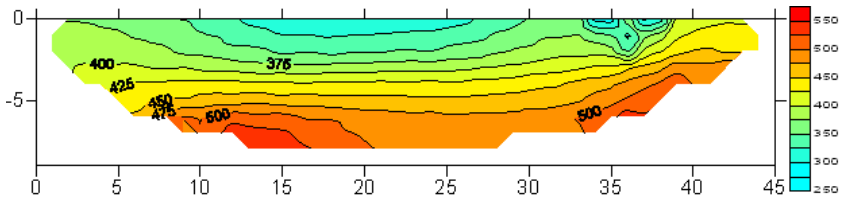


Figure 5.20 - Refraction tomography P-wave model (Carvalho et al., 2004)

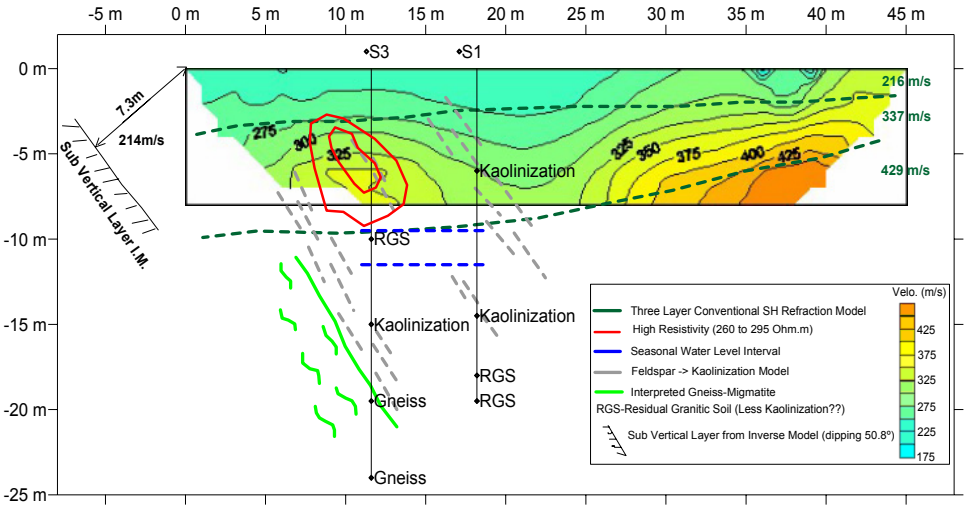


Figure 5.21 - Refraction tomography SH velocity model overlaid by geophysical results (Carvalho et al., 2004) and geological model used for seismic reflection interpretation (Almeida et al., 2004)

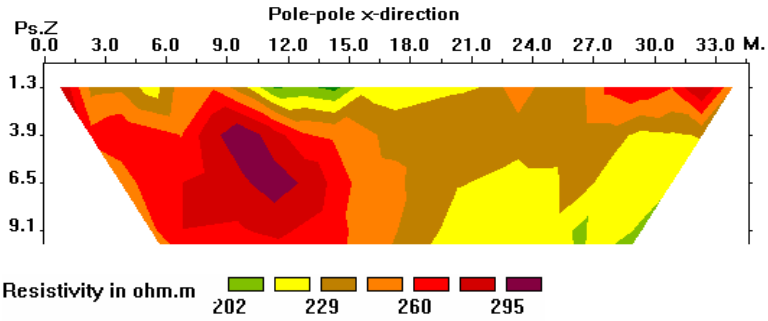


Figure 5.22 - Electric resistivity image (Carvalho et al., 2004)

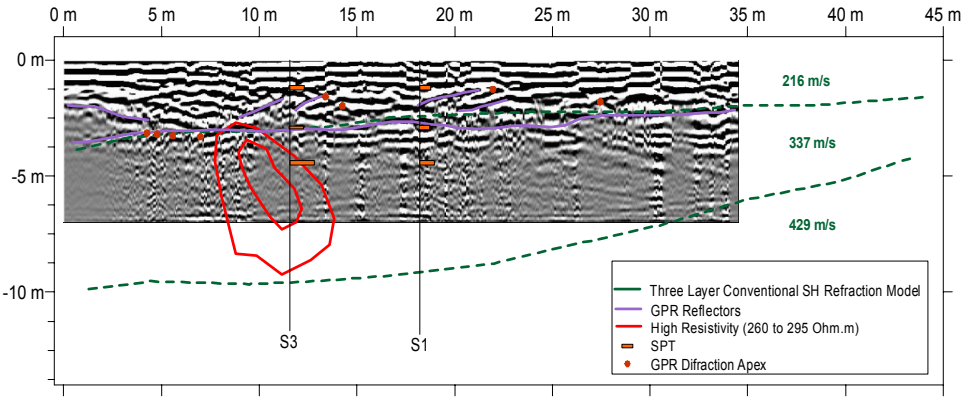


Figure 5.23 - Processed radargram with interpreted events overlaying the resistivity and CH model and N-SPT values in boreholes S3 and S1 (Carvalho et al., 2004)

In order to evaluate the response of the site to reflected S-waves, a reflection profile was done after a walk way noise test. For this test, two Seistronix Ras24 seismographs were used, having 24 and 12 available channels. The 28Hz horizontal

geophones spacing was 0.5m and minimum offset 1m with a sampling interval of 0.25ms. In order to obtaining a record with 72 channels the system was rolled over once, 5 stacks for each polarity were used and the shot was at the starting point of the seismic line. Following the processing procedures, the next step was to overlay all the information interpreted from seismic reflection, refraction, resistivity, GPR and from the geology (Figure 5.24). In Figure 5.24a, the interval velocities obtained from CMP analysis are overlaid by the RC three layers model, the high resistivity contour lines and the hypothetical lateral dipping structure model (dip: 50.8 ° E) obtained from seismic side reflections. This model is believed to be related to the identified 60 ° E dipping gneissic-migmatite local structures. In Figure 5.24b the seismic stacked section obtained is overlaid with interpreted seismic and GPR information.

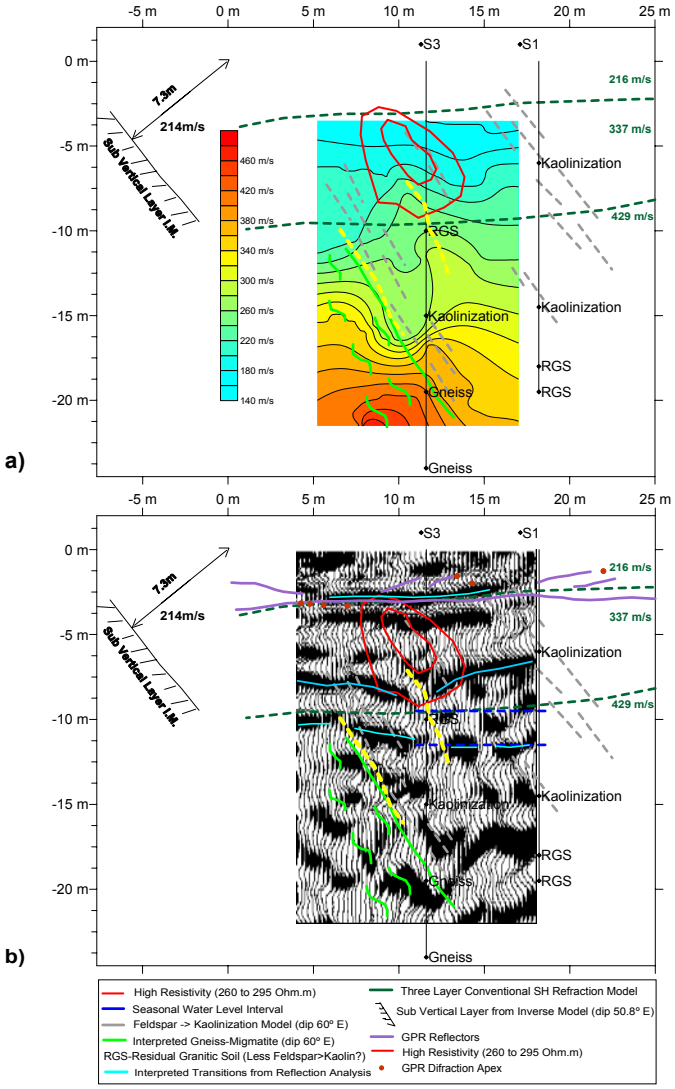


Figure 5.24 - Integration of the interpreted partial models: a) interval velocity model; b) stacked seismic reflection section (Viana da Fonseca et al., 2006)

Three boreholes, S1, S2 and S3 (Figure 5.14), were used for S and P-wave seismic CH and DH surveys. CH data acquisition took place between boreholes S1-S2, S2-S3 and S1-S3 and in borehole S3 a P- and S-wave DH survey was conducted, with a 1.5m interval between shots. These tests were carried out in July, during the dry season, when the groundwater level was positioned around 10 m deep. The obtained curves in terms of the shear moduli and Poisson's ratio are presented below in Figure 5.27.

5.3.4. Geomechanical characterization

5.3.4.1. Derived profile and results from in situ mechanical tests

In spite of the natural spatial variability of the fabric of these residual soils due to some preserved relic heritage, there is evidence of a fairly homogeneous ground profile in geotechnical terms, as demonstrated by the results obtained with continuous sampling from drilling, with the SPT sampler - schematically shown in Figure 5.25 with photos of samples obtained from borehole S3 - and from high quality samplers (Viana da Fonseca et al., 2004).

The first stage of site characterization included 4 SPT, 5 CPTU, 5 DMT, 3 PMT and several CH, DH, SASW and CSWS, while in the second stage 4 CPTU and 4 DMT were performed. The technical data of the first stage of in situ tests is summarized in Figure 5.25 to Figure 5.27. As referred above, three boreholes (S1, S2 and S3 - Figure 5.14), were used for S- and P-wave CH survey. Derived values of the shear modulus, G_0, and Poisson's ratio, ν are included in Figure 5.27.

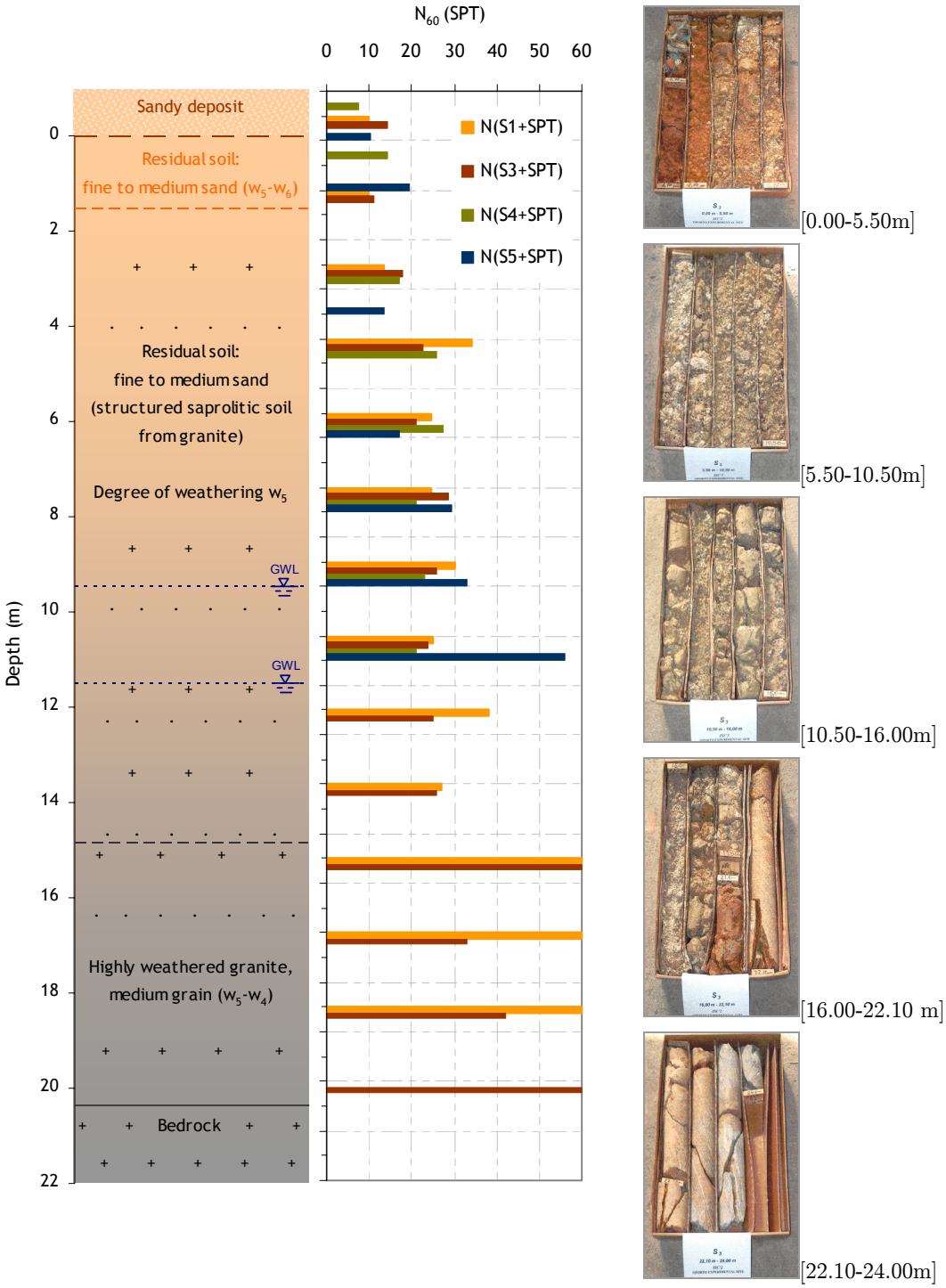
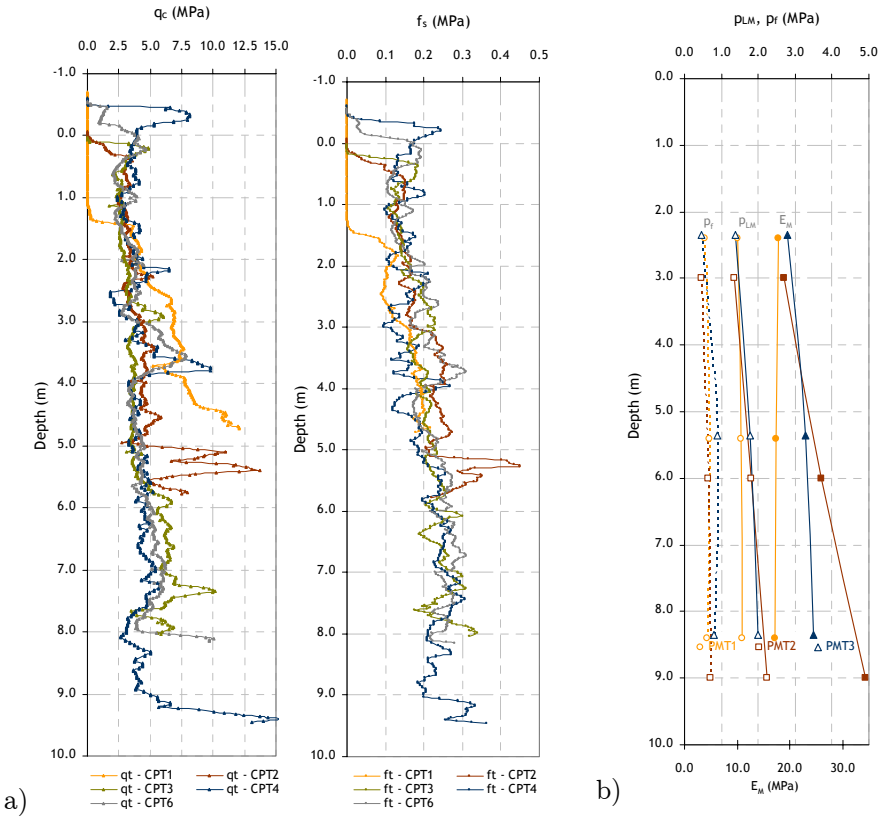


Figure 5.25 - Geotechnical profile and photos of the samples obtained in boreholes (S3 - Figure 5.14)



Note: All pore pressures measurements (u_2) are nearly null; thus qc ≅ qt and fs ≅ ft can be considered.
Figure 5.26 - In-situ tests profile: a) CPTU: q_c, f_s; b) PMT: p_f, p_{LM}, E_M; c) DMT: E_d, K_d, I_d

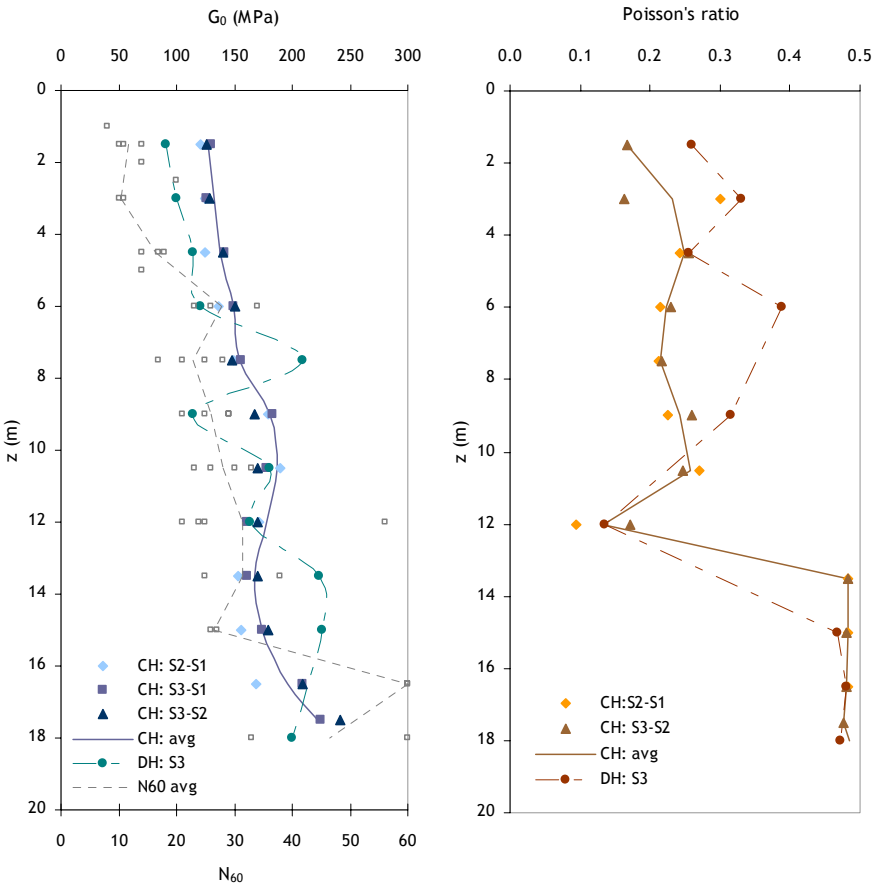


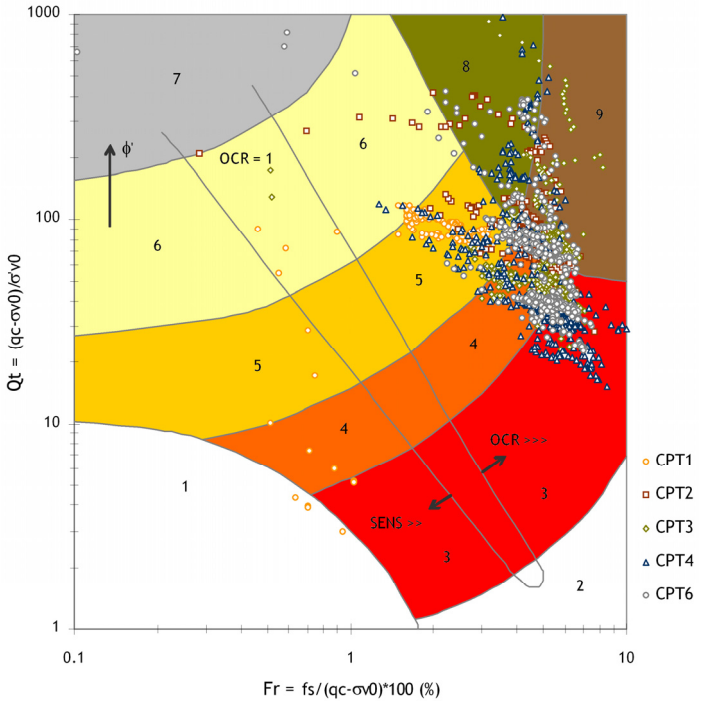
Figure 5.27 - Shear modulus and Poisson's ratio from CH sections and DH in borehole S3

As expected, G_0 and V_S variability with depth follows a similar pattern, generally smooth, although more erratic in the case of DH based values. The ν values show in general higher dispersion, except in the saturated zone below 13.5 m. While in the zone above 13.5 m the values vary around an average value of 0.25, below such level these are quite constant with values near 0.5 (around 0.48), as a clear sign of full saturation. G_0 and ν values down to 9m - the zone of highly weathered saprolitic soil - are plotted in Figure 5.27. V_S values were obtained in CH sections S3-S2 and S2-S1 and RT in boreholes S3, S2 and S1.

The highest G_0 values are located in borehole S1 showing increasing divergence with depth. The lowest ν values are located in borehole S1. The remaining ν sets have a similar trend mainly after 4.5m depth with values around 0.25.

5.3.4.2. Classification based on mechanical indices from in situ test results

Classification charts based on the piezocone (CPTU) results, such as those proposed by Roberston (1990) are presented in Figure 5.28, reflecting considerable dispersion in the material type, as this evaluation may be conditioned by unreliable pore pressure measurements.

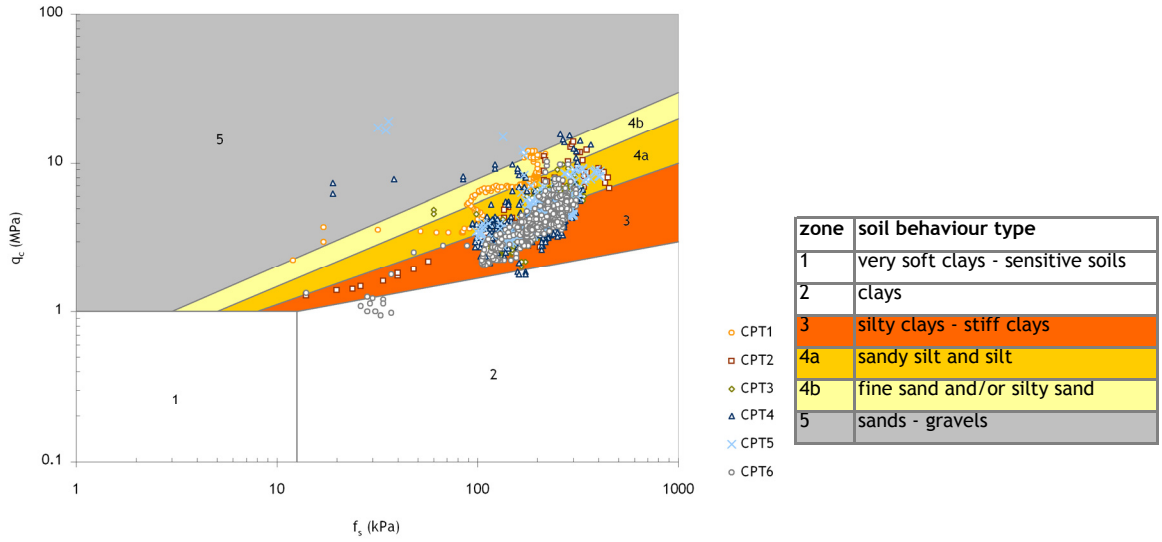


zone	soil behaviour type
1	sensitive, fine grained
2	organic soils, peats
3	clays - clay to silty clay
4	silt mixtures - clayey silt to silty clay
5	sand mixtures - silty sand to sandy silt
6	sands - clean sand to silty sand
7	gravelly sand to dense sand
8	very stiff sand to clayey sand (cemented)
9	very stiff fine grained (cemented)

Figure 5.28 - Soil behaviour classification chart (after Robertson, 1990)

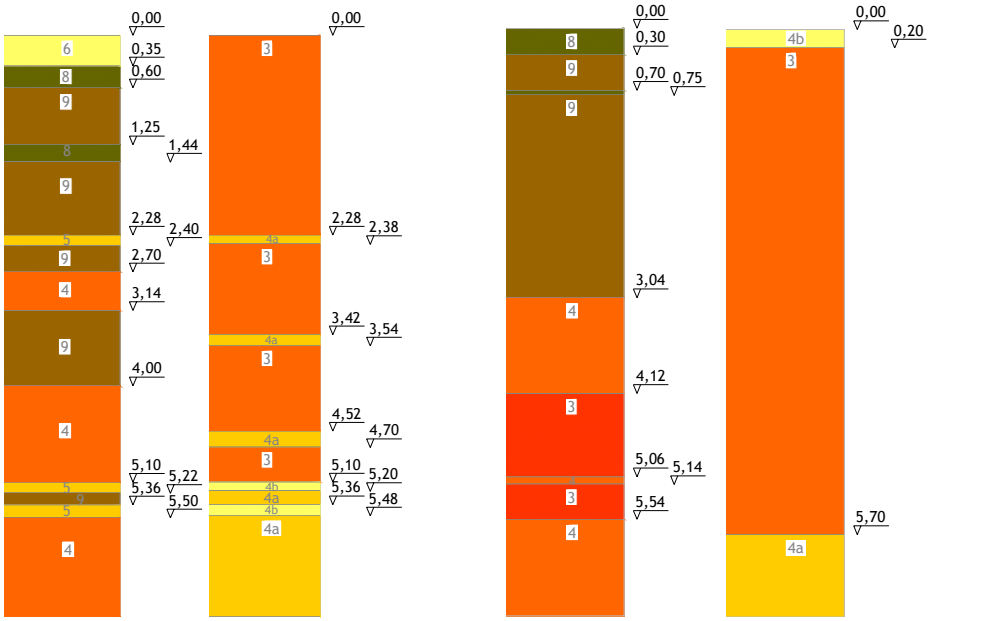
This general trend identifies this material as cemented and aged, with a grain size distribution from silty clays to clayey sands. Laboratory tests on the collected samples have confirmed it mainly as clayey silty sand, when the analysis is made by classical wet sieving and sedimentation with no use of chemical de-flocculation (Viana da Fonseca et al., 2004).

The results previously presented, namely those obtained by means of a laser beam analyser, confirm the dominant class trend of silty sands, with very low clay fraction. Another classification based on the CPTU results has been introduced by Eslami and Fellenius (1997), mainly directed to pile design but also useful for geotechnical purposes. In Figure 5.29, this chart is presented together with the results of this experimental site. After application of both classification proposals to the piezocone results in depth, Costa (2005) generated the following profiles, confirming that this profile is ruled by a typical heterogeneity of residual soils (Figure 5.30).



zone	soil behaviour type
1	very soft clays - sensitive soils
2	clays
3	silty clays - stiff clays
4a	sandy silt and silt
4b	fine sand and/or silty sand
5	sands - gravels

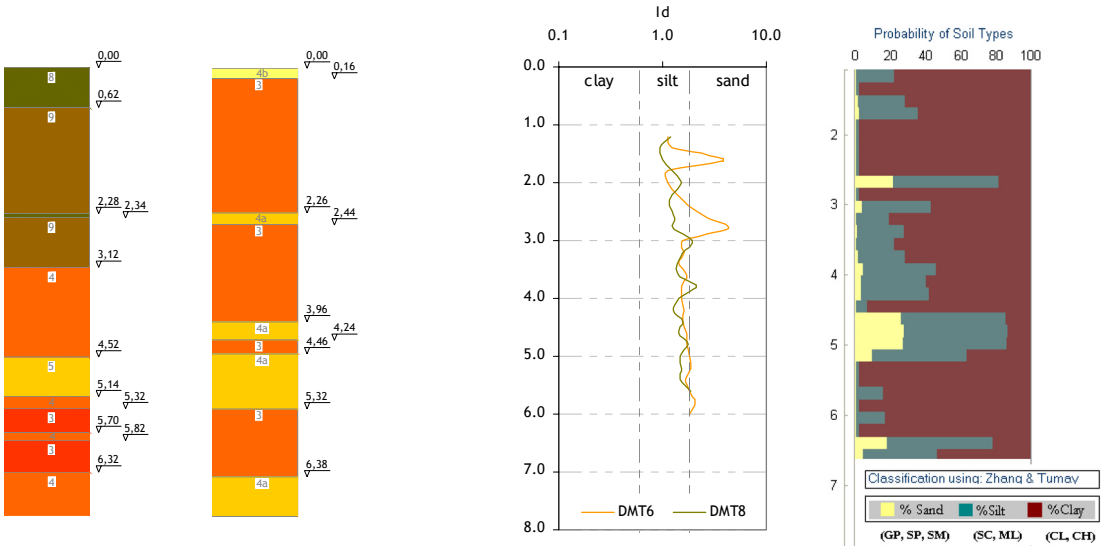
Figure 5.29 - Soil behaviour classification chart (after Eslami & Fellenius, 1997)



a) CPT2 b) CPT3

Figure 5.30 - Soil behaviour classification profiles (Costa, 2005), based on the proposals of Robertson (1990) and Eslami & Fellenius (1997)

The most surprising trend is the prevailing incidence of clayey matrices, which is not in accordance with the grain size distribution determined from laboratory tests. This diatomic behaviour was also explored by other classifications, such as those proposed by Marchetti (1980) and Zhang & Tumay (1999), and turned out to be also divergent in the percentage of fines. Figure 5.31 illustrates the discrepancies observed for one of the profiles - that of CPTU8, DMT6 and DMT8 (very close to each other).



Robertson (CPT) Eslami & Fellenius (CPT) Marchetti (DMT) Zhang & Tumay (CPTU)
Figure 5.31 - Profile identification from distinct tests based classifications

The use of these classification charts is clearly not very satisfactory, thus evidencing the specificity of these soils and the requirement of adapted versions of the classical proposals developed for transported soils, to residual profiles. This fact has been identified in other sites, namely by Mayne and Brown (2002) on Piedmont residual soils. In this case, soils are composed of fine sandy silts to silty fine sands, resulting from weathering of gneiss and schist. Classical classifications, such as the Unified Soils System, categorize these soils unsatisfactorily, since the definition of fine and coarse-grained groups are very sensitive to such an extensive grain size distribution. The authors refer to similar contradictions in identification indices, such as stress history ratios, when comparing the results from laboratory tests on undisturbed samples and those inferred from in situ test results, such as CPTU and DMT. These may be due to the high degree of non-linearity, typical of these cemented soils, distinct from those of corresponding transported soils (at similar density and water content). The authors conclude that great care should be taken in extrapolating empirical correlations to non-textbook geomaterials, being necessary to verify design parametrical findings, by performing regional inter-crossing of experimental data (with emphasis to the use of comparisons between test results on calibration chambers and prototypes of geotechnical structures).

As stated by Schnaid et al. (2004), bearing in mind that soil classification using CPTU data is indirect and relies on empirical charts developed for strata interpretation, u_2 measurements cannot always be considered useful to ensure a proper soil classification in unusual materials. Since classification charts should rely on at least two independent measurements, in the absence of pore pressure

measurements, the authors suggest that q_c should be compared with the small strain stiffness G_0. The G_0/q_c ratio provides a measure of the ratio of elastic stiffness to ultimate strength and may therefore be expected to increase with ageing and cementation, primarily because the effect of these on G_0 is stronger than on q_c. Other authors, such as Bellotti et al. (1989), Rix & Stokoe (1992), Lunne et al. (1997) and Fahey et al. (2003) have reported, in sands, some new insights by correlating G_0/q_c versus q_{c1}, where q_{c1} is defined as:

$$q_{c1} = \left(\frac{q_c}{p_a}\right)\sqrt{\frac{p_a}{\sigma'_v}} \qquad [5.2]$$

where p_a is the atmospheric pressure (note that the normalized parameter q_{c1} is dimensionless).

Once the profiles of q_c and G_0 are determined, these values can be directly used to evaluate the possible effects of stress history, degree of cementation and ageing for a given profile, as already recognised by Eslaamizaad & Robertson (1997). Data points are shown in Figure 5.32 for CPT tests carried out in residual soils (artificially cemented Monterey soils are also included), with specific emphasis to the values obtained for this experimental site (identified in the figure as Porto, Portugal). Since residual soils always exhibit a relatively bonded structure, the data fall outside and above the bands proposed by Eslaamizaad & Robertson (1997), indicated in the figure.

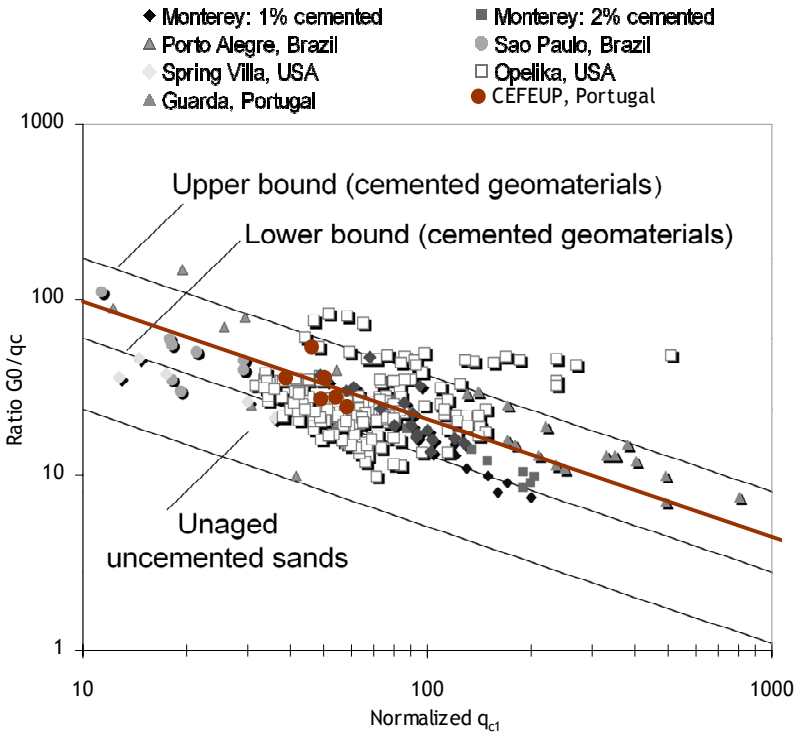


Figure 5.32 - Relationship between G_o and q_c for residual soils (after Schnaid et al., 2004)

The variation of G_0 with q_c observed in the range of sand deposits was expressed by upper and lower bounds. The upper bound for uncemented material can be assumed as a lower bound for cemented soils and a tentative new upper bound for cemented materials can be expressed as (Schnaid et al., 2004):

$$\left.\begin{array}{ll} G_0 = 800\sqrt[3]{q_c \sigma'_v p_a} & \text{upper bound : cemented} \\ G_0 = 280\sqrt[3]{q_c \sigma'_v p_a} & \text{lower bound : cemented} \\ & \text{upper bound : uncemented} \\ G_0 = 110\sqrt[3]{q_c \sigma'_v p_a} & \text{lower bound uncemented} \end{array}\right\} \quad [5.3]$$

The specific results of this experimental site (the thick line in the figure) may be expressed by:

$$G_0 = 450\sqrt[3]{q_c \sigma'_v p_a} \quad [5.4]$$

As for the CPT, Schnaid et al. (2004) point out that SPT N values can also be combined with seismic measurements of G_0 to assist in the assessment of the presence of bonding structure and its variation with depth. Such a combination is provided on Figure 5.33, which plots G_0/N_{60} against $(N_1)_{60}$ in residual soils, where $(N_1)_{60} = N_{60}(p_a/\sigma_{vo})^{0.5}$ and is analogous to q_{c1} on Figure 5.32. Values of FEUP experimental site are also included. The bond structure is seen to have a marked effect on the behaviour of residual soils, with normalised stiffness (G_0/N_{60}) values considerably higher than those observed in cohesionless materials. A guideline formulation to compute G_0 from SPT tests may be given by the equations:

$$\frac{(G_0/p_a)}{N_{60}} = \alpha N_{60}\sqrt{\frac{p_a}{\sigma'_{vo}}} \quad \text{or} \quad \frac{(G_0/p_a)}{N_{60}} = \alpha (N_1)_{60} \quad [5.5]$$

where α is a dimensionless number that depends on the level of cementation and age as well as on the soil compressibility and suction. The variation of G_0 with N can also be expressed by upper and lower boundaries, similarly to the cone penetration data (Schnaid et al., 2004):

$$\left.\begin{array}{ll} G_0 = 1200\sqrt[3]{N_{60} \sigma'_v p_a^2} & \text{upper bound : cemented} \\ G_0 = 450\sqrt[3]{N_{60} \sigma'_v p_a^2} & \text{lower bound : cemented} \\ & \text{upper bound : uncemented} \\ G_0 = 200\sqrt[3]{N_{60} \sigma'_v p_a^2} & \text{lower bound uncemented} \end{array}\right\} \quad [5.6]$$

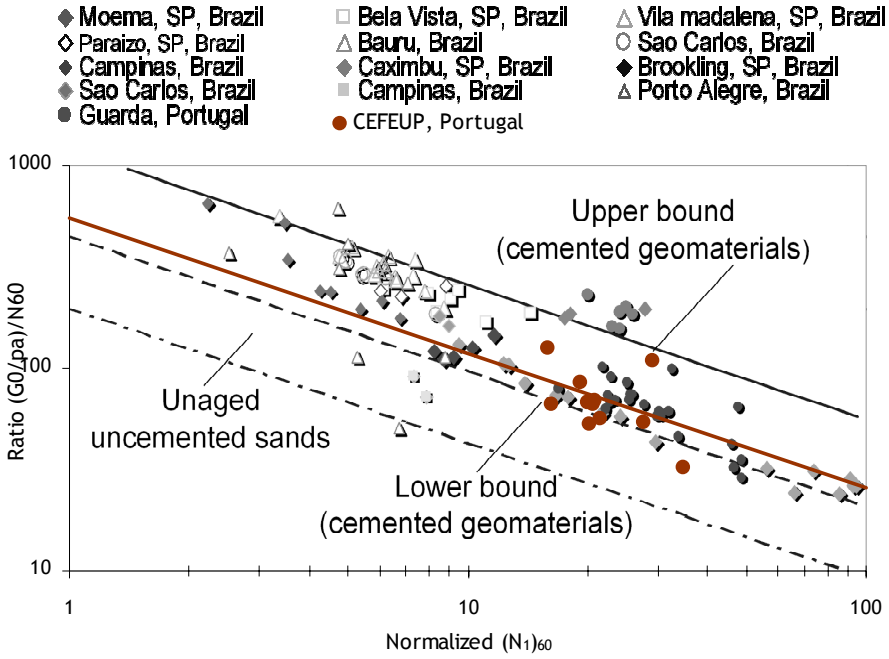


Figure 5.33 - Correlation between G_0 and N_{60} for residual soils (after Schnaid et al., 2004)

In this case, the results of the present campaign (the thick line in the figure) can be expressed by:

$$G_0 = 550\sqrt[3]{N_{60}\sigma'_v p_a^2} \qquad [5.7]$$

It can be concluded that a bonded/cemented structure produces G_0/q_c and G_0/N_{60} ratios that are systematically higher than those measured in cohesionless soils. These ratios therefore provide a useful means of assisting site characterization.

5.3.4.3. General physical properties

A vast amount of undisturbed samples were carefully taken from the experimental site, in boreholes at specific depths, using high quality piston samplers, as well as block samples, which are described and analysed in detail in the following chapters. Figure 5.34 shows the particle size distribution of the tested specimens obtained from the undisturbed samples on borehole S2, and a typical grain size distribution fuse for Porto silty sand. According to the identification tests results, and with the results previously presented, the main composition of this saprolitic soil is a fine to medium grade and low plasticity material, mainly classified as silty sand (SM). The most representative physical properties for a number of samples are presented over depth in Figure 5.35.

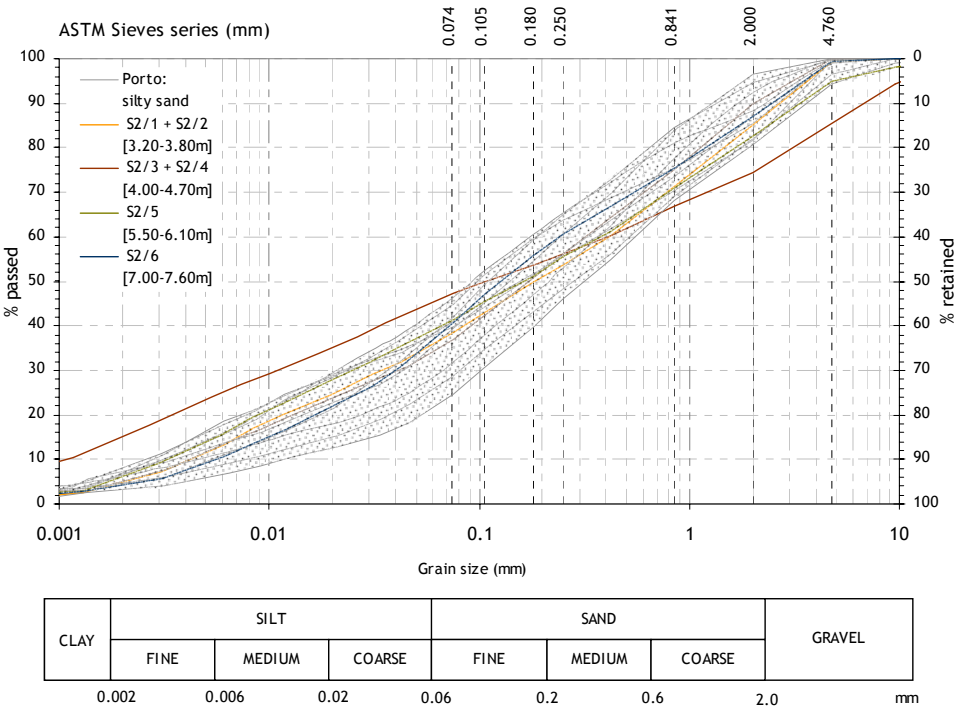


Figure 5.34 - Grain size distribution curves from ES2, compared with Porto silty sand

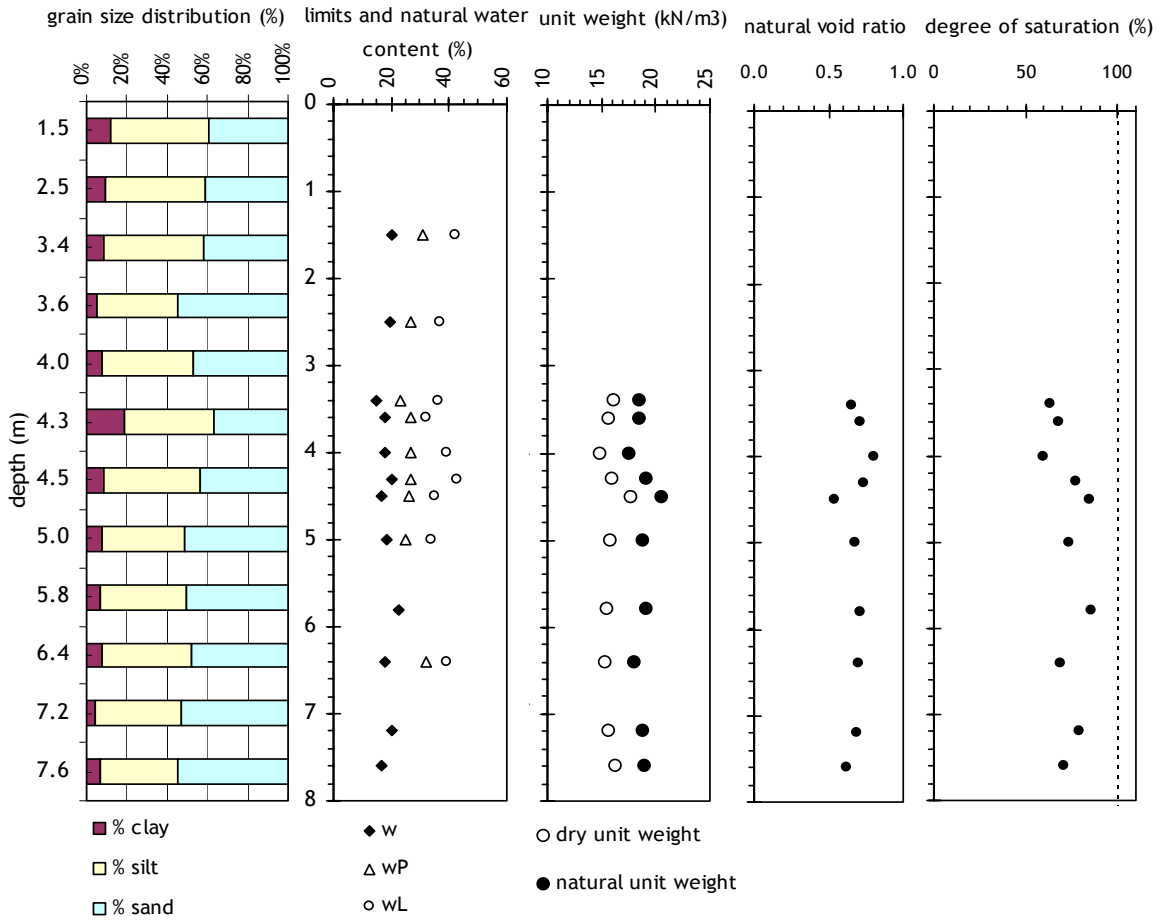


Figure 5.35 - Soil index properties in depth from a number of samples

5.3.4.4. Strength correlations

Some correlations have been derived from the results database, and described elsewhere (Viana da Fonseca et al., 2004, Carvalho et al., 2004). Values of $(N_1)_{60}$, taken from the SPT tests, allowed to derive the angle of shearing resistance from Decourt's (1989) proposal, ranging from 35 ° to 41 °, with an average of 38 °. This value coincides with those reported in similar regional soils, namely for Porto silty sand (Viana da Fonseca, 2003).

The classification chart by Robertson (1990) presented in Figure 5.28 shows some dispersion, but the general trend identifies this material as cemented and aged, with a grain size distribution from silty clays to clayey sands. Laboratory tests over collected samples have confirmed it mainly as clayey silty sand (Viana da Fonseca et al., 2004). The relation between q_c from CPT and σ'_{v0} is presented in Figure 5.36, which integrates Robertson and Campanella's (1983) curves for the estimation of the angle of shearing resistance. The CPT results reveal a moderate increase of q_c in depth. Robertson and Campanella's proposal tends to lead to higher values of ϕ', especially at lower depths, than those obtained from triaxial tests, since the effective cohesive component is not considered.

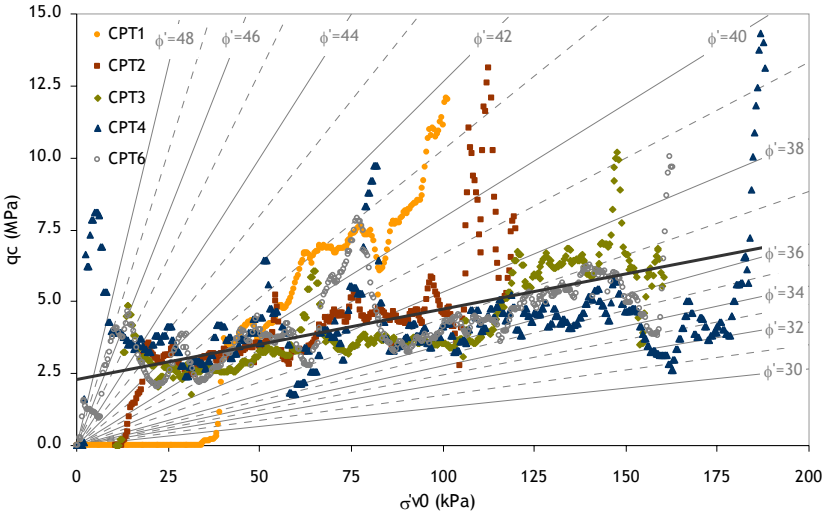


Figure 5.36 - Relation between qc values, in situ at rest effective stress, σ'_{v0}, and the angle of shearing resistance, ϕ' (adapted from Robertson and Campanella, 1983)

This reflects the simultaneous sensitivity of q_c towards frictional and cohesive components. In the present case, the CPT results are rather constant in depth, crossing a wide range of friction angles (35-42 °) with more incidence at 37 °, which

is much lower than the one obtained in the laboratory tests. This can be a consequence of the behaviour of a cohesive-frictional soil, where the lower confinement levels are dominated by the cohesive component, while the higher are mostly governed by friction.

The usefulness of correlating results from SPT and CPT tests, led to the evaluation of q_c/N_{60} ratio and its dependence on the mean grain size, D_{50} (Robertson and Campanella, 1983). For the case of the experimental site, this ratio varied from 0.17 to 0.36 (D_{50} = 0.15 mm). Different parent rocks generally produce different correlations for the same particle size distribution, due to intrinsic heterogeneity (Danzinger et al., 1998).

The Brazilian data show a general trend of lower values for the relation q_c/N_{60} with D_{50} than that expressed by Robertson & Campanella's (1983) average line. Data from this experimental site are in close agreement with those results, but somewhat contradictory with Porto silty sand data, as illustrated in Figure 33. This discrepancy is probably a consequence of the more intensive clayey content of the soil in the present experimental site (see Figure 5.28 and Figure 5.30).

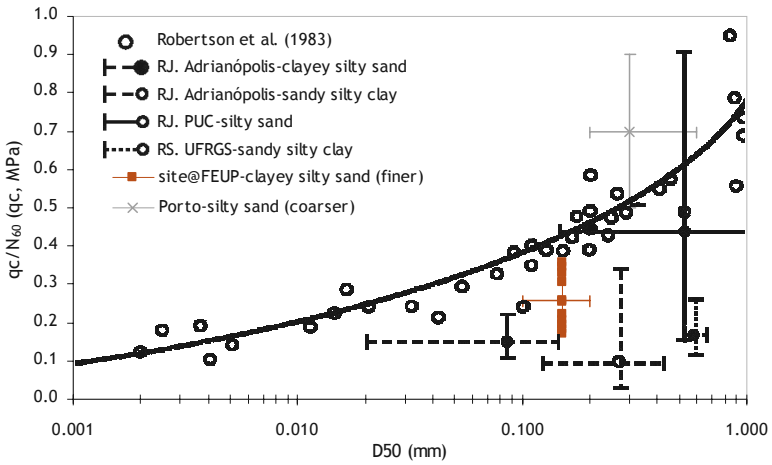


Figure 5.37 - Ranges of q_c/N versus D_{50} on Brazilian residual soils, compared with the experimental site results (based on Danziger et al., 1998)

Other reported values of the ratio q_c/N_{SPT} for different residual soils are indicated in Table 5.7, along with results from this experimental site. The percentage of fines has a clear influence in the obtained values.

Table 5.7 -Estimated values of q_c/N_{SPT} for different residual soils

Residual soil (and reference)	q_c / N_{SPT} [q_c, MPa]
Brazilian residual soils: Sandroni (1985)	0.30 - 0.78
Nigerian saprolitic and lateritic tropical soils: Ajayi and Balogum (1988)	0.40
Singaporean saprolitic granite soils: Chang (1988)	0.20
Porto silty sand (coarser): Viana da Fonseca (1996, 2003)	0.50-0.90
ES2: CEFEUP experimental site	0.17-0.36

DMT and PMT results are not discussed here in detail, but preliminary analyses of these tests results have also enabled the soil identification. As previously stated, the DMT I_d graph presented in Figure 5.26, classifies it as a silty sand to silt, which corroborates the results of the identification tests but which is not in accordance with the classification based on charts with input on penetration tests (CPT, CPTU).

It should be emphasized that the dilatometer test may be a very useful frame to evaluate the cohesive-frictional nature of these residual soils (Cruz et al., 2004). For this approach, the angle of shear resistance is determined from obtained results of DMT and CPTU tests by means of the correlations of Marchetti (1997) and Robertson and Campanella (1983). For the regional soils, a significant data has been collected and analysed, and, in general, the values of the parameter range from 35 ° to 45 °, which are globally higher than those determined under controlled conditions in triaxial tests on undisturbed samples, if the cohesive fraction is not considered. Taking into account the low influence of sampling on the evaluation of the angle of shear resistance, the registered difference on the value of ϕ' is attributed to the effects of the cemented structure on q_c and K_D parameters.

The methodology for the derivation of this cohesive component is described in Cruz et al. (1997) in a fairly simple way. Assuming that K_D reflects the overall strength of soil, it is expected that both c' and ϕ' have influence on this parameter. Then, if ϕ' deduced from triaxial testing is assumed, the corresponding K_D may be back-calculated. The difference between the two values of K_D (measured and back-calculated) will reveal the effective cohesive intercept. From available data, the cohesion obtained from DMT, c'_{DMT}, ranged from 5 to 15 kPa, which were confirmed by triaxial testing. A summary of the strength parameters, derived from in situ and laboratory tests results is presented in the Table 5.8.

Table 5.8 - Strength parameters from in situ and laboratory tests

TESTS		ϕ' [°]	c' [kPa]
In situ	SPT	38	n/a
	CPT	37	n/a
	DMT	35-38	6-10
Laboratory	TX compression	45.8	4.5
	TX extension	28	12

5.4. Summary and conclusions

In this chapter, the main features of residual soils, in general, and of the residual soil from Porto granite, in particular, were presented in detail. Two experimental sites on this geomaterial were selected for this research and the main results of the in situ characterisation were systematised in this chapter.

It was highlighted that residual soils are a product of a weathering process on a rock mass, which are usually dominated by strong heterogeneity and by natural fabric and structure (macro and micro). Structure, and especially the effect of interparticle bonding, has a significant influence in the interpretation of test data, especially from in situ tests. These singularities were addressed in this chapter, with evidence of its influence in important geotechnical design parameters such as at rest stress state, stiffness, non-linearity, strength, and permeability.

6.

Sampling and Laboratory Testing Programme

6.1. Introduction

In this chapter, the sampling programme and the subsequent laboratory testing programme will be presented with some detail. Firstly, the most common sampling methods will be introduced, from block to undisturbed tube sampling, and to disturbed soil sampling. A description of the sampling methods used in this research, for both experimental sites, will be provided. The use of different sampling methods, namely different tube samplers, enables to obtain samples with distinct qualities, that is, with different disturbances induced by the sampling processes.

In an attempt to identify the most and the least suited tube samplers for this particular soil, a comparison was made based on the shear wave velocities measured in the field and in the laboratory, for samples recovered from the first experimental site. Preliminary results obtained by Ferreira (2003) suggested that a sharp cutting edge and a large diameter were important factors towards high quality samples in this material, from which one sampler was selected for high-quality sampling in the second experimental site.

Following the description of the sampling methods and programme, the preparation procedures of natural and reconstituted samples will be introduced and discussed, in relation to its specific testing apparatus and conditions. Natural samples of this residual soil were tested in the standard triaxial, stress-path, resonant-column, true triaxial and cubical cell apparatuses, each of these requiring a different procedure for sample preparation. On the other hand, reconstituted samples were produced in the laboratory at the natural water content, high water content (w=30%) and at dry conditions. These were tested in the standard triaxial and the true triaxial apparatuses, as described below.

Finally, a brief description of the set-up and testing procedures will be presented, including a list of the main laboratory tests carried out in undisturbed and reconstituted samples from both experimental sites.

6.2. Sampling programme

6.2.1. Introduction to sampling methods

Soil disturbance due to sampling operations are of major concern to the geotechnical engineer attempting to estimate in situ properties of foundation soils by means of laboratory tests (Baligh, 1985). Over the years, considerable improvements have been made towards devising "good" sampling practices, based on engineering judgement, experimental observations and/or analytical studies.

The sampling processes used for retrieving soil specimens from the experimental sites can be divided in three types, according to the sampling methods which are directly related with the quality of the obtained samples. These are:

a) block samples
b) "undisturbed" tube samples
c) disturbed soil samples

A soil sample is considered intact or undisturbed when the soil structure and mechanical properties are kept as close as possible to those of the soil in the field.

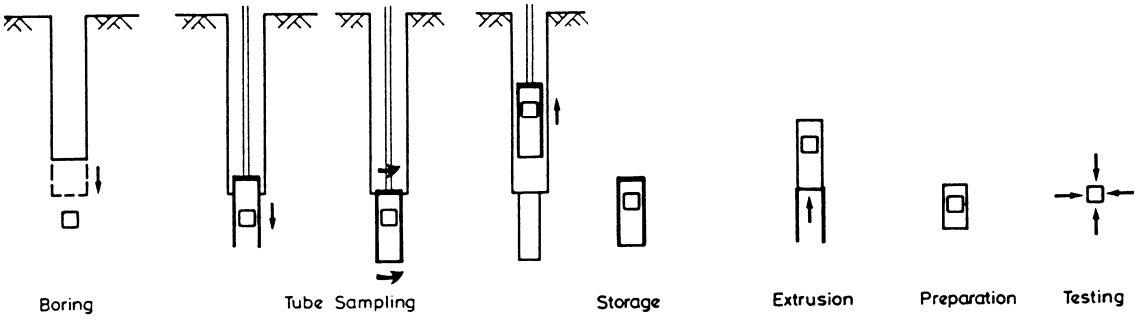


Figure 6.1 - Stages in tube sampling and soil specimen preparation for laboratory testing (after Hight, 2000)

There are a number of undisturbed tube sampling techniques in current use in Portugal, usually divided in driven samplers and rotary samplers. A few of these techniques were selected for borehole sampling in the first experimental site, from which their sampling performance was assessed. Based on the quality of the samples of the various samplers considered, one was selected for use in the second experimental site. An overview of all of the sampling techniques applied at both experimental sites is presented below, including block sampling, undisturbed tube sampling and disturbed soil sampling.

6.2.2. Block sampling

With the purpose of obtaining high quality soil samples, as undisturbed as possible, a number of block samples were collected at both experimental sites. The block sampling process can be divided essentially into the following four stages (JGS, 1995):

- rough carving of the sample: opening of the area surrounding the intended sample;
- trimming of the sample: performed with great care, in order to obtain the intended sample size, well-aligned for a perfect fit in the container;
- sealing of the sample: insertion of the container (usually a wooden box) covered with plastic film for moisture retention;
- separation from the ground: the block is cut on the bottom by means of a shovel or a long blade; the block is slowly and carefully tilted to reveal the bottom surface, which is immediately levelled, sealed and covered with the box cover.

This procedure is summarised in Figure 6.2, using diagrams adapted from the Japanese Standard No. 1231 (JGS, 1995). Photographs of the work in ES1 at

CICCOPN are presented to complement each corresponding sampling stage. At this experimental site, taking into account the position of the water table, the maximum depth for collecting block samples was about 2 meters, at which three cubical blocks of circa 400 mm were retrieved.

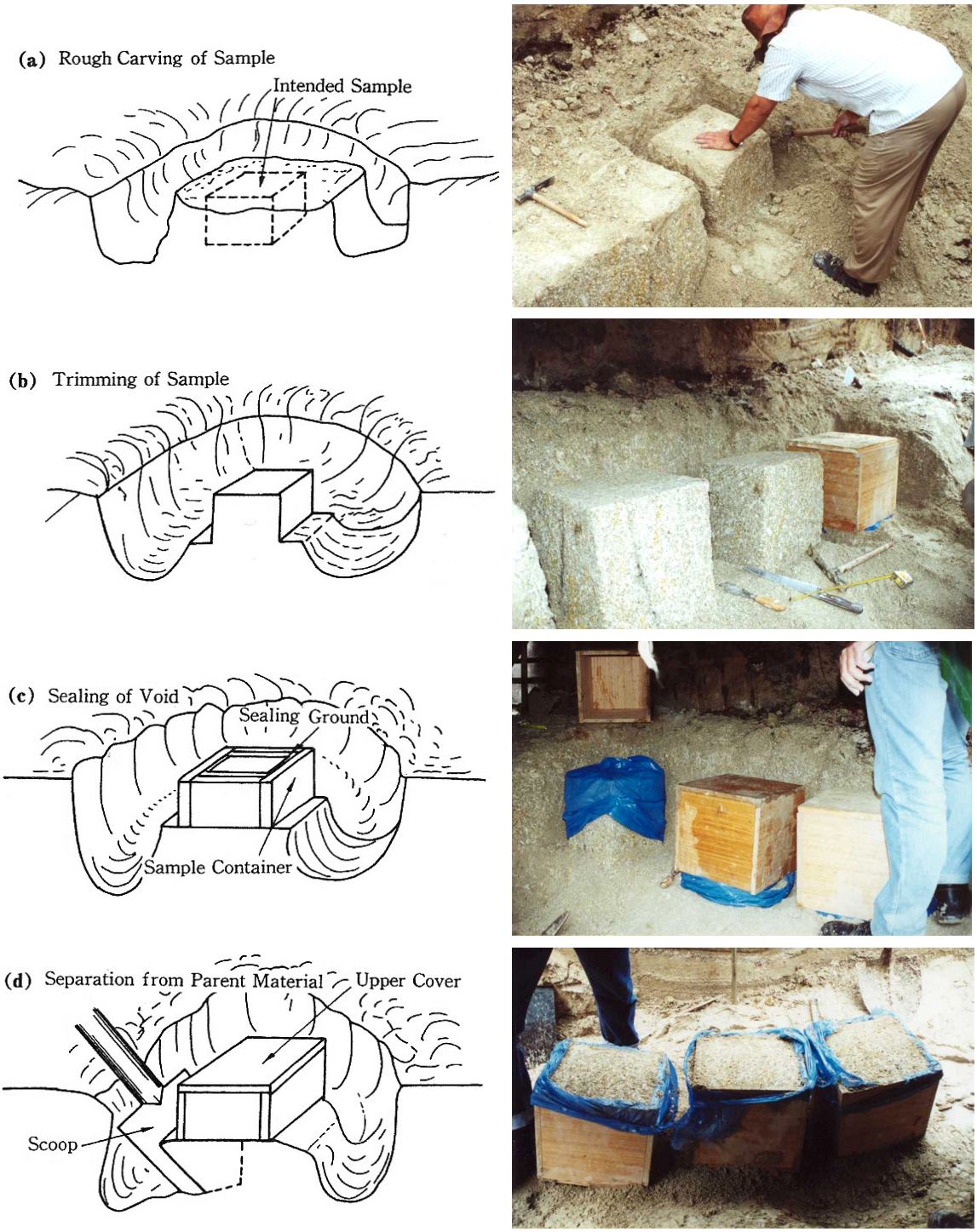


Figure 6.2 - Illustrative diagrams of the block sampling stages (after JGS, 1995) and photographs of the work at experimental site ES1 (after Ferreira, 2003)

On the other hand, at the second experimental site ES2 at CEFEUP, the position of the water table around 11 m was not an issue for block sampling. Taking the opportunity provided by the excavation of the experimental site as a result of the end of the pile prediction event (Viana da Fonseca et al. 2004a, 2004b, 2005; Santos et al., 2005), a block sampling campaign was programmed. Consequently, six block samples were collected, two at each of the three different depths: 1.65 m, 2.75 m and 4.25 m, measured from the centre of the block to the ground surface. Photographs of this work are presented below in Figure 6.3. Evidence of the excavation works for the removal of the piles is clearly visible in Figure 6.3b.

a)



b)



c)



Figure 6.3 - Photographs of the block sampling work at experimental site ES2 at different depths: a) B1 and B2 at 1.65 m; b) B3 and B4 at 2.75 m; c) B5 and B6 at 4.25 m

The location of the blocks was selected, considering a reasonable distance to the piles to avoid any disturbances produced during the construction of the piles. During these sampling operations, some material was collected for determination of the natural in situ water content. Additionally, a considerable volume of soil was collected in bags, sealed to retain its natural moisture and kept at the humid chamber, providing ample material for experimental calibration tests as well as for reconstituted specimen testing.

A second block sampling campaign was later carried out on a different location to provide more intact material for further research (Dourado, 2011).

6.2.3. Tube sampling

6.2.3.1. Overview

The sampling surveys were performed in collaboration with private engineering contractors (Mota & Ca., later Mota-Engil and CICCOPN), which were responsible for boring and extracting soil samples using the available samplers, according to their own standard procedures. The selection of the samplers used in the sites was made considering a few fundamental aspects, namely:

- the characteristics of this soil;
- some variety of geometric properties of the samplers, such as the cutting edge, the sampler driving method, the existence or not of inside clearance, the use of liner and its type;
- availability of equipment;
- level of applicability in practice;
- expected sample quality offered by the different samplers.

Considering the maximum particle size of this soil, the recommended diameter for representative samples is of about 70 mm and, thus, all samplers used have an internal diameter slightly higher than 70 mm.

As mentioned earlier in the previous chapter, the first experimental site (ES1: CICCOPN) served as ground for the assessment of the sampling quality of a variety of tools and techniques, with the purpose of selecting the most suited sampler for this soil to be used in the second, more thoroughly studied, experimental site (ES2:

CEFEUP). For the assessment of the sampling quality of the samplers, shear wave velocities measured in situ and in the collected samples at the in situ stress were compared, as will be presented and discussed in detail in Chapter 8. Preliminary results were already reported (Ferreira, 2003; Ferreira et al., 2006).

A photograph of the sampling works in ES1 (on a rainy day) is presented in Figure 6.4, including a diagram with the layout of the boreholes. A triangular arrangement with an even spacing of 4 m was selected, to facilitate seismic cross-hole testing.



a) b)

Figure 6.4 - ES1 at CICCOPN: a) view of the experimental site during sampling; b) layout of the boreholes

At ES1, a different sampler was used in each borehole and soil samples were collected at the depths of 2, 4 and 6 m. During these sampling works, the water level remained stable, approximately 3 m deep. A list of the samplers used and their characteristics is presented in Table 6.1, which are further described in the sections below.

Table 6.1 - Tube sampler used in each borehole

#	Sampler	Cutting edge [°]	Internal diameter [mm]	Liner	Sampling
S1	GMPV	30	72.0	grey PVC	dynamic
S2	ST85	5-6	75.0	PVC (often transparent)	dynamic
S3	NT81	5-7	74.0	coated steel (not stainless)	dynamic
S4	Mazier	*	74.0	blue PVC	rotary
S5	Osterberg	30	n/a	none	stationary
S6	Shelby	30	77.5	none	stationary

* sharp cutting edge ahead of the drill bit

The preliminary results obtained by Ferreira (2003) indicated considerable differences between the sampling quality of the samples recovered by each of these samplers, by the comparison of in situ and laboratory V_S. Ferreira et al (2006) concluded that the least disturbed samples had been recovered by the NT81 sampler. As a result, this sampler was adopted for undisturbed tube sampling in ES2 at CEFEUP.

6.2.3.2. GMPV sampler

The GMPV sampler is a thick-walled open-drive sampler, manufactured by the Spanish company TECSO, of about 600 mm of length, external diameter of 90 mm and internal diameter of 72 mm, and a cutting edge of 30°. In Figure 6.5 are presented photographs taken during the sampling process at ES1, together with a schematic diagram of the sampler.



a) b)

Figure 6.5 - GMPV thick-walled sampler: a) photographs of the sampling process; b) schematic diagram

6.2.3.3. ST85 sampler

The ST85 is also a thick-walled sampler, and is manufactured by TECSO. It has 600 mm of length, an internal diameter of 75 mm and an internal transparent PVC liner. The particularity of this sampler resides in its cutting shoe, which has a sharp cutting edge of 5 to 6°. This detail, which is a clear contrast from the traditional cutting shoe angles around 30°, represents an important quality step towards high quality tube samples (Ferreira, 2003).

Photographs of the sampling works using this sampler in the first experimental site are provided in Figure 6.6.



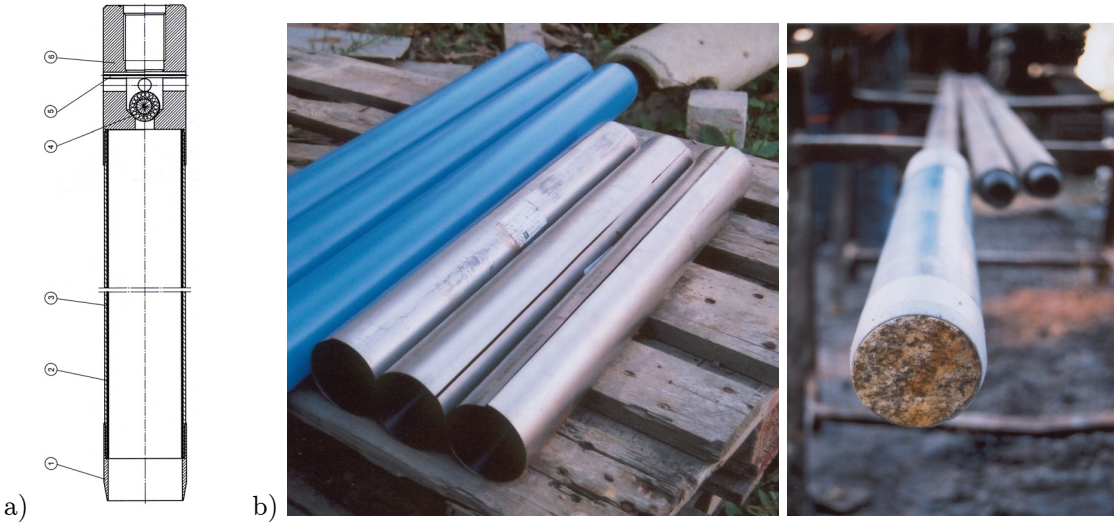
Figure 6.6 - Soil sampling with the ST85 sampler

6.2.3.4. NT81 sampler

This sampler was developed more recently by TECSO (Gomez and Solas, 2001), based on the design of the ST85, previously presented. The design changes refer to the need to comply with a legal requirement (Spanish standard NTE-CEG-75), which imposes an area ratio lower than 25%, for thick-walled samplers. It should be noted that thin-wall sampling devices are usually taken to be those with an area ratio of less than 20%, and a suitable cutting shoe taper, while thick-wall samplers are taken to have an area ratio greater than 20% (Clayton et al., 1995).

For this purpose, minor modifications were made in the ST85, which are mainly related with the change of liner material. In the NT81, the liner is thinner and usually made of steel, although thin PVC liners can also be used. To ease extraction after sampling, the steel liner is pre-cut longitudinally. The obtained sample diameter is of 74 mm. Figure 6.7 shows a simplified scheme of this sampler and its application during the sampling stage at ES1.

As previously mentioned, the performance of this sampler was considered the most suitable for this residual soil, based on the preliminary comparative analysis of field and laboratory shear velocities, reported in Ferreira (2003) and Ferreira et al (2006). The results obtained for samples recovered with this sampler were lower but comparable to those of block samples. For this reason, this sampler was selected for the undisturbed tube sampling works at the second experimental site, ES2 at CEFEUP, as shown in Figure 6.8.



a) b)

Figure 6.7 - NT 81 sampler: a) schematic diagram; b) photographs of the steel liner and of the sampler during sampling stage in ES1 at CICCOPN



Figure 6.8 - Photographs of tube sampling works in ES2 at CEFEUP using NT 81 sampler: sampling, immediate extraction of the liner and cling film wrapping

6.2.3.5. Mazier sampler

The Mazier sampler is a triple-tube swivel type retractor core barrel, whose effectiveness relies on the fact that the amount of inner barrel protrusion is controlled by a spring placed in the upper part of the device. The cutting shoe and connected inner barrel projects ahead of the bit when drilling in soil and retracts when the drilling pressure increases in harder materials (Ng and Leung, 2007). The cutting shoe on the bottom of the inner barrel is substantial, making it much less easily damaged than a thin-walled seamless tube, but introducing the problems of disturbance when the high area ratio shoe travels ahead of the core-bit (Clayton et al., 1995). This sampler, manufactured by the French company Seditech, has attracted considerable interest for sampling, due to its dual capability of static boring, in an analogy with the Laval sampler development (La Rochelle et al., 1981), and its flexibility in driving both soft and harder soils. A schematic of the details of this sampler and its operation in different soil conditions are presented in Figure 6.9.

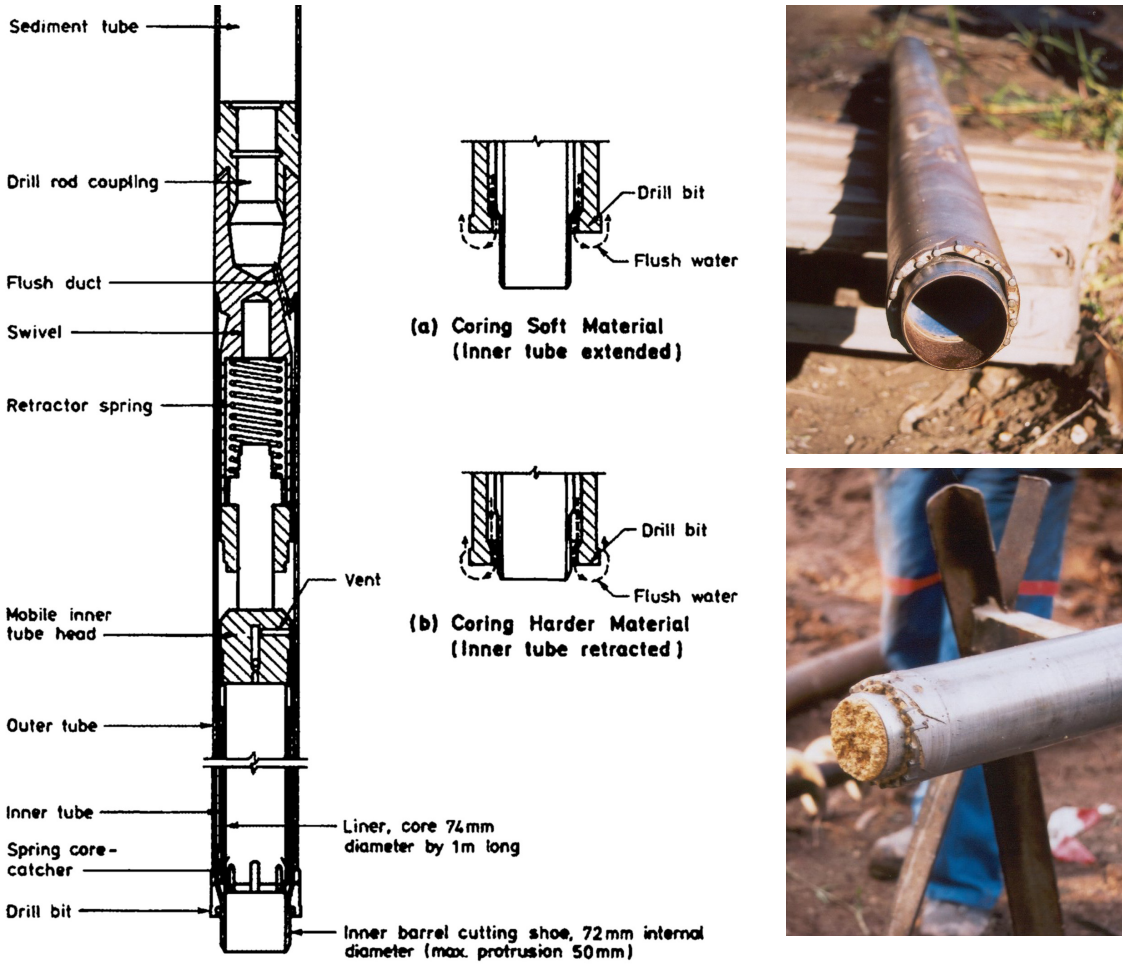


Figure 6.9 - Schematic details and principle of operation of the Mazier sampler (GCO, 1987); photographs of the sampling process with this sampler in ES1

The typical internal diameters available for this sampler range from 61 to 108.5 mm. In this sampling programme, a Mazier sampler with an internal diameter of 74 mm was used, as shown in Figure 6.9. Long samples can be retrieved, up to 1000 mm.

6.2.3.6. Osterberg sampler

The original Osterberg thin-walled hydraulic piston sampler was available in 127mm (6% area ratio) and 72mm (6.3% area ratio) diameter forms. It had vents in the sample tube to allow vacuum relief below the tube when pulled from the soil, and the sampler could be rotated before pulling, in order to shear the soil at the base of the tube. This thin-wall fixed-piston sampler was designed to sample soft soils. Very good quality clay samples have been obtained, comparable to block samples (Raymond, 1977, cited by Clayton et al., 1995). An illustration of this sampler is provided in Figure 6.10.

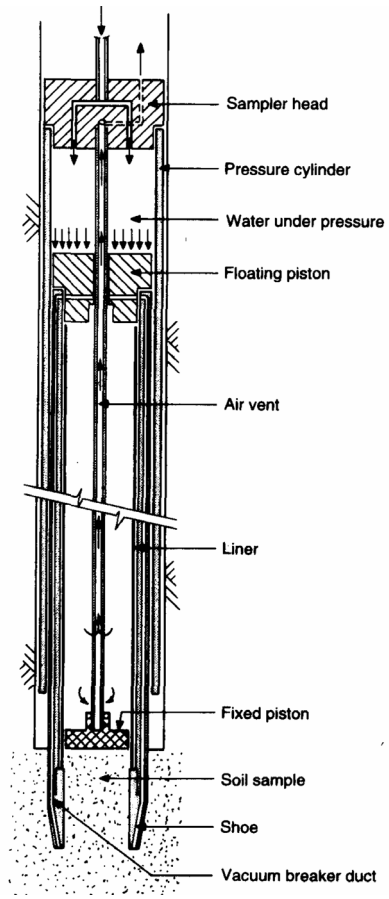
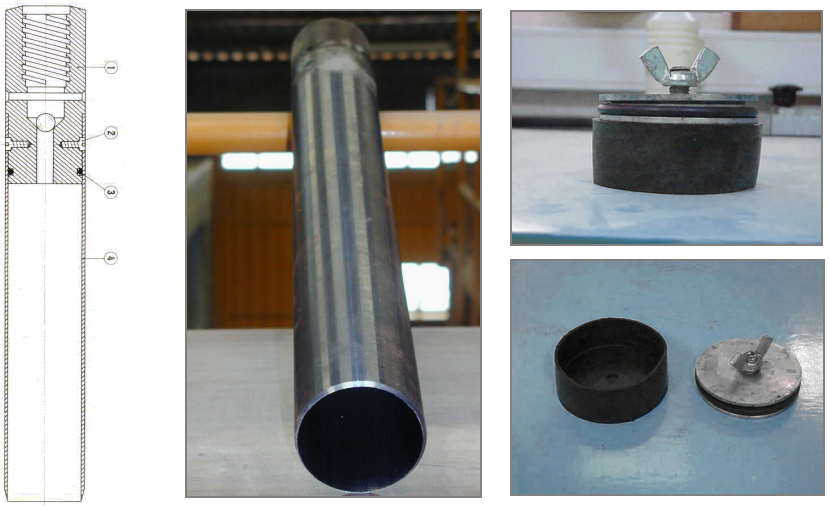


Figure 6.10 - Osterberg composite hydraulic fixed piston sampler (Osterberg, 1973, in Clayton et al, 1995).

Despite being designed to sample soft soils, its application was considered for this residual soil. The sampler was not capable of recovering any material, thus sampling this soil with the Osterberg sampler proved unsuccessful, most likely due to its coarse grained nature. This unfruitful exercise served as confirmation of the inaptitude of this sampler to operate in coarse granular geomaterials.

6.2.3.7. Shelby sampler

The thin-walled open-drive Shelby sampler was introduced in the USA in the late 1930s (Terzaghi, 1939; Hvorslev, 1949, cited by Clayton et al., 1995) and it is still commonly used in Portugal. These sampling tubes are made of steel, seamless with no inside clearance, with 500 mm of length, 77.5 mm of internal diameter and about 3 mm of wall thickness. The cutting edge angle is of 30°. The tube sealing system comprises a rubber lid, slightly wider than the tube at the base, and a double steel tip with an o-ring at the top and a lower diameter than the internal diameter of the sampler, in order to ensure a good fit with the top end of the sample.



a) b)

Figure 6.11 - Shelby thin-walled open-drive sampler: a) schematic; b) photographs of the sampler and the insulating lids

Since this is also a driven sampler, it is best suited to sampling materials with no or few coarse elements, and consequently it is less suitable for sampling residual soils. Using higher diameters may be an interesting option, but due to the smoothness of the inner walls of the sampler, sample recovery may be compromised by the risk of the sample falling out.

For the removal of the sample from the tube and considering its length and material (steel), it is necessary to use an extruder. This piece of equipment compresses the soil sample from one end of the sampling tube, pushing the sample out until it slides along the tube. This procedure involves some degree of disturbance to the samples, especially for the case of lightly bonded and structured materials, such as these residual soils.

6.2.4. Other sampling methods

Continuous borehole sampling, often combined with SPT, was also used in a few boreholes, for an immediate identification of the site characteristics and composition of the soil. Highly disturbed samples were obtained, which were still suitable for physical identification tests, such as the determination of water content and grain size distributions (Figure 6.12).



Figure 6.12 - CEFEUP site: continuous borehole sampling

As previously mentioned, disturbed soil was also collected in plastic bags and kept at its natural moisture in the humid chamber, thus providing material for tests in reconstituted conditions.

6.3. Sample preparation

6.3.1. Natural samples

The natural samples used in this research were either taken with any of the tube samplers described in the previous section or using the block sampling technique. The tube samples were used for tests in the standard triaxial, stress-path and resonant-column apparatuses. The block samples were trimmed in different shapes and sizes in order to produce cubical specimens for testing in the true triaxial and the cubical cell apparatuses, as well as cylindrical specimens for the standard triaxial, stress-path and resonant-column apparatuses. A few oedometer samples were also prepared, though

its preparation will not be directly addressed. In what follows, brief descriptions of the sample preparation processes are presented.

6.3.1.1. Standard triaxial and stress-path natural samples

Most of the natural soil samples tested in the standard triaxial (or the stress-path) apparatus were taken from undisturbed tube samplers. As previously detailed in the description of the sampling methods, most of these samplers include a liner, in which the sample is kept until the time of testing.

After inspection of the condition of the tube, the first step of tube sample preparation consists in selecting the number of samples to be prepared from each tube sample. For the case of transparent liners, this step is particularly simple, since the soil can be directly observed and any defects can be avoided. For other liners, the tube is cut along its section, about 50 mm above the end of the sample and the soil condition can then be observed. For both cases, the remaining material is cut to the size of the test specimens (140 or 200 mm in height). It should be noted that the tube samples are often not completely filled with undisturbed soil; hence the length of the tube does not correspond to the length of available material. Usually no more than two samples can be obtained from the same tube.

Each tube sample (with the correct height) needs to be extracted from the liner prior to testing. In order to minimise the disturbance of the sample during preparation, the extraction of the sample from the liner is critical. Since extrusion involves some compression of the sample to overcome wall friction, a more suitable method was devised, as shown in Figure 6.13. This method consists in cutting the liner (with a thickness of about 1.5 to 2.5 mm, depending on the sampler) into eight identical parts. This operation was carried out with great care to avoid cutting the soil in the process. When all parts are separated, each of them is removed by vertically sliding towards the bottom of the sample, so that any soil stuck to the liner is released, with minimal movement.

a)



b)

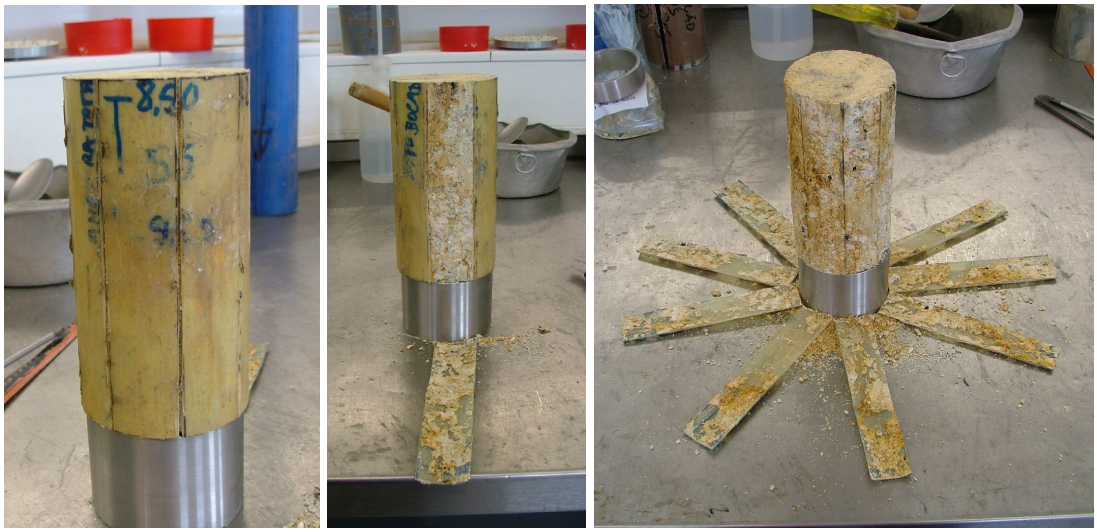


Figure 6.13 - Preparation of undisturbed tube samples: a) cutting the PVC liner into eight parts using a rotary disc; b) removing the liner by vertically sliding each part

There were obviously some cases where the sample preparation method was problematic, mainly due to the presence of large grains of quartz and mica within the sample, as illustrated in Figure 6.14.



Figure 6.14 - Example of a coarse-grained natural sample, evidencing problematic preparation

For the block samples, the preparation of these cylindrical samples consisted in trimming this shape with the use of a guiding mould, typically a PVC liner with a vertical cut to facilitate immediate extraction after trimming.



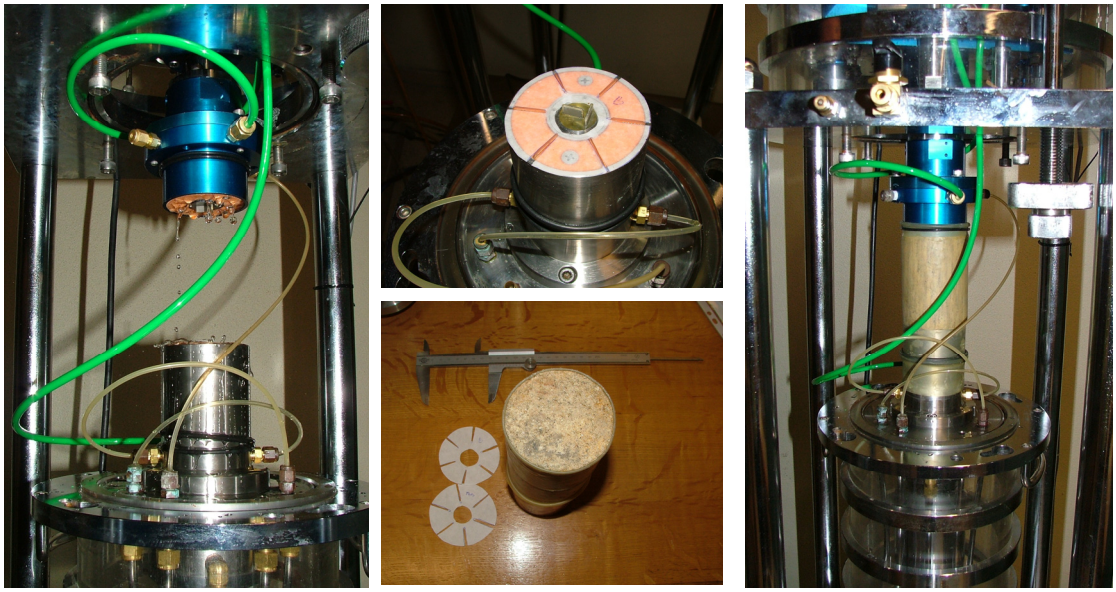
Figure 6.15 - Trimming cylindrical 70 and 100 mm diameter samples for standard triaxial testing from block samples B3 and B5.

Following either sample preparation procedures, a thin rubber membrane was stretched and placed around the sample for installation in the testing apparatus. Since most of these samples were tested using top and bottom BE, the position of these transducers was defined. The BE slots were marked, to ensure proper contact and to remove any grains that could compromise coupling or even break the transducers.

6.3.1.2. Resonant-column natural samples

The specimens for resonant-column testing were prepared in a similar manner to triaxial specimens, with the only difference being the aspect ratio. In this apparatus, the dimensions of the soil specimens are required to be 70 x 100 mm, due to the specific characteristics of this equipment.

In order to ensure adequate coupling with the blades of the top and bottom platens, slots were carved in the sample prior to its installation in the apparatus.



a) b) c)

Figure 6.16 - Preparation of a resonant-column test: a) saturation of the porous stones; b) preparation of the filter paper disc with the slots for the column blades; c) installation

6.3.1.3. True triaxial natural samples

The natural soil specimens using for tests in the true triaxial apparatus at FEUP were necessarily trimmed from the block samples, due to the large dimensions required for the samples in this apparatus. The clearest way of exposing the process of intact sample preparation and installation is by means of a sequence of photographs, as shown in Figure 6.17. The process consists of trimming the original block sample to roughly the same dimensions as the true triaxial frame, that is, about 250 x 250 x 250 mm. The area to be tested in the true triaxial is first outlined and the surplus material of the block is carved away to provide intact cylindrical specimens for standard triaxial, stress-path, resonant-column or oedometer tests, as previously described. Occasionally, cubical 100 x 100 x 100 mm specimens for the cubical cell can also be trimmed.

After trimming all other specimens, the large cubical specimen for true triaxial testing is prepared to the desired dimensions. The frame of the cube serves as a guide for the trimming process, exercising caution so as not to disturb or induce stresses in the sample in this process. When the sample fits into the frame, it is pushed over the sample and two of the side platens are mounted around it, as well as the bottom platen, which is at this stage facing upwards. The sample is then rotated through 180 ° and placed on its support base, so that the bottom platen is indeed at the

bottom of the specimen, facing downwards. This rotation reveals the uncarved top of the specimen that needs to be levelled. Finally, all the remaining platens are assembled around the sample.



Figure 6.17 - Sequence of preparation of a block sample [B2] in the true triaxial apparatus

Although not evident in the photographs in Figure 6.17, a square rubber membrane is affixed to the inside of each platen using silicone grease (or other type of grease) to minimise friction. Similarly to the standard triaxial samples, the position of each BE pair was marked and a slot was created to ensure proper contact. Whenever necessary, fine material was used to fill the BE slot or, if necessary, silicone grease.

6.3.1.4. Cubical cell natural samples

Previous work on this apparatus was carried out exclusively on dry reconstituted sands (Sadek, 2006). In this research, this apparatus was used to test natural undisturbed samples of residual soil at its natural water content (of about 20%). Due to lack of time, the first tests carried out on reconstituted samples served only to assess the performance and operation of this apparatus and were not be included in the analyses. For this reason, only test results on natural undisturbed samples of residual soil will be presented and discussed.

The natural samples to be tested in the cubical cell were initially trimmed from the ES2 block samples at FEUP. For preservation of the integrity of the soil structure, larger samples were transported to allow for possible superficial disaggregation. These trimmed samples were transported with great care from Porto to the Geomechanics Laboratory of the University of Bristol. The secondary trimming process and sample preparation from the larger samples to the appropriate size (100 x 100 x 100 mm) is best explained in the sequence of photographs below, in Figure 6.18.

An aluminium cube served as an orientation guide to the trimming of the sample. A number of tools were used to ensure verticality and orthogonal faces. Some of the extracted soil was sieved to provide fine material to cover the most significant imperfections in the faces of the sample. Once this aesthetics step was completed, the orientation of the sample was attributed and the positions of the corresponding T-shaped BE were outlined in the surface of the specimen. This enabled to ensure that the BE would penetrate with ease into the sample and thus guarantee good coupling.

As a side note, it is worth stating that the sample in the figure is B6-RS2. The natural heterogeneity, evidenced by the different colouring of the faces, does not appear to correspond to very different materials: the darker (more oxidised) material exhibited identical resistance to trimming and similar grains in relation to the remaining soil of the specimen. The same cannot be said for sample B4-RS3, in which a discontinuity was clearly visible, but composed of a completely different material from the rest of the sample, as previously discussed.



Figure 6.18 - Preparation of an undisturbed sample (B6-RS2) for the cubical cell

A box-type of rubber membrane was used to wrap the specimen. In order to facilitate the insertion of the B/EE into the soil specimen, this cubical membrane should be punctured, prior to being placed around the specimen. A T-shaped punch having exactly the same size and shape of the B/EE was used to produce a T-shaped cut in the centre of four faces of the membrane, with centricity achieved by means of a special template (Sadek, 2006), as illustrated in Figure 6.19.

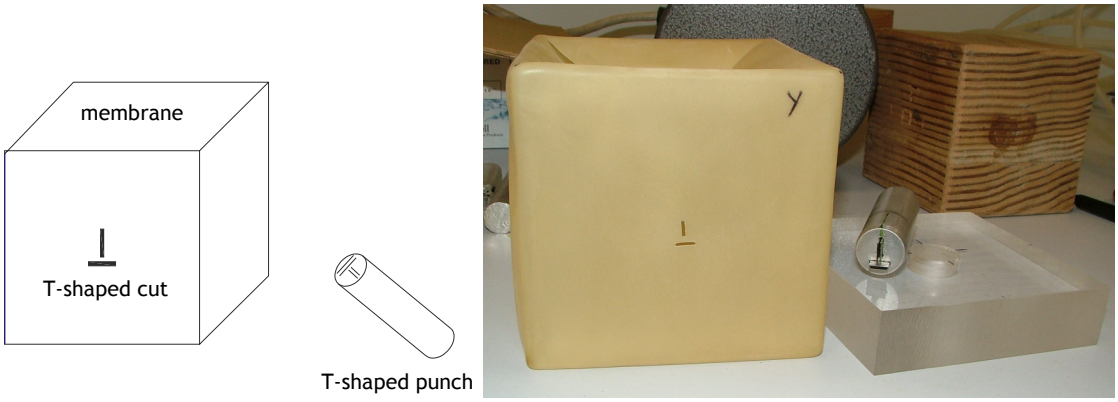


Figure 6.19 - Preparation of the cubical cell membrane for tests with BE

The T-shaped cuts on each side of the membrane were covered with adhesive tape. To enclose the sample inside the membrane, a sheet of rubber membrane was prepared with contact glue and fixed to the other sides of the membrane box, as shown in Figure 6.18. Prior to testing, the working range of the electronic pressure regulators was checked and talcum powder was sprinkled on the surface of the membrane.

The installation procedure of a natural sample in the cubical cell is illustrated in Figure 6.20. The sample was carefully placed in the cell and a vacuum/drainage tube was fed through the diagonal hole in the frame. A pressure of 15 kPa was applied to the bottom cushion (on wall Z1) in order to support the sample. On each of the faces of the sample, the adhesive tape was removed, followed by the insertion of the brass plug that houses the T-shaped pair of BE, together with a sealing grommet. Several coats of an adhesive solution ("copydex") were applied to the grommet-membrane boundary to ensure the sealing of the sample. After a curing period of about one hour, a cushion with a central hole with the diameter of the grommet was placed in the cavity of the cubical cell, enabling an O-ring to surround the grommet. The connection between the grommet and the cushion was painted with several layers of the adhesive solution, in order to guarantee an airtight pressure system. A curing time of one hour is required before mounting the wall assembly on the apparatus.

The wiring cable connected to the BE is fed through a hole in the centre of the wall assembly sealed with a specially designed threaded plug.

Subsequently, this process was repeated on the other faces, requiring the rotation of the whole apparatus, as already mentioned in Chapter 3. When the apparatus was fully assembled, a minimum pressure of 15kPa was applied to the remaining five faces of the sample. The process of installation of a soil sample is presented in the sequence of photographs in Figure 6.20.

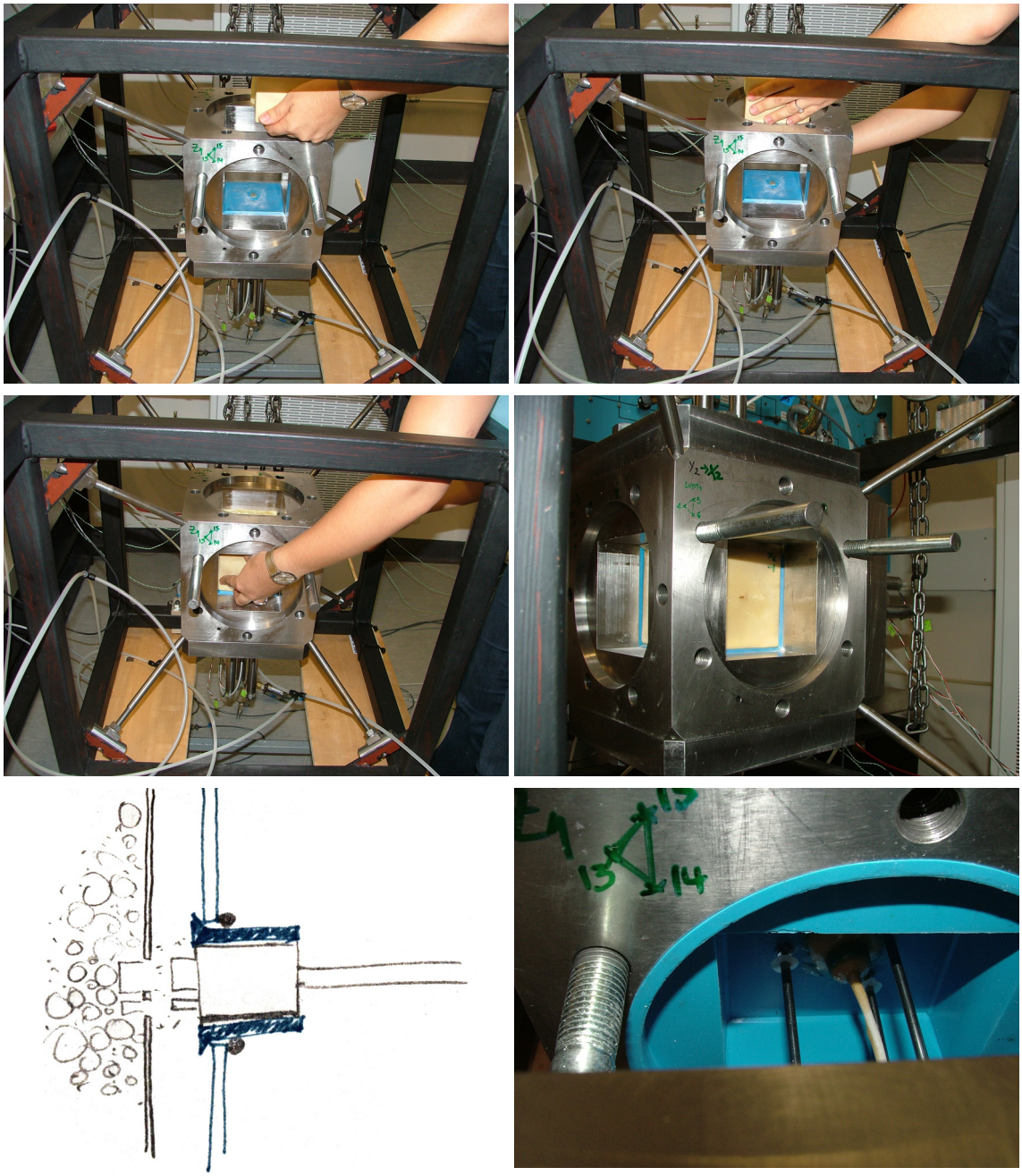


Figure 6.20 - Installation of an undisturbed natural sample in the cubical cell

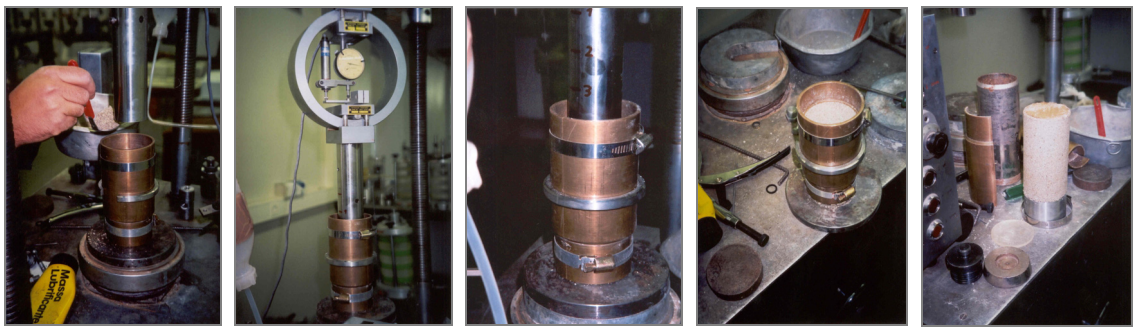
6.3.2. Reconstituted specimens

Sample reconstitution refers to the process required to produce a reference laboratory material for comparison with the natural soil. Several techniques have been proposed over the years and a clear distinction exists between the reconstitution of sands (e.g. Ishihara, 1993) and clays (e.g. Burland, 1990). An interesting observation by Cotecchia and Chandler (1997) suggested that the reconstituted samples could not be referred as "unstructured" sample, but rather that the reconstituted sample had a sedimentation structure which was different from the natural sample (Sukolrat, 2007).

In this research, reconstituted residual soil specimens were tested in the standard triaxial (or stress-path) and in the true triaxial apparatuses. Considering the grain-size distribution of this residual soil and the required densities, static compaction was generally adopted for the standard triaxial (or stress-path) specimens, while moist or dry tamping were selected for the true triaxial reconstituted specimens.

6.3.2.1. Standard triaxial specimens

A number of reconstituted specimens were prepared for comparison with the behaviour of the naturally structured samples under standard triaxial conditions. Figure 6.21 illustrates the complete preparation process of remoulded specimens for standard triaxial testing. Two distinct densities were considered to match those of the tube samples and those of the block samples, from identical water contents.



a) b) c) d) e)

Figure 6.21 - Stages of preparation of remoulded specimens: a) spooning a weighed amount of soil corresponding to one layer; b) light static compaction by layers; c) detail of the layer marks in the piston; d) remoulded specimen in the mould; e) ready for installation in the triaxial cell

In each case, the desired density was used to calculate the total weight of wet soil in relation to the internal volume of the mould. Five compaction layers were usually adopted. For each layer, a fifth of the total weight of the specimen was spooned into the mould and compacted using a hydraulic press under the adequate thickness was obtained. After static compaction of each layer, its surface was scratched to ensure good contact and continuity between layers. At the end of the fifth layer, the mould was removed, revealing a uniform and smooth soil sample, clearly different from the natural samples.

6.3.2.2. True triaxial specimens

For the preparation of the reconstituted or remoulded specimens for true triaxial tests, the sample installation process in the apparatus is inverted. In this case, the structure of the apparatus is entirely assembled, with the obvious exception of the top platen, through which the soil is poured or spooned and lightly compacted by hand. Two soil conditions have been considered: wet and dry.

Burland (1990) suggested that a reconstituted clay sample should be prepared from mixing a wet natural sample with water to the water content equal to w_L to $1.5\,w_L$. Despite referring to clay materials, analogous reasoning was considered in this research and so wet soil specimens were produced, at a water content near or above the liquid limit of the soil, in this case around 30%. The water surrounds the soil particles and the distribution of the deposited soil inside the chamber appears homogeneous and uniform. Since a high void ratio is intended as a starting point, virtually no compaction is necessary, only very soft tamping as a means of levelling the surface. This procedure is also favourable to the minimisation of any induced particle layering. As the soil sets in the chamber, some water may percolate and rise to the top of the specimen, in a self-weight consolidation process. The flow of water and the consequent water content variation are monitored using the burettes. Nevertheless, it is not possible to guarantee total saturation, that is, the absence of air bubbles trapped between the soil particles. The entrapped air may result in suction stresses, producing an additional (unaccounted for) effective stress, which in turn influences the small strain response of the soil, as measured by shear seismic waves. This uncertainty, though limited for such high water content, cannot be completely excluded, but it is not an issue when testing dry specimens.

A dry soil specimen (w below 1%) has the advantage of behaving as a particulate material, in which the interactions between the particles are related with intrinsic characteristics (particle size, shape, roughness) and its arrangement or packing. This

also represents a limitation, as the installation of a dry specimen in the testing chamber can hardly be made without the induction of particle layering and thus anisotropy. The wide grain-size distribution of this soil prevents the use of standard pluviation techniques, which would in this case result in strong segregation of particles: coarser grains are heavier, hence more rapidly pluviated and deposited, and consequently finer material would be concentrated in the upper part of the specimen, with evident heterogeneity.

Instead, the dry soil specimen was prepared by slowly pouring the soil into the chamber and occasionally spreading level. Very light tamping was applied after spreading to produce a loose sample. The density (or the weight of the sample) was not estimated *a priori*, since the intention was to obtain a sample as loose as possible. The limitation of this preparation technique is its dominant horizontal depositional direction, which cannot be eliminated.

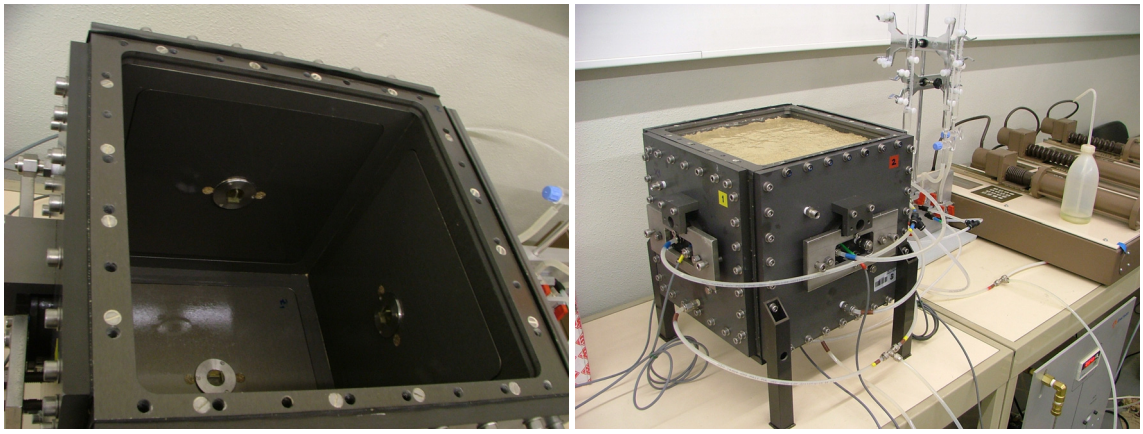


Figure 6.22 - Preparation of a wet reconstituted sample in the true triaxial apparatus

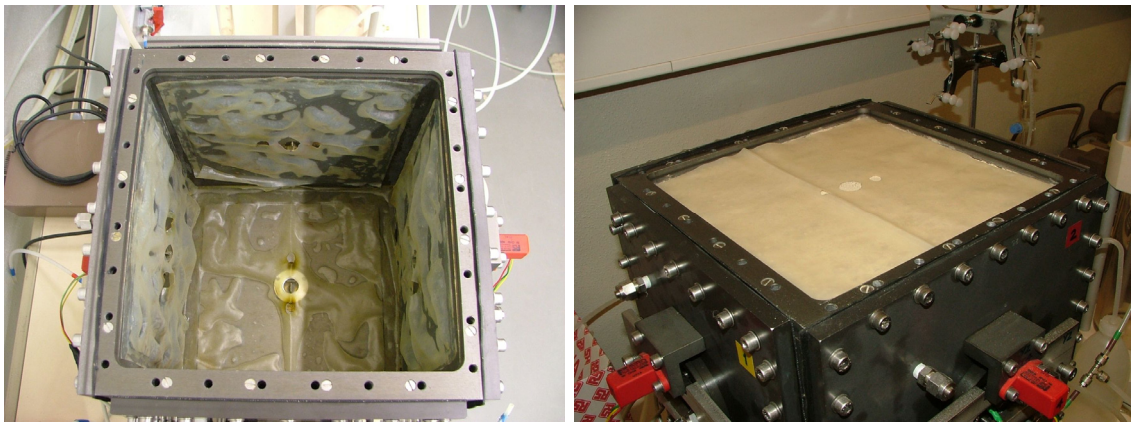


Figure 6.23 - Preparation of a dry reconstituted sample in the true triaxial apparatus

6.4. Laboratory testing programme

6.4.1. Setup and testing procedures

Following its preparation, each sample was set-up in the respective testing device. Special attention was given to the installation and coupling of the BE with the soil, in order to guarantee the best possible transmission of the seismic waves.

The testing procedures in the true triaxial and cubical cell apparatuses are described with the analyses of the laboratory tests in Chapter 7, given the variety of testing options, associated with the novelty of these testing devices. For this reason, only the generic testing procedures in standard triaxial (or stress-path) tests are presented below.

Taking into consideration the sensitive nature of the structure of this soil and also the purpose of assessing sample disturbance, the reconsolidation technique is particularly influential, as pointed out by Lo Presti et al. (1999). These authors distinguished between wet and dry setting, showing that the dry setting is preferable to the conventional setting method. Wet setting is the conventional method used to set-up a specimen prior to testing, where saturation is carried out prior to the re-establishment of the in situ stress conditions, that is, prior to the reconsolidation. During this conventional procedure, the specimen can absorb water and swell, experiencing large deformations that can cause relevant fabric changes, i.e., soil destructuration.

As suggested by Lo Presti et al. (1999), a solution to overcome this problem is the use of the dry reconsolidation setting, initially developed by Berre (1982) at NGI and also adopted in other universities worldwide (Ampadu and Tatsuoka, 1993; Lo Presti et al., 1994). In the present research, each test on a undisturbed sample was initiate with an anisotropic consolidation to the estimated in situ effective stresses, assuming a coefficient of earth pressure at rest K_0 equal to 0.50 for ES1 and variable between 0.35 and 0.50 for ES2, under drained conditions. One of the potential shortcomings of this method is associated with a potential increase in the effective stresses due to the presence of suction. For this reason, in samples with a low water content (corresponding to higher suction levels) an initial percolation of water at a low back-pressure is recommended.

After the consolidation stage, water was percolated through the sample at an average back pressure of 5 kPa (10 kPa at the bottom platen and 0 kPa at the top platen) and a minimum volume of 500 ml was considered necessary to remove most of the large air bubbles. At this point, the differences between ES1 and ES2 are clearer. While the samples from ES1 can be assumed to be saturated in the field, due to the high water table around 3 m, the same cannot be applied to the samples at ES2, where the water table lies below 10 m. For this reason, the saturation process was only carried out for ES1 samples, under otherwise stated in the analysis of results. These samples were saturated in increments of back-pressure of 30 to 50 kPa, generally up to 300 kPa or until a Skempton's B value higher than 0.90 was obtained. Taking advantage of the measurement of P-waves, it was possible to verify saturation by measuring V_P higher than 1500 m/s, as proposed by Ferreira (2003).

Studies of the non-saturated condition of this residual soil were not considered in this research, but are currently being developed by Topa Gomes (2009) on another experimental site in the similar residual soil from Porto granite and also by Dourado (2011) on ES2 site.

Nevertheless, the measurements made on the suction levels of this soil for the depths of these samples provided values below 20 kPa, from which a low effect on stiffness and strength can be expected, especially under drained conditions.

6.4.2. ES1 testing programme

For the purposes of this research, the main objective of the laboratory tests on the samples from the first experimental site ES1 at CICCOPN was the identification of sample disturbance and assessment of the sampling quality provided by different samplers in a typical homogeneous residual soil profile. As a result, most laboratory tests were carried out to replicate field conditions, in terms of consolidation and saturation conditions, and the shear loading stage was generally of standard vertical compression. Load application was particularly slow and carried out in small steps to provide time for strain stabilisation in order to measure seismic waves at a stabilised condition. Four tests on a resonant column apparatus equipped with BE were also carried out for comparison of small-strain results.

The origin, main physical properties and type of test carried out on the undisturbed and reconstituted soil samples from this experimental site are listed in Table 6.2 and Table 6.3, respectively. Some of these test results were already published in Ferreira (2003); however, due to the continued research in the same (ES1) and in another

(ES2) experimental site on a similar residual soil from granite, the compilation of results was considered valuable, as a means to better understand and characterise the behaviour of this soil. A large number of shear and compression wave measurements were made in each TXBE (triaxial test with BE measurements), as will be shown in Chapter 7.

Table 6.2 - List of the main laboratory tests on ES1 natural samples

Specimen	Sample	Approx. depth [m]	γ [kN/m³]	w [%]	e	Type of test
B2.1.70	B2	2.0	19.0	24.7	0.803	TXBE 70
B2.2.70	B2	2.0	17.6	23.4	0.877	TXBE 70
S1.2.1	S1	2.0	19.3	22.6	0.667	TXBE 70
S1.2.3	S1	2.0	19.5	22.9	0.652	RCBE
S1.2.4	S1	2.0	19.4	23.0	0.662	RCBE
S1.4.1	S1	4.0	19.2	22.7	0.660	TXBE 70
S1.6.3	S1	6.0	19.3	22.8	0.656	TXBE 70
S2.2.2	S2	2.0	19.1	21.6	0.668	TXBE 70
S2.2.3	S2	2.0	19.3	19.4	0.623	RCBE
S2.4.1	S2	4.0	19.4	22.1	0.649	TXBE 70
S2.6.1	S2	6.0	19.9	21.5	0.602	TXBE 70
S2.6.2	S2	6.0	19.5	22.4	0.644	RCBE
S3.2.1	S3	2.0	19.5	20.5	0.622	TXBE 70
S3.2.2	S3	2.0	19.5	21.1	0.642	TXBE 70
S3.4.1	S3	4.0	19.4	20.2	0.623	TXBE 70
S3.4.2	S3	4.0	19.5	19.4	0.610	TXBE 70
S4.2.1	S4	2.0	19.4	22.6	0.660	TXBE 70
S6.2.2	S6	2.0	18.9	21.8	0.718	TXBE 70
S6.6.1	S6	6.0	18.6	22.0	0.717	TXBE 70

Legend: TXBE: standard triaxial test, with BE measurements (including P- and S-waves); 70: diameter of the specimen; RCBE: resonant-column equipped with BE

Table 6.3 - List of the main laboratory tests on ES1 reconstituted specimens

Specimen	Sample	γ [kN/m3]	w [%]	e	Type of test
B2.0.70	B2	17.7	24.2	0.857	TXBE 70
S2.2.0	S2	19.2	21.2	0.662	TXBE 70

Legend: TXBE: standard triaxial test, with BE measurements (including P- and S-waves); 70: diameter of the specimen

The main results of these tests in terms of stiffness measurements and stress-strain reponse will be presented and discussed in the following chapters.

6.4.3. ES2 testing programme

The large amount of samples, including high-quality block samples, recovered from the second experimental site, provided the opportunity to test this residual soil under a variety of stress conditions, using different apparatuses, in which seismic wave velocities were consistently measured. The main physical properties and testing conditions of the undisturbed and the reconstituted soil samples from ES2 are presented in Table 6.4 and Table 6.5, respectively. It should be noted that many other undisturbed and reconstituted samples were tested, but the results were not directly comparable (namely when no seismic wave measurements were taken) and for that reason those tests were not included in this work.

Table 6.4 - List of the main laboratory tests on CEFEUP natural samples

Specimen	Sample	Approx. depth [m]	γ [kN/m^3]	w [%]	e_0	Type of test
B2-TT	B2	1.50	16.7	20.4	0.894	TT
B2-4-TX	B2	1.50	17.6	23.4	1.016	TXBE
B4-RS3	B4	2.50	16.9	26.0	0.956	CC
B4-TT	B4	2.75	18.8	25.0	0.850	TT
B5-1-RC	B5	2.50	15.4	16.9	0.994	RCBE
B5-2-RC	B5	2.50	15.4	16.9	0.994	RCBE
B5-isoSP	B5	2.50	19.0	24.7	0.801	ISOSP
B5-TT	B5	4.35	17.4	20.0	0.811	TT
B5-TX	B5	2.50	19.3	22.6	0.689	TXBE
B6-OED	B6	4.20	18.2	17.5	0.778	OED
B6-RS1	B6	4.20	17.3	17.5	0.780	CC
B6-RS2	B6	4.20	17.4	15.7	0.746	CC
S2-1-CT	S2B	8.80	18.1	11.4	0.600	CTX
S2-2-CT	S2B	11.50	18.5	19.4	0.695	CTX
S2-3-CT	S2B	14.95	19.3	13.3	0.525	CTX
S2-3-TX	S2	4.00	18.2	16.3	0.780	TXBE
S2-4-TX	S2	4.50	18.4	16.2	0.748	TXBE
S2-5-TX	S2	5.50	19.0	22.5	0.710	TXBE
S2-7-TX	S2	7.00	19.0	20.2	0.676	TXBE
S5-1-RC	S5	4.30	20.0	13.8	0.497	RC
S5-2-RC	S5	8.00	19.0	19.7	0.663	RC
S5-4-TX	S5	4.30	19.1	21.6	0.556	TXBE
S5-5-TX	S5	6.30	19.4	22.1	0.714	TXBE
S5-6-TX	S5	8.85	19.9	21.5	0.676	TXBE
S5-OED	S5	6.30	19.4	22.1	0.817	OED

Legend: (see below in the following table)

Table 6.5 - List of the main laboratory tests on CEFEUP reconstituted specimens

Specimen	γ [kN/m^3]	w [%]	e_0	Type of test
R2-isoCF1	20.0	30.8	0.909	ISOTX
R2W-ISOTT	19.1	28.4	0.770	TT
R3W-K_0TT	18.8	30.7	0.850	TT
R4D-K_0TT	14.1	1.2	0.883	TT
R8D-TT	12.7	1.0	1.067	TT

Legend: TT: true triaxial test; TXBE: standard triaxial test, with BE measurements (including P- and S-waves); 70: diameter of the specimen; ISOTX: isotropic test on the standard triaxial cell; CC: cubical cell test; RCBE: resonant-column equipped with BE test; RC: resonant column test; ISOSP: isotropic test on the stress-path cell; OED: oedometer test; CTX: conventional triaxial test

As shown in the table, from the six block samples retrieved from the ES2 at CEFEUP, only three cubical specimens were tested intact in the TT apparatus. Similarly, only three intact specimens were used in the UoB cubical cell. All other tests in these apparatus were carried out with reconstituted material from the site and, frequently, from the same blocks. The block samples B3 and B6 presented some heterogeneity, from which it was unfeasible to trim a representative 250 mm specimen. In those cases, the material was carefully selected and trimmed for small soil samples, such as those for standard triaxial (or stress-path), resonant-column, cubical cell and oedometer tests.

Further details regarding the specific testing conditions of these samples will be provided along with the presentation and analysis of the test results, in the following chapter.

6.5. Summary and conclusions

In this chapter, the sampling programme and the subsequent laboratory sample preparation, setup and testing procedures were presented with some detail. The sampling methods used on both experimental sites, from block to undisturbed tube sampling, to disturbed soil sampling were described and discussed. The use of different sampling methods resulted in samples with distinct qualities, that is, with different disturbances induced by the sampling processes. Based on the preliminary results of Ferreira (2003), the least disturbed samples in the first experimental site were obtained using the NT 81 sampler. For this reason, this sampler was selected for high-quality tube sampling in the second experimental site (ES2).

The sample preparation procedures under natural and reconstituted conditions were discussed, for each specific testing apparatus. Natural samples of this residual soil were tested in the standard triaxial, stress-path, resonant-column, true triaxial and cubical cell apparatuses, while reconstituted samples were tested in the standard triaxial and the true triaxial apparatuses.

The set-up and testing procedures were briefly introduced, and the main laboratory tests carried out in undisturbed and reconstituted samples from both experimental sites were systematised in tables for quick reference. The use of the dry setting method, that is, the option of consolidating the natural samples prior to its saturation, was adopted. This method proved very effective as a means to minimise water absorption and swelling which may cause relevant fabric changes, and thus induce soil destructuration.

Further details and specific conditions of some tests will be provided in Chapter 7, where all the results of these tests will be presented and debated. More comprehensive and integrated analyses will be made in Chapter 8.

7.

Laboratory Test Results

7.1. Introduction

In this chapter, the most relevant results provided by the laboratory tests carried out on reconstituted and undisturbed samples, listed in the previous chapter, will be presented, discussed in detail and directly compared.

The resonant-column apparatus equipped with bender elements enables to establish direct comparison of the shear modulus measured by both methods, thus enabling the assessment of the performance of the BE interpretation techniques and its calibration.

The test results were divided according to the range of strain at which the stiffness moduli were measured: a) very small strains, obtained by means of BE and RC; b) small to large strains, from the strain measuring devices of each testing apparatuses.

Preliminary conclusions are provided in each section. A more comprehensive and integrated analysis of the global results will be presented in the following chapter.

7.1.1. Theoretical background on stiffness at very small strains

As reported in Chapter 2, the propagation of shear and compression waves through the soil causes only very small movements of the soil particles, in which the behaviour can be assumed to be elastic. Hence, the measurement of the wave velocities can be used as a tool for the determination of the elastic stiffness of the soil. Shear wave velocities enable to define the shear modulus, while compression wave velocities provide the constrained modulus. Both correspond to maximum values of the respective stiffness and are usually noted as G_0 and M_0 (or G_{max} and M_{max}). The calculation of G_{max} and M_{max} is usually based on the theory of wave propagation in an infinite elastic medium, as follows (e.g. Santamarina et al., 2001):

$$G_0 = \rho \cdot V_S^{\,2} = \rho \cdot \left(\frac{L}{t_S} \right)^2 \qquad [7.1]$$

$$M_0 = \rho \cdot V_P^{\,2} = \rho \cdot \left(\frac{L}{t_P} \right)^2 \qquad [7.2]$$

where ρ is the mass density of the medium, V is the wave velocity, L is the travel length and t is the wave travel time.

The shear modulus G_0 is an important reference parameter in geotechnical design, since shear strains generally cause the greatest damage in structures. As a result, G_0 is more frequently applied in soil characterisation than M_0. In addition, the shear modulus is highly sensitive to a number of relevant factors and soil conditions. On the other hand, since compression waves travel through both solids and fluids, the response in saturated conditions is dominated by the presence of water and does not correctly characterise the behaviour of the saturated soil.

Hardin and Black (1969) were the first to systematise the more relevant factors influencing the overall shear modulus, in a generic function such as:

$$G_0 = \mathrm{f}\,(\sigma', e, H, S, \tau_{oct}, C, f, t, \xi, T) \qquad [7.3]$$

where σ' represents the effective stresses, e is the void ratio, H is the stress history, S is the degree of saturation, τ_{oct} is the octahedral shear stress, C refers to grain and mineralogical properties, f is the excitation frequency, t is time (ageing), ξ is a measure of the fabric and structure of the soil, and T is the temperature.

Clearly, the influence of each of these factors in stiffness is varied. It is widely recognised that the most important factors to which the stiffness is dependent of are the principal effective stresses in the wave propagation and wave polarisation directions, the void ratio, the structure or packing of the soil, and also the degree of saturation (mainly for clays and silts), also associated with suction levels, and the degree of cementation (natural or artificial).

Hardin and Blandford (1989) presented a formulation incorporating the fundamental and most influential parameters, as follows:

$$G_{0ij} = S_{ij} \cdot F(e) \cdot OCR^{k} \cdot p_a^{(1-n_i-n_j)} \cdot (\sigma'_i)^{n_i} \cdot (\sigma'_j)^{n_j} \quad [7.4]$$

where σ'_i and σ'_j principal effective stresses in the wave propagation direction, i, and wave polarisation direction, j; k is an empirical exponent of the overconsolidation ratio OCR depending on the plasticity index, IP; $F(e)$ is a void ratio function, S_{ij} is a non-dimensional material constant reflecting the fabric and structure of the soil; n_i and n_j are empirical stress exponents or indices (for sands, $n_i \cong n_j$ is often assumed), and p_a represents a reference stress, usually the atmospheric pressure (taken equal to 1 kPa).

According to several authors, the influence of the overconsolidation ratio can be neglected if an appropriate void ratio function is considered (Tatsuoka and Shibuya, 1992; Jamiolkowski et al., 1995; Barros, 1997; Sulkorat, 2007). For the definition of the void ratio function, three reference expressions are usually considered, as indicated in Table 7.1. These can be directly applied when no specific study is carried out to determine which is most suitable for the soil in study, or serve as a starting point for a more soil-specific analysis. The differences between these reference void-ratio functions are more evident at low void ratios, as illustrated in Figure 7.1.

Table 7.1 - Reference void ratio functions (from Ferreira, 2003)

Function	General expression	References
F(e)1	$\frac{(2.17-e)^2}{1+e}$	Hardin e Richart (1963); Iwasaki et al. (1978)
F(e)2	$\frac{1}{0.3+0.7\cdot e^2}$	Hardin (1978); Chung et al. (1984)
F(e)3	e^{-x}, with $x=1.3$	Lo Presti (1995); Jamiolkowski et al. (1991)

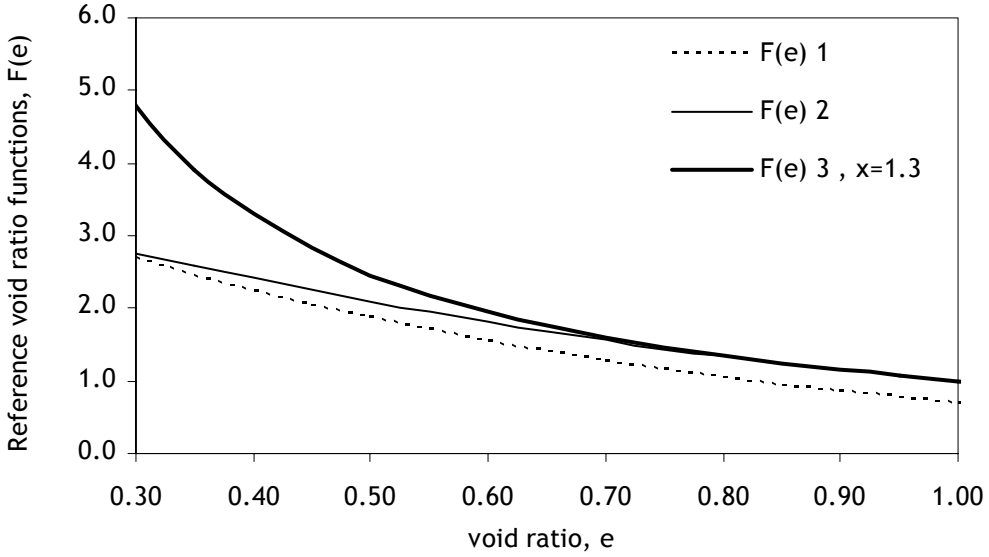


Figure 7.1 - Differences between reference void-ratio functions against void ratio

In standard triaxial testing, the stresses acting in the wave propagation and polarisation directions corresponding to the principal vertical and horizontal stresses. When only the vertically propagated shear waves are measured, the generic form of Equation 7.4 can be simplified to:

$$G_{0vh} = S \cdot F(e) \cdot (\sigma'_v \cdot \sigma'_h)^{n_{vh}} \qquad [7.5]$$

When horizontally propagated shear waves are also measured, the individual indices can be directly extracted. Strictly under K or K_0 stress conditions (where the horizontal and vertical stresses are proportional), the fundamental expression of G_{0ij} can be modified into three separate equations:

$$G_{0hv} = S_{hv} \cdot F(e) \cdot K^{n_h} \cdot \sigma'^{\,n_{hv}}_v \text{ with } n_{hv} = n_h + n_v \qquad [7.6]$$

$$G_{0hh} = S_{hh} \cdot F(e) \cdot K^{n_{hh}} \cdot \sigma'^{\,n_{hh}}_v \text{ with } n_{hh} = 2 \cdot n_h \qquad [7.7]$$

$$G_{0vh} = S_{vh} \cdot F(e) \cdot K^{n_h} \cdot \sigma'^{\,n_{vh}}_v \text{ with } n_{vh} = n_v + n_h \qquad [7.8]$$

Several authors (e.g. Pennington, 1999) have suggested that the out-of-plane stress has negligible influence on G_{0ij}. Nevertheless, the influence of all stresses involved can be assessed by considering the relationship with p', which may be especially useful towards understanding the response in three-dimensional conditions, which can be expressed as follows:

$$G_{0ij} = S_{ijo} \cdot F(e) \cdot p'^{n} \qquad [7.9]$$

This concept behind these formulations will serve as basis for the presentation, analysis and discussion of the results obtained in the laboratory tests carried out in this research. The normalisation of the different shear moduli in relation to the void ratio enables to directly compare the influence of the applied stresses and, simultaneously, identify the structure parameter S. For this purpose, the normalised shear modulus in relation to the void ratio is denoted with an asterisk:

$$G_{0ij}^{*} = \frac{G_{0ij}}{F(e)} \qquad [7.10]$$

The consideration of different approaches to the stress-dependency of the shear moduli aimed at defining which is most appropriate, mainly from the interpretation of results in true triaxial conditions.

7.2. Very small strains

7.2.1. Introduction

In what follows, the results obtained from measurements of stiffness at the very small strain range, that is, for strains lower than 10^{-5} will be presented. These results have been obtained in a variety of tests, namely resonant-column, standard triaxial and true triaxial, on reconstituted and natural residual soil samples.

7.2.2. Resonant-column and BE tests

The BE-equipped resonant-column device provides grounds for direct comparison of the shear wave velocities derived by both methods, theoretically enabling the calibration of the BE interpretation techniques.

The RC+BE tests comprised the application of isotropic and (or) anisotropic stress conditions, at various stages, on natural intact soil samples collected from both experimental sites, as outlined in Table 7.2 and Table 7.3. All tests were drained, and the samples were almost but not fully saturated during testing, maintaining the natural moisture content. At each loading stage, RC readings of the resonance frequency were made after a stabilization period of about 30 minutes, followed by the acquisition of the wave traces in the time and frequency domain with the BE.

Table 7.2 - Testing conditions and physical characteristics of ES1 specimens in the RC

Specimen	Type of test	Testing conditions
S1.2.3	RCBE	Isotropic consolidation: 8 stages up to σ'_c = 400 kPa
S1.2.4	RCBE	Isotropic consolidation: 8 stages up to σ'_c = 400 kPa, with creep (for 48 days)
S2.2.3	RCBE	Anisotropic consolidation (K_0 = 0.5) and shear: 8 stages up to σ'_v = 120 kPa
S2.6.2	RCBE	Anisotropic consolidation (K_0 = 0.5): 7 stages up to σ'_v = 400kPa

Specimen	Depth	γ	w	e	σ'_{v0}	σ'_{h0}	p'	q
	[m]	[kN/m^3]	[%]		[kPa]	[kPa]	[kPa]	[kPa]
S1.2.3	2.20	19.5	22.9	0.652	40	20	26.7	20
S1.2.4	2.10	19.4	23.0	0.662	40	20	26.7	20
S2.2.3	2.10	19.3	19.4	0.623	40	20	26.7	20
S2.6.2	6.30	19.5	22.4	0.644	80	40	53.3	40

Table 7.3 - Testing conditions and physical characteristics of ES2 specimens in the RC

Specimen	Type of test	Testing conditions
S5-1-RC	RC	Anisotropic consolidation (K_0 = 0.5) to σ'_v = 80kPa Stiffness degradation (shear strain ε_s or $\gamma = 3.8\text{x}10^{-6}$ to $2.5\text{x}10^{-4}$)
S5-2-RC	RC	Anisotropic consolidation (K_0 = 0.5) to σ'_v = 160kPa Stiffness degradation (shear strain ε_s or $\gamma = 3.6\text{x}10^{-6}$ to $3.9\text{x}10^{-4}$)
B5-1-RC	RCBE	Anisotropic consolidation (K_0 = 0.35): 13 stages to σ'_v = 500kPa Stiffness degradation (shear strain ε_s or $\gamma=4.0\text{x}10^{-6}$ to $6.7\text{x}10^{-4}$)
B5-2-RC	RCBE	Anisotropic consolidation (K_0 = 0.5): 4 stages to σ'_v = 90kPa Stiffness degradation (shear strain ε_s or $\gamma=5.5\text{x}10^{-6}$ to $8.0\text{x}10^{-4}$)

Table 7.3 (cont.) - Testing conditions and physical characteristics of ES2 specimens in the RC

Specimen	Depth	γ	w	e_0	σ'_{v0}	σ'_{h0}	p'	q
	[m]	[kN/m^3]	[%]		[kPa]	[kPa]	[kPa]	[kPa]
S5-1-RC	4.10	20.0	13.8	0.497	80.0	40.0	53.3	40.0
S5-2-RC	8.60	19.0	19.7	0.663	160.0	80.0	106.7	80.0
B5-1-RC	4.15	15.4	16.9	0.994	65.0	22.8*	36.8	42.3
B5-2-RC	4.15	15.4	16.9	0.994	65.0	22.8*	36.8	42.3

* K_0 considered equal to 0.35; all other samples, $K_0 = 0.5$

The samples from ES1 were mainly used to explore the comparison between shear moduli obtained by the bender element technique and the resonant column. On the other hand, the tests on the ES2 soil samples served primarily for the characterization of the soil rather than the analysis of the testing methods. A new RC testing method was also experimented in sample B5-1-RC, which proved to be fundamental for the understanding of BE and RC measurements.

7.2.2.1. BE interpretation process

The procedure for the interpretation of the BE data, combining time and frequency domain results, follows what was presented in Chapter 4. The test results for sample S1.2.4 will be used as example, namely for the comparison between BE and RC measurements.

Figure 7.2 shows the time domain readings on sample S1.2.4, at stage 2 [s02], for an isotropic confining pressure of 50 kPa. Input frequencies of 2, 4, 8, 10 and 15 kHz were applied, but only the first three frequencies were considered relevant and/or had sufficient amplitude for the interpretation. Note that the polarity of the input and output signals is positive, hence the start of the shear wave is expected to be ascending.

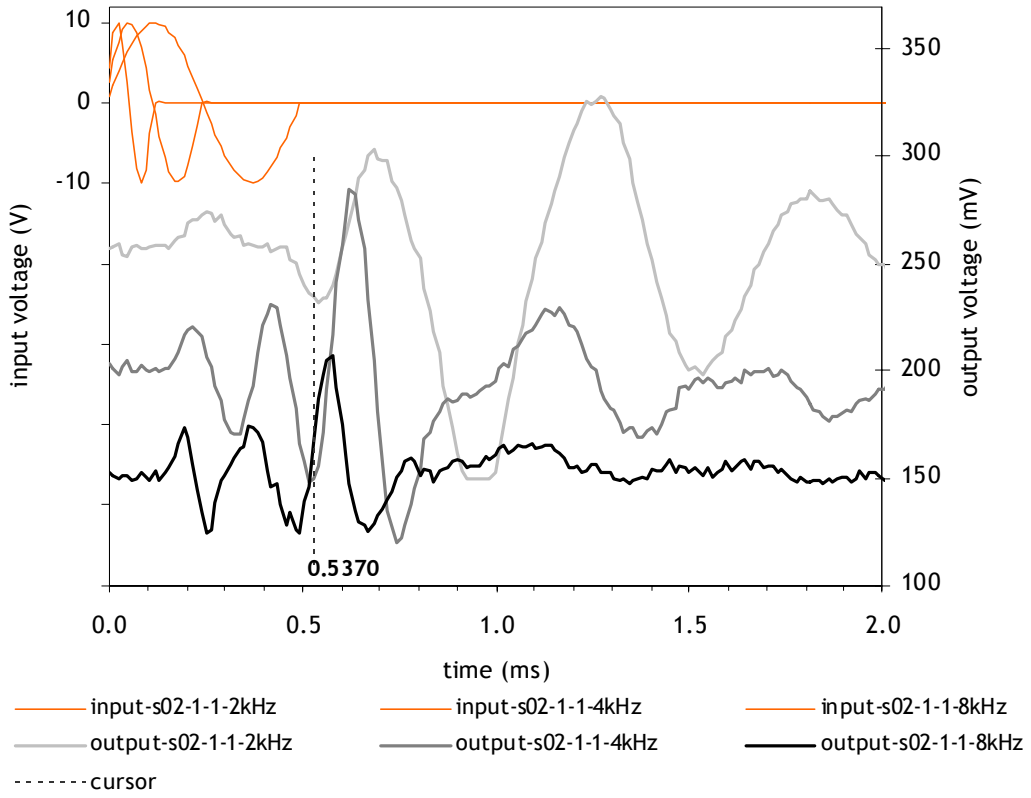
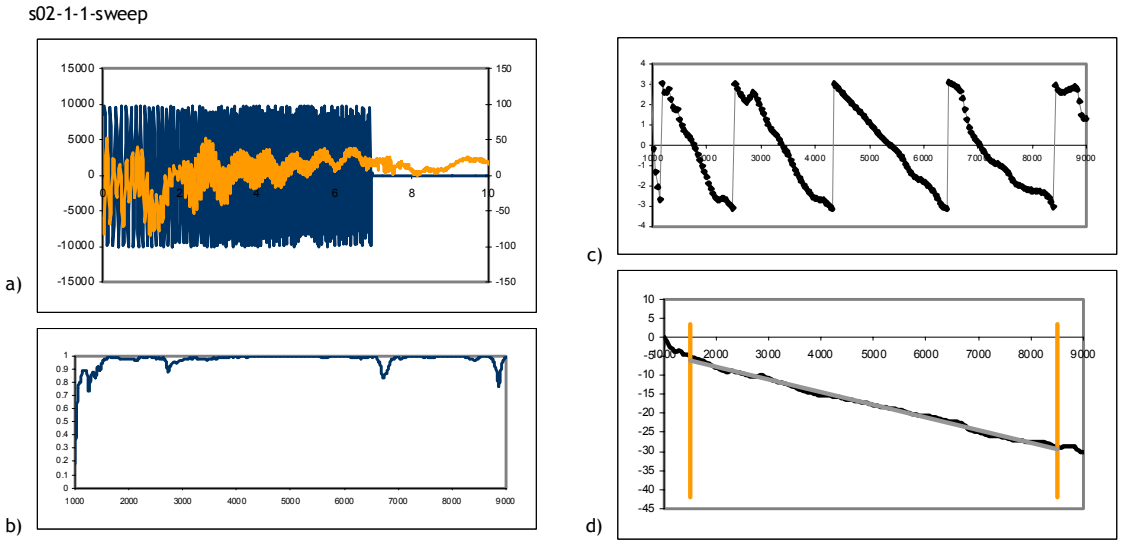


Figure 7.2 - RC+BE sample S1.2.4: TD results at 50 kPa

The TD interpretation herein used assumes the same travel time for all tested frequencies. In this figure, the dotted vertical line corresponds to the selected travel time. For an input frequency of 2 kHz, the received signal has an irregular start, but after the first trough a typical shear wave appears. This wave has a higher second peak and its main frequency is roughly the same of the transmitted signal (which can be measured directly in the oscilloscope or in the graph). For the second input frequency of 4 kHz, the initial disturbance of the received signal is stronger and likely to be associated with the arrival of a P-wave around 0.15 ms. In this case, the distinction between compression and shear waves is less clear, but the second trough of the signal is aligned with the previous selection of travel time, thus providing confidence in the selected points for shear wave arrival. The third received signal, for an input signal at 8 kHz, has nearly half the amplitude of the first received signal for a 2 kHz input signal. In addition, the amplitudes of the compression and the shear parts of the wave are almost the same, which tend to compromise the interpretation. However, the irregularities in the signal from about 0.40 ms to the selected point at 0.537 ms enable the visual separation of the two types of waves. The comparison of the three received signals is clearly beneficial to the reliability on this interpretation of the BE results in the time domain, as opposed to the use of a single input frequency.

For the frequency domain approach, the predefined input sweep signal, from 100 Hz to 20 kHz in 10 ms, was generated. The software tool ABETS was used for acquisition and processing data, which automatically produced the graphs in Figure 7.3, for the frequency range selected at the time of testing. Detailed representations of these graphs are provided and discussed below.



Frequency range: f1 =	1500	Hz
f2 =	8500	Hz
travel time =	0.524788	ms
correlation coefficient =	0.995001	
distance =	135	mm
mass density =	1976.95	kgm-3
wave velocity, V_S =	257.247	ms-1
estimate G_0 =	130.826	MPa

[NOTE: a) signals in timescale; b) coherence; c) wrapped phase angle; d) unwrapped phase angle]
Figure 7.3 - RC+BE sample S1.2.4: FD results at 50 kPa, ABETS automatic results

The representation of the complete data acquired for FD analysis is provided in Figure 7.4, showing that about four sets of raw (non-averaged) input and output signals are used in the computation. The output signal exhibits higher amplitudes for low frequencies and some noise persists during zero input, that is, between triggered sweeps. Most of this noise cancels itself out when averaged, and the same applies in this case since a few samples are acquired and applied in the calculation.

The results for the complete frequency range of application are presented in Figure 7.5. The first plot of computed results is the coherence function, which provides an indication of the relation of the two signals, as detailed in Chapter 4.

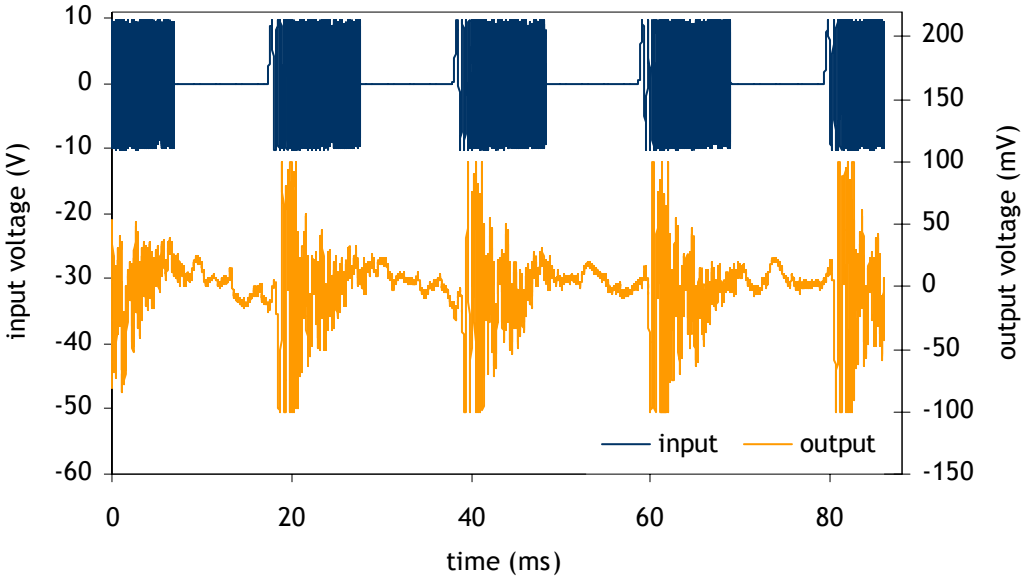


Figure 7.4 - RC+BE sample S1.2.4: FD results at 50 kPa, input and output in a timescale

The variation of phase angle between the signals is presented wrapped between π and $-\pi$ in Figure 7.5b, and unwrapped in Figure 7.5c. From the slope of the phase angle, the travel time can be promptly derived. For an unbiased selection of the frequency range between which the slope, and hence the travel time, is to be calculated, a post-processing tool, available in ABETS-plus, was applied. The overall variation of travel time against frequency, or travel time spectra, for different frequency windows (of 0.5, 1, 2, 4, 6 and 8 kHz) is illustrated in Figure 7.6.

As evidenced in Figure 7.6, narrower windows (0.5 and 1 kHz) result in high variations of travel time, while wider windows (6 and 8 kHz) produce smoother curves. For that reason, the results provided by wider windows are generally more consistent and thus considered reliable than the narrower windows. However, this cannot be taken as a rule, as will be discussed below.

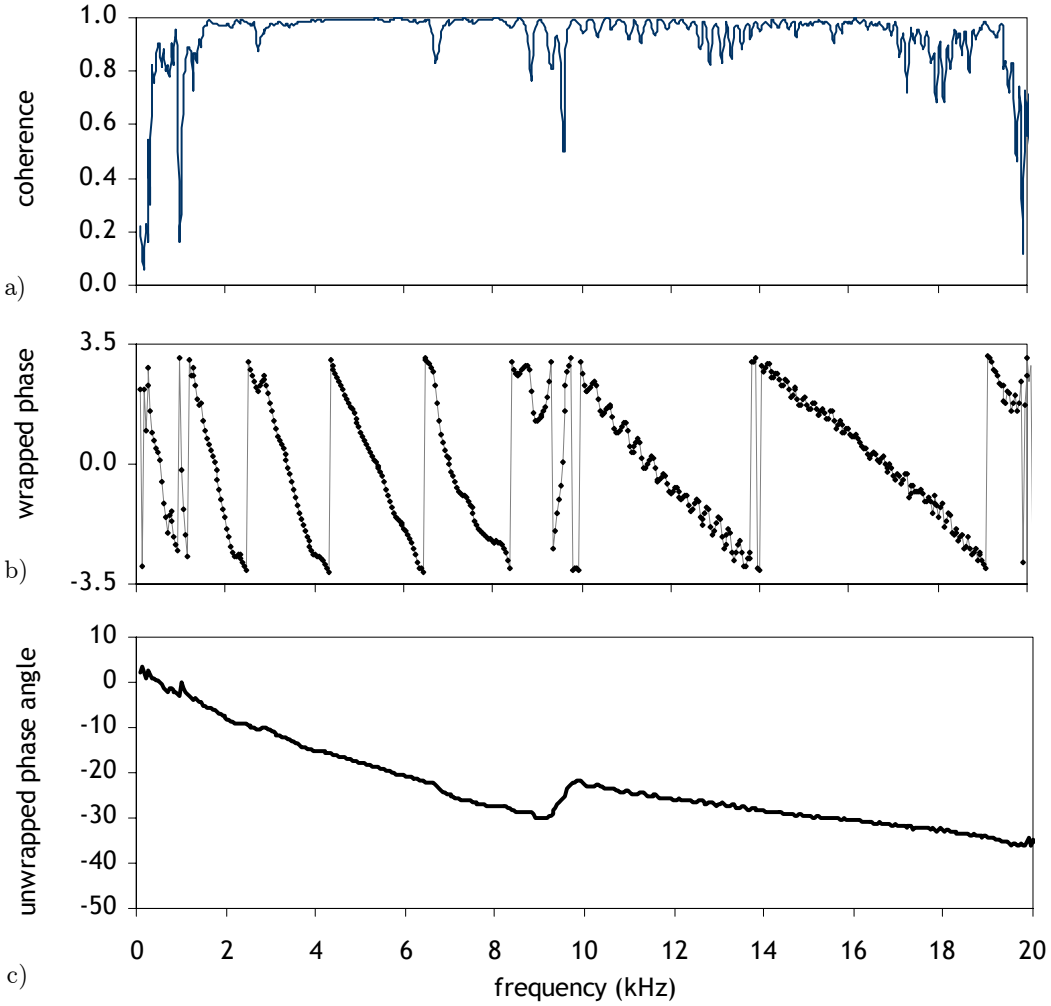


Figure 7.5 - RC+BE sample S1.2.4: FD results at 50 kPa, complete frequency range

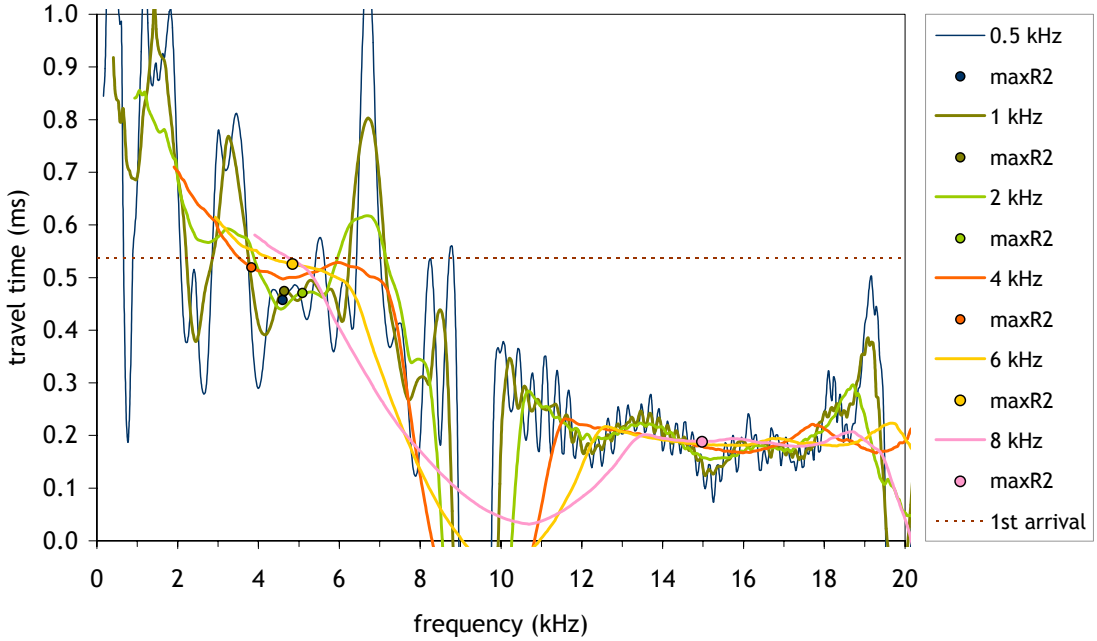


Figure 7.6 - RC+BE sample S1.2.4: FD results at 50 kPa, travel time spectra

Since the travel time is computed from the slope of the best fit line, the correlation coefficient (R^2) of the regression can be used as an indicator of the quality of its estimate. Hence, the maximum correlation coefficient should, in principle, point out the most reliable travel time associated with each frequency window. This information is included in this figure, by means of markers corresponding to the maximum correlation coefficients for each window.

An alternative and more informative graph is provided in Figure 7.7, where only the travel times associated with correlation coefficients greater than 0.98 are represented. This is a refined and simplified view of Figure 7.6 and enables to narrow down the possibilities and thus minimize the errors in the selection and determination of the travel time of the shear wave.

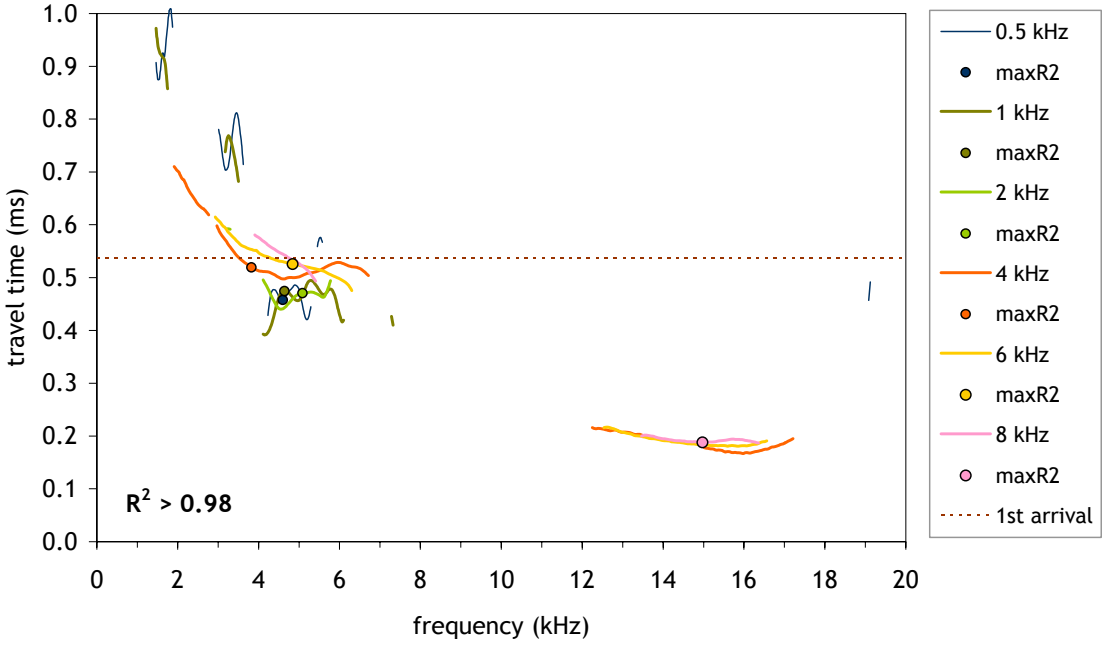


Figure 7.7 - RC+BE sample S1.2.4: FD results at 50 kPa, travel time spectra for R^2>0.98

This simplified travel time spectra clears the view and highlights the position of the markers. Most of these markers appear in this case concentrated around 4 to 5 kHz, which corresponds to the zone of highest coherence between the signals (as seen in Figure 7.5a). This information can be used to select the most suitable frequency for TD measurements, or where the interpretation of the TD results should focus for the identification of first arrival.

In this graph, the variations of travel time with respect to the window size are not as evident as in Figure 7.6. It is interesting to observe that one of the markers appears

clearly astray from all other points and that point corresponds in fact to the widest window of 8 kHz, usually taken as more reliable. In this particular case, the 8 kHz maximum-R^2 point is positioned at 0.18 ms (and 15 kHz), at a lower travel time and a much higher frequency than all other markers. It is likely to be related with the earlier arrival of the compression wave, as it is relatively close to the TD estimate of the P-wave arrival, previously discussed.

Nevertheless, since this determination of travel time is a mathematical process based on statistical analyses, there is always the possibility of obtaining erroneous or misleading results. For this reason, the use of experience and judgement is advocated in opposition to a fully-automated interpretation.

These computations have been made using open-source software and this is advantageous in the sense that the program can be adjusted and adapted to the requirements of each specific study. For example, the use of other wider or narrower frequency windows may be more appropriate for best-fitting more spread or more clustered results, respectively. On the other hand, different frequency ranges for the input sweep signal may be better suited to excite distinct soil stiffnesses, e.g. lower frequencies (100 Hz - 10 kHz) for soft soils and higher frequencies (1 kHz - 50 kHz) for stiffer materials, such as heavily compacted and/or soil-cement samples (Rios Silva et al., 2008). Obviously, these frequency ranges can only be effectively varied within the specific range of frequency response of the bender elements.

7.2.2.2. RC measurements and calculations

The resonant-column apparatus used for this work is installed at the Geotechnical Laboratory of IST, in Lisbon. As previously mentioned in the description of this equipment in Chapter 3, this is a Hardin-type oscillator. In the conventional resonant-column test (RC-CT), a cylindrical specimen is subjected to torsional vibration in the form of continuous sine excitation. At each test stage, the input frequency is manually varied until resonance is reached. Under this resonant condition, the values of the resonant frequency, current, output amplitude and displacement of the sample are recorded, from which the shear strain, shear modulus, damping ratio and void ratio are automatically computed.

Since this process is carried out manually, it becomes time-consuming, which could be improved with the use of an automated system. Within the scope of another research project (Santos et al., 2007; Camacho-Tauta, 2007, 2009), various options were analysed and the use of random noise (RC-RN) was considered an appropriate

input solution. This option was the advantage of distributing the energy by all frequencies and enables to measure very low strains (Cascante & Santamarina, 1997). The amplitude of the response varies with the frequency of the random noise, and the frequency to which the transfer function reaches a peak corresponds to the resonant frequency of the system.

For the purpose of direct comparison with the BE measurements, the shear wave velocity and corresponding travel time were back-calculated from the RC shear modulus, using the equations deduced from Equation 7.1, presented below:

$$V_S = \sqrt{\frac{G}{\rho}} \qquad [7.11]$$

$$t = L \cdot \sqrt{\frac{\rho}{G}} \qquad [7.12]$$

7.2.2.3. Comparison of BE and RC results

A summary of the test results on sample S1.2.4 in terms of travel times and shear moduli from BE in time and frequency domain and from RC are provided in Table 7.4. The travel time derived from the RC shear modulus is also presented. Figure 7.8 shows the evolution of the shear moduli obtained by the three methods in relation to the mean effective stress.

Table 7.4 - Test results on RC+BE sample S1.2.4: BE and RC small strain parameters

stage	σ'_v	σ'_h	ε_a	ts FD	ts TD	G FD	G TD	G CR	ts via CR
#	[kPa]	[kPa]	[%]	[ms]	[ms]	[MPa]	[MPa]	[MPa]	[ms]
00	0.0	0.0	0.000	0.840	0.842	25.11	24.99	24.11	0.857
01	20.0	20.0	0.229	0.671	0.650	39.10	41.67	35.50	0.704
02	50.0	50.0	0.640	0.525	0.537	63.29	60.49	54.93	0.564
03	100.0	100.0	1.356	0.428	0.440	93.71	88.67	86.72	0.445
04	200.0	200.0	1.719	0.395	0.360	109.12	131.37	123.71	0.371
05	300.0	300.0	2.168	0.348	0.324	139.17	160.55	158.46	0.326
06	300.0	300.0	2.181	0.346	0.311	140.42	174.20	160.61	0.324

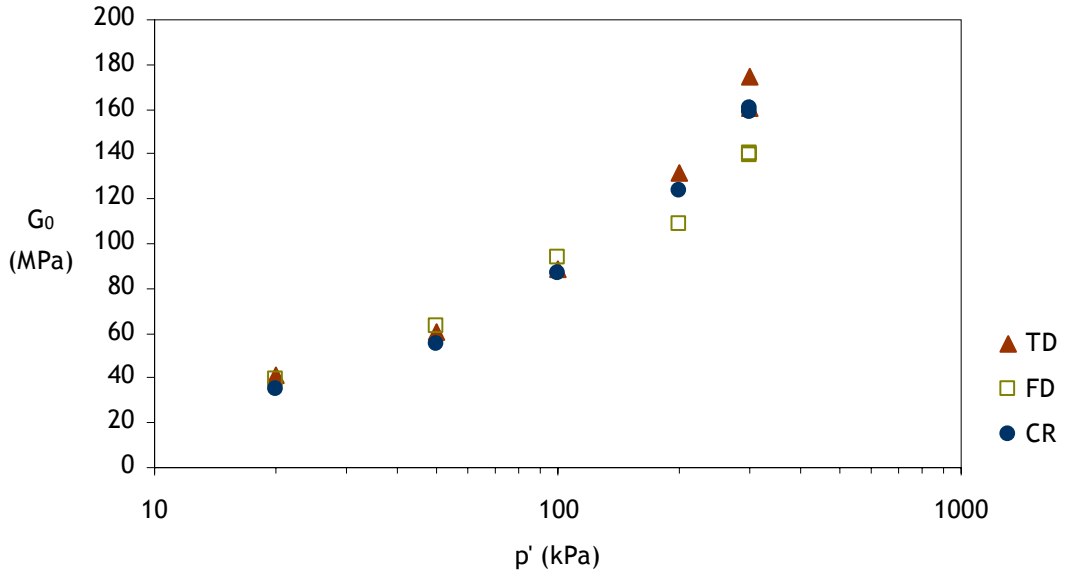
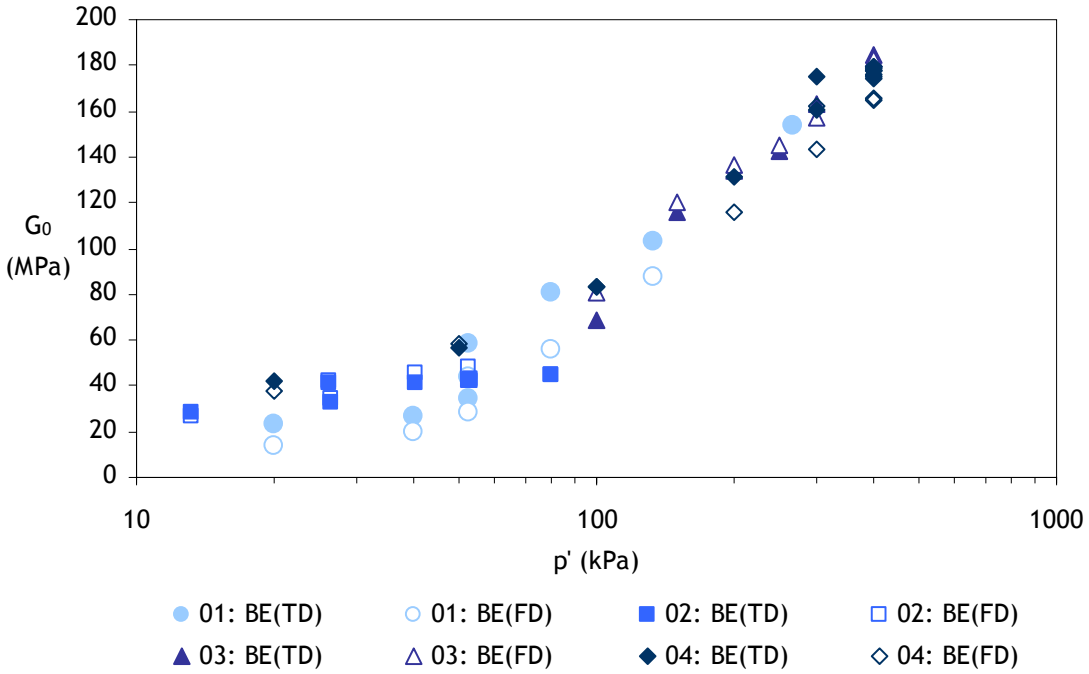


Figure 7.8 - RC+BE sample S1.2.4: evolution of G_0 with mean effective stress

These results demonstrate a relatively good agreement among the three methods, especially at lower effective stresses. Considering the evolution of the BE shear modulus presented in the table, from an initial value of about 25 MPa, an increase of more than 6 times was measured reaching 140 MPa (FD) and 174 MPa (TD). This increase of 6 times in G_0 corresponds roughly to a decrease of 2.5 times in travel time. Assuming that there might be systematic (or fixed) errors involved in the measurement of the travel time, the effect of these errors in the determination of travel time will be increased and therefore become more pronounced at higher stresses. The results presented in the graph are in agreement with this hypothesis, since the differences between the methods are increasing with stress.

The resonant-column results appear in general in-between the BE results, with TD generally providing the highest estimates of the shear modulus. The evolution of the FD results is less "stable", in the sense that it is at times the highest and at other times the lowest value.

The same interpretation procedure was followed for all other samples. The final results of the evolution of the shear modulus, determined by the two BE interpretation methods, with mean effective stress are shown in Figure 7.9, for the four specimens from ES1 (see Table 7.2).



[Note: The numbers indicate the tested specimens: 01-S2.6.2; 02-S2.2.3; 03-S1.2.3; 04-S1.2.4]

Figure 7.9 - Variation of G_0 with p' for all samples, from BE measurements in TD and FD

The measured RC shear moduli were then plotted over the BE results of the previous graph. For the comparison, the results were grouped according to the measurement technique: BE-TD, BE-FD and RC, as presented in Figure 7.10.

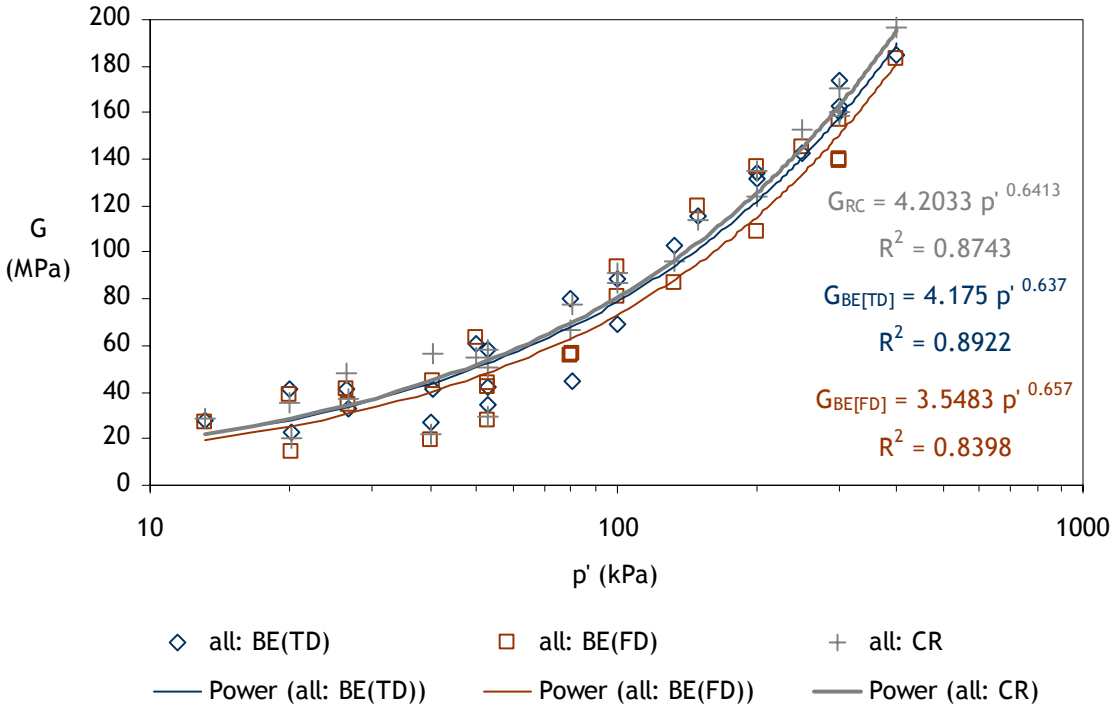


Figure 7.10 - Variation of G_0 with p' for all samples, from RC and BE measurements

The results exhibit significant similarities in terms of the G_0 versus p' relation and the dispersion between RC and the two BE methods are relatively small. The derived equations for this relation, respective to each method, evidence good convergence. These equations are merely indicative for the dependence of G_0 with p', and will be examined in detail in the following chapter, after the definition of the references indices from triaxial tests on reconstituted specimens. It is assumed that the obtained constants (multiplier and exponent) incorporate very important contributions from void ratio, structure, stress history, among others, which must be addressed separately. It is interesting to note that these are not normalized results and, despite the diverse stress paths followed in each test, the overall curve for each method appears to fit reasonably well with the whole set of points.

Assuming for the resonant-column the role of calibrator of the BE methods, the G_0 values measured by the RC were taken as reference and the relative distance between methods was assessed, as shown in Figure 7.11. This plot enables to conclude that the FD domain technique results in G_0 values that deviate from those measured by the RC by less than 7% in average. The time domain provided values of G_0 that are within an average of 2% of the RC values. The lower and upper limits of the ratio between G_0 values for the FD compared with the RC are of about 73% and 115%, respectively. These limits are similar to the ones measured in the TD, which are 72% and 122%, respectively.

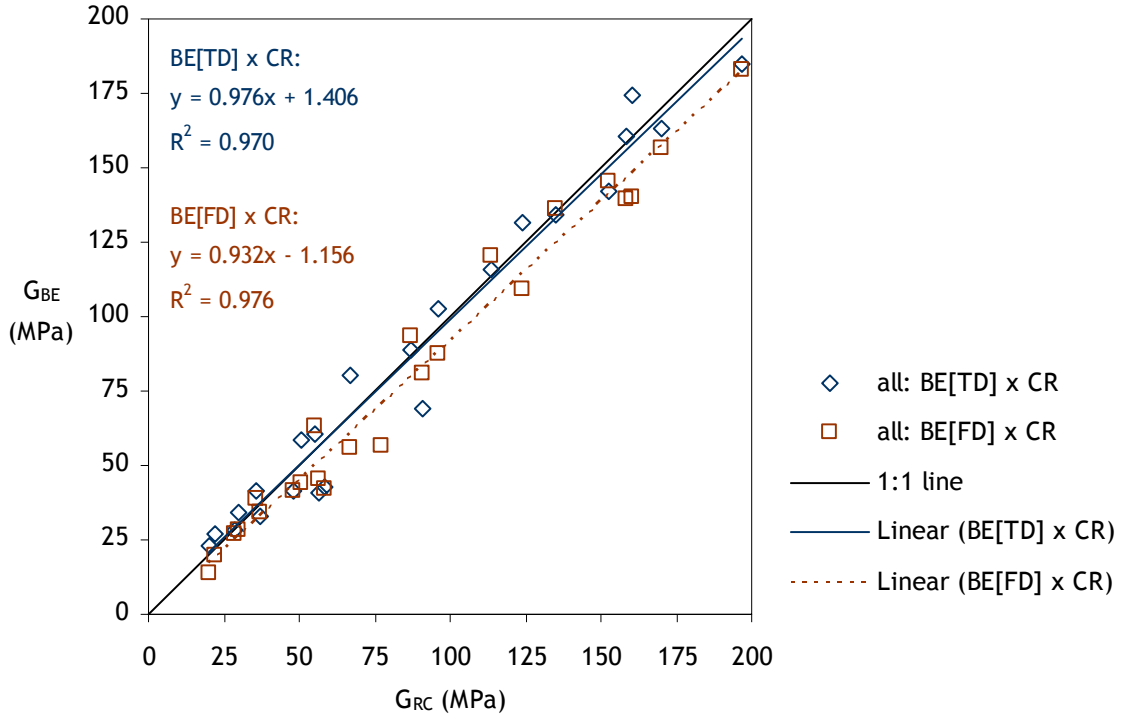


Figure 7.11 - G_0 values derived from the RC versus from the two BE methods

This graph also shows that the frequency domain results generally appear below time domain results, as previously reported by many authors (Greening et al., 2003; Greening and Nash, 2004; Alvarado and Coop, 2009).

7.2.2.4. The influence of the shear strain even at very small strains

In an attempt to investigate the reasons for the greater dispersion of the FD results, data from the test on sample S1.2.4 were used to compute the ratios between the shear moduli from BE (TD and FD) and from the RC, which are indicated in Table 7.5. These ratios were then compared with the shear strain induced by the RC at each measurement, as presented in Figure 7.12. The measurements considered in this comparison were only those obtained at the isotropic consolidation stages.

In resonant column testing, the determination of the resonant frequency from which the shear modulus is computed, requires the application of an elastic vibration to the soil specimen. With the information provided by the amplitude and current, the determination of the associated strain, induced by the vibration in resonance, is made by the application of an implemented algorithm. Despite the very low range of strains involved (around 10^{-6}), some variation exists, which is unrelated with the confining stresses, but which is directly related with the operational requirements for the measurement in the RC. Therefore, this strain is directly related with the measured small-strain stiffness parameter.

The scatter in this graph of Figure 7.12 is quite significant, so only preliminary conclusions can be drawn. While TD results seem to be less affected by the shear strain, FD results appear to line up with the increase of shear strain. This means that for RC strains below 4.2×10^{-6}, the BE-FD results are providing lower estimates of G_0, which could be interpreted as indicative of the strain level at which these bender elements are operating. On the other hand, for (slightly) higher strains, the BE-FD values of shear moduli are systematically higher than those obtained via the RC.

Table 7.5 - Test results on RC+BE sample S1.2.4: ratios of G_0 obtained by the 3 methods

stage #	σ'_v [kPa]	σ'_h [kPa]	ε_a [%]	RC ε_s [-]	G FD G RC	G TD G RC
00	0.0	0.0	0.000	4.2E-06	1.041	1.036
01	20.0	20.0	0.229	4.5E-06	1.101	1.174
02	50.0	50.0	0.640	4.7E-06	1.152	1.101
03	100.0	100.0	1.356	4.2E-06	1.081	1.022
04	200.0	200.0	1.719	4.0E-06	0.882	1.062
05	300.0	300.0	2.168	3.8E-06	0.878	1.013
06	300.0	300.0	2.181	3.8E-06	0.874	1.085

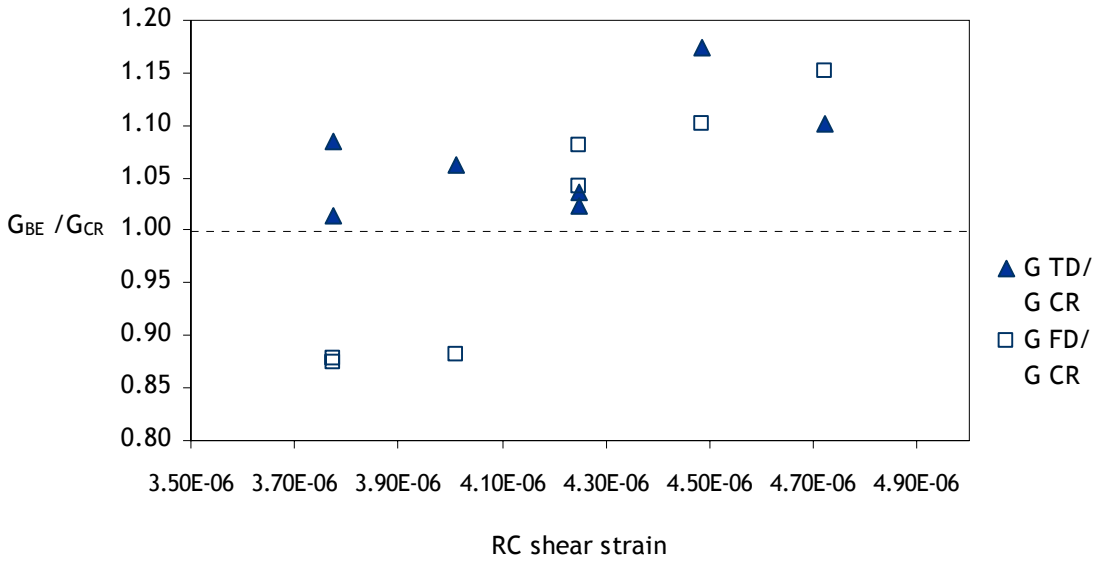


Figure 7.12 - RC+BE sample S1.2.4: evolution of the G_0 ratios with RC shear strain

These results suggest that there is an influence, even at very low strains, of the shear strain at which the measurement is made, in the measured value. Moreover, it points towards the possibility that the input signals used in TD and FD induce different strains, thus provide different values.

This hypothesis converges with another reported work in the comparison between two different types of excitation signal in resonant-column testing. Santos et al. (2007) tested an undisturbed specimen of Lisbon alluvial clay, using not only the conventional method of resonance (RC-CT) as well as a random noise excitation (RC-RN). The latter required the calculation of the transfer function, from which the resonance frequency of the system could be determined. One of the advantages is that it is possible to measure stiffness at even lower strains. The graph in Figure 7.13 shows the comparison of the results obtained by the two methods in the same test, at

different confining stresses. The non-conventional method of random noise was capable of detecting higher shear moduli at very low strains, often lower than 10^{-7}.

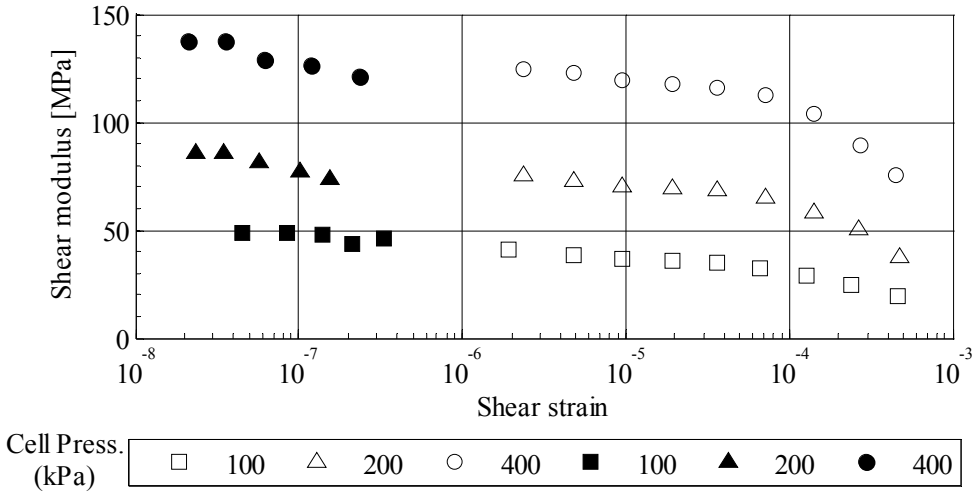


Figure 7.13 - Comparison between RC-CT (hollow symbols) and RC-RN (solid symbols) (after Santos et al., 2007)

While both RC testing methods follow approximately the same curve, the maximum shear modulus obtained by RC-RN tests is higher than the maximum shear modulus measured by RC-CT (about 20% at 100 kPa and 10% at 400 kPa). These authors were able to identify stiffness degradation, for shear strains greater than 10^{-7}.

The last RC+BE tests carried out in this research programme, namely B5-1-RC, included BE measurements both TD and FD approaches and RC measurements using the conventional method as well as the non-conventional method, with a random noise input signal. Initially, the main purpose of this test was to evaluate the performance of the RCCT and RCRN methods in a different soil and to compare it with the results obtained by Santos et al. (2007).

With the new findings in mind, this test on sample B5-1-RC provided an opportunity to complete the analysis in terms of the influence of the shear strain at very small strains, not only in RC but also in BE testing. An overview of the results obtained by means of the four methods (BE-TD, BE-FD, RCCT and RCRN) is presented in Figure 7.14. The graph shows larger differences between BE and RC results than in any other test. In particular, the results from frequency domain are clearly distanced from all other measured shear moduli.

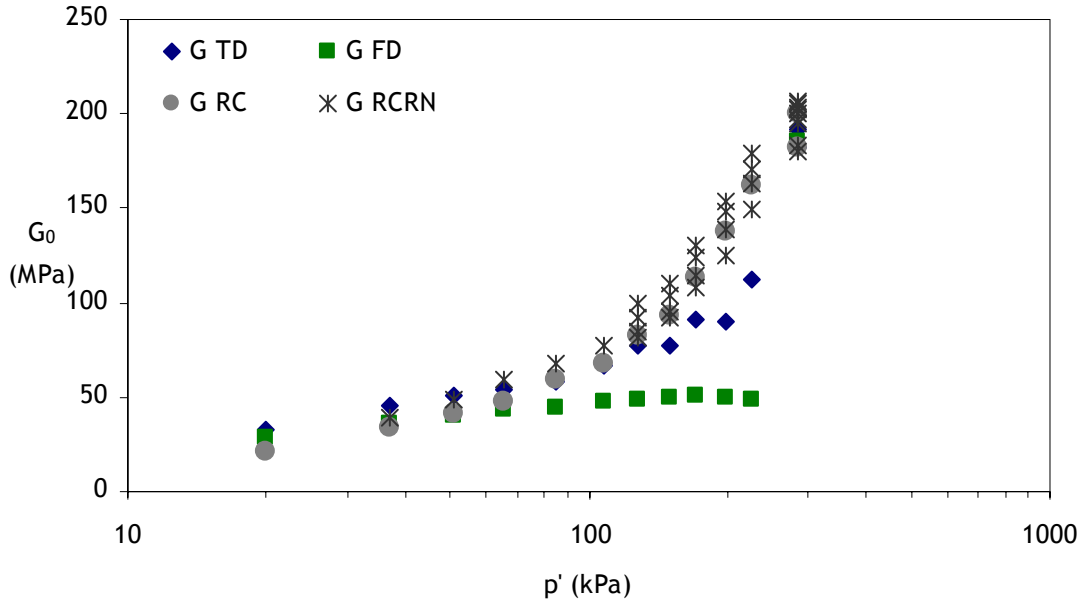


Figure 7.14 - RC+BE sample B5-1-RC: evolution of G_0 with mean effective stress

Four ratios of shear moduli measured by the two BE methods with those measured using the two RC methods can be computed from these data. The representation of the ratios against the respective shear strain at which the RC moduli were obtained is provided below, in Figure 7.15.

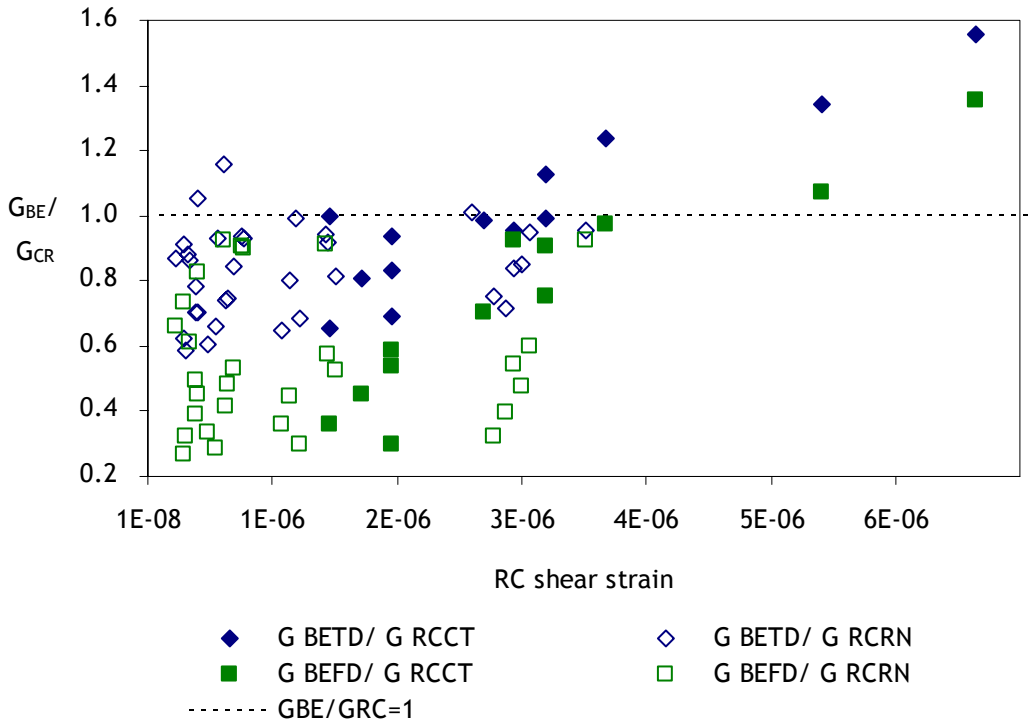


Figure 7.15 - RC+BE sample B5-1-RC: evolution of the G_0 ratios with RC shear strain

The first impression of this plot is the resemblance with that in Figure 7.12. Again, the ratios appears to increase with increasing strain levels, that is to say, at higher RC shear strains, the shear modulus measured by the BE will be greater than the corresponding RC modulus. And once again, the TD method resulted in higher values of shear modulus and, consequently, of BE-to-RC ratios than the FD method.

The plots of the two figures are, however, different in the range of the induced shear strains. In this test, since two RC methods were used, it was possible to obtain RC measurements at considerably lower strains and for a much wider range of strains. In terms of the BE, it appears that in this case TD results are also related with the shear strain, however at lower values than the FD results. As before, strains of about $4x10^{-6}$ appear to define a threshold for the shear modulus measured by the FD method: for lower strains, this method underestimates the stiffness in relation to that measured by the RC.

Before any further conclusions, it is relevant to look at all the data provided by these tests and compile the ratios of BE and RC measured shear moduli. In Figure 7.16, these results are plotted together to identify the overall similarities and differences. Despite exhibiting considerable scatter, the points from both BE techniques clearly reveal a trend, indicating a relation between the BE and RC shear moduli ratios and the shear strain at which each RC shear modulus was measured. The best-fit lines for the ratios of each BE method are also included in the graph.

This effect of strain in the measurement of G_0 at very low strains has not yet been put forward as a potential reason for the discrepancies between interpretation methods, however it appears to be influential.

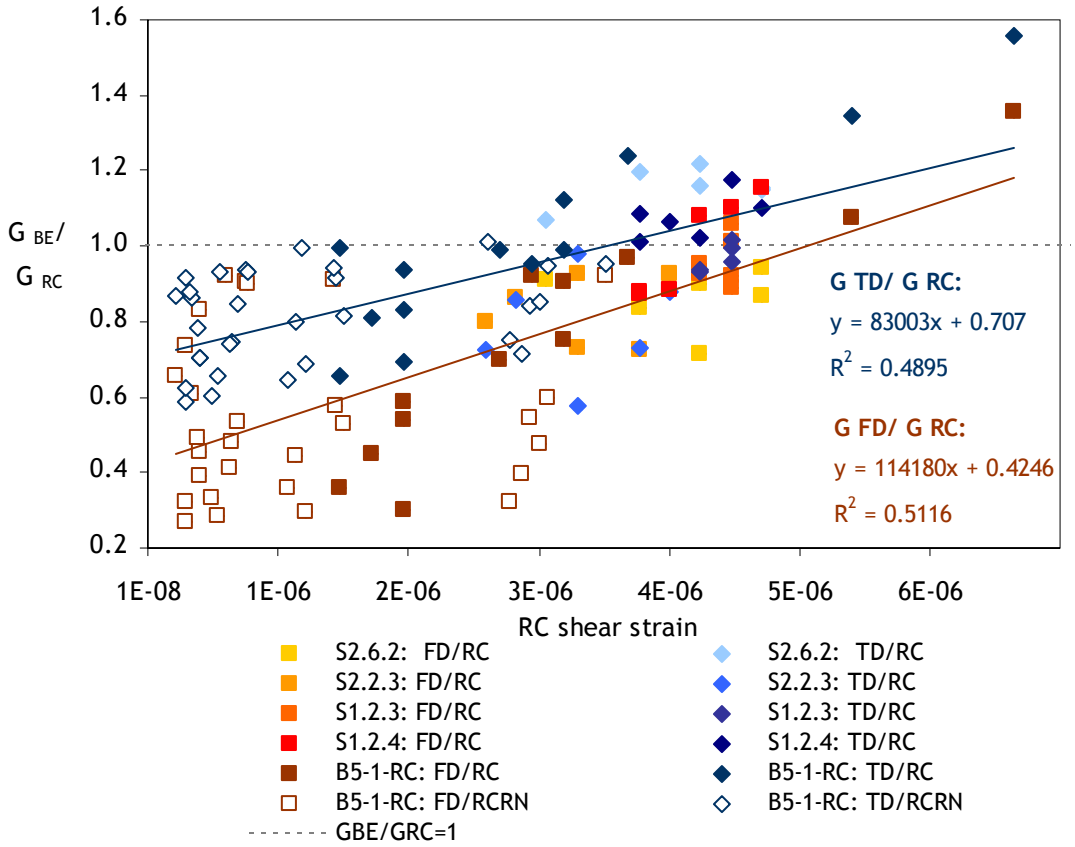


Figure 7.16 - Variation of the G_0 ratios with RC shear strain for all RC+BE tested samples

To understand these graphs and to accept the possibility of the influence of the shear strain in bender element and resonant-column measurements, it is worth revisiting some aspects regarding each method.

In bender element testing and for the frequency domain method, each BE measurement is made using the same input sweep signal at a fixed voltage amplitude (20 V_{pp} in this apparatus), thus it can only be expected that the strains induced by the BE on the soil are repeatedly the same.

For the time domain method, a number of input pulse signals are used, also at fixed voltage amplitude but at different frequencies. It is widely recognised that these different excitation frequencies induce different transducer responses with higher or lower amplitudes, as observed when calibrating a pair BE in direct contact. For example, at resonant frequency, the signal obtained at the receiver element is generally sharper and stronger (in terms of amplitude or energy), thus implying a greater movement of the bender element. Clearly, different frequencies cause a slightly different pattern of movement in the bender element in contrast with the

RC. However, these differences have always been considered negligible in terms of the measured travel time. Moreover, since a unique travel time is defined from each set of TD readings, the final value incorporates such differences. In sum, given the same nature and amplitude of the signals, the strains induced on the soil in TD measurements are also expected to be identical.

Obviously, FD sweep signal and TD pulse signals are distinct. A sweep signal is a non-harmonic continuous signal, thus producing a dynamic steady-state response. On the other hand, pulse signals, due to their finite duration, cause a transient response. Rio (2006) studied in depth the dynamic behaviour of bender elements and investigated its response to different types of excitation, namely pulse, continuous and sweep signals. For this purpose, the oscillation of two BE, with different dimensions, was monitored using a laser velocimeter. In this work, different BE displacements were observed according to the imposed excitation signal and to the boundary conditions of the transducers, that is, in free vibration in air and embedded in an artificial sample. Naturally, the highest oscillation occurred for the transducer moving in air as a free cantilever, since when embedded the movement is attenuated. The maximum amplitudes of oscillation are summarised in Table 7.6. From these results, it is not possible to directly extrapolate any conclusions regarding the response of the pairs of BE used in the present research, since the performance of BE-1 is opposite to BE-2 in relation to the type of excitation. These values are, however, indicative of the level of deformation imposed to the BE during testing.

Table 7.6 - Maximum amplitudes of oscillation for two different BE, in air and embedded in a sample for pulse and sweep signal excitation (adapted from Rio, 2006)

Transducers	Tip fixity	Pulse signals	Sweep signal
BE-1	free	8.0 μm	37.0 μm
[1.5x6.5x8.0 mm]*	embedded	2.5 μm	2.3 μm
BE-2	free	6.6 μm	5.9 μm
[1.5x12.0x10.0mm]	embedded	2.6 μm	2.9 μm

[*] dimensions as thickness x width x length

In the light of these results, it is reasonable to accept that pulse excitation signals produce different movements in the BE from those produced by continuous signals.

Many authors have attempted to determine the shear strain induced by the BE in the soil by indirect methods (Dyvik and Madshus, 1985; Leong et al., 2005; Pennington, 1999). The experiments conducted by Rio (2006) provided valuable

information regarding the deformation of the transducer in two different boundary conditions (or tip fixities), but the actual shear strain in soil could not be determined.

The information condensed in Figure 7.16 can be analysed to estimate the shear strain associated with each BE method, under the assumption that a G_{BE}/G_{RC} ratio equal to unity (represented by a dashed line) means that the measured value by the BE and the RC was made for the same shear strain.

Under this assumption, it can be said that, in this case and for this particular pair of BE, the shear strain induced by the sweep signal of the FD method is higher than the shear strain caused by the pulse signals used in the TD method. Moreover, the systematic differences, observed here and elsewhere, between TD and FD methods may be explained by the slightly different shear strains at which the BE are excited.

These results indicate that the calibration of the BE in relation to the RC is an interesting and constructive exercise, if the associated RC shear strain is taken in due consideration.

7.2.3. Triaxial tests on reconstituted specimens of residual soil

A number of reconstituted samples were prepared and tested under conventional triaxial conditions. These tests were performed mainly for the identification of the dependence of the shear modulus in relation to the void ratio, the stress conditions and directions, considering the reconstituted samples as a non-structured soil. Important issues such as structure and anisotropy can also be discussed in the light of these test results, by comparison with the undisturbed material.

From all the triaxial tests carried out on reconstituted specimens, the following section will focus on the results obtained on a few specimens. The main physical properties of the tested specimens are detailed in Table 7.7.

Table 7.7 - Reconstituted specimens used for definition of reference indices

Specimen	γ	w	e	σ'_{vc}	σ'_{hc}	p'	q
	[kN/m^3]	[%]		[kPa]	[kPa]	[kPa]	[kPa]
R2-isoCF1	20.0	30.8	0.909	1100	1100	1100	0
B2.0.70	17.69	24.2	0.857	500	500	500	0
S2.2.0	19.19	21.2	0.662	45	22.5	30	22.5

7.2.3.1. Definition of references indices from reconstituted specimens

An isotropic test on a reconstituted specimen provides a wealth of information, namely regarding the reference indices. The isotropic conditions are ideal to remove stress-induced anisotropy. On the other hand, the use of a reconstituted soil specimen enables to consider that the effect of natural structure is inexistent and, thus, the value of S_{ij} in the fundamental equation of shear modulus [Equation 7.4] is constant throughout the test.

For the definition of the void ratio function, the shear modulus should ideally be determined at different void ratios under the same state of stress. This can be achieved by performing the test with a series of unload-reload stress cycles, with repeated measurements of shear wave velocity at selected stress states.

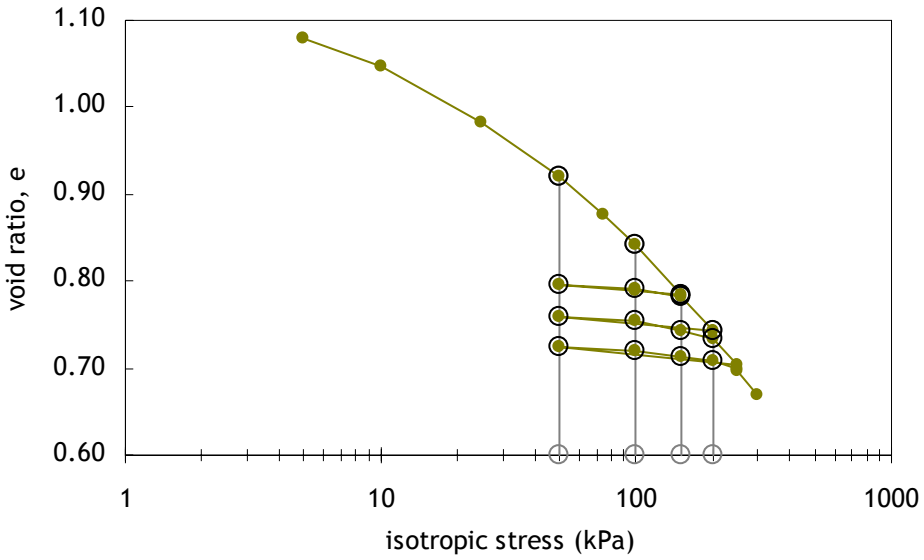


Figure 7.17 - Schematic of the stress path for the definition of the void ratio function

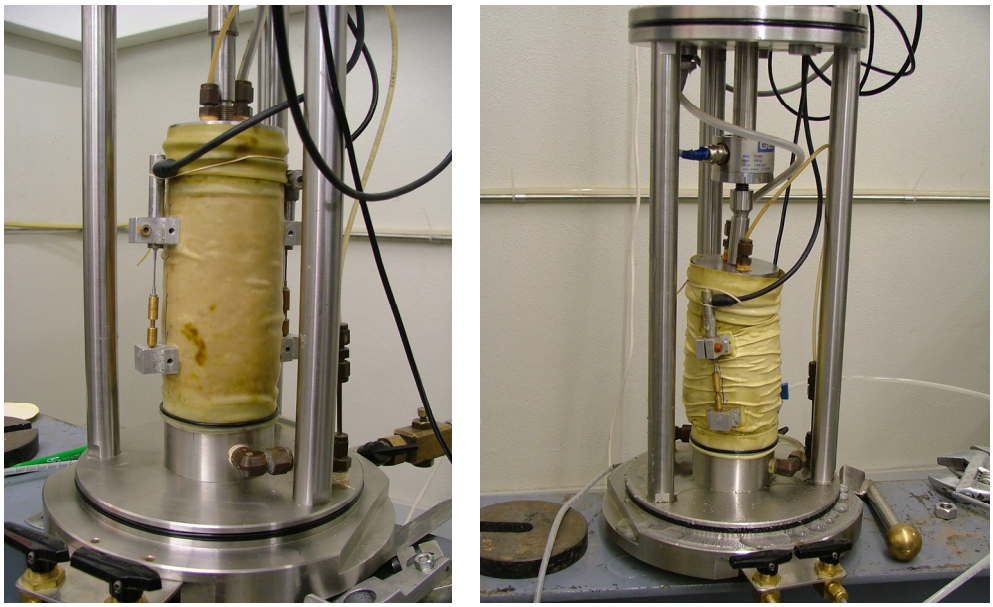
Clearly, there is an important assumption being made here, which is that the void ratio function is capable of capturing not only the effects of volume change and consequent stiffness change but also the effect of the overconsolidation.

Once the void ratio function is defined, the parameter S_{ij} and the stress indices, that is, the exponent(s) of the stress component(s) can be determined. The value of S_{ij} derived from a reconstituted sample should correspond to the minimum for this material and can be taken as a reference for those obtained in undisturbed samples.

7.2.3.2. Definition of the void ratio function in isotropic conditions

The R2-isoCF1 sample was prepared at a high moisture content (w~30%), in an attempt to minimize layering of the soil particles induced by other preparation procedures, such as static compaction. Instead, an initial loose condition was assumed and the desired density was divided by the number of layers to obtain the necessary weight of wet soil per layer. The weighed amount of soil was then spooned to the mould and lightly tamped to level at each layer.

For static measurements, two submersible axial LVDTs were installed, as shown in Figure 7.18a. For dynamic measurements, only top and bottom BE were used in this test. At the time, it was not possible to mount horizontal bender elements in the sides of the specimen. This means that only G_{vh} was measured, which represents a limitation to the scope of the conclusions to be drawn from this test in terms of the complete characterization of the elastic stiffness parameters.



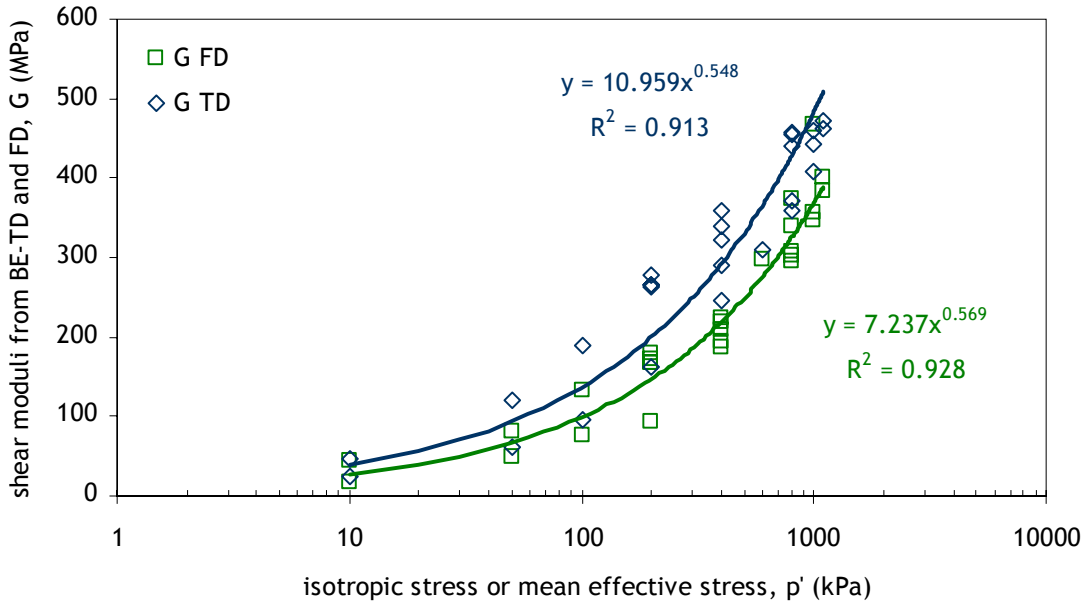
a) b)

Figure 7.18 - Isotropic test on sample R2-isoCF1: a) start and b) end of the test

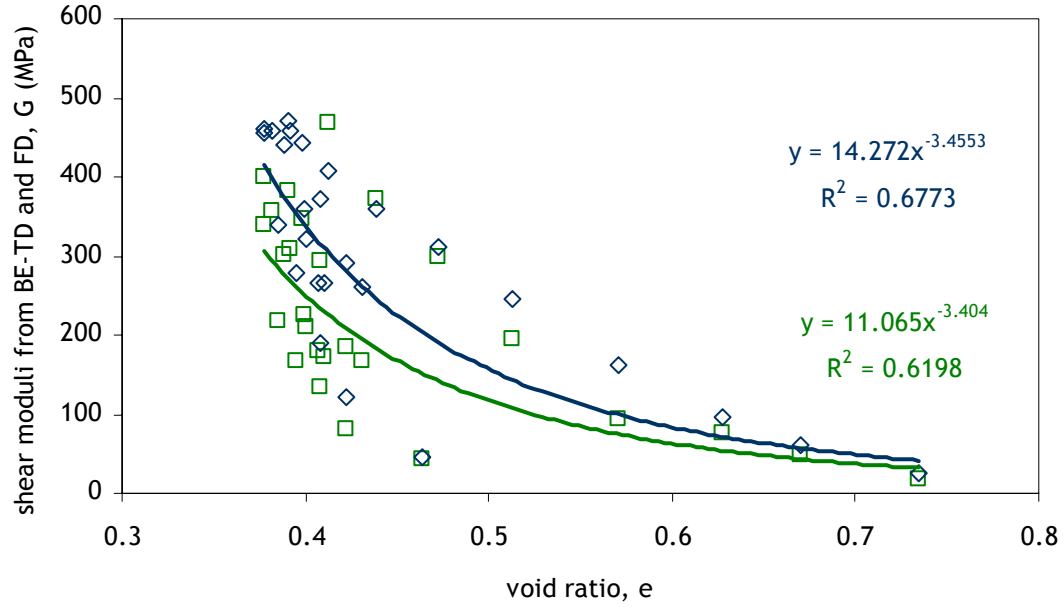
The stress-path consisted on the application of an initial isotropic confining pressure of 10 kPa, followed by saturation at an effective stress of 10 kPa, up to a back-pressure of 300 kPa. When fully saturated, the sample was isotropically loaded in increments up to the maximum applicable in the chamber, which resulted in a maximum effective stress of 1100 kPa. Several unload-reload cycles were applied to the specimen, in order to induce the same stress states. A total of twenty-seven isotropic stress stages were applied and a consolidation period of about 24 hours was

adopted, to ensure stabilisation of the deformation. After such period of time, shear wave measurements were made in the time and the frequency domain.

An overview of the global evolution of the shear moduli obtained from BE-TD and BE-FD with the isotropic stress, or mean effective stress, is presented in Figure 7.19. In Figure 7.20, the variation of the same shear moduli with void ratio is provided.



a)

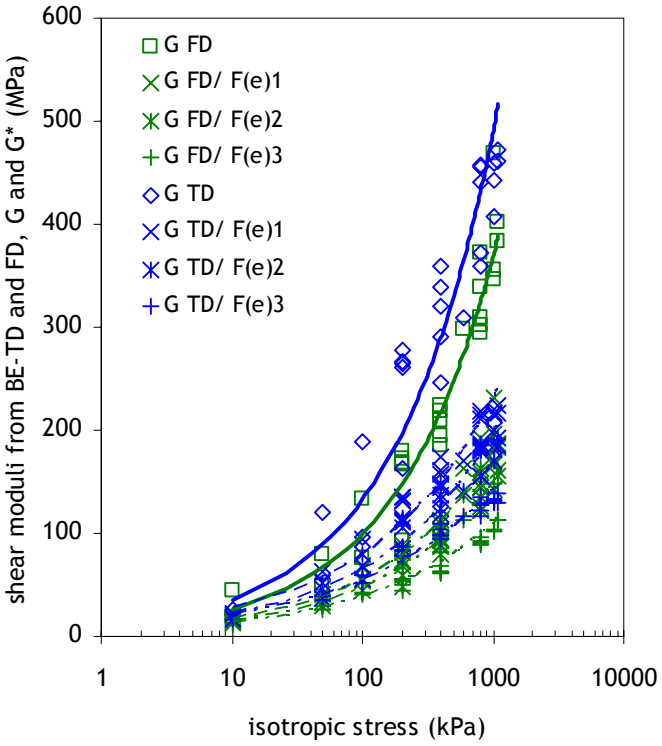


b)

Figure 7.19 - R2-isoCF1 test results: shear moduli obtained by BE-TD and BE-FD against a) mean effective stress; b) void ratio

These results exhibit significant scatter within each BE interpretation method, which is likely to be reduced when normalised to the respective parameters, stress and void ratio.

First, the shear modulus was normalized to each of the void ratio functions defined in Table 7.1, in order to assess their efficiency in improving the relationship with stress. The obtained results are presented below in Figure 7.20. The regression parameters of the best fit curves of G_0 and normalized G_0* to each void ratio function are presented in Table 7.8.



Linear regression parameters for

$$G_0 = S \cdot F(e) \cdot \sigma_{iso}{}'^{n} \text{ and}$$

$$G_0{}^* = \frac{G_0}{F(e)} = S \cdot \sigma_{iso}{}'^{n}$$

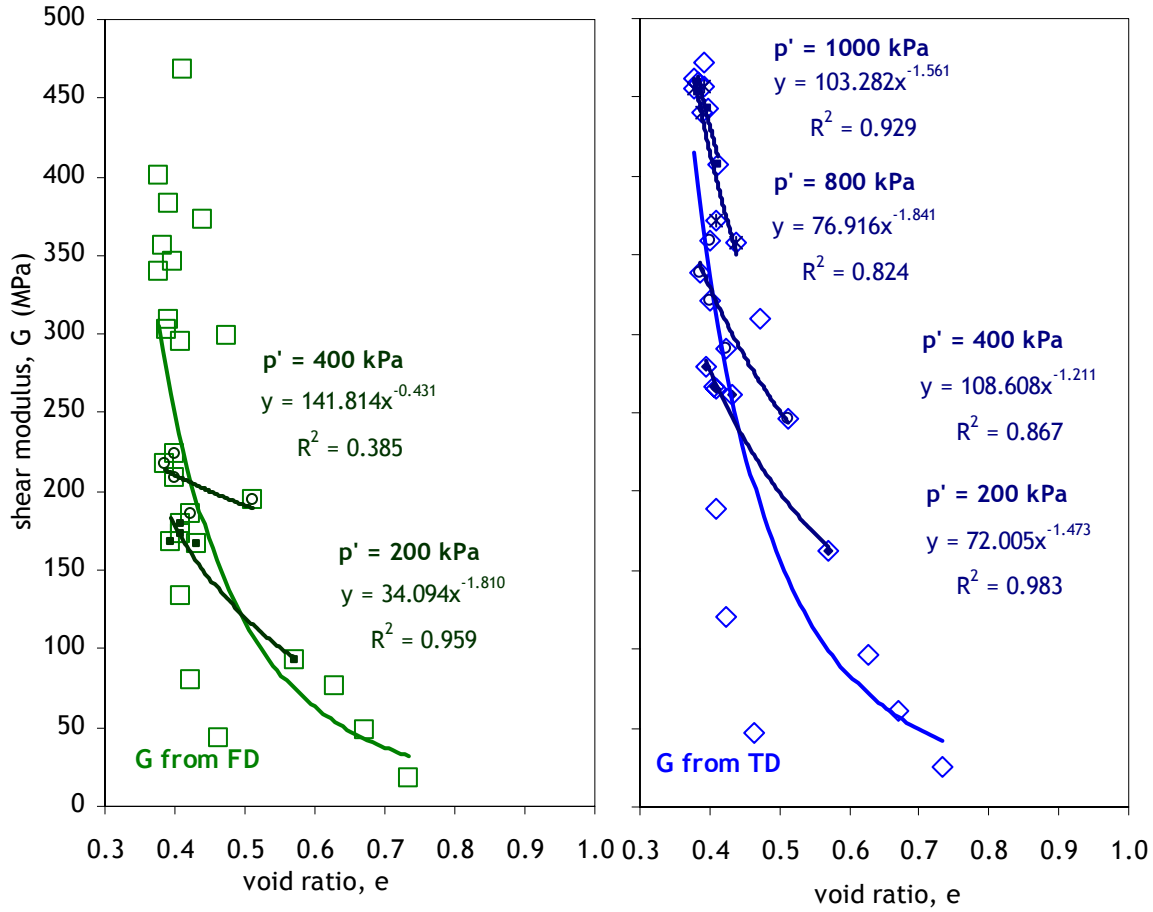
Table 7.8 - Linear regressions

	S	n	R^2
G FD	7.237	0.569	0.928
G FD/Fe1	5.998	0.489	0.959
G FD/Fe2	4.684	0.502	0.959
G FD/Fe3	4.783	0.454	0.956
G TD	10.959	0.548	0.913
G TD/Fe1	9.082	0.468	0.958
G TD/Fe2	7.094	0.481	0.957
G TD/Fe3	7.243	0.433	0.970

Figure 7.20 - R2-isoCF1 test results: shear moduli from BE-TD and BE-FD against mean effective stress and normalised to different void ratio functions

The obtained correlation parameters indicate that all three void ratio functions improve the quality of the relationship of shear modulus with effective stress, thus confirming the need to normalise the stiffness for comparative purposes.

In order to define, if possible, a more adjusted and soil-specific void ratio function, the G_0 results were grouped according to the applied stresses, that is at the same stress state, and analysed against the void ratio. The obtained results are plotted in Figure 7.21.



a) b)

Figure 7.21 - Shear moduli from BE-FD and BE-TD against void ratio, with trends taken at the same isotropic stresses

The trends presented in the above graphs show considerable variability according to the respective stress state. For the FD results, it was only possible to consider those obtained at 200 and 400 kPa, due to the low correlation coefficients obtained for other stress states. For the TD results, regressions were made for 200, 400, 800 and 1000 kPa with acceptable correlation coefficients.

These results suggest that the void ratio function is incapable of fully described the evolution of the shear modulus at the same isotropic stresses after each unload-reload cycles, which can be justified by the non-consideration of the increasing over-consolidation ratio, OCR.

The derived values for the exponent of void ratio function F(e)4 e^{-x} were quite diversified, and the average value of the trends (considering only regressions with R^2 greater than 0.80) corresponded to 1.60. Since this value is relatively close to that of

function 3 and taken into account the variability of the derived exponents, it was considered more prudent to adopt F(e) 3, that is, with x equal to 1.30. The absolute and normalised shear moduli (in relation to this void ratio function) obtained for this sample are represented in Figure 7.22.

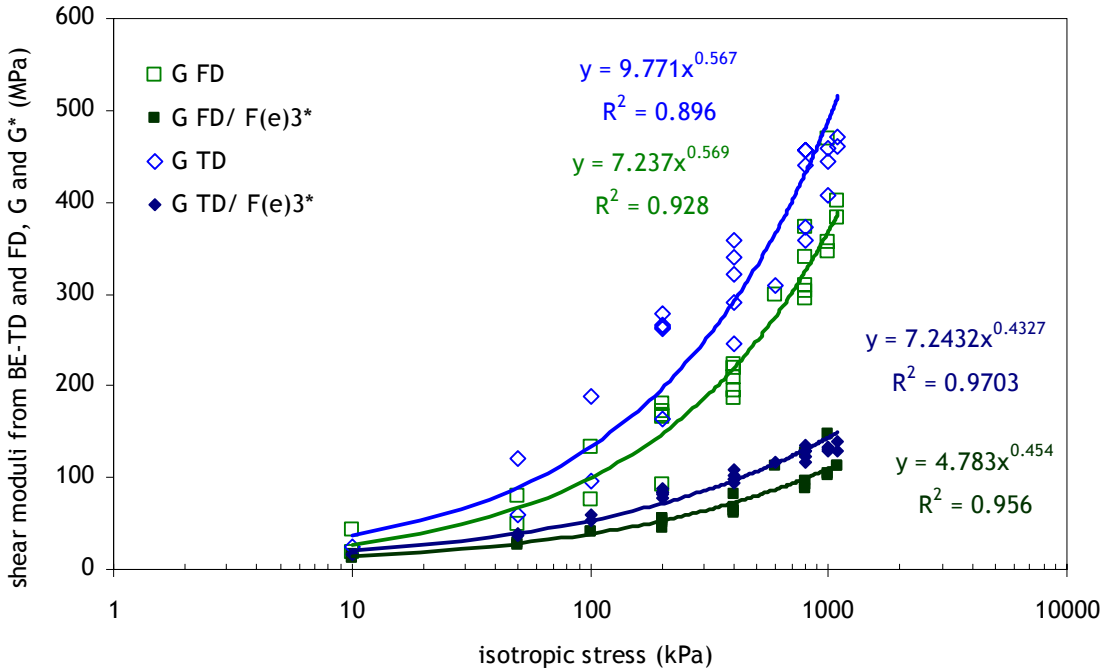


Figure 7.22 - Comparison between absolute and normalised G_0 to the defined void ratio function against isotropic stress

In the light of the previous results, two separate expressions have been derived:

$$G_{FD} = 4783 \cdot e^{-1.3} \cdot \sigma'^{0.454}_{iso} \quad [7.13]$$

$$G_{TD} = 7243 \cdot e^{-1.3} \cdot \sigma'^{0.433}_{iso} \quad [7.14]$$

It can also be concluded that, for the purpose of characterisation of the evolution of the shear modulus with stress, only normally consolidation stages should be considered, especially for the natural samples.

7.2.3.3. Definition of the stress indices from reconstituted specimens

The comparison of these results with those obtained from other reconstituted specimens enabled to extract the dependence of the shear modulus with the individual components of stress. Naturally, in the triaxial apparatus it is only possible to distinguish between the two orthogonal directions of stress, that is, the vertical and horizontal stresses. The stress-dependency of the shear modulus in

relation to its vertical and horizontal components can be made in a triaxial test when one of the stresses is kept constant, while the other is varied.

For this purpose, two other tests on reconstituted specimens of residual soil (B2.0.70 and S2.2.0 from ES1) were carried out, considering isotropic and anisotropic consolidation, respectively. The comparison between the two isotropic tests on samples R2-isoCF1 and B2.0.70 are presented in Figure 7.23.

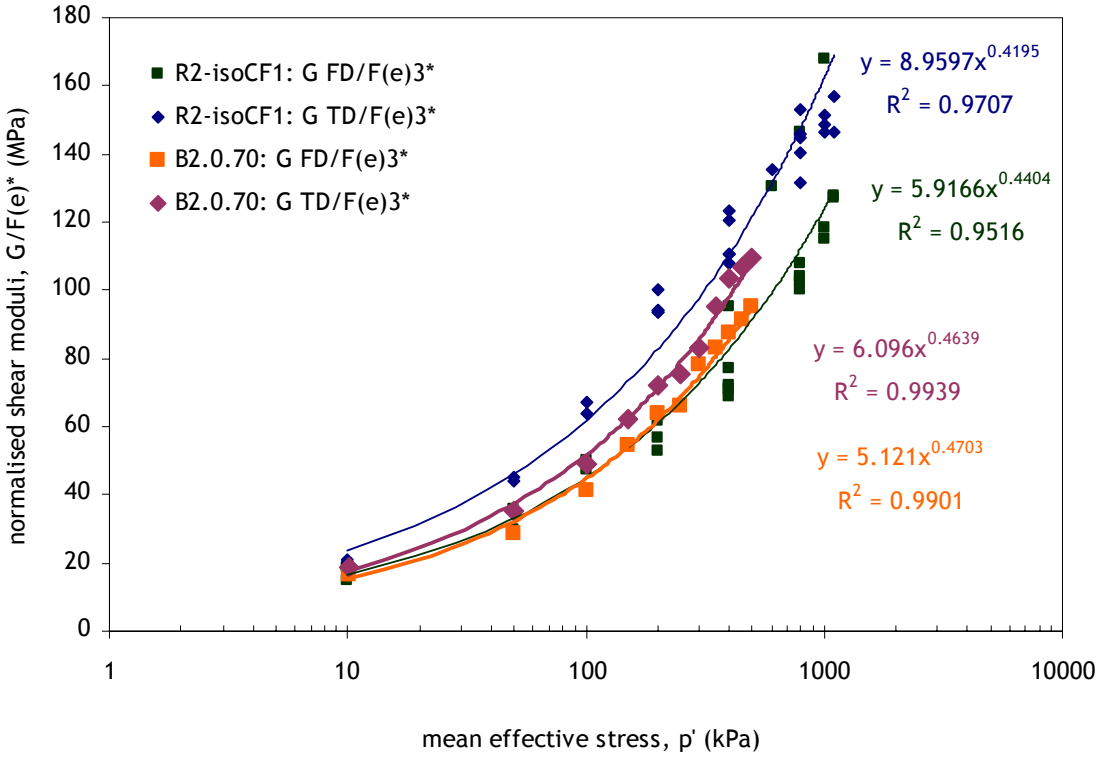


Figure 7.23 - Comparison between R2-isoCF1 (from ES2) and B2.0.70 (from ES1) of the normalised G_0 against p'

The final values of the stress dependency indices are presented in the following table. For the determination of the individual stress exponents, the measured shear moduli were normalised to the previously defined void ratio function, $e^{-1.3}$. These results refer to the initial stages of shearing, in which the vertical effective stress was gradually increased at constant horizontal stress. These results were analysed after normalisation in relation to the void ratio, as previously defined.

Table 7.9 - Values of the references stress dependency indices determined from tests on reconstituted specimens

Reconstituted specimens	G_{max} TD			G_{max} FD		
	n	n_v	n_h	n	n_v	n_h
R2-isoCF1	0.420	---	---	0.440	---	---
S2.2.0	0.432	0.104	0.328	0.432	0.086	0.346
B2.0.70	0.464	0.229	0.235	0.470	0.098	0.372
average values	0.439	0.167	0.282	0.447	0.092	0.359

The results show that the global stress exponent is similar in the time and in the frequency domain. However, the individual exponents of the vertical and horizontal effective stresses are apparently quite different. Given the reduced number of specimens from which the average values are deduced, this conclusion is strictly preliminary.

7.2.4. Triaxial tests on undisturbed samples of residual soil

7.2.4.1. Test results from ES1

A great number of conventional triaxial tests were carried out on undisturbed samples collected from both experimental sites. The majority of the samples from the first experimental site, at CICCOPN, were tested at the estimated in situ effective stresses mainly for its characterisation and for the assessment of sampling disturbance.

In general, the loading stress-path of these undisturbed samples consisted of three distinct stages, in drained conditions: 1) consolidation (generally anisotropic, at K_0 = 0.5); 2) percolation and saturation up to a back-pressure of 300 kPa; and c) shearing at constant horizontal stress, by increments of vertical stress.

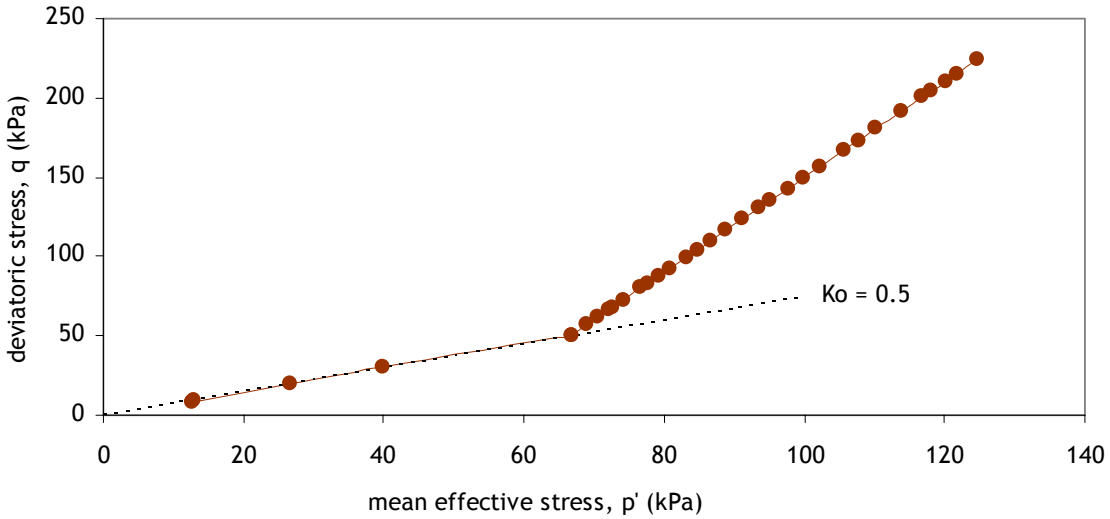


Figure 7.24 - Generic stress-path of undisturbed samples in standard triaxial tests

Some of the samples from this experimental site were tested as part of an earlier research (Ferreira, 2003). Since the results on those samples were directly influential in the selection of the sampling tools for the second experimental site, it was considered relevant to integrate all of the available data here, for a more complete analysis. The full list of samples is presented in Table 7.10.

Table 7.10 - Physical properties and testing conditions of undisturbed ES1 specimens

Specimen	γ [kN/m^3]	w [%]	e	σ'_{v0} [kPa]	σ'_{h0} [kPa]	p' [kPa]	q [kPa]	P- and S- wave records
B2.1.70	18.99	24.7	0.803	45.0	22.5	30.0	22.5	44+44
B2.2.70 #	17.60	23.4	0.877	45.0	22.5	30.0	22.5	31+31
S1.2.1 *	19.27	22.6	0.667	45.0	22.5	30.0	22.5	35+35
S1.4.1	19.22	22.7	0.660	66.7	33.3	44.4	33.3	22+22
S1.6.3	19.30	22.8	0.656	85.0	42.5	56.7	42.5	33+33
S2.2.2 *	19.10	21.6	0.668	45.0	22.5	30.0	22.5	35+35
S2.4.1 *	19.39	22.1	0.649	68.0	34.0	45.3	34.0	45+45
S2.6.1 *	19.87	21.5	0.602	86.0	43.0	57.3	43.0	54+55
S3.2.1 *	19.46	20.5	0.622	47.0	23.5	31.3	23.5	21+21
S3.2.2 *	19.47	21.1	0.642	40.0	20.0	26.7	20.0	24+24
S3.4.1	19.40	20.2	0.623	66.7	33.3	44.4	33.3	7+7
S3.4.2	19.52	19.4	0.610	66.7	33.3	44.4	33.3	23+23
S4.2.1 *	19.35	22.6	0.660	45.0	22.5	30.0	22.5	44+44
S6.2.1 *	18.87	21.8	0.715	45.0	22.5	30.0	22.5	36+36
S6.2.2 *	18.87	21.8	0.718	45.0	22.5	30.0	22.5	39+39
S6.6.1	18.62	22.0	0.717	86.0	43.0	57.3	43.0	19+19

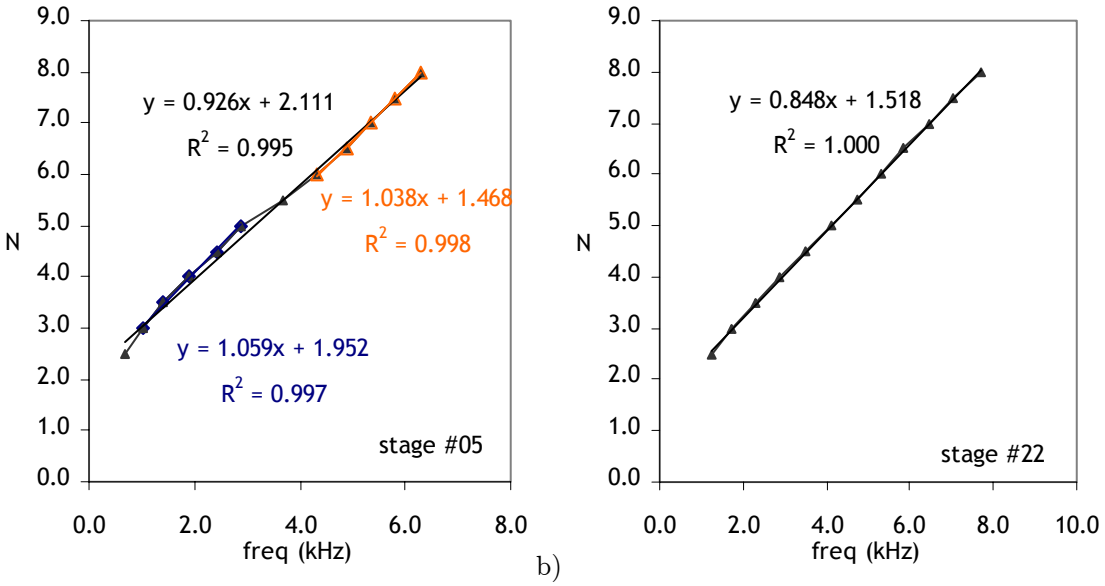
[*] original data from Ferreira (2003)

During each test, many shear and compression wave measurements were made by means of BE, B/EE and/or CT, in all three phases: consolidation (generally anisotropic, at $K_0 = 0.5$), saturation and shearing. The determination of the S-wave first arrival was made in the time domain using a number of relevant frequencies, for which a unique value for travel time was defined. A rudimental version of the frequency domain method was used in many of these tests, which consisted in the definition of the π-point phase frequencies. This method has already been described in section 4.4.4.5.

The π-points method, in its original form, is relatively time-consuming, as it requires manual sweeping of the input frequency. One if its main disadvantages is that the recorded set of frequencies at which the two signals are in- or out-of-phase is obtained without any further knowledge regarding the correlation between them. This limitation has been overcome with the use of specific software, such as ABETS or similar, where a broadband sweep is generated and an algorithm automatically calculates the coherence between the signals and the continuous phase angle function.

However, the first method was routinely used in many of the tests here analysed, as a first approach to a frequency domain interpretation of bender element test results.

The two examples in Figure 7.25, taken from the same test at different stress conditions, illustrate some of the complexities and practical limitations of the π-point method. In the absence of additional information, the determination of the travel time is generally made considering the best-fit linear regression of the set of points in relation to the number of wavelengths, N. For the case of the results in Figure 7.25a, the regression produced a very good fit to the data, however a change of slope (a "bump") is discernible between the fitted line and the data points. Visually, two different slopes can be identified and separately analysed, as displayed in the figure, which necessarily produce higher correlation parameters and distinct slope values. In this case, the selection of travel time requires a decision, which can be made considering an average value or the highest correlation fit. The latter was generally applied, whenever in doubt. On the other hand, for the results in Figure 7.25b, the regression provides a perfect fit to the data, thus the resulting travel time (taken from the slope of the best-fit line, here t=0.848 ms) can be readily accepted.



a) b)

Figure 7.25 - Examples of the application of the π-points method in test S1.2.1: a) load stage 5 (σ'v = 46.5 kPa, σ'h = 22.5 kPa) ; b) load stage 22 (σ'v = 119.2 kPa, σ'h = 22.5 kPa)

The reasons for this diverse behaviour in the same test has clearly to do with the imposed stresses, but also with the quality and relation between the two signals and also likely related with the dynamic properties of the transducers and the complete BE-soil system. The comparison of the π-point method with the automated sweep method, as debated in Chapter 4, has proved that the relationship between phase angle and frequency is identical: a perfect match between the discrete π-points and the continuous curve from the automated sweep is obtained. Other authors have reported similar conclusions, thus demonstrating that the adopted FD algorithm is correctly computing the phase angle (Greening and Nash, 2004; Viana da Fonseca et al., 2008).

The complexity or limitation of this BE interpretation inevitably introduces some subjectivity and uncertainty in the determination of the travel time. Therefore, the differences between this and the time domain method can be anticipated to be more significant, than for the automated sweep. These differences also appeared to be inconsistent from one test to another, as shown in Figure 7.26. In order to account for the different void ratios of the various samples, the results are presented in terms of G_0*, that is, normalised G_0 in relation to the established void ratio function, $e^{-1.3}$.

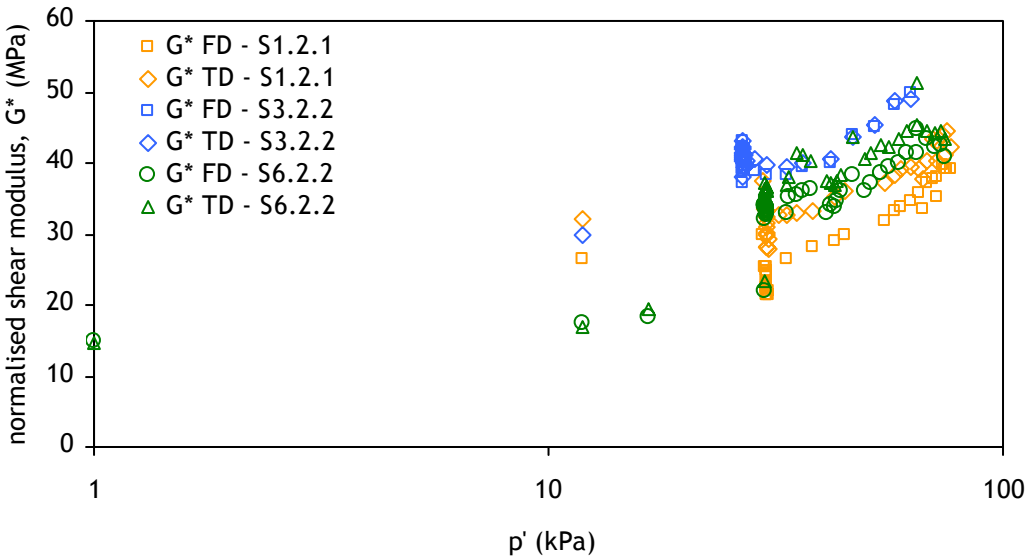


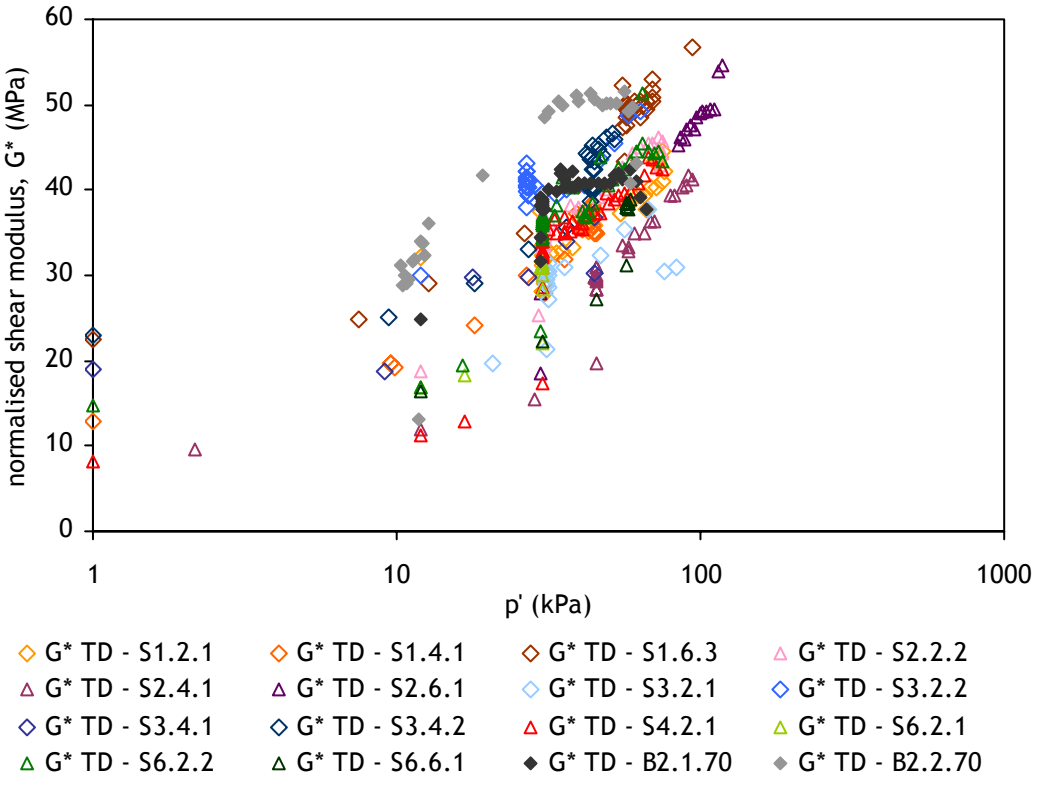
Figure 7.26 - Examples of the FD (using π-points method) and TD results for three different undisturbed samples from ES1: S1.2.1, S3.2.2 and S6.2.2 (all from a depth of 2 m)

In this figure, the differences between FD and TD methods are not systematically the same: 20% difference in G_0 for test S1.2.1, 1% for test S3.2.2 and 8% for S6.2.2. However, it is interesting to note that FD results are consistently lower than TD results and the trends of G_0 in each test are very similar.
For simplicity, the overall results are presented only for G_0* obtained from TD measurements, in relation to mean effective stress and to both stresses (σ'v.σ'h).

The relative evolution of G_0 against stress for these undisturbed samples is very similar, despite the scatter and the distinct absolute values. These differences are mainly related with the disturbance induced during sampling, as will be analysed in the following chapter.

The saturation stages are also very clear in the graph, by a vertical alignment of points at constant effective stress, in which the shear modulus tends to be reduced due to a certain collapse of the fragile cemented structure of the soil. This issue will also be discussed in greater detail in the next chapter.

a)



b)

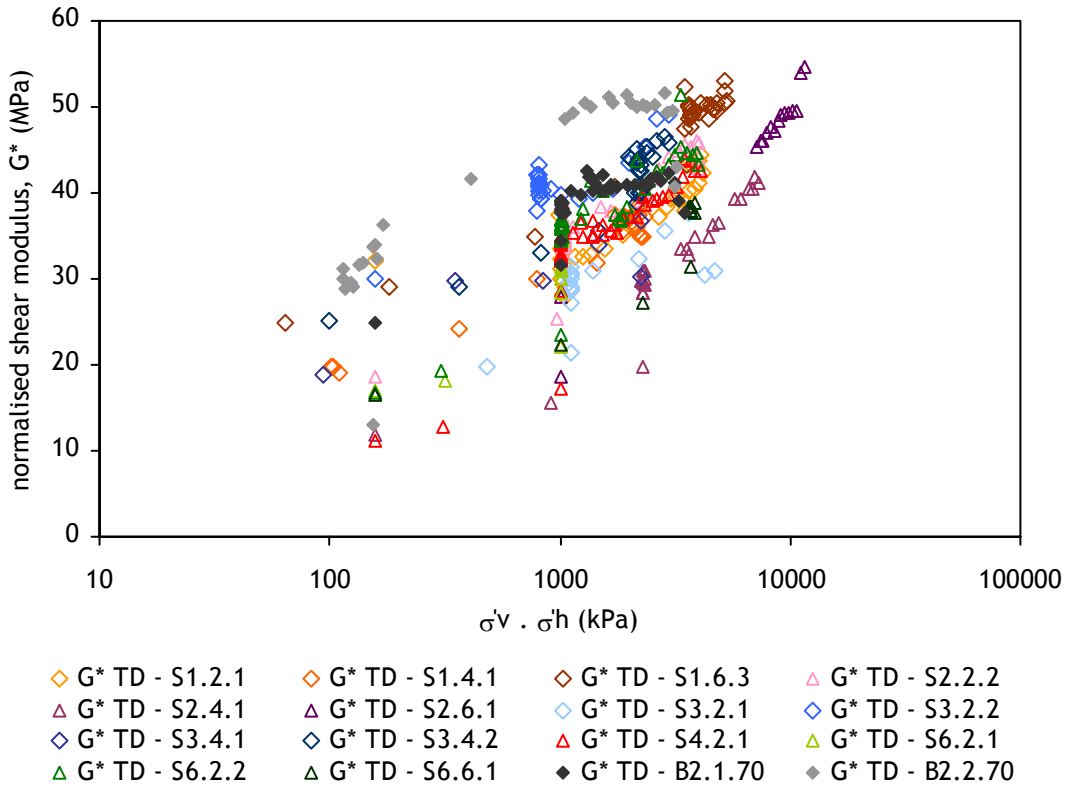


Figure 7.27 - ES1 undisturbed samples results, normalised G_0 against: a) mean effective stress, b) vertical and horizontal stresses

7.2.4.2. Test results from ES2

A series of undisturbed tube and block samples from the second experimental site (ES2) were tested in standard triaxial conditions for the determination of stiffness at the in situ stresses and also to assess its sampling quality in relation to the in situ measured stiffnesses.

Due to the specific characteristics of this experimental site, the previously adopted stress-path (Figure 7.24) had to be modified, for the reasons exposed below. As presented in Chapter 6, the ground water table in this experimental site is located at a considerable depth, around 10 m. Since many of the samples were collected at lower depths, its natural state is only partly-saturated. Within the scope of this research, it was not possible to appropriately address the issue of suction, due to a lack of measuring and testing equipment, which has recently been acquired and is now available at the Geotechnical Laboratory of FEUP. Recently, suction measurements using a tensiometer on block samples indicated negative pore pressures below 20 kPa. This observation, though limited to a very few samples, enabled to assume that the effect of suction in the measured stiffness will be limited and that the effect of natural structure (or natural cementation) will override any suction effects. In any case, considering the unsaturated condition of the natural soil, it was considered more suitable and realistic to perform the standard triaxial tests on this material in drained unsaturated conditions, at a low back-pressure of 10 kPa, to minimise any loss of water content.

As a result, the stress-path adopted for this material consisted of: 1) consolidation (generally anisotropic, at $K_0 = 0.5$), followed with application of a back pressure of 10 kPa; 2) strain-controlled shearing at constant horizontal stress.

Contrary to the tests on ES1 samples, in this case, the shear stage was carried out under automatically strain-controlled conditions. For this reason, BE measurements were limited during shearing, since the time required for each BE measurement using both TD and FD techniques was found to be too long to assume an identical soil state, both in terms of stresses and of strains.

The list of undisturbed samples tested in standard triaxial conditions is listed below, in Table 7.11. The last sample (B5-isoSP) was tested under different stress conditions, mainly in isotropic consolidation, hence it will be analysed separately.

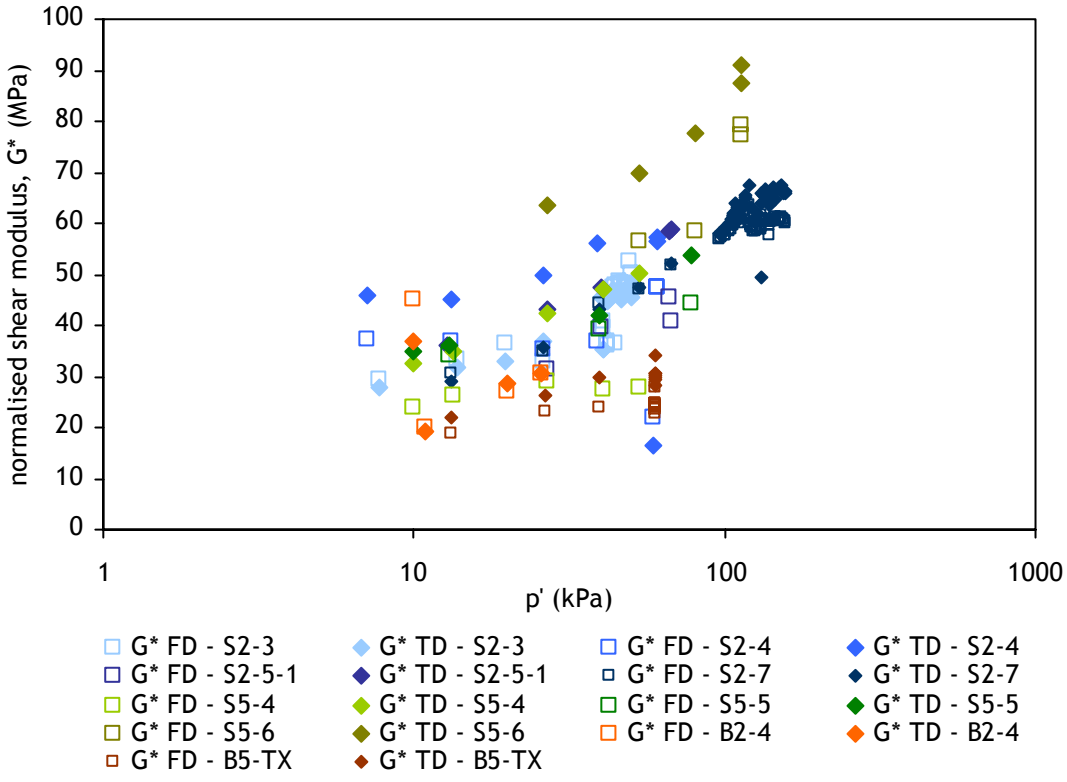
Table 7.11 - Physical properties and testing conditions of undisturbed ES2 specimens

Specimen	γ [kN/m^3]	w [%]	e	σ'_{v0} [kPa]	σ'_{h0} [kPa]
B2-4-TX	17.60	23.4	1.016	35.0	17.5
B5-TX	19.27	22.6	0.689	45.0	22.5
S2-3	18.23	16.3	0.780	60.0	30.0
S2-4	18.42	16.2	0.748	90.0	45.0
S2-5	19.00	22.5	0.710	100.0	50.0
S2-7	19.00	20.2	0.676	140.0	70.0
S5-4	19.10	21.6	0.556	45.0	22.5
S5-5	19.39	22.1	0.714	68.0	34.0
S5-6	19.87	21.5	0.676	86.0	43.0
B5-isoSP	18.99	24.7	0.801	45.0	22.5

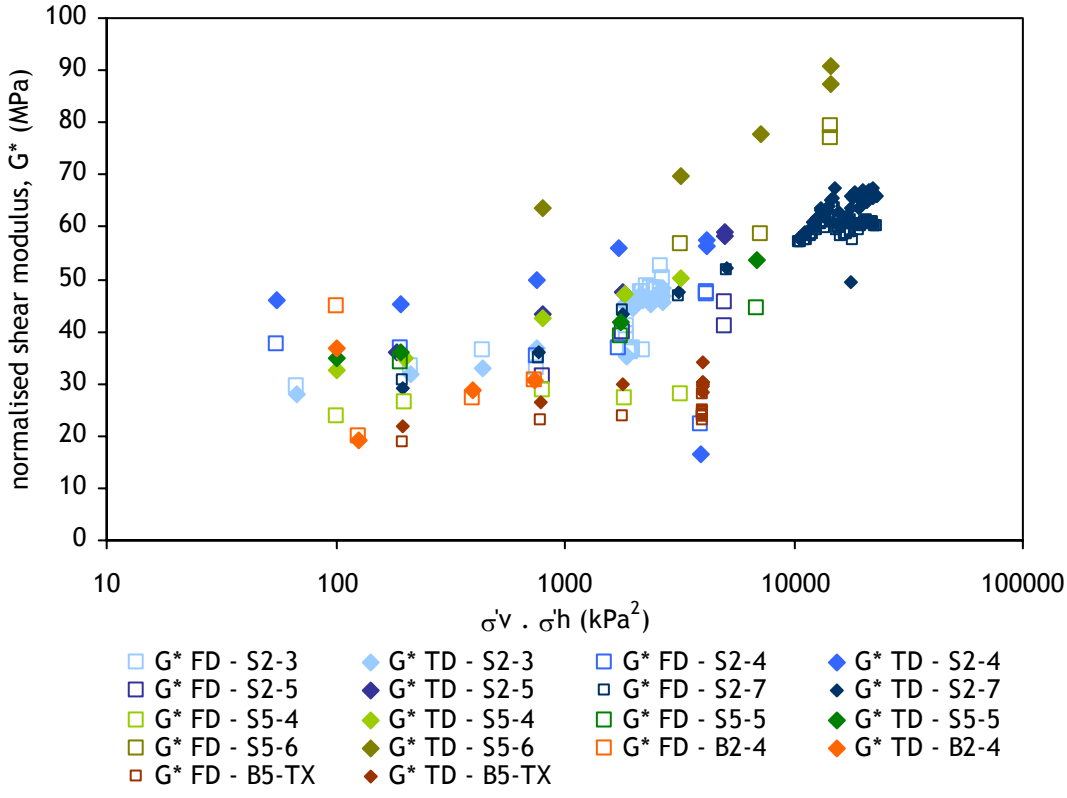
Given the variety of samples, the respective void ratios and in situ stress conditions, the overview of the small strain shear modulus with stress, presented in Figure 7.28a and b, was prepared considering the normalised modulus in relation to the void ratio. The two plots intend to show the relationship between G_0*, measured with both TD and FD methods, with mean effective stress and with the two stresses (σ'_v.σ'_h).

These results show considerable dispersion and the evolution of the shear modulus with stress is diverse among the tests. Clearly, the limited results at higher stresses, namely during shearing, concentrates the results at a narrow range of stresses, thus accentuating the differences between tests.

It is worth noting the effect of the application of a low back pressure without saturation in some samples. For example, B2-4 test results (in orange) show relatively high values of G_0* at very low stresses below 10 kPa, after which the values drop significantly. The cause of the abrupt loss of stiffness can only be attributed to the application of back-pressure at that stage. A similar effect has been observed during the complete saturation process, in which high back-pressures are necessarily applied. This effect at such low confining stresses was unexpected, demonstrating an unforeseen fragility of the natural structure of this material. This matter will be discussed in greater detail in the following chapter.



a)



b)

Figure 7.28 - ES2 undisturbed samples results, normalised G_0 against: a) mean effective stress, b) vertical and horizontal stresses

7.2.4.3. Isotropic test on an undisturbed sample from ES2

An isotropic consolidation test was carried out on one sample from block B5, in test B5-isoSP. In this test, it was possible to use and experiment side-mounted BE, complementarily to the more common vertical BE measurements. This was only made possible through the collaboration with the University of Bristol, who provided the miniature BE probes.

For this test, a different stress-path was considered, consisting of: 1) application of an initial confining stress of 10 kPa; 2) saturation up to a back-pressure of 300 kPa; 3) isotropic consolidation, with an unload-reload cycle. For limitations of the chamber, it was not possible to maintain a stable confining pressure above 500 kPa (total stress). The followed stress-path is illustrated in Figure 7.29.

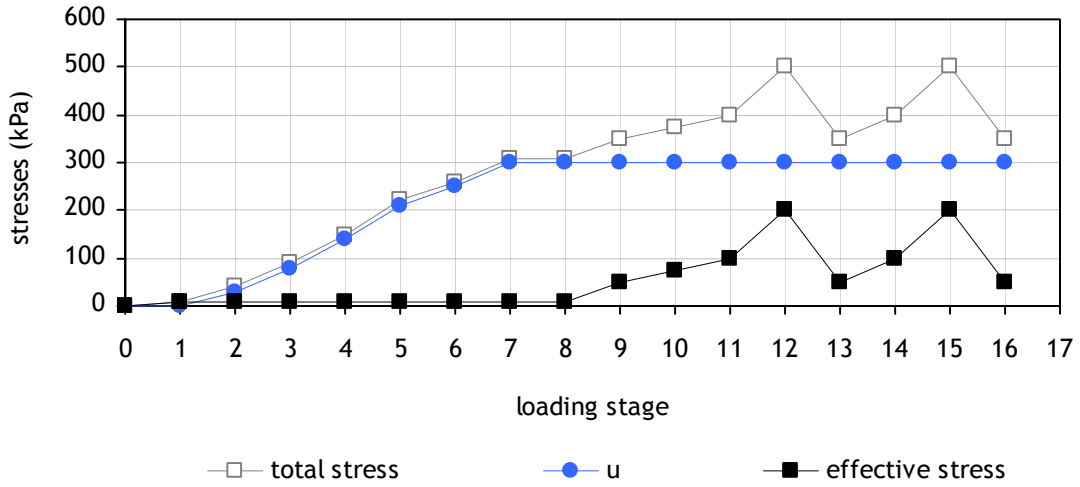


Figure 7.29 - B5-isoSP: schematic of the isotropic stress-path

The results obtained in terms of the normalised shear moduli in the three directions of the wave propagation and polarisation, against mean effective stress are presented in Figure 7.30. The obtained regression parameters are summarised in Table 7.12.

Table 7.12 - B5-isoSP: correlation parameters for the different stress-dependency approaches

	Correlation with σ'i or p'			Correlation with σ'i.σ'j		
	S_i	n_i	R^2	$S_{ij}=S_i$	$n=n_i/2$	R^2
G*vh TD	3189.8	0.585	0.990	3189.8	0.292	0.990
G*hv TD	4455.4	0.516	0.989	4455.4	0.258	0.989
G*hh TD	4106.3	0.568	0.976	4106.3	0.284	0.976
G*vh FD	3125.2	0.566	0.991	3125.2	0.283	0.991
G*hv FD	769.4	0.672	0.957	769.4	0.336	0.957
G*hh FD	1830.8	0.547	0.998	1830.8	0.274	0.998

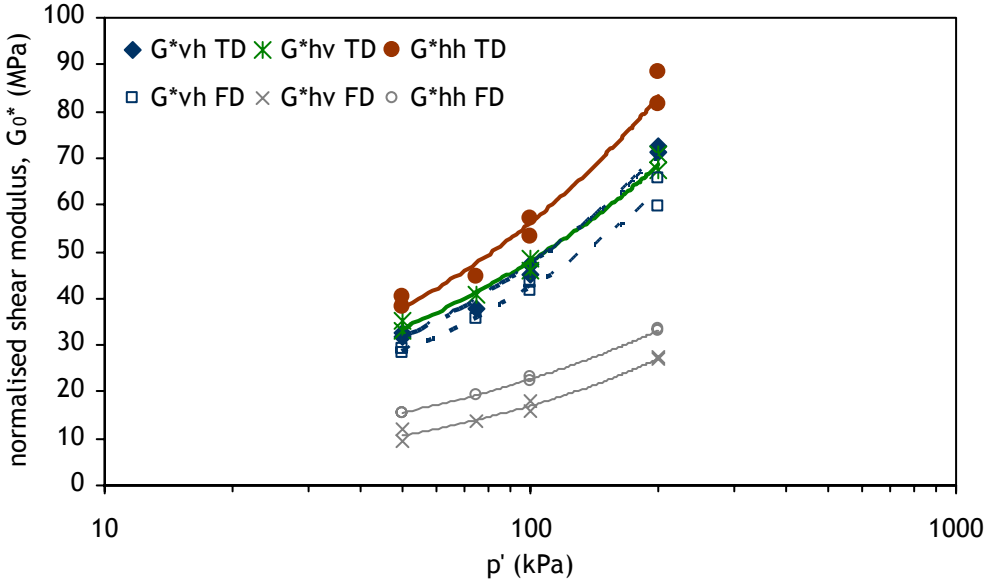


Figure 7.30 - B5-isoSP: isotropic consolidation test on an undisturbed sample, normalised G_0 against mean effective stress (or isotropic stress)

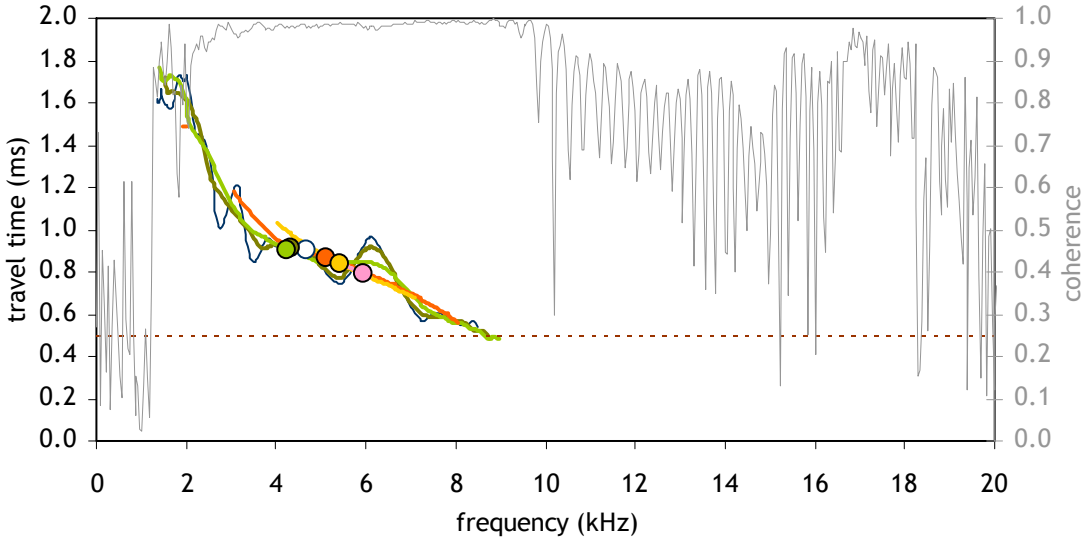
The FD results in the horizontal directions are represented in a light grey, both in the graph and in the table, because these values were considered dubious. Large discrepancies can be observed in relation to the remaining results, not only to the corresponding TD results but also to the other shear modulus (G_0*_{vh}) measured by the same method.

A greater uncertainty and difficulty in the estimate of travel time in the frequency domain was encountered for the horizontal measurements. Given the limited use of these transducers, only made available at the final testing stages of this research and only applied once in actual testing (in this test), the reasons behind this response can merely be speculated. Issues such as the coupling between the transducers and the soil, the shorter travel distance, the miniature size of the benders are possible explanations.

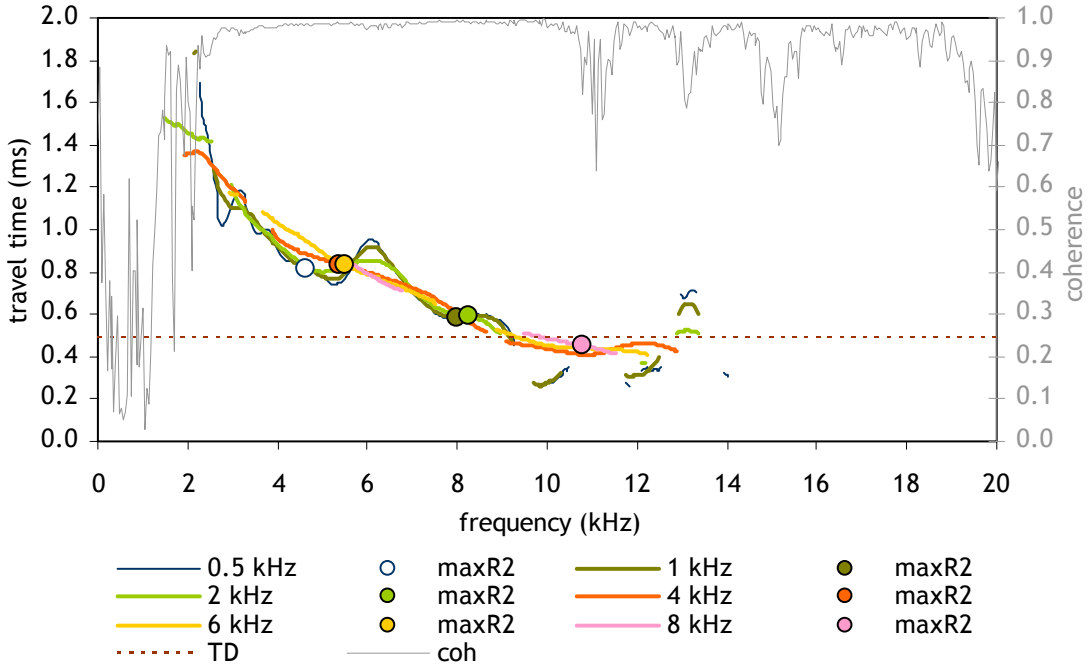
It should be emphasised that the definition of the FD travel times are in general made independently and separately in each direction, and the comparison of all results is made at the end of the interpretation method. In the graphs below in Figure 7.31, the travel time defined by the TD method has been added to better illustrate the relative positions of the results of the two methods.

At stage #11 (Figure 7.31a), the best estimates of the FD method are very close together, but considerably far from the TD time. In contrast, at stage #14 (Figure 7.31b), the estimates of the FD method appear scattered in the graph. The closest

FD estimate to the TD value is for the 8 kHz window, however the corresponding coherence is the lowest of all, hence it would not be routinely selected. These examples indicate that the FD method can be more sensitive to errors in its interpretation that the TD. The shape of the coherence functions in the two stages is significantly different, showing very low values above 10 kHz, which may also be the cause of the (presumably) "wrong" estimates of travel time.



a)



b)

Figure 7.31 - B5-isoSP: FD travel time spectra at different stages (#11 and #14) for the same isotropic stress of 400 kPa

In terms of the other measured shear moduli, it can be concluded that the highest values were measured for G_{0HH} and the values of G_{0VH} and G_{0HV} were very similar, typical of a cross-anisotropic material. It is also interesting to observe the consistent and recurrent 10% difference between FD and TD in the measurement of G_{0VH}.

7.2.4.4. Comparison between ES1 and ES2 undisturbed samples

The first comparison between the results obtained in terms of laboratory-measured stiffness can be made in a general overview of the normalised G_0* against mean effective stress, as presented in Figure 7.32.

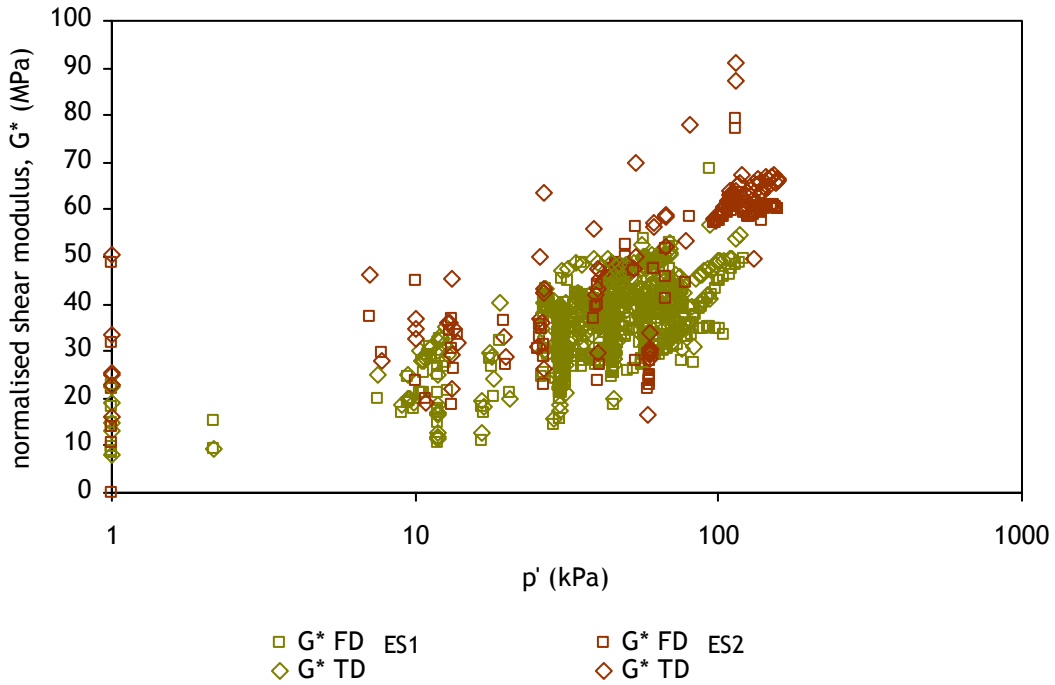


Figure 7.32 - ES1 and ES2 undisturbed samples: normalised G_0 against mean effective stress

The scatter of the results is noticeable, though not unexpected, so obviously the conclusions have to be broad and generic. Regardless of the scatter, it is clear that the materials tested from both experimental sites are similar, as the measured stiffness response and evolution with stress is comparable.

Despite the lower number of points from ES2, its results appear to be more scattered and erratic than those of ES1. The issue of the saturation conditions of the tested samples is a plausible explanation to this observation.

From practical experience, it can be noted that the unsaturated conditions of these tests negatively affect the difficulty in the interpretation of BE and thus promote the spread of results. Frequently the signals in unsaturated conditions (as well as at the start of a new test) have lower magnitudes, higher noise and often a more complex shape than when the sample is fully saturated. Obviously, saturation is not a direct influence in the *value* of the measured travel time, as water has no shear resistance. However, if analysed in the light of boundary effects (Arroyo et al., 2006, discussed in section 4.2.5), it can be argued that an unsaturated sample in triaxial conditions can be assimilated as a reflecting boundary setup, due to the higher impedances between the sample and its surroundings. In such case, larger distortions and mixed waves are more likely to appear in the output signal. Since ES1 samples were tested saturated and ES2 samples were unsaturated, the higher dispersion of the latter is acceptable or, at least, understandable.

Finally, a detailed analysis of the individual results of each undisturbed samples can be more effectively made by the comparison of the shear modulus (or shear wave velocity) measured in the laboratory at in situ stress conditions. Since this analysis is the basis of the method of assessment of sampling quality applied in this research, to be discussed in Chapter 8, it was considered more appropriate to direct this comparison to the following chapter.

7.2.5. True triaxial tests

7.2.5.1. Seismic wave measurements in the TT

As mentioned in previous chapters, one of the capabilities of the true triaxial apparatuses is the measurement of seismic wave velocities not only in all three orthogonal directions, but also in inclined directions. These measurements result in a wide array of data, often redundant but nevertheless relevant and necessary for a more robust and reliable characterisation.

Table 7.13 - Combination of possible seismic wave measurements in the TT apparatus

output / input	ch1: X2hv	ch2: X2hh	ch3: Y2hv	ch4: Y2hh	ch5: Z2vh	ch6: Z2vh
ch1: X1hv	**GXhv**		**GXYhv**		**GXZθv**	
ch2: X1hh		**GXhh**		**GXYhh**		**GZXθh**
ch3: Y1hv	**GYXhv**		**GYhv**			
ch4: Y1hh		**GYXhh**		**GYhh**		
ch5: Z1vh	**GZXθh**				**GZvh5**	
ch6: Z1vh		**GZXθh**				**GZvh6**

Note: θ is usually taken equal to 45 °

In order to consider a cross-anisotropic behaviour, it is necessary that, under isotropic stresses, the following shear stiffness moduli coincide:

$G_{Xhv} \approx G_{Yhv} \approx G_{XYhv} \approx G_{YXhv}$

$G_{Xhh} \approx G_{Yhh} \approx G_{XYhh} \approx G_{YXhh}$

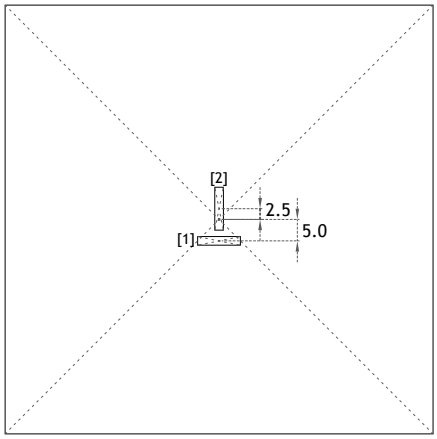
$G_{Zvh5} \approx G_{Zvh6}$

As debated in the BE interpretation section, the travel distance of seismic waves in bender element tests is usually taken as the tip-to-tip distance. For the case of most tests, the tip-to-tip distance corresponds generically to the dimension of the specimen in that direction (length or width) minus the protrusion of both transmitter and receiver BE, which may differ slightly. Obviously, in the course of a test, the dimensions of the specimen vary, hence the distance needs to be correspondingly adjusted.

For the case of inclined measurements in true triaxial or conventional triaxial, the same principle applies, only its measurement is not as straightforward, requiring

specific explicitation. Given the positioning, orientation and location of the transducers in two adjacent platens, its distance differs according to each inclined wave measurement and depends also on the deformation of the specimen in the two involved directions.

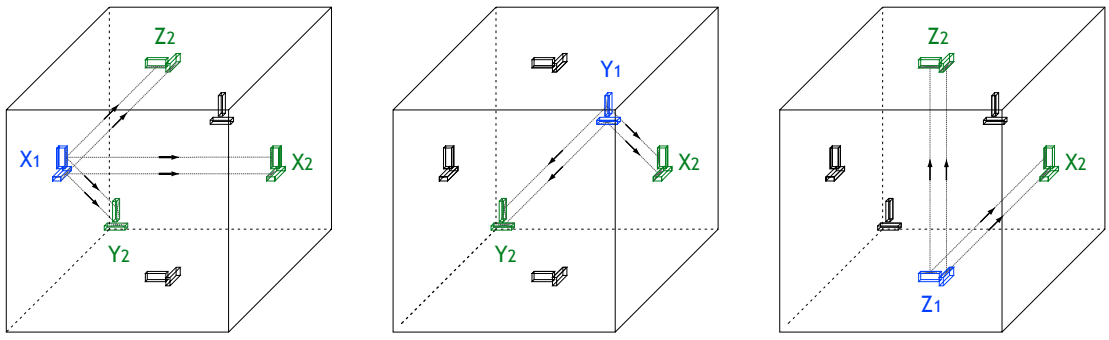
First, it is necessary to quantify the distance of the centre of each transducer in relation to the centre of the platen. Since the B/EE transducers are provided as T-shaped probes, their dimensions and positioning in the probe are identical, as assumed here for all six probes (twelve transducers). This feature facilitates the calculation of the inclined distances and reduces the error in its estimate. Since the probe is placed centred with the platen, the offset of the each individual transducer can be easily determined, as detailed in Figure 7.33. This configuration results in 14 different measurements, for which the expressions for calculation are presented in Table 7.14.



Distances to centre of the platen:
[transducer 1]: 5.0 mm below
[transducer 2]: 2.5 mm above

Protrusion of each transducer: 4.5 mm

Figure 7.33 - Schematics of a B/EE pair in one of the true triaxial platen



a) b) c)

Figure 7.34 - Direct and inclined seismic wave measurements using BE transmitters in platens: a) X1; b) Y1; c) Z1

Table 7.14 - Equations for the determination of the travel lengths of the 14 different wave measurements in the true triaxial apparatus

LX0, LY0, LZ0	[mm]	Initial dimensions in the X, Y and Z direction
PTx	[mm]	Displacements in the X direction [= PT1+PT2]
PTy	[mm]	Displacements in the Y direction [= PT3+PT4]
PTz	[mm]	Displacements in the Z direction [= PT5+PT6]
LBEx0	[mm]	= LX0-4.5*2
LBEy0	[mm]	= LY0-4.5*2
LBEz0	[mm]	= LZ0-4.5*2
LBEx	[mm]	= LBEx0-PTx
LBEy	[mm]	= LBEy0-PTy
LBEz	[mm]	= LBEy0-PTy
LBExy	[mm]	= SQRT((LBEx /2)^2+(LBEy /2)^2)
LBEx1z5	[mm]	= SQRT((LBEx /2+5)^2+(LBEz /2+5)^2)
LBEx2z6	[mm]	= SQRT((LBEx /2-2.5)^2+(LBEz /2-2.5)^2)
LBEz5x1	[mm]	= SQRT((LBEz /2-5)^2+(LBEx /2-5)^2)
LBEz6x2	[mm]	= SQRT((LBEz /2+2.5)^2+(LBEx /2+2.5)^2)

All bender elements installed in the true triaxial apparatus were calibrated in their final arrangement to determine the polarity between corresponding transmitter and receiver. In most cases, the polarity is negative, similar to those in other testing devices, namely the conventional triaxial. The information regarding the polarity of each pair of BE is recorded and recurrently checked before the identification of the first arrival in TD.

One of the complications in the use of this apparatus for seismic wave propagation is the greater likelihood of contamination of the signals with waves travelling through the apparatus or being reflected in its rigid platens, rather than through the soil. The calibration test made with the chamber filled with water enabled to verify that, when appropriately grounding, the propagation of both shear and compression waves is made solely through the medium inside the chamber and not through the apparatus, as already discussed in Chapter 3.

This calibration test can also be used to verify the computed travel distances, under the assumption that the P-wave velocity would be identical in any direction. From this test with water, the following travel times and corresponding compression wave velocities were measured (Table 7.15).

Table 7.15 - Results of the calibration test with the chamber filled with water

	estimated dimensions	measured travel time	corresponding V_P	dimensions for V_P = 1500 m/s	% error
	[mm]	[μs]	[m/s]	[mm]	
LX0, LY0, LZ0	250				
PTx, PTy, PTz	0				
L BEx	241	163.2	1476.7	244.8	1.6
L BEy	241	166.0	1451.8	247.5	2.6
L BEz	241	*			
L BExy	170.41	114.8	1484.4	172.2	1.0
L BEx1z5	177.48	122.0	1454.8	183	3.0
L BEx2z6	166.88	112.3	1486.0	168.45	0.9
L BEz5x1	163.34	*			
L BEz6x2	173.95	*			

[*] This calibration was not entirely made for the Z direction due to difficulties in ensuring the full capacity of the chamber (at the time, drainage was not completely installed). The results obtained in the other directions were considered acceptable and valid also for the Z direction.

The measured velocities were all close but below the reference value of 1500 ms^{-1}, the speed of sound in water. This value naturally depends on a number of factors, namely the quality and composition of the water, temperature, among others. Since all values are below the reference, the inverse calculation of the dimensions indicates values beyond the maximum dimensions of the apparatus, which is not possible. Given the similarity of V_P values, the calculation of the travel distances was considered correct.

The calibration made using the chamber full of water was successful, in the sense that it resulted on waves clearly travelling through the water, near the reference compression wave velocity. This fact, however, does not guarantee that wave propagation through soil will be straightforward and unambiguous. On the contrary, results obtained in tests on soil samples proved that there are interferences, probably caused by reflections at the boundaries that may mask the true first arrival of the shear wave.

Figure 7.35 illustrates one of such cases, from the test on a dry sample of residual soil, R4D-TT. The output signals for all tested frequencies of 1, 2, 4 and 8 kHz have a first deflection at 1.65 ms, which could be considered the first arrival of the shear wave. This part of the signal is however relatively short for a "typical" shear wave and it is intersected by a second wave (here considered the true shear wave), arriving

at 2.29 ms. For all frequencies, this second wave has more energy than the first, and an apparent frequency closer to that of the respective transmitted signals.

Although not evident at first inspection, the apparent first wave, at 1.65 ms, is in fact a P-wave, produced by the BE when shooting the generated shear wave signal. This compression wave travelled diagonally across the soil until it reached one of the orthogonal platens of the chamber where it was reflected back to the soil, arriving at the receiver BE earlier than the direct shear wave. A rough calculation of both velocities can be readily made. Considering the dimensions of the inner chamber equal in all directions, as a perfect cube, then the travel distance of the reflected P-wave can be expressed by:

$$L_{reflect} = 2 \cdot \sqrt{\left(\frac{L}{2}\right)^2 + \left(\frac{L}{2}\right)^2} \qquad [7.15]$$

with L the travel distance of the direct wave.

.

Assuming an approximate value of 250 mm for L, then $L_{reflect}$ results equal to 353.55 mm. The reflected wave took 1.65 ms to cover such distance, thus travelled at a velocity of 214.3 m/s. The direct shear wave arrived at 2.29 ms, which results in a velocity equal to 109.2 m/s. Both P- and S- wave velocities are consistent with the expected values for the tested soil.

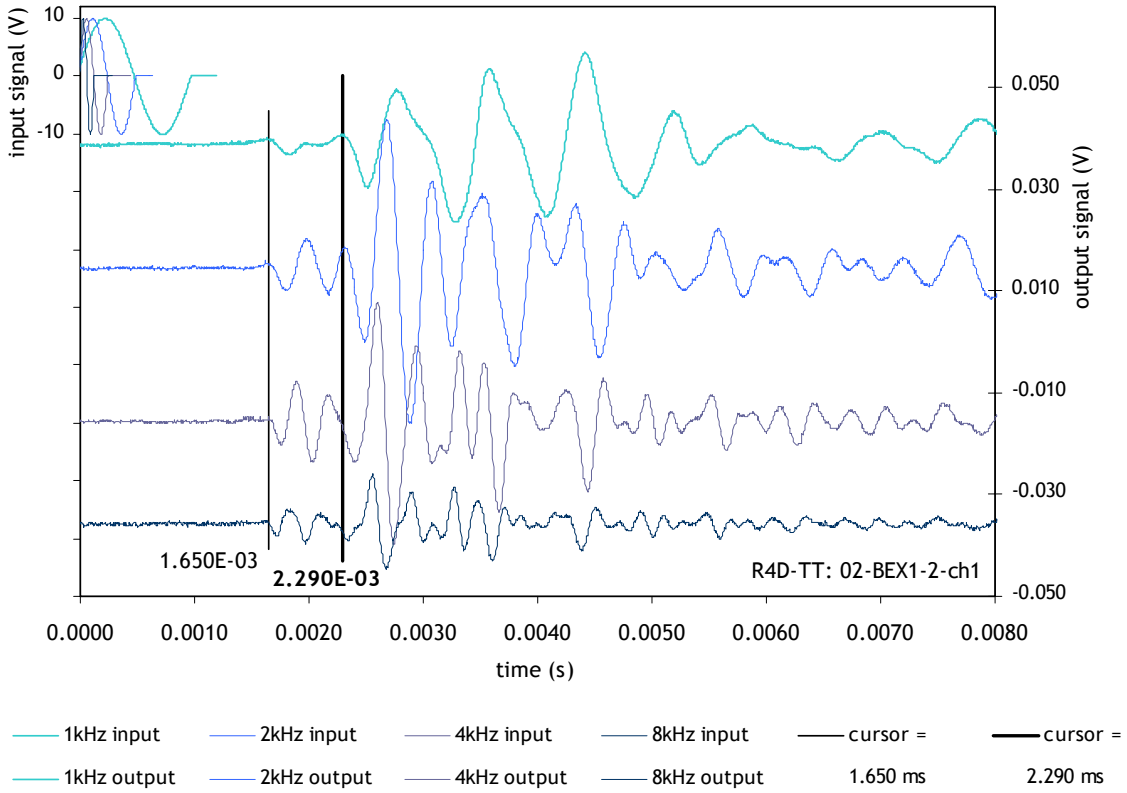
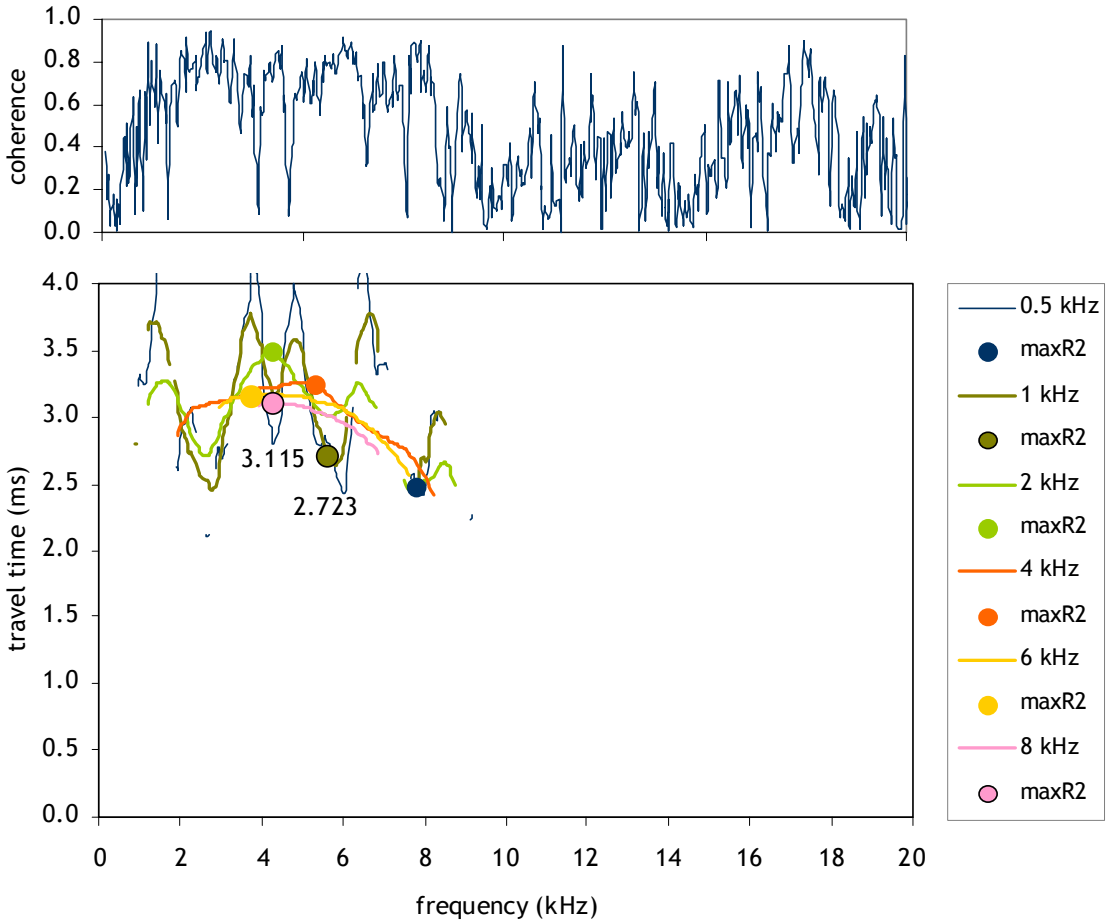


Figure 7.35 - Time domain results for sample R4D-TT, on X1ch1 direction, at stage #02 [σ'x=6 kPa, σ'y=7 kPa and σ'z=25 kPa]

The comparison with the frequency domain results for the same measurement completes the analysis. The travel time spectra (for $R^2 > 0.98$) obtained after the application of the standard input sweep signal [0.1 to 20 kHz] is presented in Figure 7.36. Two markers were highlighted (in black outline) and labelled, corresponding to 1 kHz and 8 kHz frequency windows. The 1-kHz marker was the selected value in this case, since it is associated with a higher coherence value; the 8-kHz marker could also have been selected, as it represents the widest window, thus including more data in its calculation, and is closer to the average of all markers. As previously reported, the frequency domain method provides a lower travel time than the time domain method.



NOTE: The numbers in this graph correspond to the two best estimates of travel time: the 1-kHz and 8-kHz markers

Figure 7.36 - Frequency domain for sample R4D-TT, on X1ch1 direction, at stage #02 [σ'x=6 kPa, σ'y=7 kPa and σ'z=25 kPa]: a) coherence; b) travel time spectra for R^2>0.98

Even though there is still room for dubious interpretation of the FD output, it is worth noting that these results appear to be less affected by the interferences caused by the inevitable reflected waves. The reason is likely to be related with the lower energy and different frequency content of the reflected wave. These two factors lead to low coherence values and poor correlation coefficients, which are thus eliminated in the computation of the final output results.

In summary, the two methods are complementary and both were used as often as possible for the determination of the shear wave velocities in all directions. In some of the final tests, due to time limitations, the FD approach was predominantly used, for its faster processing and ease of interpretation. Despite the convenience of this option, it was later found to be an unwise decision, in particular for BE measurement

in undisturbed samples, where unexpected spread and variability compromised the results.

seismic S-wave measurements: direct & inclined

	BE X						BE Y				BE Z			
	X1ch1HV			X1ch2HH			Y1ch3HV		Y1ch4HH		Z1ch5VH		Z1ch6VH	
stg #	↓	↘	↘	↓	↘	↘	↓	↘	↓	↘	↓	↘	↓	↘
	X2ch1	Y2ch3	Z2ch5	X2ch2	Y2ch4	Z2ch6	Y2ch3	X2ch1	Y2ch4	X2ch2	Z2ch5	X2ch1	Z2ch6	X2ch2
	TD	TD	TD	TD	TD	TD	TD	TD	TD	TD	TD	TD	TD	TD
#00	3743	---	2671	3671	---	2671	---	---	---	---	3586	2571	3543	2700
#01	2971	---	2171	2971	---	2229	---	---	---	---	2800	---	2783	---
#02	2443	---	1807	2400	---	1793	---	---	---	---	2229	---	2229	1600
#03	1629	---	1186	1586	---	1214	---	---	---	---	1557	1186	1571	1096
#04	1307	---	989.3	1307	---	996.4	---	---	---	---	1230	1000	1243	857
#05	1264	---	925	1207	---	914	---	---	---	---	1207	921	1187	896
#06	1029	---	757	975	---	750	---	---	---	---	1011	675	978	657
#07	907	---	657	879	---	671	---	---	---	---	886	600	871	589
#08	771	---	---	736	---	571	---	---	---	---	782	507	750	538
#09	671	---	441	632	---	516	---	---	---	---	653	537	675	460

Figure 7.37 - Example of a datasheet for TT travel time records (in μs)

7.2.5.2. TT tests on reconstituted residual soil specimens

Testing on a complex apparatus, with many possibilities in terms of stress application, configuration and path should be initiated with simple options, which can be easily and directly related with other, more conventional, apparatus. This is also the case for the first tests on the true triaxial apparatus. The use of a simple stress-path is favourable, as the behaviour is anticipated and any differences between tests can only be attributed to soil conditions and its state parameters. For the purpose of comparison, isotropic loading to the maximum allowable deformation was selected for stress application in a few tests. As mentioned in the description of this apparatus, the maximum allowable movement of each platen is 10 mm, hence the displacements. The isotropic consolidation was in general followed by shearing in true triaxial conditions.

A number of isotropic tests were carried out in the true triaxial apparatus using reconstituted specimens of residual soil. The first true triaxial tests were carried out in reconstituted dry ($w \approx 0$ %) and wet ($w \approx 30$ %) residual soil specimens. These rather extreme conditions are intended to reproduce the behaviour of a non-structured soil, so that the effects of structure can be isolated and analysed separately when testing intact soil specimens. The use of both in detriment to a

single non-structured soil condition is fully justifiable by some uncertainties and limitations regarding its behaviour. The dry condition enables to completely eliminate suction effects, although its preparation and reconstitution process can induce undesirable layering and heterogeneity, possibly more than the humid specimens. On the other hand, the wet condition is favourable in terms of the ease of preparation at a very high void ratio, thus producing a more homogeneous sample; however, air bubbles can still get entrapped between the soil particles, hence introducing an unmeasured amount of capillary negative pore pressure. The physical properties of the reconstituted specimens tested in this apparatus are listed in Table 7.16.

After each increase or decrease in load, the soil was left to consolidate, generally for a minimum period of 24 hours, during which continuous deformation measurements were acquired, generally at 30 s intervals. All seismic wave measurements were acquired at the end of these consolidation stages.

Table 7.16 - Summary of physical properties of the reconstituted specimens tested in the TT

Specimen	γ [kN/m^3]	w_0 [%]	e_0
R2W-TT	19.1	28.4	0.770
R3W-K_0TT	18.8	30.7	0.850
R4D- K_0TT	14.1	1.2	0.883
R8D-TT	12.7	1.0	1.067

The first successful test with this apparatus was made on sample R2W-TT. A simple isotropic loading test was carried out as shown in the stress-path of Figure 7.38. Despite its simplicity, it is presented here with the purpose of comparison and contrast with the stress-paths adopted for the other samples. In order to avoid any stress differences in the three directions, which could deviate from the intended isotropic condition, the three pressure lines were intentionally connected. Consequently, for the application and control of the isotropic stress, only one GDS controller was used.

During the course of test R2W-TT, both bender elements in the Y direction failed to work. Consequently, the analysis could only consider the results in the X and Z directions, thus imposing the assumption of a cross-anisotropic behaviour. An overview of the obtained results, in terms of direct and inclined wave measurements in and between X and Z directions, is presented in Figure 7.39a and b, derived from BE measurements interpreted in the time and frequency domain, respectively.

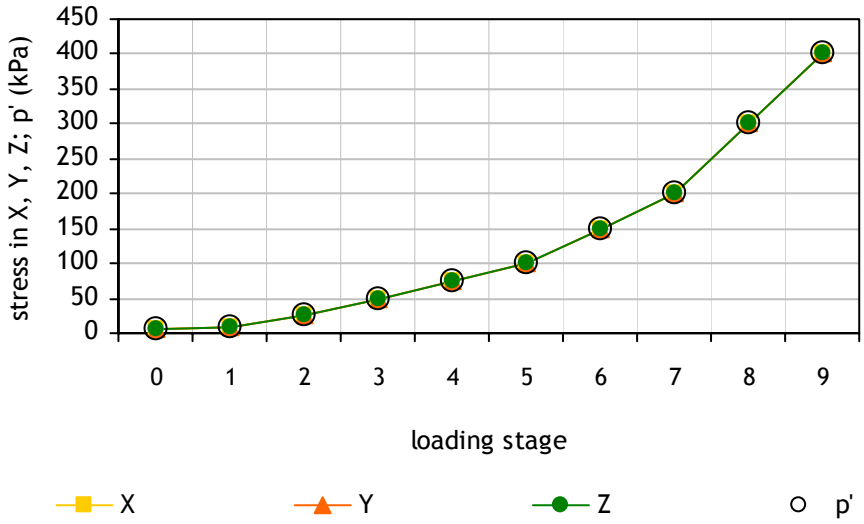
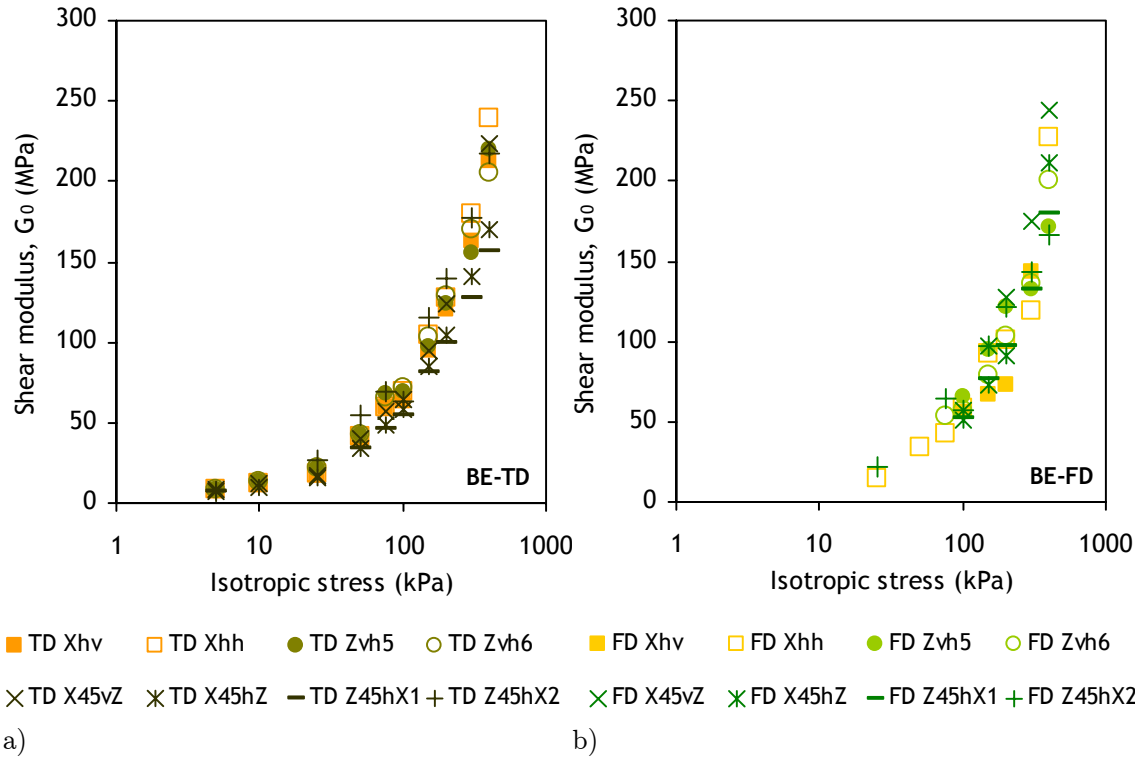


Figure 7.38 - R2W-TT: Schematic of the stress stages

In this test, as well as in some other tests carried out in different apparatuses, frequency domain measurements were not feasible immediately after sample installation, due to a high level of noise in the signals, probably caused by poor coupling between the soil and the transducer at very low confining stresses. From practical experience, it appears that this method is more demanding in terms of testing conditions that the time domain approach. In this case, FD measurements were only obtained after the application of a 25 kPa isotropic stress.



a) b)

Figure 7.39 - R2W-TT: G_0 results for direct and inclined measurements from: a) TD; b) FD

The results in the figures show remarkable similarities between all the measured direct and inclined shear moduli. The differences are more visible in the obtained regression parameters, listed in Table 7.17, where the parameter S and the stress index n vary only slightly (more in FD than in TD), compensating each other to result in identical stiffnesses. In the light of these results and since the stress conditions were always isotropic, the response of this wet reconstituted sample can be considered isotropic. Consequently, a single global shear modulus can be derived, for each BE interpretation method, as illustrated in Figure 7.40.

Table 7.17 - R2W-TT: regression parameters per wave direction, from TD and FD

	G_0* TD			G_0* FD		
Direction	**S**	**n**	**R^2**	**S**	**n**	**R^2**
Xhv	1720	0.635	0.989	1926	0.596	0.926
Xhh	1671	0.657	0.991	1090	0.699	0.957
X45vZ	1768	0.634	0.988	997	0.744	0.976
X45hZ	1613	0.618	0.988	709	0.769	0.991
Zvh5	2124	0.604	0.989	2607	0.523	0.992
Zvh6	2141	0.605	0.989	2323	0.556	0.975
Z45hX1	2038	0.564	0.994	1642	0.606	0.994
Z45hX2	2159	0.618	0.973	2805	0.529	0.926
all [*]	1890	0.617	0.973	1666	0.619	0.918

[*]: all-TD corresponds to 76 measurements; all-FD corresponds to 44 measurements

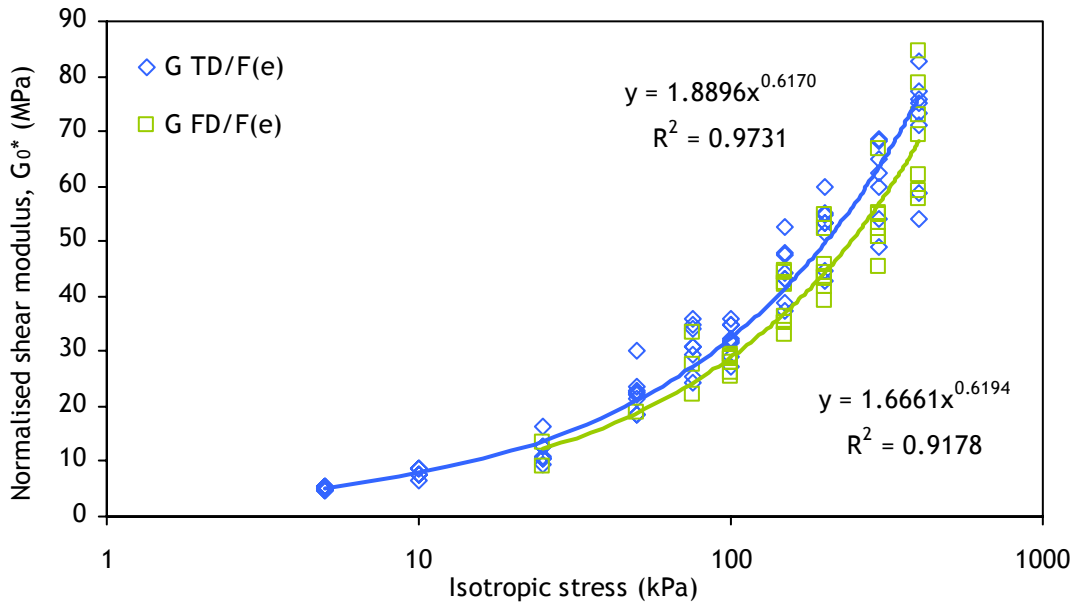


Figure 7.40 - R2W-TT: global normalised G_0 results from TD and FD measurements

Similarly to previous observations in standard triaxial conditions, these results show a difference of about 10% between BE measurements interpreted in the time and the frequency domain, for the correlation parameter S. The stress index n appear to be practically unaffected by the BE interpretation technique.

Identical analyses can be made for the results of test R8D-TT. In this test, a number of unload-reload cycles were performed, analogous to the standard triaxial test isoCF1. After those cycles, three-dimensional stress conditions were imposed at constant mean effective stress, p'.

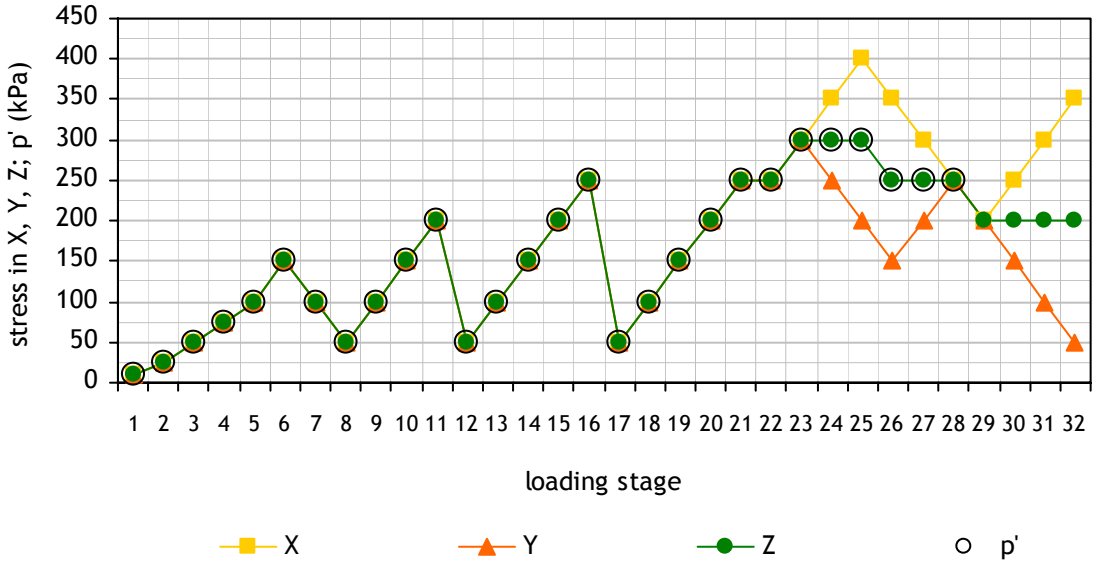


Figure 7.41 - R8D-TT: Schematic of the stress stages

The isotropic stages are analysed separately for comparison with the previous results. The maximum shear moduli obtained in each direct measurement is presented in the Figure 7.42.

The stress-path followed in this test included three unload-reload cycles, which enabled to study the influence of the void ratio in the measured stiffnesses. The procedure followed was similar to that described earlier for the standard triaxial test. The unloading and reloading cycles provided the opportunity to measure shear wave velocities repeatedly at the same stress levels but with varying void ratio due to the deformation experienced by the soil during loading. The complete set of results in terms of maximum shear modulus against void ratio is presented in Figure 7.44.

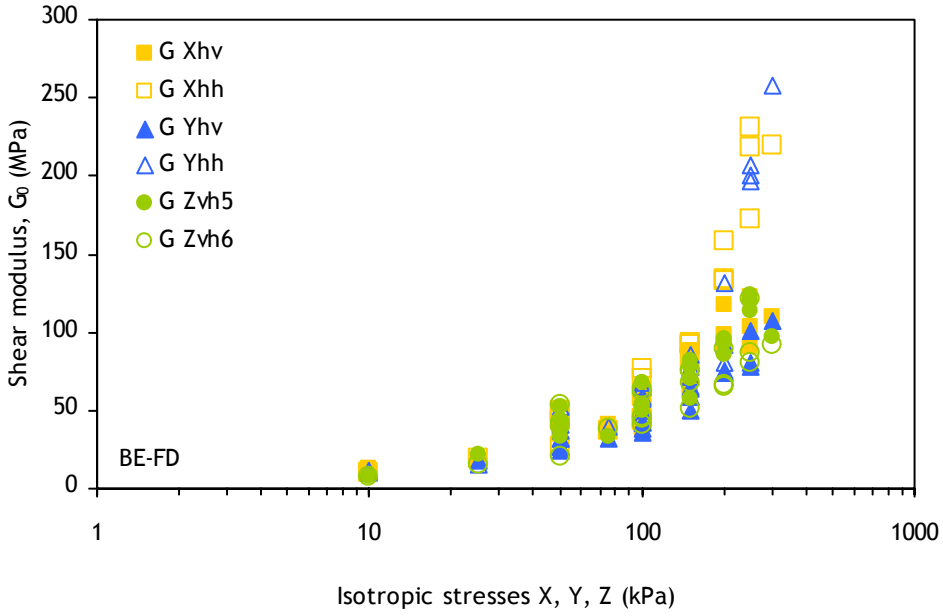


Figure 7.42 - R8D-TT: G_0 results from direct FD measurements

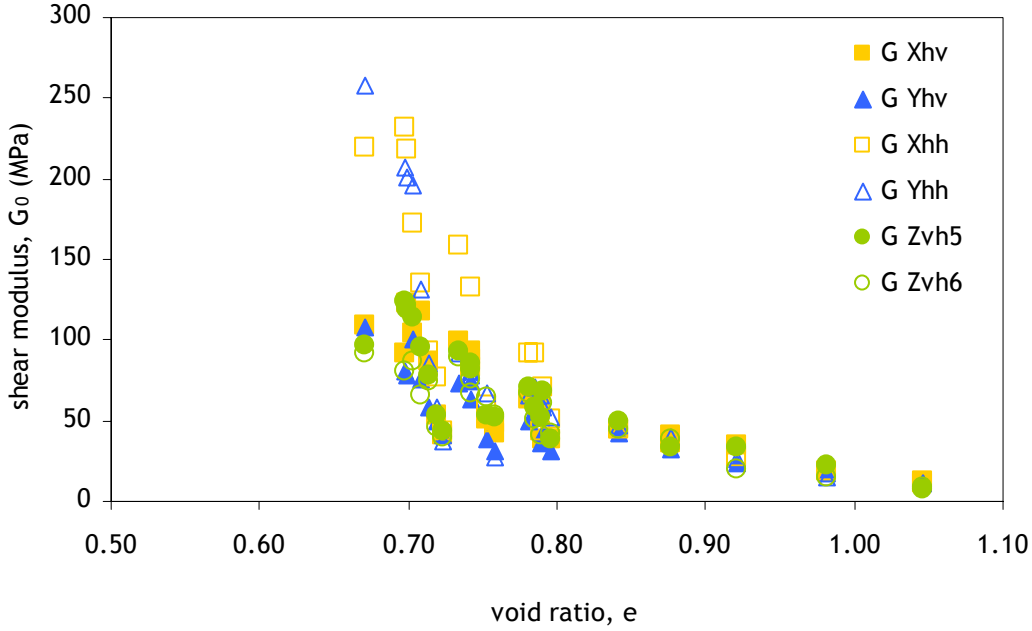


Figure 7.43 - R8D-TT: G_0 against void ratio, from direct FD measurements

In an attempt to estimate the value of exponent for the void ratio function, the results obtained at the same stresses in different stress stages were grouped for each HV, HH and VH directions, that is, V_{SXhv} and V_{SYhv}, V_{SXhh} and V_{SYhh}, V_{SZvh5} and V_{SZvh6}, respectively. At each of these isotropic stresses, the general expression can be simplified as:

$$G_{0ij} = S_{ij} \cdot F(e)_{ij} \cdot \sigma_i'^{ni} \cdot \sigma_j'^{nj} = C \cdot F(e)_{ij} \qquad [7.16]$$

where C incorporates the constant terms due to the constant stress state. The exponent of each regression should correspond to the $-x$ exponent of the void ratio function:

$$F(e)_{ij} = e^{-xij} \qquad [7.17]$$

Figure 7.44 shows an example of the void ratio analysis for the case of the HV shear moduli, where a best fit exponential regression is computed at each "repeated" isotropic stresses of 50, 100, 150 and 200 kPa (measured during loading, unloading and/or reloading).

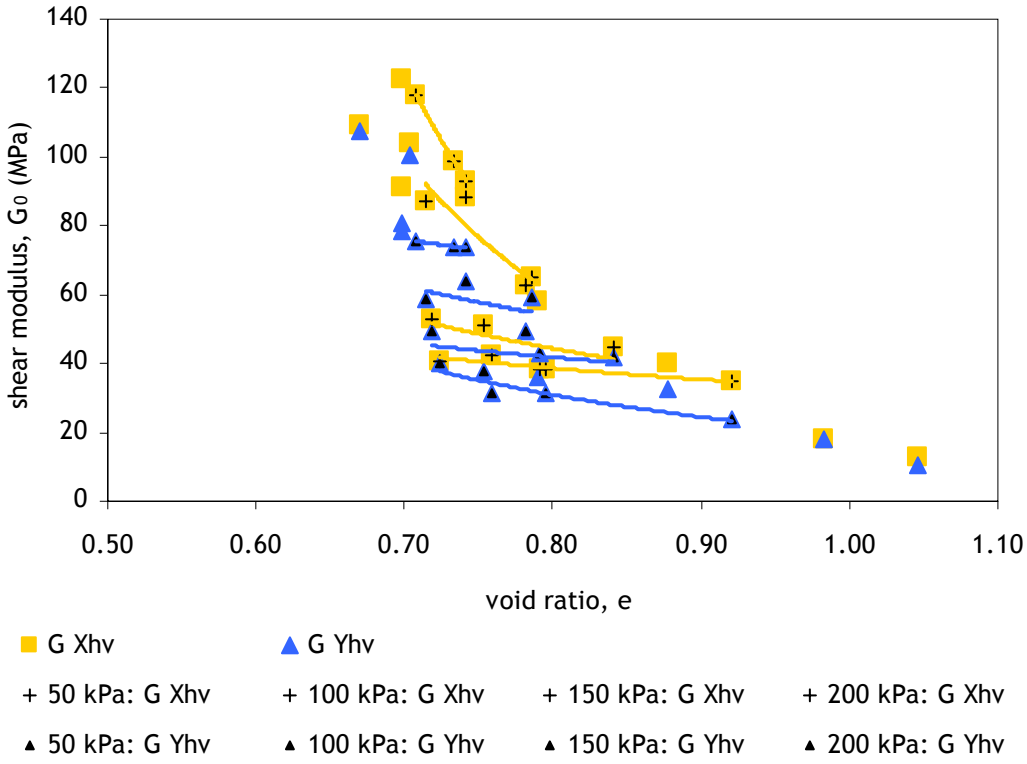


Figure 7.44 - R8D-TT: G_0 results from direct FD measurements

The spread of the data was considerably larger than that obtained in the conventional triaxial test. Moreover, the resulting correlations were in general poor. For this reason, the indices for the power functions relating G_0 to void ratios were taken from the average value of the individual exponent at each isotropic stress in each direction. The final indices corresponded to -1.92 for G_{0hv}, -1.28 for G_{0hh} and -1.34 for G_{0vh}. These values point to the existence of a directional strain-induced anisotropy, as suggested by Pennington (1999) for Gault clay. However, given the proximity of values for the exponents x_{hh} and x_{vh}, identical to the exponent previously adopted for the conventional triaxial tests, a unique non-directional value of x equal to 1.3, was considered most suitable for the void ratio function.

After the definition of the void ratio function, which confirmed the one obtained in conventional triaxial conditions, it is possible to study the stress dependency of the maximum shear modulus in each measured wave direction. For this purpose, only the measurements of the shear moduli at normally consolidated stress states should be considered, since overconsolidation influences the stress dependency.

The normalised G_{0ij} to the void ratio, G_{0ij}* against isotropic stresses, in normally consolidated (NC) conditions, for all wave directions is presented in Figure 7.45.

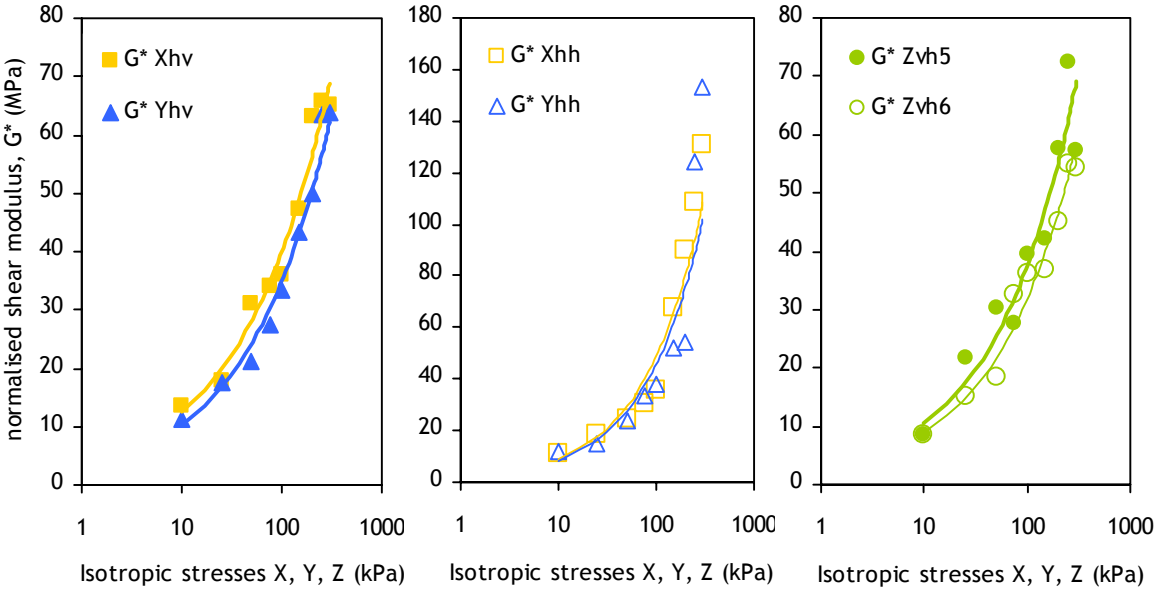


Figure 7.45 - R8D-TT: G_0* results in relation to the wave polarisation direction in normally consolidated conditions, from direct FD measurements

A clear distinction is visible in this case, between horizontally and vertically polarised wave velocities. Both G_{0Xhh} and G_{0Yhh} exhibit the highest values and stand out from the other measured velocities (note the different vertical scales in each chart). The regressions appear to be consistent and have similar patterns. The obtained correlation parameters are summarised in Table 7.18.

Table 7.18 - R8D-TT: correlation parameters for each wave direction

	$G_0^* = S\,p'^n$		
Direction	***S***	***n***	**R^2**
all HV	3553	0.512	0.980
all HH	1625	0.731	0.923
all VH	2676	0.556	0.954

There are substantial differences between horizontally- and vertically-polarized shear velocities, particularly at higher stresses. It appears that the sample preparation method, which consisted of the deposition and gentle tamping of the soil in dry conditions, has induced an unforeseen degree of 'inherent' anisotropy.

Under isotropic conditions, no distinction can be made in terms of the dependency with the different stress components acting in the propagation and polarisation directions. In order to address this issue, the results from test R4D-TT will be analysed.

Test R4D-TT was carried out to investigate the possibility of this apparatus to automatically impose a K_0 stress state condition from which the at rest stress parameters could be determined. This procedure was made possible by establishing a non-deformation imposition in the horizontal platens: the deformation recorded by the potentiometers was monitored and kept constant at a reference value, by the application of water pressures at the platens to balance the soil pressure. While this procedure is questionable for the determination of the at rest stress state in natural undisturbed samples, it appears to be acceptable for reconstituted specimens.

The stress-path consisted on the gradual increase of the vertical stress, by increments, and the measurement of the horizontal stresses required for the zero-deformation imposed in the horizontal X and Y platens. The obtained stress-path is depicted in Figure 7.46.

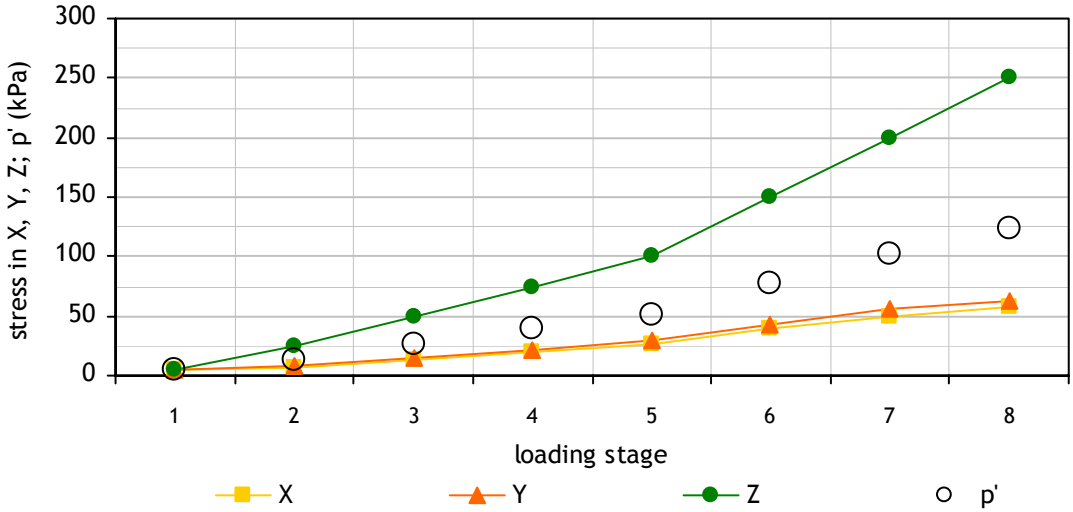


Figure 7.46 - R4D-TT: Schematic of the stress stages

An overview of the results obtained in this test in terms of maximum shear moduli against the main corresponding stresses, that is, in the direction of wave propagation,

is presented in Figure 7.47a. The shear moduli in the graph is already normalised with respect to the pre-defined void ratio function.

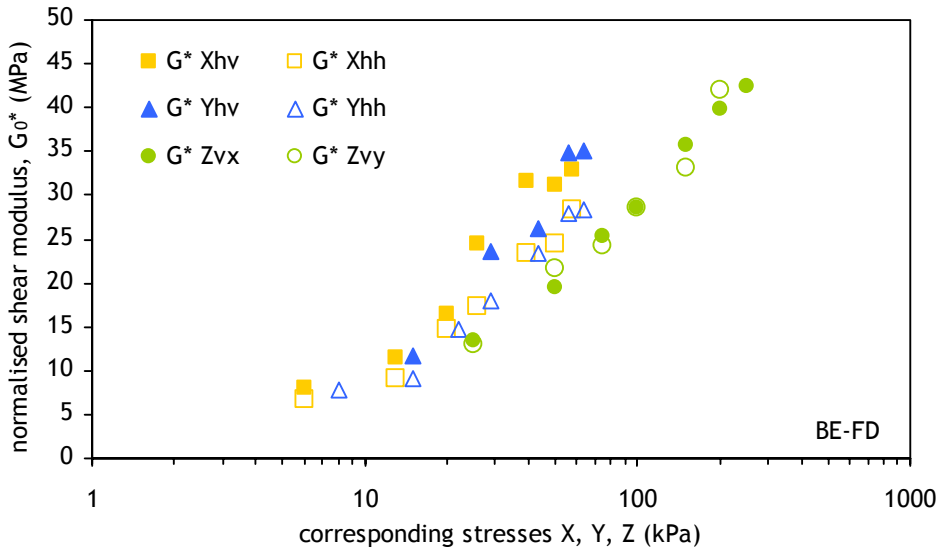
From this test, it is possible to investigate which stresses are most influential in the variation of the shear modulus. In an attempt to derive the parameters for the present case of test R4D-TT, the following graphs in Figure 7.47 were prepared, from which the correlation coefficients in Table 7.19 were obtained.

Table 7.19 - R4D-TT: correlation parameters for three stress-dependency approaches

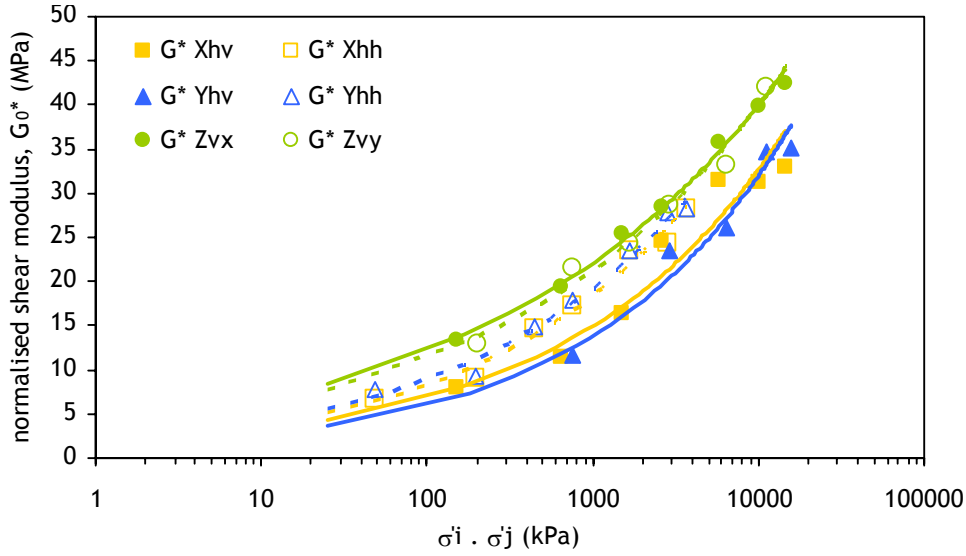
	Correlation with $\sigma'i$			Correlation with $\sigma'i.\sigma'j$			Correlation with p'		
	S_i	n_i	R^2	S_{ij}	n_{ij}	R^2	S_{ijo}	n	R^2
Xhv	916	0.675	0.95	1430	0.340	0.96	1365	0.688	0.95
Xhh	835	0.693	0.95	1706	0.343	0.98	1226	0.713	0.96
Yhv	802	0.655	0.97	1124	0.364	0.96	1185	0.667	0.98
Yhh	950	0.628	0.96	1962	0.329	0.97	1382	0.639	0.97
Zvx	2631	0.514	0.99	3700	0.259	1.00	3572	0.523	0.99
Zvy	2445	0.533	0.98	3185	0.274	0.98	3415	0.537	0.98

These results show small differences between the three possible approaches to the stress dependency of the shear moduli, possibly because there is a direct (and nearly constant) relation between the horizontal and vertical stresses. Nevertheless, higher correlations were obtained when considering the two stresses acting in the relevant wave directions of propagation and polarisation. The consideration of the influence of the three stresses also provided good approximations to the measured stiffnesses.

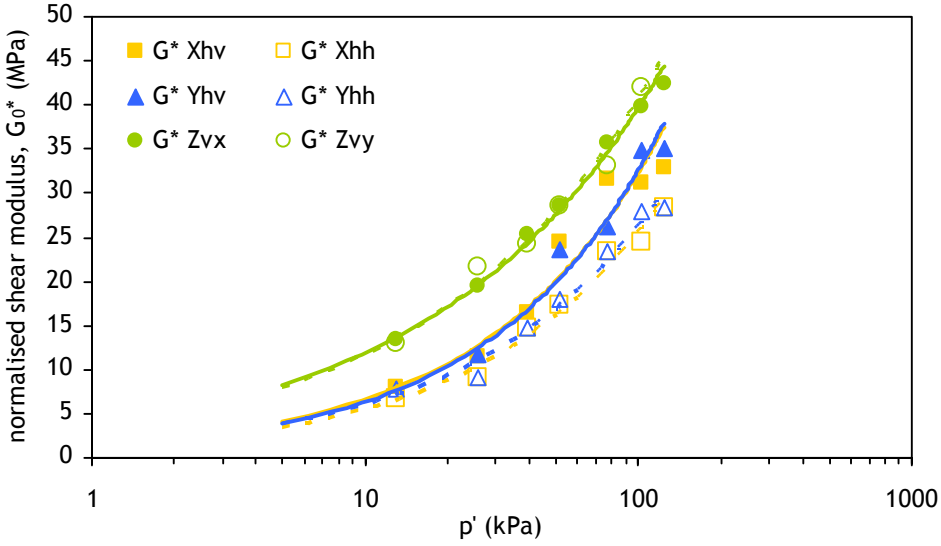
Similar comparisons will be made for other test results, namely on natural undisturbed samples.



a)



b)



c)

Figure 7.47 - R4D-TT: normalised G_0* against: a) stress corresponding to the wave propagation direction, b) mean effective stress

7.2.5.3. TT tests on natural block samples of residual soil

From the six block samples retrieved from CEFEUP-ES2, only three (B2, B4 and B5) provided suitable material for testing in its undisturbed state, in the true triaxial apparatus. The considerably large size of the required specimen (circa 250x250x250 mm) posed an additional challenge especially regarding the homogeneity of the sample. For example, block sample B3 appeared to be fairly homogeneous, however during the preparation process, a large discontinuity was revealed, which excluded the possibility of trimming a specimen for testing in the true triaxial apparatus (details in Figure 7.48).



Notes: a) after opening the wooden box where it was contained, the block sample appear to be fairly homogeneous; b) a large and persistent discontinuity was revealed when clearing the surface; c) only standard triaxial (70 and 100 mm diameter) samples were trimmed, as the larger homogeneous side (to the left in the photos) was smaller than the required dimensions of the TT apparatus; d) detail of the material at the discontinuity

Figure 7.48 - Block sample B3: impossibility of trimming a true triaxial specimen due to a large discontinuity across the sample

The shortlist of undisturbed samples appropriate for true triaxial testing is presented in Table 7.20. The numbers of the samples correspond to the block sample reference, from which each tested specimen was trimmed.

Table 7.20 - Physical properties of the natural block samples tested in the TT

Specimen	Depth [m]	γ [kN/m³]	w [%]	e	σ'_{v0} [kPa]	σ'_{h0} [kPa]
B2-TT	1.50	16.7	20.4	0.894	26.0	13.0
B4-TT	2.75	18.8	25.0	0.850		
B5-TT	4.35	17.4	20.0	0.811	75.0	37.5

Test B2-TT consisted of a simple isotropic loading stress-path with a few unload-reload cycles, for comparative analysis with the reconstituted material. A schematic of the idealised stress-path is presented below, in Figure 7.49.

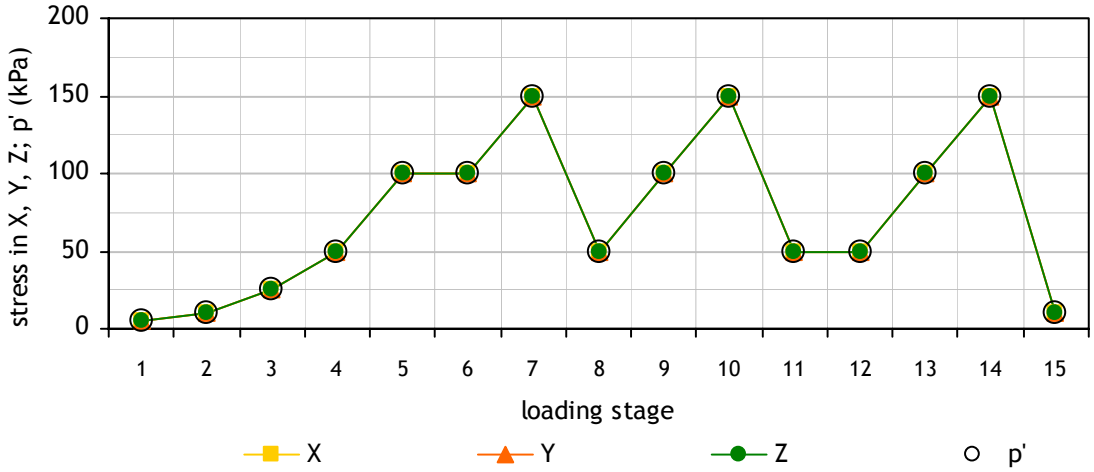


Figure 7.49 - B2-TT: schematic of the isotropic stress-path

Considering the time requirements for the complete set of BE measurements in all directions, including inclined wave measurements, and in the time and frequency domain, some concessions had to be made. Taking into account the performance of the FD method for the reconstituted specimens, it was decided to carry out most of the BE measurements exclusively by the FD method. The obtained results are summarised in Figure 7.50.

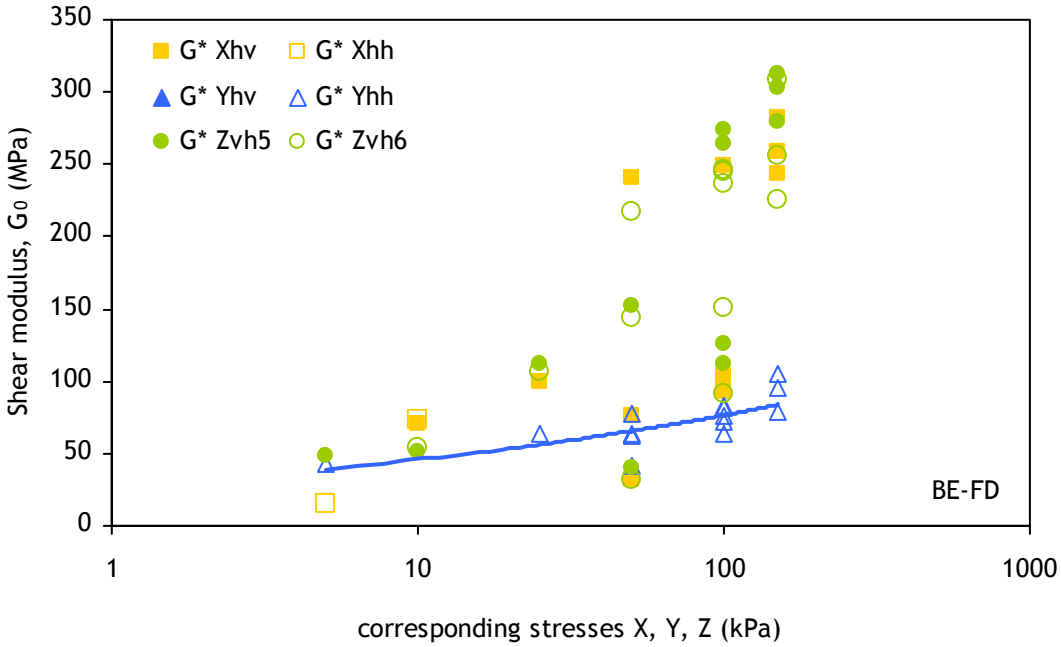


Figure 7.50 - B2-TT: G_0 results against isotropic stresses

These results are clearly unsatisfactory and have to be considered, apart from Y_{hh}, meaningless. Despite the effort in the analyses and in the optimisation of the post-processing method, it was not possible to obtain a consistent pattern for the measured shear modulus. This is more striking since the stress conditions were always isotropic, at which the differences between the stiffnesses in the three directions are expected to be moderate.

In contrast, the spread of the results was unexpectedly large. The preliminary interpretation of the FD results during the course of the test was not sufficiently detailed to identify and alert for such variability in the measured travel times, hence shear velocity and modulus.

This option, which clearly proved to be a bad one, forced a completely blind FD analysis of the BE results, that is, without the orientation of the TD results to guide the selection of the travel time provided by the algorithm, which had not yet been experimented. The most negative aspect from this experiment was the fact that it was carried out in a complex and time-consuming test, on an undisturbed, hence unique sample of residual soil.

Test B5-TT was carried out following a similar stress-path to that of the reconstituted specimen R4D-TT. The application of stresses was made by gradual increase of the vertical stress, by increments. The horizontal stresses required for the zero-deformation imposed in the horizontal X and Y platens were measured, after an initial isotropic confinement stress of 20 kPa. The obtained stress-path is presented in Figure 7.51. After loading stage #21 (σ'_x=150 kPa, σ'_y=75 kPa, σ'_z=400 kPa) the deformation control was deactivated. Instead, opposite increments of horizontal stress in the X and Y directions were applied, thus maintaining a constant mean effective stress, p' = 208 kPa.

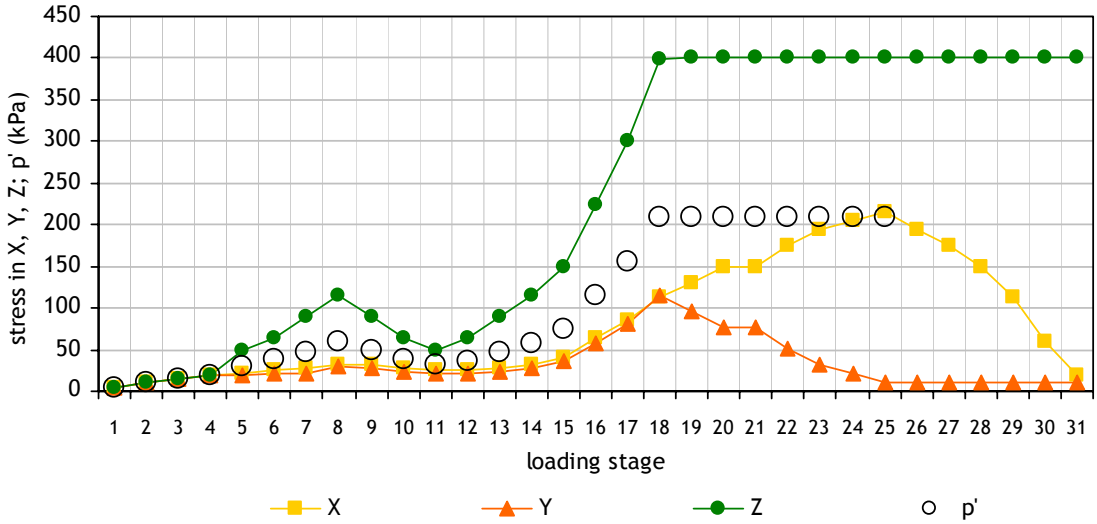
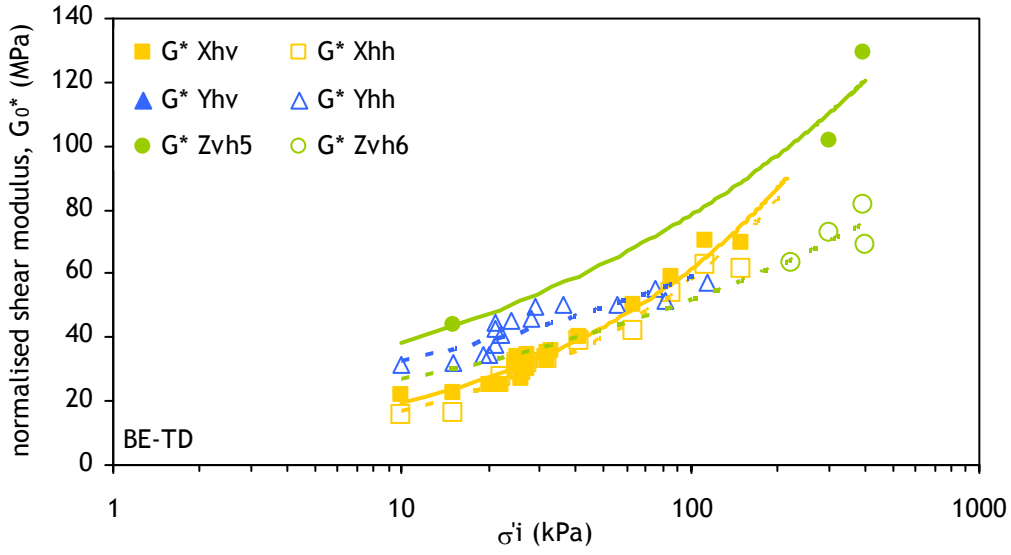


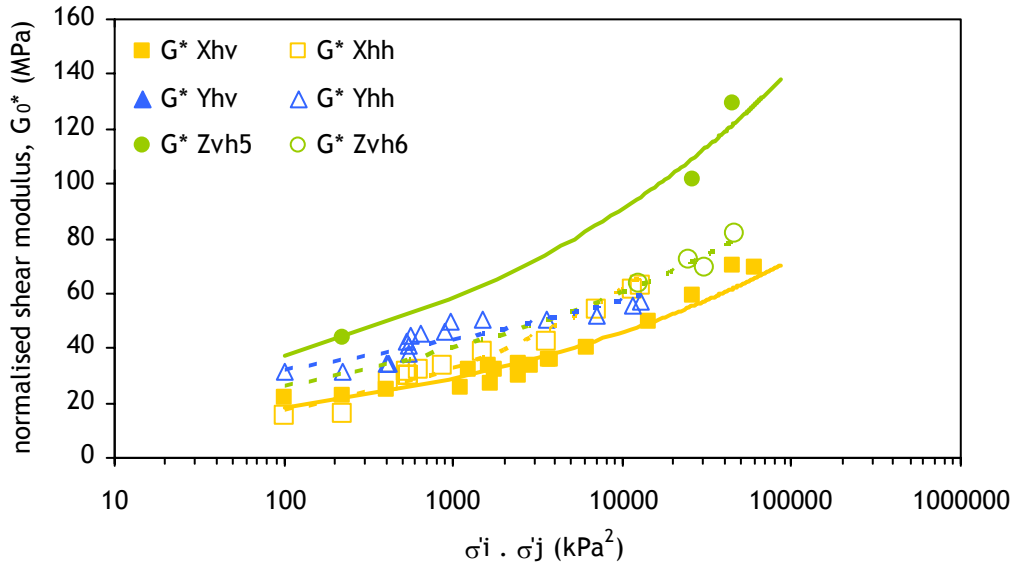
Figure 7.51 - B5-TT: stress-path followed, partially with zero horizontal deformation

In this test, BE measurements were made at all loading stages, using TD and FD interpretation methods. During the course of this test, it was not possible to obtain any BE measurements in the Y_{hv} direction, due to a lack of response from the receiver transducer. Measurements in the Z direction were not always successful, due to a high noise level in the signals, especially in Z_{VH5} (or Z_{VX}), consequently only a few measurements were effectively considered valid.

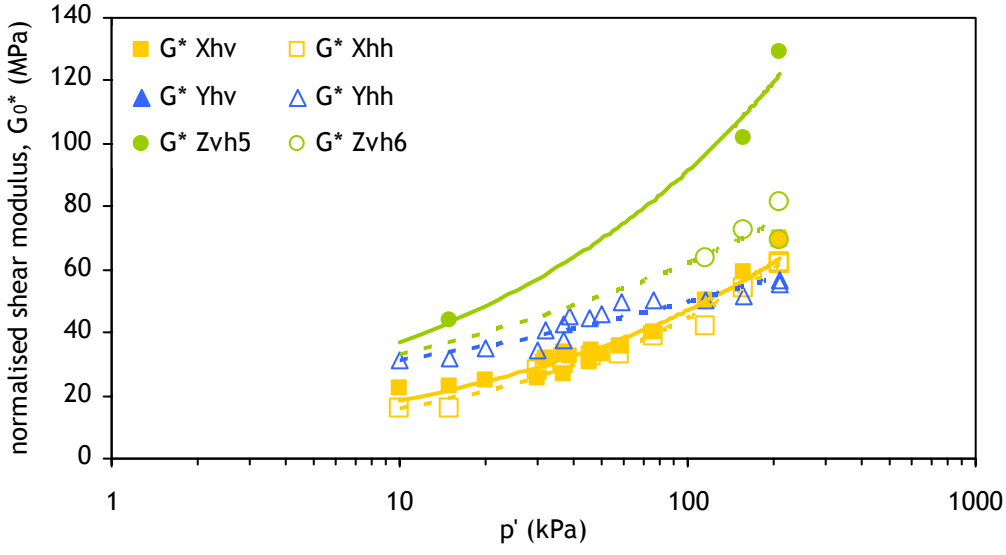
An overview of the results obtained in this test in terms of maximum normalised shear moduli in direct measurements against the three possibilities for stress dependency is illustrated in Figure 7.52. The results of the regressions are summarised in Table 7.21



a)



b)



c)

Figure 7.52 - B5-TT: normalised G_0* against: a) corresponding stresses, b) stresses in the wave propagation and polarisation directions, c) mean effective stress

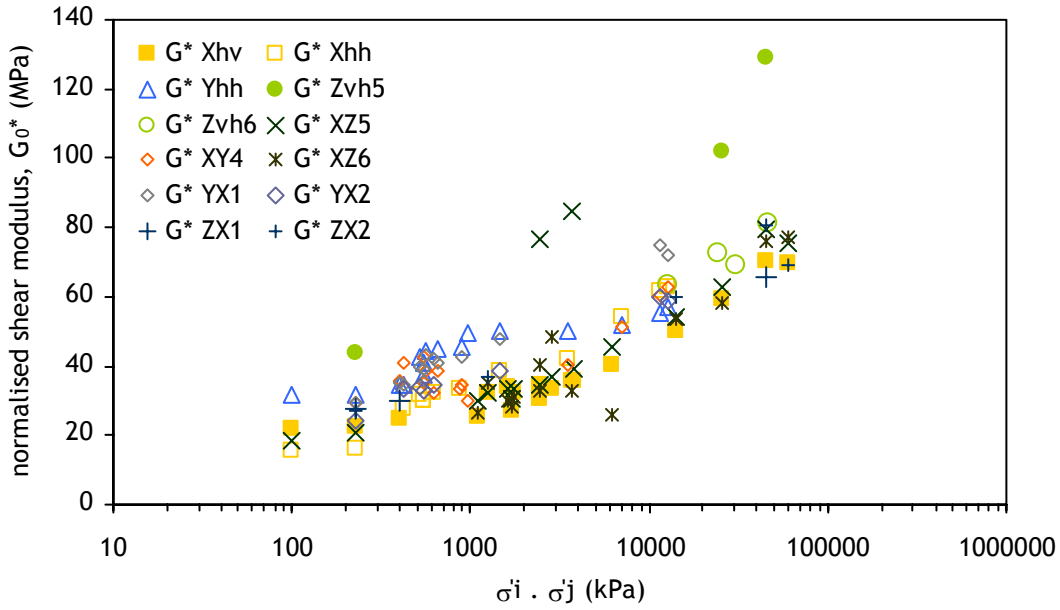
Table 7.21 - B5-TT: regression parameters for the stress-dependency approaches

	Correlation with σ'i			Correlation with σ'i.σ'j			Correlation with p'		
	Si	*ni*	R^2	*Sij*	*nij*	R^2	*Sijo*	*n*	R^2
Xhv	6106.2	0.501	0.950	7293.2	0.199	0.926	7220.7	0.407	0.934
Xhh	5111.5	0.526	0.927	4908.2	0.275	0.922	5357.6	0.448	0.966
Yhv	---	---	---	---	---	---	---	---	---
Yhh	18234	0.255	0.777	18273	0.124	0.799	19445	0.204	0.886
Zvx	18744	0.310	0.983	15161	0.194	0.987	15024	0.392	0.988
Zvy	14167	0.280	0.538	11652	0.179	0.844	17818	0.271	0.546

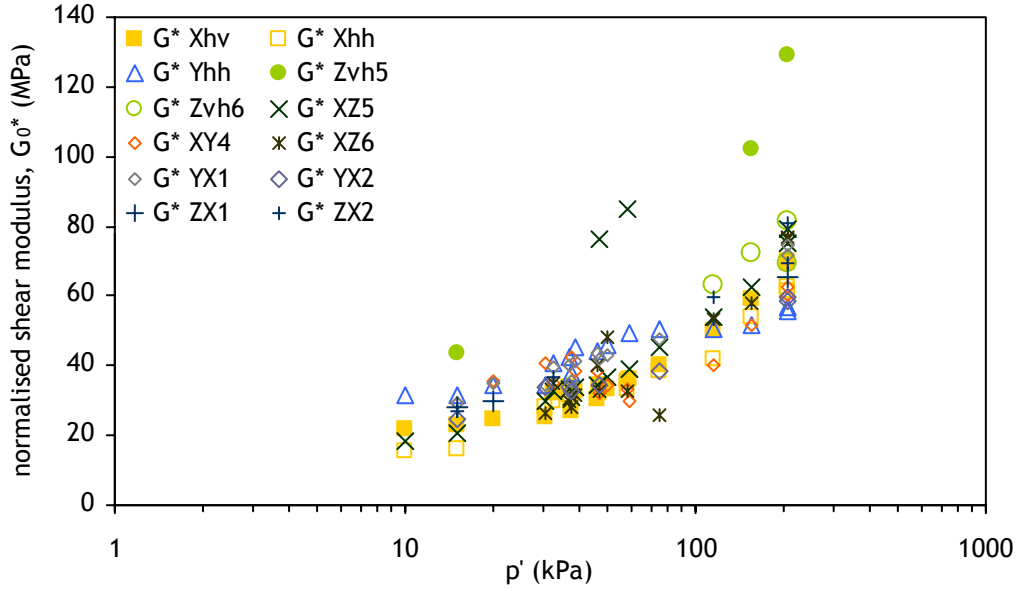
Despite the limitations in the analysis in the vertical direction, these results appear to be rather homogeneous and very consistent in relation to the considered stress components. The regressions against mean effective stress produced higher correlation coefficients, which is also evident in the graph in the adjustment of the fitted curves to the measured points. This conclusion cannot be extrapolated other true triaxial tests, since this test was carried at approximately the same horizontal X and Y stresses (as in a K_0 condition), similar to a standard triaxial test.

In addition, BE measurements of inclined waves were also carried out in this test. Almost all orientations produced clear signals, except those involving the Yhv transducers. The results of these inclined measurements are presented below in relation to both propagation and polarisation stress and to the mean effective stress.

The inclined measurements produced very similar results to the direct measurements, and also appear to be slightly better related with mean effective stress, rather than the stress in the propagation and polarisation directions. The similarity of trends in relation to stress is encouraging and suggests that, in the absence of signals in direct measurements, the measurement of inclined waves is a valid alternation to deduce the shear modulus.



a)



b)

Figure 7.53 - B5-TT: normalised G_0* against: a) stresses in the wave propagation and polarisation directions and b) mean effective stress

A final comment is due on the measured "pseudo"-coefficient of lateral earth pressure, K_0. It was designated a "pseudo"-coefficient, since in reality it is not possible to fully restore the in situ stress conditions after sampling, due to the prolonged stress relief thereafter. Hence, any laboratory measurements of K_0 can only be considered with great reserve, as a rough approximation to the real value, since it really represents a reloading process on an overconsolidated stress-path.

In this case, the measured horizontal stresses applied to the lateral platens of the apparatus, in order to fulfil the control requirement of zero-deformation in both platens, were already schematically presented in Figure 7.51. An estimate of K_0 can be directly established, since

$$K_0 = \frac{\sigma'_h}{\sigma'_v} \qquad [7.18]$$

The values of the estimate ranged from 0.41 at the lowest vertical stress of 50 kPa to 0.26 at the highest stresses, with an average value of 0.30.

It is worth recalling that the most commonly assumed K_0 value for this residual soil is 0.50, which was also considered in most of the laboratory tests carried out on the samples from both experimental sites. However, as discussed in Chapter 5, results from several in-situ tests have been analysed and correlated, suggesting values of the coefficient of lateral earth pressure closer to 0.35 (Viana da Fonseca et al., 1994; Viana da Fonseca, 1996; Viana da Fonseca and Almeida e Sousa, 2001).

One other true triaxial test was carried out on sample B4-TT. This sample was trimmed and prepared at an earlier stage from block B4, which also provide material for the cubical cell tests carried out at the University of Bristol, presented in the following section. In order to preserve as much as possible its moisture content, the large cubical sample was covered with paraffin and contained in a plastic box to prevent any accidents during storage. Finally, at the time of testing, the paraffin was removed and the sample appeared to be in very good conditions (Figure 7.54).

The adopted stress-path for this sample was also along the K_0 line but, in this case, a fixed K_0 value of 0.35 was considered, from which the horizontal and vertical stresses were accordingly defined. The purpose of this stress-path was to compare the differences in the horizontal displacements in relation to the previous test B5-TT, where the zero horizontal deformation was imposed.

Both TD and FD interpretation techniques were applied in the BE measurements. During the test, many difficulties were encountered in grounding the signals to reduce the noise level. The immediate interpretation of results was complex, as evidenced in the example of Figure 7.55. The estimated travel time of 0.126 ms was selected with some uncertainty. A very sharp P-wave is apparent, which significantly distorts the signal.



Figure 7.54 - B4-TT: preparation of the sample for testing

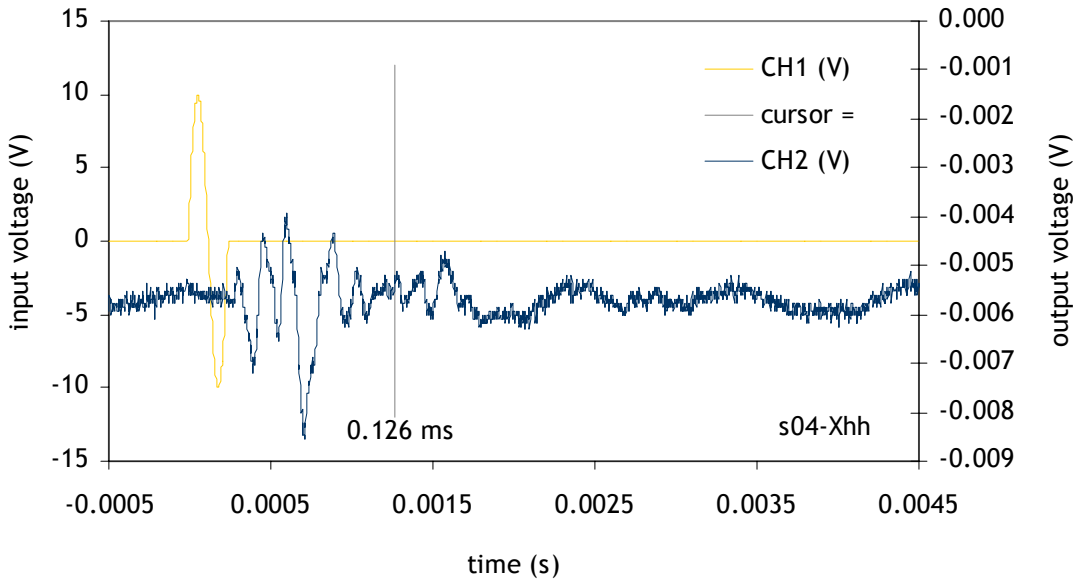


Figure 7.55 - B4-TT: BE measurement the Xhh direction at stage #4 (σ'x= σ'h=30 kPa; σ'z=65 kPa) for an input frequency of 4 kHz

These difficulties generally tend to be minimised when the whole set of results is sequentially analysed and even more so when both TD and FD techniques were applied at the time of testing. However, this case turned out to be the exception to the rule: the analyses and post-processing of the results revealed that too many inconsistencies and disparities in the results, both in the time and the frequency domain. In the absence of further reasons to justify the results, it was considered more appropriate to ignore them, for now. It is hoped that in the near future, these results can be re-analysed, eventually with the use of new and improved interpretation tools.

7.2.6. Cubical cell true triaxial tests

7.2.6.1. Introduction

The cubical cell true triaxial device was presented in detail in Chapter 3. It is a flexible boundary true triaxial apparatus, in which 100 mm cubical samples can be tested, with independent control of the three orthogonal stresses and direct measurement of strains in each side of the sample. Bender or bender-extender elements can be fitted to the apparatus. The installation of the complete set of six B/EE is not straightforward, due to the lack of support at the bottom platen, but an innovative setup procedure was successfully developed during this work, as presented earlier in section 3.5.2.

A few preparatory tests were carried out, firstly in a calibration aluminium cube and later in remoulded specimens of residual soil, which will not be discussed here. The purpose of those tests was mainly focused on the understanding of the operation and the functioning of the device, the re-calibrating of all instrumentation and the verification of the testing procedures, namely the synchronous evolution of the independent stresses.

Issues such as the preparation and installation of the specimen, the positioning and fixing of the bender elements and other operational details were also defined during the tests with the remoulded soil specimens. Seismic wave measurements were made on the remoulded material only for checking its operation and procedure but these were not systematically acquired at the time. For this reason, only the tests carried out on undisturbed soil samples will be presented and analysed.

7.2.6.2. Seismic wave measurements

As mentioned in section 3.5.2.7, the arrangement of the B/EE was different throughout the tests. Initially, the B/EE were installed only for direct measurements of seismic waves, hence their orientation in relation to those in the adjacent platens was not relevant. For the last test and with the purpose of experimenting inclined wave measurements, this arrangement had to be altered to a suitable orientation between the transducers. As a result, the B/EE in platens X and Z were rotated by 90 ° (Figures 3.45a and 3.45b).

The main implication of the different arrangements of the B/EE in the cubical cell, in terms of the analysis, is that the correspondence of the stresses acting in the wave polarisation direction needs to be shifted accordingly, from the first tests to the last.

The calculation of the tip-to-tip distances was made according the same principles described for the true triaxial device, namely for the inclined wave measurements, in Table 7.14.

7.2.6.3. CC test results on natural undisturbed samples

After the process of re-activation and testing of this apparatus and due to time restrictions, only three tests on natural undisturbed samples were successfully completed during the six-month period at the University of Bristol. The main physical properties of those samples are listed in Table 7.22. In what follows, the main results obtained on these tests, over a variety of stress conditions, will be presented.

Table 7.22 - Summary of physical properties of the undisturbed specimens tested in the CC

Specimen	γ [kN/m^3]	w_0 [%]	e_0
B6-RS1	17.33	17.5	0.780
B6-RS2	17.39	15.7	0.746
B4-RS3	16.90	26.0	0.956

The first undisturbed sample tested in the cubical cell apparatus was B6-RS1. Its main physical properties are presented in Table 7.22. The objective of this test was to experiment a variety of stress-path options, relevant to the research, and to observe the response of the soil in terms of stiffness, strains and strength as well as to

assess the performance of the apparatus. For this purpose, a rather elaborate stress-path was considered, including isotropic consolidation to the expected in situ vertical stresses, shearing at constant mean effective stress, second loading at "pseudo"-K_0 conditions simulating the in situ conditions at greater depths, and second shearing also at constant p'. This is schematically illustrated in Figure 7.56.

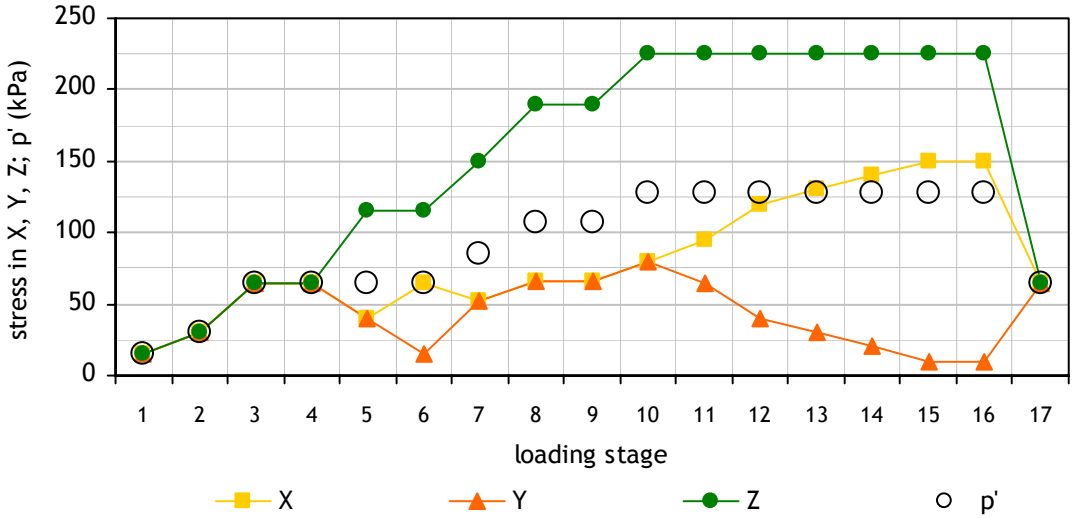
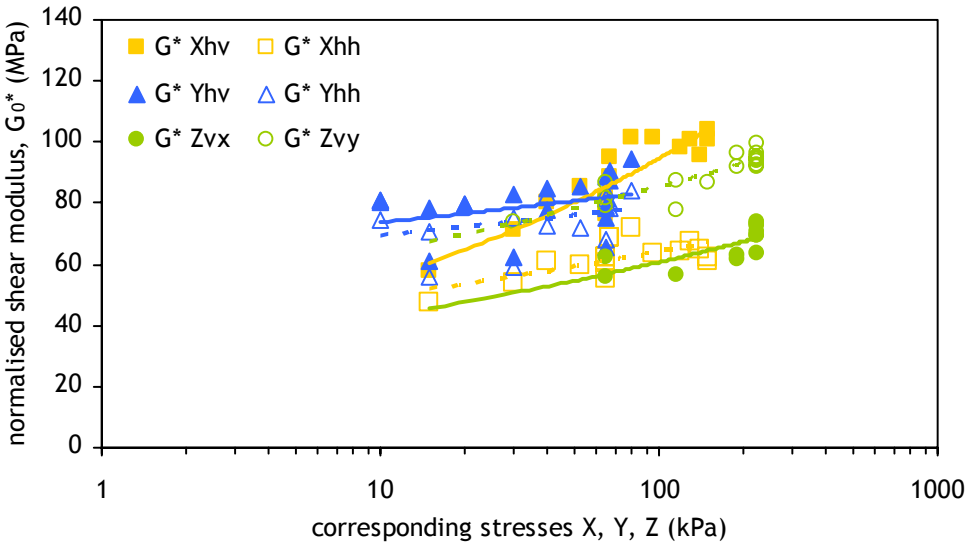


Figure 7.56 - B6-RS1: schematic of the stress-path

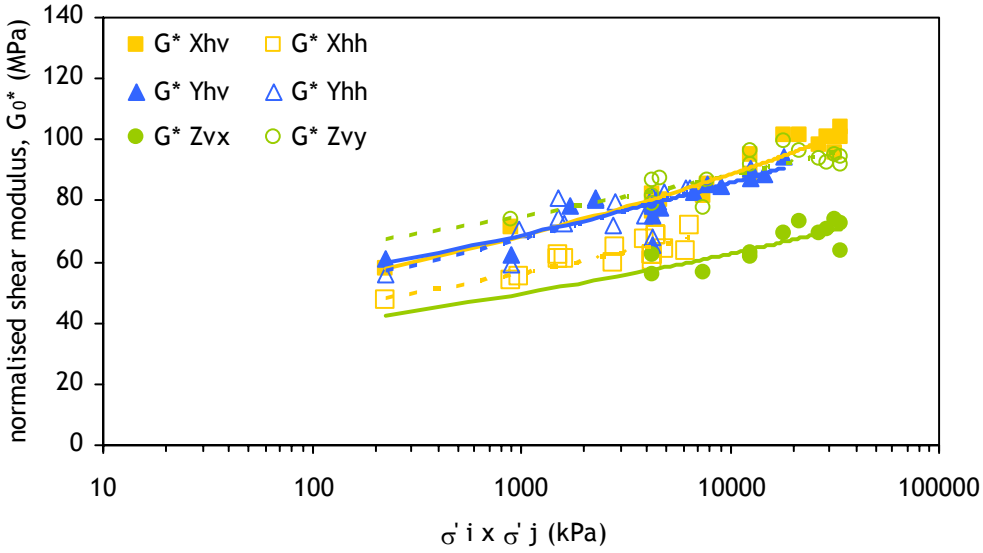
The results in terms of the shear moduli are presented in the following graphs of Figure 7.57, in relation to the three stress dependency approaches: a) corresponding stress, that is, wave propagation stress; b) wave propagation and polarisation stresses; and, c) mean effective stress, that is, including the out-of-plane stress. The correlation parameters obtained from the power regression curves are presented in Table 7.23.

Table 7.23 - B6-RS1: correlation parameters for two stress-dependency approaches

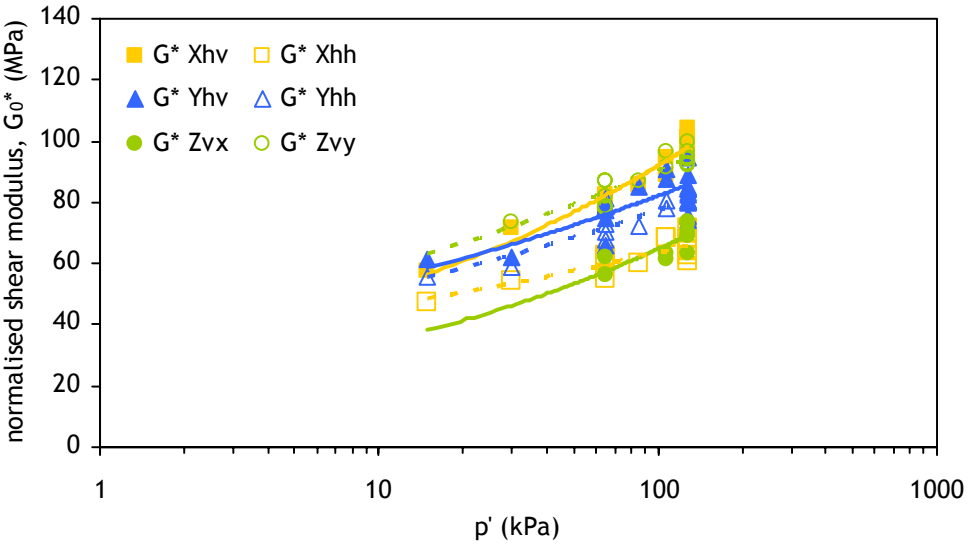
	Correlation with σ'i			Correlation with σ'i.σ'j			Correlation with p'		
	Si	*ni*	R^2	*Sij*	*nij*	R^2	*Sijo*	*n*	R^2
Xhv	31801	0.237	0.825	31522	0.112	0.945	28108	0.257	0.939
Xhh	38228	0.113	0.471	27987	0.101	0.613	32713	0.145	0.746
Yhv	64524	0.057	0.107	35497	0.096	0.785	36247	0.178	0.722
Yhh	60754	0.057	0.122	31273	0.111	0.674	34535	0.175	0.781
Zvx	30292	0.151	0.552	24462	0.102	0.643	18103	0.277	0.701
Zvy	48208	0.124	0.780	45694	0.072	0.702	37562	0.191	0.832



a)



b)



c)

Figure 7.57 - B6-RS1: normalised G_0 against: a) corresponding stresses, b) stresses in the wave propagation and polarisation directions, c) mean effective stress

Considering the three possible relationships between normalised shear moduli and the stress components, it is clear that both stresses in the wave propagation and polarisation direction have considerable influence in the measured parameter, thus both must be included in the equation to satisfactorily model the stiffness response. What is more striking is that the consideration of the influence of p' in the shear moduli is reasonable and does in some cases (that is, measured directions) provide better estimate of the evolution of the stiffness with stress. This appears to reveal that the out-of-plane stress may also play a part in the measured shear modulus.

The test on sample B6-RS2 was carried out with the intention of characterising in greater detail the soil behaviour at more relevant stress conditions, in parallel with the estimated in situ state. Its response in terms of stiffness and strains was monitored in a series of isotropic stages followed by a shearing stress-path at constant p'. This simple stress-path is illustrated in Figure 7.58. The comparison of the shear moduli of this and the previous test enabled to complement the information, regarding the most influential parameters of stiffness (Figure 7.59a, b and c)

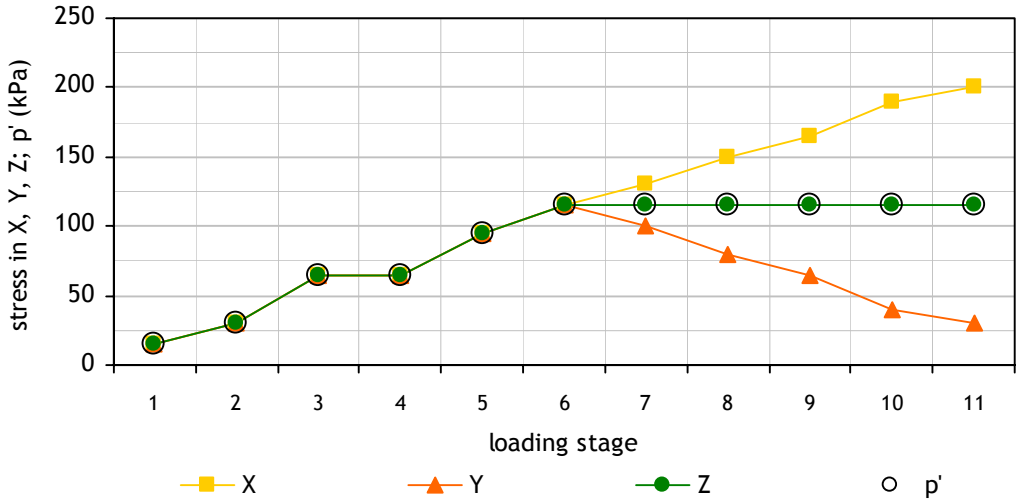
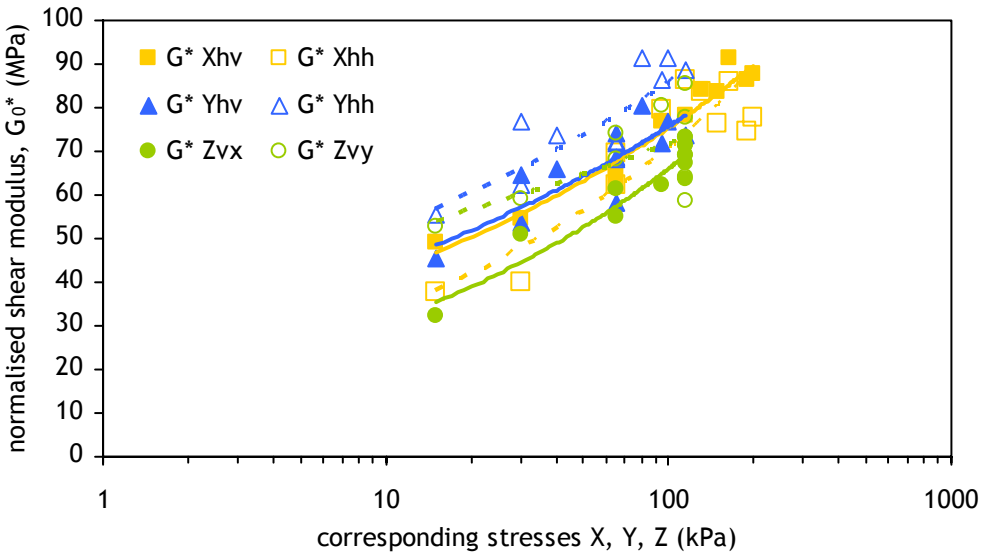
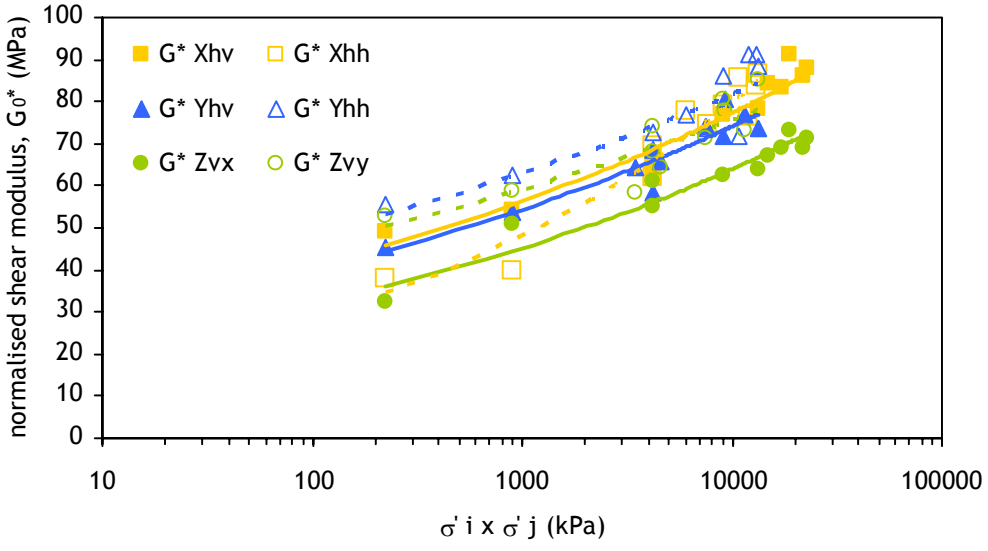


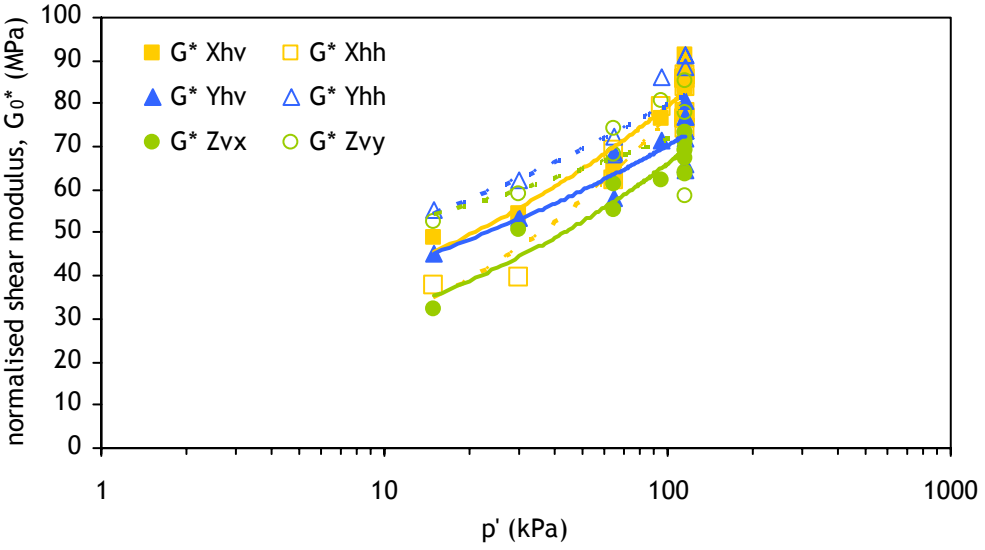
Figure 7.58 - B6-RS2: schematic of the stress-path



a)



b)



c)

Figure 7.59 - B6-RS2: normalised G_0 against: a) corresponding stresses, b) stresses in the wave propagation and polarisation directions, c) mean effective stress

Table 7.24 - B6-RS2: correlation parameters for the three stress-dependency approaches

	Correlation with σ'ij			Correlation with σ'i.σ'j			Correlation with p'		
	Si	*ni*	R^2	*Sij*	*nij*	R^2	*Sijo*	*n*	R^2
Xhv	23597	0.252	0.956	21793	0.137	0.943	29234	0.305	0.914
Xhh	15658	0.328	0.833	10476	0.220	0.929	16151	0.426	0.926
Yhv	25656	0.235	0.731	22125	0.128	0.903	34491	0.243	0.814
Yhh	31495	0.218	0.712	27562	0.121	0.823	44763	0.214	0.722
Zvx	14533	0.329	0.918	15954	0.151	0.921	20650	0.341	0.924
Zvy	36344	0.148	0.452	28239	0.107	0.762	51640	0.160	0.460

In this test, the stress components that most influence the evolution of the shear moduli are those in the wave propagation and polarisation direction. The results obtained for the regression considering p' indicate however that the combination of the three independent stresses is also influential in the measured stiffnesses.

The third test was carried out on sample B4-RS3. This sample was prepared in a similar manner as the previous ones, trimmed from a larger block to the necessary dimensions of the cubical cell of about 100 mm side length. During preparation, a large discontinuity became clearly visible in the middle of the specimen, almost dividing it into two parts in the X direction, as illustrated in the photographs below, in Figure 7.60.

This fault material had a flaky appearance and a brittle response when crushed between the fingers. After the final preparation and smoothing of the surface of the sample with some of the remaining material, the discontinuity is no longer visible. For that reason, its position was marked and noted on a sketch, to indicate the orientation of the sample inside the cell. It is anticipated that this heterogeneity will affect the results, since the other samples were considerably more homogeneous.

Considering the limitations of testing a heterogeneous sample, a simple stress-path, predominantly K_0 consolidation was considered, followed by a short shearing phase once again at constant p'. This stress-path is illustrated in Figure 7.61.

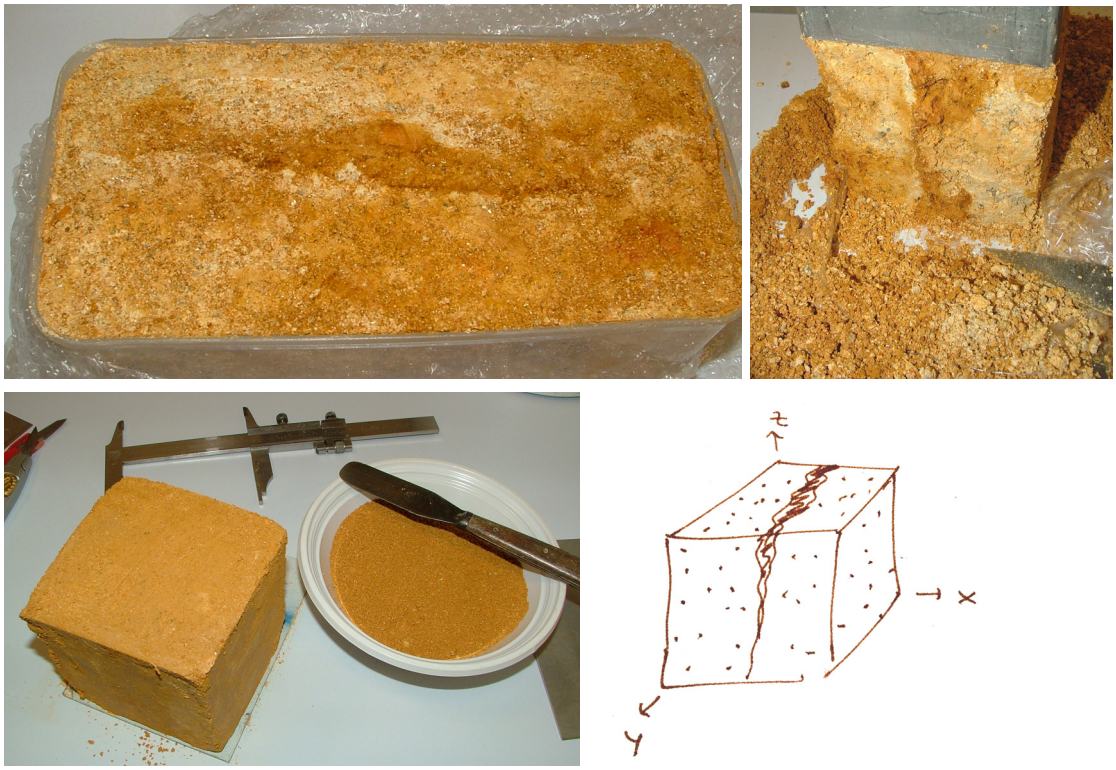


Figure 7.60 - B4-RS3: photographs of the trimming process and the evidence of a central discontinuity in the specimen (a hand-drawn sketch indicates the position pf this discontinuity in relation to the platens of the cubical cell)

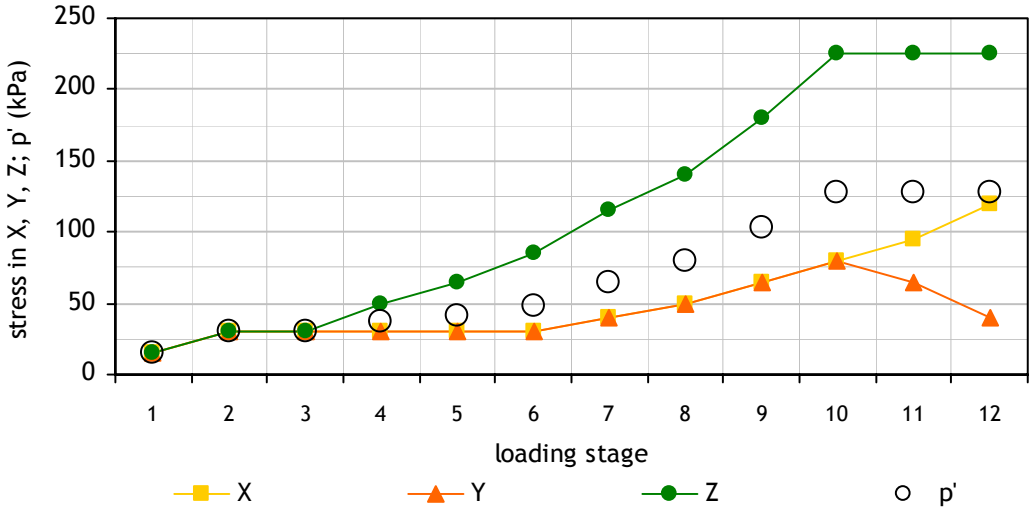


Figure 7.61 - B4-RS1: schematic of the stress-path

This test had also been planned for the measurement of not only direct but also inclined waves. Despite having been recorded and measured, its interpretation was largely affected and compromised by the heterogeneity of the tested material. For this reason, the inclined wave measurements taken on this sample were not analysed. The shear moduli obtained in each direct wave measurement are presented in Figure 7.62, again in relation to the three stress-dependency approaches.

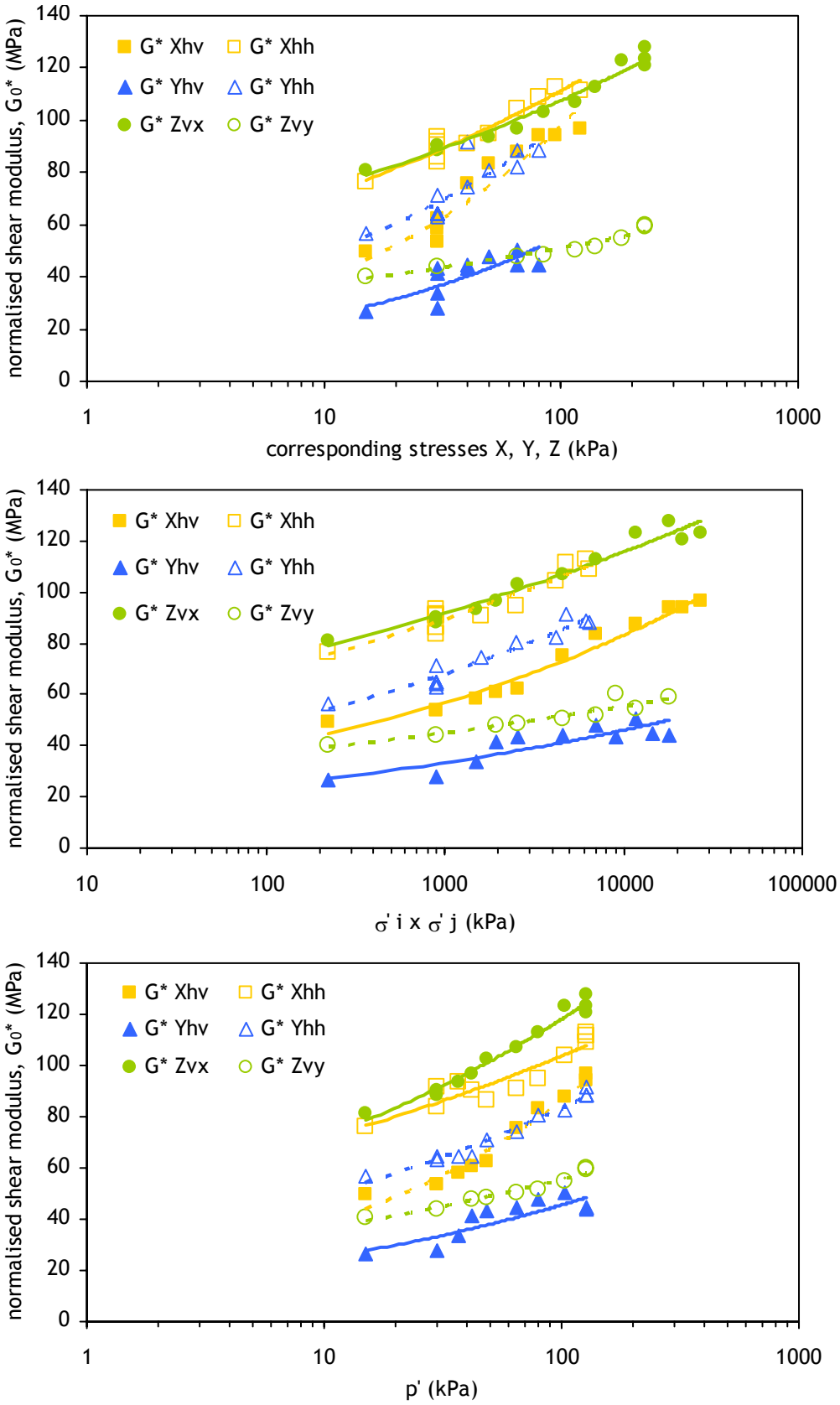


Figure 7.62 - B4-RS3: normalised G_0 against: a) corresponding stresses, b) mean effective stress, c) stresses in the wave propagation and polarisation directions

A summary of the regression parameters is presented in Table 7.25.

Table 7.25 - B4-RS3: correlation parameters for the three stress-dependency approaches

	Correlation with σ'ij			Correlation with σ'i.σ'j			Correlation with p'		
	Si	*ni*	R^2	*Sij*	*nij*	R^2	*Sijo*	*n*	R^2
Xhv	16014	0.393	0.891	18176	0.165	0.958	16959	0.352	0.959
Xhh	45828	0.193	0.923	41042	0.113	0.912	49462	0.161	0.862
Yhv	11096	0.349	0.604	12610	0.141	0.777	13747	0.260	0.723
Yhh	24180	0.304	0.769	23925	0.151	0.933	29446	0.226	0.969
Zvx	50647	0.164	0.970	45900	0.100	0.965	43785	0.215	0.977
Zvy	27300	0.136	0.940	24213	0.090	0.911	24251	0.179	0.969

The results of this test show larger differences between corresponding velocities in the same directions, as indicated by high V_{Xhh} and the low V_{Yhv}. Since a discontinuity was clearly visible in the sample during preparation, as illustrated in Figure 7.60, these different velocity measurements are in fact expected.

This observation confirms the aptitude of the shear wave velocities to detect irregularities, discontinuities or other changes in soil properties, thus demonstrating its usefulness and applicability in soil characterisation.

7.2.6.4. Comparison of results for the three CC undisturbed samples

Finally, it is interesting to plot all the obtained results together, for comparison of the responses of the three undisturbed samples, provided in Figure 7.63.

The convergence and overlap of the shear moduli measured in the three samples in most directions, namely in the X_{hv}, Y_{hh}, and also in Z_{vy}. On the other directions, the results of the last sample B4-RS3 appear detached from the others, which is, as previously mentioned, a result of a local heterogeneity, thus not characteristic of the soil.

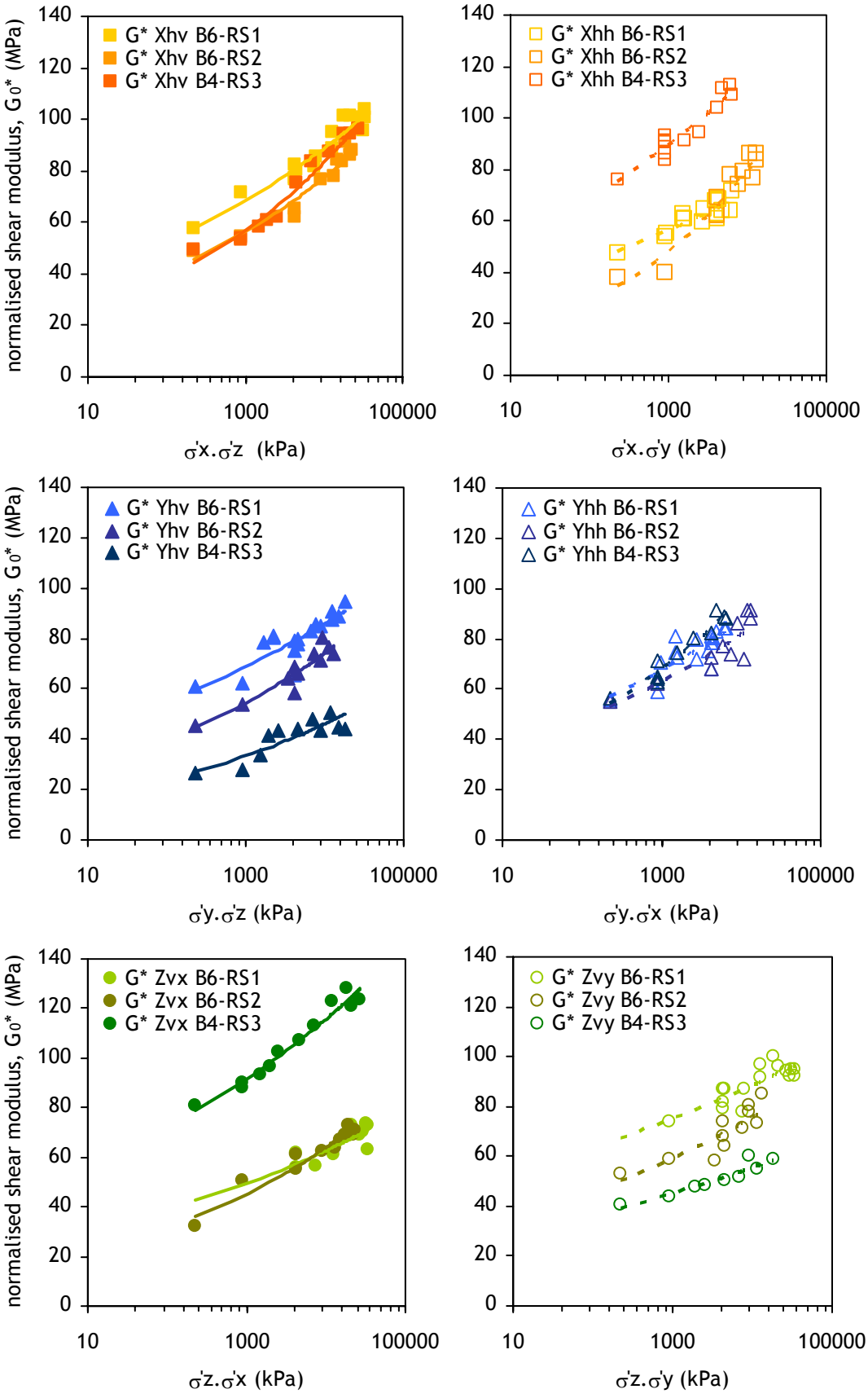


Figure 7.63 - Normalised G_0 against corresponding stresses for the 3 CC samples

7.3. Small to large strains

7.3.1. Introduction

In this section, the most relevant results in terms of stiffness at small to large strains (10^{-5} to 10^{-2}) will be presented, from measurements obtained in resonant-column, standard triaxial and true triaxial tests. Since the main focus of this work is the application of wave velocities in the measurement of stiffness, these results will be mainly used for its comparison towards medium to large strain levels, as its value is a function of the strain level, and therefore necessary for a good definition of the stiffness degradation curves.

7.3.2. Resonant-column tests

The primary aim of tests carried out in the resonant-column device equipped with BE, partly presented in section 7.2.2, was the determination of the maximum shear stiffness from RC and BE measurements. For the case of the samples from ES2, after the consolidation stages, these samples were subjected to increasing levels of shear strain (distortion), in which the stiffness tends to decrease, as shown in Figure 7.64. At these increasing strain stages, only RC measurements are taken.

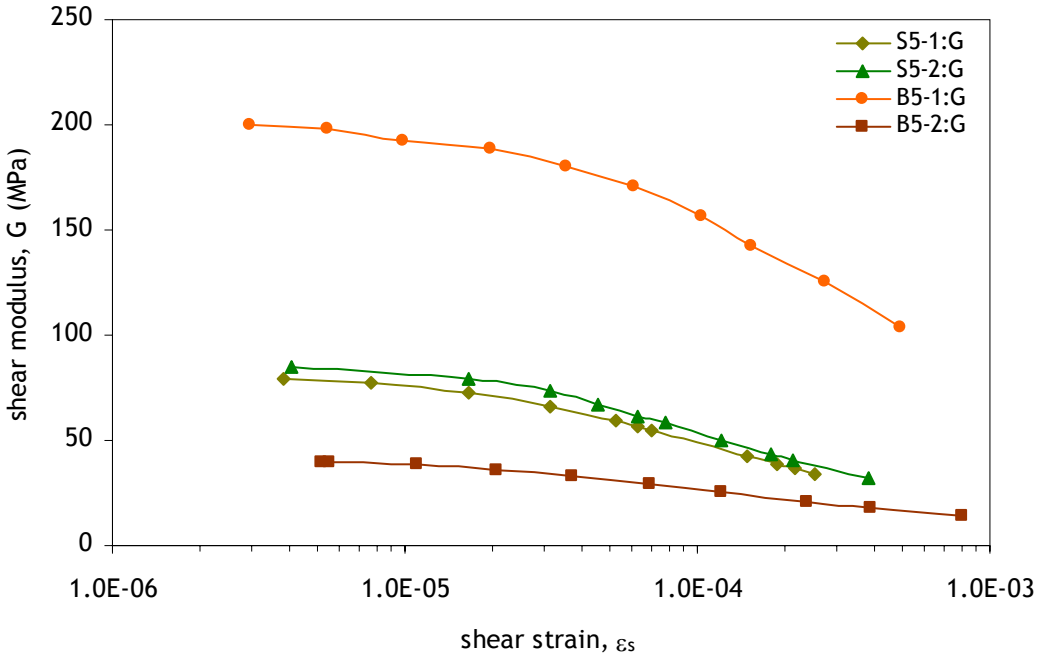


Figure 7.64 - Resonant-column test results on ES2 samples: stiffness versus shear strain, for different confining stresses

This reduction in stiffness, also called degradation, is generally expressed as a plot of G/G_0 versus shear strain γ, where G_0 is the "elastic", very small shear strain modulus (Fahey, 1992). The normalized stiffness G/G_0 and the damping ratio D obtained on these samples are plotted as a function of the shear strain in Figure 7.65.

Despite the similarity of the trends in the degradation curves, it is not possible to directly derive a unique relationship between the normalised stiffness modulus and the shear strain level. This is mainly due to the different stress conditions in each of the tests, as indicated in the legend of Figure 7.65.

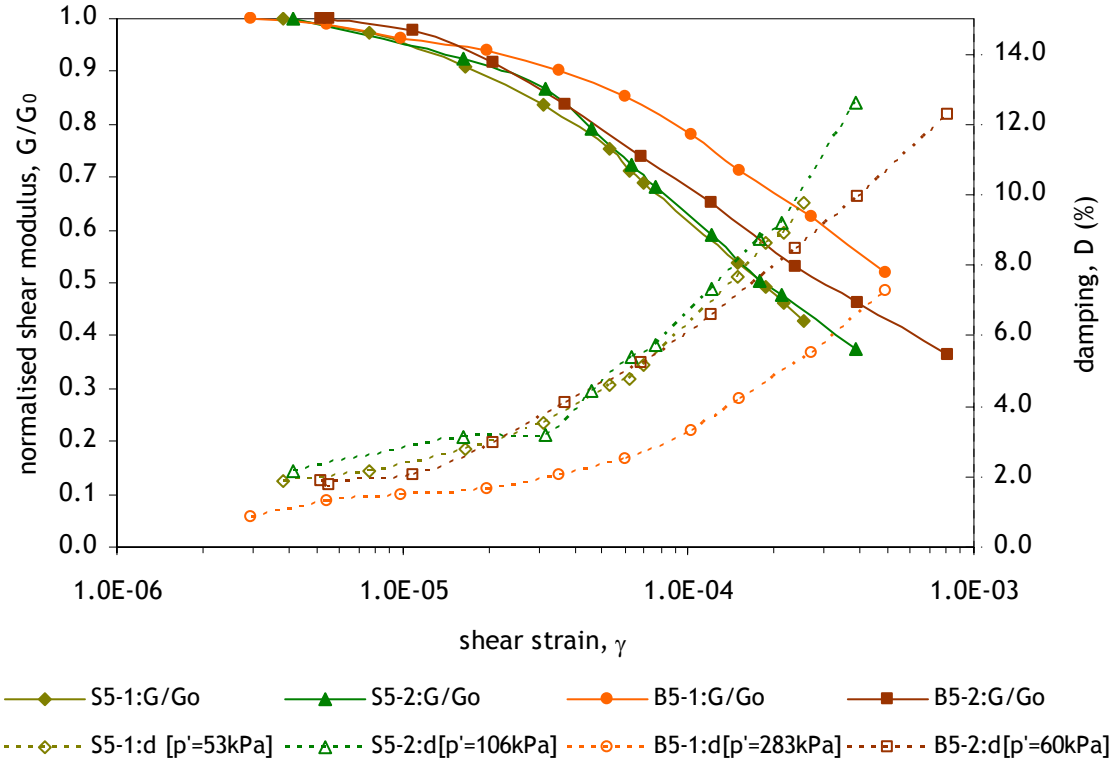


Figure 7.65 - Resonant-column test results on ES2 samples: normalized stiffness and damping ratio versus shear strain, for different confining stresses

Hardin and Drnevich (1972a, 1972b) were the first to identify the non-unique relationship between G/G_0 and shear strain γ (or ε_s), thus suggesting the use of a plot of G/G_0 versus γ/γ_r, where γ_r is the reference shear strain (Fahey, 1992). A quasi-unique "reference behaviour" curve has been proposed by Santos (1999), where the reference threshold shear strain γ_r corresponds to a stiffness degradation factor G/G_0 of 0.7, that is, $\gamma_{0.7} = \gamma_r$. This normalisation is closely related with the concept of volumetric threshold shear strain, and represents the limit beyond which changes in

soil structure are irreversible (Vucetic, 1994). In practical terms, the reference threshold shear strain defines the beginning of significant stiffness degradation and increase of hysteretic damping (Gomes Correia et al., 2001). For the shear strain range of 10^{-6} to 10^{-2}, this normalised stiffness and strain relationship appears to be almost unaffected by the type of soil, plasticity index, confining pressure, overconsolidation ratio or degree of saturation (Viana da Fonseca and Coutinho, 2008).

The test results on the four undisturbed samples from ES2 were normalised in relation to the corresponding shear strain, presented in Figure 7.66 and summarised in Table 7.26. In this normalised plot, it is possible to integrate reference stiffness degradation curves, namely the upper and lower bounds proposed by Santos (1999) for sands, and the curve for a non-plastic soil proposed by Vucetic and Dobry (1991).

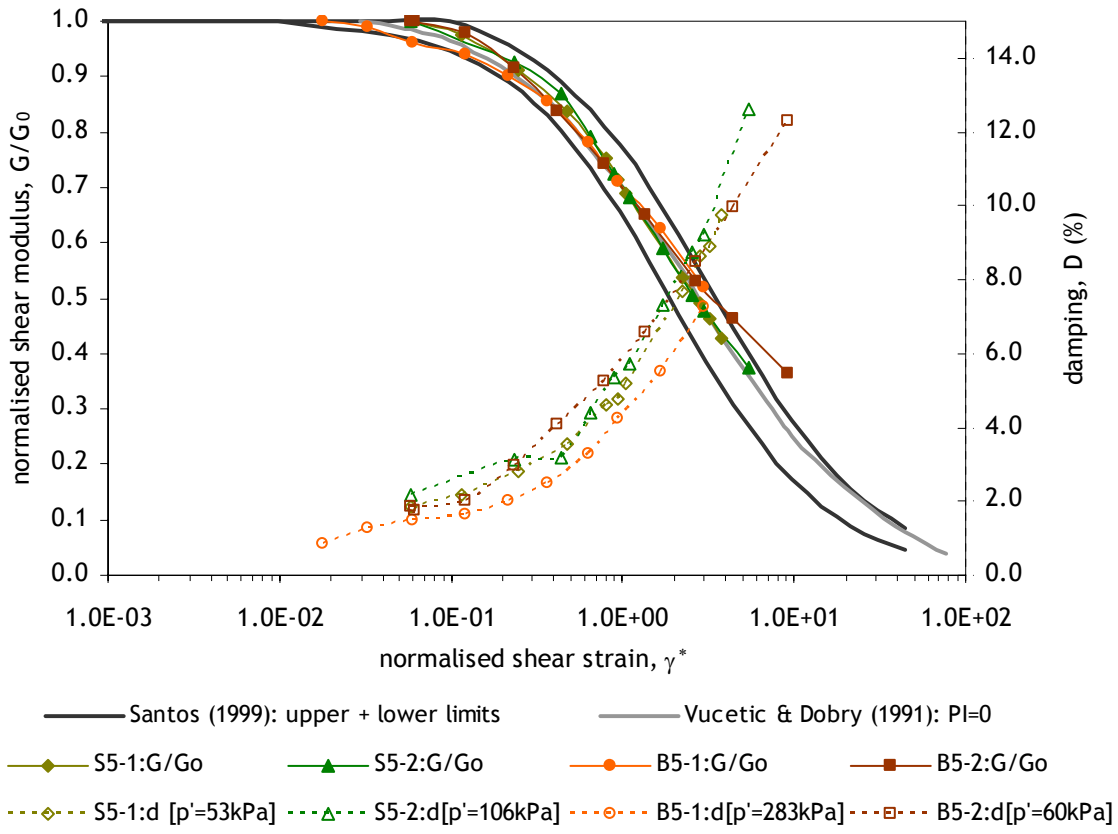


Figure 7.66 - Resonant column results: normalized stiffness and damping ratio versus normalised shear strain

The results clearly show that the stiffness-strain response of this soil is well defined and framed within these reference curves. The values of the reference shear strain, indicated in Table 7.26, suggest some variability, possibly due to the different stress conditions, since at higher stresses, the values of γ_r (or ε_{sr}) tend to be higher. This

relationship is analysed in Figure 7.67, where two additional curves for saprolitic and lateritic soils have been included, after the proposal of Gomes Correia et al. (2001) derived from a large number of RC tests on these soils.

Table 7.26 - RC+BE samples: summary of stiffness degradation results

RC+BE sample	e	p' (kPa)	G_0 (MPa)	minimum shear strain, γ or ε_s	reference shear strain, γ^* or ε_s^*
S5-1	0.462	53.33	79.44	3.84E-06	6.65E-05
S5-2	0.568	106.67	85.25	4.11E-06	7.09E-05
B5-1	0.885	283.33	200.43	2.951E-06	1.63E-04
B5-2	0.852	60.00	39.54	5.50E-06	8.90E-05

The results clearly show that the stiffness-strain response of this soil is well defined and framed within these reference curves. The values of the reference shear strain, indicated in Table 7.26, suggest some variability, possibly due to the different stress conditions, since at higher stresses, the values of γ_r (or ε_{sr}) tend to be higher. This relationship is analysed in Figure 7.67, where two additional curves for saprolitic and lateritic soils have been included, after the proposal of Gomes Correia et al. (2001) derived from a large number of RC tests on these soils.

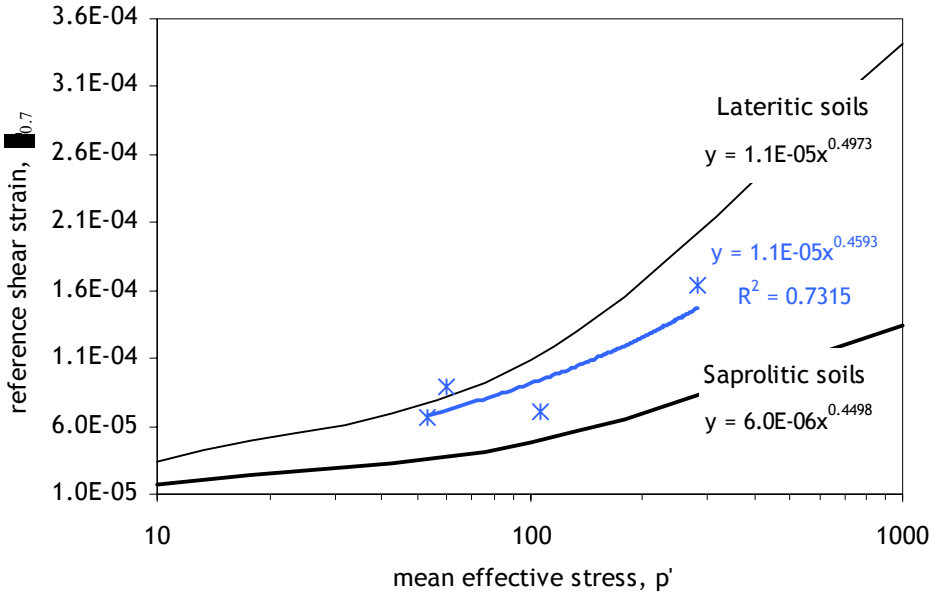


Figure 7.67 - RC+BE samples: reference shear strain, as a function of mean effective stress

The results for this soil appear to fit well within the proposed curves. Despite the saprolitic nature of the soil in study, its response in terms of the reference shear strain, that is of the beginning of the stiffness degradation, is intermediate between the response of a lateritic and a saprolitic soil.

7.3.3. Triaxial tests

Most of the standard triaxial tests carried out in this research included a shearing stage for the characterisation of the strength parameters of the soil samples. As previously mentioned, in order to allow sufficient stabilisation of the stresses during shearing prior to BE testing, a large number of tests were carried out considering a manual increment of the stresses. In such cases, the acquisition of the stress and strain results was also manually recorded, hence without the use of automatic acquisition.

With the objective of defining the stiffness versus strain relationship, this acquisition method poses some limitations, namely in the interpretation in the unload-reload cycles, due to the small number of points. In any case, the results presented below enable to observe a clear reduction of stiffness with increasing strain levels. For clarity, the presentation of the results has been divided according to the origin of the samples.

7.3.3.1. Internal versus external strain measurements

Before presenting the results, it is important to address the observed differences between internal (or local) and external measurements of strain. The example in Figure 7.68 refers to sample S2-3-TX, randomly selected. In this test, two LDT were used, directly fixed to opposite sides of the sample, as well as an external LVDT, fixed to the loading piston. The results presented in the figure clearly illustrate that the externally-measured strain is systematically larger than the internally-measured, particularly at small strains. At higher strains, the difference between the three measurements appears to remain the same.

For this reason, the calculation of the secant stiffness at small and medium strains was made considering the average of the two internal strain measurements. In cases where the strain level exceeded the limit of the internal transducers, namely the LDT beyond 10% strain, external measurements were used.

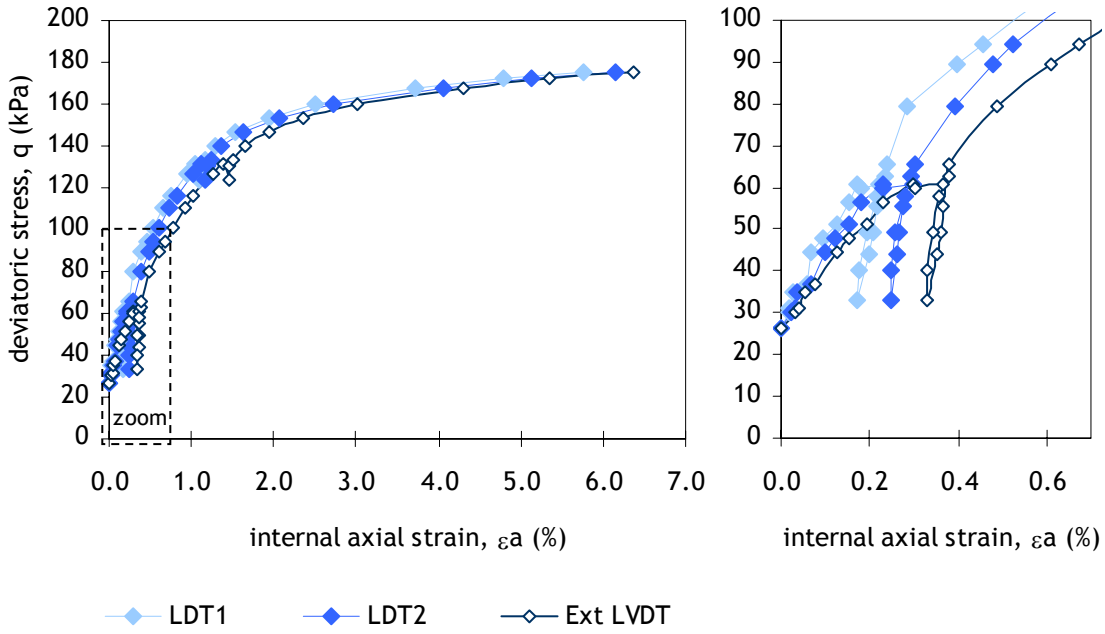


Figure 7.68 - ES2 test S2-3-TX: example of internal and external strain measurements, a) full test data; b) measurements below 100 kPa and 0.7%

7.3.3.2. Stress-strain response of undisturbed samples from ES1

The shearing stress-path obtained from the standard triaxial tests, on the undisturbed samples from ES1, is presented in Figure 7.69. The data points correspond to the end of each stress increment at which the measurements were taken.

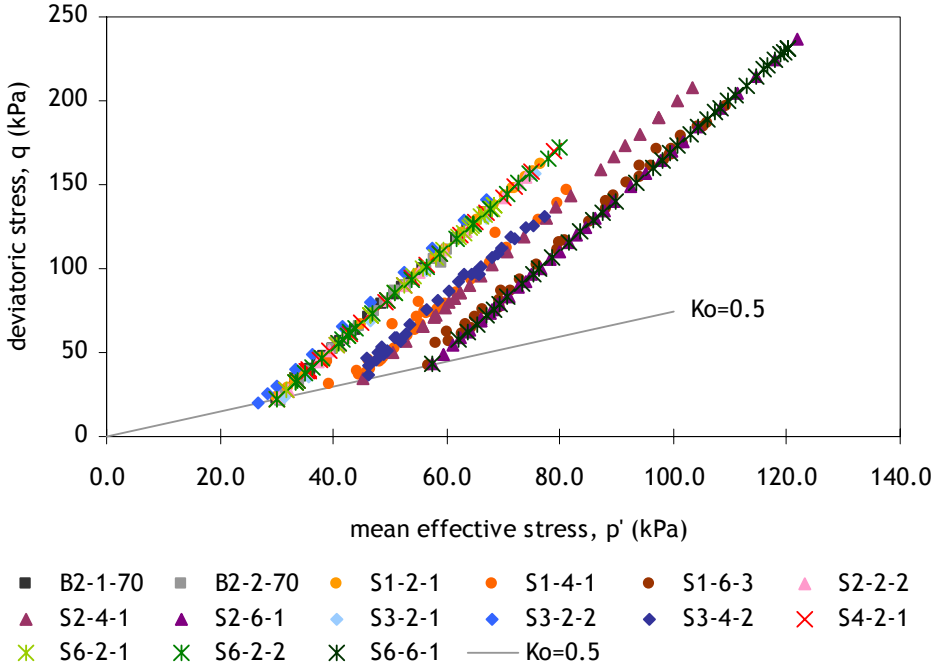
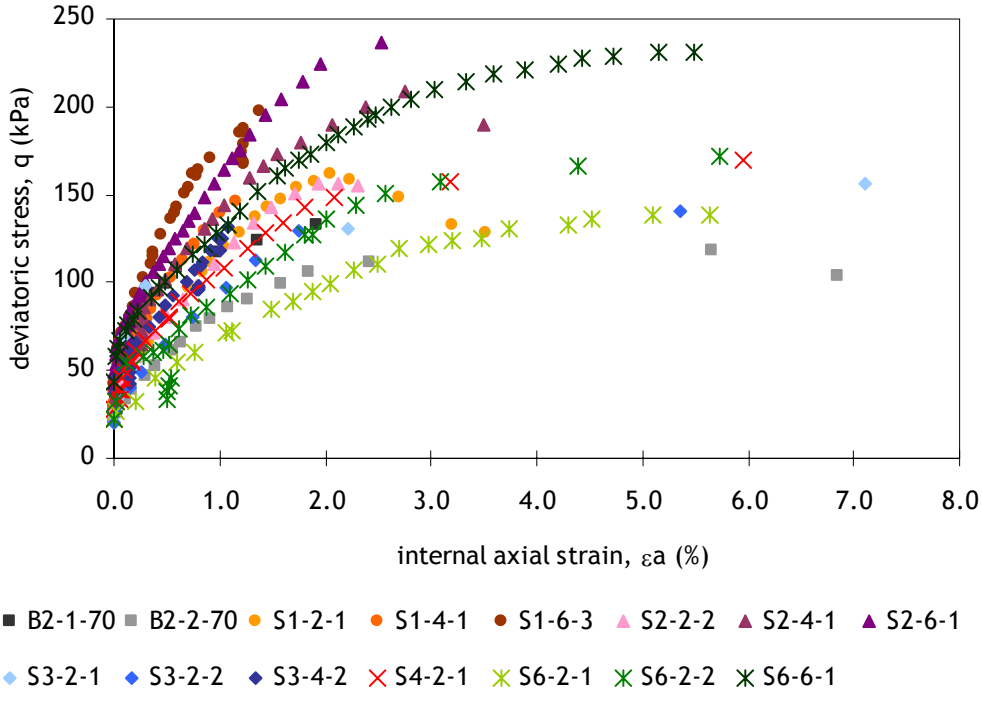
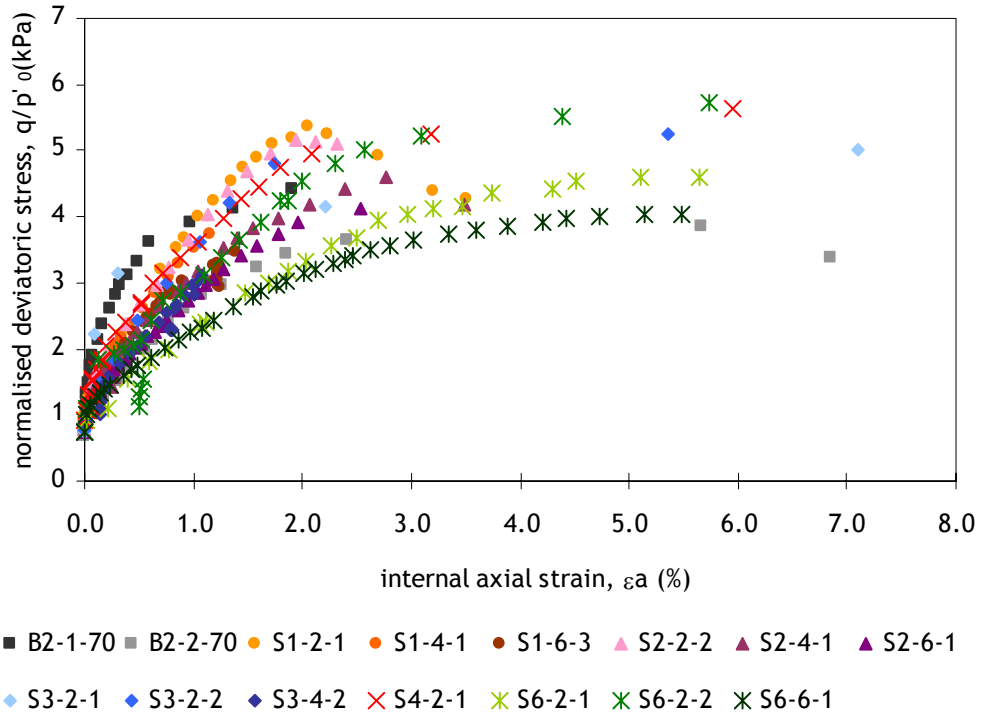


Figure 7.69 - ES1 undisturbed samples: summary of stress-paths

The obtained stress-strain curves are illustrated in Figure 7.71a and b, in terms of deviatoric stress q versus internal axial strain ε and normalised deviatoric stress in relation to the consolidation mean effective stress, q/p'_0, respectively. The evolution of volumetric versus axial strains is presented in Figure 7.71c.



a)



b)

Figure 7.70 - ES1 undisturbed samples: summary of the stress-strain curves, a) deviatoric stress against internal axial strain; b) normalised deviatoric stress against internal axial strain

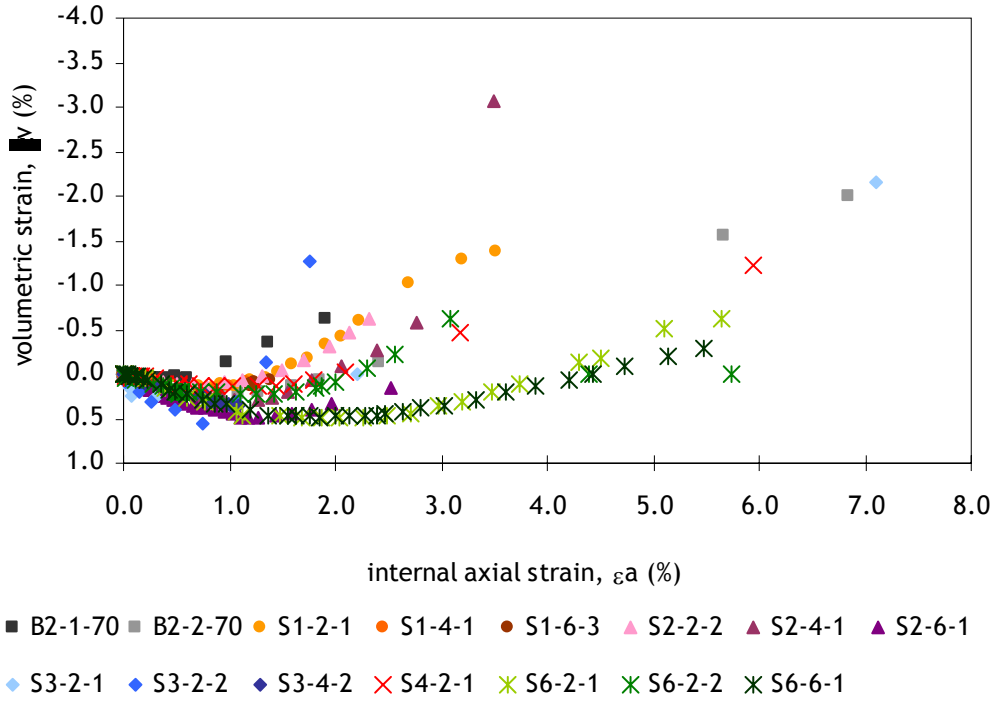


Figure 7.71 - ES1 undisturbed samples: volumetric against internal axial strains

Considerable differences can be observed in the stress-strain response of the tested undisturbed samples, which can be attributed to a number of influencing factors, namely to state (void ratio and water content) conditions, structural damage caused by the different sampling processes, adopted stress conditions in relation to actual in-situ stress state, ageing, etc. The analysis of all these factors is beyond the scope of this research.

7.3.3.3. Stiffness-strain response of undisturbed samples from ES1

The internal (and, if necessary, external) strain measurements can be used to determine the stiffness of the soil. Since in most tests only vertical internal strain transducers were used, the derived stiffness corresponds to the Young's modulus of the soil in the vertical direction, E_v. The stiffness can be defined as either secant or tangent. In this work, only the secant stiffness was used, which can be determined from the ratio of the difference in stress and strain from the start of the shearing phase. Its determination is less influenced by data scattering and its interpretation is simpler, when compared to the tangent stiffness (Sukolrat, 2007).

The stiffness-strain response can be analysed considering the evolution of the vertical secant stiffness with the measured local axial strain, illustrated in Figure 7.72. For

simplicity, in this representation, the strains are indicated as percentage, since that is the usual notation in standard triaxial testing.

Also included in the figure are the estimates of E_{v0} derived from the shear modulus determined by BE measurements at the final consolidation stage, immediately before the start of the shearing stage. These estimates were computed assuming that a good approximation of the vertical Young's modulus can be obtained from the following equation:

$$E_{v0BE} = 2 \cdot (1 + \nu) \cdot G_{\text{vhBE}} \qquad [7.19]$$

and assuming a value for the Poisson's ratio ν equal to 0.30, as previously adopted by other authors to characterise this soil (Viana da Fonseca, 1996). In accordance with the discussion in section 7.2.2.4, the strain at which this elastic moduli was determined in the BE measurements, was considered equal to $3x10^{-6}$ (that is, $3x10^{-4}$% in the graph).

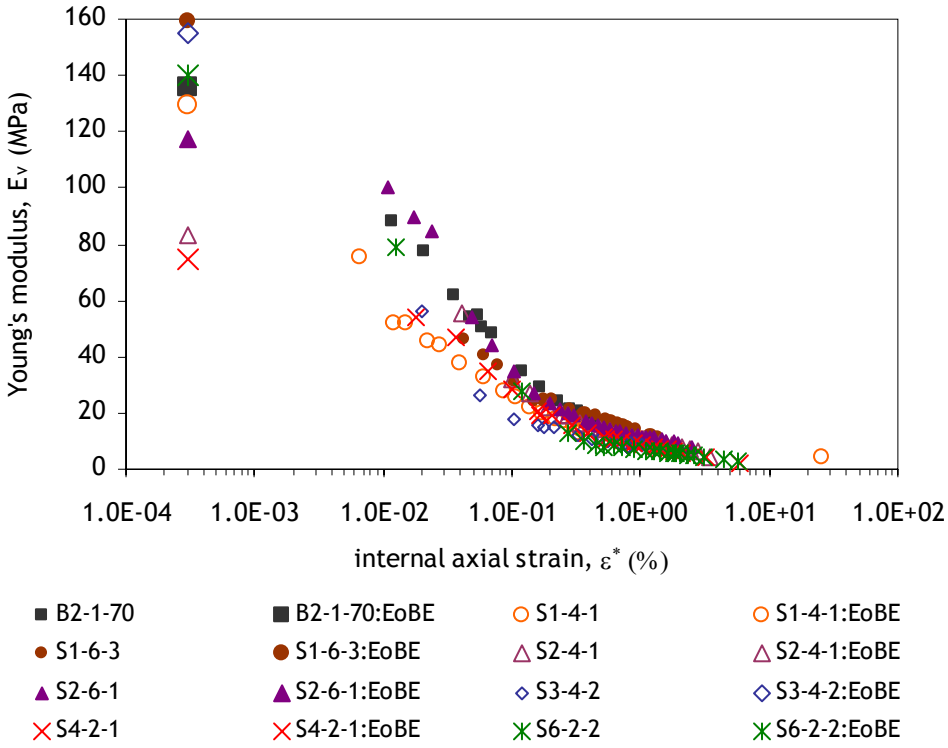


Figure 7.72 - ES1 undisturbed samples: summary of the stiffness-strain curves, including the estimate of E_0 from BE measurements

From the figure, it can be concluded that there is not a direct correspondence between the relative positions of the elastic stiffness E_0 (from G_{0BE})and the stiffness

degradation curve of the tested samples. For example, the results from sample S2-6-1 (solid triangle) indicate the highest Young's modulus from static measurements, whereas its elastic modulus is below the average value of all samples. One of the reasons for this discrepancy is certainly related with the limitations of the use of manual acquisition, as opposed to automatic acquisition. Other causes can be anticipated, associated with the behaviour of the soil, which were not explored in this study. Nevertheless, this plot provides a clear indication of the reduction of stiffness with increasingly larger strains.

Despite the limitations of the data, these results can be further analysed, using the hyperbolic model proposed by Hardin and Drnevich (1972a) and further developed by Fahey and Carter (1992) and Fahey (1998). According to these authors, a much more informative method of showing the modulus degradation is to plot G/G_0 versus shear stress, normalised by the shear strength (that is, τ/τ_{max}), since for a true hyperbolic relationship, this plot results in a straight line. In order to compare the results from monotonic tests with the hyperbolic relationship, it is more appropriate to consider the secant Young's modulus normalised by the initial (for $q=q_0$) secant Young's modulus E_s/E_{s0} versus the deviatoric stress normalised by the maximum deviatoric stress or shear strength, both corrected to the consolidation deviatoric stress: $(q\text{-}q_0)/(q_{max}\text{-}q_0)$. The general expression of this hyperbolic model is:

$$\frac{E}{E_0} = 1 - f\left(\frac{q}{q_{ult}}\right)^g \qquad [7.20]$$

The obtained plot of E_s/E_{s0} versus (q/q_{max}) is presented in Figure 7.73.

Alternatively, the analysis of the hyperbolic relationship can be analysed in terms of axial strains in relation to a reference strain ε_r, by means of the expression:

$$\frac{E_s}{E_{s0}} = \frac{1}{1+\left(\frac{\varepsilon - \varepsilon_{el}}{\varepsilon_r - \varepsilon_{el}}\right)^n} \qquad [7.21]$$

where ε_{el} is the threshold strain for elastic behaviour, considered equal to 10^{-5} and E_{s0} was determined from the initial secant modulus or, when available, from unload-reload cycles.

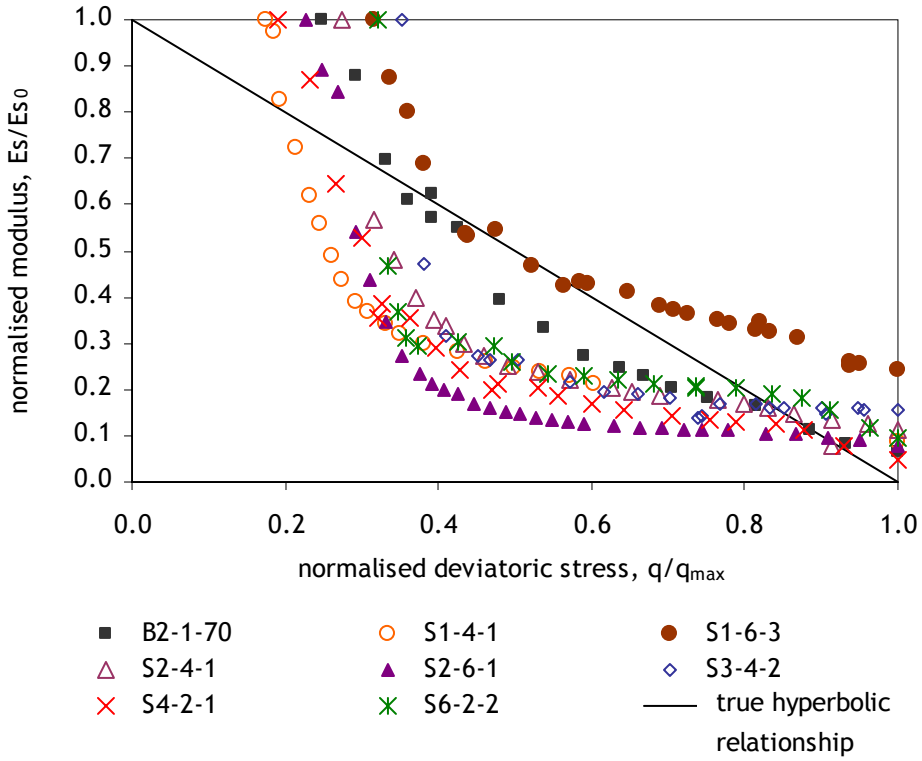


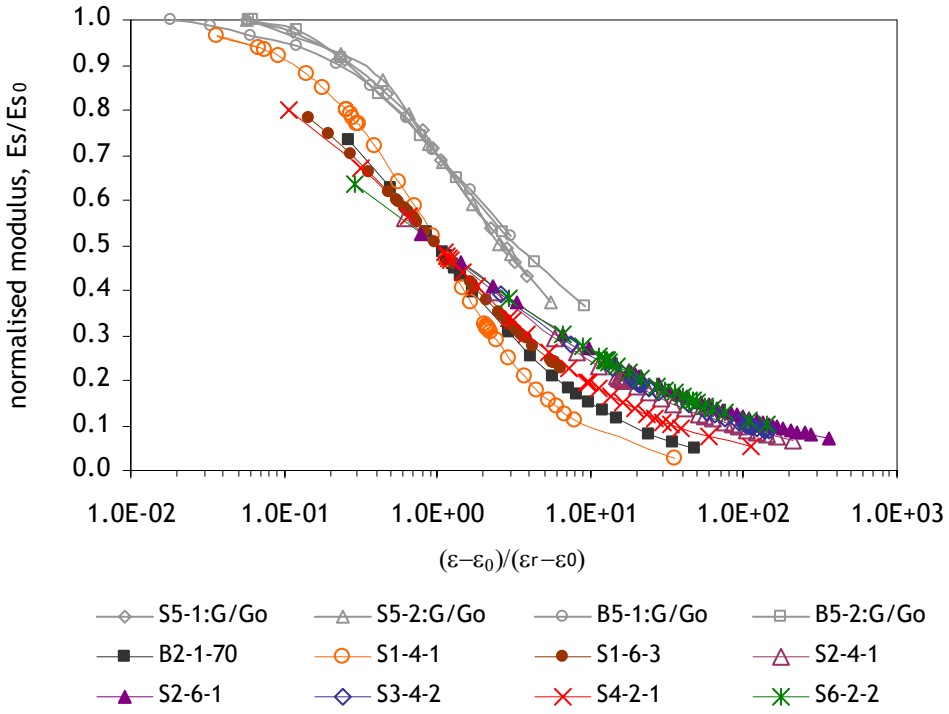
Figure 7.73 - ES1 undisturbed samples: Young's modulus degradation curves plotted as E_s/E_{s0} versus (q/q_{max})

The values of the reference strain ε_r and the exponent n can be determined by rewriting the previous equation to expose these parameters as follows:

$$\log\left(\frac{E_{s0}}{E_s}-1\right)=n\log(\varepsilon-\varepsilon_{el})-n\log(\varepsilon_r-\varepsilon_{el}) \qquad [7.22]$$

The computation of these parameters for the test results of the undisturbed samples from ES1 provided the data for the construction of the following plot in Figure 7.74. The RC degradation curves obtained on samples from ES2 are also included in this figure.

The curves presented in the figure evidence the difference between static and dynamic determination of stiffness and suggest distinct levels of stiffness degradation.



Note: S5-1, S5-2, B5-1 and B5-2 represent resonant-column tests on ES2 undisturbed samples

Figure 7.74 - ES1 undisturbed samples: normalised Young's modulus versus normalised strain

7.3.3.4. Stress-strain response of undisturbed samples from ES2

An identical analysis procedure was adopted for the identification of the stress-strain response of the undisturbed samples from ES2. The shearing stress-path obtained from the standard triaxial tests on these samples is presented in Figure 7.75. In this case, a number of tests were recorded using automatic acquisition, which can be immediately identified by the continuous curves of the graph.

The resulting stress-strain curves of these samples are plotted in Figure 7.76a and b, in terms of deviatoric stress q versus internal axial strain ε and normalised deviatoric stress in relation to the consolidation mean effective stress, q/p'_0, respectively.

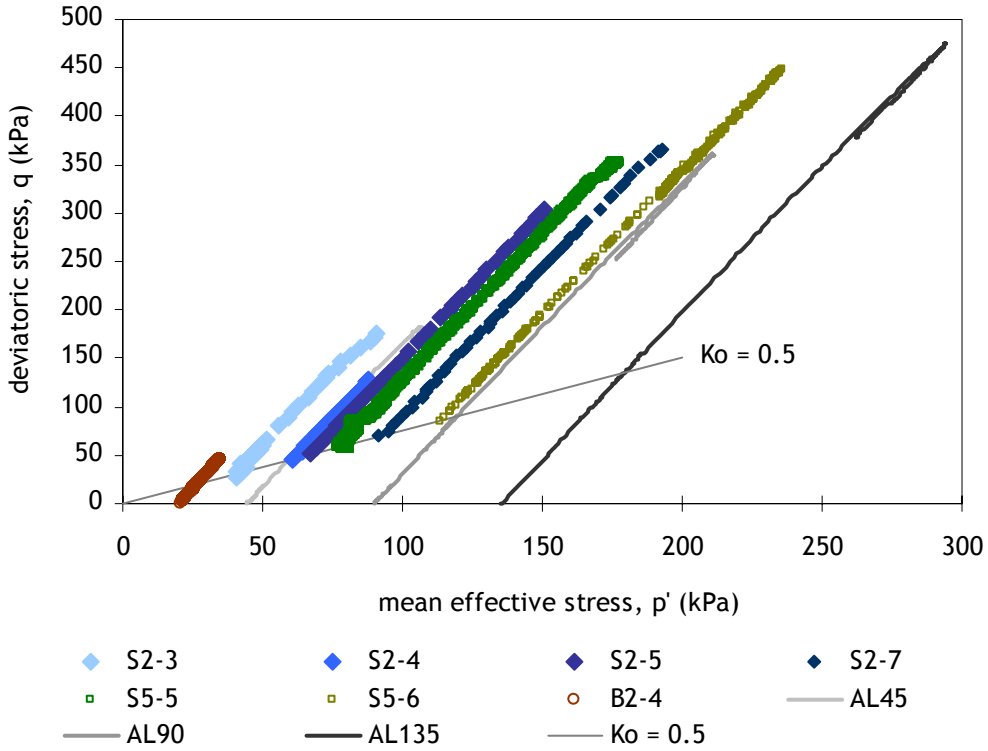
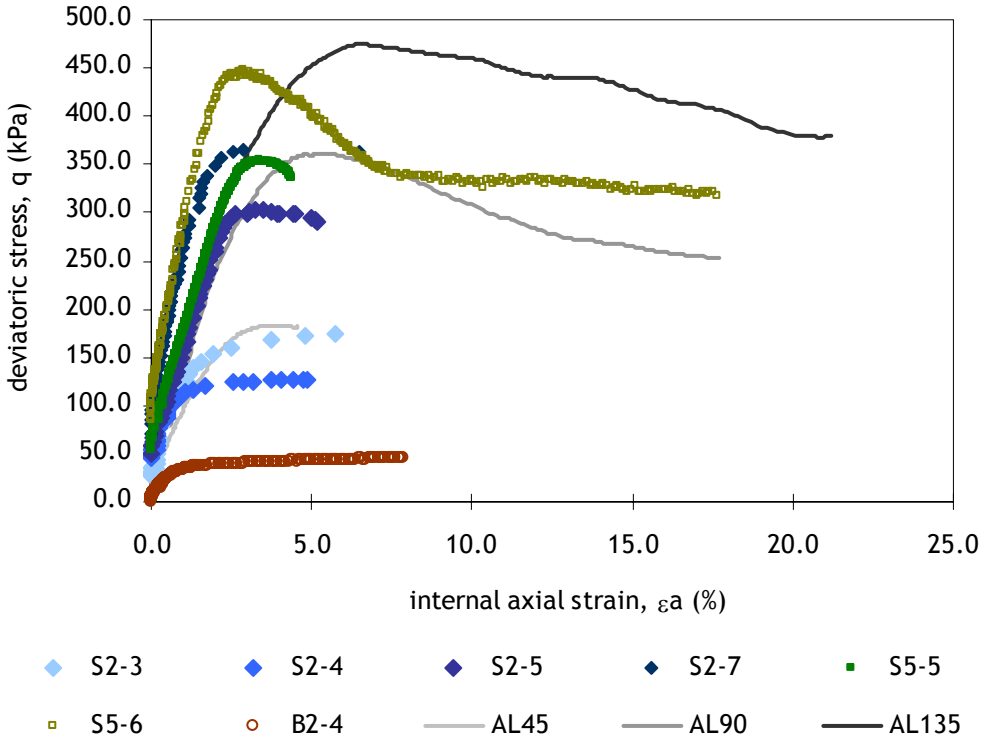


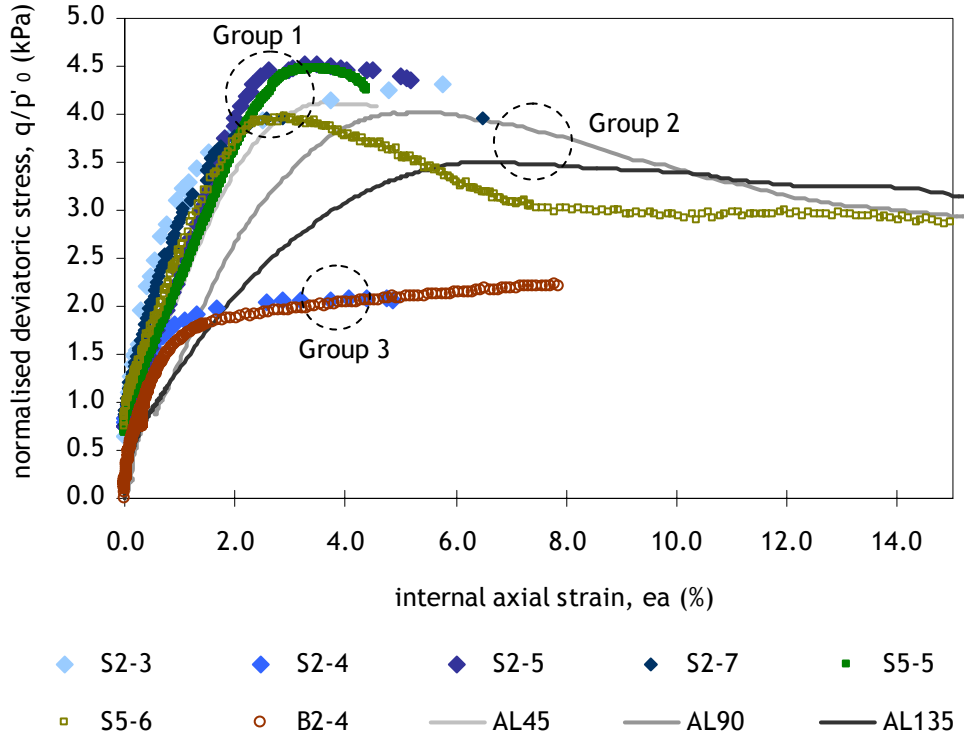
Figure 7.75 - ES2 undisturbed samples: summary of the stress-paths

The normalised stress against strain curves provide an interesting plot, where three distinct responses can be identified, as indicated in the figure. The first and the third group of samples appear to define the boundaries of the behaviour and the second group is relatively in the middle of both. The differences between these three groups can be attributed to various causes, namely sampling effects, storage (including storage time), different weathering profiles or even issues related with sample preparation.

These data have also been analysed in terms of the Young's modulus degradation curves, as previously shown for ES1. The obtained curve is presented in Figure 7.77.



a)



b)

Figure 7.76 - ES2 undisturbed samples: summary of the stress-strain curves, a) deviatoric stress and b) normalised deviatoric stress, against internal axial strain

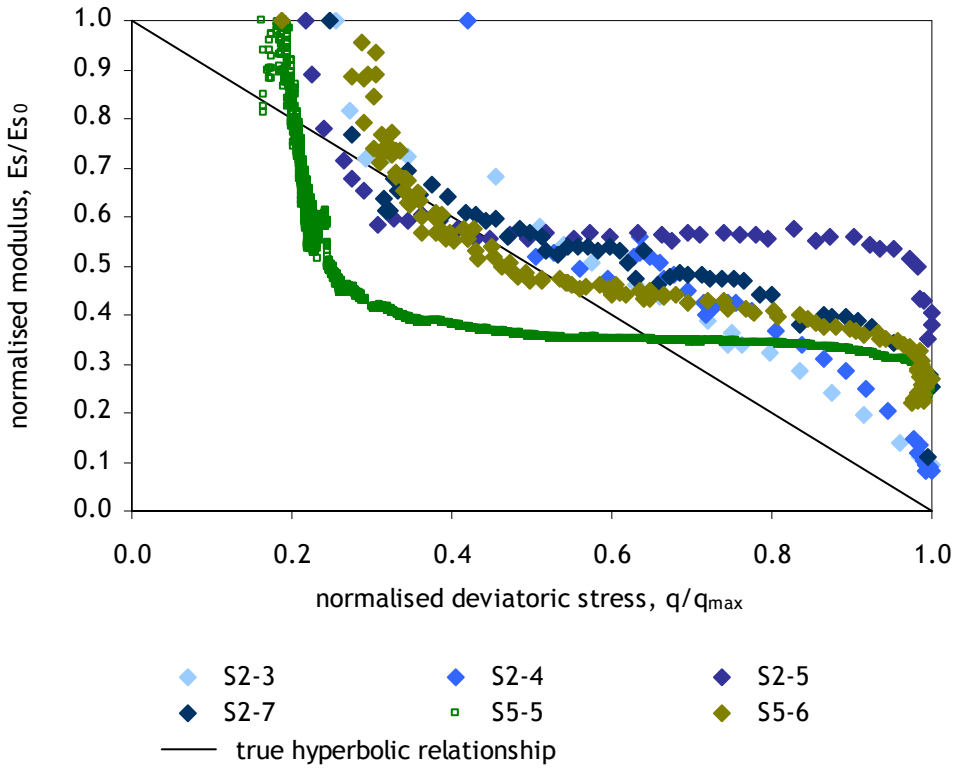


Figure 7.77 - ES2 undisturbed samples: Young's modulus degradation curves plotted as E_s/E_{s0} versus (q/q_{max})

7.3.4. True triaxial tests

The measurement of the stress in each direction and the displacements of each platen of the true triaxial apparatus provided interesting information regarding the stress-strain response as well as the stiffness to stress to strain relationships of this material under 3D loading. In what follows, the main results obtained in these true triaxial tests will be presented, divided according to the type of soil specimen: reconstituted or undisturbed.

Since the principal axes of the true triaxial apparatus coincide with the X, Y and Z reference directions of the soil specimen, the distortional stress q, also referred to as 3D deviatoric stress, can be calculated from the following expression (Muir Wood, 2004, Sadek, 2006):

$$q = \sqrt{\frac{(\sigma'_y - \sigma'_z)^2 + (\sigma'_z - \sigma'_x)^2 + (\sigma'_x - \sigma'_y)^2}{2}} \qquad [7.23]$$

Similarly, the distortional strain ε_q can be determined by the expression:

$$\varepsilon_q = \frac{1}{3}\sqrt{2[(\varepsilon_y - \varepsilon_z)^2 + (\varepsilon_z - \varepsilon_x)^2 + (\varepsilon_x - \varepsilon_y)^2]} \quad [7.24]$$

For the true triaxial and cubical tests where three-dimensional stress paths were applied, the stress-strain results will also be presented in the form of q against ε_q.

7.3.4.1. Stress-strain-stiffness response of reconstituted samples

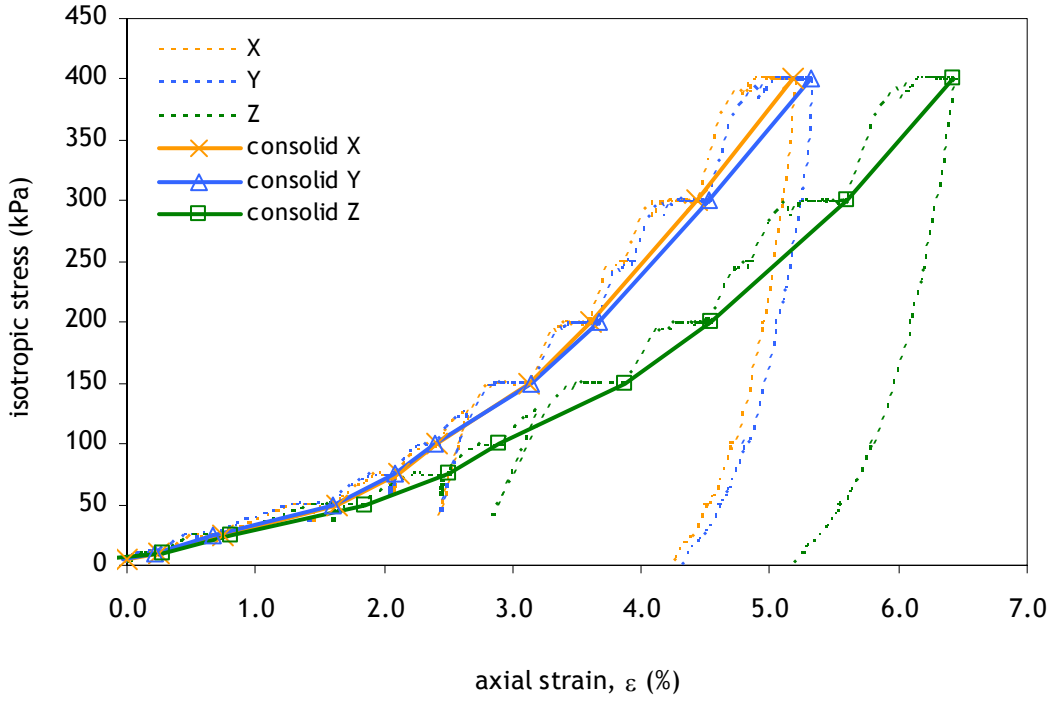
The true triaxial test on sample R2W-TT followed an isotropic stress-path, from which the following stress-strain curves, presented in Figure 7.78, were obtained. The data in the graph of Figure 7.78a includes the complete set of data, evidencing the strains involved at each consolidation stage until stabilisation, and the consolidation curve, where the markers also indicate the stages of BE measurements. In Figure 7.78b, those stages were plotted in a three-dimensional form to better represent the overall stress-strain response.

The symmetry of the 3D plot in Figure 7.78b is particularly illustrative of a similar stress-strain response in the two horizontal directions. Since higher strains were measured in the vertical direction, the behaviour of this sample can be considered cross-anisotropic. Taking into account the isotropic nature of the stress conditions, the anisotropy is inherent of the soil, possibly due to the tendency of layering of the soil particles during sample preparation, by deposition in wet conditions.

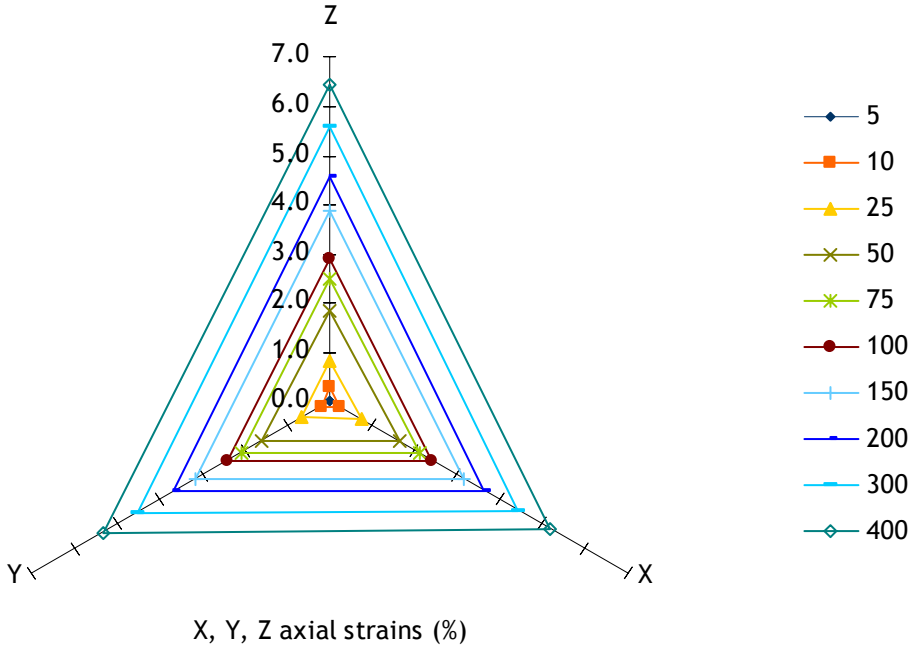
Inherent anisotropy can also be assessed by the analysis of the stiffness moduli derived from these measurements, presented against stress in Figure 7.79. G_0 results from BE measurements were also included for comparison and discussion.

The initial Young's moduli at very low stresses are extremely variable, but also considerably higher than those measured at increasing higher stresses. After 50 kPa, the evolution of the stiffness moduli with stress appears to be more consistent and similar to that observed for the maximum shear moduli from BE measurements.

It is interesting to note that the overlap of the E_{sX} and E_{sY}, thus confirming the stress-strain response and the assumption of horizontal isotropy and cross-anisotropy. The Young's modulus in the vertical direction E_{sZ} follows the same variation of the other moduli, but consistently lower values.

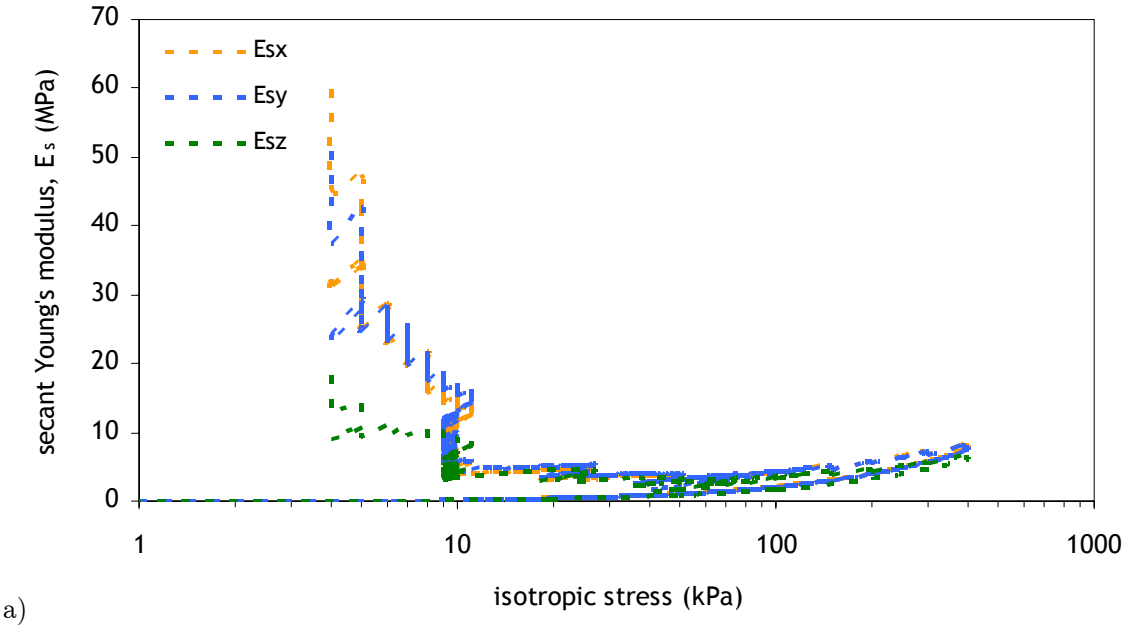


a)

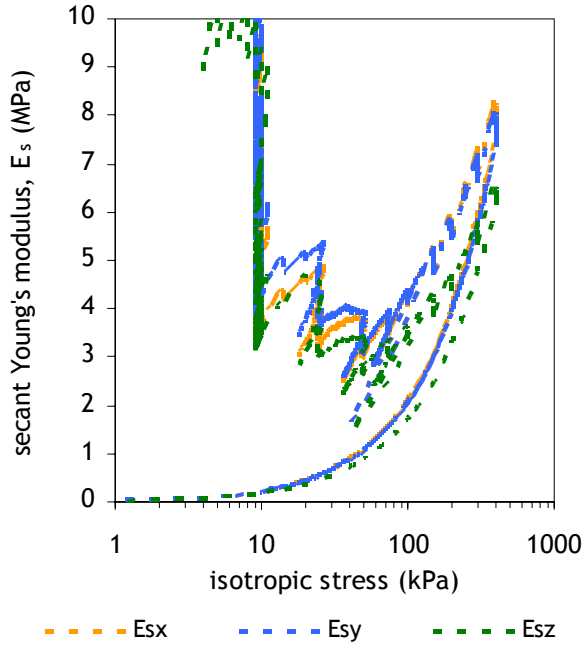


b)

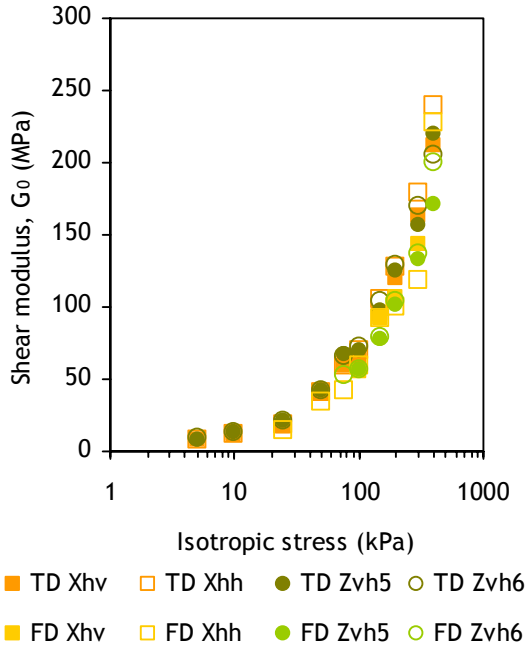
Figure 7.78 - R2W-TT: stress-strain curves: a) complete data and consolidation curves per stress direction; b) 3D plot of axial strains



a)



b)



c)

[Note the distinct vertical scales]

Figure 7.79 - R2W-TT: stiffness moduli against mean effective stress during isotropic consolidation: a) secant Young's modulus, E_s; b) zoom on secant Young's modulus to observe variations at high stresses; c) maximum shear modulus, G_{0BE}.

The comparison between the E_s and G_0 plots is particularly revealing. In terms of the relative evolution of stiffness with stress, the graphs are very similar. The differences between the horizontal and the vertical moduli are more pronounced for the longitudinal stiffness than for the shear stiffness. In fact, while from Figure 7.39, the

behaviour of the soil could be assimilated as isotropic, from Figure 7.79b and c, the soil stiffness is lower in the vertical direction, hence the behaviour of the soil tends towards cross-anisotropy. The analysis can be assisted by the computation of the respective anisotropy ratios:

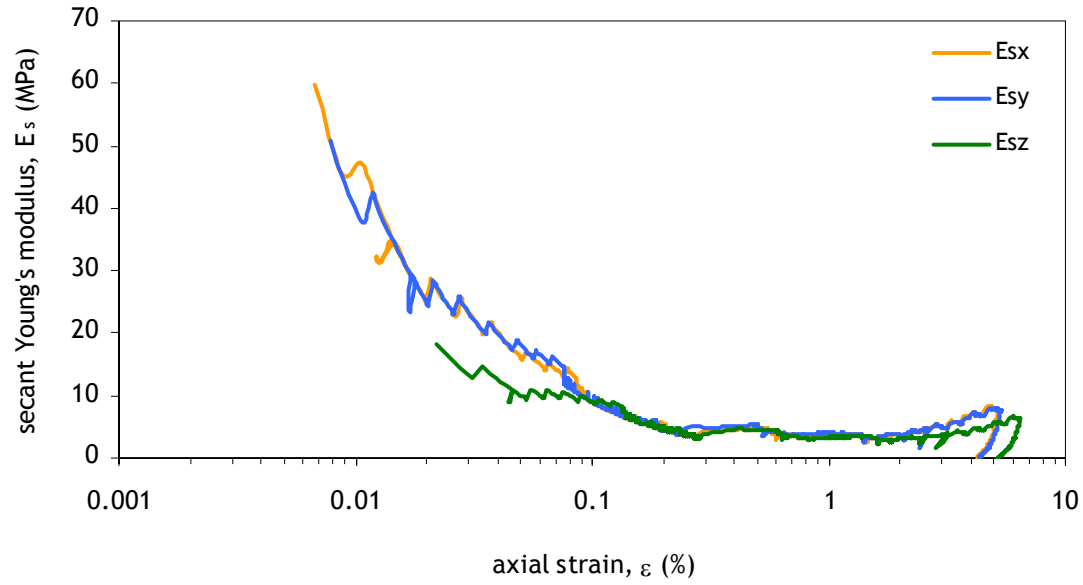
$$\alpha_{Ex} = \sqrt{\frac{E_{hX}}{E_{vZ}}} = 1.10 \text{ and } \alpha_{Ey} = \sqrt{\frac{E_{hY}}{E_{vZ}}} = 1.11 \quad [7.25]$$

and

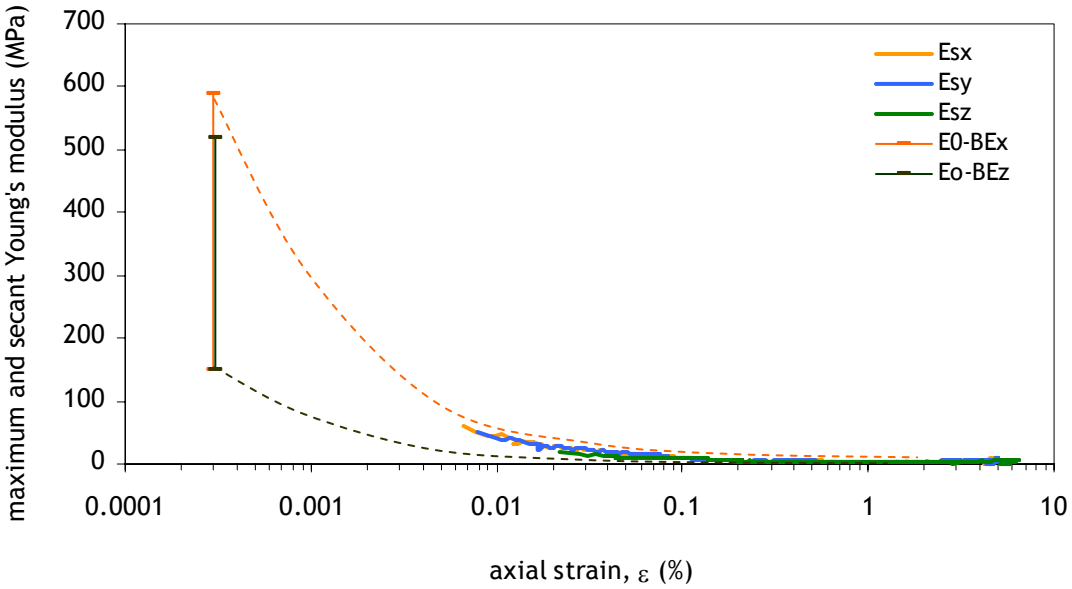
$$\alpha_{G_0} = \frac{G_{0hX}}{G_{0vZ}} = 1.06 \text{ [via TD] and } \alpha_{G_0} = \frac{G_{0hX}}{G_{0vZ}} = 1.03 \text{ [via FD]} \quad [7.26]$$

These values of α (computed from the average of all stress stages) indicate that the level of cross-anisotropy is small. The different values of α can be attributed to the stiffness modulus E_s and G_0 used for its determination. Similar observation was made by Pennington (1999), who determined values of α_E equal to 1.99 and α_{Go} equal to 2.25 for Gault clay.

The differences between E_s and G_0 are, however, impressive. If the maximum Young's modulus were computed from G_0, at 400 kPa for example, the value of E_{0X} would be about 625 MPa (from a G_{0X} equal to 240 MPa, considering as before ν=0.30). On the other hand, the highest secant Young's modulus determined from static strain measurements at that stress level was only 8.1 MPa. This considerable stiffness reduction is clearly related with the strain level at which the moduli were measured, but also with the rapid decay of stiffness of this particular geomaterial. The graphs in Figure 7.80 illustrate these observations. For the representation of E_0 from BE measurements, a strain of $3x10^{-6}$ (that is, $3x10^{-4}$%) was adopted, as previously estimated and discussed.



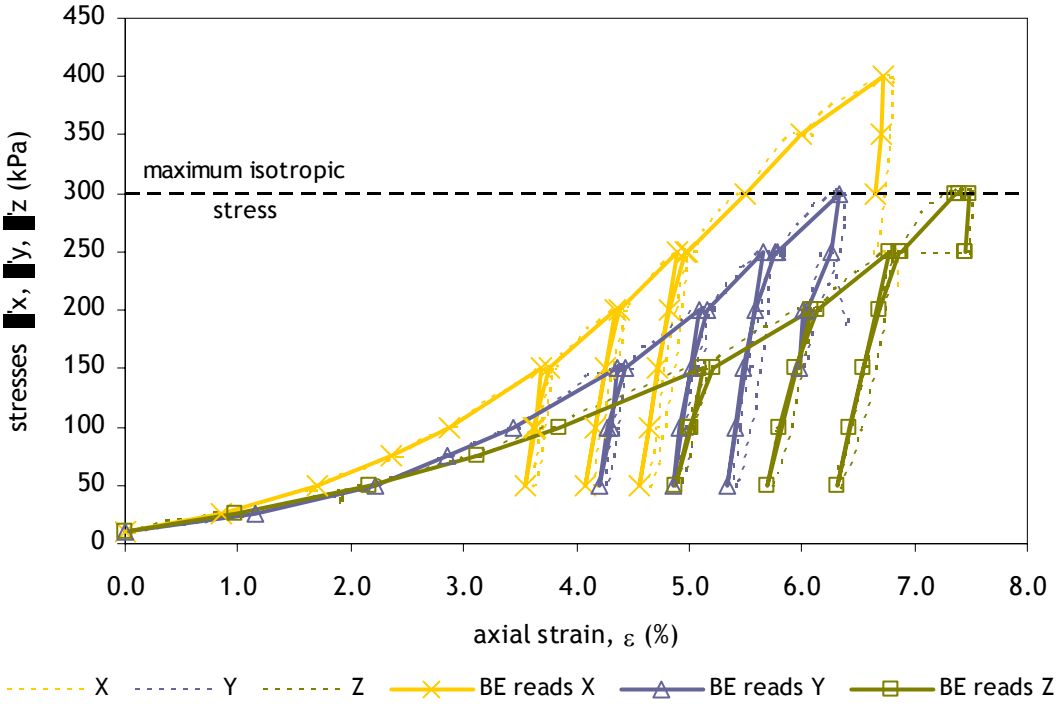
a)



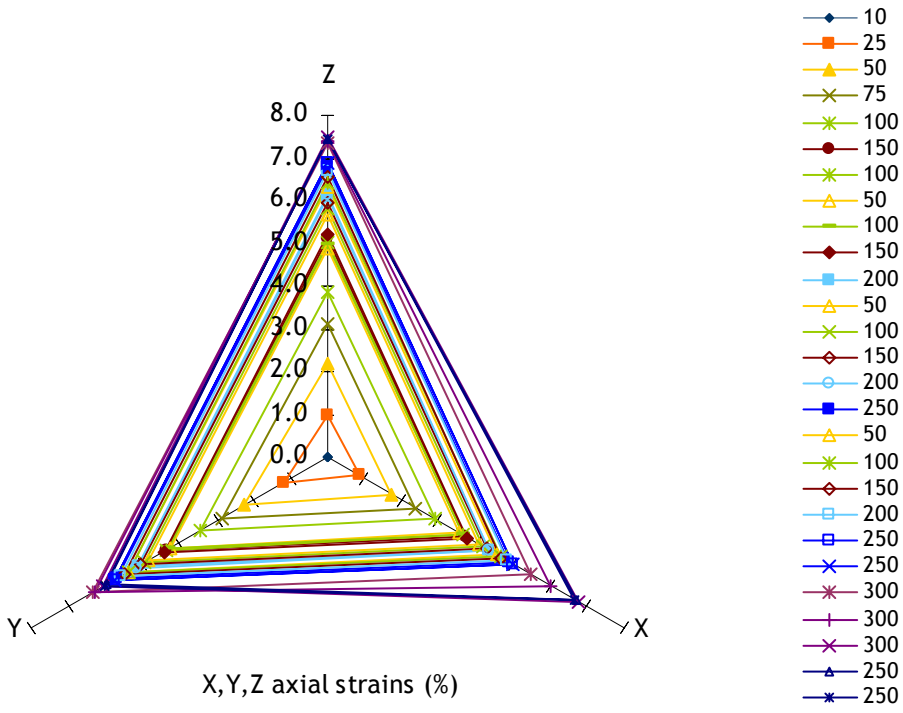
b)

Figure 7.80 - R2W-TT: Young's moduli against axial strain: a) E_s from X, Y and Z axial strain measurements; b) E_0 from BE measurements

Another true triaxial test was carried out on reconstituted sample R8D-TT. Contrary to the previous test, in this case the reconstituted sample was tested in dry conditions ($w \approx 0\%$). This test consisted of isotropic consolidation with unload-reload loops up to the deformation limits, followed by three-dimensional shear at constant p'. Twenty-five increments/decrements of isotropic pressures were applied, to a maximum of 300 kPa, corresponding to maximum strains of 5.50%, 6.33% and 7.33% in X, Y and Z directions, respectively. Figure 7.81 presents the deformation curves in a conventional stress-strain plot as well as in a three-dimensional view.



a)



b)

Figure 7.81 - R8D-TT stress-strain results: a) conventional plot; b) 3D view of axial strains

It can be seen from the figures that, despite the three curves having similar shapes, compressibility in the Z direction is greatest, which can be expected from the method of deposition of the particles (with a significant percentage of mica) during sample preparation. Having been prepared in dry conditions, the effects of deposition are

likely to be more pronounced than when prepared at high water content, such as sample R2W-TT ($w \approx 30\%$).

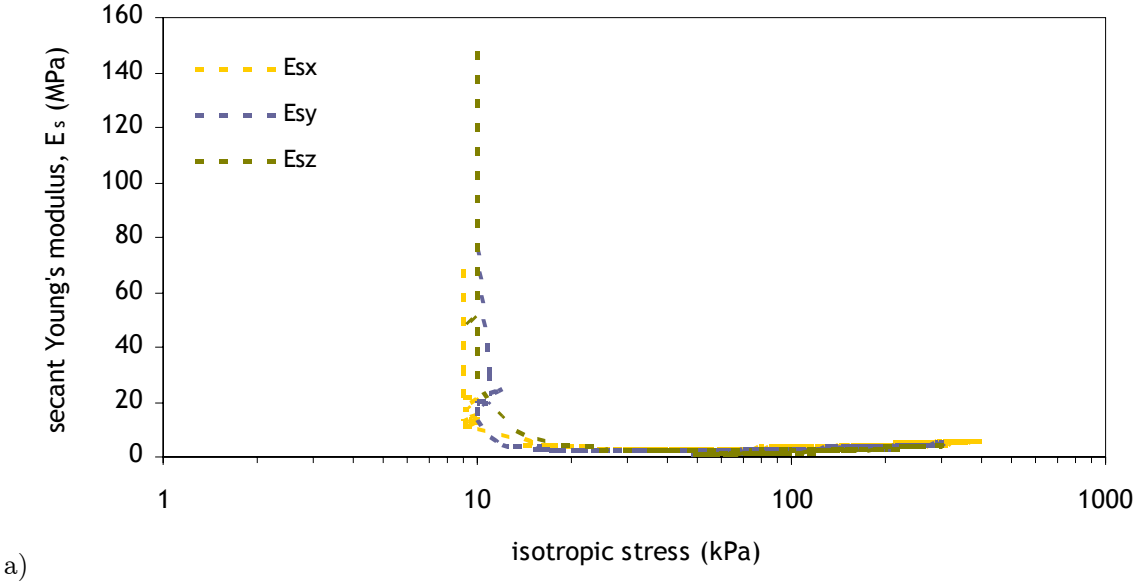
X and Y directions exhibit different compressibilities but the reasons for this are not obvious. It appears in Figure 7.81a, that higher deformation occurred in the Y direction at low stresses, since in that direction the strain had already exceeded 1% at 25 kPa. A local rearrangement of the grains or an adjustment of the platen to the soil may have caused this higher strain. It is not expected that this is a direct reflection of the behaviour of soil, especially considering the results previously obtained with another reconstituted specimen.

The secant Young's modulus was computed from the stress and strain measurements, resulting in the curves of Figure 7.82a. At low stresses, there is considerable variation of stiffness, with a rapid decay at roughly the same stress level, around 10 kPa. In order to identify the variation of E_s with stress, it is more convenient to zoom in the graph and adopt a smaller vertical scale, as shown in Figure 7.82b. For the comparison with the elastic stiffness, the plot of G_0 obtained from direct BE measurements, is presented side-by-side in Figure 7.82c.

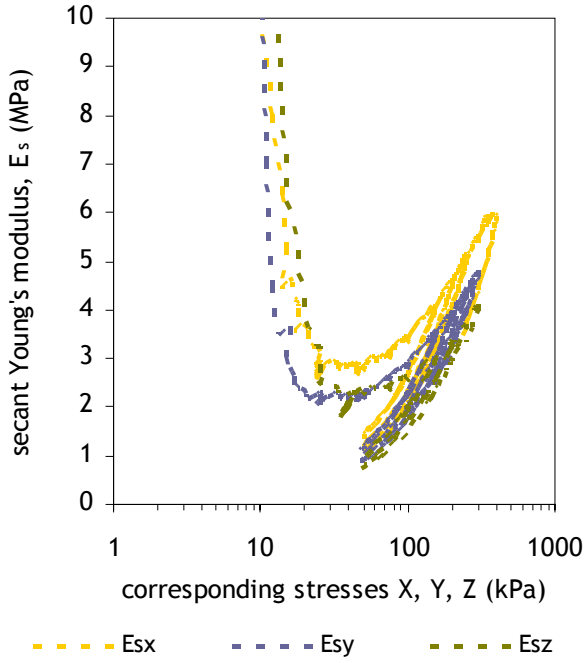
These figures show very similar results, regardless of the direction of the Young's moduli. The evolution of E_s and G_0 is comparable after the application of isotropic stresses at about 50 kPa, where in both cases an increase of stiffness with stress can be observed.

It is also interesting to present the relationship between the secant Young's modulus and strain, illustrated in Figure 7.83. As previously, the values of E_0 from BE measurements were derived using Equation 7.18, with a Poisson's ratio $\nu = 0.3$.

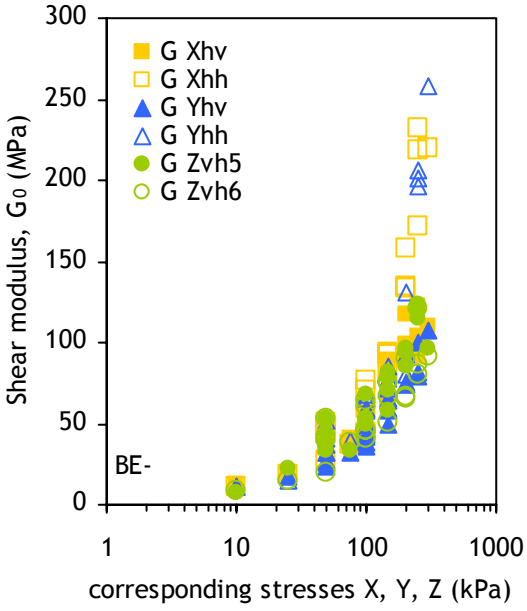
In the plot of Figure 7.83a, the similarity between the stiffness moduli is more explicit. Once again, the stiffness rapid decays with the strain increase. For illustrative purposes, additional lines were drawn in the graph to represent possible decay curves, which highlight the sensitivity of this soil to the imposed strain level and its subsequent stiffness degradation.



a)



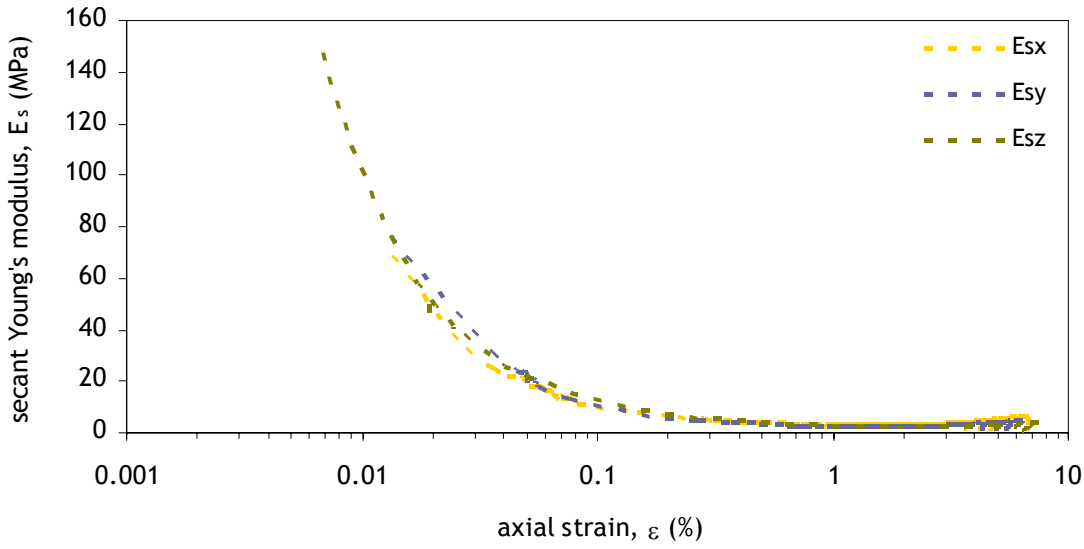
b)



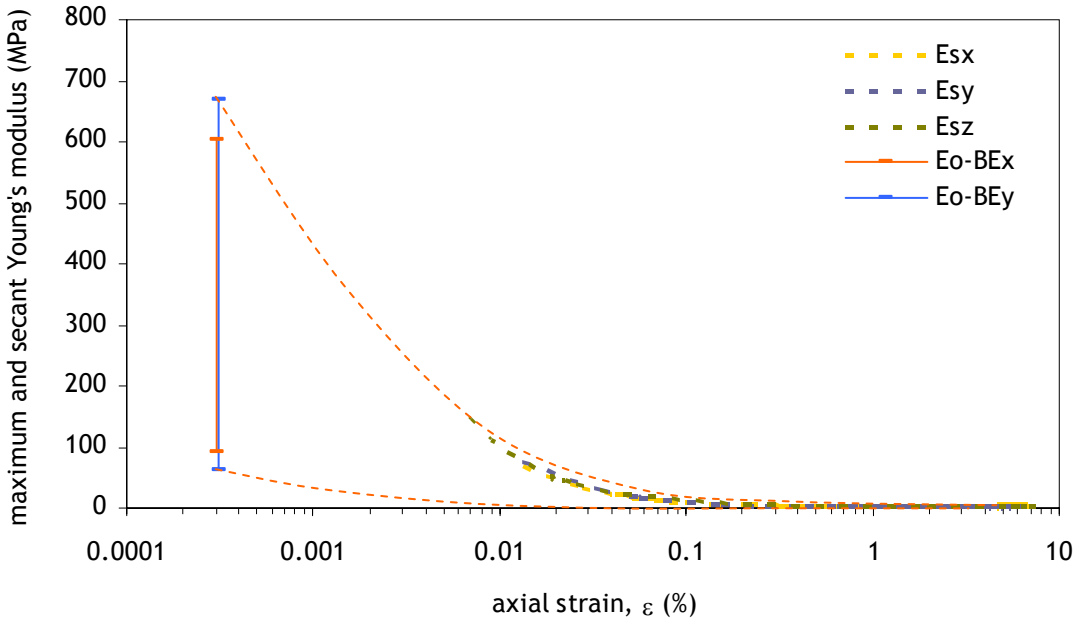
c)

[Note the distinct vertical scales]

Figure 7.82 - R8D-TT: stiffness moduli against mean effective stress during isotropic consolidation: a) secant Young's modulus, E_s; b) zoom on secant Young's modulus to observe variations at high stresses; c) maximum shear modulus, G_{0BE}.



a)



b)

Figure 7.83 - R8D-TT: Young's moduli against axial strain: a) E_{s0}; b) E_0 from BE and E_{s0}

Another true triaxial test carried out on the reconstituted soil sample, R4D-TT. As previously presented, this test comprised the indirect determination of the stresses necessary to comply with a null horizontal deformation requirement, in an attempt to investigate the potential of this apparatus for the purpose of defining K_0, or more accurately, a pseudo-K_0. In this particular test, the average of the ratios between horizontal and vertical stresses was calculated, from which a value of K_0 equal to 0.27 was obtained.

Due to this specific stress-path, the measured displacements refer almost entirely to the Z direction, as shown in Figure 7.84.

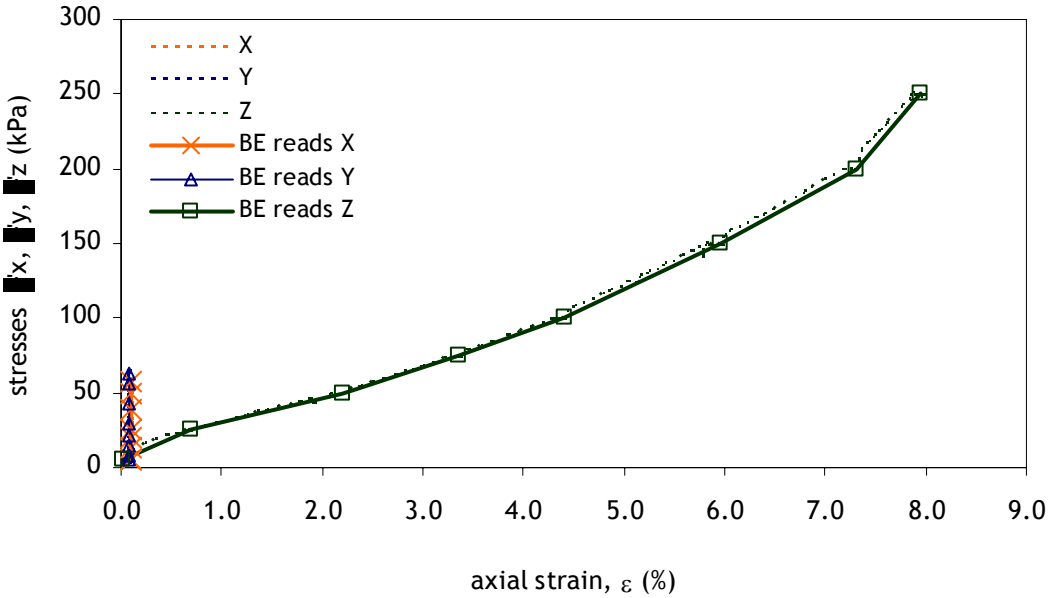
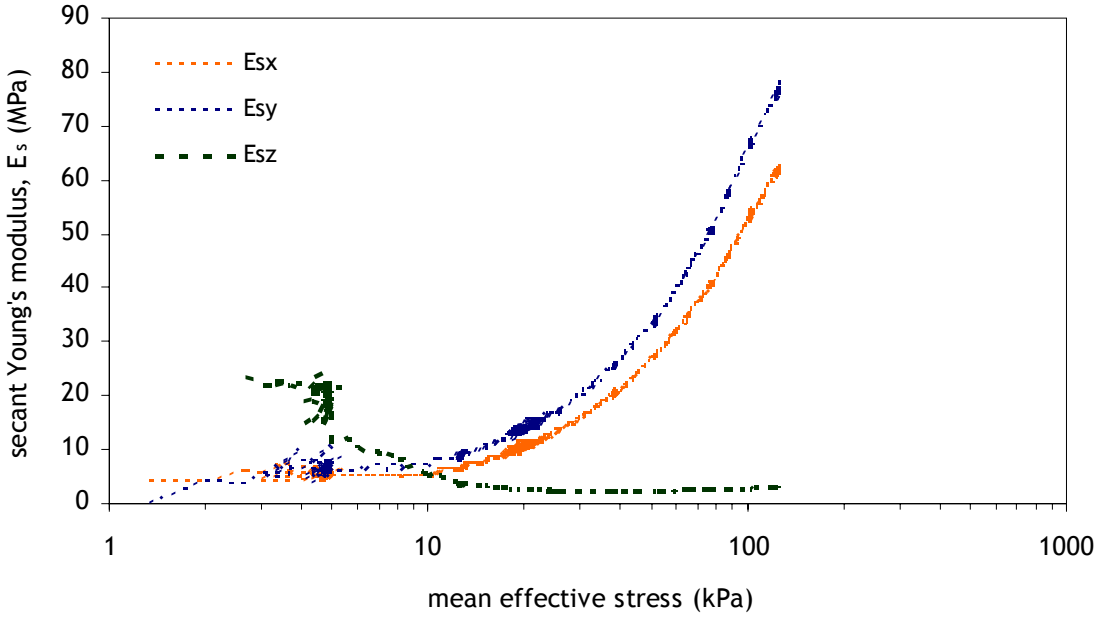


Figure 7.84 - R4D-TT: stress-strain results (test under K_0 conditions, so strains are only visible in the Z direction)

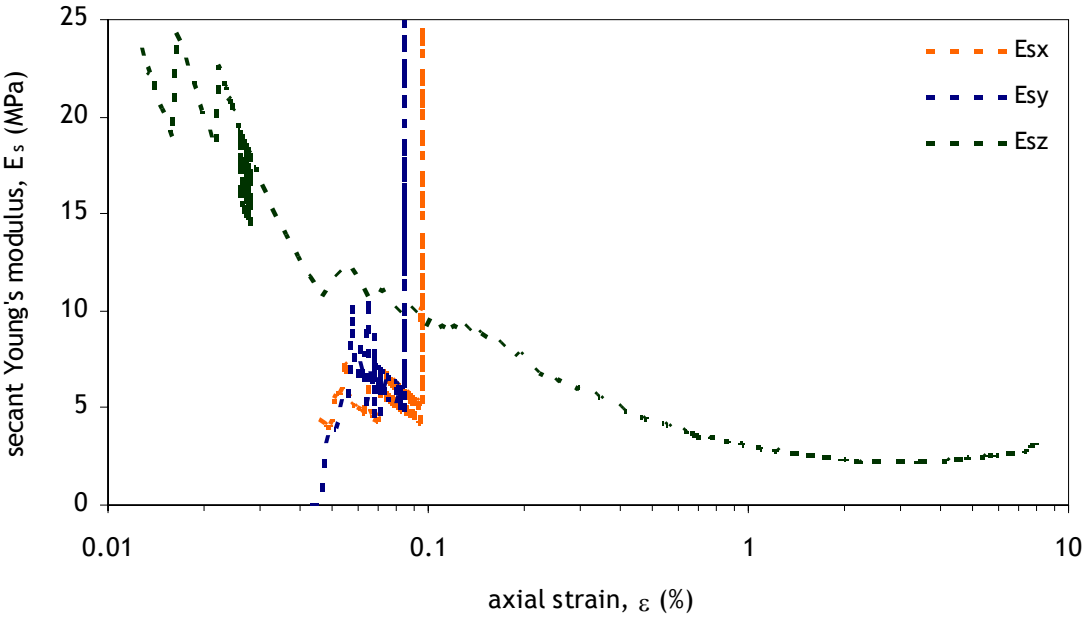
The secant Young's moduli in the three directions were computed from the stress and strain measurements, and the relationship with the applied stresses and strains is illustrated in Figure 7.85. In this case, the mean effective stress was considered more suitable to describe the stiffness to stress relationship.

Since in the two X and Y horizontal directions the deformation was kept constant, the increase of stiffness in those directions is predominantly related with the stress increase and does not truly represent the stress-strain response of the soil. For this reason, the scale of the graph in Figure 7.85b was readjusted to evidence the variation of E_s in the vertical direction.

In this test, the comparison with the elastic stiffness measured using BE was not established, since only the static results in the Z direction are actually comparable with the BE derived values.



a)



b)

Figure 7.85 - R4D-TT: secant Young's moduli against a) stresses; b) axial strains

As a final note, it is interesting to combine the results from the three reconstituted samples in these true triaxial tests. For this purpose, the stiffness response in terms of E_s of the three samples was plotted together in Figure 7.86. The figure demonstrates the similarity and convergence of the measured values. Since a large part of the measurements of E_s was made at large strains, the comparison with the elastic moduli provided by the BE measurements is limited and complex, involving differences of several orders of magnitude.

Considering the differences between the stress-paths applied in each samples, the graph combining the stress-strain response were not included in this final comparison.

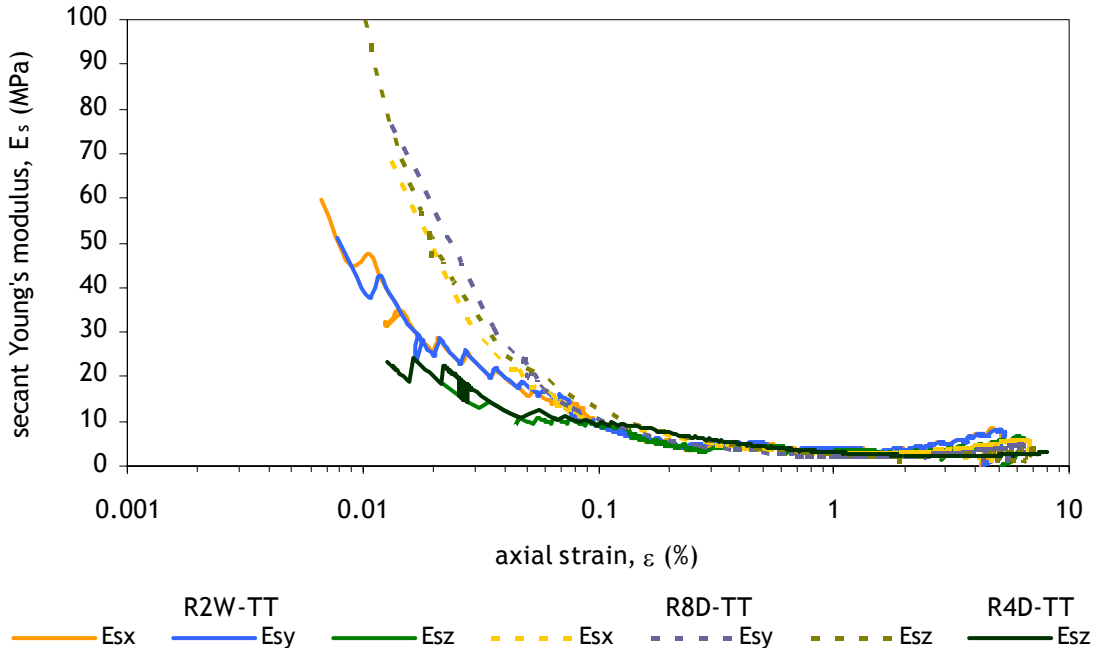
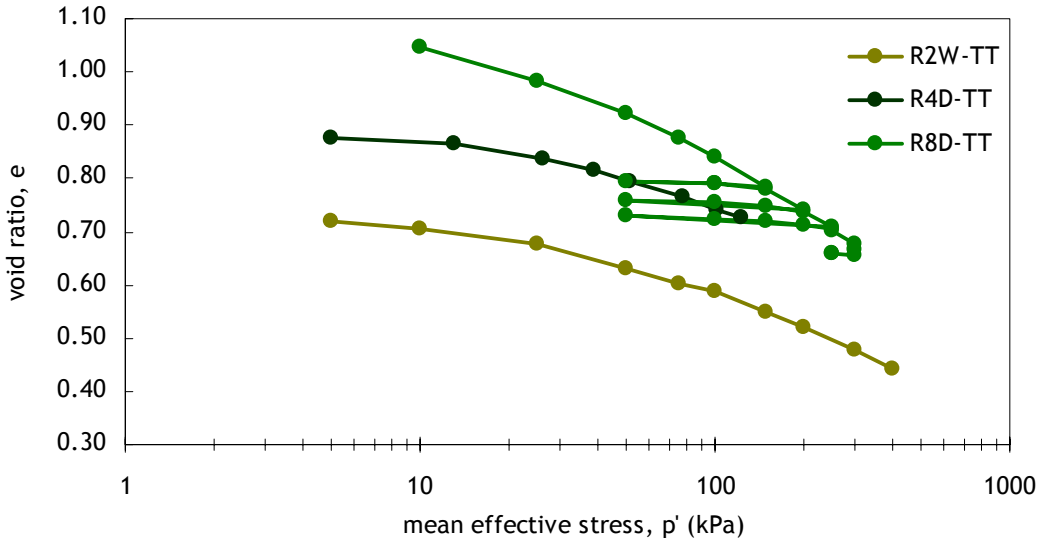


Figure 7.86 - Secant Young's moduli against strain for the 3 reconstituted samples

Instead, the compressibility curves of Figure 7.87 were found to be more illustrative. Clearly, the samples prepared in dry conditions enable to create looser samples, especially in this apparatus where the reconstituted samples can be produced against the walls of the device, fully containing the specimen.



Note: RW- reconstituted wet specimen; RD-reconstituted dry specimen

Figure 7.87 - Compressibility curves for reconstituted samples in true triaxial conditions

The shape of the compressibility curves of the three samples is very similar, which can be interpreted as an indicative of a characteristic response of this material in reconstituted, that is, unstructured conditions.

7.3.4.2. Stress-strain-stiffness response of undisturbed samples

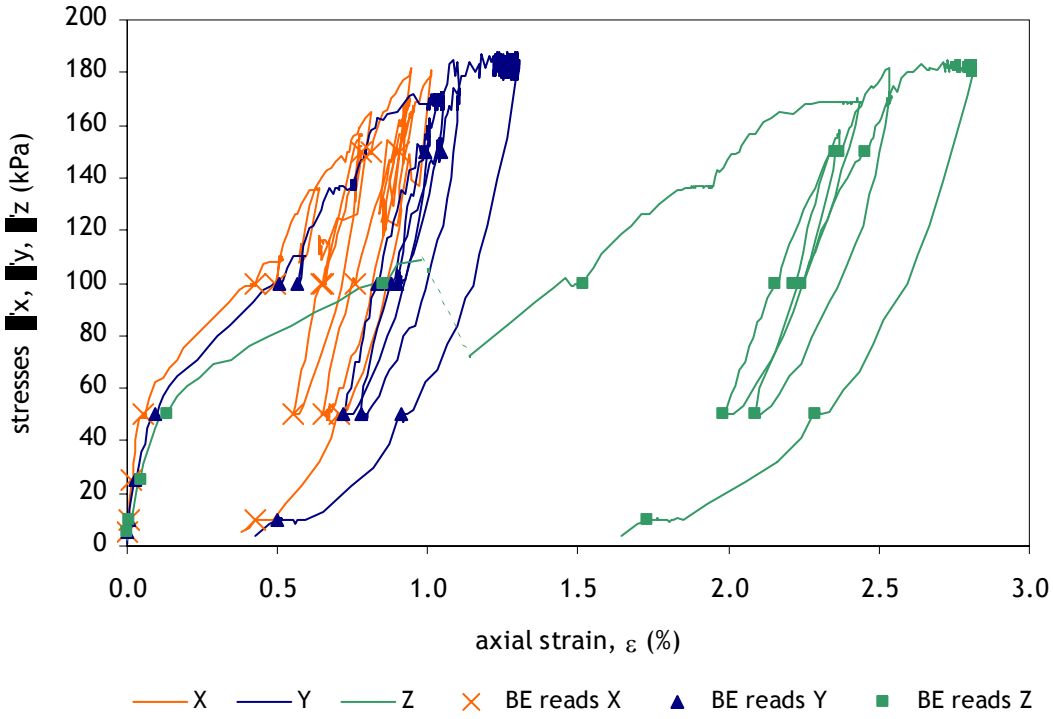
The results from the true triaxial tests on undisturbed samples from ES1 were analysed in a similar manner as the reconstituted specimens. Since these samples were prepared by trimming a large block sample, one of the difficulties is in ensuring a good contact between each face of the sample and the respective platen of the apparatus. In the case of irregularities at the surface of the sample, the measurement of displacements and strains can be misleading. For this reason, the surfaces were levelled with great care and prior to the actual start of each test, an isotropic pre-load of 5 to 10 kPa (according to the response of the soil) was applied.

The true triaxial tests carried out on natural undisturbed samples comprised different stress-paths, from isotropic stress conditions to K_0 conditions to excursions in the deviatoric plane at constant mean effective stress. Despite the limited number of samples, some interesting and comparable results were obtained.

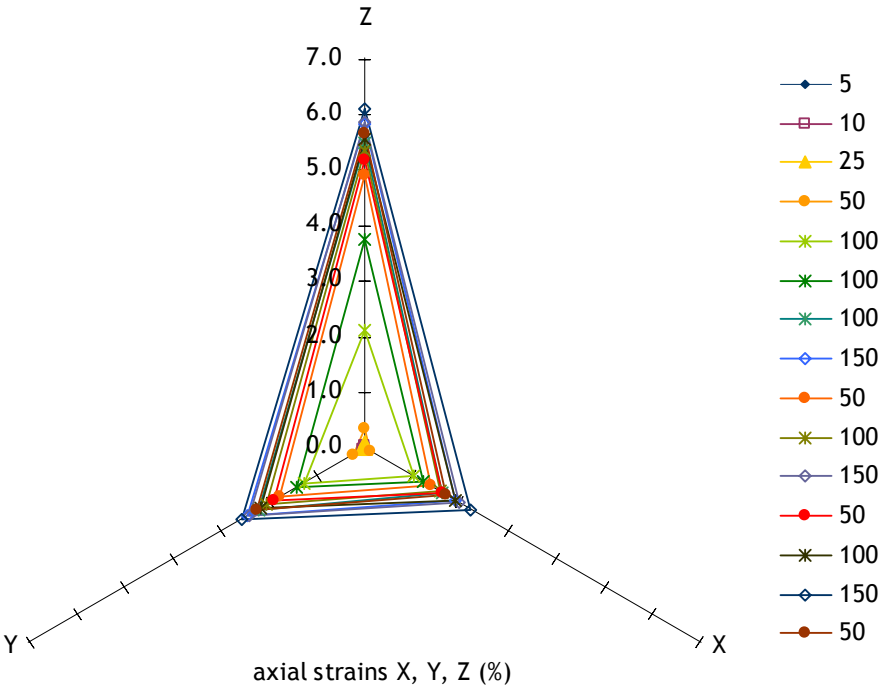
In test B2-TT, the sample was isotropically consolidated, with a few unload-reload cycles, as presented earlier in section 7.2.5.3. The stress-strain curves in the three directions are depicted in Figure 7.88a in a conventional plot and in Figure 7.88b in a three-dimensional representation.

The figures show a clear distinction between the horizontal and vertical strains. This can be directly interpreted as a cross-anisotropic response, since the differences in the two horizontal directions are relatively small and can be considered negligible.

The response in the vertical direction is discontinued between 1% and 1.5% axial strain, where a reduction in stress occurred with strain increase. This is possibly due to some readjustment of the platens in the Z direction and it is not expected to be associated with an actual deformation of the sample.



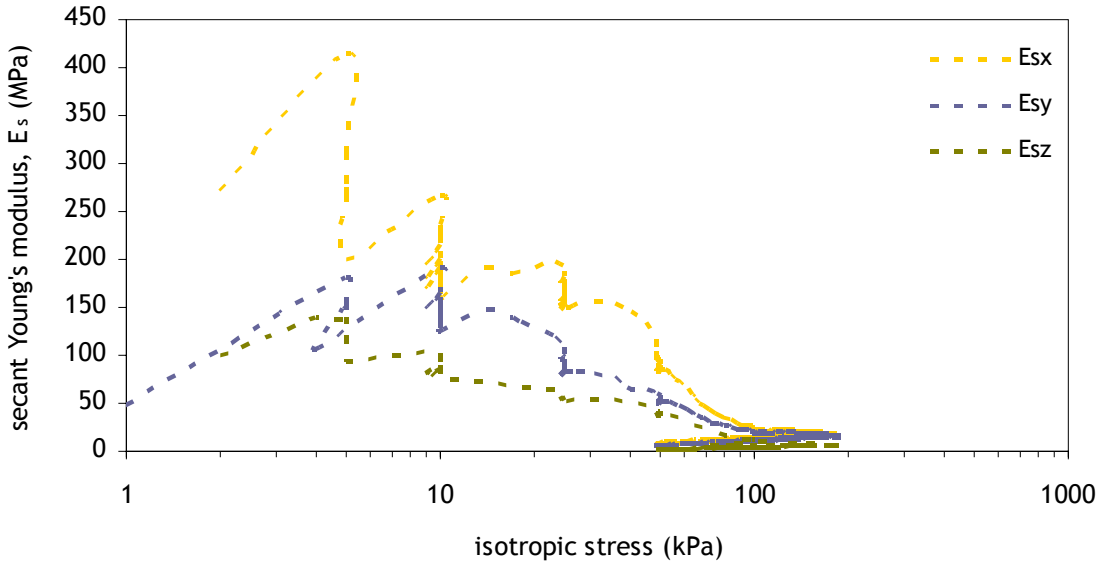
a)



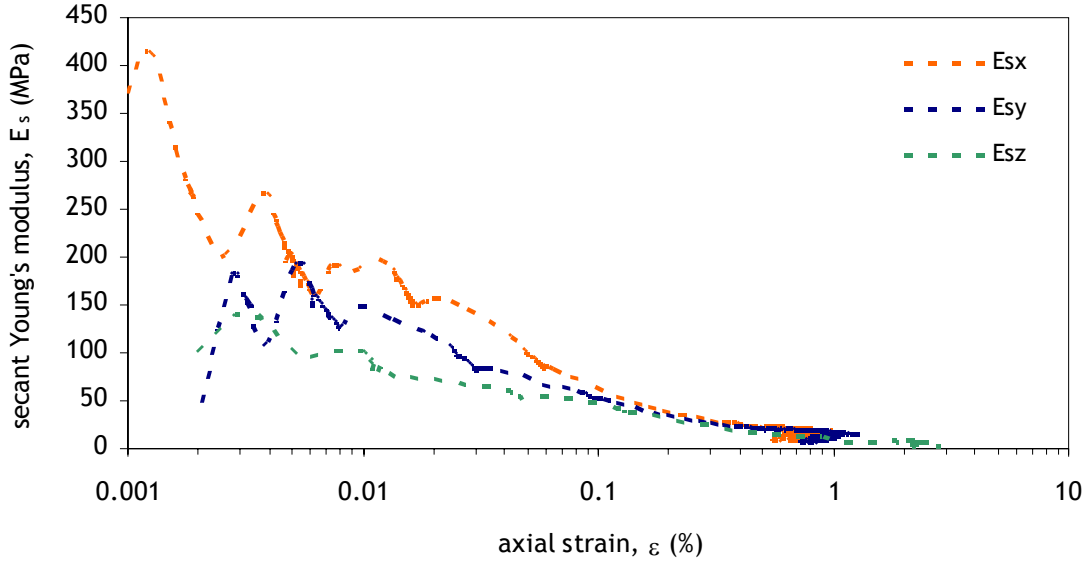
b)

Figure 7.88 - B2-TT: stress-strain curves: a) conventional plot; b) 3D view of axial strains

The stiffness was also computed, namely the secant Young's modulus, based on the stress and strain measurements. The obtained results are summarised in Figure 7.89a and b, as a function of the applied isotropic stress and the axial strains.



a)



b)

Figure 7.89 - B2-TT: secant Young's moduli against a) isotropic stress; b) axial strains

These results indicate a smooth decay of stiffness with stress and also with strain. In these figures, the stiffnesses in the three directions appear to be distinct, inclusively in the X and Y directions. The analysis of the anisotropy can be made by the computation of the respective anisotropy ratios. In this case, the values of α_{Ex} and α_{Ey} were calculated, according to Equation 7.24, for the complete series of data. These ratios are plotted in Figure 7.90 against mean effective stress, where two linear regression curves were also included.

The average values of α_{Ex} and α_{Ey} were 1.67 and 1.51, respectively. It seems reasonable to accept that these anisotropy ratios reflect only a small level of anisotropy in the horizontal plane. Furthermore, as shown in the figure, the ratios

tend to converge to the same value with the stress increase. Therefore, a cross-anisotropic behaviour can be assumed. The anisotropy of the sample, defined from these secant stiffness moduli, can then be calculated from the average of these anisotropy ratios, resulting in α equal to 1.60.

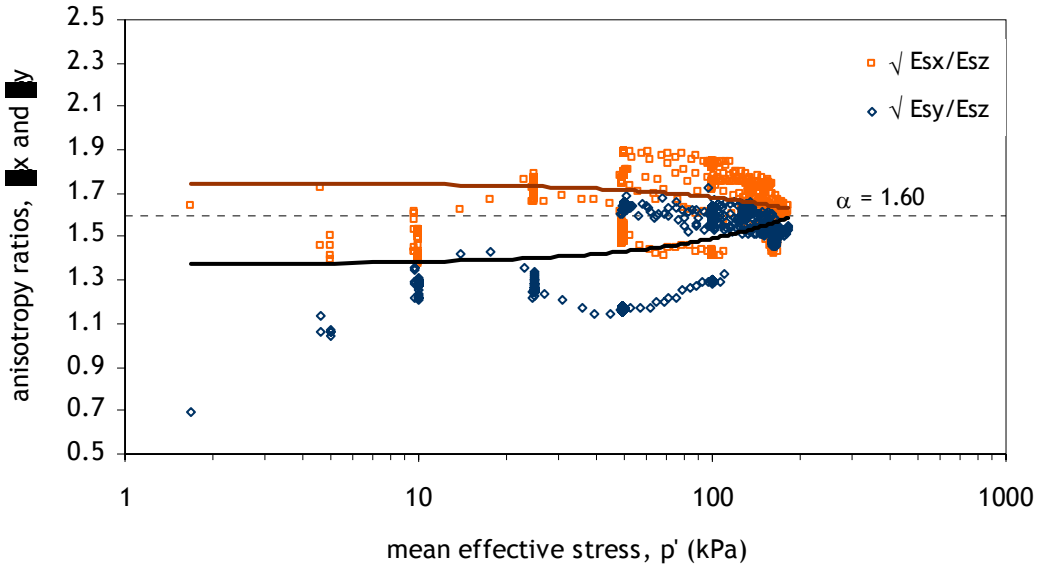
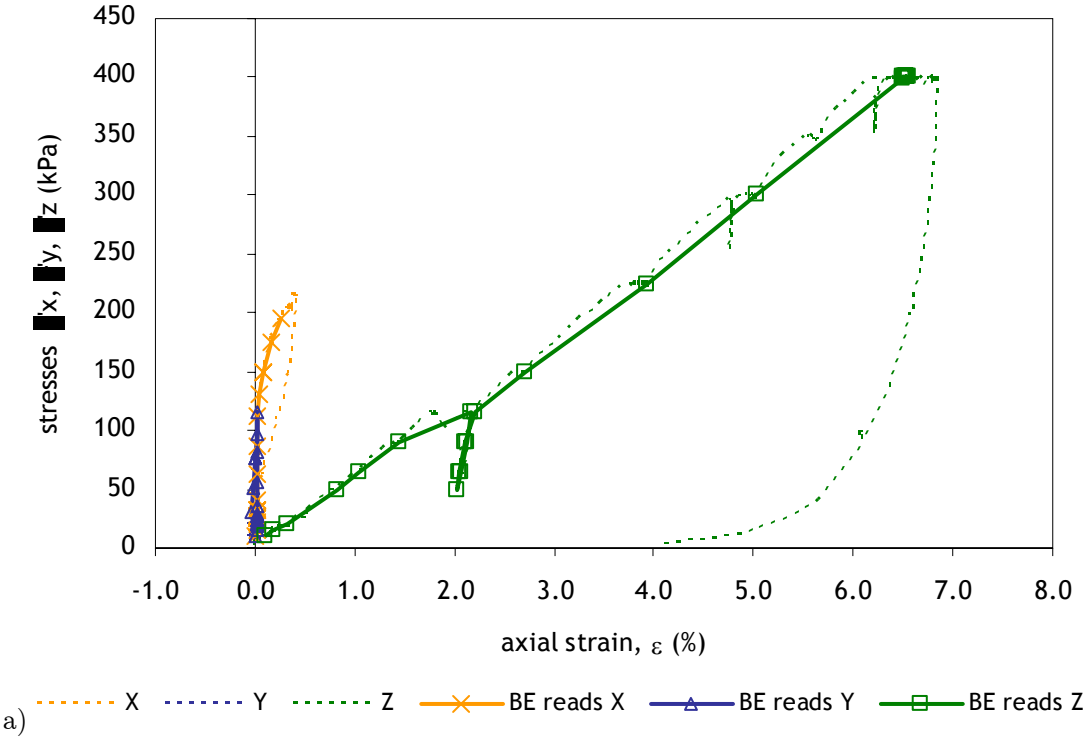


Figure 7.90 - B2-TT: anisotropy ratios for the two X and Y horizontal directions in relation to the Z vertical direction

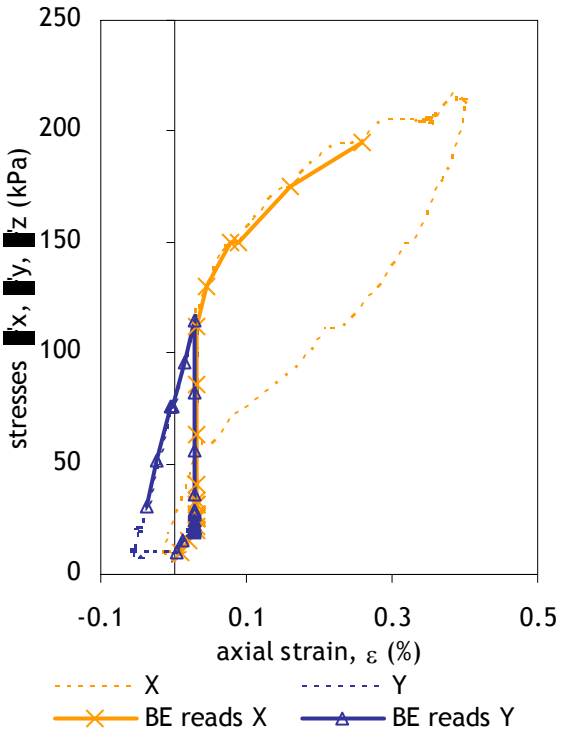
Due to suspicions regarding the BE results (discussed earlier in this chapter), the comparison between static and dynamic measurements of stiffness was not considered.

The second test on undisturbed sample B5-TT followed a stress-path which included a phase with increase of vertical stress at a controlled zero-horizontal deformation, similar to that used in sample R4D-TT. After this consolidation phase, the sample was sheared in the deviatoric plane, at constant mean effective stress. The resulting stress-strain curve is presented in Figure 7.91. Since the strains experienced by the soil in the two horizontal directions was controlled to remain nearly zero, it is necessary to zoom in the graph in Figure 7.91a in order to visualise the differences of behaviour between the X and Y directions.

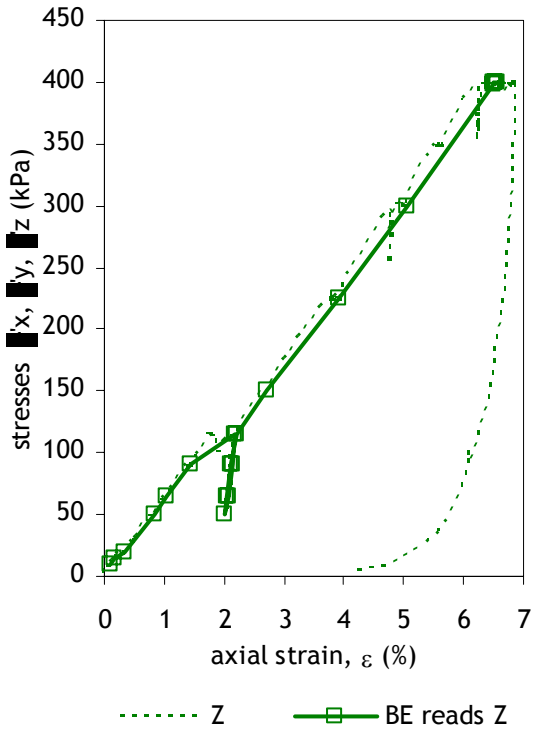
It is interesting to see in Figure 7.91b the complementary curves formed by the two X and Y stresses in the shearing phase at constant p'.



a)



b)



c)

Figure 7.91 - B5-TT: stress-strain curves: a) complete results; b) strains in the X and Y directions; c) strains in the Z direction

In order to better illustrate the stress-strain relationship, namely in true triaxial conditions, it is possible to compute the distortional stress and strain, as introduced

in the beginning of this section. For the present test, the distortional stress-strain plot was prepared and is presented in Figure 7.92.

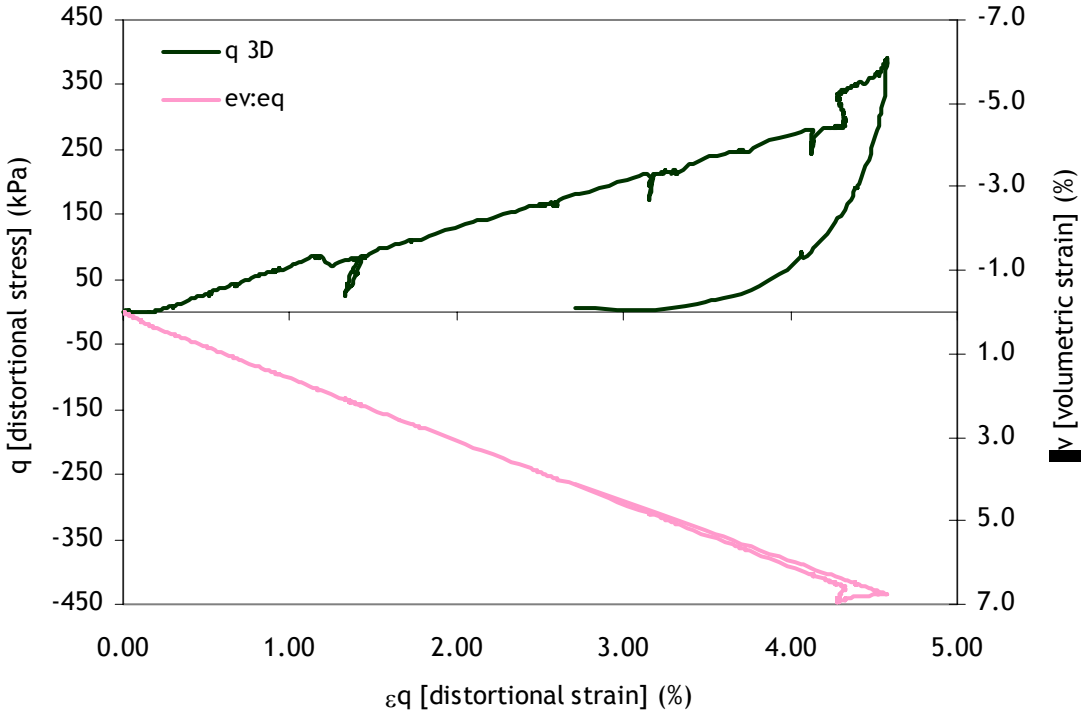
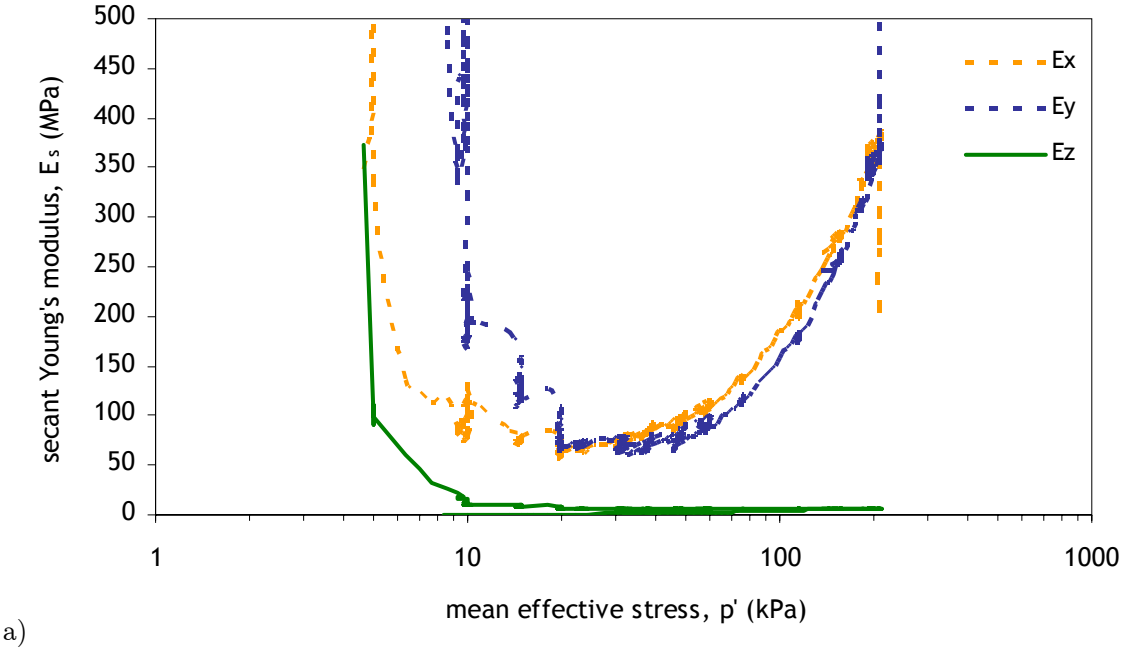


Figure 7.92 - B5-TT: distortional stress and volumetric strain against distortional strain

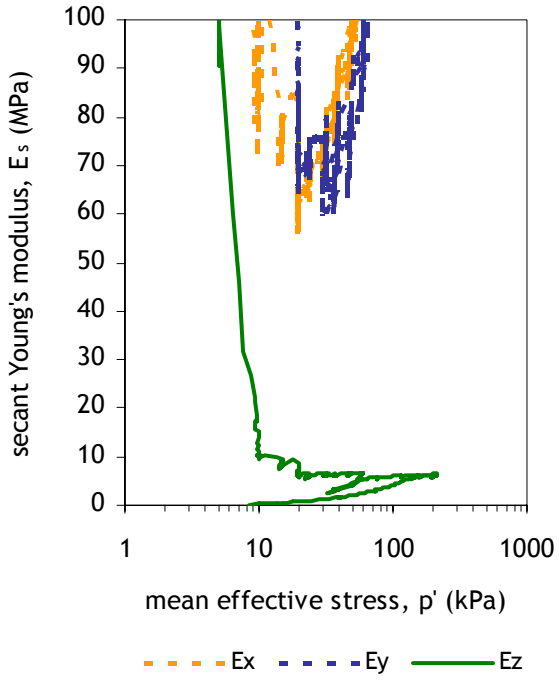
This plot does not evidence any signs of loss of structure of the soil. On the contrary, the sample appears to be steadily compressing without any visible destructuration, softening or hardening.

The secant Young's modulus was once again calculated in each direction from the stress and strain measurements. For the interpretation of the evolution of stiffness with stress, it was considered more appropriate the use of mean effective stress instead of the corresponding stress in the stiffness direction. The resulting graph is presented in Figure 7.93.

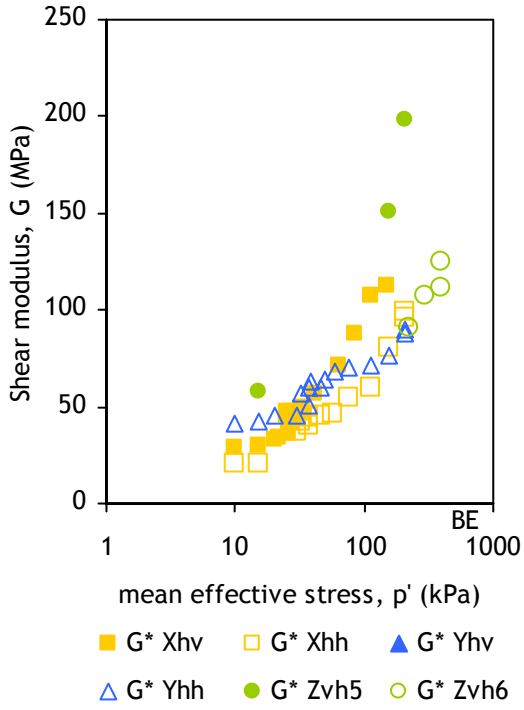
Similarly to the results from R4D-TT, in this test the deformation in the two X and Y horizontal directions was controlled and kept constant around zero. For this reason, the calculation of stiffness in those directions is strongly related with the stress increase, thus it does not truly represent the stress-strain response of the soil. For this reason, the scale of the graph in Figure 7.85b was readjusted to evidence the variation of E_s in the vertical direction.



a)



b)

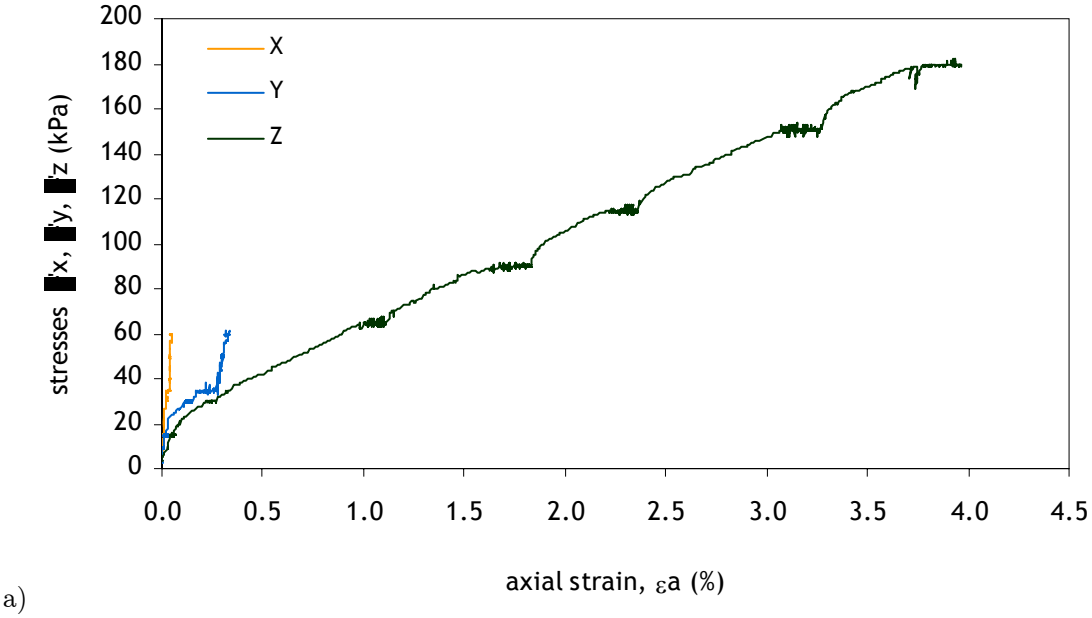


c)

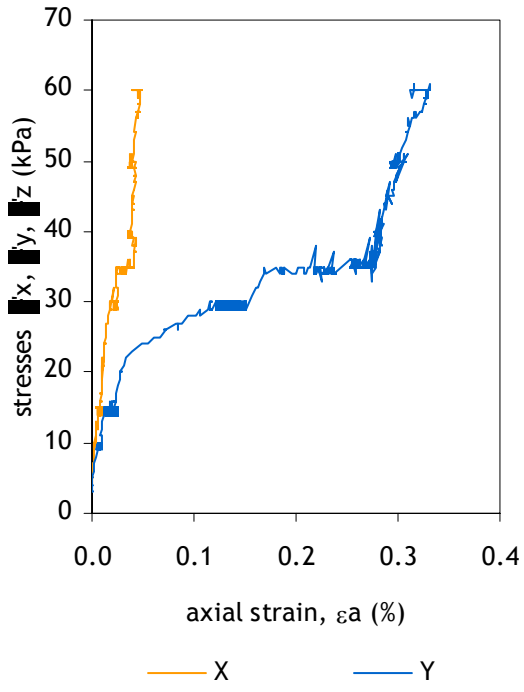
Figure 7.93 - B5-TT: secant Young's moduli against mean effective stress

Even at this scale (Figure 7.93b), the values of E_{sZ} are hardly perceptible and its variation with stress is very small. The comparison between the static and the dynamic measurements of stiffness is, in this case, particularly complex. Additionally, only a few BE measurements in the Z direction were possible. As a result, this comparative analysis is inconclusive.

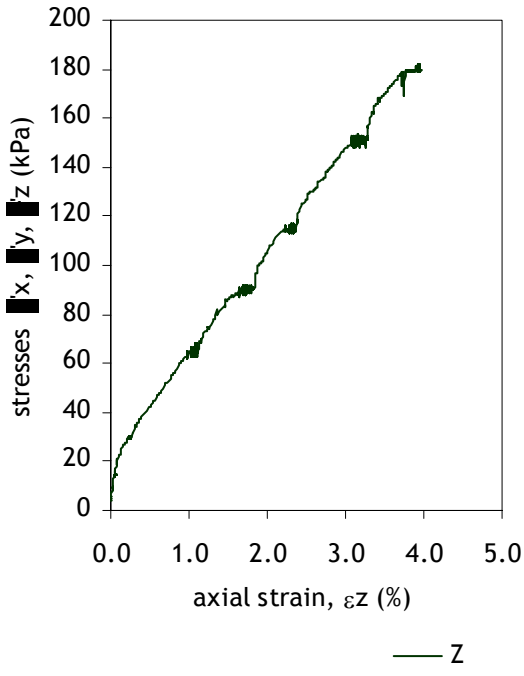
The last test to be discussed here in the context of the true triaxial tests was carried out on sample B4-TT. In this test, the sample was consolidated to an estimated in-situ stress state, where K_0 was considered equal to 0.35, in order to take into account the most recent results of tests on this material. The stress-strain curves obtained in this test are presented in Figure 7.94. As before, separate plots of the stresses in the horizontal and the vertical directions were prepared so that the displacements in the X and Y directions could be discernible (Figure 7.94b and c).



a)



b)



c)

Figure 7.94 - B4-TT: stress-strain curves, a) complete set of data; b) zoom-in for horizontal stresses; c) vertical stress

The results indicate that, despite the low coefficient of at rest state, some deformation occurred in the horizontal directions, especially in the Y direction. This deduction can only be considered in relative terms, by comparison with other works of the same nature. As previously mentioned, after the stress relief caused by the removal from the ground, irreversible damage is caused to the sample, the extent of which depends on a number of factors namely the sampling method, storage conditions, soil properties, among others. As a consequence, at the time of testing and for the corresponding in-situ stresses, the response of the sample will be more or less over-consolidated, depending on its disturbance.

Considering the three-dimensional stress-path of this test, the deviatoric stress and strain were calculated and shown in Figure 7.95.

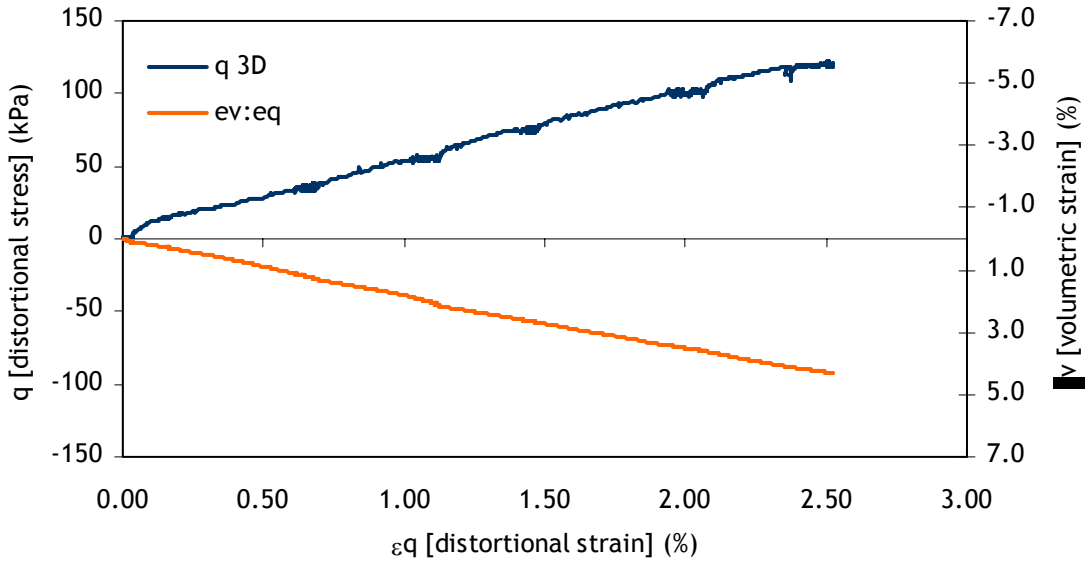


Figure 7.95 - B4-TT: distortional stress and volumetric strain against distortional strain

According to this figure, the applied consolidation stress-path did not induce any destructuration of the sample, as the response is nearly linear.

The obtained secant Young's modulus are presented in Figure 7.96a and b, as a function of mean effective stress and axial strains, respectively.

The variation of the directional stiffness moduli is very similar, with highest values for E_{sX}. Since in this test, BE measurements were unfeasible, the comparison between the static and dynamic stiffnesses cannot be established.

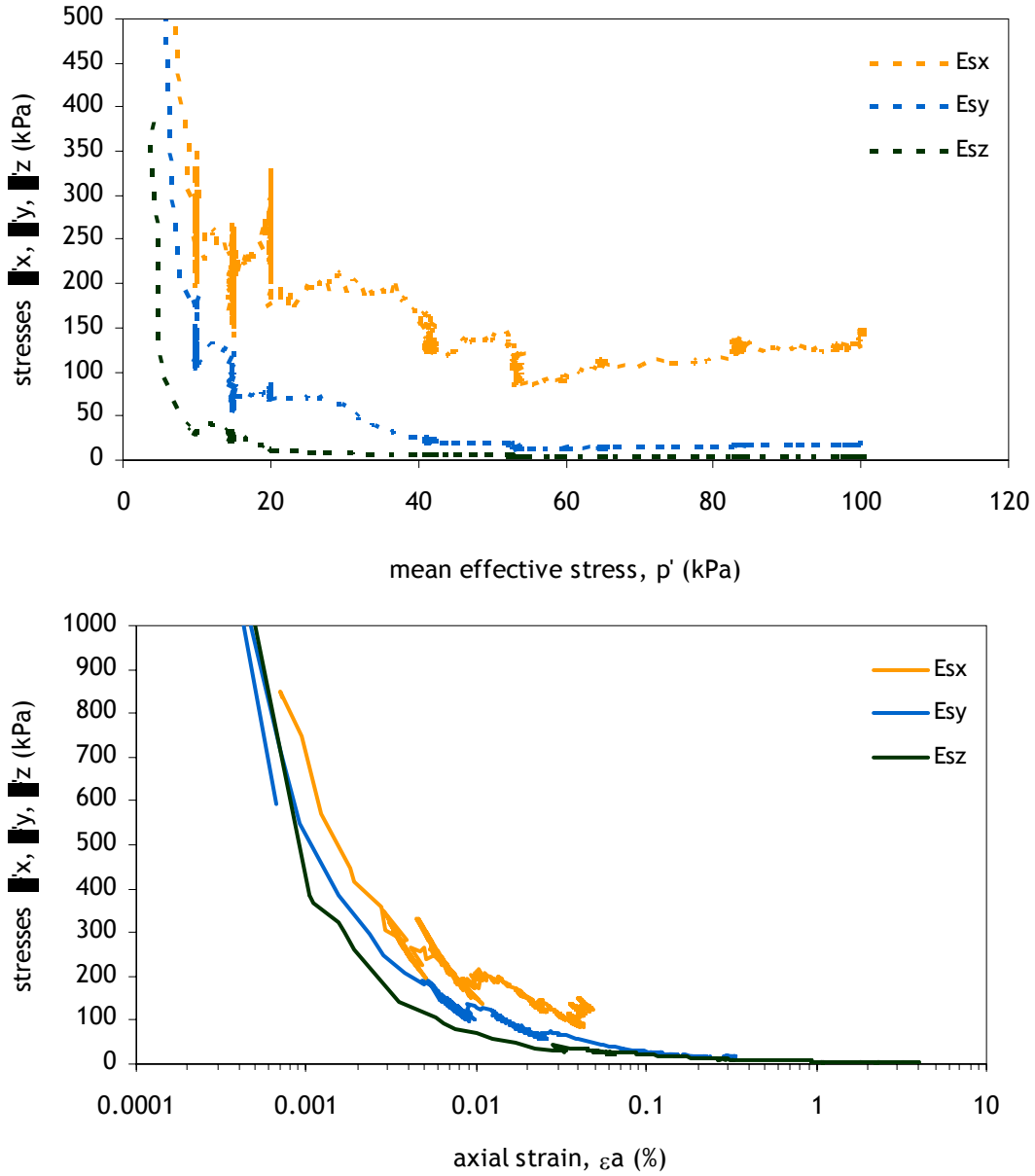


Figure 7.96 - B4-TT: secant Young's moduli against a) mean effective stress; b) axial strains

7.3.4.3. Comparison between undisturbed and reconstituted samples

To finalise this section on the laboratory results on small to large strains in the true triaxial apparatus, the comparison of some of the obtained results will be presented as follows. A combined plot containing the stress-strain results of all of these samples would be too "crowded" and few conclusions could be derived. Instead, the comparison will focus on a few simple representations of the tests and also on the direct comparison of similar tests, namely those with isotropic and K_0 consolidation.

The first plot, presented in Figure 7.97, refers to the comparison of the compressibility of the tested undisturbed and reconstituted samples. As shown in the figure, the results from the undisturbed samples are well framed within the curves of reconstituted samples. The void ratios adopted for the reconstituted samples were representative of the typical soil state conditions. The reconstituted samples are more compressible than the undisturbed, as would be expected, given the natural structure of this soil.

Due to the characteristics of this apparatus, the compressibility curves are relatively short. The limitation of this apparatus is the maximum strain of 8%, for which the highest applied pressure corresponded to only 400 kPa. The comparison of these results with those of oedometer tests, where higher stresses were applied, would provide further insight on the compressibility characteristics of this soil.

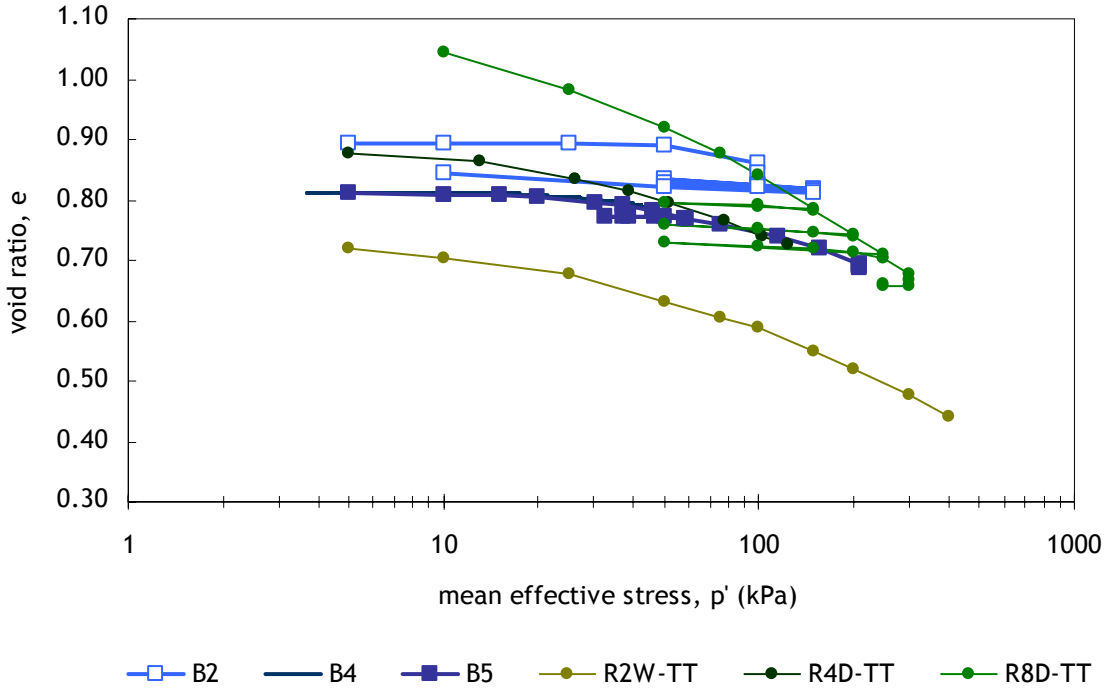


Figure 7.97 - Compressibility curves of the undisturbed and reconstituted samples

Another comparison can be made between the reconstituted and the undisturbed samples, grouped by the stress-path applied. For example, samples R2W-TT and B2-TT followed an isotropic consolidation stress-path, while an anisotropic K_0 condition (imposed by a null horizontal deformation control) was adopted for both samples R4D-TT and B5-TT.

For the isotropically consolidated samples, the comparison of the stiffnesses defined by the secant Young's moduli is established in Figure 7.98, against the axial strains. A similar graph would be obtained for the relationship with mean effective stress.

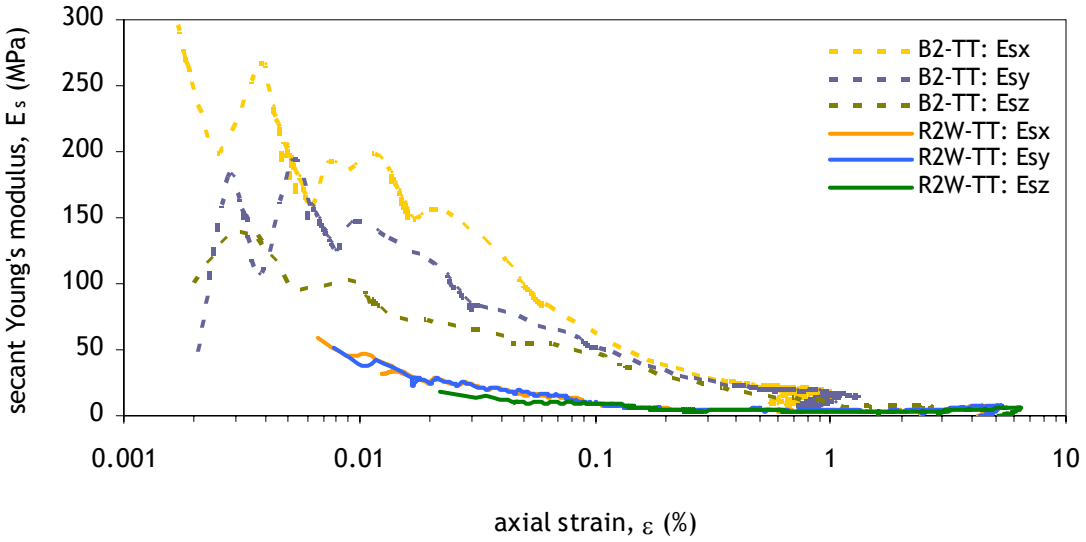


Figure 7.98 - Secant Young's moduli obtained from isotropic consolidation: comparison between undisturbed B2 and reconstituted R2W samples

The results in the figure show considerable differences between the stiffnesses. The undisturbed material exhibits much higher stiffness moduli in all directions than the reconstituted sample. This conclusion was clearly anticipated, but this direct comparison is useful and informative. Moreover, it provides a good indicator of the performance of this apparatus for stiffness measurement at small to large strains.

For the anisotropically consolidated samples, tested at zero horizontal deformation, it is more appropriate to establish the comparison of the Young's moduli as a function of mean effective stress. The stiffness results are combined in the plots of Figure 7.99a and b, which were divided in the horizontal and vertical directions. The objective for this division is to provide a clearer and more satisfactory view of the differences between corresponding stiffnesses. In these two tests, due to the adopted stress-path, the stiffness in the horizontal directions is much higher than in the vertical direction.

Once again, the Young's moduli of the undisturbed sample are substantially higher than those of the reconstituted sample. Even for the horizontal directions where the moduli are considerably amplified by the division of a nearly zero value (the reference zero deformation), the values for the undisturbed material are greater than for the reconstituted material.

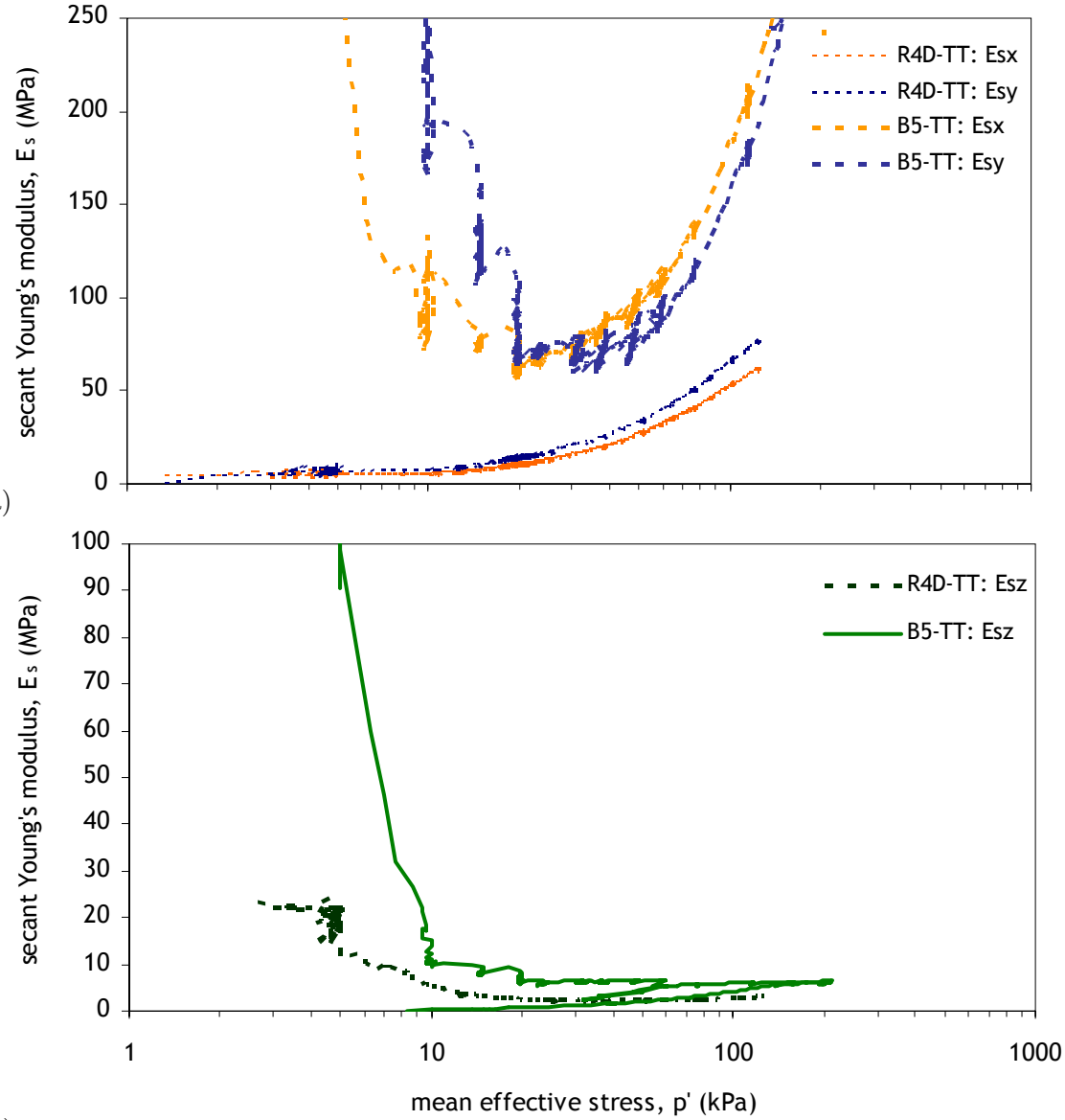


Figure 7.99 - Secant Young's moduli from anisotropic K_0 consolidation, comparison between undisturbed B5 and reconstituted R4D samples: a) X and Y horizontal direction; b) Z vertical direction

There are many more possibilities of comparison and combination of these true triaxial results. These were considered most relevant for the identification of the soil

behaviour and response under diverse stress conditions, as well as for the assessment of the performance of this device for the intended purposes: independent control and measurement of stresses and strains (from small to large), and small strain measurement of stiffness by means of BE.

7.3.5. Cubical cell tests

The stress-strain results of the tests carried out in the cubical cell apparatus, from the University of Bristol, will be briefly presented. The description of the tested samples, testing conditions and stress-path was already introduced earlier in this chapter, in section 7.2.6.

The complex stress-path adopted for sample B6-RS1 resulted on the stress-strain curves illustrated in Figure 7.100.

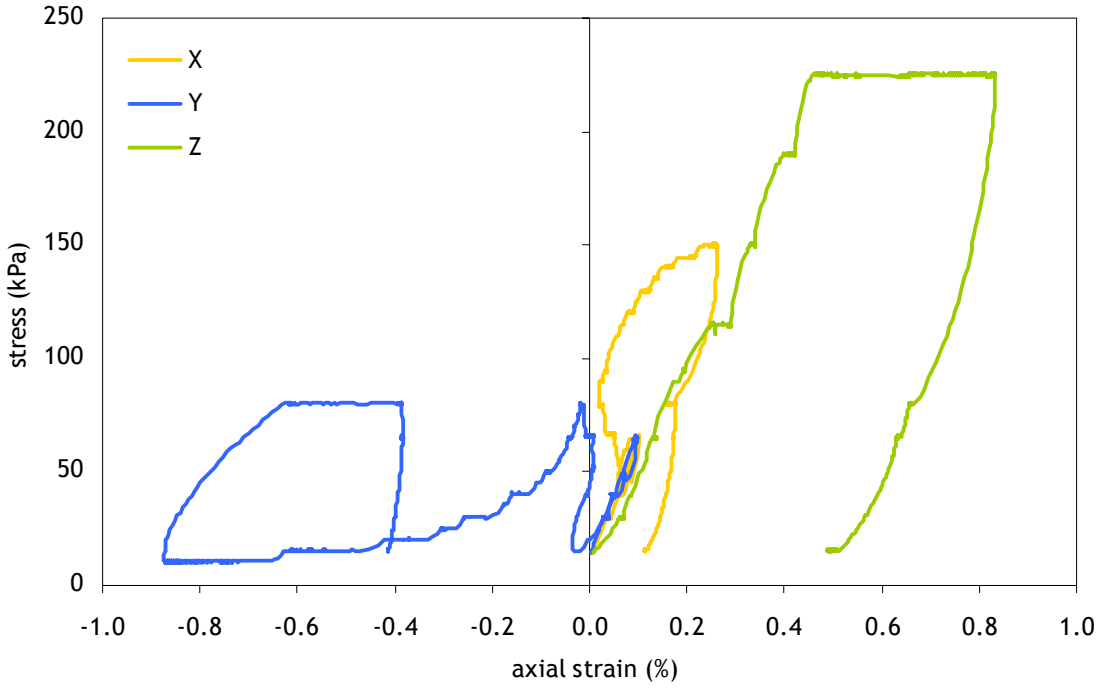


Figure 7.100 - B6-RS1: stress-strain curves

This deviatoric stress-path at constant mean effective stress, with identical but opposite sign variations of the stresses in the two horizontal directions, produces stress-strains in X and Y that appear to complement each other. This has already being observed in the true triaxial tests, for sample B5-TT.

The secant Young's moduli were also computed, as presented in Figure 7.101 as a function of the axial strains. Since an extension stress-path was applied in the Y direction, in this case, negative E_s were measured.

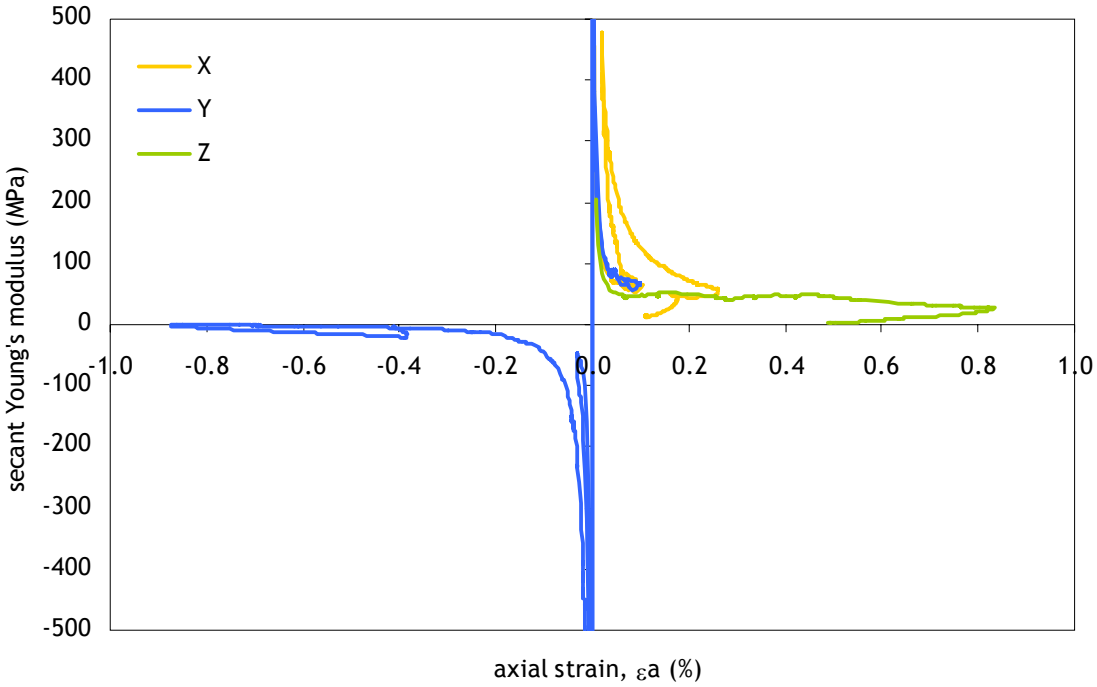


Figure 7.101 - B6-RS1: secant Young's moduli against axial strains

Similar analyses were made for the test on sample B6-RS2. The obtained stress-strain curves are plotted in Figure 7.102.

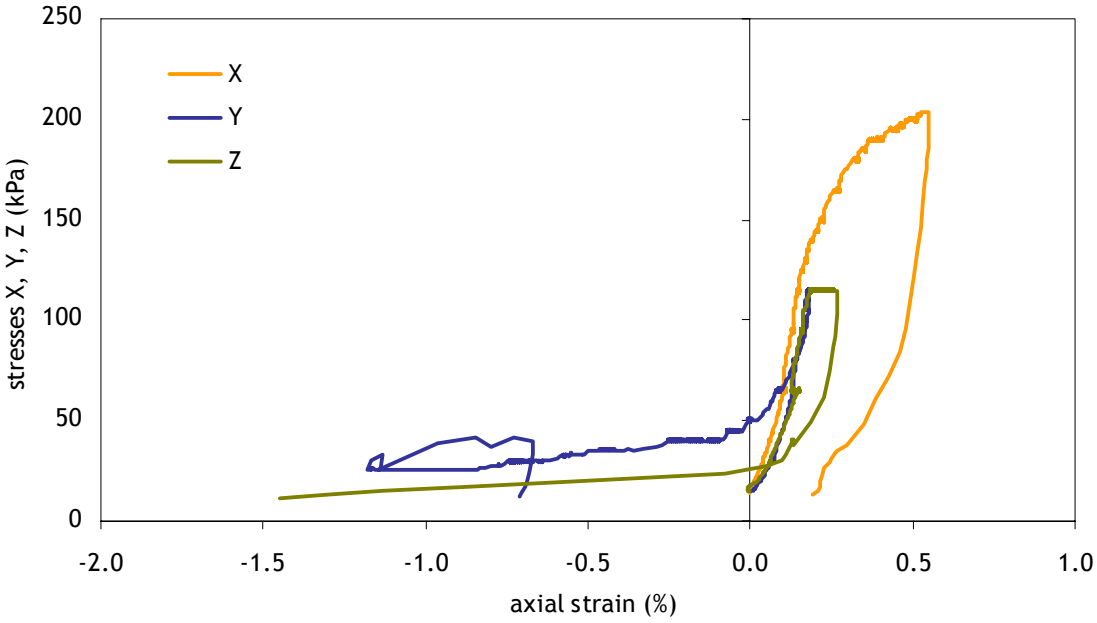


Figure 7.102 - B6-RS2: stress-strain curves

The secant Young's moduli in the three directions were computed from the stress and strain measurements, as illustrated in Figure 7.103.

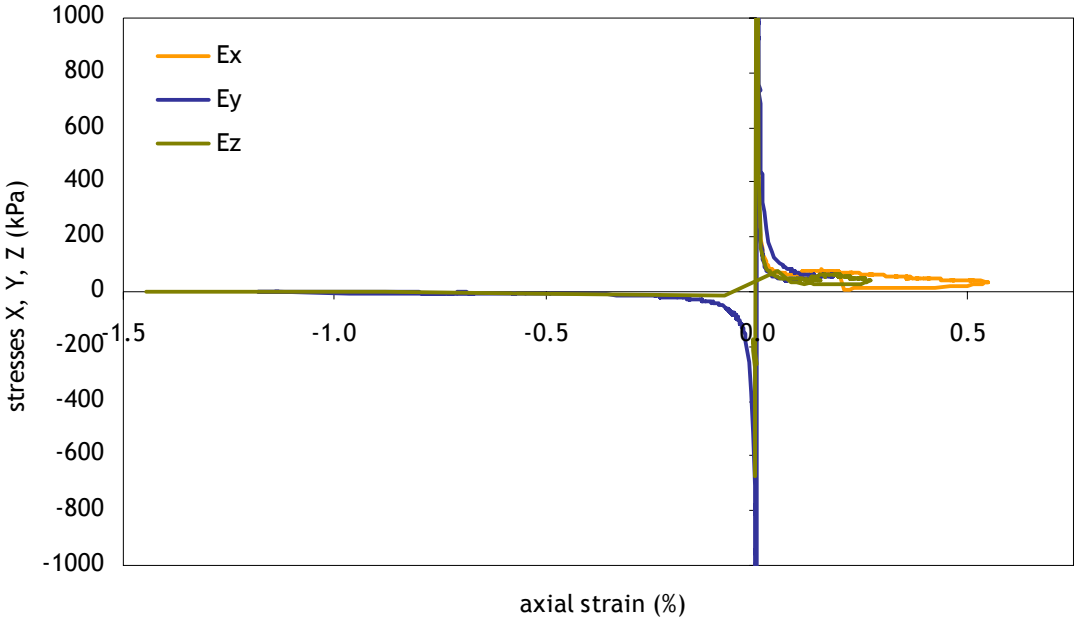


Figure 7.103 - B6-RS2: secant Young's moduli against axial strains

In this case, a clear reversal of stiffness can be observed not only on the Y direction, but also on the vertical direction.

Finally, the test on sample B4-RS3 provided the following stress-strain curves, presented in Figure 7.104. The stiffness results are plotted in Figure 7.105.

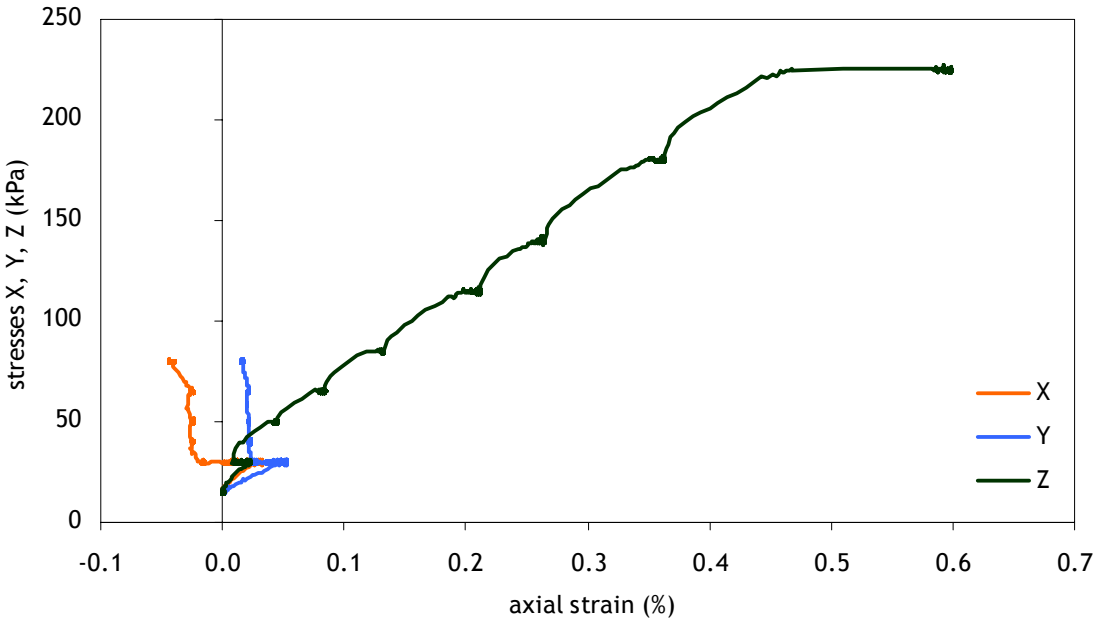


Figure 7.104 - B4-RS3: stress-strain curves

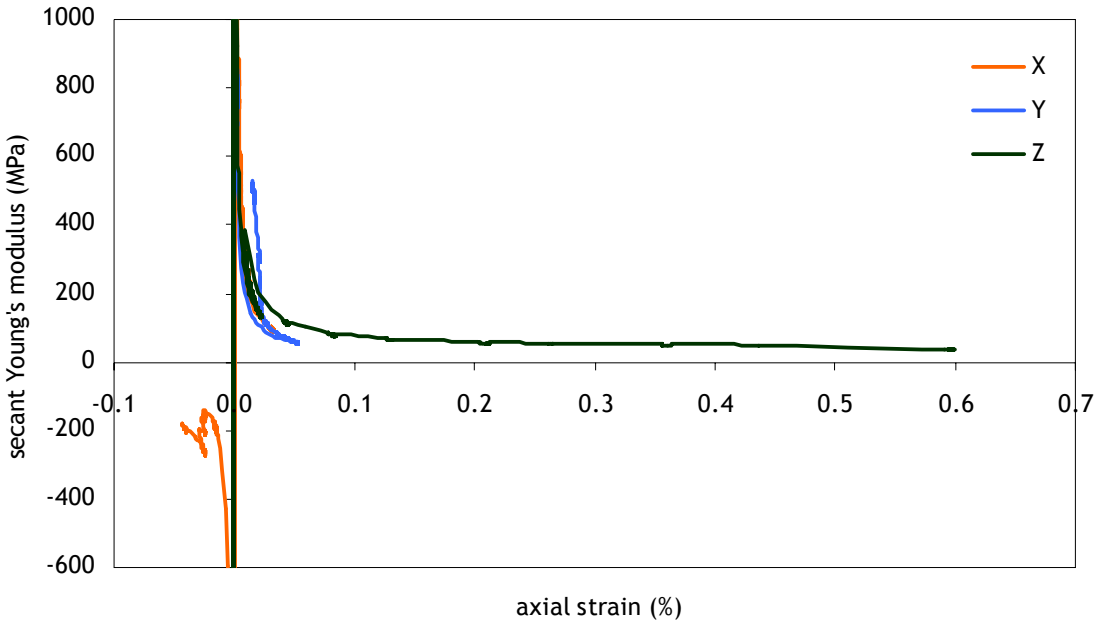


Figure 7.105 - B4-RS3: secant Young's moduli against axial strains

The distortional stress and strain were calculated from the data in order to better illustrate the response of the soil in the deviatoric plane. These results are reproduced in Figure 7.106.

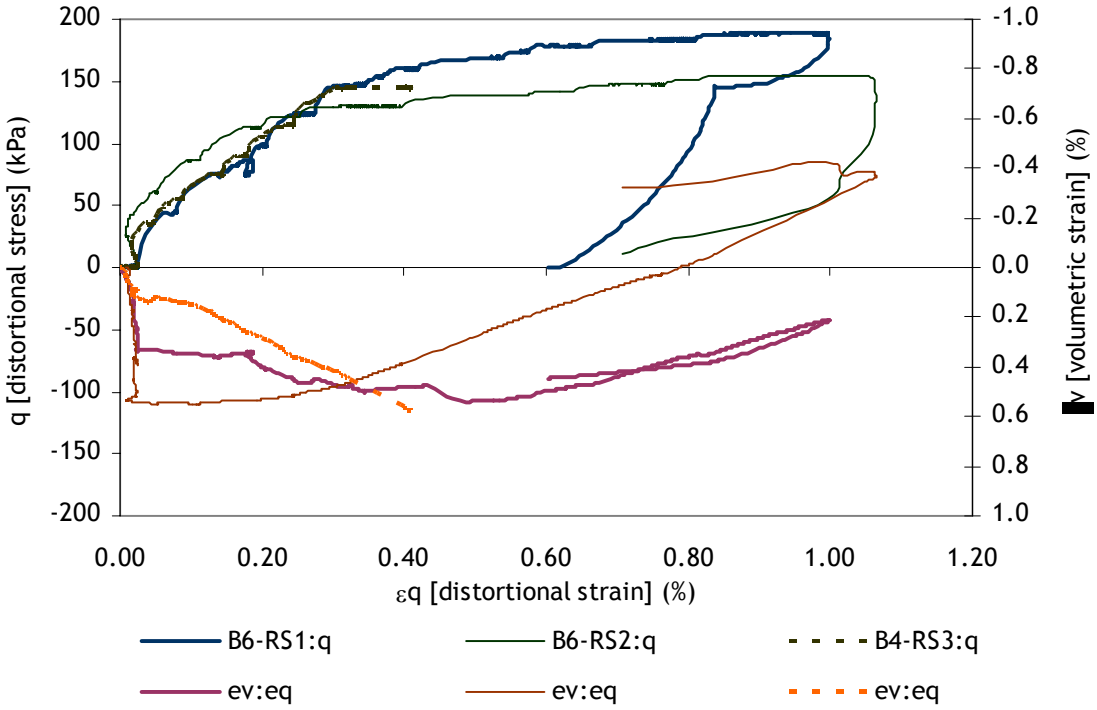


Figure 7.106 - Distortional stress and volumetric strain against distortional strain for all tested CC specimens

Contrary to previous tests in the true triaxial apparatus, in this cubical cell, since there are virtually no restrictions in terms of the mobilised strains, it was possible to induce much larger deformations and reach failure in the two of the samples, namely B6-RS1 and B6-RS2. For example, in test B6-RS2, the sample clearly failed and a shear wedge was visible once it was removed from the cubical cell, as shown in Figure 7.107.



Figure 7.107 - B6-RS2: end of the test

7.4. Summary and conclusions

In this chapter, the most relevant laboratory test results were presented, obtained from testing natural residual soil from granite in the resonant-column, standard triaxial and true triaxial apparatuses. The results were grouped in terms of very small strains, measured by means of BE, and small to large strains, provided by the local strain measuring devices. Focus was given to the stiffness response in relation to stress and strain conditions, observed in these different testing apparatuses.

The comparison between resonant-column and BE tests provided new insights on the likely influence of the shear strain induced by the measurement, even at very small strains. This effect of strain in the measurement of G_0 at very low strains has not yet been put forward as a potential reason for the discrepancies between interpretation methods, however it appears to be influential. Under this assumption, it can be said that, in this case and for this particular pair of BE, the shear strain induced by the sweep signal of the FD method is higher than the shear strain caused by the pulse signals used in the TD method. Moreover, the systematic differences, observed here and elsewhere, between TD and FD methods may be explained by the slightly different shear strains at which the BE are excited. These results indicate that the calibration of the BE in relation to the RC is an interesting and constructive exercise, if the associated RC shear strain is taken in due consideration.

The very small strain results were presented from reconstituted specimens to natural undisturbed samples, in isotropic and anisotropic conditions, in standard triaxial, true triaxial and cubical cell tests. The parameters that describe the dependency of the shear stiffness with stress, void ratio and structure were derived for the different sample conditions and stress states.

The comparison between the results obtained from tests on undisturbed samples from both experimental sites presented similar stiffness response and evolution with stress, thus confirming that the soil of the two sites is similar. The very small strain stiffness results from ES2 were found to be more scattered than those of ES1. The most plausible cause for this discrepancy is related with the different saturation conditions of the two soils, which affect the interpretation of BE tests. An unsaturated sample in a triaxial cell can be assimilated to a reflecting boundary setup, in which case, larger distortions are introduced in the BE output signal.

The interpretation of the BE tests in true triaxial conditions was found to be more complex than in the cubical cell, possibly due to the nature of the boundaries. In the

TT tests, the use of the proposed methodology of BE interpretation was mandatory in order to obtain realistic estimates of travel time. Nevertheless, the tests on natural samples provided less data in terms of very small strain stiffness, which may be related with the greater difficulty in ensuring contact between the BE and the soil.

Finally, the results obtained at small to large strains were also summarily presented. Large differences were encountered between the maximum stiffness and those determined at increasing higher strains, especially in the true triaxial tests. These results suggest that the installation of BE in any laboratory testing apparatus is beneficial, in order to obtain more accurate estimates of the maximum stiffness of the tested material.

The analysis of these results will follow with the combination and integration of the data obtained in diverse apparatuses under comparable conditions, namely the comparison between two- and three-dimensional behaviour, in Chapter 8.

8.

Discussion

8.1. Introduction

In this chapter, the combination of results obtained from different laboratory testing techniques will be presented. Despite the distinct nature and characteristics of the testing equipments used in this research, the obtained results can be compared and contrasted as a means to highlight and provide a more complete understanding of the behaviour of the geomaterial in study. Moreover, by demonstrating the similarities and differences between laboratory results, it will be possible to assess the performance and highlight the potentialities and limitations of the novel non-conventional testing methods used in this research work.

Subsequently, some important geotechnical applications will be discussed derived from the comparison between laboratory and/or in situ test results. Emphasis will be given to the application of shear wave velocities in the assessment of sampling quality, structure and anisotropy, and in the evaluation of porosity.

8.2. Developments in bender testing

8.2.1. BE testing methods and interpretation techniques

A number of BE interpretation techniques have been reported over the years in the literature. In the present work, a framework was proposed for combining two fundamentally different BE testing methods, in the time and the frequency domain. The method in the time domain was derived from the traditional and most common method of identification of first arrival in the output wave. In this work, this method is extended to the use of various input frequencies and complementary measurement of P-waves, in order to reduce the subjectivity of the interpretation.

The other method in the frequency domain uses a broad-band input signal, thus energizes a wide range of frequencies, and the response of the system is analysed using Fast-Fourier transforms to obtain the phase-angle between the two signals, from which the travel time of the shear wave is derived. Early results using this method showed that the estimates of travel time were considerably sensitive to slight changes in the moving window used for its computation. As a result, an automated tool was conceived to provide unbiased information regarding such variations. This procedure enabled to deal with the variability, even at high coherence values, of the results from the sweep method and to deduce the travel time from the highest correlation coefficient obtained from different moving windows.

From the test results presented in the previous chapter, it can be concluded that the FD method is more demanding in terms of the testing conditions, since it requires better coupling between the transducer and the soil and lower environment noise than the TD method. The exclusive use of either method is not advocated, as the interpretation of the results may be unreliable.

The most important conclusion from the work is that the combined use of time-domain and frequency-domain methods can aid effectively in the analysis and interpretation of BE tests in the laboratory. The use of both interpretation techniques brings the advantages of the two together and thus minimizes their weaknesses, since it is possible and acceptable to directly compare results and decide accordingly.

8.2.2. Comparison of RC and BE measurements

In the previous chapter, the small-strain stiffness moduli obtained in the resonant-column were compared with those measured by means of bender elements, in a RC device purposely equipped with BE. In this apparatus, a considerable amount of tests were carried out on a number of undisturbed samples of residual soil, under a variety of stress conditions and stress-paths. The proposed framework for BE testing was used, that is, BE measurements were made in the time and the frequency domain. Resonant-column tests were made using the conventional testing (RC-CT) method, but on the last two samples, an alternative method was also applied, using random-noise excitation (RC-RN).

Some differences were encountered between the estimates of the "maximum" shear modulus by those testing methods. In an attempt to understand and justify those differences, the final results were re-analysed. It was found that the strain at which the G_0 measurement was made has some influence in its result, even in the very small strain domain.

The strains associated with each RC measurement are variable. However, these can be calculated from the output of the acquisition, namely the amplitude and current. On the other hand, while relatively unknown, the strains induced by each BE technique can be assumed constant, if the same pair of transducers, the same voltage and the same range of frequencies are employed. The use of pulse signals for the time domain (BE-TD) method is expected to produce lower strains than the sweep signals for the frequency domain (BE-FD) method, considering the steady state nature of the sweep signal.

In the absence of more accurate data or of direct measurement of the BE deformation when fully embedded into the soil, the strains associated with each BE method must be estimated, either based on other research results or from the comparison with the RC results. The second option was considered, since there are no reports on the measurement of the BE deformation during a test on a soil specimen. For this purpose, the best-fit lines of the data points relating the ratios of shear moduli defined by each BE method with those defined by each RC method were drawn. Identical plots have already been presented in the previous chapter, but these are repeated here to explain the process used to define the best estimate of the BE shear strain. Under the assumption that, if two methods measure G_0 at the same strain then their results should be identical, the shear strain induced by each BE method should correspond to the intersection of the best fit line with the line of

G_{BE}/G_{RC} equal to unity. This procedure is illustrated in Figure 8.1, from which the shear strains of $3.5x10^{-6}$ and $5.0x10^{-6}$ have been associated with the TD and the FD methods, respectively.

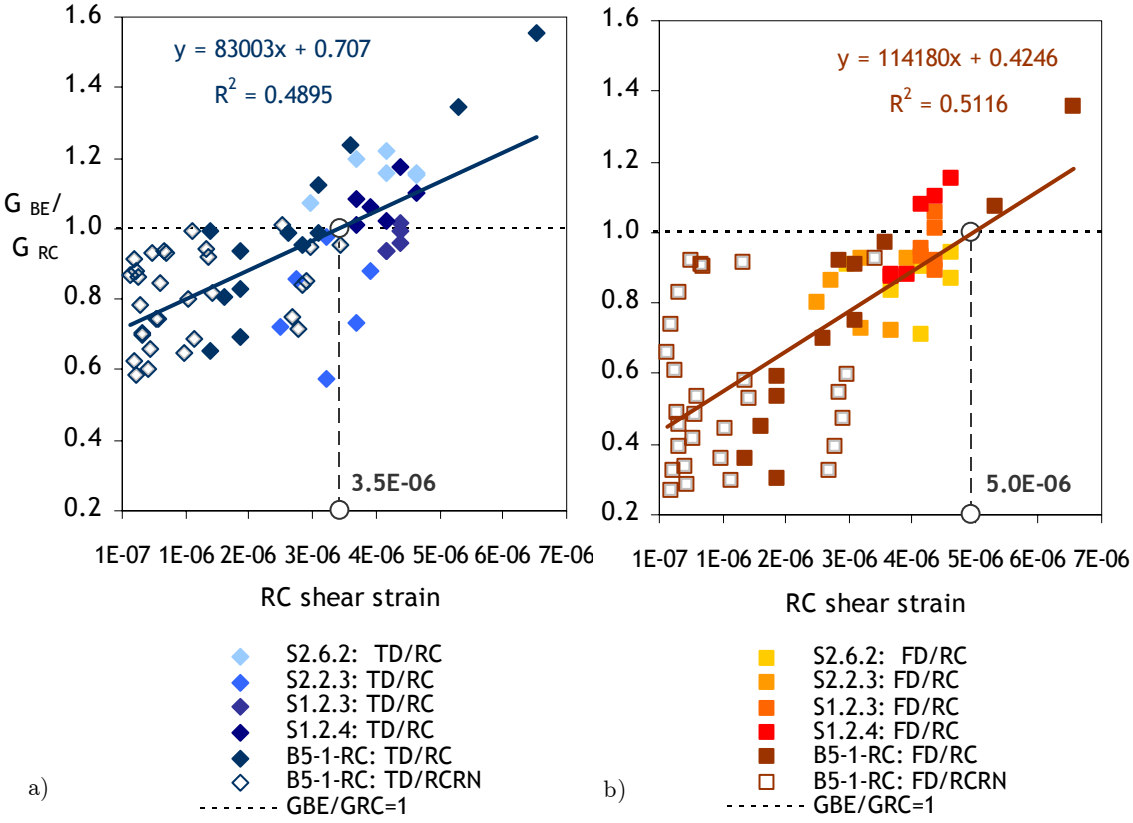


Figure 8.1 - Variation of the ratios of G_0 measured by BE methods with those determined by RC methods: a) FD; b) TD

The hypothesis formulated, based on the obtained results, is that since different strains are induced by the different methods for the determination of G_0, the results are necessarily different.

To illustrate this observation, an additional graph has been produced, which relates the stiffness moduli with the strain of measurement, and is presented in Figure 8.2. This graph features two degradation curves from the tests on samples B5-1 and B5-2, which were anisotropically consolidated to the mean effective stresses of 283.3 kPa and 60 kPa, respectively. Results from BE-TD, BE-FD, RC-CT and RC-RN measurements, from the test on sample B5-1 are also included, at p' equal to 283.3 kPa and 65 kPa (the closest stress stage considered in B5-1 to the stress conditions of B5-2).

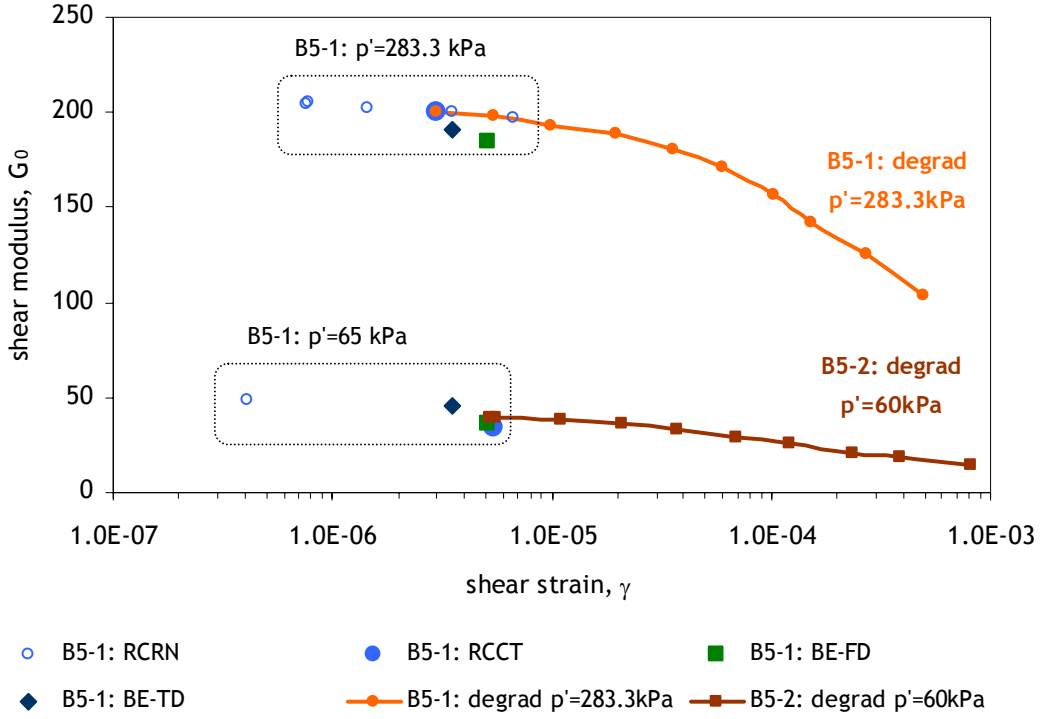


Figure 8.2 - Maximum shear moduli measured by RC-CT, RC-RN, BE-TD and BE-FD as a function of the shear strain of measurement

This graph shows that at low stresses (B5-1 at 65 kPa) the RC-CT method provided the lowest value of G_0, but this measurement induced the highest shear strain. Conversely, at higher stresses (B5-1 at 65 kPa) both RC methods provided higher values of G_0 but the corresponding induced shear strains were considerably lower than those at lower stress and also those estimated for the BE methods. Hence, the variability of G_0 values appears to be related with the shear strain induced by the measurement. The estimates of the shear strains associated with each BE method seem to fit reasonably well with the two shear moduli degradation curves.

Other factors can be proposed to explain the differences between the methods for the determination of the shear modulus. However, in the light of these results, it can be concluded that the shear strain at which the shear modulus is measured should also be considered, even for measurements in the very small strain domain (below 10^{-5}).

8.3. Comparison of stiffness measurements in the laboratory

Despite the distinct nature and characteristics of the testing equipment used in this research, the obtained results can be compared and contrasted to highlight the behaviour of the tested soil. Moreover, the comparison of results enables to assess the performance and capabilities of the non-conventional testing devices.

For this purpose, some of the laboratory results previously presented in Chapter 7 will be grouped and analysed side-by-side. Considering the focus of this work on the measurement of stiffness by means of seismic wave velocities, the discussion of results will be fundamentally made in terms of the very small strain stiffness.

The analyses must be made between comparable results, that is, when only a few controlling parameters are different. Therefore, in order to establish comparisons between tests in different apparatuses, some aspects of the tests have to be identical or similar, such as:

- the seismic wave directions
- the type of soil specimen: reconstituted or undisturbed
- the stress conditions: isotropic, anisotropic or other

Moreover, to account for the natural variability of the tested soil samples, the consideration of soil state, namely the void ratio, will be made by analysing the results in terms of normalised shear moduli (in relation to the established void ratio function).

8.3.1. Resonant-column and standard triaxial results

The comparison between RC and standard TX tests enables to verify whether the shear wave measurements by means of BE are producing identical results in different apparatuses. For this purpose, the soil specimens should be as similar as possible, in order to minimize the variability associated with the tested material.

From the same block sample [B5], it was possible to prepare a few cylindrical specimens to be tested in different apparatus: i) sample B5-1-RC was tested in the BE-equipped resonant column under anisotropic (K_0=0.35) conditions; ii) sample B5-isoSP was tested in the stress-path cell under isotropic conditions; and iii) sample B5-TX was tested in the standard triaxial apparatus under anisotropic (K_0=0.50) conditions.

The results obtained in terms of the normalised shear moduli are presented in Figure 8.3. Despite the same origin of the three samples, the respective void ratios are different, hence the need to normalise the moduli prior to this comparison.

The figure shows a fairly good agreement between the different shear moduli, except for the FD method in the resonant-column test on sample B5-1-RC. The comparison with the other results suggests the possibility of errors in the FD interpretation, especially at higher stresses, as previously discussed in the analyses of the RC results. The reasons of this unsuccessful FD interpretation on that test are unclear, and may be related with the application of higher stresses and the use of a different acquisition system.

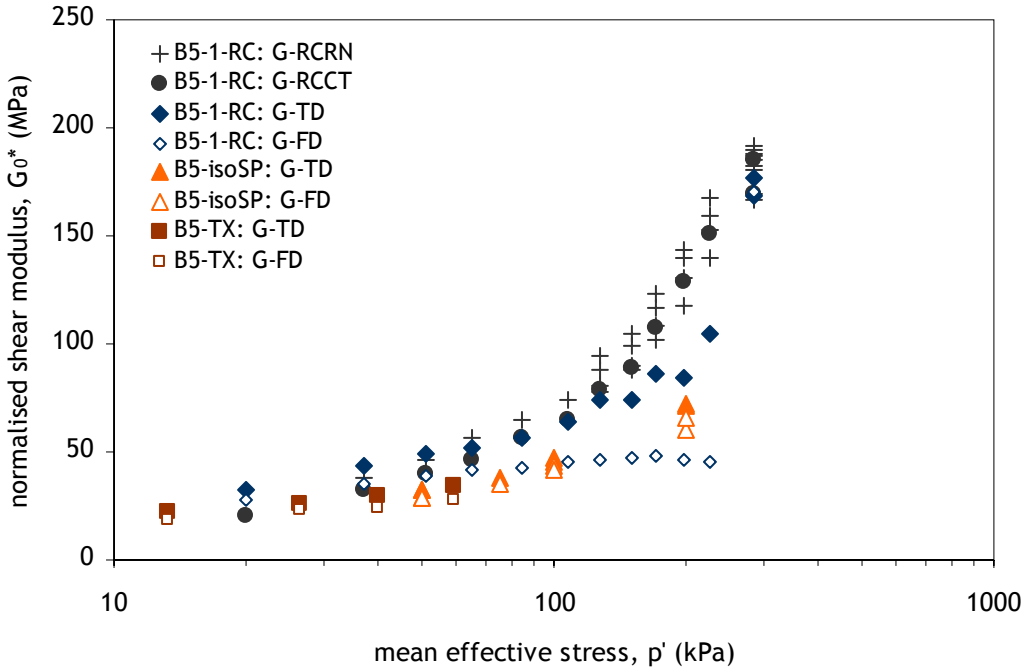


Figure 8.3 - Normalised G_0 of three specimens from block B5, tested in the resonant-column and the standard triaxial apparatuses

At higher stresses, the BE results are considerably lower than those provided by the RC, which can be justified by the lower strain level induced by the RC in those measurements, as discussed in the previous section.

The overall differences between the three tests can be considered acceptable and justified by the different stress conditions. It can be concluded that the BE measurements in these apparatuses (resonant-column, standard triaxial and stress-path) appear to be directly comparable.

8.3.2. Standard triaxial and true triaxial results

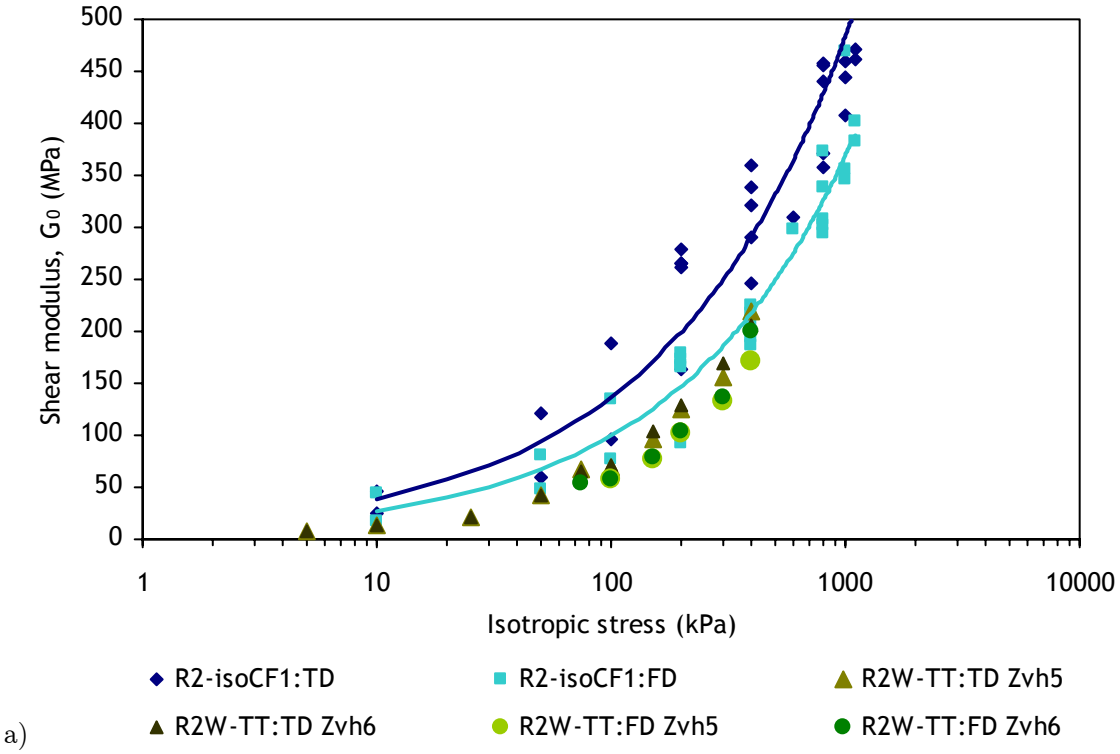
Similar comparisons can be established between seismic wave measurements carried out in standard triaxial and in true triaxial conditions. For this purpose, two different analyses can be made from the available test results, according to the type of tested soil specimens: a) reconstituted; b) undisturbed.

The comparisons between reconstituted specimens can be directly made and enables to assess the quality of the defined reference indices. Moreover, the different sample geometry conditions can be contrasted to identify its effects on the interpretation of BE results, namely the differences between TD and FD interpretation methods.

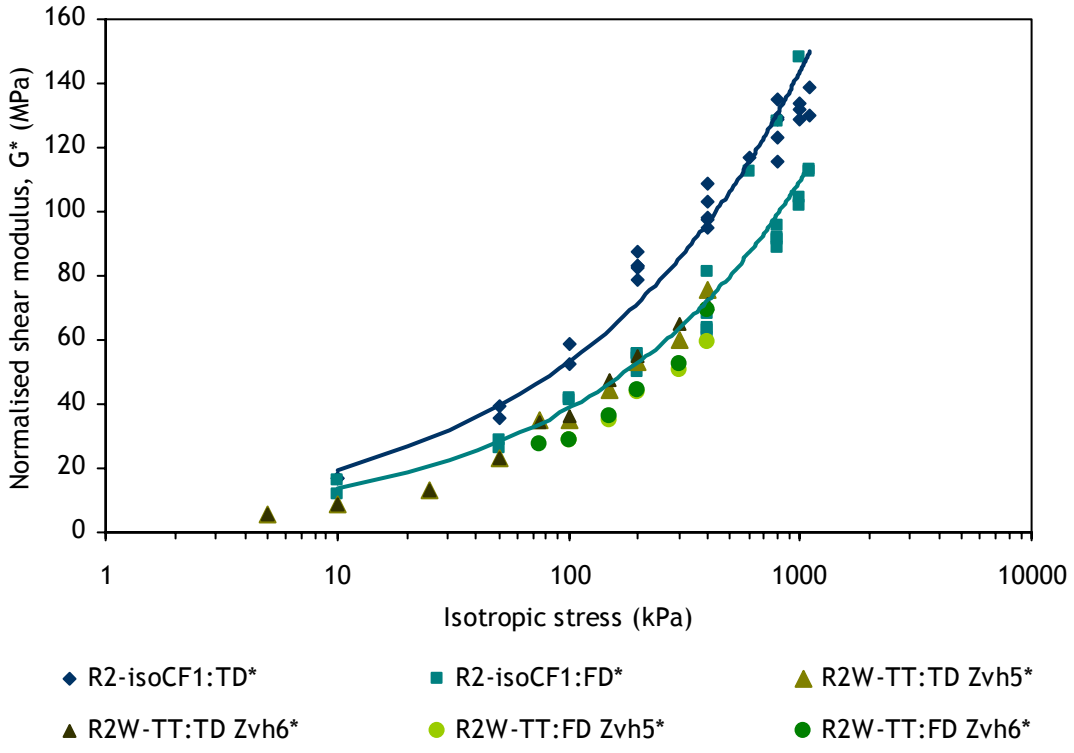
For this purpose, the results from isoCF1-TX, tested in standard triaxial apparatus, and R2W-TT, tested in the true triaxial apparatus, both under isotropic stresses were compared. The comparison between these reconstituted samples in isotropic conditions was made in relation to G_0 and $G_0{}^*$ (normalised to the void ratio function) against stress, as shown in Figure 8.4a and b, respectively. For the test on sample isoCF1-TX, only vertically propagated velocities were measured. For this reason, it is only reasonable to compare the true triaxial results obtained in the Z direction.

From the two figures, it is clear that the normalisation of the shear moduli in relation to the void ratio is effective in the reduction of the number of influential parameters and thus enables to establish more realistic comparisons.

Focusing on Figure 8.4b, it can be concluded that the BE measurements in the TX and TT apparatuses provided identical results, with very similar trends in relation to the applied isotropic stresses. The differences between the TD and FD methods are smaller in the true triaxial test and these results are almost identical to those obtained in the standard triaxial test for the FD interpretation. This observation suggests that the factors that lead to the divergence in the time and frequency domain technique are less relevant in the true triaxial apparatus. Considering the differences between TX and TT in terms of the BE setups, it can be preliminarily concluded that the sample geometry and especially the symmetrical boundary conditions of the true triaxial apparatus are more favourable to the reduction of the wave dispersion phenomena associated with BE testing. However, the comparison between TX and TT results does not provide sufficient evidence to state which method provides more realistic, and thus reliable, measurements of the shear modulus.



a)



b)

Figure 8.4 - Comparison between reconstituted samples in isotropic conditions in the standard triaxial and the true triaxial: a) G_0 against stress; b) G_0* against stress

An analogous comparison can be made from standard triaxial and true triaxial tests on undisturbed samples. Again, the tests on different samples trimmed from block sample B5 will be compared, namely the results from two tests on standard triaxial

conditions (B5-TX and B5-isoSP) and the true triaxial test on B5-TT. The stress conditions were different, but the consideration of the evolution with mean effective stress is sufficient to incorporate the diverse stresses. The comparison of results is established in Figure 8.5, for the normalised shear moduli G_0*. In this case, the comparison was only possible using TD results, given the limited data from the FD technique (further commented in Chapter 7). Ideally, the comparison should be made for corresponding seismic waves in terms of the propagation and polarisation directions. Only G_{vh} was measured on sample B5-TT, but for sample B5-isoSP the other two horizontal shear moduli were also measured, G_{hv} and G_{hh}. In addition, only a few points were obtained in B5-TT for the Z direction. Considering that the tests on B5-isoSP and B5-TT were carried out under isotropic stresses, the shear moduli in the three directions should be compared, and its differences should only be affected by the natural inherent anisotropy (to be discussed later), which is expected to be relatively small. For this reason, all the results from the directional shear moduli from the three tests were plotted together.

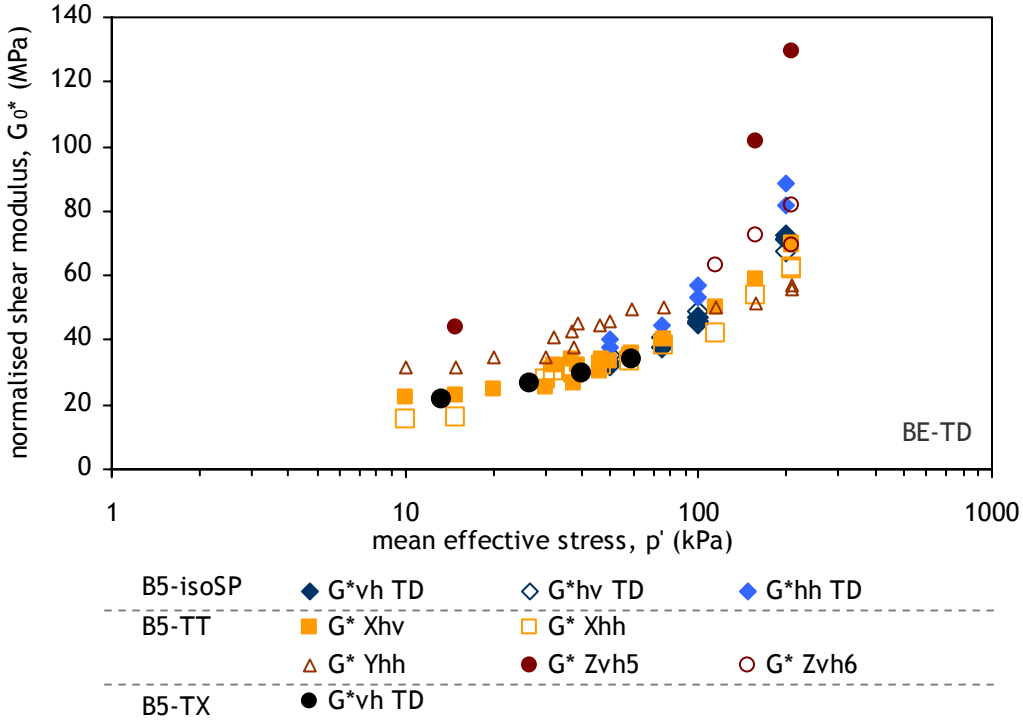


Figure 8.5 - Comparison of G_0* against stress between undisturbed samples in different stress conditions in the standard triaxial and the true triaxial

The results in the figure show small differences and very similar evolutions with the applied stresses, with the exception of the $G_{vh\text{-}Z5}$ results on B5-TT. Considering the difficulties encountered during measurements, it is possible that these values of $G_{vh\text{-}Z5}$ were incorrectly determined.

8.3.3. True triaxial and cubical cell results

Finally, it is interesting to compare the results obtained under true triaxial conditions, considering the different types of boundaries of the two apparatuses. The true triaxial apparatus at FEUP is a rigid-boundaries apparatus, while the cubical cell at UoB is a flexible-boundaries apparatus.

For this comparison, it was not possible to consider tests on identical samples, due to lack of data. Instead, all the results obtained from the tested block samples in the cubical cell were considered for comparison with those obtained on sample B5-TT tested in the true triaxial. In order to simplify the graphical display, the results were separated into horizontal and vertical propagated seismic wave moduli, in Figure 8.6 and Figure 8.7, respectively. The results were plotted against the product of the effective stresses acting on the corresponding wave propagation and polarisation directions to better account for the stress conditions of these tests.

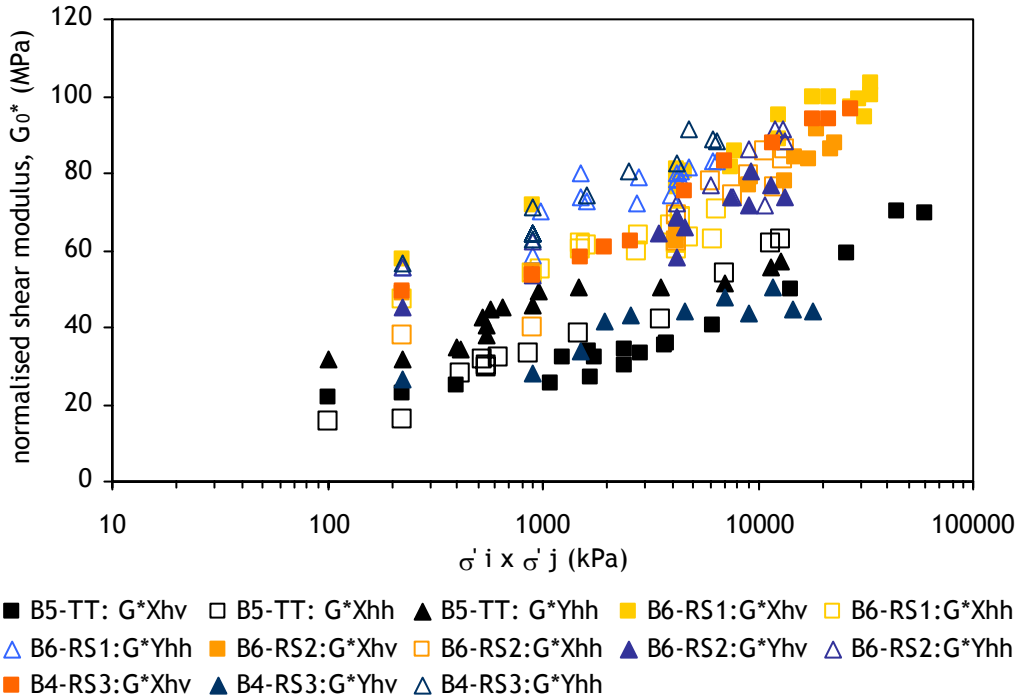


Figure 8.6 - Comparison of G_0* in X and Y directions against stresses, from undisturbed samples in different stress conditions in the true triaxial and the cubical cell apparatuses

The darkest markers in the figure correspond to the TT results, which are considerably different from the CC results. The shear moduli obtained in the TT follow the same evolution with stresses as the cubical cell results, but the absolute

results appear to be shifted to the right. Despite the fewer number of points from B5-TT in the vertical direction, in this case the obtained results in the CC and the TT evidence similar trends, as shown in Figure 8.7.

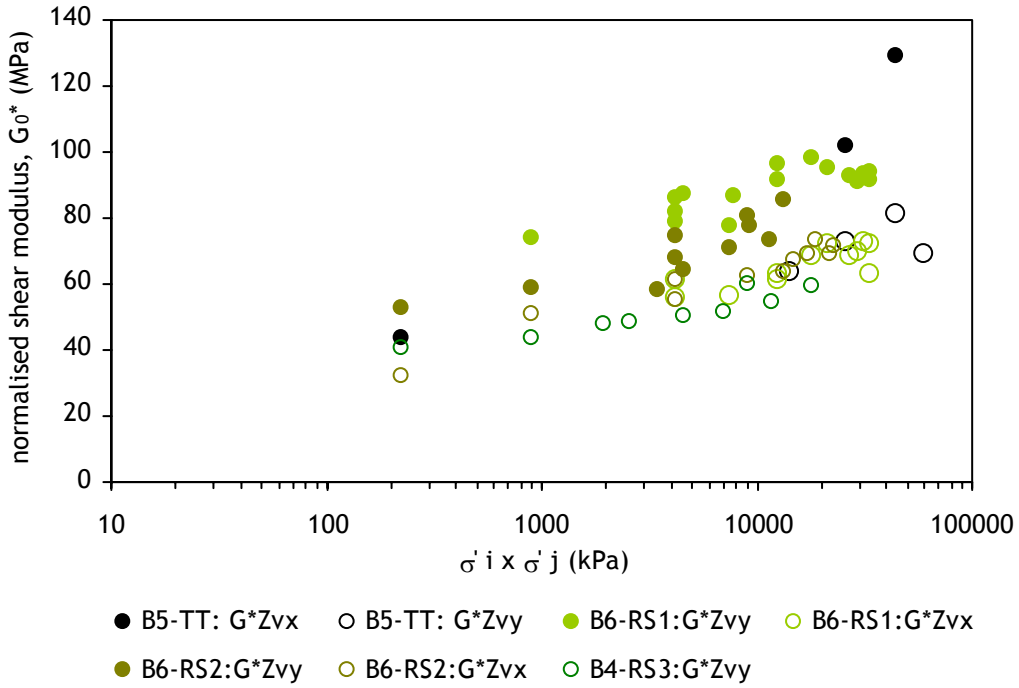


Figure 8.7 - Comparison of G_0* in the Z direction against stresses, from undisturbed samples in different stress conditions in the true triaxial and the cubical cell apparatuses

It is suspected that the different nature of the boundaries of the two apparatuses may have some influence of this observation. In fact, while the flexible boundaries of the cubical cell enable the application of uniform stresses, the rigid platens of the true triaxial apparatus impose uniform strains and the applied stress corresponds to an average of the actual stress installed in the area of the platen. This response can be assimilated to that of the contact pressure at the base of a rigid footing. Computations based on the theory of elasticity demonstrate that the contact pressure below a rigid footing increases from a low value at centreline to a maximum (infinite) value at the edges (Terzaghi et al, 1996). Due to the symmetry of the apparatus, the variations between minimum and maximum stresses are expected to be relatively small, but it is conceivable that the actual stress acting on the centre of the specimen in each direction, and thus affecting the measured stiffness, is somewhat lower than the applied stress. This could partly explain the differences between the cubical cell and the true triaxial results.

Unfortunately, since this comparison involves only one TT test, these conclusions are limited and should be complemented with further parallel tests in the future.

8.4. Assessment of sampling quality

8.4.1. Introduction

A laboratory-based characterisation of the behaviour of a soil is directly dependent on the samples selected for testing, from which the model will be constructed, and therefore dependent on their representativeness and quality in relation to the in situ conditions. Consequently, it is important to be able to assess the quality of the samples, to guarantee that only high quality samples will be used for extensive laboratory characterisation. In this context, this section addresses the issue of sampling quality and its assessment, especially by means of the comparison of field and laboratory shear wave velocities, applied to the two experimental sites considered in this research work.

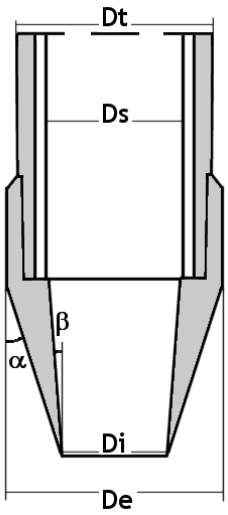
Perfect sampling represents one of the greatest challenges in geotechnical engineering. A sample of soil obtained by any sampling process will suffer disturbance, which can be divided into two main sources. Mechanical disturbance is induced by the penetration of the sampler into the soil. This produces shear distortions and subsequent compression of the soil closer to the inner wall of the sampler (Bashar et al., 1997). Baligh et al. (1987) listed some of the causes for soil disturbance during tube sampling, namely: changes in soil conditions ahead of the advancing borehole during drilling operations; penetration of the sampling tube and sample retrieval to ground surface; water content redistribution in the tube; extrusion of the sample from the tube; drying and/or changes in water pressures; and, trimming and other processes required to prepare specimens for laboratory testing. While some of these disturbances can be attributed to the sampling tools and equipment, others cannot be reduced by improving sampling operations.

The second main source of disturbance is caused as a result of the stress relief due to the removal of the sample from the ground to zero total stress state in the laboratory. The inevitable changes of stress may modify the mechanical properties of the recovered soil sample including strength, stiffness and pore pressure or volume change responses (Atkinson et al., 1992).

As discussed by Clayton et al (1998), numerous researchers have investigated the extent and nature of disturbance during sampling and laboratory testing (Kallstenius, 1958; Skempton and Sowa, 1963; Davis and Poulos, 1967; Adams and Radakrishna, 1971; Lefebvre and Poulin, 1979; La Rochelle et al., 1981; Kirkpatrick and Khan,

1984; Hight et al., 1985; Graham and Lau, 1988; Clayton et al., 1992). However, most of this research has been focused on comparative experimental investigations.

One of the most significant advances in the last decades in understanding disturbance by tube sampling has been the introduction of the strain path method (Baligh, 1985; Baligh et al., 1987) and its application to the deep penetration of a sampling tube into the ground, thus providing an analytical basis upon which the effects of sampling could be evaluated (Hight, 1993, Hight, 2000). This method was further extended by Clayton et al (1998) to examine the effects of different details of sampling tube geometry, including inside clearance ratio (ICR), outside cutting edge angle (OCA), inside cutting edge angle (ICA) and area ratio (AR), as defined in Figure 8.8.



- inside clearance ratio (ICR), which controls internal friction:

$$ICR = \frac{Ds - Di}{Di} 100 \quad [8.1]$$

- outside cutting edge angle (OCA), α
- inside cutting edge angle (ICA), β
- area ratio (AR), which relates the volume of displaced soil with the volume of the sample:

$$AR = \frac{De^2 - Di^2}{Di^2} 100 \quad [8.2]$$

Figure 8.8 - Definition of the geometric parameters of a tube sampler

These authors identified the major factors controlling the magnitude of tube sampling strains as the increasing AR or increasing OCA, both of which contribute significantly to the peak axial strain in compression, and increasing ICR which has a strong influence on the peak axial strain in extension. Their results emphasise the sensitivity of imposed strain levels to details of sampling tube geometry.

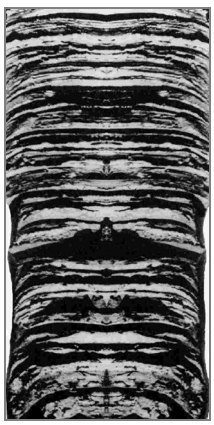
In summary, the predicted effects of the strains induced by tube sampling include: a reduction in mean effective stress; damage to structure, manifest by the shrinking of the bounding surface of the soil; and, an increase in water content in the centre of the sample (Hight, 2000). Though mainly developed for sampling of soft clays, these studies can be generalised to any sensitive and/or structured.

As pointed out by Long (2001), the need to assess the degree of sample disturbance prior to interpretation of parameters derived from laboratory tests on soil samples is now well accepted. A number of methods for the assessment of sampling quality, that is, the level of sampling disturbance have been proposed over the years. According to Hight (2000), the most common methods are:

- Fabric inspection
- Measurement of initial mean effective stress, p'
- Measurement of strains during reconsolidation
- Comparison of in situ and laboratory measurements of seismic wave velocities

8.4.2. Fabric inspection

The visual inspection of the fabric of a soil sample is the most immediate and simple method of identifying potential damaged samples. It is an empirical technique hence involves some subjectivity; however, it is particularly important for assessing water content redistribution between adjacent sand and clay layers. Only large distortions are visible, generally in the peripheral zones of the sample; the relatively small strains, associated with yield and damage to a bonded structure, usually occurring around the centreline of the sample, are hardly detected. In Figure 8.9 two examples are provided, where the disturbance caused by the penetration of the sampling tube is clearly visible.



a)



b)

Figure 8.9 - Fabric inspection: a) disturbance on a laminated clay sample with sand and silt layers spaced every 10 mm (Morecombe Bay), Rowe (1972); b) clearly disturbed residual soil sample collected from CEFEUP experimental site (ES2)

In summary, this method cannot directly indicate the effects of sampling on the behaviour of the soil, but serves as a good indicator for a preliminary selection of the samples for subsequent laboratory testing.

8.4.3. Measurement of initial mean effective stress

The initial mean effective stress, p' corresponds to the effective stress in the sample after its extraction from the ground. This parameter may change during sample, transportation, storage and even during specimen preparation. Measurements of initial effective stress, p', in samples taken from the ground and set up in the laboratory, have been advocated for many years, e.g. Ladd and Lambe (1963) (Hight, 2000). Ladd and DeGroot (2003) proposed a hypothetical stress-path showing potential sources of sample disturbance, which cause the degradation of the initial stress in a sample from sampling to laboratory testing.

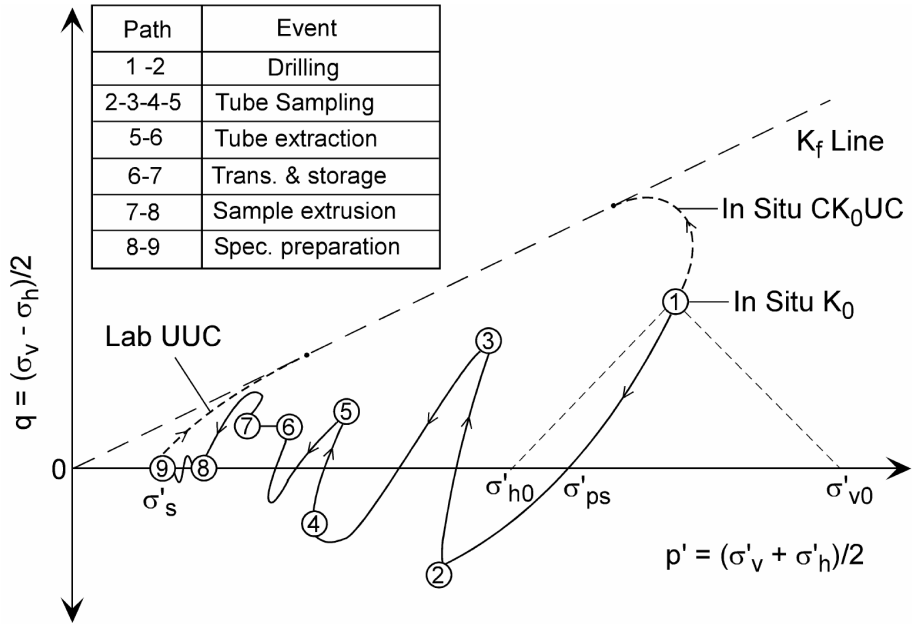


Figure 8.10 - Stress-path during tube sampling and specimen preparation of centreline element of low OCR clay (Ladd and Lambe, 1963, Baligh et al., 1987, in Ladd and DeGroot, 2003)

The potential causes for changes in mean effective stress have been considered, showing that most processes induce a decrease in p'. Comparison of p' with its value for perfect sampling, p_s, provides an indicator of level of disturbance. However, the measurement of p' alone is not sufficient, as it cannot indicate the amount of destructuration that has occurred (Hight, 2000).

8.4.4. Measurement of strains during reconsolidation

In the reconsolidation to in situ stresses, the strains experienced by the sample will depend on the reduction in effective stress resulting from sampling and from destructuration. Andresen and Kolstad (1979) proposed that increasing sample disturbance should result in increasing values of volumetric strains at the overburden vertical stress. This approach was also adopted by Terzaghi et al (1996), who introduced the term SQD (Specimen Quality Designation), with sample quality ranging from A (best) to E (worst), corresponding to ε_{v0} of 1% and 12%, respectively. More recently, Tanaka et al. (2002) concluded that this parameter cannot be universally applied for representing sample quality. As noted by Hight (2000), the absolute value of the strains will depend on the reconsolidation path followed and the soil compressibility.

An alternative method was developed by Lunne et al. (1997), who proposed the use of volume strains in terms of $\Delta e/e_0$, where Δe is the change in void ratio and e_0 the initial void ratio. Their criteria were based on tests results on marine clays covering a wide range of plasticity indices, overconsolidation ratios and water contents, from which the following categories of sample quality (in Table 8.1) have been defined.

Table 8.1 - Criteria for the assessment of sampling quality from volumetric strains (from Lunne *et al.*, 1997)

	$\Delta e/e_0$	OCR	
		1-2	2-4
Quality [*]	Very good to excellent	< 0.04	< 0.03
	Good to fair	0.04 - 0.07	0.03 - 0.05
	Poor	0.07 - 0.14	> 0.14
	Very poor	0.05-0.10	> 0.10

[*] this description refers to the use of the soil sample for characterization of the mechanical properties

This method was applied to a number of samples from this experimental testing programme, namely to various tube and block samples from ES1, where a greater variety of tube samplers were used. The obtained results in terms of $\Delta e/e_0$ are summarised in Table 8.2.

Despite the clear differences between the various samples collected in ES1, the values of $\Delta e/e_0$ obtained in this exercise were all below the minimum proposed value of 0.04, except for one of the reconstituted samples, which are obviously not included in the

evaluation of sample quality. From this exercise, it can be concluded that this method is not appropriate for assessing the sampling quality in this material, since it would classify all samples as very good to excellent quality samples. Clearly, the relatively low compressibility of this soil compromises the direct application of this method.

Table 8.2 - Example of the application of the method of Lunne et al. (1997) for assessing sample quality, from the initial and reconsolidation void ratios from ES1 samples

Specimen	Type of sample	e_0	e_c	$\Delta e/e_0$
B2.1.70	block	0.803	0.801	0.0025
B2.2.70	block	0.877	0.874	0.0034
S1.2.1	tube	0.647	0.639	0.0124
S1.4.1	tube	0.739	0.729	0.0135
S1.6.3	tube	0.680	0.675	0.0074
S2.2.2	tube	0.668	0.661	0.0105
S2.4.1	tube	0.686	0.674	0.0175
S2.6.1	tube	0.790	0.783	0.0089
S3.2.2	tube	0.674	0.668	0.0089
S3.4.2	tube	0.679	0.671	0.0118
S4.2.1	tube	0.665	0.652	0.0195
S6.2.1	tube	0.715	0.705	0.0140
S6.2.2	tube	0.718	0.713	0.0070
S6.6.1	tube	0.726	0.708	0.0248
B2.0.70*	reconstituted	0.857	0.687	0.1984
S2.2.0*	reconstituted	0.667	0.657	0.0150

* Note: these reconstituted samples are not part of the assessment of sampling quality and have been included exclusively for comparative purposes

In order to establish a more suitable sample quality classification, different limits for each category would have to be defined for this type of soils. This method is however useful for a qualitative and comparative analysis of the tested samples.

8.4.5. Comparison between laboratory and in situ measurements of seismic wave velocities or maximum shear modulus

As largely debated in the previous chapters, the potentialities of shear wave velocities for the characterisation of soil properties and state and stress conditions are remarkable. The sensitivity of the shear waves enables to distinguish different structure or fabric arrangements, as well as stress conditions and void ratio. Thus, the comparison between laboratory and in situ measurements of seismic wave

velocities (or maximum shear modulus) has been increasingly accepted as one of the most promising for the assessment of sampling quality, especially in natural structured soils (Viana da Fonseca and Coutinho, 2008).

For the comparisons to be valid, the laboratory samples must be representative and should be restored to their in situ stress state, because of the dependence of V_S on stress state. In order to account for the influence of void ratio, allowances must be made for changes in void ratio during reconsolidation to in situ stresses (Hight, 2000). Measurements of V_S should also be made with shear wave propagation in the same direction as in the field, with the same plane of polarisation (see the directions of propagation and polarisation associated with the most common geophysical methods in Chapter 2). For this reason, vertically propagated shear waves (V_{SVH}), as typically measured in standard triaxial setups, should be preferably compared with Down-Hole results, as schematically illustrated in Figure 8.11.

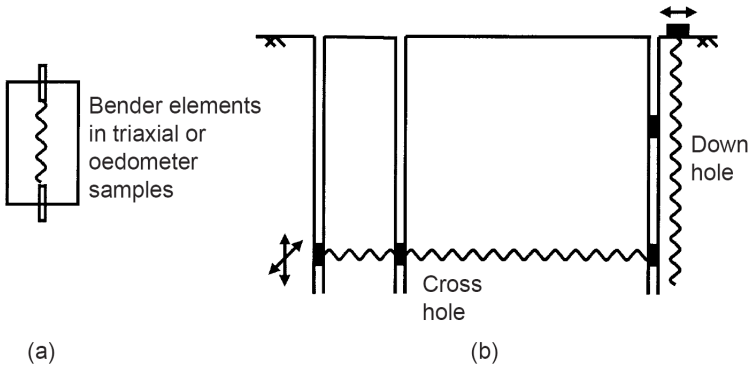


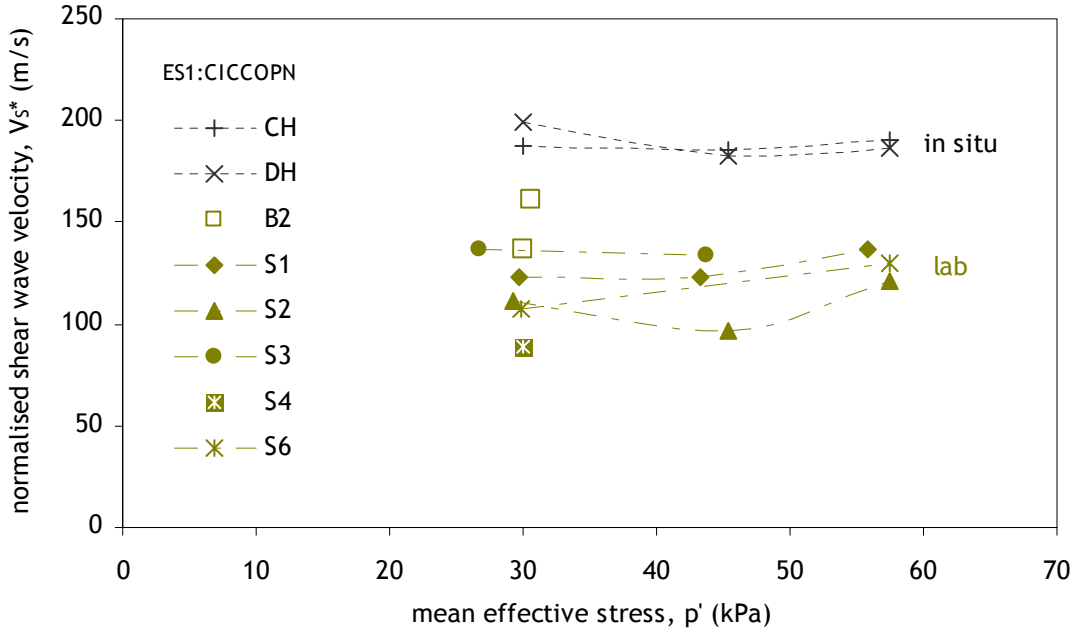
Figure 8.11 - Measurement of G_0 from shear wave velocities in: a) laboratory tests; b) in situ tests (Atkinson, 2000)

The results obtained for the tested specimens of both experimental sites studied in this work, at the estimated in situ stresses, are presented in the following figures. For a more consistent comparison, the shear wave velocities were normalised to the respective void ratio. The normalisation of the in situ values was made considering the void ratio of the block samples. For the ES1 samples, shown in Figure 8.12, only V_{Svh} were measured. In this study, the differences between V_{SHV} (from cross-hole tests) and V_{SVH} (from down-hole) will not be considered.

The similarity of V_S trends in depth from both in situ and laboratory tests is evident and the differences encountered can be mainly attributed to disturbances associated with the sampling processes.

In terms of the tube samples (S1 to S6), the results show that the geometric characteristics of the sampler (introduced in Chapter 6) were determinant, both in

terms of the cutting edge angle as well as of the area ratio. The sampler with the lowest outside cutting edge angle (S3) provided the highest stiffnesses. The good performance of the Shelby sampler (S6) is worth mentioning, which is most likely associated to the difference between the internal diameter of the sampling tube and the final diameter of the tested specimens, requiring the trimming of the sample to the appropriate size, after its extrusion from the sampler. This process, despite being quite delicate, enables to eliminate the peripheral areas of the sample which have experienced greater distortions during both sampling and extrusion, pointing out to the relevance of careful laboratory sample preparation techniques.



Note: samples from B2- Block; S1- GMPV; S2- ST85; S3- NT81; S4- MAZIER; S6- SHELBY
Figure 8.12 - Normalized shear wave velocities for ES1 specimens

Finally, samples collected by the Mazier sampler are unexpectedly damaged. Its disturbance is probably related with the operational requirement of applying high water injection pressures at the cutting shoe, in order to reduce the friction and abrasion between the cutting tools and the coarse quartz grains of the soil. The injected water literally washes away the fragile bonds between the particles, severely damaging the natural structure of the soil. Ageing may also explain why the in situ shear wave velocities differ from that of same soil in laboratory with the same state of effective stress and void ratio, as well as between laboratory samples tested in different occasions.

For the second experimental site (ES2), only one tube sampler was used for collecting all the samples: the same tube sampler used for borehole S3 in ES1, that is, NT81.

This tube sampler was selected for its good performance in terms of sampling quality of the residual soil from ES1. In this case, a fewer number of samples was tested at the estimated in-situ stresses, as presented in Figure 8.13.

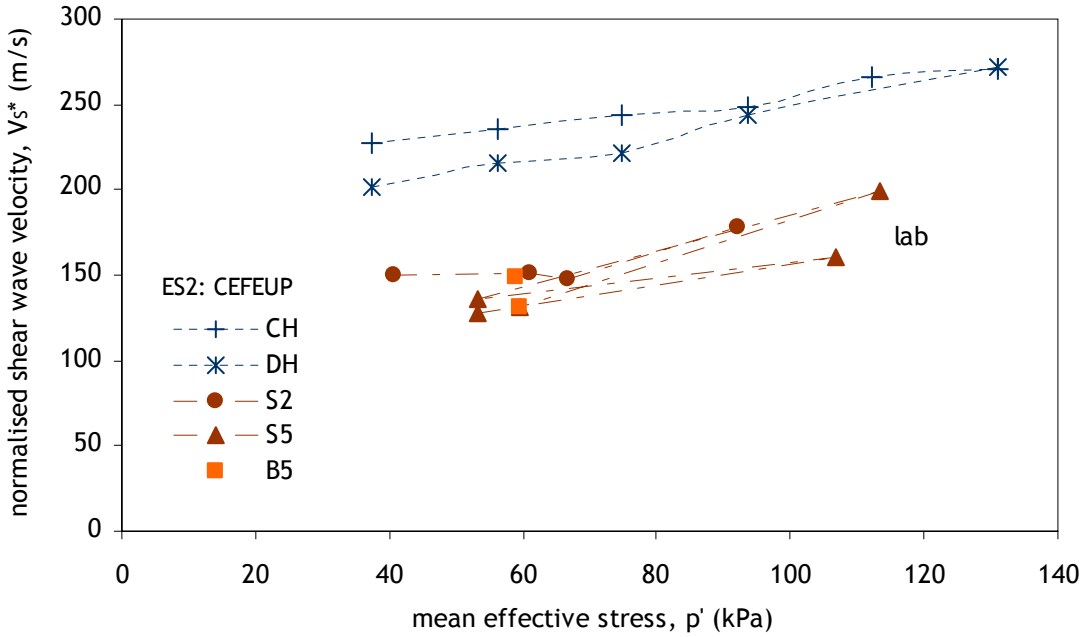


Figure 8.13 - Normalized shear wave velocities for ES2 specimens

The figure shows that the differences between the shear wave velocities of different samples are smaller than those observed for the samples of ES1. This was anticipated since all samples were collected by the same sampler. The evolution of the laboratory and in situ velocities with stress, that is, with depth, is relatively similar, and it is unclear whether sample disturbance is affected (or not) by the depth of sampling.

Contrary to the results for ES1 samples, in this case, the block samples appear to have the same loss in shear wave velocity in relation to the in situ value as the tube samples. This would mean that those blocks have the same level of disturbance, which is unlikely. A more plausible explanation for the unexpectedly lower values of the block sample results may reside on the fact that the two block samples were tested much later than the tube samples. Ageing during storage is an influential parameter in the shear stiffness of a soil, which however was not explicitly and systematically addressed in the context of this research.

The combination of the results from both experimental sites can be made by plotting the laboratory V_S values against the corresponding in situ values (for the same depth, or mean effective stress), as shown in Figure 8.14. Perfect agreement of laboratory

and field results would fall on the 1:1 line; below this line, the points indicate that laboratory values are lower than in situ values.

As would be expected, all points appear below the 1:1 line. The slope of the line connecting each point (or the best fit line for a group of points from the same borehole) to zero provides an indication of the loss of shear wave velocity in relation to the field, which can be considered a measure of the sample disturbance. The obtained results are summarised in Table 8.3.

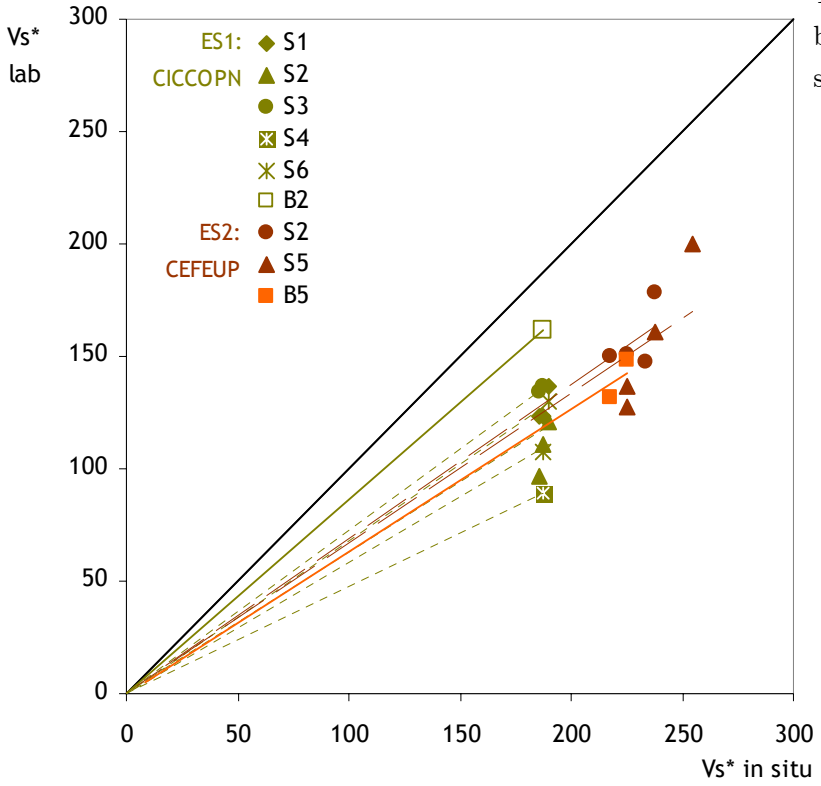


Figure 8.14 - Normalized shear wave velocities for all tested specimens

Table 8.3 - Differences between V_s* measured in situ and in the laboratory

Sample		% loss
ES1	S1	32%
	S2	42%
	S3	28%
	S4	52%
	S6	37%
	B2	14%
ES2	S2	32%
	S5	33%
	B5	37%

The percentages of loss indicated in the table refer to shear wave velocity, but could also be associated with stiffness or natural structure. The conclusions are similar to what was already commented in the analysis of each experimental site, but from this plot, it is possible to define different categories of sample quality (or sample disturbance). The least disturbed sample was block sample B2 from ES1, with 14% of loss. Considering the stages of a sample from sampling to storage to preparation to laboratory testing, shear velocity losses below 15% appear to be minimal and therefore acceptable as an indicative of an excellent quality sample. A gradual scale can be then empirically and experimentally established: below 30% for a very good quality sample; below 40% for a good sample; below 50% for a fair quality sample.

Above 50% of V_S loss, the quality of the sample is poor and the sample should be considered disturbed, thus inappropriate for careful laboratory testing.

From these results, a classification of sampling quality (or sample condition) based on the comparison of normalised shear wave velocities in the field and in the laboratory is proposed, as indicated in Figure 8.15 and Table 8.4. In this figure, the result obtained for a laboratory reconstituted specimen (R2), consolidated to the same in situ stresses as all corresponding samples from ES1 is also presented.

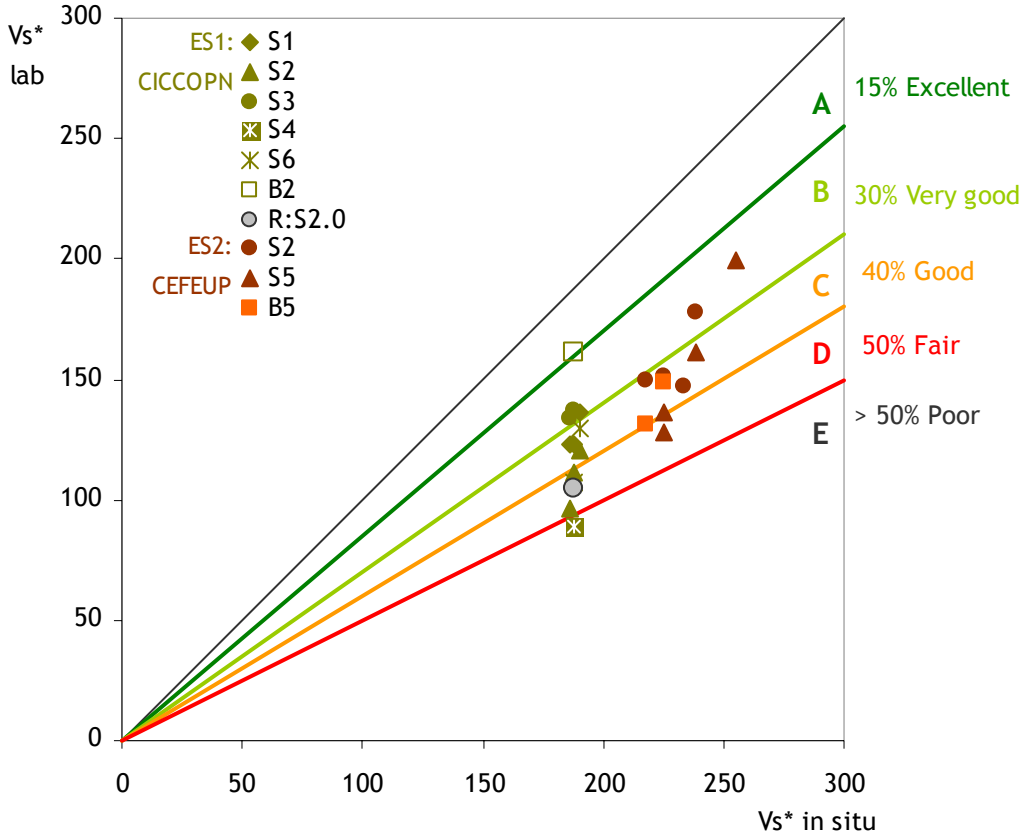


Figure 8.15 - Proposed classification of sampling quality based on the comparison of normalised shear wave velocities in the field and in the laboratory

Table 8.4 - Proposed classification of sampling quality and sample condition based on the comparison of normalised shear wave velocities in the field and in the laboratory

Quality zone	% loss in V_S*	$V_S*_{lab}/V_S*_{in\ situ}$	Sample quality	Sample condition
A	≤ 15%	≤ 0.85	Excellent	Perfect
B	15% - 30%	0.85 - 0.70	Very good	Undisturbed
C	30% - 40%	0.70 - 0.60	Good	Fairly undisturbed
D	40% - 50%	0.60 - 0.50	Fair	Fairly disturbed
E	> 50%	> 0.50	Poor	Disturbed

It is worth noting the position of the reconstituted sample, located at quality zone D, therefore not corresponding to the lowest shear wave velocity value. Two tube samples (from S2 and S4) appear below the reconstituted sample, which is indicative of their poor quality, thus enabling to confirm the proposed limits of this classification.

There is some parallelism between this new classification and that proposed by Landon et al. (2007) based upon tests on Boston blue clay. In their research, these authors compared laboratory and in situ shear wave velocities and used the reconsolidation strains method by Lunne et al. (1997) to define the categories of sample quality. However, their classification is less restrictive than the one proposed in Table 8.4: the ratio $V_{lab}/V_{in\ situ}$ from 0.6 to 0.8 corresponded to good to excellent quality samples; poor quality samples had a ratio of 0.35-0.6 and very poor quality samples exhibit values of $V_{lab}/V_{in\ situ}$ lower than 0.35.

Finally, it is interesting to plot the shear wave velocities measured in different directions (besides V_{Svh}, also V_{Shh} and V_{Shv} were measured) on true triaxial and cubical cell tests. Only three tests were carried out considering an anisotropic stress-path approximately at the in situ stresses and therefore comparable with the in situ data: B5-TT on the true triaxial; and, B6-RS1 and B4-RS3 on the cubical cell apparatus.

Since the block samples are considered to be the most representative and less disturbed samples, their void ratios can be assumed indicative of those in the field. For this reason, the normalisation of the shear wave velocities is unnecessary. The obtained results are presented in Figure 8.16.

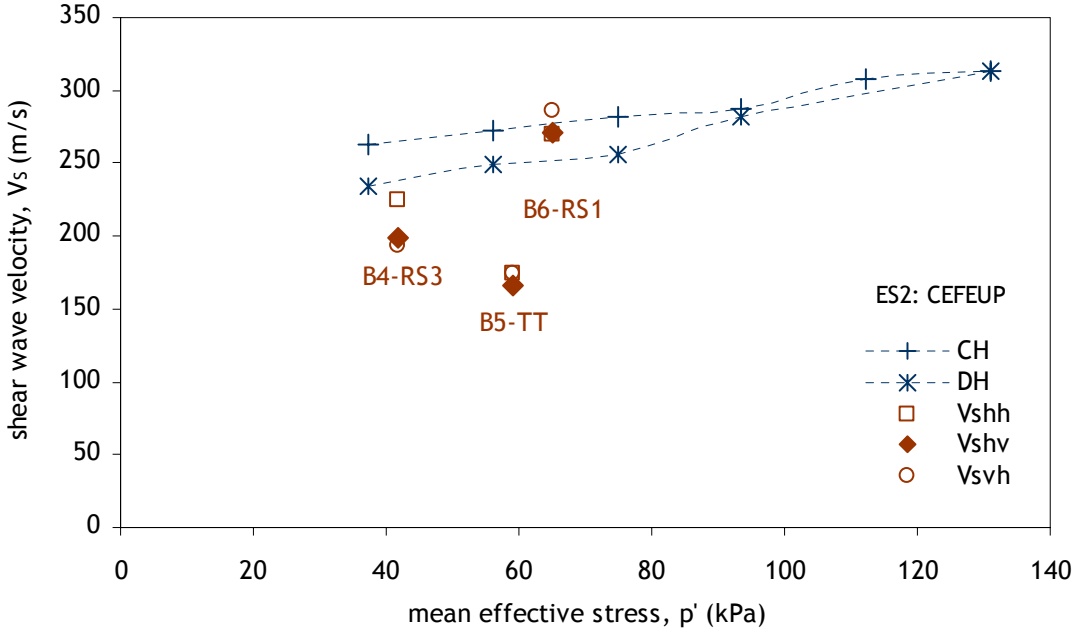


Figure 8.16 - Shear wave velocities for ES2 block samples tested in true triaxial conditions

The results in the figure are rather unexpected. Both block samples tested in the CC apparatus (B4-RS3 and B6-RS1) provided V_S values near or above the in situ values, and the relative positions of the directional velocities are also different between them, or in relation to the in situ results. On the other hand, the sample tested in the TT exhibited considerably lower velocities, closer to those measured in standard triaxial conditions. The reasons for such high laboratory V_S in the cubical cell are unclear.

8.5. Other applications of seismic wave measurements

8.5.1. Assessment of structure

The differences in the behaviour of natural and reconstituted soils are well recognised and the term 'structure' has been used to refer to the distinctive fabric and bonding that characterise intact natural soils (Burland, 1990; Leroueil and Vaughan, 1990, Nash et al., 2006). The expression 'microstructure' has also been used to refer to both the arrangement of the soil particles (microfabric) and the bonding between them (Burland et al., 1996). As discussed in the previous section, sampling disturbance causes changes to the microstructure of the soil that cannot be completely reversed after the application of the estimated in-situ effective stresses.

The small strain shear modulus G_0 fundamentally depends on the following factors (Jamiolkowski et al. 1995, Nash et al., 2006):

- the soil structure and fabric resulting from deposition, ageing processes and strain history
- the soil state described by a combination of stresses and void ratio

The expression for the dependency of the shear modulus with these factors can be written as:

$$G_{0ij} = S_{ij} \cdot F(e) \cdot (\sigma'_i)^{n_i} \cdot (\sigma'_j)^{n_j} \quad [8.3]$$

or

$$G_{0ij} = S_{ijo} \cdot F(e) \cdot p'^{n} \quad [8.4]$$

The structure of a soil, as defined by the structural term S_{ij}, can be examined using the shear stiffness normalisation to the void ratio function, as suggested by Jamiolkowski et al. (1995). The expected relationships between void ratio, G_0 and effective stress can be schematically represented by an idealised structural framework, presented in Figure 8.17, defined for a natural structured clay, but generically applicable to most structured soils (Nash et al., 2006, Sukolrat, 2007).

As shown in the figure, the state of the natural soil is located above the non-structured state for the same initial effective stress (point A), with higher shear stiffness than that of the non-structured soil. The shear stiffnesses tend to converge when the natural sample is loaded beyond its yield stress (point B) as a consequence of destructuration. The non-structured sample when subjected to unloading to the initial stress state (point A_2), exhibits higher shear stiffness. This increase is related with the reduction of void ratio, and, with appropriate void ratio normalisation, a unique curve is obtained, reflecting a constant structural term S_{ij}. As suggested by Sukolrat (2007), if the same void ratio function obtained from the non-structured material is used to normalise the shear stiffness of natural soil, the degradation of its structure can be examined.

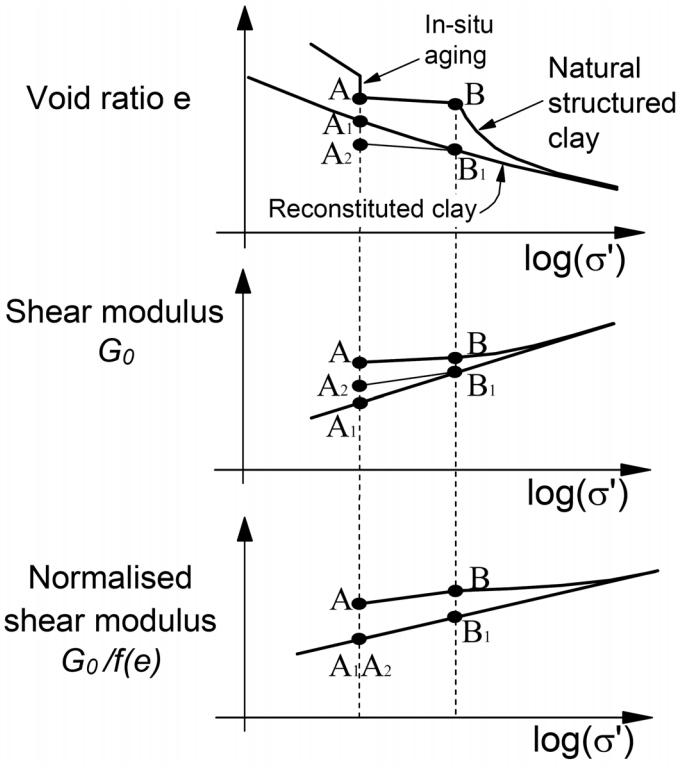


Figure 8.17 - Structural framework for a natural clay (Nash et al., 2006)

This concept has been implicit in many of the results presented, as well as in the analyses and discussions. The aim of its separate analysis in this section is to summarise the obtained results in terms of the structure of the tested samples, which is closely connected to the assessment of sampling quality.

For the illustration of the capabilities of shear wave velocities in the assessment of the structure of the residual soil in study, the results from the tests on undisturbed and reconstituted specimens of ES2 (CEFEUP) were selected, as presented in Figure 8.18. The reason for selecting these test results is related with the fact that the samples were collecting either with the same tube sampler or trimmed from a block. This means that the effect of sampling method is less influential to the analysis and enables to focus the attention to the comparison and distinction between undisturbed and reconstituted/remoulded specimens.

The parameters of the dependency of the normalised shear stiffness with the product of the effective stresses ($\sigma'_v.\sigma'_h$) are summarised in Table 8.5.

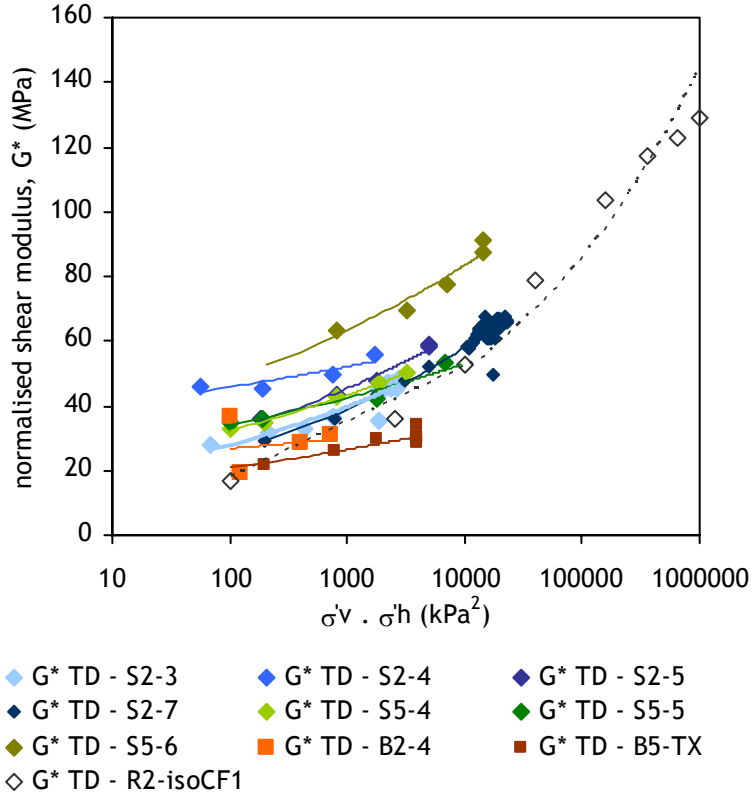


Table 8.5 - Parameters of the shear stiffness dependency with stress ($\sigma'_v.\sigma'_h$)

	(from Eq. 8.3)	
	S_{ij}	$n_i=n_j$
R2-isoCF1	6299	0.23
B2-4-TX	21617	0.05
B5-TX	12987	0.10
S2-3	13850	0.15
S2-4	35255	0.06
S2-5	16313	0.15
S2-7	11586	0.18
S5-4	18023	0.13
S5-5	21699	0.10
S5-6	27709	0.12

Figure 8.18 - Assessment of structure, from the normalised G_0 as a function of the effective stresses for undisturbed and reconstituted specimens

The results in the figure appear to be rather mixed, in the sense that the reconstituted specimen has higher shear stiffness than some of the natural samples, especially at increasing stress levels. The interpretation is facilitated with the analysis of the summary of the dependency parameters in Table 8.5.

The structure of this soil can not be exclusively analysed by the parameter S_{ij} but should also integrate the exponent n. A more structured material should exhibit higher values of S and, simultaneously, lower values of n.

The reconstituted material exhibits the lowest structure term S_{ij} associated with the highest stress exponent. This can be interpreted as its initial condition is nearly unstructured and that it is strongly dependent of the applied stresses, hence the high value of n. There is not a clear distinction between the tube and the block samples, which would be unexpected if the block samples had not been tested at a much later time. Long-term effects were not considered in this research as influential to the measurement of stiffness, but in the light of these results, time appears to play a relevant role. The significant reduction of the natural structure of the block samples is likely related with storage time.

Given the similar response of tube and block samples, the comparison with the reconstituted material includes both types of undisturbed samples. The natural structure of this soil appears to be only slightly dependent of the applied stresses, as demonstrated from the low values of the exponent ranging from about 0.05 to 0.18. The values of the structural parameter are quite varied, but the lowest is about twice the corresponding value of the reconstituted material.

This exercise serves to demonstrate the potentialities of shear wave measurements in the direct detection of natural structure and in the comparison between samples of different origins, namely between undisturbed and reconstituted conditions.

8.5.2. Assessment of anisotropy

Soil stiffness anisotropy plays a significant role in many geotechnical problems, as recognised by many researchers (Bjerrum, 1973; Jardine, 1994; Hight, 1998; Kuwano et al., 2000). Due to anisotropy, the strength and deformation characteristics of the residual soils are dependent of the shearing loading direction.

Casagrande and Carrillo (1944) were the first to suggest a distinction between two components of soil anisotropy: "inherent" and "induced" anisotropy (Arroyo, 2002; Reis et al., 2003). Inherent anisotropy is caused by the arrangement of the soil fabric and related with a preferred particle orientation of the soil originated during the formation process of the deposit. These authors defined this component of anisotropy as a physical characteristic inherent to the material and entirely independent of the applied stresses and strains.

On the other hand, induced anisotropy is a direct consequence of the stress states which the soil has been subjected to, which cause a directional redistribution of particle contacts. Induced anisotropy can then be defined as a physical characteristic caused by the strain associated with the applied stresses and strains (Casagrande and Carrilo, 1944). Ladd (1991) also discussed anisotropy as related to an inherent and an initial component. The first component is caused by the initial one-dimensional deposition and K_0 consolidation, and the second component exists prior to the application of stresses.
In most field situations, the soil has been subjected to complex stress histories due to geological and other processes, from which a combination of inherent and induced anisotropy can be expected.

The definition of the anisotropic elasticity parameters requires the determination of the relationships between the six stress components and the six strain components, in a total of 36 components. Due to the equivalence of some of these components, the number of determinations can be reduced to 21 components (Love, 1927). Different formulations have been proposed to describe these parameters (Graham and Houlsby, 1983, Muir Wood, 1990, Lings, 2001). As pointed out by Lings (2001), the most appropriate form of anisotropy to describe soils with a one-dimensional strain history is cross-anisotropy. Five independent elastic parameters are required, usually chosen to be two Young's moduli, E_v and E_h, two Poisson's ratios, ν_{vh} and ν_{hh} and a shear modulus, G_{vh} (= G_{hv}). For the geomaterials tested in this research, the hypothesis of cross-anisotropy was assumed throughout, even for the tests in true triaxial conditions.

As reported by Ng et al. (2004), field seismic measurements have revealed inherent anisotropy in the stiffness of natural soils (Sully and Campanella, 1995; Hight et al., 1997; Stokoe and Santamarina, 2000). The use of seismic wave velocities for laboratory investigation of shear stiffness of soils has also shown various degrees of anisotropy because of inherent anisotropy, stress-induced anisotropy, or both (Thomann and Hryciw, 1990; Stokoe et al., 1994; Pennington et al., 1997; Pennington, 1999; Fioravante, 2000; Kuwano et al., 2000).

The assessment of stiffness anisotropy by means of the shear wave velocities has already been suggested and briefly analysed in the previous chapter. Direct measurements of shear wave velocities propagated and/or polarised in different directions enabled to identify distinct stiffnesses in the corresponding directions, from which the level of anisotropy can be determined. However, these measurements were only carried out on a limited amount of samples, thus the analysis of anisotropy of this residual soil is only preliminary.

Following the proposal of Graham and Houslby (1983), also adopted by Pennington (1999) and Sukolrat (2007), the assessment of anisotropy was made by means of the anisotropy ratio, α, which reflects the relationship between the horizontal and vertical shear moduli:

$$\alpha_{G_0} = \frac{G_{0hh}}{G_{0vh}} \qquad [8.5]$$

The results obtained in terms of the shear stiffness anisotropy ratios of the reconstituted specimens, measured in true triaxial conditions, are summarised in Table 8.6.

Table 8.6 - Anisotropy ratios for reconstituted specimens

Specimens	Type of test	hh/hvX	hh/hvY	hh/vhZ1	hh/vhZ2	hv/vhZ1	hv/vhZ2
R2W-TT	TT (iso)	1.06	---	0.99	0.97	0.91	---
R4D-TT	TT (K)	0.80	0.81	0.58	0.61	0.73	---
R8D-TT	TT (iso)	1.20	1.31	1.20	1.22	1.02	0.94

The anisotropy ratios obtained for the reconstituted specimens are relatively different. Sample R2W-TT was tested in isotropic conditions and the observed anisotropy was very small, suggesting a nearly isotropic behaviour. Since there was no further stress-induced anisotropy, this sample can be considered inherently isotropic. This result confirms that the preparation of reconstituted specimens at high water content enables to produce a fairly isotropic sample.

On the other hand, sample R8D-TT was also tested in isotropic conditions but the results suggest a certain level of anisotropy. By comparison with sample R2W-TT, the main reason for this anisotropy may reside on its preparation, which was carried out in dry conditions. The sample preparation procedure consisted of deposition of the soil and gentle tamping, which apparently was sufficient to induce an unforeseen degree of 'inherent' anisotropy.

Sample R4D was prepared in the same manner as R8D, so its response in isotropic conditions can be assumed to be identical. However, this sample was tested under anisotropic conditions, at an imposed zero-horizontal deformation, and the obtained shear stiffness ratios clearly appears to be affected by these stress conditions. The difference between the ratios of the two stress states, from 1.20 in isotropic conditions to 0.80 under K_0 loading, provide an indication regarding the stress-induced anisotropy of this specimen.

Similar analyses can be made from the shear stiffness anisotropy ratio obtained on the undisturbed specimens, mostly tested under true triaxial conditions, as provided in Table 8.7.

Table 8.7 - Anisotropy ratios for undisturbed specimens

Specimens	Type of test	hh/hvX	hh/hvY	hh/vhZ1	hh/vhZ2	hv/vhZ1	hv/vhZ2
B5-isoSP	TX (iso)	1.17	---	---	---	1.02	---
B4-TT	TT (K)	1.19	1.08	---	---	---	---
B5-TT	TT (K_0)	0.91	1.24	---	---	---	---
B6-RS1	CC (3D)	0.71	0.95	0.71	1.21	1.01	1.21
B6-RS2	CC (iso)	0.94	1.15	1.01	1.27	1.08	1.12
B4-RS3 *	CC (K_0)	*1.36*	*1.88*	*0.91*	*1.47*	*0.68*	*0.81*

[*] the results of this sample are not representative, due to the visible heterogeneity of the sample (as detailed in Chapter 7)

The stiffness anisotropy ratios obtained for the undisturbed samples are also diverse, and can be related with the stress-path followed in each test. Of the two isotropic tests where sufficient directional shear waves were measured, one was carried in the standard triaxial and another in the cubical cell. The results indicate a small level of natural inherent anisotropy. If compared with the reconstituted specimens, it appears that the natural structure may be responsible for approximately 15% of the anisotropy of natural undisturbed samples.

The samples tested under anisotropic K_0 or three-dimensional stress conditions generally exhibit lower anisotropy ratios, which are in agreement with the lower horizontal stress applied. The exception is sample B4-TT where higher stiffness ratios were obtained.

Finally, the results of sample B4-RS3 indicate a considerably high level of anisotropy, which can be largely attributed to the discontinuity of the sample in an approximately vertical plane, as shown in Figure 7.60, and discussed in the previous chapter.

These results and analysis serve to demonstrate the capabilities of the shear wave velocities to the assessment and identification of anisotropy in reconstituted and undisturbed soil specimens. For this purpose, it is necessary to have not only top and bottom (vertically-propagated) shear wave measurements, but also horizontally-propagated wave measurements.

8.5.3. Evaluation of porosity

A technique to derive soil porosity from seismic wave measurements has been proposed, triggered by the difficulty of obtaining adequate samples for porosity estimate in many fragile and granular soils (Foti et al., 2002; Foti and Lancellotta,

2004). With this purpose in mind, most of the supporting evidence presented by those authors related to dynamic field measurements and the technique used the Biot poroelastic model to invert the wave velocity measurements. More specifically, porosity was deduced from cross-hole measurements with independent laboratory determinations on a group of samples. The agreement thus obtained between the directly measured and the inferred porosity value was generally very good, thus proving the attractiveness of the proposed technique (Arroyo et al., 2006).

In this context, the potential of the porosity dynamic measurement technique in laboratory saturated triaxial conditions was explored, using the results obtained in this research work. While the advantage of obtaining estimates of porosity in the field is clear, it may also be beneficial in laboratory testing, as it can provide an alternative measure of full saturation and of volume change in saturated conditions.

Additionally, this technique can be employed in a different way: instead of using seismic measurements to obtain porosity, the independently measured porosity may be employed to check the coherence of the measured velocities and/or to improve the means of interpreting the seismic test results (Arroyo et al., 2006).

The poroelastic Biot model results in dispersive wave propagation, i.e. wave velocities that are generally dependent on frequency (see, for instance, Miura et al., 2001). This dependency is negligible below a certain frequency range. The upper limit of the frequency range is given by the characteristic frequency (Foti et al. 2002):

$$f_c = \frac{n \cdot g}{2\pi \cdot k} \qquad [8.6]$$

where f_c is the characteristic frequency in Hz, g is 9.81 m/s^2, n is the porosity and k is the permeability of the soil.

For the residual soil in study, the characteristic frequency of natural samples is slightly above 60 kHz, whereas for the reconstituted samples it can reach 6 MHz. Consequently, some of the P-wave measurements on undisturbed samples may have been taken close to this limit.

Under the assumption of a very high bulk modulus of the soil particles, Foti et al.(2002), derived the following formula:

$$n = \frac{\rho^S - \sqrt{(\rho^S)^2 - \dfrac{4(\rho^S - \rho^F)K^F}{V_P{}^2 - 2\left(\dfrac{1-\nu^{SK}}{1-2\nu^{SK}}\right)V_S{}^2}}}{2(\rho^S - \rho^F)} \qquad [8.7]$$

where porosity, n, is defined as a function of the shear and compression wave velocities, V_S and V_P, and of the mass density of the soil particles and of the fluid, ρ^S and ρ^F, the fluid bulk modulus, K^F, and the Poisson's ratio of the soil skeleton, ν^{SK}.

The previous equation can be easily inverted to give the shear velocity as:

$$V_S = \sqrt{\frac{\left(1-2\nu^{SK}\right)}{2\left(1-\nu^{SK}\right)} \cdot \left(V_P^2 - \frac{K^F}{n^2\left(\rho^F - \rho^S\right) + n\rho^S}\right)} \qquad [8.8]$$

It is also interesting to appreciate that a lower bound of the compressive wave velocity, neglecting the skeleton soil stiffness, is given by

$$V_P \geq V_F \sqrt{\frac{1}{n^2 + n(1-n)\dfrac{\rho^S}{\rho^F}}} \qquad [8.9]$$

V_F is the value of the velocity of sound in the saturating fluid. The fluid is water and its velocity, V_F, at 20 ° C is 1483.7 m/s (Marczak, 1997). This is equivalent to a bulk modulus of $K^F = 2.2\text{x}10^6$ kPa.

The measured and estimated values of the seismic wave velocities using Equations 8.7 and 8.8 are discussed in detail in Arroyo et al. (2006), in parallel with a similar analysis for Bothkennar clay. These authors conclude that, by means of simple poroelastic formulae, it is possible to check the measured wave velocities using the conventionally measured porosity.

Considering a Poisson's ratio of 0.30, a few samples from ES1 were selected, where a considerable number of V_S and V_P measurements had been made after full saturation, during the shearing stage. The porosity estimated from Equation 8.7 was then compared with the measured porosity, as illustrated in Figure 8.19.

The results in the figure evidence a generally good agreement between the measured and the estimated values of porosity. The conclusions to be drawn are threefold: the proposed technique for measuring porosity is applicable to laboratory seismic wave

measurements in this material; and, the measured shear and compression waves were relatively well determined, considering the convergence of results.

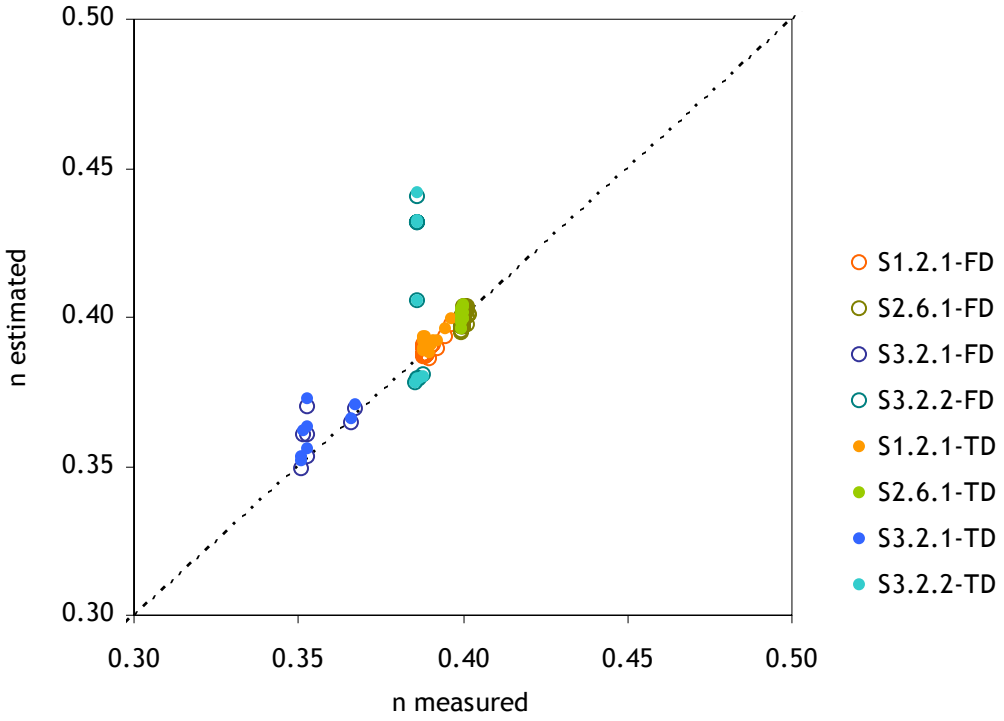


Figure 8.19 - Comparison of estimated and measured porosity

Although not explicit in the figure, this process of computation of porosity enables to detect any conditions of incomplete saturation, in which circumstances the value of porosity cannot be extracted as it results in an error.

This evaluation of porosity was carried out as an experiment of the novel technique and thus it was not systematically applied to all tests. However, the obtained results enable to conclude that this calculation of porosity can be directly and successfully applied to this material.

8.6. Other correlations between laboratory and in situ tests

The comparison between stiffness moduli is most relevant, in order to provide adequate geotechnical design parameters, namely for serviceability conditions. As stated by several authors and summarised by Tatsuoka et al. (1997), field loading

tests are preferred in the cases where sample disturbance may negatively affect the laboratory test results. Different approach levels have been proposed (Tani, 1995; Viana da Fonseca et al., 2003), which include:

- definition of design parameters through empirical relationships with index properties; for example, the empirical use of penetration tests (SPT or CPT) and even intrusive dilatometers (such as DMT) for deriving Young's modulus;
- definition of an average stiffness deduced by linear analysis, dependent on the involved characteristic axial and shear strains; these strains are obviously different in pressuremeter tests, PMT and plate loading tests, PLT;
- non-linear stress-strain relationship, interpreted from a non-linear analysis of the test results, considering an initial stiffness value determined by seismic tests.

Considering the variety of tests carried out in ES1 for the characterisation of stiffness, the following analyses were made in order to position the different experimental methods for evaluation of the stiffness moduli, in relation to the specific ranges of stress-strain levels. These analyses are a result of the work of Vieira de Sousa (2002) and Viana da Fonseca et al. (2003).

The laboratory tests over undisturbed samples had the purpose of characterising the constitutive model of this soil, as well as the measurement of seismic wave velocities in triaxial specimens, reconsolidated to the at-rest stress state conditions. The stiffness values obtained in BE tests followed the trend of the in situ CH and DH tests, as previously presented. From the results, it can be concluded that:

- the elastic stiffness moduli are almost constant with the confinement stress, both the seismic-derived values and those determined by local instrumentation in small unload-reload cycles, following the pattern of V_S (CH/DH) with depth;
- the Young's modulus derived from the initial tangent slope, inferred from an hyperbolic approach, increases with confinement stress (thus, with depth); this is also true in the unload-reload modulus, on intermediate cycles, and should be addressed with care, when compared to true elastic values (above); this higher dependence with the confinement stress converges to the observed increase of PMT modulus

in depth; E_{pm} is clearly an elasto-plastic modulus, therefore closer to the concept of a secant modulus to intermediate strain levels.

Table 8.8 summarizes some representative values deduced from triaxial tests over high quality samples. The values of E_{el}, E_{ur} and E_{ti} are quite sensitive to data adjustments and should be considered less reliable. The trend is however clear: there is a marked sensitivity to the adopted range of stress-strain for the calculation of the stiffness moduli.

Table 8.8 - Stiffness (Young's) moduli E deduced in triaxial tests on undisturbed samples

Depth	$E_{0(BE)}$	E_{el}	E_{ur}	E_{ti}
2.0	134.11	80.07	65.48	41.48
4.0	117.11	103.29	78.17	53.77
6.0	113.08	123.74	88.65	64.64

[E values in MPa]

E_0: "elastic" (derived from BE shear wave velocities)

E_{el}: "pseudo-elastic", from the initially linear reload branch of an intermediate unload-reload cycle;

E_{ur}: "unload-reload", between vertices of the cycle;

E_{ti}: hyperbolic tangent modulus, from the small strain range

Ratios between distinct values of stiffness moduli inferred from in situ and laboratory tests have the interest of fulfilling the needs of geotechnical designers to use data from different origins for each specific purpose, mainly in accordance with the different strain levels involved. From the available data from this experimental site, some interesting correlations can be made, including ratios between stiffness moduli obtained at different strain levels in the field (Table 8.9); ratios between SPT or CPT parameters and Young's modulus (Table 8.10); and values of directly-determined Young's modulus at different strain levels in the laboratory (Table 8.11).

Some remarks should be made with regard to the stiffness moduli taken from in situ tests, with loading actions. It is recognized that the Menard pressuremeter measures an "equivalent" modulus E_{pm}, which clearly stands in the range of medium to large strains, around 1% of average strain (Gambin et al., 2002). This modulus is, in fact, a tangent value, as it is determined between two stress stages.

On the other hand, plate loading tests are usually interpreted in order to define a secant modulus. Recent models, based on the parameter of these PLT tests, have shown that the strain levels of the modulus taken from unload-reload cycles are in

the range of about 0.1%, though there is not a sound validation of this value, which results from cumulative data.

Table 8.9 - Ratios between Young's moduli from in situ tests

$\frac{E_0(CH)}{E_{s1\%}(PLT)}$	$\frac{E_0(CH)}{E_{ur}(PLT)}$	$\frac{E_0(CH)}{E_{pm}(PMT)}$
≅ 8 - 15	≅ 2 - 3	≅ 20 - 30

Table 8.10 - Average ratios between Young's modulus and in situ tests

$\frac{E_0(CH)}{N_{60}(SPT)}$	$\frac{E_0(CH)}{q_c(CPT)}$	$\frac{E_0(CH)}{q_d(DPL)}$	$\frac{E_0(CH)}{p_1(PMT)}$
≅ 10	≅ 30	≅ 50	≅ 8 MPa^{-1}

Table 8.11 - Ratios between Young's moduli determined in triaxial tests and in situ CH tests

$\frac{E_0(CH)}{E_0(BE)_{tx}}$	$\frac{E_0(CH)}{E_{el}(LI)_{tx}}$	$\frac{E_0(CH)}{E_{ur}(LI)_{tx}}$	$\frac{E_0(CH)}{E_{ti}(LI)_{tx}}$
≅ 2.0	≅ 2.4	≅ 3.1	≅ 4.5

Triaxial tests (TX): seismic waves velocities determined by bender elements (BE) and modulus in elastic loops (el) or between vertices on unload-reload cycles (ur), and secant to 10% of failure ($s_{10\%}$), using local instrumentation (LI).

From these tables, it is clear that the relative position of each stiffness determination has a considerable influence on the obtained values. These stiffness ratios demonstrate the highly non-linear constitutive response of this soil. The implications of this behaviour can be assumed by the selection of suitable geotechnical design parameters, based on the correlation of results from different in situ testing methods and on the use of appropriate stiffness ratios, according to the available data and the estimated strain levels.

8.7. Key findings

This chapter included the combination of results obtained from different laboratory testing techniques, namely resonant-column and BE measurements, standard triaxial and true triaxial tests, true triaxial and cubical cell tests. Despite the distinct nature and characteristics of the testing equipments used in this research, the comparisons made using identical or comparable soil specimens enabled to assess the performance of the various testing methods used in this research work. Some potentialities and limitations were encountered, namely:

- a interpretation framework combining time and frequency domain BE measurements has been proposed and its application effectively reduced the uncertainty and subjectivity often associated with BE testing; on the other hand, the exclusive use of either method proved to be unreliable;
- the shear strain induced by each BE and RC measurement is different and depends on the method used, which partly explains why the differences between the obtained stiffness moduli are not systematic but variable, according to the shear strain of each RC measurement;
- the comparison between standard triaxial and true triaxial results showed greater differences between TD and FD methods in TX conditions, pointing towards the influence of the sample geometry and boundary conditions to the interpretation of BE results;
- the analysis of true triaxial and cubical cell tests, though limited to a few samples, led to the conclusion that the actual stresses applied in each face of the sample in the TT are lower than the imposed stresses in each platen; this conclusion needs to be verified by a series of parallel tests, possibly using other more repetitive soils.

Some important geotechnical applications were also discussed, mainly derived from the comparison between laboratory and/or in situ test results. The application of shear wave velocities in the assessment of sampling quality was demonstrated. A new classification of sample quality was proposed for this structured soil, from the comparison of the normalised shear wave velocities in the laboratory and in the field, in terms of the ratio $V_S{}^*_{lab}/V_S{}^*_{in\ situ}$ as follows:

- perfect samples correspond to ratios above 0.85;
- undisturbed samples correspond to ratios between 0.70 and 0.85;
- fairly undisturbed samples correspond to ratios between 0.60 and 0.70;
- fairly disturbed samples correspond to ratios between 0.50 and 0.60;

- disturbed samples (not appropriate for subsequent careful laboratory characterisation) correspond to ratios below 0.50

It should be highlighted that, among the commonly used methods for assessing sample quality, this method is the only one capable of effectively considering the effects of destructuration at very low reconsolidation strains, as is the case of this geomaterial.

The application of shear wave velocities to the assessment of structure and anisotropy were also briefly discussed. Due to the large variability in void ratio, these analyses were systematically established in terms of normalised shear wave velocities and stiffnesses, to a pre-defined void ratio function. The assessment of structure is analogous to sampling quality, in the sense that a more structured sample will in general be a less disturbed sample. The results obtained in terms of the evolution of the normalised shear moduli with mean effective stress showed not only an increase of the structure term S_{ij} with increasing structure levels, but also a decrease in the stress exponent, n.

Anisotropy was also addressed, despite the limited number of tests with vertical and horizontal seismic wave measurements. Cross-anisotropy was assumed, since no distinction was made between the two horizontal directions. The analyses of tests under isotropic stress conditions for reconstituted and undisturbed specimens enabled to define the inherent anisotropy of this soil. An estimated value of 1.15 was adopted for the anisotropy ratio of the shear moduli in undisturbed conditions, which corresponds to a low inherent cross-anisotropy. This value is not unexpected, considering the rather homogeneous and isotropic effect of natural structure of this residual soil.

The evaluation of porosity, following the proposal of Foti et al. (2002) and Foti and Lancellotta (2004) for field geophysics, was experimented using laboratory seismic wave data, namely V_P and V_S measured by BE or other piezoelectric transducers. The results obtained from the seismic waves (estimated) and the measured values of porosity during each test were found to be very similar, thus successfully proving the applicability of this technique as an additional tool for the assessment of volume change in laboratory testing. Finally, different stiffness moduli obtained from a variety of laboratory and in situ testing methods were compared, highlighting the non-linear response of this soil. These moduli were translated into ratios, for a more immediate application to the definition of geotechnical design parameters, which should be made in view of the expected strain level.

9.

Conclusions

9.1. Key findings revisited

The use of seismic wave velocities is undoubtedly an optimal method for the measurement of stiffness moduli and for the derivation of a series of relevant soil properties and parameters.

In the laboratory, the most widely-used method for determining V_s is the bender element method. The applications of bender element results are numerous, as detailed in the previous chapters, including:

- definition of the elastic stiffness parameters
- assessment of sampling quality
- assessment of structure
- assessment of anisotropy
- process monitoring, namely consolidation and saturation (using complementary P-wave measurements)
- evaluation of porosity (also with P-waves)
- comparison of dynamically- and statically-determined stiffnesses

While the potential and benefit of bender element testing is clear, the interpretation of its results, unfortunately, is not as straightforward, particularly if only one interpretation method is used. In an attempt to overcome this important limitation, a new interpretation framework combining time and frequency domain BE measurements has been proposed and its application effectively reduced the uncertainty and subjectivity often associated with BE testing.

The interpretation of the BE tests in true triaxial conditions was found to be more complex than in the cubical cell, possibly due to the nature of the boundaries. In the TT tests, the use of the proposed methodology of BE interpretation was mandatory in order to obtain realistic estimates of travel time. Nevertheless, the tests on natural samples provided less data in terms of very small strain stiffness, which may be related with the greater difficulty in ensuring contact between the BE and the soil.

The comparison between resonant-column and BE tests provided new insights on the likely influence of the shear strain induced by the measurement, even at very small strains. This effect of strain in the measurement of G_0 at very low strains has not yet been put forward as a potential reason for the discrepancies between interpretation methods, however it appears to be influential. Under this assumption, it can be said that, in this case and for this particular pair of BE, the shear strain induced by the sweep signal of the FD method is higher than the shear strain caused by the pulse signals used in the TD method. Moreover, the systematic differences, observed here and elsewhere, between TD and FD methods may be explained by the slightly different shear strains at which the BE are excited. These results indicate that the calibration of the BE in relation to the RC is an interesting and constructive exercise, if the associated RC shear strain is taken in due consideration.

The analysis of the results obtained from tests on undisturbed samples from both experimental sites presented similar stiffness response and evolution with stress, thus confirming that the soil of the two sites is similar. The very small strain stiffness results from ES2 were found to be more scattered than those of ES1. The most plausible cause for this discrepancy is related with the different saturation conditions of the two soils, which affect the interpretation of BE tests. An unsaturated sample in a triaxial cell can be assimilated to a reflecting boundary setup, in which case, larger distortions are introduced in the BE output signal.

Seismic wave velocities in soils are influenced by a number of factors, such as the stress state, void ratio, structure, inherent anisotropy, among others, and it is important to be able to isolate each of these factors. The ability to measure wave velocities in different propagation and polarization directions in a general fully-controlled three-dimensional stress state is made possible in true triaxial apparatuses, where the influence of each of the different factors has been investigated. For this purpose, numerous tests were carried out in natural and reconstituted conditions, in diverse states of stress.

Large differences were encountered between the maximum stiffness and those determined at increasing higher strains, especially in the true triaxial tests. These results suggest that the installation of BE in any laboratory testing apparatus is beneficial, in order to obtain more accurate estimates of the maximum stiffness of the tested material, since this is a reference parameter for geotechnical design.

One of the greatest challenges in laboratory testing is the quality and representativity of the available samples. In order to assess the quality of laboratory samples, a number of methods are available, though not universally applicable to any soils. For this purpose, the comparison between in situ and laboratory shear wave velocities was made, where the differences encountered in terms of normalised velocities (to the respective void ratio function) are directly related with sample quality. Based on the database of results from the two experimental sites studied in this research, a new classification of sampling quality was subsequently proposed. It should be highlighted that, among the commonly used methods for assessing sample quality, this method is the only one capable of effectively considering the effects of destructuration in soils with low reconsolidation strains, as in the present case.

9.2. Further work and limitations

In the finishing line of this research work, it is clear that much remains to be investigated and understood. The following thoughts for future developments have risen as the more relevant and urgent.

In terms of the bender element technology and interpretation:

- the definition of a completely automated yet flexible BE interpretation tool for unbiased and reliable measurements

- the use of self-healed measurements by automatic and continuously monitoring the response of the BE; thus would eliminate the problem of unknown transfer functions and minimise errors
- the development of a numerical model simulating the testing conditions of the cubical cell and the true triaxial apparatus, that is, considering the effect of flexible and rigid boundaries; in BE wave propagation, these two conditions can be assimilated to absorbing and reflecting boundaries

In terms of the testing apparatuses and new devices:

- the comparison between cubical cell and true triaxial results using the same geomaterial, preferably a well-known and calibrated soil, for example, Hostun or Toyoura sand; it is still unclear as to what extent does size effects and boundary effects influence the stress-strain response, especially at very small strains

In terms of the enhanced characterization of soils, and of residual soils in particular:

- the comparison between different stress-paths in the Bishop-Wesley stress-path cell and the true triaxial apparatus
- the consideration of time effects, as an additional disturbance
- the analysis of the influence of suction in the stress-strain-stiffness behaviour of these soils

In terms of other geotechnical applications of the testing methods herein employed:

- the assessment of liquefaction potential in cyclic triaxial tests, fully equipped with BE

The limitations encountered in the course of this work are most related with the duration of the tests, especially for the true triaxial tests, mainly due to the amount of compression and shear wave measurements at each loading stage, which sum up to 28 measurements. The volume of data to process and the integration of the results from various measuring devices in the same test were also challenging. Nevertheless, the opportunity to experiment new and complex equipments, to develop new software tools, to contribute to the scientific knowledge and development, largely surmounts any challenges.

Like a child placed before natural phenomena which impress him like a fairy tale...

References

Abbiss, C.P. (1981). Shear wave measurements of the elasticity of the ground. Géotechnique, Vol. 31, No. 1, pp. 721-726.

Adams, J.L. and Radakrishna, H.S. (1971). Loss of strength due to sampling in a glacial lake deposit. Symposium of Sampling of Soil and Rock, ASTM, STP 483, pp.109-120.

Aggour, M.S., Tawfiq, K.S., and Taha, M.R. (1988). Impulse and random testing of soils. Recent advances in ground-motion evaluation. American Society of Civil Engineers, Geotechnical Special Publication No. 20, pp. 346–358.

Airey, D.; Mohsin, A.K.M.; Donohue, S. (2003). Obtaining reliable G_{max} measurements, Proceedings of the Workshop on Current Practices of the Use of Bender Element Technique. Lyon, France.

Airey, D.W.; Muir Wood, D. (1988). The Cambridge true triaxial apparatus. Advanced Triaxial Testing of Soil and Rock, ASTM STP 977, Robert T. Donaghe, Ronald C. Chaney, Marshall L. Silver (eds.). American Society for Testing and Materials, Philadelphia, pp. 796-805.

Ajayi, L. A. and Balogun, L. A. (1988). Penetration testing in tropical lateritic and residual soils - Nigerian experience. Penetration Testing – 1988. (Edited by De Ruiter). Proc. ISOPT-1, Orlando, Vol. 1, pp. 315-328. A. A. Balkema Pub., Rotterdam.

Aki, K., and Richards, P.G. (2002). Quantitative Seismology. Second Edition. University Science Books.

Alarcon-Guzman, A.; Chameau, J.L.; Leonards, G.A. (1986). New apparatus for investigating the stress-strain characteristics of sands. Geotechnical Testing Journal, Vol. 9, No. 4, pp. 204-212.

Alawaji, H., Alawi, M., Ko, H. Y., Sture, S., Peters, J. F. & Muir Wood, D. (1990) Experimental Observations of Anisotropy in some Stress-Controlled Tests on Dry Sand. Yielding, Damage and Failure of Anisotropic Soils, EGF5, Mechanical Engineering Publications, London, 251-264.

Almeida, F., Hermosilha, H., Carvalho, J.M., Viana da Fonseca, A., Moura, R. (2004). ISC'2 experimental site investigation and characterization - Part II: From SH waves high resolution shallow reflection to shallower GPR tests. Geotechnical and Geophysical Site Characterization. Viana da Fonseca and Mayne (Eds). Vol.1, pp. 419-426. Millpress, Rotterdam

Alvarado, G. and Coop, M.R. (2009). On the performance of bender elements in triaxial tests. Submitted to Géotechnique.

Alvarado, G.; Coop, M. R. (2004). Experience of bender element measurements on a variety of materials, Workshop on Bender Element Testing of Soils, University College London.

Amini, F., Tawquif, K.S. and Aggour, M.S. (1988). Cohesionless soil behavior under random noise excitation. Journal of Geotechnical Engineering Division, ASCE, Vol.114, No. 8, pp.896-914.

Ampadu, S.F.; Tatsuoka, F. (1993). A hollow cylinder torsional simple shear apparatus capable of a wide range of shear strain measurement. Geotechnical Testing Journal, Vol. 16, No. 1, pp. 3-17.

Anderson, D.G. and Woods, R.D. (1975) Comparison of field and laboratory shear moduli, Proceedings of the Conference on In Situ Measurement of Soil Properties. Specialty Conference of the Geotechnical Engineering Division, ASCE. North Carolina. Vol.1, pp.69-92.

Andresen, A.; Kolstad, P. (1979). The NGI 54mm samplers for undisturbed sampling of clays and representative sampling for coarser materials. Proceedings of the International Symposium on Soil Sampling. Singapore, pp. 13-21.

Andrus, R.D. and Stokoe, K.H. II (1997). Liquefaction Resistance Based on Shear Wave Velocity. Proceedings, NCEER Workshop on Evaluation of Liquefaction Resistance of Soils, T.Y. Youd and I.M. Idriss, Eds., Buffalo, NY.

AnhDan, L. Q. and Koseki, J. (2003) Anisotropic deformation properties of dense granular soils by large-scale true triaxial tesrts. Proceedings of the 3rd Int. Symposium on Deformation Characteristics of Geomaterials. Di Benedetto et al. (eds), Swets & Zeitlinger, 305-312.

Arroyo, M. (2001). Pulse tests in soil samples, PhD Thesis, University of Bristol, UK.

Arroyo, M., Greening, P., Muir Wood, D. (2003a) An estimate of uncertainty in current pulse test practice. Rivista Italiana di Geotecnica 37, 1, 17-35

Arroyo, M., Muir Wood, D., Greening, P. D., Medina, L. and Rio, J. (2006). Effects of sample size on bender-based axial G_o measurements, Géotechnique 56, No. 1, 39-52.

Arroyo, M.; Greening, P.D. (2002). Phase and amplitude responses associated with the measurement of shear-wave velocity in sand by bender elements: Discussion (paper by Blewett, J.; Blewett, I.J. & Woodward, P.K.). Canadian Geotechnical Journal, Vol. 39, pp. 483-484.

Arroyo, M.; Medina, L. and Muir Wood, D.(2002). Numerical modelling of scale effects in bender-based pulse tests, NUMOG VIII, Pande, G.N. and Pietruszczak, S. (eds), pp. 589-594.

Arroyo, M.; Muir Wood, D. and Greening, P.D.(2003). Source near-field effects and pulse tests in soil samples, Géotechnique. Vol.53, N° 3, pp. 337-345.

Arthur, J. R. F., ; Menzies, B. K. (1972) Inherent anisotropy in a sand. Géotechnique 22, No. 1, 115-128.

Arthur, J.R.F. (1988). Cubical devices: versatility and constraints. Advanced Triaxial Testing of Soil and Rock, ASTM STP 977, Robert T. Donaghe, Ronald C. Chaney, Marshall L. Silver (eds.). American Society for Testing and Materials, Philadelphia, pp. 743-765.

Arulnathan, R.; Boulanger, R.W.; Riemer, M.F. (1998). Analysis of bender element tests. Geotechnical Testing Journal, Vol. 21, No. 2, pp. 120-131.

ASTM D2487-85 (1989). Classification of soils for engineering purposes. 1989 Standards Annual Book. Vol. 04.08, pp.288-297. ASTM, Philadelphia.

ASTM D4015 (2000). Standard Test Methods for modulus and Damping of Soils by the Resonant-Column Method.

Atkinson, J.H. (2000). Non-linear soil stiffness in routine design. Géotechnique, Vol. 50, No. 5, pp. 487-508.

Atkinson, J.H.; Richardson, D.; Stallebrass, S.E. (1990). Effect of recent stress history on the stiffness of overconsolidated soil. Géotechnique, Vol. 40, No. 4, pp. 531-540.

Atkinson, J.H.; Sallfors, G. (1991). Experimental determination of soil properties. Proceedings of the 10th European Conference on Soil Mechanics and Foundation Engineering, Firenze, Vol. 3, pp. 915-956.

Baldi, G.; Hight, D.W.; Thomas, G.E. (1988). A reevaluation of conventional triaxial tests methods. Advanced Triaxial Testing of Soil and Rock, STP 977, pp. 219-262. Ed. Donaghe, Chaney e Silver. ASTM, Philadelphia.

Baligh, M.M. (1985). Strain Path method. Journal of Geotechnical Engineering, ASCE, Vol. 111, No. 9, pp. 1108-1136.

Baligh, M.M.; Azzouz, A.S.; Chin, C.-T. (1987). Disturbances due to ideal tube sampling. Journal of Geotechnical Engineering, ASCE, Vol. 113, No. 7, pp. 739-757.

Barros, J.M.C. (1996). Shear dynamic modulus of tropical soils. PhD thesis. University of Sao Paulo, Brazil (in Portuguese).

Barton, N.R.; Lien, B.; Lunde, J. (1974). Engineering classification of rock masses for the design of tunnel support. Rock Mechanics, Vol. 6, No. 4, pp.189-236.

Bashar, M.A.; Siddique, A.; Safiullah, A.M.M. (2001). Influence of 'perfect' sampling disturbance on shear properties of a coastal soil. Proceedings of the 14th International Conference on Soil Mechanics and Foundation Engineering, Hamburg, Germany, Vol. 1, pp. 1-4.

Bates, C.R. (1989). Dynamic soil property measurements during triaxial testing. Géotechnique, Vol. 39, No. 4, pp. 721-726.

Begonha, A. (1989). Alteração das Rochas Graníticas do Norte e Centro de Portugal. Uma Contribuição. Dissertação apresentada à Universidade Nova de Lisboa para obtenção do grau de Mestre em Geologia.

Bellotti, R.; Ghionna, V.N.; Jamiolkowski, M.; Robertson, P.K. (1989). "Design parameters of cohesionless soils from in situ tests". Transportation Research Board Conference, Washington.

Bellotti, R.; Jamiolkowski, M.; Lo Presti, D.C.F.; O'Neill, D.A. (1996). Anisotropy of small strain stiffness in Ticino sand. Géotechnique, Vol. 46, No. 1, pp. 115-131.

Bieniawski, Z.T. (1976). Rock Mass Classification in Rock Engineering. Proc. of the Symposium on Exploration for Rock Engineering. Vol. 1. Cape Town. South Africa.

Binns, A. (1998). Rotary coring in soils and soft rocks for geotechnical engineering. Proceedings of the Institution of Civil Engineers. Geotechnical Engineering, Vol. 131, No. 4, pp. 63-74.

Biot, M. A. (1956a). Theory of propagation of elastic waves in a fluid-saturated porous solid. I – Low frequency range. Journal of Acoustical Society of America,Vol. 28, No.2, pp. 168-178.

Biot, M. A. (1956b). Theory of propagation of elastic waves in a fluid-saturated porous solid. II - Higher frequency range. Journal of Acoustical Society of America,Vol. 28, No.2, pp. 179-191.

Bjerrum, L. (1973). Problems of soil mechanics and construction on soft clays and structurally unstable soils, State-of-the-art report, Session IV, Proc. 8th Int. Conf. Soil. Mech. and Found. Eng., Moscow, Volume 3, pp. 111-159.

Blewett, J.; Blewett, I.J. ; Woodward, P.K. (1999). Measurement of shear-wave velocity using phase-sensitive detection techniques. Canadian Geotechnical Journal, Vol. 36, pp. 934-939.

Blewett, J.; Blewett, I.J. ; Woodward, P.K. (2000). Phase and amplitude responses associated with the measurement of shear-wave velocity in sand by bender elements. Canadian Geotechnical Journal, Vol. 37, pp. 1348-1357.

Blight, G.E. (1997). Mechanics of residual soils. Balkema, Rotterdam.

Bodare, A.; Massarsch, K.R. (1984). Determination of shear wave velocity by different Cross-Hole methods. Proceedings of the 8th World Conference on Earthquake Engineering, San Franscisco, pp. 39-45.

Brand, E.W. and Phillipson, H.B. (1985). A review of international practice for the sampling ans testing of residual soils. Technical Committee on sampling and testing of residual soils. ISSMFE.

Brignoli, E.G.M.; Gotti, M.; Stokoe, K.H.II (1996). Measurement of shear waves in laboratory specimens by means of piezoelectric transducers. Geotechnical Testing Journal, Vol. 19, No. 4, pp. 384-397.

Brocanelli, D. and Rinaldi, V., 1998, Measurement of low strain material damping and wave velocity with bender elements in the frequency domain, Canadian Geotechnical Journal, Vol. 35, pp. 1032–1040.

Burger, H.R. (1992). Exploration Geophysics of the shallow subsurface, Prentice Hall, Englewood Cliffs.New Jersey.

Burland, J.B. (1979). Contribution to discussion on Session 4. Proceedings of the 7th European Conference on Soil Mechanics and Foundation Engineering. Brighton, UK, Vol. 4, pp. 137.

Burland, J.B. (1990). On the compressibility and shear strength of natural clays. 30th Rankine Lecture. Géotechnique, Vol. 40, No. 3, pp. 329-378.

Burland, J.B., (1989), Small is beautiful - the stiffness of soils at small strains (Ninth Laurits Bjerrum Memorial Lecture), Canadian Geotechnical Journal. No. 26, pp. 499-516.

Burland, J.B.; Symes, M. (1982). A simple axial displacement gauge for use in the triaxial apparatus. Geotechnique, Vol. 32, No. 1, pp. 62-65.

Butcher, A.P.; Powell, J.M. (2000a). Deformation properties of soil from in situ and laboratory tests. , pp. 51-54.

Butcher, A.P.; Powell, J.M. (2000b). Determining the modulus of the ground from in-situ geophysical testing. , pp. 449-452.

Callisto, L. and Calabresi, G. (1998) Mechanical behaviour of natural soft clay. Géotechnique 48, No. 4, 495-513.

Callisto, L. and Rampello, S. (2002) Shear strength and small-strain stiffness of a natural clay under general stress conditions. Géotechnique 52, No. 8, 547-560.

Camacho-Tauta, J., Santos, J.A. and Viana da Fonseca, A. (2008a). Two bender-receivers test. Proceedings of the 4th International Symposium on Deformation Characteristics of Geomaterials (IS-Atlanta 2008).

Camacho-Tauta, J.; Ferreira, C.; Santos, J. A.; Viana da Fonseca, A. (2008b). Moving Windows Algorithm to Reduce Uncertaintities in Bender Element Testing. 11 ° Congresso Nacional de Geotecnia, 7 a 11 de Abril de 2008, Coimbra.

Campanella, R.G. (1994). Field methods for dynamic geotechnical testing. Dynamic Geotechnical Testing II (STP1213), ASTM, West Conshocken, PA., 3-23.

Campanella, R.G., Robertson, P.K., and Gillespie, D. (1986). Seismic cone penetration test. Use of in situ tests in geotechnical engineering, Proceedings, In Situ '86, ASCE Geotechnical Specialty Publication No. 6, Samuel P. Clemence (ed.), Balcksburg, VA, June, pp. 116-130.

Carvalho, J.M.; Viana da Fonseca, A.; Almeida, F.; Hermosilha, H (2004), ISC'2 experimental site invest.and characterization - Part I: Conventional and tomographic P and S waves refraction seismics vs. electrical resistivity. Geotechnical & Geophysical Site Characterizaton. Viana da Fonseca and Mayne (Eds). Vol.1, pp. 433-442. Millpress, Rotterdam

Casagrande, A and Carrillo, N. (1944). Shear failure of anisotropic materials. Proc. Boston Soc. of Civil Eng. Vol. 31, pp. 74-87.

Cascante, G. and Santamarina, J.C. (1997). Low-Strain Measurements Using Random Noise Excitation, ASTM Geotechnical Testing Journal , vol. 20, no. 1, pp. 29-39.

Chang, M. F. (1988). In-situ testing of residual soils in Singapore. Geomechanics in Tropical Soils. Proc. Sec. Int. Conf., Singapore, Vol. 1, pp. 97-108. A. A. Balkema Pub., Rotterdam.

Chung, R.M.; Yokel, F.Y.; Wechsler, H. (1984). Pore pressure buildup in resonant column tests. Journal of the Geotechnical Engineering Division, ASCE, Vol. 110, No. 2, pp. 247-261.

Clayton C. R. I., Matthews M.C., Simons N.E., (1995). Site Investigation. Second Edition. Blackwell Science, Oxford. 584 pp. [also available as an e-book at http://www.geotechnique.info/]

Clayton, C. R. I., Theron, M. ; Best, A. I. (2004). The measurement of vertical shear-wave velocity using side-mounted bender elements in the triaxial apparatus. Geotechnique, Vol. 54, No. 7, pp. 495-498.

Clayton, C.R.I. (1989). Sample disturbance and BS5930. Geological Society, Engineering Geology Special Publication, No. 2, pp. 33-41.

Clayton, C.R.I.; Gordon, M.A.; Matthews, M.C. (1994). Measurement of stiffness of soils and weak rocks using small strain laboratory testing and field geophysics. Pre-failure Deformation of Geomaterials. Shibuya, Mitachi & Miura (eds). Balkema, Rotterdam, Vol. 1, pp. 229-234.

Clayton, C.R.I.; Hight, D.W.; Hopper, R.J. (1992). Progressive destructuring of Bothkennar clay: implications for sampling and reconsolidation procedures. Géotechnique, Vol. 42, No. 2, pp. 219-239.

Clayton, C.R.I.; Siddique, A. (2001). Discussion on tube sampling disturbance - forgotten truths and new perspectives (author's reply). Proceedings of the Institution of Civil Engineers. Geotechnical Engineering, Vol. 149, No. 3, pp. 195-200.

Clayton, C.R.I.; Siddique, A.; Hopper, R.J. (1998). Effects of sampler design on tube sampling disturbance - numerical and analytical investigations. Géotechnique, Vol. 48, No. 6, pp. 847-867.

Cole, K.W.; Burland, J.B. (1972). Observation of retaining wall movements associated with a large excavation. Proceedings of the 5th European Conference on Soil Mechanics and Foundation Engineering. Madrid, España.

Collins, R. (1985). Towards characterisation of tropical soil microstructure. Proc. 1st Int. Conf. on Geomech. in Tropical Lateritic and Saprolitic Soils, Brasilia, Vol.1, pp.85-96; Discussion, Vol.3, pp.207-209.

Cook, J. R. and Newill, D. (1988). The field Idescription and identification of tropical residual soils. Proceedings of the 2nd International Conference on Geomechanics in tropical soils, Singapore, December 1988, 1, 3–10. A. A. Balkema, Rotterdam.

Cooley, J. W. and Tukey, J. W. (1965), An algorithm for the machine calculation of complex Fourier series, Mathematics of Computation. Vol. 19, No. 90, pp. 297–301.

Coop, M.R.; Jovicic, V.; Atkinson, J.H. (2001). Comparisons between soil stiffnesses in laboratory tests using dynamic and continuous loading. , pp. 267-270.

Costa Filho, L.M. ; Vargas Jr., E.A. (1985). Hydraulic properties. Mechanical and Hydraulic Properties of Topical Lateritic and Saprolitic Soils. Progress Report of the ISSMFE Technical Committee (1985), pp. 67-84. ABMS, Brasília, Brazil.

Costa, C.F.G. (2008). Development of a monitoring and control system for triaxial tests in soils. MSc thesis on Automation, Instrumentation and Control, FEUP. Porto (in Portuguese).

Costa, E. (2005). Tests and response analysis of piles in residual soils from granite under vertical loads. MSc Thesis, University of Porto, Portugal (in Portuguese).

Costa, J.C.; Teixeira, C. (1957). Nota explicativa da folha 9-C - Porto. 'Carta Geológica de Portugal' na escala 1:50000. Serviços Geológicos de Portugal, Lisboa.

Cotecchia, F. and Chandler, R.J. (1997). The influence of structure on the prefailure behaviour of a natural clay. Géotechnique, 47, No.3, 523-544.

Crampin, S. (1981) A review of wave motion in anisotropic and cracked elastic-media. Wave Motion 3, 343-391.

Cresswell, A. (2001). Block sampling and test sample preparation of locked sands. Géotechnique, Vol. 51, No. 6, pp. 567-570.

Cruz, N., Viana da Fonseca, A. and Neves, E. (2004), Evaluation of effective cohesive intercept on residual soils by DMT data. Geotechnical & Geophysical Site Characterizaton. (Edited by. A. Viana da Fonseca & P.W.Mayne). Vol.2, pp. 1275-1278. Millpress, Rotterdam.

Cruz, N., Viana da Fonseca, A., Coelho, P. and Lemos, J. (1997), Evaluation of Geotechnical Parameters by DMT in Portuguese Soils. XIV Int. Conf. on Soil Mechanics and Foundation Engineering, pp 77-80. Balkema, Rotterdam.

Cruz, N.B. (1995). A avaliação de parâmetros geotécnicos pelo dilatómetro de Marchetti. Dissertação apresentada na Universidade de Coimbra para obtenção do grau de Mestre em Engenharia Civil, FCTUC, Coimbra.

Cuccovillo, T.; Coop, M. R. (1997). The measurement of local axial strains in triaxial tests using LVDTs. Géotechnique 47, No. 1, 167-172.

Danzinger, F.A.B., Politano, C.F. and Danzinger, B.R. (1998), CPT-SPT correlations for some Brazilian residual soils. First International Conference on Site Characterization - ISC'98. Atlanta, Vol. 2, pp. 907-912. Balkema, Rotterdam.

Davis, E.H.; Poulos, H.G. (1968). The use of elastic theory for settlement prediction under three-dimensional conditions. Géotechnique, Vol. 18, N ° 1, pp. 67-91.

Dearman, W.R. (1976). Weathering classification in the characterisation of rock: a revision. Bull. Int. Assoc. Eng. Geol., N ° 13, pp. 123-127.

Decourt, L. (1989), The standard penetration test. State of the Art Report. Proc. XII ICSMFE, Rio de Janeiro. Balkema, Rotterdam. Vol. 4, pp. 2405-2416.

Deere, D. U., and Patton, F. D. (1971). Slope stability in residual soils. Fourth panamerican conference on soil mechanics and foundation engineering, American Society of Civil Engineers, pp. 87-170.

Dewoolkar, M., Goddery, T., Sture, S. & Ko, H. Y. (1997) Multiaxial cubical cell apparatus for cohesive and cohesionless soils: Description and users manual. Department of Civil, Environmental and Architectural Engineering, University of Colorado, Boulder.

Di Benedetto, H., Geoffroy, H. and Sauzéat, C. (1999), Sand behaviour in very small to medium strain domain, Proceedings of the 2nd Int. Conference on Pre-failure Deformation Characteristics of Geomaterials. Jamiolkowski, Lancellotta and Lo Presti (eds), Balkema, Rotterdam, pp. 89-96.

Dihoru, L.; Muir Wood, D.; Sadek, T. and Lings, M. (2005). Neural Network Framework for Error prediction in a True Triaxial Apparatus with Flexible Boundaries. Computers and Geotechnics, Vol.21, N ° 2, 2005, pp.59-71.

Dobrin, M.B. and Savit, C.H. (1988). Introduction to Geophysical Prospecting, Fourth Edition, McGraw-Hill Book Company.

Dourado, K. (2011). Modelling the behaviour of bored piles in residual soils from granite. PhD thesis, University of Recife (under development).

Drnevich, V.P., Hardin, B.O., and Shippy, D.J. (1978). "Modulus and damping of soils by the resonantcolumn method," Dynamic Geotechnical Testing, ASTM STP 654, American Society of Testing and Materials, pp. 91-125.

Dyvik, R.; Madshus, C. (1985). Lab measurements of Gmax using bender elements. Proceedings ASCE Annual Convention: Advances in the art of testing soils under cyclic conditions, Detroit, Michigan, pp. 186-197.

Dyvik, R.; Olsen, T.S. (1989). Gmax measured in oedometer and DSS tests using bender elements. Proceedings of the Twelfth International Conference on Soil Mechanics and Foundation Engineering, Rio de Janeiro, Vol. 1, pp. 39-42.

Elmore, W.C.; Heald, M.A. (1969). Physics of waves. Dover Editions, pp. 225-229.

Eslaamizaad, S.; Robertson, P.K. (1996) A Framework for In-situ determination of Sand Compressibility. 49th Canadian Geotechnical Conference; St John's Newfoundland.

Eslami, A.; Fellenius, B.H. (1997) Pile Capacity by Direct CPT and CPTU Methods Applied to 102 Case Histories. Canadian Geotechnical Journal, Vol. 34, pp. 886-904.

Fahey, M. (1992). Shear modulus of cohesionless soil: variation with stress and strain level. Canadian Geotechnical Journal, Vol. 29, pp. 157-161

Fahey, M. (1998). Deformation and in situ stress measurement. Geotechnical Site Characterization. Robertson & Mayne (eds.). Balkema, Rotterdam, pp. 49-68.

Fahey, M. (2001). Soil stiffness values for foundation settlement analysis. Proc. 2nd Int. Conf. on Pre-failure Deformation Characteristics of Geomaterials, Torino, Italy, Vol. 2, 1325-1332, Balkema, Lisse.

Fahey, M., Lehane, B. & Stewart, D.P. (2003). Soil stiffness for shallow foundation design in the Perth CBD. Australian Geomechanics, 38(3): 61–89.

Fahey, M., Schneider, J. M. & Lehane, B. (2007). Self boring pressuremeter testing in Spearwood dune sand. Australian Geomechanics, in press - December.

Fahey, M.; Carter, J.P. (1993). A finite element study of the pressuremeter test in sand using a nonlinear elastic plastic model. Canadian Geotechnical Journal, Vol. 30, pp. 348-362.

Fam, M. A.; Cascante, G.; Dusseault, M. B. (2002). Large and Small Strain Properties of Sands Subjected to Local Void Increase, Journal of Geotechnical and Geoenvironmental Engineering, Vol. 128, No.12, pp. 1018-1025.

Fam, M.; Santamarina, C. (1995) Study of geoprocesses with complementary mechanical and electromagnetic wave measurements in an oedometer, Geotechnical Testing Journal, ASTM. Vol.18, No. 3, pp. 307-314.

Fannin, C.A. (1997). Design of an analog adaptive piezoelectric sensoriactuator. Department of Mechanical Engineering, Faculty of Virginia Polytechnic Institute and State University.

Ferreira, C., (2003). Implementation and Application of Piezoelectric Transducers for the Determination of Seismic Wave Velocities in Soil Specimens. Assessment of Sampling Quality in Residual Soils. MSc Thesis, Faculty of Engineering, University of Porto (In Portuguese).

Ferreira, C., 2004, Analysis of the application of different interpretation techniques on bender element measurements on Toyoura sand, Workshop on Bender Element Testing of Soils, University College London. (http://www.civeng.ucl.ac.uk/staff/pdg/benders/UCL-cristiana.ppt, last accessed at 5 December 2007).

Ferreira, C.; Viana da Fonseca, A. (2005). International Parallel Tests on Bender Elements at theUniversity of Porto, Portugal. Report for TC29 of ISSMGE. Available at https://www.fe.up.pt/si/publs˙pesquisa.formview?p˙id=14204

Ferreira, C.; Viana da Fonseca, A. and Santos, J.A. (2007). Comparison of simultaneous bender elements and resonant column tests on Porto residual soil, Soil Stress-Strain Behavior: Measurement, Modeling and Analysis. A Collection of Papers of the Geotechnical Symposium in Rome, 2006, Ling, Callisto, Leshchinsky & Koseki (Eds.). Springer. pp. 523-535.

Fioravante, V. (2000) Anisotropy of small strain stiffness of Ticino and Kenya sands from seismic wave propagation measured in triaxial testing. Soils and Foundations 40, No. 4, 129-142.

Fioravante, V. and Capoferri, R. (2001). On the use of multi-directional piezoelectric transducers in triaxial testing. Geotechnical Testing Journal, Vol. 24, No. 3, pp. 243-255.

Fioravante, V.; Jamiolkowski, M.; Lo Presti, D.C.F.; Manfredini, G.; Pedroni, S. (1998). Assessment of the coefficient of the earth pressure at rest from shear wave velocity measurements. Géotechnique, Vol. 48, No. 5, pp. 657-666.

Foti, S. (2000). Multistation methods for geotechnical characterisation using surface waves. PhD thesis, Politecnico di Torino.

Foti, S.; Lai, C.G.; Lancellota, R. (2002). Porosity of fluid-saturated porous media from measured seismic wave velocities, Géotechnique. Vol.52, N ° 5, pp. 359-373.

Foti, S.; Lancellotta, R. (2004) Soil porosity from seismic velocities, Géotechnique, Vol. 54, No. 8, pp. 551-554.

Fratta, D. ; Santamarina, J.C. (1996). Wave propagation in soils: Multi-mode, wide-band testing in a waveguide device. Geotechnical Testing Journal, Vol. 19, No. 2, pp. 130-140.

Fuertes, A.V. (1999). The use of piezoelectric transducers in the measurement of elastic moduli of soils. Internal Report, Department of Civil Engineering, University of Bristol, UK.

Gabriels P.; Snieder R. & Nolet G. (1987) In situ measurementof shear wave velocity in sediments with higher-moderayleigh waves, Geophysical prospecting, 35, 187-196.

Gajo, A., Fedel, A. & Mongiovi, L. (1997). Experimental analysis of the effects of fluid–solid coupling on the velocity of elastic waves in saturated porous media. Géotechnique 47, No. 5, pp. 993–1008.

Ganji, V., and Gucunski, N. (1998). Automated inversion procedure for spectral analysis of surface waves,ASCE, Journal of Geotechnical and Geoenvironmental Engineering, pp. 757-770.

GCO (1987). Guide to Site Investigation. Reprint. Geo-technical Engineering Office. Hong Kong.

GDS Instruments (2001). The GDS Standard Pressure/Volume Controller STDDPC. www.gdsinstruments.com (last accessed in 31st January 2008)

Geoffroy, H.; Di Benedetto, H.; Duttine, A.; Sauzéat, C.(2003). Dynamic and cyclic loadings on sands: results and modelling for general stress–strain conditions, Proceedings of Deformation Characteristics of Geomaterials, Lyon, France, 22-24 September, Lyon, France. Balkema, pp. 353-363.

Gomes Correia, A., Barros, J.M.C., Santos, J.A., Sussumu, N. (2001). An approach to predict shear modulus of soils in the range of 10-6 to 10-2 strain levels. 4th International Conference on Recent Advances in Geotehcnical Earthquake Engineering and Soil Dynamics, 26-31 March 2001, San Diego, California.

Gomes Correia, A., Viana da Fonseca, A. and Gambin, M. (2004). Routine and advanced analysis of mechanical in situ tests. Results on saprolitic soils from granites more or less mixed in Portugal. Proceedings ISC-2 on Geotechnical and Geophysical Site Characterization, Viana da Fonseca & Mayne (eds.). Millpress, Rotterdam. pp.75-95.

Gomez, A.; Solas, J.P.R. (2001). Toma muestras TECSO NT-81. Actas da Workshop Técnicas de Amostragem em Solos e Rochas Brandas e Controlo de Qualidade. FEUP, Porto.

Gordon, M.A.; Clayton, C.R.I (1997). Measurement of stiffness of soils using small strains triaxial testing and bender elements. Modern Geophysics in Engineering Geology. McCann, D.M.; Eddleston, M.; Fenning, P.J. & Reeves, G.M. (eds.). Geological Society Engineering Geology Special Publication, No. 12, pp. 365-371.

Goto, S.; Tatsuoka, F.; Shibuya, S.; Kim, Y.S.; Sato, T. (1991). A simple gauge for local small strain measurements in the laboratory. Soils and Foundations, Vol. 31, No. 1, pp. 169-180

Graham, J. & Lau, S. L.-K. (1988). Infiuence of stress release disturbance, storage, and reconsolidation procedures on the shear behaviour of reconstituted underwater clay. Geotechnique 38, No. 2, 279-300.

Graham, J. and Houlsby, G. T. (1983). Anisotropic elasticity of a natural clay. Geotechnique Vol. 33, No. 2, pp. 165-180.

Greening, P.D. (2000). Development in seismic laboratory testing using piezo-ceramic transducers. Research project proposal, University of Bristol.

Greening, P.D. ; Nash, D.F.T. (2004) Frequency domain determination of G0 using bender elements, ASTM Geotechnical Testing Journal, 27, 3, 1-7

Greening, P.D.; Nash, D.F.T.; Benahmed, N.; Viana da Fonseca, A. and Ferreira, C., 2003, Comparison of shear wave velocity measurements in different materials using time and frequency domain techniques, Proceedings of Deformation Characteristics of Geomaterials, Lyon, France, 22-24 September, Lyon, France:Balkema, pp. 381-386.

Grolewski, B.; Zeng, X. (2001). Measurement of Gmax and K0 of saturated clay using bender elements. Proceedings of the Fourth International Conference on Recent Advances in Geotechnical Earthquake Engineering and Soil Dynamics, San Diego, California, No. 1.47.

Hambly, E. C. (1969) A new true triaxial apparatus. Géotechnique 19, No. 2, 307-309.

Hardin, B. O., Drnevich, V.P. (1972a), Shear modulus and damping in soils: measurement and parameter effects," Journal of Soil Mechanics and Foundation Engineering Div., ASCE, Vol. 98 No. SM6, June, pp 603-624.

Hardin, B.O. (1965). Dynamic versus static shear modulus for dry sand. Materials Research and Standards, ASTM, Vol. 5, No. 5, pp. 232-235.

Hardin, B.O. (1978). The nature of stress-strain behaviour of soils. Proceedings of the Earthquake Engineering and Soil Dynamics Conference, ASCE. Pasadena, California, Vol. 1, pp. 3-39.

Hardin, B.O., Drnevich, V.P. (1972b). Shear modulus and damping in soils: design equations and curves. Journal of the Soil Mechanics and Foundations Division, ASCE, Vol. 98, No. 7, pp. 667-692.

Hardin, B.O.; Black, W.L. (1969). Closure to: Vibration modulus of normally consolidated clays. Journal of Soil Mechanics and Foundation Division, ASCE, Vol. 95, No. 6, pp. 1531-1537.

Hardin, B.O.; Blandford, G.E. (1989). Elasticity of articulate materials. Journal of Geotechnical Engineering, ASCE, Vol. 115, No. 6, pp. 788-805.

Hardin, B.O.; Richart, F.E.Jr. (1963). Elastic wave velocities in granular soils. Journal of Soil Mechanics and Foundation Division, ASCE, Vol. 89, No. 1, pp. 33-65.

Hardy, S.; Zdravkovic, L. and Potts, D.M., 2002, Numerical interpretation of continuously cycled bender element tests, Numerical Models in Geomechanics (NUMOG VII, Pande and Pietruszczak (eds), Swets and Zeitlinger, Lisse, pp. 595-600.

Hardy, S.; Zdravkovic, L.; Potts, D.M. (2002). Numerical interpretation of continuously cycled bender element tests. Numerical Models in Geomechanics (NUMOG VII). Pande & Pietruszczak (eds.). Swets & Zeitlinger, Lisse, pp. 595-600.

Hayano, K., Tatsuoka, F., Koseki, J. & Sato,T. (1999) Small strain deformation characteristics of sedimentary soft mudstone from true triaxial tests. Proceedings of the 2nd Int. Conference on Pre-failure Deformation Characteristics of Geomaterials. Jamiolkowski, Lancellotta & Lo Presti (eds), Balkema, Rotterdam, 191-198.

Head, K.H. (1985). Manual of soil laboratory testing. Vol.III - Effective stress tests. Pentech Press, London.

Hight, D. W. (1993). A review of sampling effects in clays and sands. Offshore Site Invest. Found. Behav. Soc. Underwater Technol. 28, 115-146.

Hight, D. W. (1998). "Soil characterization: The importance of structure and anisotropy." 38th Rankine Lecture, British Geotechnical Society, London.

Hight, D. W., Gens, A. and Jardine, R. J. (1985). Evaluation of geotechnical parameters from triaxial tests on offshore clay. Proceedings of an international conference on offshore site investigation, Society for Underwater Technology, London, pp. 253-268.

Hight, D.W. (1996). Moderator's report on Session 3: drilling, boring, sampling and description. Advances in site investigation practice, Thomas Telford, London, pp. 337-360.

Hight, D.W. (2000). Sampling methods: Evaluation of disturbance and new practical techniques for high quality sampling in soils. Actas do 7° Congresso Nacional de Geotecnia, Porto, Portugal.

Hight, D.W., Bond, A.J., Legge, J.D., Characterization of the Bothkennar clay: an overview, Géotechnique 42, 2, 303-347

Hight, D.W.; Bennell, J.D.; Chana, B.; Davis, P.D.; Jardine, R.J. and Porovic, E., 1997, Wave velocity and stiffness measurements of the Crag and Lower London Tertiaries at Sizewell, Géotechnique. Vol.47, N° 3, pp. 451-474.

Hight, D.W.; Higgins, K.G. (1995). An approach to the prediction of ground movements in engineering practice: background and application. Pre-failure Deformation of Geomaterials, Shibuya, Mitachi & Miura (eds.). Balkema, Rotterdam, Vol. 2, pp. 909-945.

Hoar, R.J.; Stokoe, K.H.II (1978). Generation and measurement of shear waves in-situ. Dynamic Geotechnical Testing, ASTM-STP 654, pp. 3-29.

Hoffman, K. Varuso, R. and Fratta, D., 2006, The Use of Low-Cost MEMS Accelerometers in Near-Surface Travel-Time Tomography, GeoCongress 2006 Conference, Atlanta, GA, 1-6.

Huang, A.B., Huang, Y.T. and Ho, F.J. (2005). Assessment of liquefaction potential for a silty sand in Central Western Taiwan. Proceedings of 16th ICSMGE, Osaka.

Hvorslev, M .J. (1949) Subsurface Exploration and Sampling of Soils for Civil Engineering Purposes, Waterways Experimental Station, Vicksburg, USA.

Ibsen, L.B. and Praastrup, U. (2002). The Danish rigid boundary true triaxial apparatus for soil testing. Geotechnical Testing Journal, Vol. 25, No. 3, 1-12.

Ishihara, K. (1982). Evaluation of soil properties for use in earthquake response analysis. Proceedings of the International Symposium on numerical models in geomechanics, Zurich, pp. 237-259.

Ishihara, K. (1993). Dynamic properties of soils and gravels from laboratory tests. Soil Dynamics and Geotechnical Earthquake Engineering, Sêco e Pinto (ed.), Balkema, Rotterdam, pp. 1-17.

Ishihara, K.; Tsuchiya, H.; Huang, Y.; Kamada, K. (2001). Recent studies on liquefaction resistance of sand - effect of saturation (Keynote Lecture). Proceedings of the 4th International Conference on Recent Advances in Geotechnical Earthquake Engineering and Soil Dynamics, San Diego, California.

Ismail, M. A. and Hourani, Y., 2003, An innovative facility to measure shear-wave velocity in centrifuge and 1-g models, Proceedings of Deformation Characteristics of Geomaterials, Lyon, France, 22-24 September, Lyon, France. Balkema, pp. 21-29.

Ismail, M. A. and Rammah, K. I. (2005). Shear-plate transducers as a possible alternative to bender elements for measuring G_{max}, Géotechnique, Vol. 55, No. 5, pp. 403–407.

Ismail, M.; Ferreira, C. & Fahey, M. (2004). Influence of Cement Type on Gmax of a Carbonate Sand. Proceedings of the A. W. Skempton Memorial Conference, Londres, Inglaterra. ISBN: 0727732641. Thomas Telford, London.

Ismail, M.A., Sharma, S.S. and Fahey, M. (2005). A small true triaxial apparatus with wave velocity measurement, Geotechnical Testing Journal, American Society for Testing and Materials, Vol. 28, No. 2, pp.1□10.

Iwasaki, T. and Tatsuoka, F., 1977, Effects of Grain Size and Grading on Dynamic Shear Moduli of Sands, Soils and Foundations, Vol. 17, No. 3, pp. 19-35.

Iwasaki, T.; Tatsuoka, F.; Takagi, Y. (1978). Shear moduli of sands under cyclic torsional shear loading. Soils and Foundations, Vol. 18, No. 1, pp. 39-56.

Jamiolkowski, M.; Lancellotta, R.; Lo Presti, D.C.F. (1995). Remarks on the stiffness at small strains of six Italian clays. Pre-failure Deformation of Geomaterials. Shibuya, Mitachi & Miura (eds). Balkema, Rotterdam, pp. 817-836.

Jamiolkowski, M.; Leroueil, S.; Lo Presti, D.C.F. (1991). Design parameters from theory to practice. Theme Lecture. Proceedings of Geo-Coast'91, Yokohama, Vol. 2, pp. 877-917.

Jardine, R.J. (1995). One perspective of the pre-failure deformation characteristics of some geomaterials. Pre-failure Deformation of Geomaterials. Shibuya, Mitachi & Miura (eds). Balkema, Rotterdam, pp. 855-885.

Jardine, R.J. and Shibuya, S., 2005, TC29 workshop: Laboratory tests. Report, Proceedings of the 16th International Conference on Soil Mechanics and Geotechnical Engineering, Osaka. Vol.5, pp. 3275-3276.

Jardine, R.J.; Fourie, A.B.; Maswoswse, J.; Burland, J.B. (1985). Field and laboratory measurements of soil stiffness. Proceedings of the 11th International Conference on Soil Mechanics and Foundation Engineering, San Francisco, Vol. 2, pp. 511-514.

JGS (1995). Standards of the Japanese Geotechnical Society for soil sampling - standards and explanations - JGS 1221; JGS 1222; JGS 1223; JGS 1224; JGS 1231.

Jovičić, V., 2004, Rigorous bender element testing, Workshop on Bender Element Testing of Soils, University College, London.

Jovicic, V.; Coop, M.R. (1997). Stiffness of coarse-grained soils at small strains. Géotechnique, Vol. 47, No. 3, pp. 545-561.

Jovicic, V.; Coop, M.R. (1998). The measurement of stiffness anisotropy in clays with bender element tests in the triaxial apparatus. Geotechnical Testing Journal, Vol. 21, No. 1, pp. 3-10.

Jovicic, V.; Coop, M.R.; Atkinson, J.H. (2001). Laboratory measurements of small strain stiffness of a soft rock. , pp. 323-326.

Jovicic,V.; Coop, M.R.; Simic, M. (1996). Objective criteria for determining Gmax from bender element tests. Géotechnique, Vol. 46, No. 2, pp. 357-362.

Kaarsberg, E.A. (1975). Elastic wave velocity measurements in rocks and other materials by phase-delay methods. Geophysics, Vol. 40, pp. 855-901.

Kirkpatrick, W. M. & Khan, A. J. (1984). The reaction of clays to sampling stress relief. GeØotechnique 34, No.1, 29-42.

Klotz, C., Beutinger, P.H., Vermeer, P.A. (2003). Effects of inherent anisotropy and mode of shearing on the behaviour of geomaterials. Proceedings of the 16th ASCE Engineering Mechanics Conference. http://www.ce.washington.edu/em03/proceedings/papers/371.pdf

Ko, H. Y. & Scott, R. F. (1967). A new soil testing apparatus. Géotechnique, Vol. 17, No. 1, pp. 40-57.

Kondner, R.B, (1963). Hyperbolic stress-strain response: cohesive soils. Journal of Soil Mechanics and Foundations Division, Vol. 89, No SM 1, pp. 115-143.

Krautkrämer, J.; Krautkrämer, H., 1990, Ultrasonic Testing of Materials, 4th Edition. Springer-Verlag.

Kuwano, R., Connolly, T.M., and Jardine, R.J. (2000). Anisotropi stiffness measurements in a stress-path triaxial cell. Geotechnical Testing Journal, 23(2): 141–157.

Kuwano, R.; Connolly, T. M.; Kuwano, J. (1999). Shear stiffness anisotropy measured by multidirectional bender element transducers. Proc. International Symposium on Pre-failure Deformation of Geomaterials, M. Jamiolkowski et al., eds., Vol. 1, pp. 205-212.

La Rochelle, P.; Sarrailh, J.; Tavenas, F.; Roy, M.; Leroueil, S (1981). Causes of sampling disturbance and design of a new sampler for sensitive clays. Canadian Geotechnical Journal, Vol. 18, No. 1, pp. 52-66.

Ladd, C. C., and DeGroot, D. J. (2003). Recommended practice for softground site characterization: Arthur Casagrande lecture. Proc., 12th Panamerican Conf. on Soil Mechanics and Geotechnical Engineering, Boston, 3–57.

Ladd, C.C. (1991). Stability evaluation during staged construction. ASCE Journal of Geotechnical Engineering 117 (4), 540-615.

Ladd, C.C.; Lambe, T.W. (1963). The strength of undisturbed clay determined from undrained tests. Symposium on laboratory shear testing of soils, ASTM, STP 361, pp. 342-371.

Lade, P. V. and Duncan, J. M. (1973) Cubical triaxial tests on cohesionless soils. Journal of Soil Mechanics and Foundation. ASCE, 99(10), 793-812.

Landon, M.M., DeGroot, D.J. and Sheahan, T.C. (2007). Nondestructive sample quality assessment of a soft clay using shear wave velocity. Journal of Geotechnical and Geoenvironmental Engineering, ASCE. Vol. 133, No. 4, pp.424-432.

Lawrence, F.V. (1963). Propagation of ultrasonic waves through sand. Research report R63-8. Massachusetts Institute of Technology, Cambridge, MA.

Lawrence, F.V. (1965). Ultrasonic shear wave velocity in sand and clay. Research report R65-05, Soil Publication No. 175. Massachusetts Institute of Technology, Cambridge, MA.

Lee, J. S. (2003). High resolution geophysical techniques for small-scale soil model testing, PhD thesis, Georgia Institute of Technology, Atlanta, Georgia.

Lee, J. S. and Santamarina, C. (2005). Bender Elements: Performance and Signal Interpretation, Journal of Geotechnical and Geoenvironmental Engineering, Vol. 131, No. 9, pp. 1063-1070.

Lee, J.-S., Santamarina, J.C., Li, Z. and Kutter, B.L. (2005). Geophysical process monitoring in scaled models. Proceedings of 16th ICSMGE, Osaka, pp. 711-715.

Lefebvre, G., and Poulin, C. (1979). "A new method of sampling in sensitive clay." Can. Geotech. J., Vol. 16 No. 1, pp. 226–233.

Leong, E.C.; Yeo, S.H. and Rahardjo, H., 2005, Measuring shear wave velocity using bender elements, Geotechnical Testing Journal, ASTM. Vol.28, N ° 5, pp. 488-498.

Leroueil, S and Vaughan, P.R. (1990). The general and congruent effects of structure in natural clays and weak rocks. Géotechnique, Vol 40, pp. 467- 488.

Leroueil, S. (1997). Critical state soil mechanics and the behaviour of real soils. Recent Developments in Soil and Pavement Mechanics, Almeida (ed.). Balkema, Rotterdam, pp. 41-80.

Leroueil, S.; Hight, D.W. (2003). Behaviour and properties of natural and soft rocks. Characterization and Engineering Properties of Natural Soils. Eds. Tan et al. Vol.1, pp.29-254. Swets & Zeitlinger, Lisse.

Lewin, P. I. and Allman, M. A. (1992) Three-dimensional tests on reconstituted Bothkennar soil. Predictive soil mechanics: Proceedings of Wroth Memorial Symposium, London: Thomas Telford, 436-448.

Lings, M. L. (2001) Drained and undrained anisotropic elastic stiffness parameters. Géotechnique 51, No. 6, 555-565.

Lings, M.L.; Greening, P.D. (2001). A novel bender/extender element for soil testing. Géotechnique, Vol. 51, No. 8, pp. 713-717.

Lings, M.L.; Pennington, D.S.; Nash, D.F.T. (2000). Anisotropic stiffness parameters and their measurement in a stiff natural clay. Géotechnique, Vol. 50, No. 2, pp. 109-125.

Little, A.L. (1969). The engineering classification of residual tropical soils, Proc. 7th International Conference on Soil Mechanics and Foundation Engineering, Mexico. Vol. 1, pp. 1-10.

Lo Presti, D.C.F. (1995). General report: Measurement of shear deformation of geomaterials in the laboratory. Pre-failure Deformation of Geomaterials. Shibuya, Mitachi & Miura (eds). Balkema, Rotterdam, pp. 1067-1088.

Lo Presti, D.C.F.; Jamiolkowski, M.; Pallara, O.; Cavallaro, A.; Pedroni, S. (1997). Shear modulus and damping of soils. Géotechnique, Vol. 47, No. 3, pp. 603-617.

Lo Presti, D.C.F.; Pallara, O.; Cavallaro, A.; Jamiolkowski, M. (1999). Influence of reconsolidation techniques and strain rate on the stiffness of undisturbed clays from triaxial tests. Geotechnical Testing Journal, ASTM, Vol. 22, No. 3, pp. 211-225.

Lo Presti, D.C.F.; Pallara, O.; Costanzo, D.; Impavido, M. (1994). Small strain measurements during triaxial tests: many problems, some solutions. Pre-failure Deformation of Geomaterials. Shibuya, Mitachi & Miura (eds). Balkema, Rotterdam, Vol. 1, pp. 11-16.

Lo Presti, D.C.F.; Pallara, O.; Lancellota, R.; Armandi, M.; Maniscalco, R. (1993). Monotonic and cyclic loading behaviour of two sands at small strains. Geotechnical Testing Journal, Vol. 16, No. 4, pp. 409-424.

Lo Presti, D.C.F.; Shibuya, S.; Rix, G.J. (2001). Innovation in soil testing. Proceedings of the 2nd International Conference on Pre-failure Deformation Characteristics of Geomaterials (IS Torino 99), Jamiolkowski, Lancellota & Lo Presti (Eds). Balkema, Rotterdam, Vol. 2, pp. 1027-1076.

Lohani, T.N.; Imai, G.; Shibuya, S. (1999). Determination of shear wave velocity in Bender Element Test. Earthquake Geotechnical Engineering, Sêco e Pinto (ed.), pp. 101-106.

Long, M. (2001). Discussion on tube sampling disturbance - forgotten truths and new perspectives (paper by Clayton, C.R.I.; Siddique, A.). Proceedings of the Institution of Civil Engineers. Geotechnical Engineering, Vol. 149, No. 3, pp. 195-200.

Long, M. (2001). The influence of plasticity on sample disturbance in soft clays. International conference on in situ measurements of soil properties and case histories, Bali, pp. 385-389.

Lopes, I.; Strobbia, C.; Almeida, I. Teves-Costa, P.; Deidda, G.P.; Mendes, M.; Santos, J.A. (2004). Joint acquisition of SWM and other seismic techniques in the ISC'2 experimental site. Proceedings ISC'2 on Geotechnical and Geophysical Characterization, Viana da Fonseca & Mayne (eds), Porto, Milpress, Vol.1, pp. 521-530.

Love, A.E.H. (1927). A treatise on the mathematical theory of elasticity. Dover Editions, pp. 293-309.

Lumb, P. (1962) The properties of decomposed granite. Géotechnique. Vol.12, No. 3, pp.226-243. London.

Lunne, T.; Berre, T.; Strandvik, S. (1997). Sample disturbance effects in soft low plastic Norwegian clay. Recent Developments in Soil and Pavement Mechanics, Almeida (ed.). Balkema, Rotterdam, pp. 81-102

Macari, E. J. and Hoyos Jr, R. (2001) Mechanical behaviour of unsaturated soil under multi-axial stress states. Geotechnical Testing Journal 24, No. 1, 14-22.

Mair, R. J. (1993). Developments in geotechnical engineering research: applications to tunnels and deep excavations. Unwin Memorial Lecture 1992. Proc. Instn Civ. Engrs Civ. Engng, 3, pp. 27-41

Mancuso, C., Simonelli, A.L., and Vinale, F. 1989. Numerical analysis of in-situ S-wave measurements. In Proceedings of the 12th International Conference on Soil Mechanics and Foundation Engineering, Rio de Janeiro, Aug., Vol. 3, pp. 277–280.

Marchetti, S. (1980). In situ tests by flat dilatometer. J. Geotech. Eng. Div., ASCE. Vol. 106, GT3, 299-321.

Marchetti, S. (1997). The Flat Dilatometer Design Applications. III Geotechnical Engineering Conference, Cairo University.

Marczak, W. (1997). Water as a standard in the measurements of speed of sound in liquids, Journal of the Acoustical Society of America, Vol. 102, No. 5, pp. 2776-2779.

Matsuoka, H., Sun, D., Kogane, A., Fukuzawa, N., Ichihara, W. (2002). Stress–strain behaviour of unsaturated soil in true triaxial tests. Canadian Geotechnical Journal, Vol. 39, pp. 608-619.

Mayne, P.W., and Rix, G.J. (1993) Gmax-qc relationships for clays, Geotechnical Testing Journal, ASTM, 16 (1), pp. 54-60.

Mayne, P.W.; Brown, D.A. (2002). Site characterization of Piedmont residuum of North America. Characterization and Engineering Properties of Natural Soils, Vol. 2, Swets & Zeitlinger, Lisse, pp.1323-1339.

Menke, W. (1989). Geophysical Data Analysis: Discrete Inverse Theory, Academic Press.

Michelis, P. (1988) A True Triaxial for Soil and Rock. Advanced Triaxial Testing of Soil and Rock. Donaghe, Chaney & Silver (eds), ASTM STP 977, 806-818.

Miura, K.; Yoshida, N.; Kim, Y.-S. (2001). Frequency dependent property of waves in saturated soil. Soils and Foundations, Vol. 41, No. 2, pp. 1-19.

Mohsin, A.K.M. and Airey, D.W., 2003, Automating G_{max} measurements in triaxial tests, Proceedings of the 3rd International Symposium on Deformation Characteristics of Geomaterials, IS-Lyon '03, 24 September, 2003. Lyon, France, pp. 73-80.

Moncaster, A.M. (1997). The shear modulus of sand at very small strains. MSc thesis. Department of Civil Engineering, University of Bristol, UK.

Muir Wood, D. (1974). Some aspects of the mechanical behaviour of Kaolin under truly triaxial conditions of stress and strain. PhD thesis, University of Cambridge.

Muir Wood, D. (1981) True triaxial tests on Boston Blue clay. Proceedings of the 10th Int. Conference on Soil Mechanics and Foundation Engineering, Stockholm 1, 825-830.

Muir Wood, D. (1990) Soil behaviour and critical state soil mechanics, Cambridge University Press, Cambridge, UK.

Muir Wood, D. (2004). Geotechnical modelling. Taylor & Francis. ISBN 0-419-23730-5, 488 pp.

Nakagawa, K.; Soga, K.; Mitchell, J.K. (1997). Observation of Biot compressional wave of the second kind in granular soils. Géotechnique, Vol. 47, No. 1, pp. 133-147.

Nash, D.F.T., Lings, M.L., Benahmed, N., Sukolrat, J. and Muir Wood, D. (2006). The effects of controlled destructuring on the small strain shear stiffness Go Bothkennar clay. In Tatsuoka Geotechnical Symposium. Rome.

Nash, D.F.T.; Greening, P. (2001). The use of bender elements in the assessment of sample disturbance. Actas da Workshop Técnicas de Amostragem em Solos e Rochas Brandas e Controlo de Qualidade. FEUP, Porto, Portugal.

Nash, D.F.T; Pennington, D.S.; Lings, M.L. (1997). The dependence of anisotropic G0 shear moduli on void ratio and stress level for reconstituted Gault clay.

Nazarian, S. and K. H. Stokoe (1984). In situ shear wave velocities from spectral analysis of surface waves. 8th World Conference on Earthquake Engineering, pp. 31–38.

Nazarian, S., Yuan, D., and Baker M.R. (1994). Automation of spectral analysis of surface waves method, Dynamic Geotechnical Testing II, ASTM STP1213, pp 88-100.

Ng, C. W. W. & Leung, E. H. Y. (2007). Determination of Shear-Wave Velocities and Shear Moduli of Completely Decomposed Tuff. Journal of Geotechnical and Geoenvironmental Engineering, Vol. 133, No. 6, pp. 630-640. ASCE.

Ng, C. W. W., Leung, E. H. Y., and Lau, C. K. (2004). "Inherentanisotropic stiffness of weathered geomaterial and its influence on ground deformations around deep excavations." Can. Geotech. Journal, Vol. 41, No.1, pp. 12–24.

Nishio, S.; Tamaoki, K. (1988). Measurement of shear wave velocities in diluvial samples under triaxial conditions. Soils and Foundations, Vol. 28, No. 2, pp. 35-48.

NRC (2000). "Seeing into the Earth," Committee for Noninvasive Characterization of the Shallow Subsurface for Environmental and Engineering Applications, P.R. Romig, Chair, 129 pp.

Osterberg, J.O. (1973). An improved hydraulic piston sampler, Proc. 8th International Conference on Soil Mechanics and Foundation Engineering, Moscow, Volume 1.2, pp. 317-321.

Park, C.B.; Miller, R.D. & Xia, J. (1999) Multichannel analysis of surface waves. Geophysics, Vol. 64, No. 3, pp. 800-808.

Pearce, J. A. (1970) The behaviour of soft clay in a new true triaxial apparatus. PhD thesis, University of Cambridge.

Pennington, D.S. (1999). The anisotropic small strain stiffness of Cambridge Gault clay. PhD thesis, Department of Civil Engineering, Univ. Bristol.

Pennington, D.S., Nash, D.F.T. and Lings, M.L. (2001). Horizontally-mounted bender elements for measuring anisotropic shear moduli in triaxial clay specimens. Geotechnical Testing Journal, ASTM. Vol. 24, N. 2, pp. 133-144.

Pennington, D.S.; Nash, D.F.T.; Lings, M.L. (1997). Anisotropy of G0 shear stiffness in Gault Clay. Géotechnique, Vol. 47, No. 3, pp. 391-398.

Penumadu, D. and Prashant, A. (2005). Automated Flexible-Boundary True Triaxial System for Cohesive Soils.

Pereira, E. (1992). Geological Map of Portugal, on Scale 1:200 000, Sheet n.1., INETI, Porto (in Portuguese).

Piezo Systems, Inc. (1994). History of Piezoelectricity. www.piezo.com.

Porovic, E. (1995). Investigations of soil behaviour using a resonant-column torsional-shear hollow cylinder apparatus. PhD thesis, Imperial College, University of London.

Prevost, J.H.; Keane, C.K. (1989). Shear stress-strain curve generation from simple material parameters. Journal of the Geotechnical Engineering Division, ASCE, Vol. 116, No. 8, pp. 1255-1263.

Rampello, S.; Viggiani, G.M.B. (2001). Pre-failure deformation characteristics of geomaterials. Proceedings of the 2nd International Conference on Pre-failure Deformation Characteristics of Geomaterials (IS Torino 99), Jamiolkowski, Lancellota & Lo Presti (Eds). Balkema, Rotterdam, Vol. 2, pp. 1279-1289.

Rampello, S.; Viggiani, G.M.B.; Amorosi, A. (1997). Small-strain stiffness of reconstituted clay compressed along constant triaxial effective stress ratio paths. Géotechnique, Vol. 47, No. 3, pp. 475-489.

Randolph, M.F., Carter, J.P. and Wroth, C.P. (1979). Driven piles in clay – the effects of installation and subsequent consolidation. Geotechnique, Vol. 29, No. 4, pp.361-393.

Raymond, G.P. (1977). Effect on soil sampling on the drained properties of Leda Clay, Proc. Speciality Session 2 on Soil Sampling, 9th International Conference on Soil Mechanics and Foundation Engineering, Tokyo, pp. 47-55.

Reddy, K. R., Saxena, S. K. & Budiman, J. S. (1992) Development of a true triaxial testing apparatus. Geotechnical Testing Journal, Vol. 15, No. 2, 89-105.

Richart, F.E.Jr.; Hall, J.R.Jr.; Woods, R.D. (1970). Vibrations of soils and foundations. Prentice-Hall, Inc., Englewood Cliffs, NJ.

Rio, J. (2006). Advances in laboratory geophysics using bender elements, PhD Thesis, University College London, University of London.

Rio, J.; Greening, P. and Medina, L. (2003). Influence of sample geometry on shear wave propagation using bender elements, Proceedings of Deformation Characteristics of Geomaterials, Lyon, France, 22-24 September, Lyon, France:Balkema, pp. 963-967.

Rios Silva, S.; Ferreira, C.; Viana da Fonseca, A. (2008). Our experience with the use of bender elements in compacted soil-cement samples and natural soils. FEUP report

Rix, G. J., Lai, C. G. and Spang, A.W. (1994). In Situ Measurement of Damping Ratio Using Surface Waves," Journal of Geotechnical and Geoenvironmental Engineering, ASCE, 126, Vol. 5, 472-480, 2000.

Rix, G.J. and Stokoe, K.H. (1992), Correlations of initial tangent modulus and cone resistance. Proc. Int. Symp. Calibration Chamber Testing. Potsdam, New York: 351-362. Elsevier.

Robertson, P.K. (1990) Soil classification using the cone penetration test. Canadian Geotechnical Journal, Vol. 27, pp. 151-158.

Robertson, P.K. (1991) Estimation of foundation settlements in sand from CPT. ASCE Geot. Special Pub. N. 27, Vol. II, pp. 764-778. New York.

Robertson, P.K.; Campanella, R.G. (1983) Interpretation of cone penetration tests. Part I: Sand; Part II: Clay. Canadian Geotechnical Journal, Vol. 20, N. 4, pp. 718-745.

Rodriguez, J.A.D.; Carrizales, P.M.; Flores, L.L (2001). A study of soil microstructure using bender elements. Proceedings of the Fourth International Conference on Recent Advances in Geotechnical Earthquake Engineering and Soil Dynamics, San Diego, California, No. 1.39.

Roesler, S. (1979). Anisotropic shear modulus due to stress anisotropy. Journal of the Geotechnical Engineering Division, ASCE, Vol. 105, No. 7, pp. 871-880.

Rowe, P.W. (1972). The relevance of soil fabric to site investigation practice. 12th Rankine Lecture. Géotechnique, Vol. 22, No. 2, pp. 195-300.

Saada, A. & Puccini , P. (1988) The development of a data base using the case hollow cylinder apparatus. Proceeding of the Int. Workshop on Constitutive Equations for Granular Non-Cohesive Soils. Saada & Bianchini (eds), Balkema, Rotterdam, 33-40.

Saada, A.S.; Towsend, F.C. (1981). State of the art: laboratory strength testing of soils. Laboratory Shear Strength of Soil, ASTM-STP 740, pp. 7-77.

Sadek, T. (2006). The multiaxial behaviour and elastic stiffness of Hostun sand, PhD Thesis, University of Bristol, UK.

Salem, H.S. (2000). Poisson's ratio and the porosity of surface soils and shallow sediments, determined from seismic compressional and shear wave velocities. Géotechnique, Vol. 50, No. 4, pp. 461-463.

Sánchez-Salinero, I.; Roesset, J. M.; Stokoe, K.H., II (1986). Analytical studies of body wave propagation and attenuation, Geotechnical report No GR86-15, Civil Engineering Department, University of Texas at Austin.

Sandroni, S. S. (1985). Sampling and testing of residual soils in Brazil. Sampling and testing of Residual Soils. A Review of International Practice. (Edited by Brand and Phillipson). Technical Committee for Sampling and Testing. of Residual Soils, ISSMFE, pp. 31-50. Scorpion Press, Hong Kong.

Santamarina, J. C. and Fratta, D. (1998), Introduction to Discrete Signals and Inverse Problems in Civil Engineering, ASCE Press, Reston, 327p.

Santamarina, J.C., Klein, K.A., and Fam, M.A (2001). Soils and waves - Particulate materials behavior, characterization and process monitoring. John Wiley & Sons, New York.

Santamarina, J.C.; Fam, M.A. (1997). Discussion on interpretation of bender element tests (paper by Viggiani e Atkinson, 1995). Géotechnique, Vol. 47, No. 4, pp. 873-877.

Santos, J. A.; Camacho-Tauta, J.; Parodi, M.; Viana da Fonseca, A.; Ferreira, C. (2007). Use of random vibrations to measure stiffness of soils. Proceedings of EVACES'07: International Conference on Experimental vibration analysis for civil engineering structures. 24-26 October 2007. Cunha & Caetano (Eds.). FEUP, Portugal. ISBN: 978-972-752-095-4, pp. 1169-1178.

Santos, J.A., (1999). Soil characterization by means of dynamic and cyclic torsional tests. Application to the study of the behaviour of piles under static and dynamic horizontal loads, PhD Thesis, Technical University of Lisbon UNL-IST (in Portuguese).

Sasche, W.; Pao, Y-H (1978). On the determination of phase and group velocities of dispersive waves in solids. Journal of Applied Physics, Vol. 49, No. 8, pp. 4320-4237.

Schmertmann, J.H. (1975). Measurement of in situ shear strength. State of the art report, Session II, Proc. Speciality Conference on In Situ Measurement of Soil Properties, Raleigh, June, Vol. II, pp. 57-138. ASCE, New York.

Schnaid, F.; Fahey, M.; Lehane, B. (2004). In situ test characterisation of unusual geomaterials. Keynote Lecture.. Geotechnical and Geophysical Site Characterization. Ed. A. Viana da Fonseca & P.W.Mayne. Vol. 1, pp. 49-74. Millpress, Rotterdam.

Schneider, J.A., Hoyos, L., Jr., Mayne, P.W., Macari, E.J., and Rix, G.J. (1999), Field and laboratory measurements of dynamic shear modulus of Piedmont residual soils, Behavioral Characteristics of Residual Soils, GSP 92, ASCE, Reston, VA, pp. 12-25.

Scholey, G.K.; Frost, J.D.; Lo Presti, D.C.F.; Jamiolkowski, M. (1995). A review of instrumentation for measuring small strains during triaxial testing of soil specimens. Geotechnical Testing Journal, Vol. 18, No. 2, pp. 137-156.

Schultheiss, P. J., 1983, The influence of packing structures on seismic wave velocity in sediments, Marine Geological Report No. 83/1, University College of North Wales.

Seed, H.B.; Idriss, I.M. (1970). Soil moduli and damping factors for dynamic response analyses. Report No. EERC 70-10. Earthquake Engineering Research Center, University of California.

Seed, H.B.; Lee, K.L. (1966). Liquefaction of saturated sands during cyclic loading. Journal of Soil Mechanics and Foundation Division, ASCE, Vol. 92, No. 6, pp. 105-134.

Shapiro, S. & Yamamuro, J. A. (2003) Effects of Silt on Three-Dimensional Stress-Strain Behaviour of loose Sand. Journal of Geotechnical and Geoenvironmental Engineering 129, No. 1, 1-11.

Shibuya, S. (2000). Assessing structure of aged natural sedimentary clays. Soils and Foundations, Vol. 40, No. 3, pp. 1-16.

Shibuya, S. (2001). Progress Report of TC-29. Pre-failure Deformation Characteristics of Geomaterials. Jamiolkowski, Lancellota & Lo Presti (eds). Balkema, Rotterdam, Vol. 2, pp. 1265-1275.

Shibuya, S.; Hwang, S.C.; Mitachi, T. (1997). Elastic shear modulus of soft clays from shear wave velocity measurement. Géotechnique, Vol. 47, No. 3, pp. 593-601.

Shibuya, S.; Tatsuoka, F.; Abe, F.; Kim, Y.S.; Park, C.S.; Mukabi, J.N. (1991). A new look at stress strain relations of soils and soft rocks. Proceedings fo the 9th Asian Regional Conference on Soil Mechanics and Foundation Engineering, Bangkok, Vol. 1.

Shirley, D. J. and Hampton, L. D. (1978). Shear wave measurements in laboratory sediments, Journal of Acoustic Society of America 63, No. 2, pp. 607-613.

Shirley, D. J., (1978). An improved shear wave transducer, Journal of Acoustic Society of America 63, No. 5, pp. 1643-1645.

Shirley, D.J.; Anderson, A.L. (1975). Acoustical and engineering properties of sediments. Report No. ARL-TR-75-58, University of Texas, Austin.

Shirley, D.J.; Hampton, L.D. (1978). Shear wave measurements in laboratory sediments. Journal of the Acoustical Society of America, Vol. 63, No. 2, pp. 607-613.

Silva Cardoso, A. (1986). Ensaios triaxiais dos solos residuais da cidade do Porto. Geotecnia, n° 47, pp. 103-124. SPG, Lisboa.

Silvestri, V., Yong, R. N. & Mohamed, A. M. O. (1988) A true triaxial testing cell. Advanced Triaxial Testing of Soil and Rock. Donaghe, Chaney & Silver (eds), ASTM STP 977, 819-833.

Simons, N.E.; Menzies, B.K. (2000). A short course in Foundation Engineering. (2nd Edition) Thomas Telford, London.

Skempton, A.W. (1954). The pore-pressure coefficients A and B. Géotechnique, Vol. 4, No. 4, pp. 143-147.

Skempton, A.W.; Sowa, V.A. (1963). The behaviour of saturated clays during sampling and testing. Géotechnique, Vol. 13, pp. 269-290.

Souto, A.; Hartikainen, J. and Ozudogru, K. (1994). Measurement of dynamic parameters of road pavement materials by the bender element and resonant column tests, Géotechnique. Vol.44, N° 3, pp. 519-526.

Stokoe, K. H. and Woods, R. D. (1972) In situ shear wave velocity by cross-hole method, Journal of the Soil Mechanics and Foundations Div., ASCE 98, No. SM5, pp. 443-460.

Stokoe, K. H., Hwang, S. K., Lee, J. N. K. & Andrus, R. D. (1995) Effects of various parameters on the stiffness and damping of soils at small to medium strains. Proceedings of the Int. Symposium on Pre-failure Deformation of Geomaterials. Shibuya, Mitachi & Mura (eds), Hokkaido, Saporo 1, 785-815.

Stokoe, K.H. II; Joh, S.-H. and Woods, R.D., 2004, Some contributions of in situ geophysical measurements to solving geotechnical engineering problems, Proceedings of ISC-2: Geotechnical and Geophysical Site Characterization. Viana da Fonseca and Mayne (eds), Porto, Portugal. 19-22 Sept., Millpress Science Publishers, Rotterdam, Netherlands. Vol.1, pp. 97-132.

Stokoe, K.H., II, Wright, S.G., Bay,J.A. and J.M. Roesset (1994), "Characterization of geotechnical sites by SASW method," Geophysical Characteristics of Sites, ISSMFE, Technical Committee 10 for XIII ICSMFE, International Science Publishers, New York, pp. 15-25.

Stokoe, K.H.; Santamarina, J.C. (2000). Seismic-Wave-Based Testing in Geotechnical Engineering. Proceedings of the GeoEng 2000 Conference. Melbourne, Australia, November 2000, pp. 1490-1536.

Stokoe, K.H.II; Lee, S.H.H.; Knox, D.P. (1985). Shear moduli measurements under the triaxial stresses. Advances in the art of testing soil under cyclic conditions, ASCE, New York, pp. 166-185.

Stoll, R.D., Bryan, G.M., and Bautista, E.O. (1994). "Measuring lateral variability of sediment geoacoustic properties," J Acoustical Soc. Of Am., 96 (1), pp 427-438.

Strobbia, C. (2003) Surface Wave Method. Acquisition, processing and inversion. PhD Thesis, Politecnico di Torino, 317p.

Sukolrat, J. (2007) Destructuration of Bothkennar Clay. PhD Thesis, University of Bristol.

Sully, J.P.; Campanella, R.G. (1995). Evaluation of in situ anisotropy from crosshole and downhole shear wave velocity measurements. Géotechnique, Vol. 45, No. 2, pp. 267-282.

Sully, J.P.; Campanella, R.G. (1996). Discussion: Evaluation of in situ anisotropy from crosshole and downhole shear wave velocity measurements. Géotechnique, Vol. 46, No. 3, pp. 565-569.

Tanaka, H. (2000). Sample quality of cohesive soils: Lessons from three sites, Ariake, Bothkennar and Drammen. Soils and Foundations, Vol. 40, No. 4, pp. 57-74.

Tanaka, H., Ritoh, R., and Omukai, N. (2002). Quality of samples retrieved from great depth and its influence on consolidation properties. Can. Geotech. J., 39, No.6, 1288-1301.

Tanaka, H.; Sharma, P.; Tsuchida, T.; Tanaka, M. (1996). Comparative study on sample quality using several types of samplers. Soils and Foundations, Vol. 36, No. 2, pp. 57-68.

Tanaka, Y.; Kudo, K.; Nishi, K.; Okamoto, T. (1994). Shear modulus and damping ratio of gravelly soils measured by several methods. Pre-failure Deformation of Geomaterials, Shibuya, Mitachi & Miura (eds.). Balkema, Rotterdam, Vol. 1, pp. 47-53.

Tanaka, Y.; Kudo, K.; Nishi, K.; Okamoto, T.; Kataoka, T.; Ueshima, T. (2000). Small strain characteristics of soils in Hualien, Taiwan. Soils and Foundations, Vol. 40, No. 3, pp. 111-125.

Tani, K. (1995). Measurement of shear deformation of geomaterials - Field test. General report. Proceedings of the IS Hokkaido-94, Vol. 2, pp. 1115-1131.

Tatsuoka, F. (1988). Some Recent Developments in Triaxial Testing Systems for Cohesionless Soils. In Proceedings of Advanced Triaxial Testing of Soil and Rock, ASTM STP 977. (Ed: Donaghe et al.), Philadelphia, 7-67.

Tatsuoka, F. and Silver, M.L. (1980), "New method for the calibration of the inertia of resonant column devices", ASTM Geotechnical Testing Journal, Vol. 3 No. 1, pp. 30-34.

Tatsuoka, F.; Jardine, R.J.; Lo Presti, D.; Di Benedetto, H.; Kodaka, T. (1997). Characterising the pre-failure deformation properties of geomaterials (Theme Lecture). Proceedings of the XIV International Conference on Soil Mechanics and Foundation Engineering, Hamburg. Balkema, Rotterdam, Vol. 2, pp. 2129-2164.

Tatsuoka, F.; Kohata, Y. (1995). Stiffness of hard soils and soft rocks in engineering applications. Pre-failure Deformation of Geomaterials. Shibuya, Mitachi & Miura (eds). Balkema, Rotterdam, Vol. 2, pp. 947-1063.

Tatsuoka, F.; Shibuya, S. (1992). Deformation characteristics of soils and rocks from field and laboratory tests. Report of the Institute of Industrial Science, University of Tokyo, Vol. 37, No. 1, pp. 1-136.

Tatsuoka, F.; Shibuya, S.; Teachavorasinskun, S.; Park, C.-S. (1990). Discussion: An experimental and theoretical comparison between static and dynamic torsional soil tests (paper by Bolton, M.D.; Wilson, J.M.R., 1989; Géotechnique 39, No. 4, 585-599). Géotechnique, Vol. 40, No. 4, pp. 659-664.

Taya, Y.; Hatanaka, M.; Uchida, A. (1999). Effect of principal stress ratio and stress history on Vs for undisturbed sand and gravel samples. Proceedings of the 2nd International Conference on Pre-failure Deformation Characteristics of Geomaterials (IS Torino 99), Jamiolkowski, Lancellota & Lo Presti (Eds). Balkema, Rotterdam, Vol. 1, pp. 331-334.

Terzaghi, K. (1939). Soil mechanics - a new chapter in engineering science, James Forrest Lecture, J. Inst. Civ. Eng., 12, pp. 106-142.

Terzaghi, K., Peck, R.B. and Mesri, G. (1996). Soil Mechanics in Engineering Practice. John Wiley & Sons, New York.

Theron, M., Clayton, C. R. I. & Best, A. I. (2003). Interpretation of side-mounted bender element results using phase shift and group velocity. ISLyon'03: International symposium on deformation behaviour of geomaterials (eds H. Di Benedetto, T. Doanh, H.Geoffroy and C. Sauzeat), pp. 127–132. Balkema, Rotterdam.

Thomann, T. G. and R. D. Hryciw (1990). Laboratory measurement of small strain shear modulus under ko conditions. Geotechnical Testing Journal 13(2), 97–105.

Timoshenko, S.P.; Goodier, J.N. (1970). Theory of elasticity. McGraw-Hill International Editions, pp. 485-508.

Tokimatsu, K. (1995). "Geotechnical site characterization using surface waves," First International Conference on Earthquake Geotechnical Engineering, Vol. 3, Kenji Ishihara, editor, Tokyo, pp. 1333-13368.

Toll, D.G. (1993). A computer control system for stress path triaxial testing. In Developments in Civil Construction Engineering Computing. (Ed: Topping, B.V.) Civil-Comp press, Edinburgh. 107-117.

Topa Gomes, A. M. (2009). Elliptical shafts by the method of vertical sequential excavation. The case of Metro do Porto. PhD thesis, University of Porto (in Portuguese)

Tsukamoto, Y., Ishihara, K., Nakazawa, H., Kamada, K. ; Huang, Y. (2002) Resistance of partly saturated sand to liquefaction with reference to longitudinal and shear velocities, Soils & Foundations, 42, 6, 93-114

Vaughan, P.R. 1988. Characterising the mechanical properties of in-situ residual soils. Geomechanics in Tropical Soil. Proc. Sec. Int. Conf., Singapore, Keynote paper, Vol. 2, pp. 469-486. A.A. Balkema, Rotterdam.

Viana da Fonseca, A. (1988). Caracterização geotécnica de um solo residual do granito da região do Porto. Dissertação apresentada na Universidade do Porto para obtenção do grau de Mestre em Engenharia Civil, FEUP, Porto.

Viana da Fonseca, A. (1996). Geomechanics in residual soils from Porto granite. Criteria for the design of shallow foundations. PhD Thesis, University of Porto. (in Portuguese)

Viana da Fonseca, A. (2003). Characterising and deriving engineering properties of a saprolitic soil from granite, in Porto, Characterisation and Engineering Properties of Natural Soils. Swets and Zeitlinger, Lisse, pp. 1341-1378.

Viana da Fonseca, A. and Coutinho, R.Q. (2008). Characterization of residual soils. ISC3. Taiwan.

Viana da Fonseca, A.; Almeida e Sousa, J. (2001) At rest coefficient of earth pressure in saprolitic soils from granite. Proc. XIV ICSMFE, Istanbul, Vol. 1, pp. 397-400.

Viana da Fonseca, A.; Carvalho, J. M.; Ferreira, C.; Santos, J. A.; Almeida, F.; Hermosilha, H. (2005). Combining geophysical and mechanical testing techniques for the investigation and characterization of ISC'2 residual soil profile. Proceedings of the 16th International Conference on Soil Mechanics and Geotechnical Engineering, 12-16 Setembro 2005, Osaka, Japan. Vol. 2, pp. 765-769.

Viana da Fonseca, A.; Carvalho, J.; Ferreira, C.; Santos, J. A.; Almeida, F., Pereira, E., Feliciano, J., Grade, J., and Oliveira, A. (2006). Characterization of a profile of residual soil from granite combining geological, geophysical and mechanical testing techniques, Geotechnical and Geological Engineering, Vol. 24, No. 5, pp. 1307-1348.

Viana da Fonseca, A.; Carvalho, J.M.; Ferreira, C.; Costa, E.; Tuna, C.; Santos, J. A. (2004a) Geotechnical characterization of a residual soil profile: the ISC'2 experimental site, FEUP. Proceedings of the 2nd International Site Characterization Conference (ISC'2), Porto, Portugal - Geotechnical and Geophysical Site Characterization, Viana da Fonseca & Mayne (eds.) ISBN 90-5966-009-9, Vol. 2, pp. 1361-1370. Millpress, Rotterdam.

Viana da Fonseca, A.; Carvalho, J.M.C.; Pessoa, J.M.C. (2002). Ensaios crosshole em perfis de alteração de granito do Porto. Parâmetros elásticos e correlações. Actas do 8° Congresso Nacional de Geotecnia, LNEC, Lisboa, Vol. 1, pp. 73-92.

Viana da Fonseca, A.; Ferreira, C., Carvalho, J.M. (2004b). Tentative evaluation of K0 from shear waves velocities determined in Down-Hole (Vs vh) and Cross-Hole (Vs hv) tests on a residual soil. Proceedings of the 2nd International Site Characterization Conference (ISC'2), Porto, Portugal - Geotechnical and Geophysical Site Characterization, Viana da Fonseca & Mayne (eds.) ISBN 90-5966-009-9, Vol. 2, pp. 1755-1764. Millpress, Rotterdam.

Viana da Fonseca, A.; Ferreira, C.; Fahey, M. (2009). A Framework for Interpretation of Bender Element Tests, Combining Time-Domain and Frequency-Domain Methods. Geotechnical Testing Journal, ASTM. Volume 32, No. 2, pp. 1-17.

Viana da Fonseca, A.; Matos Fernandes, M.; Silva Cardoso, A. E Barreiros Martins, J. (1994). Portuguese experience on geotechnical characterization of residual soils from granite in Proceedings XIII International Conference on Soil Mechanics and Foundation Engineering-New Delhi 1994, (ed. Mohan Primlani), Oxford IBH Publishing CO PVT. Ltd, vol. 1, pp. 377-380.

Viana da Fonseca, A.; Vieira de Sousa, J., Ferreira, C. (2003). Deriving Stiffness Parameters from "Simple" in Situ Tests and Relating them with Reference Values on Saprolitic Soils from Granite. Actas da 12th Panamerican Conference on Soil Mechanics and Geotechnical Engineering – SoilRock America 2003 - MIT, Cambridge, USA. Culligan et al. (Eds). Verlag Gluckauf Gmbh, Essen. Vol. 1, pp. 321-328.

Vieira de Sousa, J. F. (2002). Modelação de ensaios de carga considerando a variação da rigidez dos solos em profundidade. Parametrização recorrente de ensaios complementares in situ e em laboratório. Dissertação apresentada na Universidade do Porto para obtenção do grau de Mestre em Engenharia Civil, FEUP, Porto.

Viggiani, G.; Atkinson, J.H. (1995). Interpretation of bender element tests. Géotechnique, Vol. 45, No. 2, pp. 149-154.

Viggiani, G.; Atkinson, J.H. (1997). Interpretation of bender element tests: Discussion. Géotechnique, Vol. 47, No. 4, pp. 873-877.

Vucetic, M. (1994). Cyclic threshold shear strains in soils. Journal of Geotechnical Engineering Division, ASCE, Vol. 120, No. 12, pp. 2208-2228.

Wang, Q. and Lade, P. V. (2001) Shear banding in true triaxial tests and its effect on failure in sand. Journal of Engineering Mechanics 127, No. 8, 754-761.

Woods, R.D. (1978). Measurement of dynamics soil properties. Conference on Earthquake Enineering and Soil Dynamics, Pasadena, Calif. Geotechnical Engineering Division, American Society of Civil Engineers, New York, Vol. 1., pp. 91–179.

Woods, R.D. (1994). Laboratory measurement of dynamic soil properties. Dynamic Geotechnical Testing II, ASTM-STP 1213, pp. 165-190.

Wroth, C.P. (1975). In situ measurement of initial stresses and deformation characteristics. Proceedings of the Geotechnical Engineering Division Specialty Conference on In Situ Measurement of Soil Properties, ASCE, Vol. 2, pp. 181-230.

Wroth, C.P. (1982). "British experience with self-boring pressuremeter". Proc. Symp. on the Pressuremeter and its Marine Applications, Institut du Pétrole. Technic, Collection Colloques et Seminaires 37, pp. 134-164. Lab. des Ponts et Chaussées, Paris.

Yamashita, S., Fujiwara, T., Kawaguchi, T., Mikami, T., Nakata, Y. and Shibuya, S., 2007, International Parallel Test on the Measurement of G_{max} Using Bender Elements Organized by Technical Committee 29 of the International Society for Soil Mechanics and Geotechnical Engineering (http://www.jiban.or.jp/e/tc29/BE˙Inter˙PP˙Test˙en.pdf, last accessed at 5 December 2007).

Yang, J. (2002). Liquefaction resistance of sand in relation to P-wave velocity. Géotechnique, Vol. 52, No. 4, pp. 295-298.

Yu, P.; Richart, F.E.Jr. (1984). Stress ratio effects on shear modulus of dry sands. Journal of the Geotechnical Engineering Division, ASCE, Vol. 110, No. 3, pp. 331-345.

Zeng, X. and Grolewski, B. (2005). Measurement of G_{max} and estimation of K_0 of saturated clay using bender elements in an oedometer, Geotechnical Testing Journal, ASTM. Vol.28, N ° 3, pp. 264-274.

Zeng, X., Figueroa, J.L., and Fu, L. (2002). Measurement of base and sub-grade layer stiffness using bender element technique. Proceedings of 15th ASCE Engineering Mechanics Conference, June 2-5, New York, NY.

Zeng, X.; Ni, B. (1998). Application of bender elements in measuring Gmax of sand under K0 conditions. Geotechnical Testing Journal, Vol. 21, No. 3, pp. 251-263.

Zhang Z., and Tumay M.T. (1999), Statistical to fuzzy approach toward CPT soil classification. ASCE Journal of Geotech. & Geoenvir. Engineering. Volume 125, No.3, pp. 179-186.